Spray Evaporation on Enhanced-Surface Tube Bundles with Low-GWP Refrigerants

by

Joshua Allan Rothe

A dissertation submitted to the Graduate Faculty of
Auburn University
in partial fulfillment of the
requirements for the Degree of
Doctor of Philosophy

Auburn, Alabama
May 6, 2023

Keywords: low-GWP refrigerants, spray evaporation, enhanced surfaces, tube bundles

Approved by

Dr. Lorenzo Cremaschi, Chair, Professor of Mechanical Engineering
Dr. Sushil Bhavnani, Associate Department Chair and Professor of Mechanical Engineering
Dr. Jeyhoon Khodadadi, Professor of Mechanical Engineering
Dr. Hans-Werner van Wyk, Associate Professor of Mathematics and Statistics
Dr. David Ennis, Associate Professor of Physics

Abstract

With the development of new low-GWP HFO refrigerants and increasingly stringent regulation of existing HVAC&R systems, the heat transfer performance of these refrigerants and the effects of various enhancement techniques are of particular interest. Refrigerant distribution via pressurized liquid spray in a shell-and-tube heat exchanger is one such recently developed enhancement technique that has the potential to decrease refrigerant inventory in industrial systems while matching or exceeding the heat transfer performance of the much more common flooded evaporator. A limited number of studies have been performed on HFO refrigerants and spray evaporation separately, but no published studies have combined these elements with other enhancement factors such as low-finned tube outer surfaces or different tube bundle pitch configurations. A specialized test apparatus was constructed in order to perform such a study, and shell-side heat transfer coefficients of R134a, R1234ze(E), and R1233zd(E) were investigated on bundles of tubes with two different enhanced-surface types and in two different bundle geometries at various refrigerant saturation temperatures.

The results showed a weak dependence of bundle heat transfer coefficients on refrigerant saturation temperature and spray nozzle type, provided that sufficient refrigerant distribution was realized. However, heat transfer performance depended strongly on refrigerant properties, tube heat flux, enhanced-surface type, bundle geometry, and refrigerant inlet subcooling. With a low-finned tube surface designed to enhance condensation heat transfer, performance was comparable to that of nucleate pool boiling; with the surface designed to enhance evaporation heat transfer, an average enhancement of 200% was realized compared to the former. Enhancement due to the triangular-pitch bundle geometry was approximately 26% compared to the square-pitch bundle

due to differences in the bundle effect, and variations in inlet subcooling between 0.5 °C and 2.0 °C resulted in an enhancement of up to 74% at the lower limit. Performance at high heat fluxes was significantly affected by refrigerant dryout at the bottom of the bundle which caused significant decreases in lower row heat transfer coefficients and represents a significant challenge in the design and implementation of a spray evaporator. The performance of R1234ze(E) was comparable to that of R134a, the refrigerant it is meant to replace. The empirical results reported in this work are meant to provide a point of comparison for engineers tasked with designing similar heat transfer equipment.

A semi-empirical model was also developed to correlate the data collected in the experiments. Found in a survey of the literature, the model on which it was based was used to correlate average bundle Nusselt numbers for similar spray evaporation experiments using ammonia. The model was modified in the current work to correlate individual row Nusselt numbers, and a method for calculating local Reynolds numbers throughout the bundle was developed. A factor was added to account for the enhancement effects of different surface types, bundle geometries, and refrigerant inlet subcooling. The model was found to be an adequate fit for the data that most closely represented real operating conditions and is intended to be applicable to the design of similar multi-row shell-and-tube heat exchangers.

Acknowledgments

I would firstly like to thank my advisor Dr. Lorenzo Cremaschi for his guidance, encouragement, and support throughout my time in graduate school and my efforts on this project, without whom this work would not have been possible. I would also like to thank the Auburn University faculty members who served on my doctoral advisory committee, Dr. Sushil Bhavnani, Dr. Jay Khodadadi, Dr. Hans-Werner van Wyk, and Dr. David Ennis. I would also like to extend a special thanks to ASHRAE, the members of Technical Committees 1.3 and 8.5, and especially the industry expert ASHRAE members who served on the Project Management Subcommittee for RP-1800: Dr. Zahid Ayub (Chair), Dr. Joseph Huber, Dr. Brian Fricke, Dr. Kashif Nawaz, and Dr. Achim Gotterbarm.

From among my colleagues in the BEST Lab, past and present, I would like extend my gratitude to Dr. Pratik Deokar, whose assistance in construction of the test setup and LabVIEW programming was invaluable. I would also like to acknowledge and give a very special thanks to Jerin Ebanesar, whose contributions in all aspects of RP-1800, from data collection to troubleshooting, were absolutely essential to the completion of the project. My appreciation also goes out to Christian Fauer, Logan Nichols, and all other unmentioned colleagues whose friendships kept my spirits high and helped me to persevere.

I would like to acknowledge my family and friends outside the lab whose encouragement kept me motivated. Many thanks and love go out to my Dad, whose support has allowed me to maintain focus on my work. Very special thanks and much love go out to my Mom, with whom I have celebrated my successes, who has always inspired me to do my best, and on whose recommendation I began my studies in mechanical engineering some eight years ago. Last but not least, my whole-hearted thanks go out to Daniel for his understanding, patience, and support.

Table of Contents

List of Tables

List of Figures

List of Abbreviations and Nomenclature

A	Nominal outer surface area of a heater tube
$a_{1,2,3,4,5}$	Empirical constants used in Eq. (5.1)
BF	Bundle factor based on differences in tube bundle geometry
$c_{1,2,3}$	Constants used in the Chun-Seban correlation as found in Eq. (2.3)
c_{pl}	Specific heat at constant pressure of a liquid as found in Eq. (2.1)
C_{sf}	Constant representing the liquid-surface combination as found in Eq. (2.1)
CFC	Chlorofluorocarbon
CHF	Critical Heat Flux
D	Heater tube outer diameter
EF	Enhancement factor based on differences in enhanced surface type
EGW	Ethylene Glycol/Water
g	Gravitational constant
GWP	Global Warming Potential
h	Convective heat transfer coefficient
h_{fg}	Enthalpy of vaporization of a refrigerant
h_{in}	Enthalpy of the refrigerant before the spray nozzles
h_{lv}	Enthalpy of vaporization of a fluid as found in Eq. (2.1)
h_{mac}	Macroconvective heat transfer used in the Chen correlation as found in Eq. (2.2)
h_{mic}	Microconvective heat transfer used in the Chen correlation as found in Eq. (2.2)
h_{out}	Enthalpy of the refrigerant after exiting the spray nozzles
$h_{Row\,j}$	Local heat transfer coefficient of a given row of tubes
HCFC	Hydrochlorofluorocarbon

HFC	Hydrofluorocarbon
HFO	Hydrofluoroolefin
j	Number of active tube rows in a given test
k	Number of active tubes in a given row
k_{ref}	Thermal conductivity of the refrigerant
k_{copper}	Thermal conductivity of copper
L_{tube}	Nominal length of a heater tube
m	Number of data points in a single test
$\dot{m}$	Mass flow rate
$\dot{m}_{Row\,j}$	Local refrigerant liquid mass flow rate at a given row of tubes
$\dot{m}_{total}$	Total refrigerant mass flow rate entering the test section
n	Number of embedded thermocouples in a given heater tube
Nu	Nusselt number
Nu_{bundle}	Average Nusselt Number for the entire tube bundle
$Nu_{Row\,j}$	Local Nusselt number for a given row of tubes
ODP	Ozone Depletion Potential
P/D	Tube bundle pitch-to-diameter (ratio)
$p_{1,2,3,4}$	Constants used in the Parken correlation as found in Eq. (2.4)
P_{box}	Refrigerant pressure in the test section
P_{inlet}	Refrigerant pressure at the test section inlet
P_{sat}	Refrigerant saturation pressure
Pr	Prandtl number of liquid refrigerant
Pr_l	Liquid Prandtl number as found in Eq. (2.1)

q''	Tube wall heat flux
Q_{htr}	Average electrical power supplied to one tube cartridge heater
Q_r	Total heat rate provided by a single cartridge heater
r_1	Heater tube inner radius
r_2	Heater tube outer radius
Re	Liquid film Reynolds number
$Re_{Row\ j}$	Local Reynolds number at a given tube row
SC	Subcooling factor based on the refrigerant subcooling at the test section inlet
T_{EES}	Refrigerant inlet temperature calculated in EES according to Eq. (3.4)
T_{inlet}	Refrigerant temperature measured at the spray nozzle inlet
T_{out}	Refrigerant temperature at spray nozzle outlet calculated according to Eq. (3.4)
T_{ref}	Refrigerant reference temperature
T_{sat}	Refrigerant saturation temperature
$T_{sat}(P_l)$	Saturation temperature of a liquid at a given pressure as found in Eq. (2.1)
$T_{Thermocouple}$	Tube wall temperature recorded using tube embedded thermocouples
T_w	Temperature of a heated surface as found in Eq. (2.1)
T_{wall}	Tube surface temperature calculated according to Eq. (3.5)
y	Nozzle factor
$z_{1,2,3,4,5}$	Constants used in the Zeng correlation as found in Eq. (2.5)

Greek Symbols

Γ_l	Refrigerant flow rate per unit length of the heater tubes
$\Gamma_{Row\ j}$	Local liquid refrigerant flow rate per unit length of the heater tubes in a given row
Δ	Finite change in some quantity

μ Dynamic viscosity

μ_l Dynamic viscosity of a liquid as found in Eq. (2.1)

ν Kinematic viscosity

π Pi, mathematical constant

ρ_l Density of the liquid phase of a substance as found in Eq. (2.1)

ρ_v Density of the vapor phase of a substance as found in Eq. (2.1)

σ Surface tension of a liquid as found in Eq. (2.1)

Chapter 1: Introduction

The phasing out of CFC and HCFC refrigerants and increasing regulation on existing HFC refrigerants has created a need to develop and implement more environmentally-friendly refrigeration alternatives and practices. In 1974, Molina and Rowland first identified the link between stratospheric ozone depletion and gaseous chemical substances containing chlorine in their makeup, which included a majority of the refrigerants in use in both residential and industrial applications at the time. It was reported that these substances, upon being released either due to leaks in refrigeration systems or for disposal, can make their way to the upper stratosphere, where they can remain for periods of time on the order of 40-150 years. Though chemically inert, it was discovered that these compounds dissociate upon the absorption of a sufficient amount of ultraviolet radiation energy, after which the free chlorine atoms react with O_3 (ozone) molecules to form O_2 (oxygen) and ClO (chlorine oxide). These chlorine oxide molecules then dissociate upon encountering another free oxygen atom to form O_2 and thus leaving the chlorine atom free again. It is estimated that a single free chlorine atom can destroy over 100,000 ozone molecules before it is removed from the stratosphere. Importantly, oxygen molecules are not nearly as effective as ozone molecules at absorbing ultraviolet radiation from the sun before it reaches Earth's surface, and the formation of ozone molecules happens much more slowly than the dissociation of these molecules, especially when the dissociation process is accelerated by free chlorine atoms. The Montreal Protocol, which was finalized in 1987 and took full effect in 1996, effectively banned the production and use of these chlorofluorocarbon and hydrochlorofluorocarbon refrigerants, also known as CFCs and HFCs, respectively.

As a result, a new generation of hydrofluorocarbon refrigerants was developed as an alternative, some as drop-in replacements for existing compounds and some that required significant research and development efforts in the creation of specialized equipment. The hydrofluorocarbon refrigerants, or HFCs, currently in use have an Ozone Depletion Potential (ODP) rating of zero, meaning they do not deplete the ozone layer as did the previous refrigerants that contained chlorine in their chemical makeup. However, it has been discovered that these HFCs do contribute significantly to the atmosphere's greenhouse effect. The Global Warming Potential (GWP) of these HFC refrigerants is often hundreds or thousands of times more severe than that of carbon dioxide, the most abundant greenhouse gas emitted by human activities. While naturally-occurring fluids such as propane and even carbon dioxide are being explored as alternatives, new hydrofluoroolefin (HFO) compounds are also being developed both as potential drop-in replacements in existing equipment and as primary working fluids in the next generation of refrigeration systems. Like HFCs, HFOs are also made up of hydrogen, fluorine, and carbon, but their chemical structure is such that they have a much less severe greenhouse effect than HFCs and some even less than that of carbon dioxide. Because many of these HFOs are in the experimental stage of development, their thermodynamic performance has not been well studied or characterized in literature.

Increasing regulation and ever-present economic concerns simultaneously encourage the development of refrigeration systems that are more efficient, both in terms of energy consumption and materials usage. The working fluids themselves represent a significant cost associated with these systems and as such, it is desired to minimize refrigerant inventory wherever possible, especially in large industrial applications. The shell-and-tube heat exchanger, a configuration that is commonly found in such applications because of its relative simplicity and ease of maintenance, represents a major obstacle in achieving this goal. The typical flooded tube evaporator requires a substantial refrigerant charge on the shell side in order to keep the tubes fully submerged so that high heat transfer coefficients associated with pool boiling can be maintained. The spray evaporator was invented as an alternative to the flooded tube evaporator to improve upon this disadvantage while also maintaining heat transfer performance. A spray evaporator is a shell-and-tube heat exchanger that utilizes nozzles to distribute a pressurized stream of refrigerant over a tube bundle in order to remove heat from the secondary fluid flowing through the tubes via evaporation. The primary advantage of the spray evaporator configuration is a significantly reduced system refrigerant charge leading to a lower cost associated with refrigerant usage and a reduced environmental risk in the event of refrigerant discharge. Spray evaporators are often not much more complex in terms of design and materials usage than their flooded evaporator counterparts and provide similar or even improved performance compared to the flooded tube configuration. Comparatively, however, this configuration is both much more complex in terms of the fluid dynamics of the refrigerant and not as well studied or characterized. Even refrigerant distribution is essential for proper function in order to avoid dryout, a phenomenon that ruins heat transfer performance and can even lead to tube burnout, depending on the application. Because of these factors, spray evaporators have been of particular and increasing interest to industrial and academic researchers looking to better understand, model, and utilize this configuration.

Enhancement of heat transfer is also of particular interest in improving the efficiency of refrigeration systems and reducing power consumption. The benefits of extended surfaces for this purpose have long been realized and studied, and the use of extended surfaces in heat transfer equipment is almost ubiquitous. Consequently, the development of new, specialized, and sometimes proprietary finned surfaces is ongoing, as is the need to characterize the performance of these enhancements.

The American Society of Heating, Refrigerating, and Air-Conditioning Engineers, commonly known as ASHRAE, is a professional organization whose mission is to promote and advance sustainable technologies for the built environment for the benefit of human well-being. ASHRAE was formed in the year 1959 via the merger of two similar pre-existing professional organizations, The American Society of Heating and Air-Conditioning Engineers (ASHAE) and The American Society of Refrigerating Engineers (ASRE). Today, ASHRAE is a society of more than 50,000 members from industry and academia that focuses on all types of building energy and conditioning systems, refrigeration, efficiency and sustainability. To that end, the society organizes conferences, industry expositions, professional development sessions, and educational seminars. Perhaps most importantly, ASHRAE also funds and publishes research and writes regulatory standards based on its own and other industry research for the design and operation of HVAC&R equipment. ASHRAE's research is overseen by a series of technical committees composed of leading experts in the field of HVAC&R which are also responsible for writing and updating the standards contained in the ASHRAE Handbook.

The work presented in this dissertation was part of a larger ASHRAE-sponsored project entitled *RP-1800: Spray Evaporation on Enhanced Tube Bundles with Low GWP Pure Refrigerants and Refrigerant/Miscible Oil Mixtures*. The project was conceived by its principal investigator, Dr. Lorenzo Cremaschi, who is also a member of ASHRAE, and was based on similar ASHRAE-sponsored research that had been conducted in the past. It was jointly sponsored by ASHRAE Technical Committees 1.3, Heat Transfer and Fluid Flow, and 8.5, Liquid-to-Refrigerant Heat Exchangers, and was overseen by a project management subcommittee composed of members of both technical committees. The main objectives of the project were to measure convective heat transfer coefficients due to liquid refrigerant spray over bundles of enhanced surface tubes in a shell-and-tube evaporator test section, to visually record and report on evaporation phenomena, and to evaluate the applicability and accuracy of pre-existing heat transfer coefficient correlations from technical literature. The objectives of the research in this dissertation were the same save for the added objective of formulating new heat transfer coefficient correlations to characterize specifically the heat transfer performance of the refrigerants, enhanced surfaces, and tube bundle geometries used for this project. The funding provided by ASHRAE on behalf of the technical committees made possible the modification of the test facility in the Building Energy Systems and Technologies (BEST) Lab at Auburn University, including construction of a specialized test section and instrumentation necessary for data collection. This work contained in this report encompasses the first part of the project title, that is, spray evaporation on enhanced-surface tube bundles with pure low-GWP refrigerants. The work on spray evaporation using the same tube bundles with mixtures of the low-GWP refrigerants and miscible oils will be contained in a future dissertation.

Chapter 2: Literature Review

A survey of the technical literature related to the work performed in this dissertation is presented in this chapter. The literature review will focus heavily on other work performed with spray evaporation, enhanced heat transfer surfaces, tube bundles, low-GWP refrigerants, and combinations of these topics. Studies on plain surfaces, falling film evaporators, other refrigerant types, and nucleate boiling will also be examined. The review will be divided into two main sections: an experimental section containing information on other test setups and reported data, and a modeling section containing analytical and empirical correlations developed in previous studies.

2.1 Experimental Work

Modern shell-and-tube heat exchangers have existed since the earliest days of refrigeration and air-conditioning technology, but were first used in the oil industry in the early 1900s as oil heaters and coolers, condensers, and reboilers (Taborek, 2014). Even before the days of oil refining, primitive shell-and-tube heat exchangers existed as the heat exchangers used to produce steam for the earliest steam engines and locomotives. As the design was adapted for use in refrigeration, usually in larger industrial applications, the flooded evaporator arrangement became almost ubiquitous due to the recognition of extremely high heat transfer coefficients on the shell side afforded by nucleate boiling of the refrigerant and the relative availability and limited regulation of early refrigerants. It was realized in early work that the mechanism by which nucleate boiling occurs on the surface of a horizontal tube is much different than that which occurs on a flat surface, meaning that new studies and correlations were needed specifically for the horizontal tube geometry. More recently, the falling film evaporator and spray evaporator have seen increased focus due to the desire to decrease refrigerant inventory in HVAC&R systems. Much work has been done on investigation of shell-side boiling and evaporation heat transfer coefficients using water and various refrigerants from early CFCs to more recent HFOs.

Boiling on Plain Tubes

A kettle reboiler is a type of shell-and-tube heat exchanger in which the cold fluid enters at the bottom of the shell at some velocity induced by a pressure gradient and passes upwards over a bundle of heated tubes, thus undergoing a change of phase from liquid to gas. As such, most kettle reboilers operate in the flow boiling regime on the shell side in which heat transfer can be attributed to a combination of forced convection and nucleate boiling and is dominated by one or the other depending on flow conditions. This arrangement is very similar to the shell-and-tube flooded evaporator, in which the liquid to be boiled may enter from above or below the tube bundle and may or may not have some flow velocity imparted upon it by an induced pressure gradient. Though the kettle reboiler and flooded evaporator were not the configurations used for this work, it will be useful to compare typical shell-side heat transfer coefficients and flow patterns from those configurations to those obtained during these experiments. A very comprehensive review of literature available at the time concerning boiling heat transfer coefficients on the shell side of horizontal tube bundles can be found in (Jensen, 1988). At that time and even today, detailed knowledge about nucleate boiling heat transfer was limited due to the difficulty in characterizing such complicated phenomena that are involved. Most early literature reported only average bundle heat transfer coefficients, but there was some limited study into local variations in heat transfer coefficients within a tube bundle. A study by Palen and Taborek (1962) found that, in a kettle reboiler, the overall heat transfer coefficient for a bundle of plain tubes was higher than that observed for a comparable single tube, but the critical heat flux (CHF) and therefore the onset of film boiling occurred at a much lower wall superheat. Heat transfer coefficients between approximately 2 kW/m^2-K and 22 kW/m^2-K were reported for the tube bundle in the nucleate boiling regime, and wall heat flux increased exponentially with superheat according to a traditional nucleate boiling curve. In a more detailed study by Leong and Cornwell (1979), local heat transfer coefficients and flow patterns in a kettle reboiler using R113 as the boiling fluid were investigated. Tube heat transfer coefficients between approximately 1.4 kW/m^2-K and 8.5 kW/m^2-K at a heat flux of 20 kW/m^2 were reported, with lower values recorded towards the bottom and outer sides of the bundle and increasing values recorded near the bundle centerline and at the upper rows. These patterns were replicated in a study by Hwang and Yao (1986) in which it was found that flow boiling heat transfer coefficients were higher for a bundle of tubes than for a single tube in a pool of R113. It was stated that this phenomenon was due to increased flow velocity for tubes higher in the bundle caused by thicker quality boundary layers on lower tubes and the increased quality of refrigerant passing over tubes that were higher in the bundle. This effect would eventually come to be called the "bundle effect" or "bundle factor" and would be variously defined and studied for different heat exchanger geometries in later studies. The same trend was confirmed again in a study by Marto and Anderson (1992) in which the highest heat transfer coefficients in a small bundle of tubes were measured in the top row with decreasing values for each subsequent lower row. The differences were much larger in the forced convection regime and, though smaller, were still significant after the onset of nucleate boiling. It was theorized in this study that, in addition to the enhancement effects mentioned previously, the formation and departure of vapor bubbles from lower tubes in a bundle and subsequent interaction of these bubbles with the surfaces of upper tubes increases the enhancement of heat transfer on the upper tubes. Similar results were reported in a much more recent study by Swain, et al. (2017) using distilled water on plain tubes in which heat transfer coefficients were highest for the topmost row of tubes and decreased with row depth in the bundle. For a bundle with a pitch-to-diameter ratio of 1.9, bundle heat transfer coefficients between approximately 2.0 kW/m^2-K and 5.0 kW/m^2-K were reported for heat fluxes between 19 kW/m^2 and 28 kW/m^2. Bundle pitch-to-diameter ratio was also varied in this study, with P/D ratios of 1.25, 1.6, and 1.95 used. The lowest bundle heat transfer coefficients were reported for the bundle with a P/D ratio of 1.95; bundle heat transfer coefficients were approximately 10% higher for a P/D ratio of 1.25 and 15% higher for a P/D ratio of 1.6. In a pool-boiling study using water by Nelson and Burnside (1985), bundle heat transfer coefficients between approximately 3 kW/m^2-K and 6 kW/m^2-K were reported for heat fluxes between 15 kW/m^2 and 40 kW/m^2. A very extensive compilation of heat transfer coefficient data on plain surface tube bundles is available in (Cornwell & Houston, 1994), in which it was observed from the literature that nucleate boiling heat transfer coefficients in water were generally higher than those observed in the common refrigerants in use at the time, namely R113, R11, and R12. These differences were smaller at lower heat fluxes and became much more exaggerated at heat fluxes over 100 kW/m^2, which were generally only achievable with water. In a more detailed experiment by Cornwell and Einarrson (1990), it was shown that individual tube boiling heat transfer coefficients were influenced significantly by the upward velocity imposed on the fluid surrounding the tube. In a test performed at a heat flux of 25 kW/m^2, the peak heat transfer coefficient was observed to increase from approximately 2.6 kW/m^2-K at a fluid velocity of 0.00 m/s to nearly 3.2 kW/m^2-K at a velocity of 0.37 m/s. Similar results were found in single-tube experiments using R113 by Yilmaz and Westwater (1980) in which, for a heat flux of 30 kW/m^2, an increase in flow velocity from 0.0 m/s to 6.8 m/s caused an increase in heat transfer coefficient from 1.5 kW/m^2-K to 4 kW/m^2-K. It was noted in this study that the enhancement effect of higher fluid velocity decreased with increasing heat flux until it became negligible near the critical heat flux. In a study comparing the nucleate boiling performance of refrigerants on a plain tube, Chiou, et al. (1997) reported the following heat transfer coefficients for heat fluxes between approximately 1 kW/m^2 and 50 kW/m^2 at a saturation temperature of 4.4 °C: for R124, values were between 0.3 kW/m^2-K and 40 kW/m^2-K; for R22 and R134a, values were between 0.7 kW/m^2-K and 60 kW/m^2-K. It was noted that heat transfer coefficients for R124 were significantly lower than those for R22 and R134a at a given saturation temperature due to the lower saturation pressure of R124, thus highlighting the influence of refrigerant saturation pressure on boiling heat transfer coefficients. In a study by Chongrungreong and Sauer (1980) using a single plain 15.8 mm diameter copper tube in a still bath of R11, nucleate boiling heat transfer coefficients between 0.6 kW/m^2-K and 3.2 kW/m^2-K were reported for heat fluxes between 6 kW/m^2 and 63 kW/m^2. Of particular note in thus study was that the experimental data were predicted very well by the widely-used nucleate boiling heat transfer correlation proposed by Stephan and Abdelsalam (1980). In a very thorough study by Jung, et al. (2003), nucleate boiling heat transfer coefficients were measured on the outside of a plain 19.0 mm diameter copper tube at a liquid pool temperature of 7 °C for refrigerants R123, R11, R142b, R134a, R12, R22, R125, and R32. For all refrigerants, heat transfer coefficients increased with increasing heat fluxes between 10 kW/m^2 and 80 kW/m^2 with the lowest values recorded for R123 and the highest recorded for R32. Of particular interest in these data were the values for R123, which were between 0.7 kW/m^2-K and 3.5 kW/m^2-K, because of its similar properties to the R1233zd(E) used in this work. Also of interest were the results for R134a, which were between 2.2 kW/m^2-K and 9.5 kW/m^2-K, because of its use in this work and the similarity of its properties to R1234ze(E). In a study of nucleate boiling heat transfer coefficients on plain tube bundles, Krasowski and Cieśliński (2011) studied the effects of bundle pitch-to-diameter ratio and operating pressure in addition to heat flux. For water at atmospheric pressure between 15 kW/m^2 and 50 kW/m^2, bundle heat transfer coefficients were between 1.9 kW/m2-K and 3.0 kW/m2-K for a P/D ratio of 1.7. These were notably higher than those calculated for R141b at the same conditions, which were between 1.3 kW/m^2-K and 2.0 kW/m^2-K. Some enhancement was seen for R141b in a bundle with a P/D ratio of 2.0, for which heat transfer coefficients were between 1.5 kW/m^2-K and 2.3 kW/m^2-K over the same heat flux range. Row heat transfer coefficients were measured as in some previous studies, and it was found that among the 5 rows in the bundle, the highest heat transfer coefficients were recorded in the topmost row with values decreasing for each subsequent lower row in accordance with the bundle effect. It was also noted that the experimental data for the bundle with a P/D ratio of 2.0 compared favorably with experimental data collected by Chang and Chiou (1999) for spray evaporation with R141b, which will be discussed in a later section. Nagata, et al. (2016) were some of the first to study nucleate boiling heat transfer coefficients on plain single tubes using the new low-GWP refrigerants R1234ze(Z), R1234ze(E), and R1233zd(E), the latter two of which were used in this work. At a saturation temperature of 10 °C, heat transfer coefficients between 0.5 kW/m^2-K and 3.7 kW/m2-K were reported for R1234ze(E) for heat fluxes between 1.5 kW/m^2 and 20 kW/m^2, while those reported for R1233zd(E) were between 0.2 kW/m^2-K and 1.5 kW/m^2-K over the same range. The lower values for R1233zd(E) were attributed to differences in thermophysical properties, specifically its higher critical pressure and thus lower reduced pressure at a given saturation temperature. It was also noted that the heat transfer coefficient values were R1234ze(E) were approximately 20% to 25% lower than those recorded for R134a in the same study at the same operating conditions. Their results for R134a were very similar to those recorded by

Dewangan, et al. (2020), also at 10 °C, in which values between 2.5 kW/m^2-K and 4.5 kW/m^2-K were reported for heat fluxes between 10 kW/m^2 and 20 kW/m^2. These experiments were extended all the way to a heat flux of 70 kW/m^2, but the value of approximately 7.5 kW/m^2-K at a heat flux of 40 kW/m^2 will be a much more useful comparison. As a summary and for ease of reference, some of the heat transfer coefficient data have been compiled and are listed in Table 2.1. The sources in the table are listed in the order in which they were referenced in this section.

Boiling on Enhanced Tubes

Since the early development of the subject of thermodynamics and the study of convective heat transfer, surface enhancements have been recognized as a very effective method, from both cost and materials perspectives, for increasing the efficiency of heat exchange equipment (Bergles, 1988). Surfaces with enhancements such as fins, grooves, pores, non-wetting coatings, and other such treatments have shown marked improvements in performance over plain surfaces. In fact, it has been shown in some cases that the enhancement of heat transfer on an enhanced surface, such as on an integral fin tube, is greater than the increase in tube surface area over a plain tube due to the addition of the fins (Stephan, 1995). An extensive review of boiling heat transfer coefficient data on both plain tubes and enhanced surface tubes can be found in both (Browne & Bansal, 1999) and (Thome, 1996). Because both reviews were published around 25 years ago, they mostly contain data pertaining to earlier CFC and HCFC refrigerants and whatever commercially-available enhanced surfaces existed at the time. As early as the mid-1950s, Katz, et al. (1955) published a report in which they recorded a nucleate boiling heat transfer enhancement factor of 1.8 for an integral-fin tube over a similar plain tube at a heat flux of 80 kW/m^2 in R12.

Table 2.1: Summary of plain-surface pool boiling heat transfer coefficient data from the literature

Source	Evaporating Fluid	Tube Material	Tube Diameter [mm]	Saturation Condition	Configuration	Heat Flux [kW/m^2]	Heat Transfer Coefficients [kW/m^2-K]
Leong and Cornwell (1979)	R113	Stainless Steel	19.1	T_{sat} = 47.6 °C	Square Bundle	20	1.4 - 8.5
Swain, et al. (2017)	Distilled Water	Stainless Steel	20.0	T_{sat} = 100 °C	Triangular Bundle	19 - 28	2.0 - 5.0
Nelson and Burnside (1985)	Water	Aluminum Alloy	19.0	T_{sat} = 100°C	Square Bundle	15 - 40	3.0 - 6.0
Cornwell and Einarrson (1990)	R113	Stainless Steel	27.1	T_{sat} = 47.6 °C	Single Tube	25	2.6 - 3.2
Yilmaz and Westwater (1980)	R113	Copper	6.4	T_{sat} = 47.6 °C	Single Tube	30	1.5 - 4.0
Chiou, et al. (1997)	R124	Copper	17.8	T_{sat} = 4.4 °C	Single Tube	1 - 50	0.3 - 40
	R22, R134a						0.7 - 60
Chongrungreong and Sauer (1980)	R11	Copper	15.9, 22.2, 28.6	T_{sat} = 23.8°C	Single Tube	6 - 63	0.6 - 3.2
Jung, et al. (2003)	R123	Copper	19.0	T_{sat} = 7 °C	Single Tube	10 - 80	0.7 - 3.5
	R134a						2.2 - 9.5
Krasowski and Cieśliński (2011)	Water	Stainless Steel	10.0	T_{sat} = 100 °C	Triangular Bundle	15 - 50	1.9 - 3.0
	R141b			T_{sat} = 32.1 °C			1.3 - 2.3
Nagata, et al. (2016)	R1234ze(E)	Copper	19.1	T_{sat} = 10 °C	Single Tube	1.5 - 20	0.5 - 3.7
	R1233zd(E)						0.2 - 1.5
Dewangan, et al. (2020)	R134a	Copper	25.4	T_{sat} = 10 °C	Single Tube	10 - 40	2.5 - 7.5

Since then, numerous studies have focused on characterizing the performances of different enhanced surface types and trying to determine which characteristics have the greatest effects on heat transfer coefficients. Memory, et al. (1995a) published a study in which eight different enhanced surfaces, including five finned surfaces (GEWA-K, GEWA-T, and GEWA-YX), two structured surfaces (Thermoexcel-HE and Turbo-B), and one porous surface (High Flux), were tested for single tubes (i.e. not in a bundle) in a pool of R114. Given that heat transfer coefficients for a plain tube varied from 0.5 kW/m^2-K at 5.0 kW/m^2 to 7.4 kW/m^2-K at 80 kW/m^2, the following enhancement factors were recorded over the same range of heat flux for the corresponding surface types: 4.0 to 1.8 for GEWA-K (19 fpi); 3.1 to 1.7 for GEWA-K (26 fpi); 5.4 to 2.0 for GEWA-T (19 fpi); 5.2 to 2.4 for GEWA-T (26 fpi); 4.8 to 2.6 for GEWA-YX (26 fpi); >20 to 2.8 for Thermoexcel-HE; >20 to 3.3 for Turbo-B; and 18.0 to 3.6 for the High Flux surface. It was noted that all heat transfer enhancement factors were greatest at low heat flux and decreased with increasing heat flux, some to nearly unity approaching 100 kW/m^2. Among the best performing surfaces in the nucleate boiling regime were the structured surfaces Thermoexcel-HE and Turbo-B, and the porous surface High Flux. In a follow-up study by Memory, et al. (1995b) on bundles of enhanced-surface tubes, the following bundle heat transfer coefficients were recorded for heat fluxes ranging from 5 kW/m^2 to 80 kW/m^2 for the corresponding enhanced surfaces: 1.28 kW/m^2-K to 4.67 kW/m^2-K for smooth tubes; 3.38 kW/m^2-K to 11.11 kW/m^2-K for GEWA-K (19 fpi); 6.49 kW/m^2-K to 15.10 kW/m^2-K for Thermoexcel-HE; and 6.33 kW/m^2-K to 19.75 kW/m^2-K for High Flux. Again, the highest performing surfaces were the structured and porous surfaces, though the finned surface also showed a significant improvement in heat transfer performance over the plain tube bundle. In a reversal of the trend observed in the single tube tests, bundle heat transfer coefficients actually increased with increasing. As such, it was noted that the use of single tube data to form heat transfer coefficient correlations for bundles would be conservative for the finned and structured tubes, but may overestimate performance for the porous-surface tube bundles. Jung, et al. (2004) conducted a study in which the same Turbo-B surface was used, in addition to a Thermoexcel-E and a low-fin surface, in refrigerants R22, R134a, R125, and R32. For all surfaces including the plain surface, the heat transfer coefficients reported for R32 were the highest while those for R134a were among the lowest. For heat fluxes between 10 kW/m^2 and 80 kW/m^2 in a pool of R134a, the following nucleate boiling heat transfer coefficients were recorded for each corresponding surface: between 2.2 kW/m^2-K and 9.5 kW/m^2-K for the plain surface; between 3.5 kW/m^2-K and 12.0 kW/m^2-K for the low-fin surface; between 10.1 kW/m^2-K and 23.0 kW/m^2-K for Turbo-B; and between 19.4 kW/m^2-K and 24.3 kW/m^2-K for Thermoexcel-E. As in the previously-mentioned study, the heat transfer performances of the structured surfaces were superior to the others, but the finned surface still produced significant heat transfer enhancement factors between 1.2 and 1.6 over the plain surface. Higher heat transfer enhancement factors have been reported by other investigators such as Thome (1989), who recorded heat transfer enhancement factors between 4 and 10 for an improved GEWA-TX finned surface compared to a plain-surface tube under the same conditions. In another similar investigation by Webb and Pais (1992), nucleate boiling heat transfer coefficients for five different refrigerants (R11, R12, R22, R123, and R134a) were recorded for a single plain tube and for four different types of enhanced surface. Among the most relevant results of that study were the heat transfer coefficients reported for R123 and R134a at a saturation temperature of 4.4 °C. For R134a, the following values were reported for each surface for heat fluxes ranging from 8 kW/m^2 to 65 kW/m^2: 2.5 kW/m^2-K to 8.5 kW/m^2-K for a plain tube; 10.0 kW/m^2-K to 21.0 kW/m^2-K for Turbo-B; 5.0 kW/m^2-K to 12.0 kW/m^2-K for GEWA-K (26fpi); 7.0 kW/m^2-K to 17.0 kW/m^2-K for GEWA-SE; and 4.0 kW/m^2-

K to 10.0 kW/m^2-K for GEWA-TX (19fpi). For R123 for the same operating conditions, the following values were reported: 0.8 kW/m^2-K to 3.5 kW/m^2-K for a plain tube; 5.0 kW/m^2-K to 10.1 kW/m^2-K for Turbo-B, 1.7 kW/m^2-K to 7.0 kW/m^2-K for GEWA-K (26fpi); 1.7 kW/m^2-K to 8.0 kW/m^2-K for GEWA-SE; and 1.5 kW/m^2-K to 7.5 kW/m^2-K for GEWA-TX (19fpi). All enhanced surfaces showed significantly increased heat transfer coefficients over the plain surface with the structured Turbo-B surface generally outperforming the finned surfaces. Also of note in these results were the increased heat transfer coefficients reported for R134a compared to those for R123 under the same conditions because of the previously discussed differences in thermophysical properties. More recently, there has been increased interest in the nucleate pool boiling performance of low-GWP refrigerants on enhanced-surface tubes in both single tube and bundle configurations. An excellent review of published literature on this work can be found in (Lin & Kedzierski, 2019). Among the most thoroughly studied low-GWP refrigerants up to this point have been the so-called natural refrigerants, such as propane (R290) and iso-butane (R600a), but some work has been done using the new HFOs. Van Rooyen and Thome (2013) conducted a pool boiling study using R134a and R1234ze(E) in order to compare their performances on Turbo-B5 and GEWA-B5 enhanced surfaces. For the Turbo-B5 tube, boiling heat transfer coefficients remained largely steady for heat fluxes between 20 kW/m^2 and 70 kW/m^2 and did not show any dependence on refrigerant saturation temperature. Reported values were approximately 28 kW/m^2-K for both R134a and R1234ze(E). For the GEWA-B5 tube, heat transfer coefficients were observed to decrease with increasing heat flux from around 35 kW/m^2-K to 24 kW/m^2-K for R134a and from around 40 kW/m^2-K to 25 kW/m^2-K for R1234ze(E). Thus, heat transfer performance for both refrigerants was comparable on the Turbo-B5 surface for all heat fluxes and was slightly improved for R1234ze(E) compared to R134a, especially at low heat fluxes. Those values were somewhat higher than those recorded by Kumar and Wang (2022) who, for heat fluxes ranging from 10 kW/m^2 to 90 kW/m^2, reported values on the order of 11.0 kW/m^2-K to 19.0 kW/m^2-K for R1234ze(E) and between 12.0 kW/m^2-K and 23.0 kW/m^2-K for R134a at a saturation temperature of 10 °C on a GEWA-B5H tube. For the comparable smooth tube, values were between 2.5 kW/m^2-K and 7.5 kW/m^2-K for R134a and between 2.0 kW/m^2-K and 5.5 kW/m^2-K for R1234ze(E) under the same conditions. Thus, the GEWA-B5H enhanced surface still increased heat transfer performance markedly, but the performance of R134a was greater than that of R1234ze(E) in this case. This was also the case in a study performed by Byun, et al. (2017) on two different structured-type enhanced surfaces in pools of R134a, R1234ze(E), and R1233zd(E). On a plain tube, nucleate boiling heat transfer coefficients for heat fluxes from 15 kW/m^2 to 50 kW/m^2 were reported for the corresponding refrigerants at a saturation temperature of 4.4 °C: 2.8 kW/m^2-K to 6.2 kW/m^2-K for R134a; 2.7 kW/m^2-K to 5.3 kW/m^2-K for R1234ze(E); and 1.1 kW/m^2-K to 2.8 kW/m^2-K for R1233zd(E). For the surface Enhanced-1 under the same conditions, the following values were reported: 8.0 kW/m^2-K to 14.0 kW/m^2-K for R134a; 7.5 kW/m^2-K to 12.0 kW/m^2-K for R1234ze(E); and 1.3 kW/m^2-K to 5.8 kW/m^2-K for R1233zd(E). Similar increases in performance were observed for the Enhanced-2 surface as well. Most interestingly, it was calculated that heat transfer coefficients were 11.5% and 66.5% lower on the Enhanced-1 surface for R1234ze(E) and R1233zd(E), respectively, and were 15.2% and 41.2% lower on the Enhanced-2 surface for R1234ze(E) and R1233zd(E), respectively. Where they were listed specifically, some of the heat transfer coefficient data from this section have been tabulated and are shown in Tables 2.2 and 2.3 in the order in which they were referenced.

Table 2.2: Summary of enhanced-surface pool boiling heat transfer coefficient data from the literature

Source	Evaporating Fluid	Tube Material	Tube Diameter [mm]	Saturation Condition	Configuration	Surface Name/Features	Heat Flux [kW/m^2]	Heat Transfer Coefficients [kW/m^2-K]	Enhancement Factor [-]
Memory, et al. (1995a)	R114	Copper	15.9	T_{sat} = 2.2 °C	Single Tube	GEWA-K (19 fpi)	5 - 80	0.6 - 8.0	4.0 - 1.8
						GEWA-K (26 fpi)		0.4 - 8.0	3.1 - 1.7
						GEWA-T (19 fpi)		1.0 - 8.0	5.4 - 2.0
						GEWA-T (26 fpi)		0.6 - 10.2	5.2 - 2.4
						GEWA-YX (26 fpi)		0.7 - 10.5	4.8 - 2.6
						Thermoexcel-HE		10.2 - 10.5	>20 - 2.8
						Turbo-B		10.7 - 10.8	>20 - 3.3
						High Flux		9.0 - 10.9	18.0 - 3.6
Memory, et al. (1995b)	R114	Copper	15.9	T_{sat} = 2.2 °C	Triangular Bundle	Plain Tubes	5 - 80	1.3 - 4.7	-
						GEWA-K (19 fpi)		3.4 - 11.1	4.0 - 1.8*
						Thermoexcel-HE		6.5 - 15.1	>20 - 2.8*
						High Flux		6.3 - 19.8	18.0 - 3.6*
Jung, et al. (2004)	R134a	Copper	18.6 - 18.8	T_{sat} = 7 °C	Single Tube	Plain Surface	10 - 80	2.2 - 9.5	-
						Low-fin Surface		3.5 - 12.0	-
						Turbo-B		10.1 - 23.0	>20 - 3.3*
						Thermoexcel-E		19.4 - 24.3	-
Thome (1989)	Hydrocarbon Mixture	Copper	18.7	-	Single Tube	GEWA-TX	2 - 200	-	4 - 10
Webb and Pais (1992)	R134a	Copper	17.5 - 19.1	T_{sat} = 4.4 °C	Single Tube	Plain Surface	8 - 65	2.5 - 8.5	-
						Turbo-B		10.0 - 21.0	>20 - 3.3*
						GEWA-K (26 fpi)		5.0 - 12.0	3.1 - 1.7*
						GEWA-SE		7.0 - 17.0	-
						GEWA-TX (19 fpi)		4.0 - 10.0	5.4 - 2.0*
	R123			T_{sat} = 4.4 °C		Plain Surface		0.8 - 3.5	-
						Turbo-B		5.0 - 10.1	>20 - 3.3*
						GEWA-K (26 fpi)		1.7 - 7.0	3.1 - 1.7*
						GEWA-SE		1.7 - 8.0	-
						GEWA-TX (19 fpi)		1.5 - 7.5	5.4 - 2.0*

*As reported in Memory, et al. (1995a)

Table 2.3: Summary of enhanced-surface pool boiling heat transfer coefficient data from the literature, continued

Source	Evaporating Fluid	Tube Material	Tube Diameter [mm]	Saturation Condition	Configuration	Surface Name/Features	Heat Flux [kW/m^2]	Heat Transfer Coefficients [kW/m^2-K]	Enhancement Factor [-]
van Rooyen and Thome (2013)	R134a	Copper	18.9 - 19.1	T_{sat} = 5 °C - 25 °C	Single Tube	Turbo-B5	20 - 70	28	>20 - 3.3*
						GEWA-B5		35 - 24	-
	R1234ze(E)					Turbo-B5		28	>20 - 3.3*
						GEWA-B5		40 - 25	-
Kumar and Wang (2022)	R134a	Copper	25.5	T_{sat} = 10 °C	Single Tube	Plain Surface	10 - 90	2.5 - 7.5	-
						GEWA-B5H		11.0 - 19.0	-
	R1234ze(E)					Plain Surface		2.0 - 5.5	-
						GEWA-B5H		12.0 - 23.0	-
Byun, et al. (2017)	R134a	Copper	19.0 - 19.1	T_{sat} = 4.4 °C	Single Tube	Plain Surface	15 - 50	2.8 - 6.2	-
						Enhanced-1		8.0 - 14.0	-
						Enhanced-2		13.0 - 25.0	-
	R1234ze(E)					Plain Surface		2.7 - 5.3	-
						Enhanced-1		7.5 - 12.0	-
						Enhanced-2		10.5 - 20.0	-
	R1233zd(E)					Plain Surface		1.1 - 2.8	-
						Enhanced-1		1.3 - 5.8	-
						Enhanced-2		8.0 - 15.0	-

*As reported in Memory, et al. (1995a)

Falling Film Evaporation on Plain Tubes

A falling film evaporator is a shell-and-tube type heat exchanger in which the liquid to be evaporated is allowed to fall over and wet the tube walls in thin liquid layers. Falling film evaporators have applications in mixture separation processes, in which the tubes are usually oriented vertically and the evaporating liquid passes either on the insides or the outsides of the tubes. Since the phasing-out of CFC refrigerants, falling film evaporators have also been of some interest to the HVAC&R sector as a means of reducing refrigerant inventory in the evaporator heat exchanger compared to a flooded evaporator.In refrigeration applications, the tubes are usually oriented horizontally and the evaporating liquid is distributed from above the tube bundle and dropped over the outsides of the tubes. Since the 1990s, research and experimentation on shell-side heat transfer coefficients has become more popular as researchers investigate whether the falling film evaporator could be used as a viable alternative to the nearly ubiquitous flooded evaporator in larger industrial applications. An extensive review of such literature can be found in (Ribatski & Jacobi, 2005) and also in (Abed, Alghoul, Yazdi, Al-Shamani, & Sopian, 2015). Both reviews highlight the reluctance of the HVAC&R industry to adopt this configuration into widespread use and point to some of the challenges associated with its design and implementation. In conducting a review of the literature for this project, it was desired by the investigators to learn about these challenges and about how various factors have affected the performance of falling film evaporators to allow for optimization of the test section despite using a different mode of refrigerant delivery. Actually, one of the most important design factors in configuring a falling film evaporator is the refrigerant delivery itself. Mitrovic (1986) described three different falling-film flow patterns, which are illustrated in Figure 2.1.

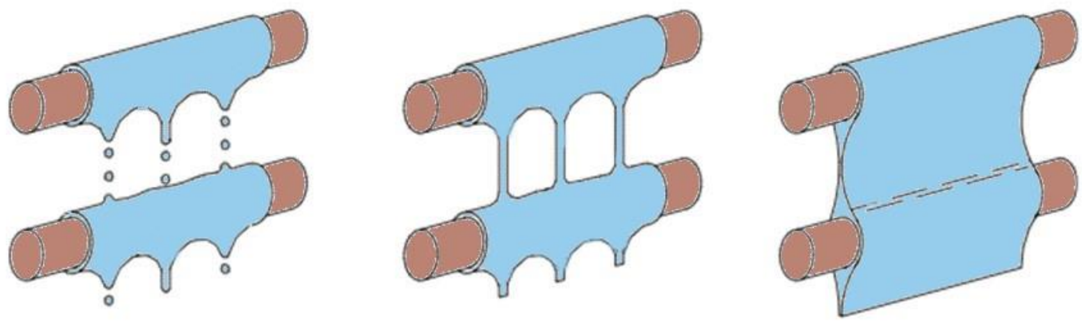

Figure 2.1: Inter-tube falling film modes in an evaporator – adapted from Mitrovic (1986)

The mode depicted on the left was termed the droplet mode, in which discrete droplets of liquid refrigerant drip on the outer tube surface. The mode depicted in the middle was termed the jet mode, in which liquid falls onto a tube's outer surface in continuous columns. The mode depicted on the right was termed the sheet mode, in which entire continuous sheets of liquid fall onto the outer tube surface along the majority of the tube's length. Of the three, the sheet mode is the one that occurs at the highest film Reynolds number and thus requires not only the highest refrigerant flow rate but also a carefully designed refrigerant distributor. For this reason, very few experiments have been conducted in the sheet mode regime, while most have utilized the droplet and jet modes. In an early study by Fletcher, et al (1974) on a single plain-surface 25.4 mm diameter copper-nickel tube using water as the evaporating fluid, heat transfer coefficients between 7.1 kW/m^2-K and 8.0 kW/m^2-K were measured for heat fluxes between 36 kW/m^2 and 60 kW/m^2 at a saturation temperature 49 °C. At a much higher saturation temperature of 126 °C, heat transfer coefficients were around 11.5 kW/m^2-K over the same range. At the lower saturation temperature, heat transfer coefficients decreased with increasing heat flux because the tube was in the nucleate boiling regime as observed through a test section window, whereas heat transfer coefficients were largely independent of heat flux at the higher saturation temperature because the test section was operating in the nonboiling regime. In a later publication, Parken, et al. (1990) also studied the effect of feed water temperature and flow rate on tube heat transfer coefficients over smooth tubes of both 25.4 mm and 50.8 mm diameter. In the nonboiling regime for heat fluxes between 47 kW/m^2 and 79 kW/m^2 and at a constant flow rate, tube heat transfer coefficients were largely independent of heat flux within ±10% and showed a steady increase from approximately 5.0 kW/m^2-K to 6.0 kW/m^2-K with increasing feed water temperature from 40 °C to 120 °C for both diameters. Results were much different in the boiling regime, however, where heat transfer coefficients for the larger 50.8 mm diameter tube climbed steadily starting at 40 °C, peaked at 100 °C (the saturation temperature for these tests) and then steeply declined. Heat transfer coefficients for the smaller tube, while lower than those of the larger tube, remained mostly constant for all temperatures. It was thought that this was caused by the greater circumference, and thus greater distance of travel for the liquid film, around the larger tube which also provided more surface area for bubble nucleation. Values peaked around 11.0 kW/m^2-K for the larger tube and around 7.5 kW/m^2-K for the smaller tube. In both the boiling and nonboiling regimes, heat transfer coefficients were observed to increase with increasing feed water flow rate. Given the results, it was thought that smaller diameter tubes (closer to 25.4 mm) would produce more consistent performance over a broad range of operating conditions at the expense of lower peak heat transfer coefficient values. Zhao, et al. (2016) later performed similar experiments on single smooth tubes using R134a. It was found that, for a saturation temperature of 6 °C and low heat fluxes around 20 kW/m^2, heat transfer coefficients were lowest for a small 16.0 mm diameter tube, higher for a 19.05 mm diameter tube, and highest for a 25.35 mm diameter tube over a large range of refrigerant flow rates. At moderate heat fluxes around 40 kW/m^2, values were nearly equal for the two larger diameter tubes and lower for the smallest tube. At higher heat fluxes around 60 kW/m^2 however, the highest values were recorded for the 19.05 mm diameter tube for most film Reynolds numbers. Refrigerant saturation temperature was also varied from 6 °C to 10 °C and 16 °C. At low and moderate heat fluxes, the highest heat transfer coefficients were recorded for the highest saturation temperature of 16 °C, while at higher heat fluxes, the dependence on refrigerant saturation temperature largely disappeared. It was theorized that, at higher heat fluxes, increases in saturation temperature had the effect of decreasing refrigerant viscosity, thus making it easier for refrigerant to drip around the tube but decreasing film thickness such that the film is more easily disrupted by nucleate bubbles. Evaporation heat transfer, then, is a balancing act between these effects at high heat fluxes. In all cases, heat transfer coefficients increased with increasing refrigerant flow rate. On the 19.05 mm tube at 80 kW/m^2, values increased from around 5.0 kW/m^2-K to around 10.0 kW/m^2-K with an increase in film Reynolds number from 700 to 2400. Similar results were obtained in another study by Jin, et al. (2019) using R134a. Heat transfer coefficients were observed to increase rapidly with increasing film Reynolds numbers from 200 to 800, after which they plateaued up the highest flow rate corresponding to a film Reynolds number of 2200. Heat transfer coefficients also increased with increasing heat flux from 2.8 kW/m^2-K at 10 kW/m^2 to as high as 7.5 kW/m^2-K at 60 kW/m^2. The investigators used their data to propose two heat transfer coefficient correlations, one for use in the wetted regime and the other for use in partial dryout conditions, which were functions of the Reynolds, Prandtl, and Boiling numbers. Jige, et al. (2019) also conducted a study on a single plain-surface tube using R1234ze(E). Heat transfer coefficients showed little dependence on refrigerant flow rate for film Reynolds numbers between 100 and 1000, but did increase with increasing heat flux from 2.5 kW/m^2 to 20 kW/m^2. Values obtained in this study were relatively low, peaking at around 6.0 kW/m^2-K for a saturation temperature of 15 °C and a heat flux of 40 kW/m^2. Fujita and Tsutsui (1998) extended the work on falling films to tube bundles by measuring heat transfer coefficients on a 5x3 bundle of plain tubes in the droplet and jet modes with R11 as the evaporating fluid. Interestingly, it was found that the heat transfer coefficient for the topmost tube in the bundle was lower than that of the tube directly below it despite the direct supply of refrigerant to the top tube. It was surmised that this was because of the uneven distribution of refrigerant to the topmost tube due to the design of the refrigerant liquid feeder followed by a more even refrigerant distribution to the second and all subsequent tubes caused by virtue of having passed over tubes higher in the bundle, thus evening the distribution. Bundle heat transfer coefficients were largely independent of tube heat flux below the incipience of boiling, for which the second through fifth rows had almost identical local heat transfer coefficients, and that of the first row was approximately 10% to 20% lower. Most notable, however, was the breakdown of refrigerant flow at the lower tube rows as heat flux increased or refrigerant flow rate decreased. The evaporation of a majority of the refrigerant by the upper tube rows caused significant unwetted areas on the lower tubes which caused an increase in wall temperatures and thus a decrease in bundle heat transfer coefficients. Thus, it was concluded that maintaining an adequate supply of refrigerant and thus a well-developed liquid film over all rows was essential to the operation of the falling film evaporator. Similar conclusions were also made in studies by Liu (1975) and Owens (1978) in which heat transfer coefficients were observed to be independent of heat flux in nonboiling conditions. A more thorough investigation of the local dryout condition was later performed by Ribatski and Thome (2007) using R134a films on a bundle of plain-surface tubes. They found that, in a tube bundle with a pitch of 22.25 mm, heat transfer coefficients were largely independent of the film flow rate in the regime in which all tube rows were sufficiently wetted. By maintaining a constant heat flux and decreasing refrigerant flow rate, the onset of dryout could be observed by a sudden increase in tube wall temperatures and thus a decrease in heat transfer coefficients. Interestingly, it was also found that the highest local heat transfer coefficients belonged to the uppermost tubes in the bundle, likely because of the more careful design of the liquid distributor. By varying tube heat flux, refrigerant saturation temperature, and film Reynolds number systematically, they were able to form one correlation to predict the onset of the dryout condition in the bundle and another two-part correlation, composed of wet and dry components, to predict bundle heat transfer coefficients. Yan, et al. (2019) performed a visual study of falling film flow patterns over three plain-surface copper tubes arranged in the same vertical plane. Two different liquid feeder arrangements were used to investigate the effects of liquid distribution from the feeder on liquid film thickness and flow development lower in the bundle. Images captured during testing showed that, for a given refrigerant flow rate, a feeder with more widely spaced liquid outlets (i.e. one with outlets spaced along the entire length of the heated tube instead of more closely spaced outlets towards the center of the tube) produced much thicker liquid films over the tubes and much more even distribution of liquid refrigerant over tubes in lower rows. Liquid films for the more closely spaced outlets were observed to become much thinner on the lower half of the tube surfaces, whereas the more evenly spaced outlets produced a much more consistent film thickness over the entire tube circumference. Additionally, the closely spaced outlets created liquid flow that coalesced on the surface of the upper tube and dripped to subsequent rows in only one or two distinct columns, whereas the flow for the widely spaced outlets tended to remain separated and dripped more evenly along the axial length of subsequent tubes. These phenomena were observed for all refrigerant flow rates and heat fluxes tested, though significant differences in heat transfer coefficients for the two lower tubes were not observed except in high heat flux, high flow rate conditions. In all tests, the heat transfer coefficient for the uppermost tube was the highest, followed by that of the second tube and subsequently that of the third tube. At a heat flux of 20 kW/m^2 and a refrigerant flow rate of 150 mLPM, heat transfer coefficients reached a maximum of approximately 4.0 kW/m^2-K at the top tube, followed by 2.2 kW/m^2-K and 1.8 kW/m^2-K for the second and third tubes, respectively. Thus it was concluded that, in addition to an adequate supply of refrigerant, an adequate distribution of refrigerant must be ensured to maximize performance. Some of the heat transfer coefficient data from this section have been compiled for ease of reference and are listed in Table 2.4.

Falling Film Evaporation on Enhanced Tubes

Owing to the fairly recent interest in the falling film evaporator and the pre-existence of enhancement techniques for heat transfer surfaces, a larger percentage of the research work conducted on the characterization of falling film heat transfer has included the use of enhanced-surface tubes than has the work on nucleate pool boiling. Bock, et al. (2019) conducted a study on the enhancement of falling film heat transfer over what is perhaps the simplest enhanced surface: one that has only been roughened with sandpaper. Copper, mild steel, and stainless steel tubes were tested first with polished surfaces and then with sanded surfaces with mean roughness ranging from 0.11 μm to 1.37 μm. For the copper tube in a control pool boiling test using R134a at a saturation temperature of 5 °C and with heat fluxes ranging from 20 kW/m^2 to 90 kW/m^2, heat transfer coefficients increased from 4.0 kW/m^2-K to 12.0 kW/m^2-K for a tube with a roughness of 0.12 μm but ranged from 5.5 kW/m^2-K to 14.0 kW/m^2-K for a surface roughness of 1.37 μm. Heat transfer coefficients for a 25 °C saturation temperature test were approximately 50% higher over the whole range. The falling film heat transfer coefficients for a film Reynolds number of approximately 2100 were even higher, ranging from 7.0 kW/m^2-K to 17.0 kW/m^2-K for a saturation temperature of 5 °C and from 10 kW/m^2-K to 23 kW/m^2-K for a saturation temperature

Table 2.4: Summary of plain-surface falling film heat transfer coefficient data from the literature

Source	Evaporating Fluid	Tube Material	Tube Diameter [mm]	Saturation Condition	Configuration	Heat Flux [kW/m^2]	Heat Transfer Coefficients [kW/m^2-K]
Fletcher, et al. (1974)	Water	Copper-Nickel	25.4, 50.8	T_{sat} = 49 °C	Single Tube	36 - 60	7.1 - 8.0
				T_{sat} = 126 °C			11.5 - 11.1
Parken, et al. (1990)	Water	Brass	25.4, 50.8	T_{sat} = 100 °C	Single Tube	47 - 79	7.5 - 11.0
Zhao, et al. (2016)	R134a	Copper	19.0	T_{sat} = 6 °C - 16 °C	Single Tube	20 - 80	5.0 - 10.0
Jin, et al. (2019)	R134a	Copper	19.1	T_{sat} = 6 °C	Single Tube	10 - 60	2.8 - 7.5
Jige, et al. (2019)	R1234ze(E)	Copper	19.0	T_{sat} = 15 °C	Single Tube	2.5 - 20	1.5 - 6.0

of 25 °C. Falling film enhancement factors (i.e. enhancement over pool boiling) were between 1.2 and 1.3 for the tube with the highest surface roughness over the whole range of heat fluxes for both saturation temperatures. It was also found that, among the three tube materials, the highest heat transfer coefficients were recorded on the outside of the copper tubes because of copper's much higher thermal effusivity. Given this finding and the popularity of copper tubes in real applications where material compatibility allows, it was decided to use copper tubes in the present study. Zheng, et al. (2017) performed a study with copper tubes that had surfaces modified with hydrophilic and superhydrophilic spray coatings. They found that, in the droplet, jet, and sheet flow regimes, both spray coatings significantly enhanced heat transfer coefficients by increasing the wettability of the tube outer surface and thus improving liquid flow distribution over the whole surface. These effects were especially noticeable at low film Reynolds numbers for which liquid distribution over the plain tube surface was especially poor. Ubara, et al. (2020) noticed similar results in another investigation into spray coatings on copper using R134a. They reported a heat transfer enhancement factor of up to 5.2 for the spray-coated surface over the smooth surface and also recorded higher heat transfer coefficients for the spray-coated surface in the falling film regime compared to the pool boiling regime, whereas falling film heat transfer coefficients were actually lower for the smooth surface than in pool boiling. In a follow-up study by Ubara, et al. (2021), R1233zd(E) was used as the evaporating fluid over the same smooth and spray-coated surfaces. It was found that, for both pool boiling and falling film evaporation, heat transfer coefficients for R1233zd(E) were lower than those for R134a due to the former's higher surface tension and lower vapor density. Despite that, heat transfer enhancement factors in R1233zd(E) of 2.1 to 4.8 were observed for the spray-coated surface compared to the smooth surface in falling film evaporation. Heat transfer coefficients in the falling film regime for the enhanced surface were between approximately 5.0 kW/m^2-K and 10.5 kW/m^2-K for heat fluxes between 10 kW/m^2 and 65 kW/m^2. In an early study of commercially-available enhanced-surface tubes, Chyu and Bergles (1989) studied the enhancement effects of the GEWA-T, Thermoexcel-E, and High Flux surfaces. Even for the plain tubes used as a control, heat transfer coefficients were much higher for falling film evaporation than for pool boiling at heat fluxes below approximately 50 kW/m^2. Values between 9.1 kW/m^2-K and 10.0 kW/m^2-K were recorded for heat fluxes ranging from 10 kW/m^2 to 100 kW/m^2. Such comparisons for all three enhanced surfaces over the same heat flux range were similar with each one having higher heat transfer coefficients in the falling film regime. For GEWA-T, values were between 20.0 kW/m^2-K and 33.3 kW/m^2-K and were between 150% (at higher heat flux) and 500% (at low heat flux) greater than those for pool boiling. For Thermoexcel-E, values ranged from 12.5 kW/m^2-K to 43.5 kW/m^2-K; these were approximately 100% higher than the pool boiling values at low heat flux but became nearly equal at high heat flux. For High Flux, values ranged from 6.6 kW/m^2-K to 15.0 kW/m^2-K but were only 40% higher at low heat fluxes and largely the same above 30 kW/m^2. Thus, enhancement factors from 2 to 4 were observed for the better-performing GEWA-T and Thermoexcel-E surfaces. Similar enhancement factors were observed by Li, et al. (2011) for the Turbo-CAB (19 fpi) and Turbo-CAB (26 fpi) surfaces using a falling water film with film Reynolds numbers ranging from 10 to 110. In a comparison of pool boiling to falling film evaporation on a smooth and finned tube in R245fa, Chien, et al. (2019) found significant enhancement for the finned tube over the smooth tube in both the falling film and pool boiling regimes. For the smooth tube over a heat flux range of 5 kW/m^2 to 50 kW/m^2 at a saturation temperature of 5 °C, pool boiling heat transfer coefficients were 0.8 kW/m^2-K to 3.0 kW/m^2-K and falling film heat transfer coefficients were between 1.7 kW/m^2-K and 2.5 kW/m^2-K. For the finned tube, pool boiling values were between 1.5 kW/m^2-K and 5.3 kW/m^2-K and falling film values were between 5.0 kW/m^2-K and 12.5 kW/m^2-K. Interestingly, heat transfer coefficients for the smooth tube were nearly the same in the pool boiling and falling film regimes, whereas for the finned tube, enhancement factors were around 2 for pool boiling and between 3 and 5 for the falling film. In a different approach, Yang and Wang (2011) performed a numerical simulation investigation into factors that affect the performance of a falling film evaporator using computational fluid dynamics. Their findings were largely the same as those that have been observed in experimentation, namely: fluid distribution at the top of the bundle is one of the most important factors in designing a falling film or similar type evaporator as maldistribution can seriously decrease heat transfer performance; enhanced surfaces such as the Turbo-B or other similar fin structures can promote significant enhancement to heat transfer; refrigerant flow rate affects performance insofar as insufficient flow can cause dry patches to develop on tube surfaces; and tube bundle geometry (i.e. tube pitch, layout, etc.) can either improve or impair refrigerant distribution in a bundle, especially in lower tube rows, thus also affecting heat transfer performance. For reference, some of the heat transfer coefficient data specifically mentioned in this section have been compiled and are shown in Table 2.5.

Table 2.5: Summary of enhanced-surface falling film heat transfer coefficient data from the literature

Source	Evaporating Fluid	Tube Material	Tube Diameter [mm]	Saturation Condition	Configuration	Surface Name/Features	Heat Flux [kW/m^2]	Heat Transfer Coefficients [kW/m^2-K]
Bock, et al. (2019)	R134a	Copper	19.1	$T_{sat} = 5$ °C	Single Tube	Roughened, $R_a = 0.12$ μm	20 - 90	4.0 - 12.0
						Roughened, $R_a = 1.37$ μm		5.5 - 14.0
				$T_{sat} = 25$ °C		Roughened, $R_a = 0.12$ μm		6.7 - 14.0
						Roughened, $R_a = 1.37$ μm		10.0 - 23.0
Ubara, et al (2020)	R134a	Copper	19.1	$T_{sat} = 20$ °C	Single Tube	Spray Coated	15 - 85	18.0 - 27.0
Ubara, et al (2021)	R1233zd(E)	Copper	19.1	$T_{sat} = 20$ °C	Single Tube	Spray Coated	10 - 65	5.0 - 10.5
Chyu and Bergles (1989)	Water	Copper	25.4	$T_{sat} = 100$ °C	Single Tube	Plain Surface	10 - 100	9.1 - 10.0
						GEWA-T		20.0 - 33.3
						Thermoexcel-E		12.5 - 43.5
						High Flux		6.6 - 15.0
Chien, et al. (2019)	R245fa	Copper	19.0	$T_{sat} = 5$ °C	Single Tube	Plain Surface	5 - 50	1.7 - 2.5
						Finned		5.0 - 12.5

Spray Evaporation

Spray evaporation is a further development of falling film evaporation technology for a shell-and-tube heat exchanger designed for the purpose of decreasing refrigerant inventory in a system. However, spray evaporation is distinct in that the liquid to be evaporated on the shell side is distributed over the tubes via a nozzle or nozzles which create a fine mist or atomized spray and through which the liquid experiences a finite pressure drop. The result is that the liquid impinges on the tube surfaces at a higher velocity than it would if it were simply allowed to fall and in the form of small droplets instead of large droplets, liquid columns, or sheets. These distinctions from falling film evaporation were often not made clear in early literature but should be noted as spray nozzle type and configuration can have significant effects on refrigerant distribution and thus heat transfer coefficients in a tube bundle. One of the earliest studies on spray evaporation was conducted by Moeykens and Pate (1994) as part of an ASHRAE-sponsored research project not unlike this one. In it, R134a was sprayed over plain-surface tubes of 12.7 mm and 19.1 mm diameter at a saturation temperature of 2.0 °C using two different spray nozzle configurations. For the 19.1 mm single tube, heat transfer coefficients between approximately 3.0 kW/m^2-K and 4.2 kW/m^2-K were reported for heat fluxes between 20 kW/m^2 and 40 kW/m^2. These data have been reproduced and are shown in Figure 2.2 as a point of reference for the present work. For the 12.7 mm single tube, heat transfer coefficients between 3.0 kW/m^2-K and 4.5 kW/m^2-K were recorded and increased steadily for heat fluxes between 10 kW/m^2 and 25 kW/m^2 for mass flow rates above 2.7 kg/min. However, for a lower flow rate of 2.3 kg/min, a distinct peak in the heat transfer coefficient around 4.0 kW/m^2-K was noticed at approximately 21 kW/m^2, after which the value began to decrease.

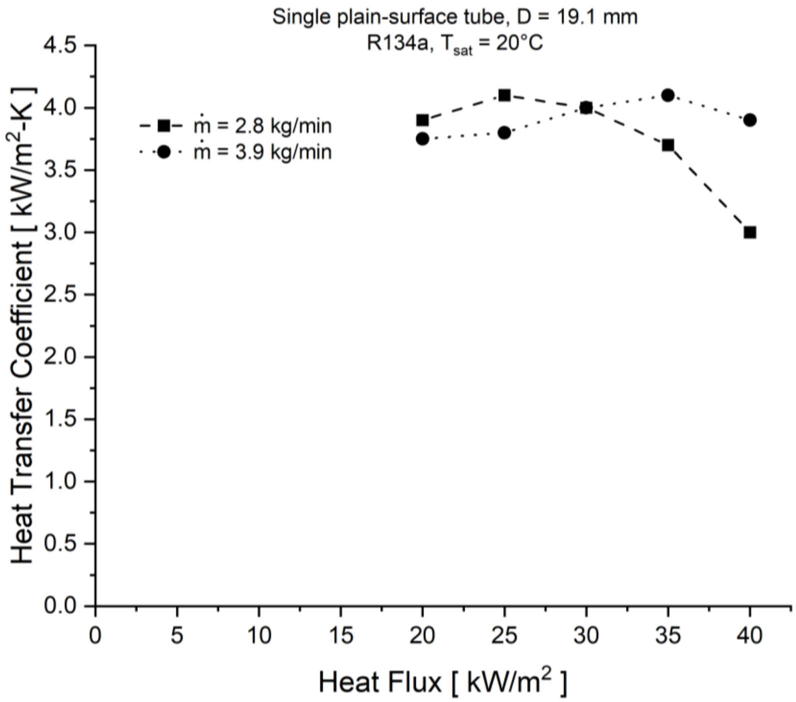

Figure 2.2: Single tube spray evaporation heat transfer coefficients - reproduced from Moeykens and Pate (1994)

A similar effect was noticed with the larger diameter tube, where a peak in heat transfer coefficient was recorded at 25 kW/m^2 at a flow rate of 2.8 kg/min and at a higher heat flux of 32 kW/m^2 for a higher flow rate of 3.0 kg/min. In both cases, the peak heat transfer coefficient value was around 4.0 kW/m^2-K. This effect was exacerbated in a test in which two 12.7 mm diameter tubes were used at once with the second positioned directly below the first. The second tube experienced a peak in values at a heat flux as low as 14 kW/m^2 for a flow rate of 2.3 kg/min and as high as 17 kW/m^2 for a flow rate of 3.0 kg/min, both of which were much lower heat fluxes than those of the first tube's peak values. Heat transfer coefficients for the second tube were 10% lower than those of the first tube at the peak, and this difference grew larger with an increase in heat flux. Pool boiling tests were also conducted for reference, and it was found that spray evaporation heat transfer coefficients were 5% to 10% higher than those for nucleate boiling at low heat fluxes but became nearly equal near their peaks. The peaks in heat transfer coefficients were demonstrative of the dryout condition, near which refrigerant flow rate has a significant effect on heat transfer performance. It was also reported that, of the two nozzle types used, the set of high-pressure-drop nozzles yielded slightly improved heat transfer coefficients over the low-pressure-drop nozzles mostly because of refrigerant impingement velocity. It was noted, however, that this effect would be negligible in a bundle of tubes as the lower tube rows would not benefit from increased impingement velocity. A follow-up study was later performed by Moeykens and Pate (1995) to study specifically the effects of nozzle height and type on spray evaporation over an enhanced-surface tube bundle. Eight different nozzle configurations were tested, including nozzles with three different orifice sizes of 4.0 mm, 4.8 mm, and 5.6 mm; two different spray pattern shapes, circular and square; and two different nozzle heights above the top of the tube bundle, 41.3 mm and 66.7 mm. It was found that, among the nozzle configurations tested, several produced heat transfer coefficients higher than those recorded in the pool boiling study using the same tube and bundle configuration. Heat transfer performance was affected significantly by nozzle orifice size as the 5.6 mm orifice nozzles produced heat transfer coefficients that were between 15% and 50% greater than the 4.8 mm nozzles, which in turn were 10% to 20% greater than those for the 4.0 mm nozzles. In contrast, heat transfer performance was only weakly dependent on the actual spray pattern, with square and circular pattern values within ±5% and groupings for the two different heights also within ±5% of each other. Follow-up tests using a liquid collector in place of the tube bundle revealed that the nozzles with larger orifices delivered more refrigerant to the bundle, thus increasing bundle heat transfer coefficients. Some of the data from that study have been reproduced as a reference for this work and are shown in Figure 2.3. It should be noted that the circular cone nozzles utilized extensively throughout the present work had an orifice diameter of 3.58 mm.

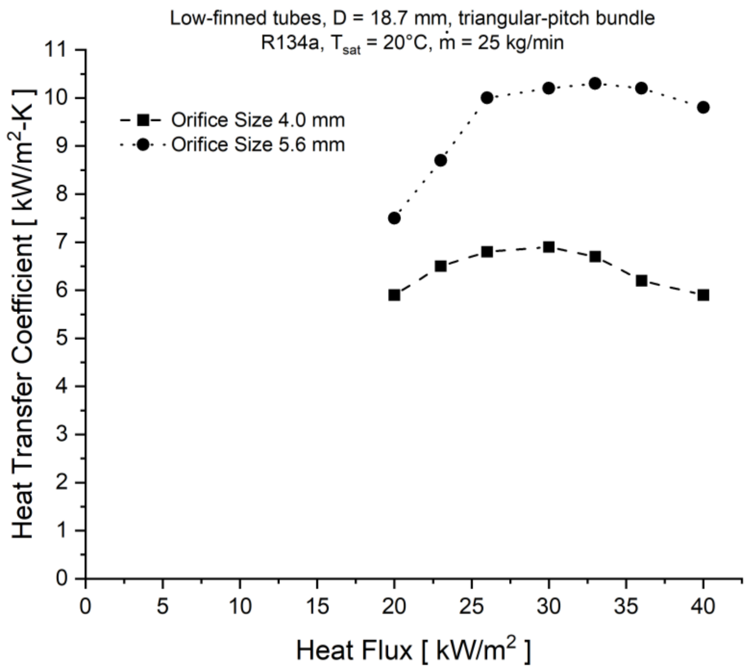

Figure 2.3: Effects of nozzle orifice size on bundle heat transfer coefficients - reproduced from Moeykens and Pate (1995)

Still another study was performed by Moeykens, et al. (1995) to more thoroughly investigate the effects of enhanced surface type, refrigerant flow rate, and tube bundle geometry on heat transfer performance in a spray evaporator. Five different tube surfaces, including four enhanced surfaces (Tu-Cii, Tu-B, W-SC and W-40 fpi), were tested in square and triangular bundle geometries with refrigerant overfeed ratios ranging from 1.4 to 7.9. It was reported that, for all surfaces and bundle geometries, shell side heat transfer coefficients showed moderate dependence on refrigerant mass flow rates that varied between 15 kg/min and 45 kg/min. These differences became more noticeable at high heat fluxes and were in excess of ±20% for the Tu-Cii surface. Also, this dependence was greater for the triangular bundle geometry over the square geometry over the whole range of flow rates tested and up to two times greater at high heat fluxes approaching 40 kW/m^2. Heat transfer coefficients also showed a significant dependence on heat flux, with most bundles experiencing an increase in values at low heat fluxes followed by a peak and decrease at higher heat fluxes. Again, this behavior was emblematic of the dryout condition in the boiling regime and was more pronounced for the surfaces W-SC and W-40 fpi which, because of their fin geometry, limited refrigerant flow in the axial direction on the tubes. This meant that, all other things equal, dry spots developed on lower tube rows at lower heat fluxes which could not be compensated by increasing refrigerant flow rate. Still, all enhanced surfaces showed an increase in heat transfer coefficients in the spray evaporation regime over a bundle of plain-surface tubes with enhancement factors in excess of 15 reported for the Tu-Cii surface. Some of the data from this study have been reproduced and are shown in Figure 2.4 as a reference for the present work.

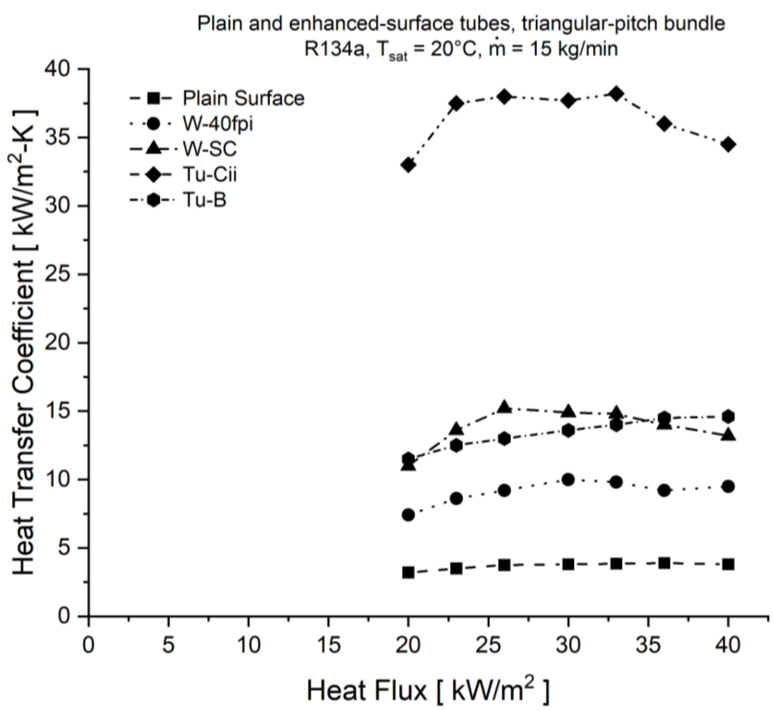

Figure 2.4: Effects of enhanced-surface type on bundle heat transfer coefficients - reproduced from Moeykens, et al. (1995)

For heat fluxes between 20 kW/m^2 and 40 kW/m^2, the W-40 fpi surface had the lowest heat transfer coefficients of the enhanced surfaces of around 6.0 kW/m^2-K to 11.0 kW/m^2-K, while the W-SC and Tu-B surfaces were between 10.0 kW/m^2-K and 15.0 kW/m^2-K and the Tu-Cii values were between 30.0 kW/m^2-K and 42.0 kW/m^2-K. Also, spray evaporation heat transfer coefficients for the Tu-Cii bundle were reported to be 100% higher than those for the Tu-B bundle operating in a flooded nucleate boiling regime. Given these results, it was decided for the present study that both square and triangular bundle geometries should be tested along with at least one enhanced surface designed to enhance boiling heat transfer coefficients (similar to Tu-Cii) and one designed to enhance condensation heat transfer coefficients (similar to W-SC). Similar studies were also performed with ammonia as the evaporating fluid as part of a subsequent ASHRAE-sponsored research project. In Zeng, et al. (1995) ammonia was sprayed on a single plain-surface tube using standard-angle and wide-angle nozzles at saturation temperatures between -23.3 °C and 10 °C and heat fluxes ranging from 8 kW/m^2 to 60 kW/m^2. At saturation temperatures below about -2 °C, heat transfer coefficient values showed little dependence on refrigerant mass flow rate. At -23.3 °C, spray evaporation heat transfer coefficients were nearly identical to pool boiling heat transfer coefficients recorded during the same study and were between 0.5 kW/m^2-K and 2.5 kW/m^2-K for heat fluxes between 10 kW/m^2 and 55 kW/m^2. At -12.2 °C, however, spray evaporation values were approximately 50% to 75% higher than those for the pool boiling values at the same temperature, with similar differences observed at -1.1 °C and 10 °C. Refrigerant mass flow rate had the largest effect on heat transfer coefficients at a saturation temperature of 10 °C for which values at 2.98 kg/min were 10% to 20% higher than those for 0.28 kg/min, with the difference growing larger as heat flux increased. Some of these data have been reproduced and are shown in Figure 2.5 for reference. It should be noted that, for the entire experimental campaign in the present work, refrigerant mass flow rates were varied between 0.7 kg/min and 7.5 kg/min. For single tube spray evaporation tests in the present work, which were most similar to the data reported in Figure 2.5, refrigerant mass flow rates were varied between approximately 2.0 kg/min and 4.6 kg/min.

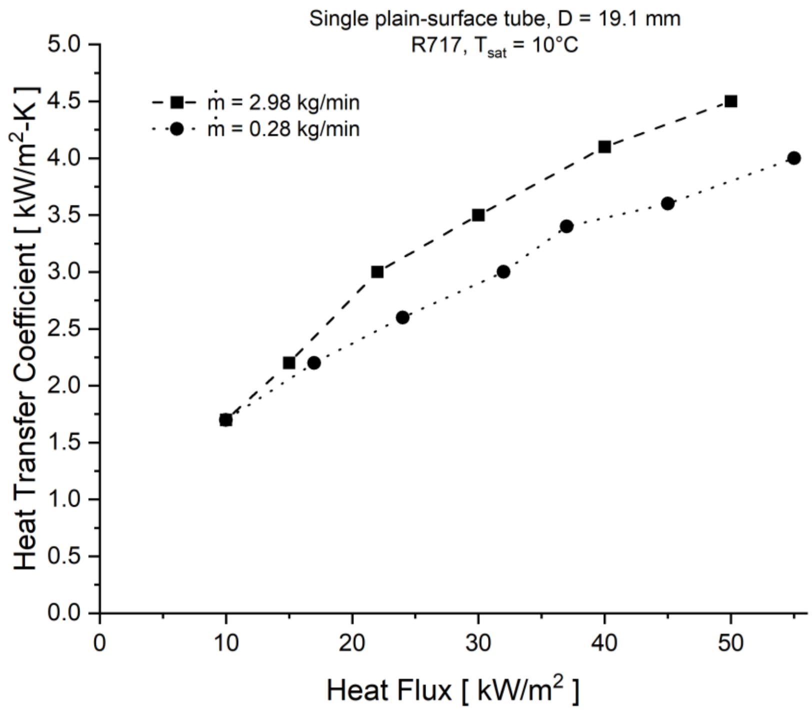

Figure 2.5: Effect of refrigerant mass flow rate on heat transfer coefficients - reproduced from Zeng, et al. (1995)

Heat transfer coefficients were also consistently higher for higher refrigerant saturation temperatures with values at 10 °C between 80% and 150% higher than those reported at -23.3 °C. For all saturation temperatures, nozzle height had little effect (within ±5%) on heat transfer performance, and differences in nozzle type were only seen at saturation temperatures above -2 °C. At those temperatures, the standard-angle nozzles consistently produced higher heat transfer coefficients than the wide-angle nozzles because of the greater amount of refrigerant that impinged on the tube instead of bypassing it at a given mass flow rate. Given these findings, it was decided that the present study should employ the use of a variety of nozzle types and that the nozzle configuration should be adjusted to minimize the amount of refrigerant bypassing the bundle. In a follow-up study by Zeng, et al. (1997) using a square-pitch bundle of plain-surface tubes, similar results were obtained. Bundle heat transfer coefficients were consistently higher at higher flow rates and higher saturation temperatures, while the enhancement effect of the standard-angle nozzles was magnified at higher saturation temperature and little effect was noticed due to differences in nozzle height. Also, for the 3x3 bundle configuration tested, individual tube heat transfer coefficients were generally highest for the topmost tubes in the bundle and lowest for the tubes in the lowest row. These differences also increased with increasing saturation temperature. At a saturation temperature of 10 °C, bundle heat transfer coefficients between 0.75 kW/m^2-K and 3.5 kW/m^2-K were reported for heat fluxes between 5 kW/m^2 and 35 kW/m^2. For reference, these data have also been reproduced and are shown in Figure 2.6. It should be noted that in the present work, the refrigerant mass flow rate per unit length of the tubes, Γ_l, was varied within a range of 0.038 kg/s-m and 0.403 kg/s-m.

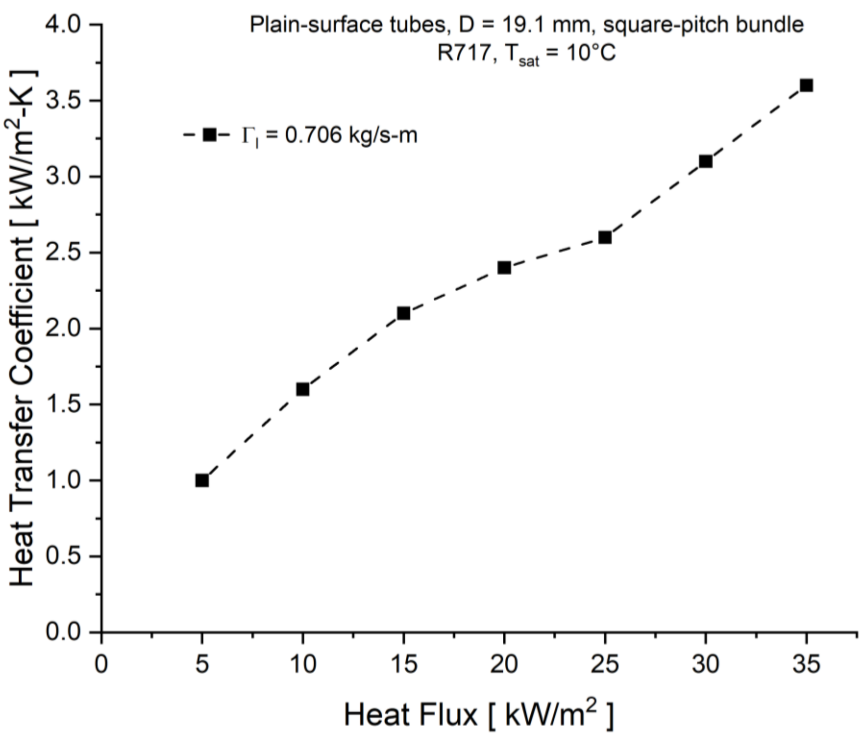

Figure 2.6: Bundle heat transfer coefficients for plain-surface tubes in ammonia - reproduced from Zeng, et al. (1997)

Later, a similar study was performed by Zeng, et al. (2001a) under the same conditions using a 3-2-3 triangular pitch bundle with a focus on investigating the tube bundle effect. As before, individual tube heat transfer coefficients varied little from each other at low saturation temperatures with differences becoming more significant at higher saturation temperatures. Values were consistently highest for the uppermost tubes in the bundle, but interestingly, the next highest values were observed for the leftmost and rightmost (i.e. towards the outside of the bundle) tubes in the lowest row. The two tubes in the middle row of the bundle had among the lowest heat transfer coefficients, similar to those of the middle tube in the bottom row, because they were blocked from receiving sufficient refrigerant flow by the outermost tubes. In this way, the bundle effect differed from that seen in the previous square-pitch bundle in which heat transfer coefficients decreased with increasing depth into the bundle as refrigerant from the upper tubes dripped directly onto tubes in subsequent lower rows. That said, the square-pitch bundle still exhibited a larger tube bundle effect, that is, a larger difference in heat transfer coefficients between the highest and lowest tubes in the bundle. Slightly higher bundle heat transfer coefficients were observed for the triangular bundle compared to the square bundle for the same conditions because of the decreased space and thus increased fluid velocity between tubes in the triangular pitch. Also, it was pointed out that the triangular geometry increased the chances for droplet and bubble impingement on the tubes as the fluid had to zig-zag through the bundle and could not pass straight through. These findings placed emphasis on the need to test both the triangular and square tube geometries in the present study. A similar study by Chang and Chiou (1999), which utilized a 3-2 triangular-pitch bundle of plain-surface tubes, was performed using R141b. At a saturation temperature of 20 °C and mass flow rate of 1.4 kg/min, the highest heat transfer coefficients were recorded for the middle tube in the top row. The next highest values belonged to the leftmost and rightmost tubes in the top row, which were nearly identical, followed by the lowest values which were recorded for the two tubes in the bottom row, which were again nearly identical to each other. Bundle heat transfer coefficients showed little dependence on mass flow rate at low heat flux but, at a mass flow rate of 0.8 kg/min, the onset of dryout occurred at much lower heat flux than it did at the higher flow rate, thus significantly decreasing heat transfer coefficients in that regime. The data from this comparison have been reproduced and are shown in Figure 2.7.

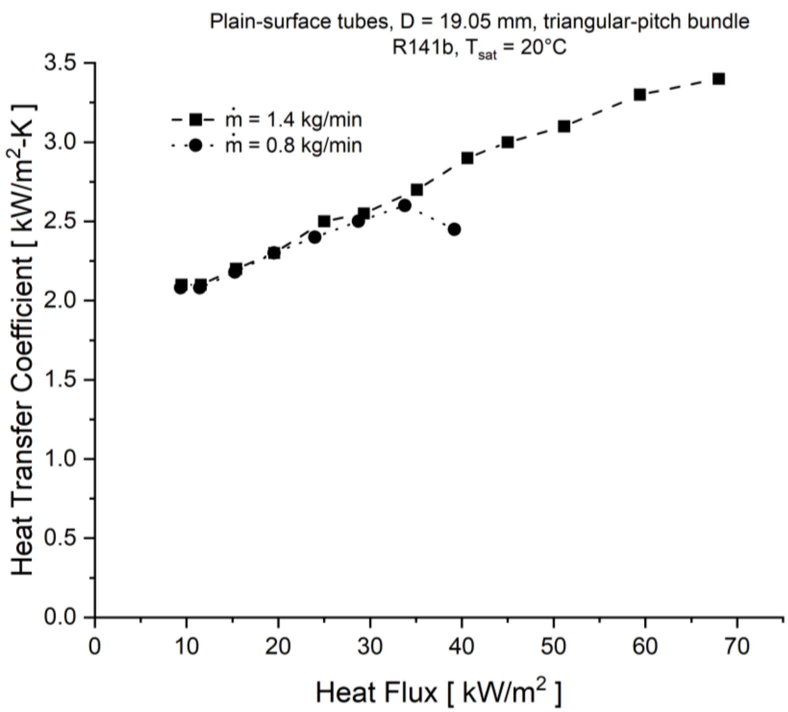

Figure 2.7: Effects of mass flow rate on the onset of dryout - reproduced from Chang and Chiou (1999)

For comparison, pool boiling tests were also conducted. Nucleate boiling heat transfer coefficients were lower than those for spray evaporation at low heat flux but became nearly identical at moderate heat fluxes and eventually surpassed spray evaporation values after the onset of dryout. A follow-up study by Chang (2006) was conducted to investigate specifically the effects of spray nozzle configuration on the heat transfer performance of the same 3-2 bundle configuration using low-finned enhanced-surface tubes. Three different nozzle types, with orifices of 1.0 mm, 1.5 mm, and 2.0 mm diameter were tested at heights of 35 mm and 54 mm above the top of the bundle. For heat fluxes between 10 kW/m^2 and 100 kW/m^2, it was found that the 1.0 mm orifice nozzles returned the poorest performance in both their high and low settings. Heat transfer coefficients for the 1.5 mm and 2.0 mm orifice nozzles in both low and high settings were very similar at heat fluxes below 50 kW/m^2 and were approximately 5% to 10% greater than those for the 1.0 mm nozzles. Only at heat fluxes above 60 kW/m^2 did the heat transfer coefficients for the 2.0 mm nozzles become higher than those for 1.5 mm nozzles, and only by about 5% to 10%. At all heat fluxes and for all nozzle types, nozzle height above the bundle had little effect on performance. Some representative data from the study have been reproduced for reference and are shown in Figure 2.8.

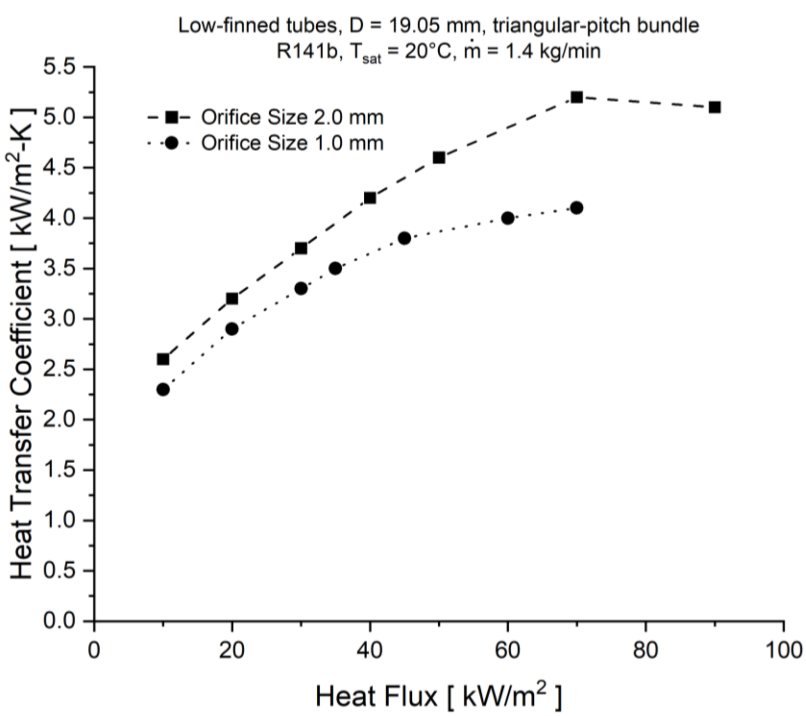

Figure 2.8: Effects of nozzle orifice size on bundle heat transfer coefficients - reproduced from Chang (2006)

Given these findings, it was concluded that nozzles an orifice diameter of at least 2.0 mm should be used in the present study. Tatara and Payvar (2001) conducted a study on a five-row triangular-pitch bundle of integral-fin tubes using a unique setup in which refrigerant R11 liquid was dripped onto the tubes from above and sprayed into the middle of the bundle in all directions by two spray tubes that took the place of heater tubes. Using this setup, they were able to improve refrigerant distribution within the bundle to such an extent that the highest tube heat transfer coefficients were recorded in the bottom tube row and values decreased with increased height in the bundle. This was consistent with the findings in their single tube drip and spray tests in which spray evaporation heat transfer coefficients were higher than those for the falling film evaporation. Bundle heat transfer coefficients at 24 kW/m^2 with a flow rate of 9.2 kg/s-m^2 were around 5.0 kW/m^2-K to 7.5 kW/m^2-K with bottom row values as high as 11.0 kW/m^2-K. Additionally, the proportion of liquid spray to liquid drip was varied and heat transfer coefficients were observed to increase slightly with an increase in the proportion of sprayed refrigerant.

2.2 Modeling Work

Though nucleate boiling and evaporation phenomena are extremely complex and often difficult to characterize, much work has been done to develop empirical, semi-empirical, and analytical correlations to better predict heat transfer behavior under such conditions. Perhaps the most widely-used correlation to predict pool boiling heat transfer coefficients is the semi-empirical Rohsenow correlation (Rohsenow, 1952) based on analogies with forced convection processes. Rearranged to solve explicitly for boiling heat flux, the equation is as follows:

$$q" = \mu_l h_{lv} \left[\frac{g(\rho_l - \rho_v)}{\sigma}\right]^{1/2} \left[\frac{c_{pl}[T_w - T_{sat}(P_l)]}{C_{sf} h_{lv}}\right]^{1/r} Pr_l^{-s/r} \tag{2.1}$$

where μ_l is the dynamic viscosity of the liquid, h_{lv} is the enthalpy of vaporization of the fluid, g is gravitational acceleration, ρ_l and ρ_v are the densities of the liquid and vapor phases, respectively, σ is the surface tension, c_{pl} is the specific heat at constant pressure of the liquid, T_w is the temperature of the heated surface, $T_{sat}(P_l)$ is the saturation temperature of the fluid at the given pressure, C_{sf} is a constant that depends on the liquid-surface combination, Pr_l is the liquid Prandtl number, and s and r are constants. Though originally developed for nucleate boiling on flat surfaces, this correlation has been modified and applied to predict heat transfer coefficients on cylindrical surfaces as well. Saiz-Jabardo, et al. (2004) performed an investigation into the Rohsenow correlation for use on copper, brass, and stainless steel surfaces of varying roughness with refrigerants R11, R123, R12, and R134a. They found that changes in surface material and roughness and refrigerant type had little effect on the correlation's exponents, and they subsequently fit the correlation to their experimental data to find values for the C_{sf} constant. After the fitting procedure, they found that deviations between the experimental data, including some that had been collected in previous studies, and the correlation were within acceptable ranges. Another widely-used correlation, one that was encountered many times in the literature referenced in this work, is the empirical Stephan-Abdelsalam correlation (Stephan & Abdelsalam, 1980) proposed by its namesakes. In contrast to that of Rohsenow, the Stephan-Abdelsalam correlation is empirical and based on dimensional analysis and regression fits of over 5000 data points. The correlation consists of different formulas for use with different substances like water, hydrocarbons, refrigerants, and cryogenic fluids, but the single correlation proposed for use with all substances was shown to agree reasonably well with experimental data with a mean absolute error of 22.3%. It has also been shown to agree closely with experimental data collected for nucleate boiling on plain and enhanced-surface tubes in many of the studies referenced in this review. Early work on falling film correlations, such as that presented by Dukler (1960), was mostly analytical and developed for use with vertical tubes as that configuration of falling film evaporator was much more common at the time. At around the same time, Chen (1966) published a study on a very thorough investigation into convective flow boiling of saturated fluids and developed an accompanying two-part correlation of the form

$$h = Fh_{mac} + Sh_{mic} \tag{2.2}$$

where h is the overall convective heat transfer coefficient, h_{mac} is the macroconvective heat transfer described by a modified form of the Dittus-Boelter equation, h_{mic} is the microconvective heat transfer according to Forster and Zuber's formulation, F is the forced convection multiplier, and S is the suppression factor, the latter two of which are functions of the two-phase Reynolds number. This correlation was found to be close fit for early data available at the time and was verified to be well suited for prediction of shell-side heat transfer performance in a flooded refrigerant evaporator in the work of Webb, et al. (1989). Significant developments were made for falling film heat transfer on vertical plain-surface tubes by Chun and Seban (1971) who collected experimental data in the laminar and turbulent regimes and proposed semi-empirical curve fits. For turbulent film evaporation of water, their correlation was of the form

$$\bar{h}\left(\frac{\nu^2}{gk_{ref}^3}\right)^{1/3} = c_1 Re^{c_2} Pr^{c_3} \tag{2.3}$$

where $\bar{h}$ is the average heat transfer coefficient, ν is the liquid kinematic viscosity, g is the gravitational acceleration constant, k_{ref} is the liquid thermal conductivity, Re and Pr are the Reynolds and Prandtl numbers, respectively, and c_1, c_2, and c_3 are coefficients determined based on experimental data. Owens (1978) then successfully applied this correlation to nonboiling ammonia film evaporation on horizontal tubes. Later, Parken, et al. (1990) proposed a modified form for use with water films on horizontal tubes as follows:

$$\bar{h}\left(\frac{\nu^2}{g k_{ref}^3}\right)^{1/3} = p_1 Re^{p_2} Pr^{p_3} q"^{p_4} \tag{2.4}$$

where $q"$ is the heat flux and p_1, p_2, p_3, and p_4 are coefficients determined based on experimental data. Thus, Parken's modified form accounted for the effects of varying heat flux which had been found to be significant based on experimentation. This formulation was then modified again by Zeng, et al. (1997) to correlate data they had collected on spray evaporation of ammonia on a bundle of horizontal enhanced-surface tubes, and appeared as follows:

$$Nu = z_1 Re^{z_2} Pr^{z_3} P_{red}^{z_4} \Phi^{z_5} \tag{2.5}$$

where

$$Nu = \frac{h}{k_{ref}}\left(\frac{\nu^2}{g}\right)^{1/3} \tag{2.6}$$

$$Re = \frac{2\Gamma_l}{\mu} \tag{2.7}$$

$$\Phi = \frac{q"D}{(T_{crit} - T_{sat})k_{ref}} \tag{2.8}$$

where Nu, Re, and Pr are the Nusselt, Reynolds, and Prandtl numbers, respectively, P_{red} is the reduced pressure of the refrigerant, h is the bundle heat transfer coefficient, k_{ref} is the liquid refrigerant thermal conductivity, ν is the liquid refrigerant kinematic viscosity, g is the gravitational acceleration constant, Γ_l is the spray flow rate, μ is the liquid refrigerant dynamic viscosity, $q"$ is the heat flux, D is the tube diameter, T_{crit} is the refrigerant critical temperature, T_{sat} is the refrigerant saturation temperature, and z_1, z_2, z_3, z_4, and z_5 are coefficients determined based on a curve fit of experimental data. A method for determining the flow rate Γ_l in the Reynolds number was described in Chyu, et al. (1995) whereby only the refrigerant that contacts the tube bundle should be measured and that which misses the bundle should not be taken into account. The investigators examined the spray flow patterns produced by different types of nozzles and developed an analytical method in which these flow patterns could be overlaid on the top projection of a tube bundle. Accordingly, the refrigerant that interacts with the bundle is represented by the areas in which the two projections overlap and the flow rate can be estimated based on the portion of the spray flow area that is included in the overlap. They compared these calculations to another study by Zeng, et al. (1994) in which they had taken direct measurements of Γ_l by replacing a bundle of tubes with a liquid collector under a set of spray nozzles and found excellent agreement between the data and the analytical method. This correlation was later used by Zeng, et al. (2001b) in a follow-up study on spray evaporation over a triangular-pitch bundle of plain-surface tubes in which a curve fit was applied and the data were successfully correlated within ±20%. Since its development, the correlation in this form has been used in many similar studies including the one by Chien, et al. (2019) in which the flow rate parameter Γ_l was described by the formula

$$\Gamma_l = \frac{\dot{m}}{2L_t} \tag{2.9}$$

such that the film Reynolds number was then

$$Re = \frac{4\Gamma_l}{\mu} \tag{2.10}$$

where $\dot{m}$ is the mass flow rate of refrigerant that impinges on the tubes, and L_t is the length of the tubes in the bundle. Effectively, the film Reynolds number then became

$$Re = \frac{2\dot{m}}{\mu L_t} \tag{2.11}$$

such that the flow rate parameter Γ_l can best be described as the refrigerant mass flow rate that impinges on the bundle per unit length of the tubes.

In order to predict the most likely range of expected heat transfer coefficient values for the current work, the three correlations from Chun and Seban, Parken, et al., and Zeng, et al. were used to calculate bundle heat transfer coefficients using the properties of the three refrigerants and the geometry of the test section to be used in this project. The calculations for R134a, R1234ze(E), and R1233zd(E) are shown in Figures 2.9, 2.10, and 2.11, respectively. As shown, the Chun-Seban correlation could be used to predict only a single heat transfer coefficient value for a given refrigerant and set of operating conditions, one that did not vary with changes in tube wall heat flux.

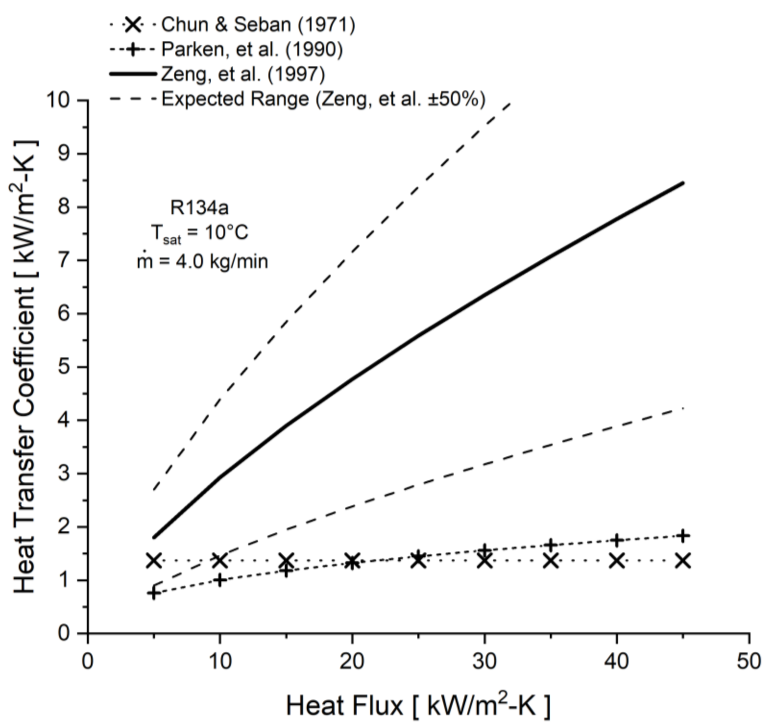

Figure 2.9: Calculated heat transfer coefficients for the current work for refrigerant R134a using the correlations of Chun & Seban (1971), Parken, et al. (1990), and Zeng, et al. (1997)

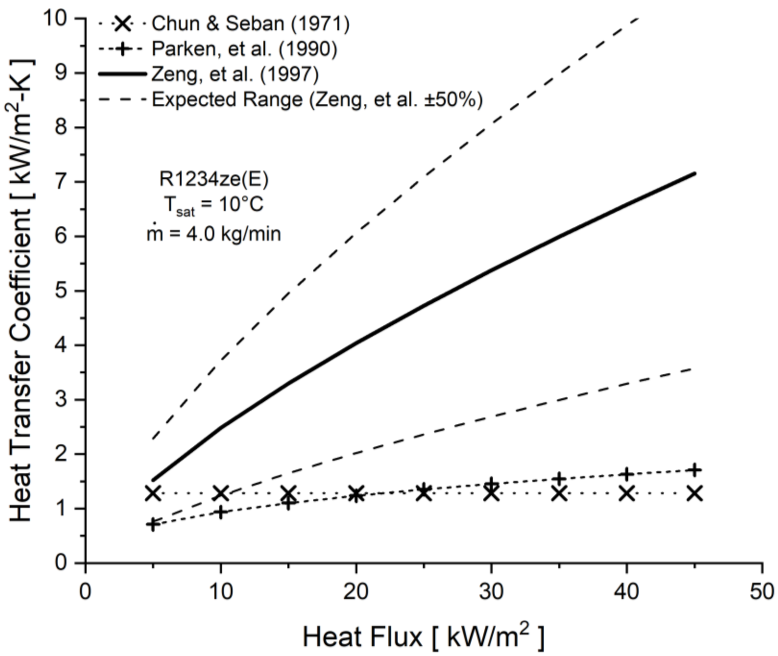

Figure 2.10: Calculated heat transfer coefficients for the current work for refrigerant R1234ze(E) using the correlations of Chun & Seban (1971), Parken, et al. (1990), and Zeng, et al. (1997)

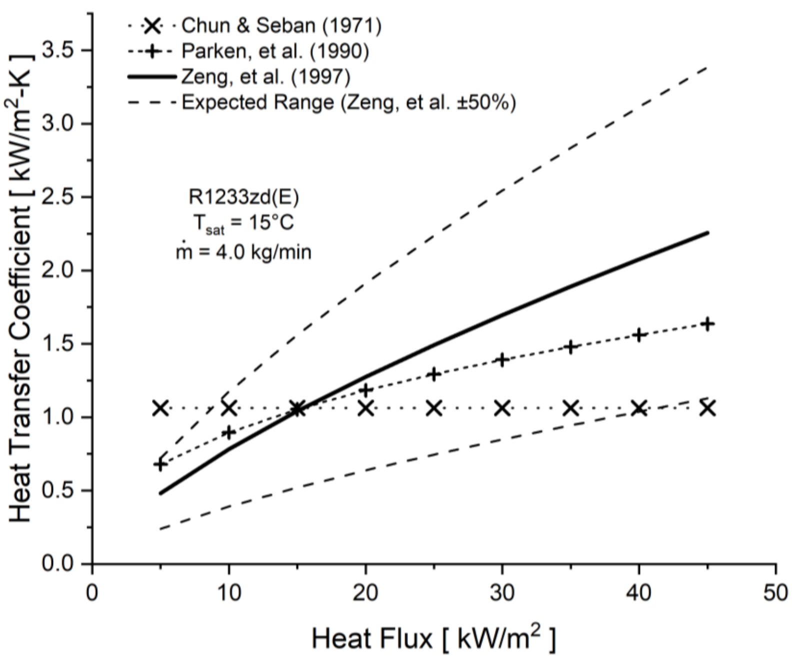

Figure 2.11: Calculated heat transfer coefficients for the current work for refrigerant R1233zd(E) using the correlations of Chun & Seban (1971), Parken, et al. (1990), and Zeng, et al. (1997)

The lack of a provision to account for the effects of heat flux on heat transfer performance thus represents a major limitation for this particular correlation and makes it unfit for meaningful predictions. Using this correlation, bundle heat transfer coefficient values of approximately 1.4 kW/m^2-K, 1.3 kW/m^2-K, and 1.1 kW/m^2-K were calculated for refrigerants R134a, R1234ze(E), and R1233zd(E), respectively, for heat fluxes ranging from 5 kW/m^2 to 45 kW/m^2. The Parken correlation, though it does include a provision for variances in heat flux, consistently returned heat transfer coefficient values within ±60%, or within about 1.0 kW/m^2-K at such low values, of those returned by the Chun-Seban correlation. The predicted values showed a near linear increase with increases in wall heat flux from 5 kW/m^2 to 45 kW/m^2: for R134a, values were between 0.8 kW/m^2-K and 1.8 kW/m^2-K; for R1234ze(E), values were slightly lower at 0.7 kW/m^2-K to 1.7 kW/m^2-K; and for R1233zd(E), values were lower still at 0.6 kW/m^2-K to 1.6 kW/m^2-K. The most realistic predictions were calculated using the Zeng correlation, which is also the most comprehensive of the three with provisions for heat flux and additional refrigerant properties compared to the previous two. Over the same heat flux range, predictions for R134a were between 1.8 kW/m^2-K and 8.5 kW/m^2-K; for R1234ze(E), between 1.5 kW/m^2-K and 7.2 kW/m^2-K; and for R1233zd(E), between 0.5 kW/m^2-K and 2.3 kW/m^2-K. Thus for the operating conditions to be used in the current work, R134a was consistently predicted to have the best heat transfer performance, followed by that of R1234ze(E) at about 80% and then R1233zd(E) at about 25% as calculated using the Zeng correlation. Given its seemingly realistic predictions, versatility, popularity and applicability to spray evaporation data in other studies, it was decided to utilize a modified version of this correlation in the modeling work for the present study as described in Chapter 5.

2.3 Summary of the Literature Review and Lessons Learned

In summary, convective and boiling heat transfer on the outsides of tubes and tube bundles is of great interest to designers and manufacturers of shell-and-tube heat exchangers which are largely found in industrial process applications. Up to this point, much work has been conducted on the most basic of such configurations, the flooded evaporator with plain-surface and enhanced-surface tubes. An extensive review of the literature on this configuration found studies dating back to the mid-1950s (though unpublished industrial research had likely existed even before that time) and data on shell-side heat transfer coefficients for single tubes and tube bundles is readily available. Though most such early studies were performed using water as the evaporating fluid, more recent studies have utilized CFC, HCFC, HFC, and even natural refrigerants as those are the fluids that have been and are typically used in industrial refrigeration applications. The flooded evaporator configuration has been nearly ubiquitous in such large-scale applications because of the early recognition that nucleate boiling heat transfer offers significant advantages in heat transfer performance compared to single-phase gas or liquid convection. Shell-side heat transfer coefficients on the order of 1.0 kW/m^2-K to 10.0 kW/m^2-K have been widely reported for flooded evaporators with plain-surface tubes, and enhancement factors on the order of 2 to 10 have been reported for various low-finned, integral fin, and enhanced surface types. Though geometries vary greatly among process application, tube diameters of approximately 20 mm are among the most popular and the most extensively studied, and bundle sizes have ranged from only a few to many tens of tubes in a single heat exchanger. The bundle effect as it applies to flooded evaporators, in which bundle heat transfer coefficients are often higher than those for single tubes in nucleate pool boiling conditions, has also been widely recognized.

However, recent efforts have been made to find and study alternative heat exchanger configurations with the intent of decreasing system refrigerant inventories. As such, the falling film evaporator configuration has also been of interest as a possible alternative. Early studies were performed as far back as the 1970s, but serious focus on the configuration did not arise until the 1990s. Even so, shell-side heat transfer coefficient data and even limited numerical studies are still readily available with water, natural refrigerants, and some more recent synthetic refrigerants. For plain-surface tubes, shell side heat transfer coefficients equivalent to those in the flooded evaporator configuration have been widely reported. Significant gains in heat transfer performance have also been realized with enhanced-surface tubes, but reported enhancement factors were usually on the order of 2 to 5 as opposed to the ten times enhancement reported in some studies of the flooded evaporator. The falling film configuration by nature also introduces a significant design challenge in ensuring sufficient liquid refrigerant supply to all tubes within a bundle, one that becomes more difficult as bundle sizes grow or staggered tube pitches are utilized. For designs in which appropriate refrigerant distribution is not ensured, any potential heat transfer performance enhancements over nucleate pool boiling are largely negated. In this configuration, the bundle effect adopts a different meaning: one in which heat transfer coefficients are highest for the tubes at the top of a bundle and thus closest to the liquid refrigerant distributor and decreased for lower rows as tubes as refrigerant is evaporator, deflected, and dispersed by the upper tubes.

Even more recently, spray evaporation as a means of shell-side refrigerant distribution has been explored as another alternative. The earliest studies on this configuration date back to the mid-1990s, but research has been sparse and development has been slow given the industry's reluctance to adopt the spray evaporator over the flooded evaporator. Even so, in the limited literature that could be found, the use of a pressurized liquid refrigerant spray has shown the potential to produce equivalent or increased heat transfer performance over nucleate pool boiling on bundles of tubes. Additionally, because the tube bundle does not need to be submerged in a pool of liquid refrigerant, this configuration simultaneously allows for a decrease in system refrigerant inventory without the need for changes to the rest of the system. Ensuring proper refrigerant distribution throughout the bundle still represents a significant design challenge, however, as this configuration has been shown to be especially susceptible to the dryout phenomenon on lower tube rows which is exacerbated by the bundle effect. Various studies have shown significant dependence on such factors as nozzle spray pattern, orifice size, and height above the tube bundle, enhanced surface type, bundle geometry, liquid flow rate, refrigerant properties, and tube heat flux, but virtually none made any mention of refrigerant quality or degree of liquid subcooling upon entering the heat exchanger. Among the limited studies performed in this area, most have utilized water, ammonia, or HFC refrigerants as the evaporating fluid even as the industry is being forced to find new low-GWP alternatives because of evolving regulations. As such, there exists very little data on external heat transfer coefficients (via nucleate pool boiling, spray evaporation, or otherwise) of new HFO refrigerants on single tubes and virtually no data on shell-side heat transfer coefficients of HFOs on bundles of tubes. The main objective of this research work, to measure and report shell-side heat transfer coefficients on bundles of enhanced-surface tubes, was proposed to address this issue. Based on previous experiments, newly-developed state-of-the-art enhanced surfaces, one designed to enhance condensation heat transfer and the other to enhance evaporation heat transfer, would be utilized in square-pitch and triangular-pitch bundle geometries as are common in real applications to provide points of comparison for each. Two different nozzle spray patterns would be utilized and the configurations of each would be adjusted to provide optimal refrigerant distribution within each bundle. A wide range of refrigerant flow rates and saturation temperatures would be tested over a similarly wide range of tube heat flux levels in order to characterize the effects of each, as would inlet subcooling so that its effects could also be identified. A sufficiently large tube bundle would be utilized and the test section instrumented to allow for row-by-row characterization of heat transfer performance especially as it pertained to the bundle effect and the dryout phenomenon. Most importantly, two new low-GWP HFO refrigerants would be the focus of the experimental campaign and would be compared to a widely-used HFC refrigerant in the same experimental apparatus as a performance baseline. As such, it was desired that this data could be used by academic and industrial researchers as a starting reference and point of comparison for future research and development work on similar shell-and-tube spray evaporators.

Given that experimental work on the spray evaporator configuration is limited, the modeling work is even sparser. Only one or two computational or numerical studies could be found, and none of them proposed a succinct method for correlating bundle heat transfer coefficients to the factors described previously. Among the experimental work, only one study on shell-side heat transfer coefficients using ammonia could be found with an acceptable semi-empirical correlation that accounted for the effects of refrigerant properties, mass flow rate, and tube heat flux on heat transfer performance. However, this model was designed to correlate and predict bundle average heat transfer coefficients and was nearly linear for increasing tube heat flux with all other operating conditions constant. As such, this model would not account for differences in enhanced-surface type, bundle geometry, or refrigerant inlet subcooling with a single set of coefficients and would not at all account for the effects of the dryout phenomenon. The secondary objective of this research, to prescribe a succinct preliminary model to correlate the experimental data while accounting for these factors with a single set of coefficients, was proposed to address this issue. Given that dryout is a row-wise phenomenon that produces nonlinear heat transfer coefficient curves as observed in some of the literature, the model would have to be formulated to correlate and predict row-by-row heat transfer coefficients. Provisions would have to be developed in order to account for the bundle effect and decreases in refrigerant mass flow rate for lower tube rows to reflect decreased heat transfer performance at heat fluxes above the onset of dryout. In calculating bundle heat transfer coefficients as an average of several individual row heat transfer coefficients, the curves could be made nonlinear to reflect the dryout condition. Several other enhancement factors would also be prescribed to account for differences in enhanced surface type, bundle geometry, and refrigerant inlet subcooling if necessary. In doing so, it was the aim of this modeling work to both correlate the data collected during the experimental campaign and to provide a convenient method to predict shell-side heat transfer performance of spray evaporation of two new HFO refrigerants for use in future academic and industrial research work.

Chapter 3: Experimental Setup

The details of the pre-existing experimental facility and the test section that was designed, constructed, and instrumented to carry out the work in this dissertation are presented in this chapter. The “experimental facility” refers to the equipment and components used to condition the refrigerant in the circulation loop before and after the test section. The “test section” refers to the apparatus used to house the enhanced-surface tube bundles, refrigerant spray nozzles, and the thermocouples used for measuring temperatures associated with spray evaporation phenomena. Refrigerant test conditions and experimental testing procedures are also presented at the end of this chapter.

3.1 Experimental Facility

Refrigerant Loop

The refrigerant loop consisted of a series of pumps, heat exchangers, valves, and instrumentation connected via stainless steel and copper tubing. The thermodynamic cycle of the loop was meant to replicate the change in phase of refrigerant from liquid to vapor in the evaporator section of a vapor-compression refrigeration cycle. A schematic of the refrigerant loop is shown in Figure 3.1. Liquid refrigerant was moved from the primary pump (either the gear pump or the diaphragm pump, depending on refrigerant type and test conditions) through the Coriolis mass flow meter, at which a measurement of total loop refrigerant mass flow rate was taken. From there, refrigerant passed into the ethylene-glycol preheater section which consisted of one of the system’s two brazed-plate heat exchangers and a tube-in-tube heat exchanger. There, the refrigerant was heated by a passing ethylene-glycol water solution that was continuously conditioned by the ethylene-glycol pump module and Syltherm cryogenic chiller (both of which will be examined

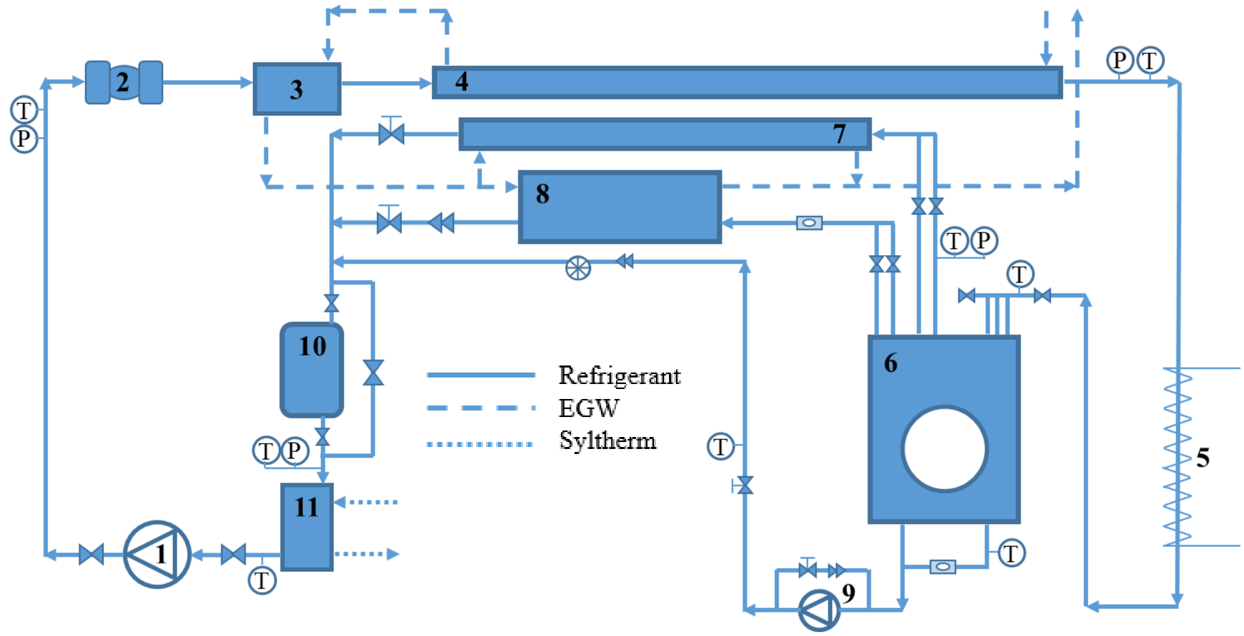

Number	Name	Elevation [m]	Relevant Length [m]
1	Primary liquid refrigerant pump: Gear pump	0.7	-
1	Primary liquid refrigerant pump: Diaphragm pump	0.1	-
2	Coriolis mass flow rate meter	2.4	-
3	Brazed-plate heat exchanger (preheater)	2.5	-
4	Tube-in-tube heat exchanger (preheater)	3.0	5.5
5	Electric preheater section	0.4	6.7
6	Test Section	1.2	-
7	Tube-in-tube heat exchanger (condenser)	2.4	3.4
8	Shell-and-tube heat exchanger (condenser)	2.4	0.8
9	Secondary liquid refrigerant pump: centrifugal pump	0.1	-
10	Refrigerant liquid receiver	1.2	-
11	Brazed-plate heat exchanger (subcooler)	0.7	-

Figure 3.1: Schematic of the refrigerant loop

later in this chapter). From there, the refrigerant passed into a section of exposed copper tubing around which were wrapped three electric tape heaters, which was referred to as the electric preheater section. Refrigerant then passed into the test section, where it was evaporated by the heaters contained within. Refrigerant vapor exited the test section through one of four outlets on the top and proceeded into either the tube-in tube condenser or the shell-and-tube condenser, both of which received the same ethylene-glycol solution that was passed through the preheater section. Liquid refrigerant exited through a drain in the bottom of the box and was recirculated by a secondary liquid refrigerant pump to a point just before the liquid receiver, thus bypassing both condenser heat exchangers. From the liquid receiver, refrigerant then flowed through the second brazed plate heat exchanger, known as the subcooler, wherein it was cooled to the lowest temperature in the loop by the Syltherm from the cryogenic chiller, after which it was sufficiently subcooled in its liquid phase to be passed through the primary pump and begin the cycle again. Other auxiliary tubes and valves were configured such that the system could be operated in various bypass modes. One such mode that was useful for initiating refrigerant flow was to bypass the test section completely and allow refrigerant to flow from the preheater section directly to the condenser section and then back to the pump. The liquid receiver could also be bypassed as doing so decreased the refrigerant charge necessary to attain a stable flow rate in the system. Similarly, either condenser heat exchanger could be bypassed individually if the heat load introduced in the test section was not great enough to warrant the use of both. An oil separator (not shown) was positioned in the loop just before the inlet to the test section and could be used while the system was operating in the test section bypass mode, but it was never used for the work presented in this dissertation as the refrigerant miscible oil tests and results are included as part of another project.

Test Section

The test section used for all experiments performed during this project was a rectangular box meant to resemble a shell-and-tube heat exchanger. It was constructed of 6.35 mm (0.25 in) thick steel plates and had interior dimensions of approximately 41 cm tall, 30 cm wide and 30 cm deep. The test section had four openings, one on either side, one on the front and one on top, to which a standard 15.2 cm (6 in) size pipe cap could be mounted using flanges and bolts that were fixed to the box. This was meant to create flexibility in the design of the heat exchanger for instrumentation, heater tube layout and orientation, nozzle layout and location, and the inclusion of a window for direct observation of evaporation phenomena. A 3D rendering of the test section with some exterior dimensions is depicted in Figure 3.2. All dimensions shown in Figure 3.2 are in centimeters unless otherwise noted.

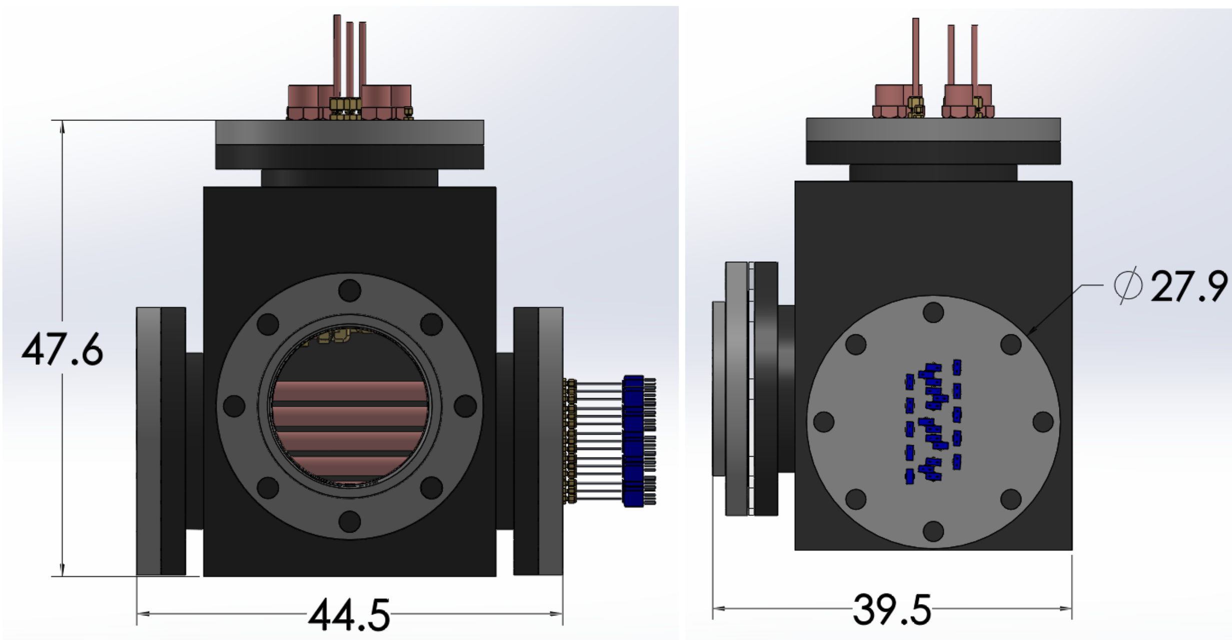

Figure 3.2: Front elevation (left) and right side elevation (right) 3D renderings of the test section

Refrigerant entered the test section from the top and was distributed to the spray nozzles which directed the flow downward onto a bundle of fifteen enhanced-surface copper heater tubes oriented horizontally and arranged in three columns of five tubes each. Some illustrations of the test section's internals in the form of 3D renderings are shown in Figures 3.3 and 3.4. All dimensions in Figures 3.3 and 3.4 are in centimeters unless otherwise noted.

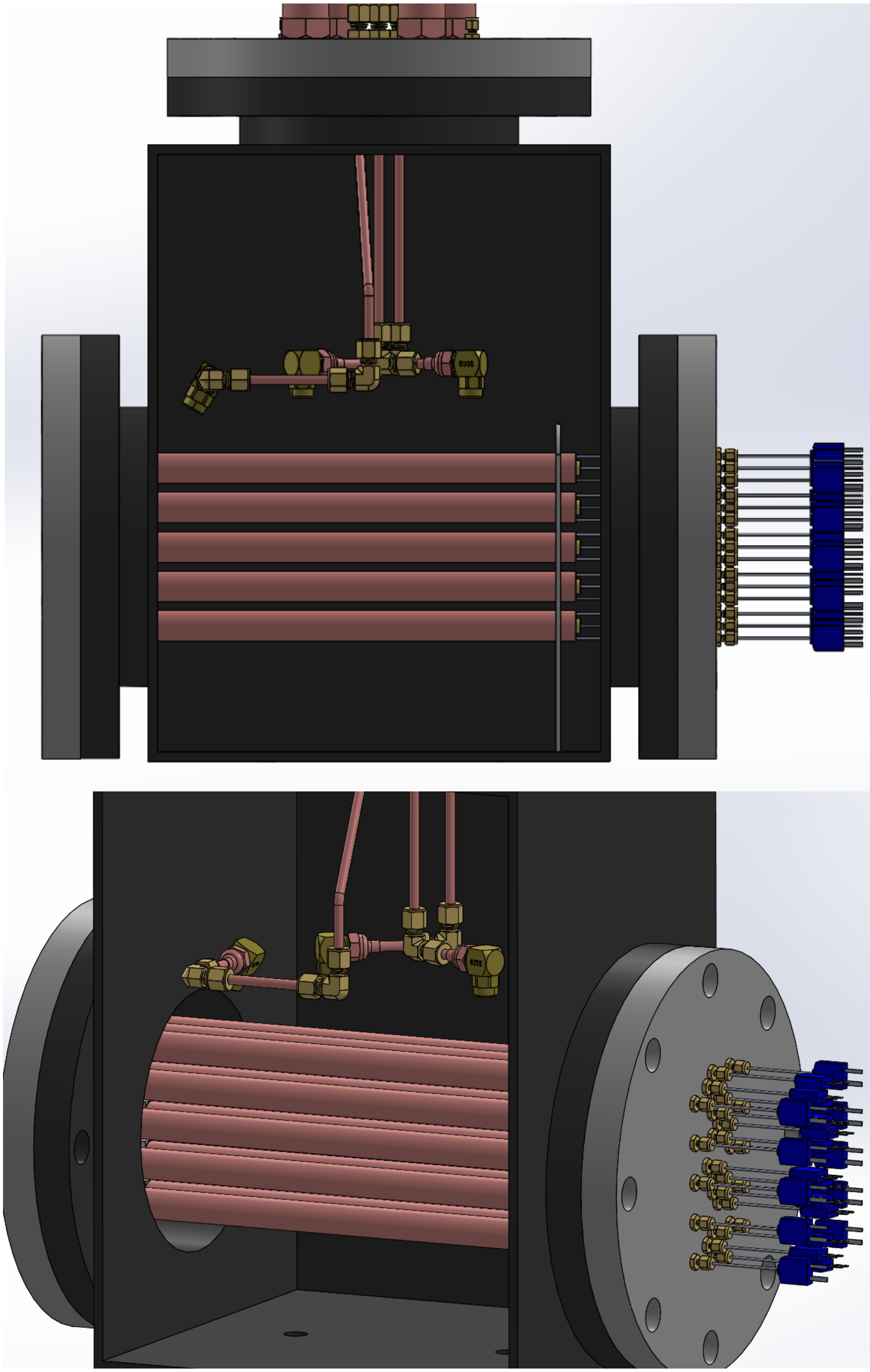

Figure 3.3: 3D renderings of the test section internals showing the square bundle geometry and circular cone spray nozzle configuration

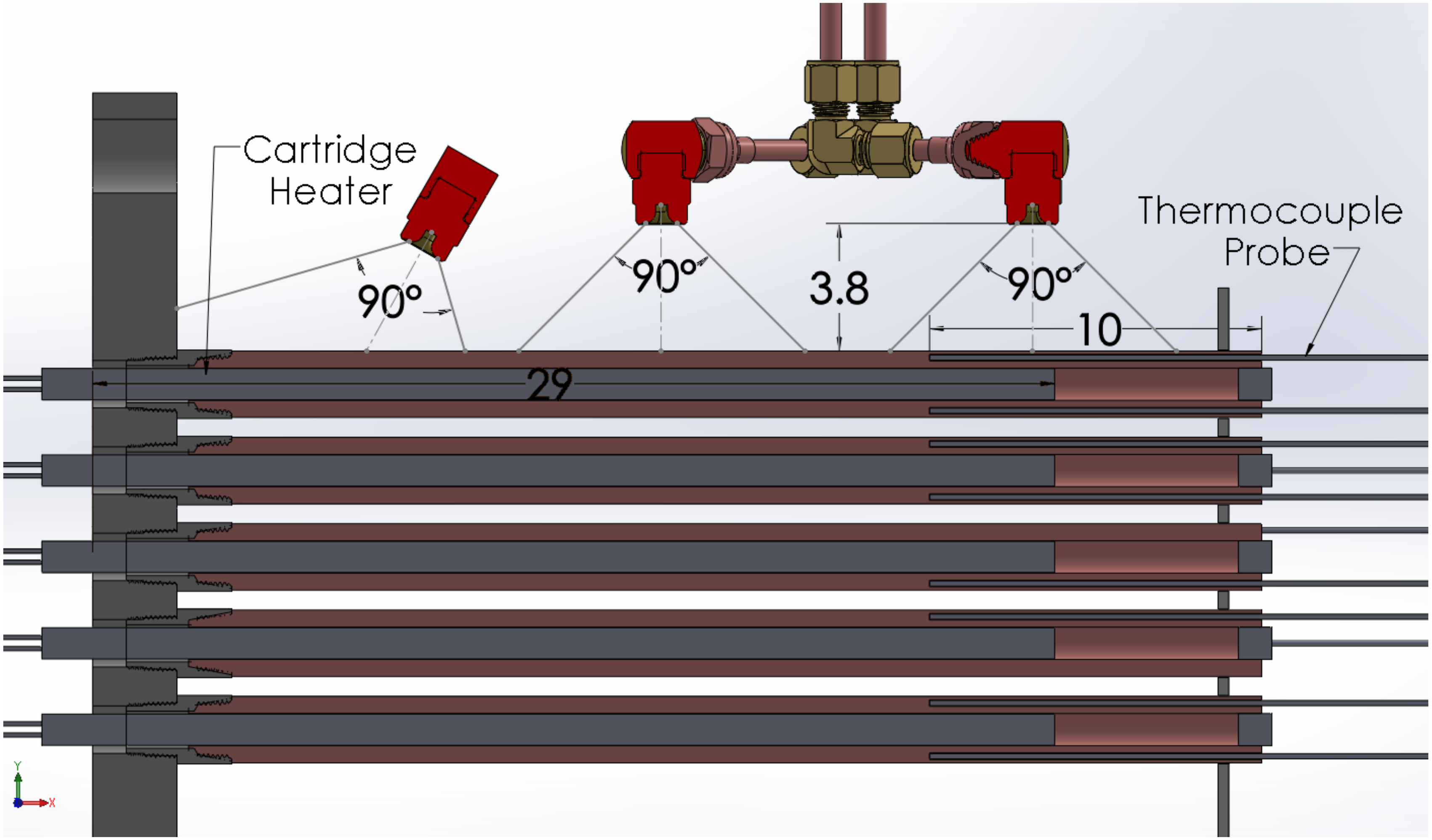

Figure 3.4: Cutaway rendering of the test section internals showing the relative positions of the circular cone spray nozzles, thermocouples probes, and cartridge heaters

As shown, the heater tubes were fixed to the flange attached to the left side of the box while a series of T-type thermocouples were supported by the flange on the right side. The inlet nozzles and their accompanying tubing, along with four vapor outlets and two pressure taps were all fixed to the top flange. Two pictures of the test section from various angles are shown in Figure 3.5.

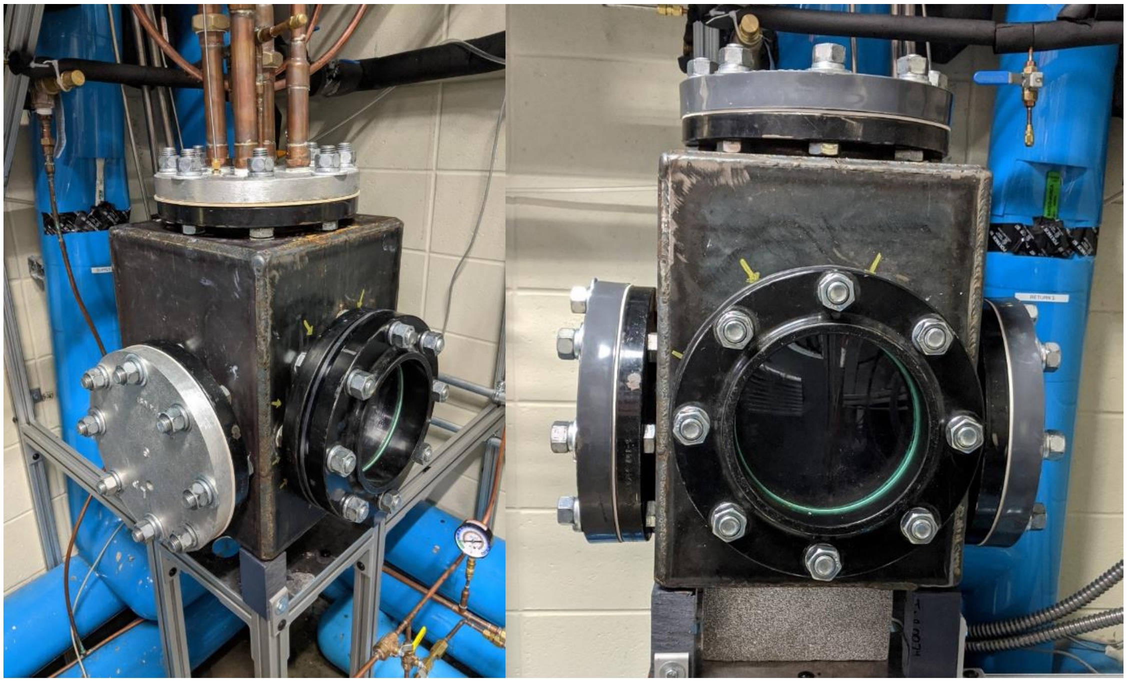

Figure 3.5: Spray evaporator test section, uninsulated

Heater Tubes

The heater tubes were the specially-constructed devices that allowed for the use of electric resistance cartridge heaters to evaporate the refrigerant inside the test section and t-type thermocouples to measure and record the temperature near the surface of the tubes themselves. All heater tubes used for this experiment were constructed of copper metal and measured approximately 300 mm in length and 20 mm in diameter with a 9.525 mm (nominal) diameter bore running the full length of each tube. The outer surface of each tube consisted of a proprietary finned structure which was designed to enhance heat transfer on the outer surfaces. Two different types of enhanced surface were used for this work, which will be referred to as the “Tube-C” Condenser Tubes and “Tube-B” Evaporator (Boiling) Tubes. Detailed pictures of both types of enhanced surface are shown below in Figure 3.6.

Figure 3.6: Tube-C condensing surface (left) and Tube-B evaporation surface (right)

The condensing surface was designed specifically to aid with liquid drainage from the outer surface of the tubes, thereby aiding in condensation heat transfer, while the evaporation surface was designed to enhance nucleate boiling from the outer tube surface in a shell-and-tube heat exchanger. Each tube also had either one, two, or three channels, 2 mm in diameter, drilled lengthwise from the closed end of the tube to a depth of either 100 mm or 150 mm and within 1 mm of the tube outer surface. These channels were meant to accommodate T-type thermocouple probes that were used to collect tube surface temperature readings during testing. Over the course of experimentation, the tubes were arranged in two different bundle configurations, the first being a staggered or triangular bundle arrangement and the second being an aligned or square bundle arrangement. In the triangular bundle arrangement, the tubes had a transverse pitch of 26 mm and a longitudinal pitch of 26 mm. The second and fourth rows of tubes were offset by a transverse distance of 13 mm for a diagonal pitch of approximately 29 mm and a bundle pitch-to-diameter ratio of 1.3. In the square bundle arrangement, the tubes had both a transverse pitch and longitudinal pitch of 26 mm with no offset on the second and fourth rows, again creating a pitch-to-diameter ratio of 1.3 for the bundle. The two bundle arrangements are shown in Figure 3.7.

Figure 3.7: Triangular tube arrangement (left) and square tube arrangement (right)

Electric Resistance Heaters

Each tube contained a resistive cartridge heating element, all of which together provided both the thermal energy needed to evaporate the refrigerant in the test section and a convenient way to accurately measure energy input to the test section. The cartridge heaters were manufactured by Watlow Electric Manufacturing Co. and were marketed under the name FIREROD®. They had a nominal outer diameter of 9.42 mm (3/8 in), a nominal total length of 305 mm (12 in), and a nominal heated length of 279 mm (11 in) such that the 25 mm section of the rods nearest the wires were unheated. Each heater was rated for a power input of 1393 Watts at 208 Volts with a nominal resistance of 28 Ω. The outer sheath of each heater was made of Incoloy 800 metal alloy. An example is pictured below in Figure 3.8.

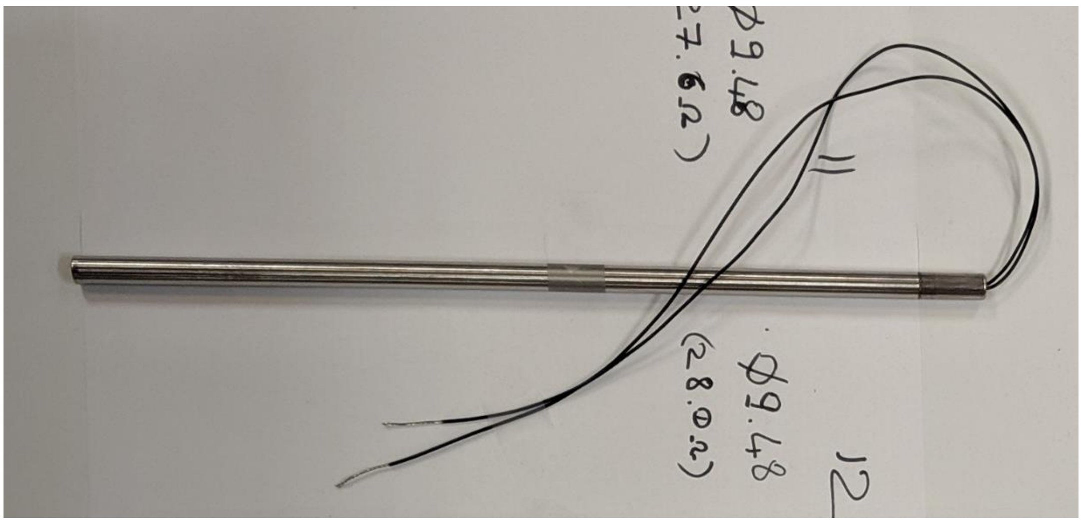

Figure 3.8: Watlow FIREROD® cartridge heater

The test section used a total of 15 of these cartridge heaters, split into five groups of three. Each group of three heaters was wired in a delta configuration, and each delta was powered by one of two combination power supply/controllers.

Deflected Flat Spray Nozzles

For the first test campaign, a set of six 303 stainless steel deflected flat spray nozzles with a flat spray pattern were used in the test section to distribute refrigerant to the tube bundle. The nozzles were manufactured by Bex and marketed as flooded nozzles with part number 1/4FL2.5. Each nozzle had an orifice of diameter 1.4 mm and was rated for a liquid flow rate of 0.53 LPM – 2.31 LPM with a nominal spray angle of 88° – 152° for a liquid pressure range of 20 kPa – 415 kPa. All six nozzles were positioned approximately 25 mm above the top surface of the topmost tubes in the bundle with two nozzles centered transversely over each of the three tubes in the topmost row. Longitudinally, the nozzles were arranged in two groups of three with the groups spaced approximately 150 mm from each other and equidistant from the middle of the heater tubes. These nozzles were only used for the condenser tubes in the triangular bundle configuration. The deflected flat nozzle arrangement is pictured in Figure 3.9.

Figure 3.9: Deflected flat spray nozzle arrangement

Full Cone Spray Nozzles

For the second test campaign, which represents a majority of the tests run as part of this dissertation, a set of three brass wide-angle spray nozzles with a full cone spray pattern were used in the test section. The nozzles were manufactured by Spraying Systems Co. and marketed as FullJet® nozzles with part number 1/4GGA-14W. Each nozzle had an orifice of diameter 3.58 mm and was rated for a liquid flow rate of approximately 3.9 LPM – 13.6 LPM with a nominal spray angle of 103° – 120° for a liquid pressure range of 34.5 kPa – 552 kPa. Some 3D renderings of the nozzle positions relative to the bundle are shown in Figure 3.10. All dimensions in the figure are in centimeters unless otherwise noted. The actual full cone nozzle arrangement as installed in the test section is pictured in Figure 3.11.

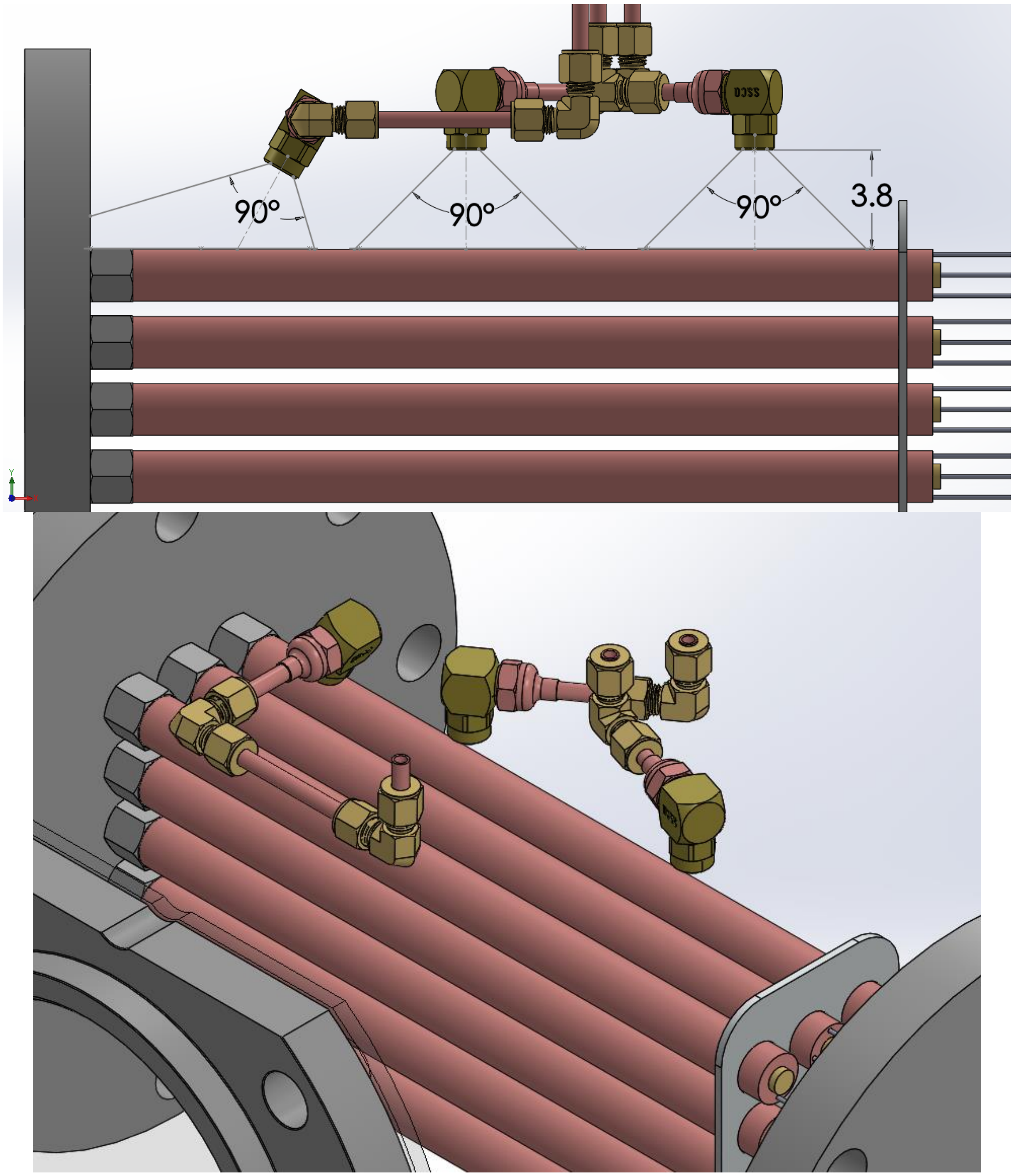

Figure 3.10: Front elevation (top) and isometric (bottom) 3D renderings of the nozzle positions

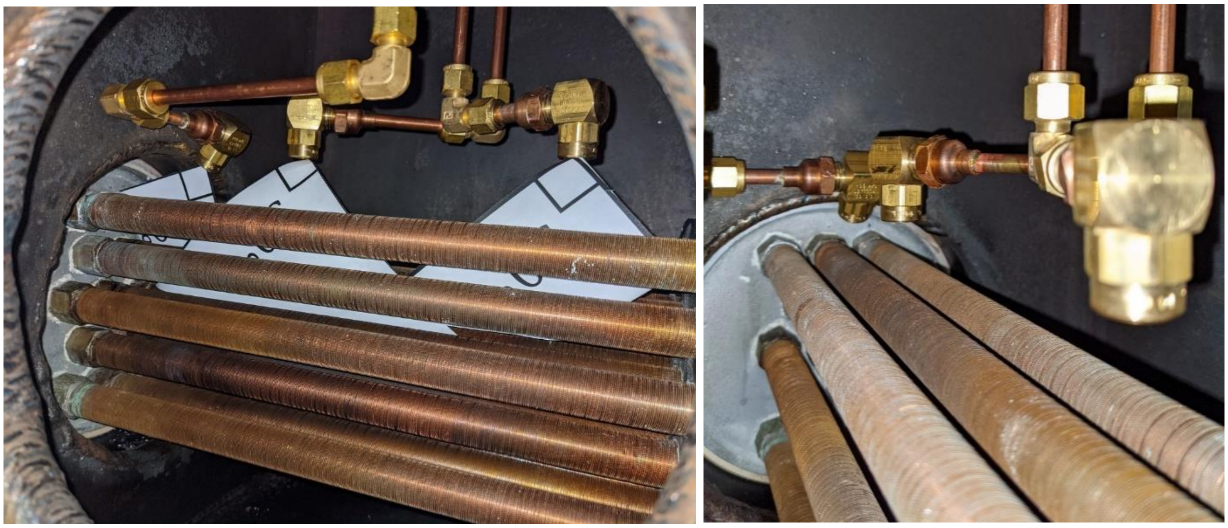

Figure 3.11: Full cone spray nozzle arrangement

All three nozzles were positioned approximately 38 mm above the top surface of the topmost tubes in the bundle and were centered transversely above the center tube in the topmost row for both the triangular and square bundles. Longitudinally, the nozzles were spaced approximately 100 mm from each other with the center nozzle positioned 150 mm, or halfway, along the heater tube. Using the nozzle specifications and installed positions, the approximate spray pattern and minimum coverage area were also rendered, as shown in Figures 3.12 and 3.13. This coverage area, along with the pattern depicted in Figure 3.10a, were in close agreement to an actual spray pattern observed during testing, which is pictured in Figure 3.14.

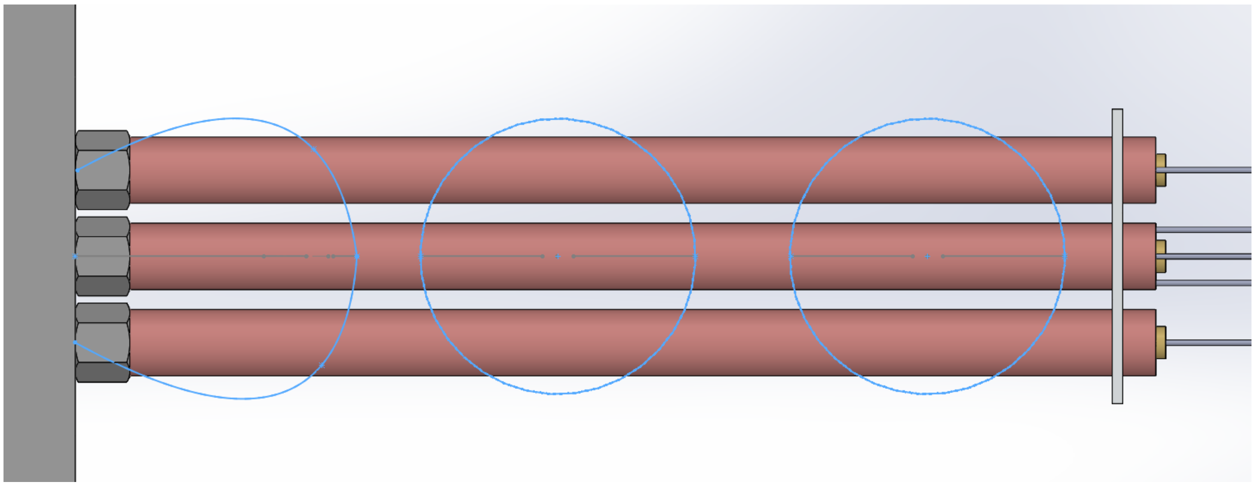

Figure 3.12: 3D rendering of the minimum coverage area for the full cone spray nozzles

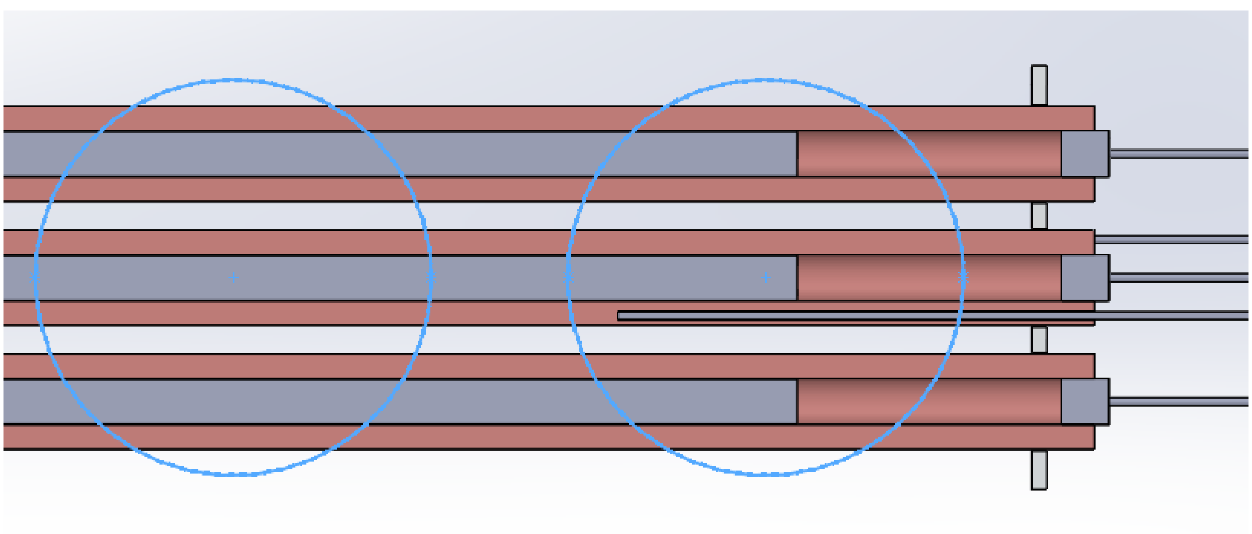

Figure 3.13: Cutaway rendering of the thermocouple probe position within a heater tube with an overlay of the minimum coverage area

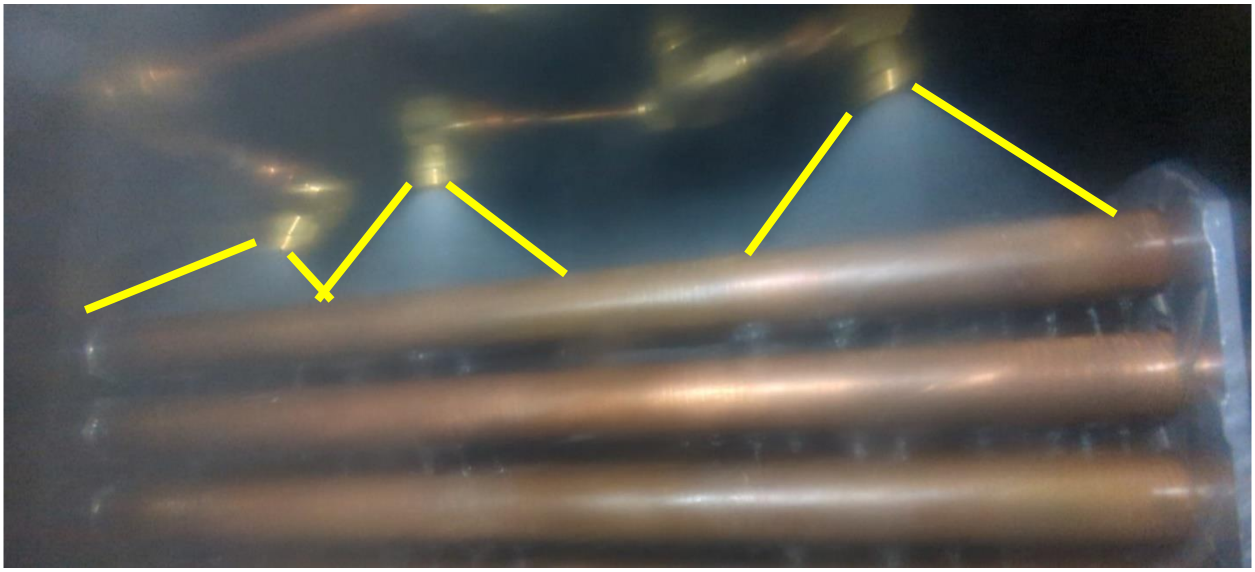

Figure 3.14: Actual full cone nozzle spray pattern observed during testing

Primary Refrigerant Gear Pump

One of the primary pumps used in the refrigerant loop was a MicroPump GC-M25.JF5S.E gear pump manufactured my Micropump, Inc. coupled to a Baldor Reliance SuperE Motor. The pump was rated for a maximum flow rate of 13.9 LPM at a maximum rated differential pressure of 8.6 bar. The gear pump is pictured in Figure 3.15.

Primary Refrigerant Diaphragm Pump

The other primary refrigerant pump used in the loop was a Hydra-Cell D04-991-2400A diaphragm pump manufactured by Wanner Engineering, Inc. coupled with a Baldor Reliance SuperE Motor and supplied by Voigt-Abernathy. The pump was rated for a maximum capacity of 11.0 LPM at a maximum rated pressure of 170 bar. The diaphragm pump is pictured in Figure 3.15.

Figure 3.15: Refrigerant gear pump (left) and refrigerant diaphragm pump (right)

Ethylene Glycol Preheater Section

The ethylene glycol preheater section consisted of two liquid-to-liquid heat exchangers. The first was a brazed-plate heat exchanger consisting of 40 plates, made of 316L stainless steel and rated for a capacity of 205 kW in a water-to-water application at a flow rate of 190 LPM. It was manufactured by Bell & Gossett, Inc. with part number BPN410-40 LCA. The second was a straight counter flow tube-in-tube heat exchanger made of stainless steel with a total length of 5.5 m. The inner tube featured an inner diameter of 9.5 mm and the annulus featured an inner diameter of 25.4 mm. The heat exchangers received a supply of cooled EGW from the pump module to raise the temperature of the refrigerant before entry into the electric preheater section. Both heat exchangers are pictured in Figure 3.16.

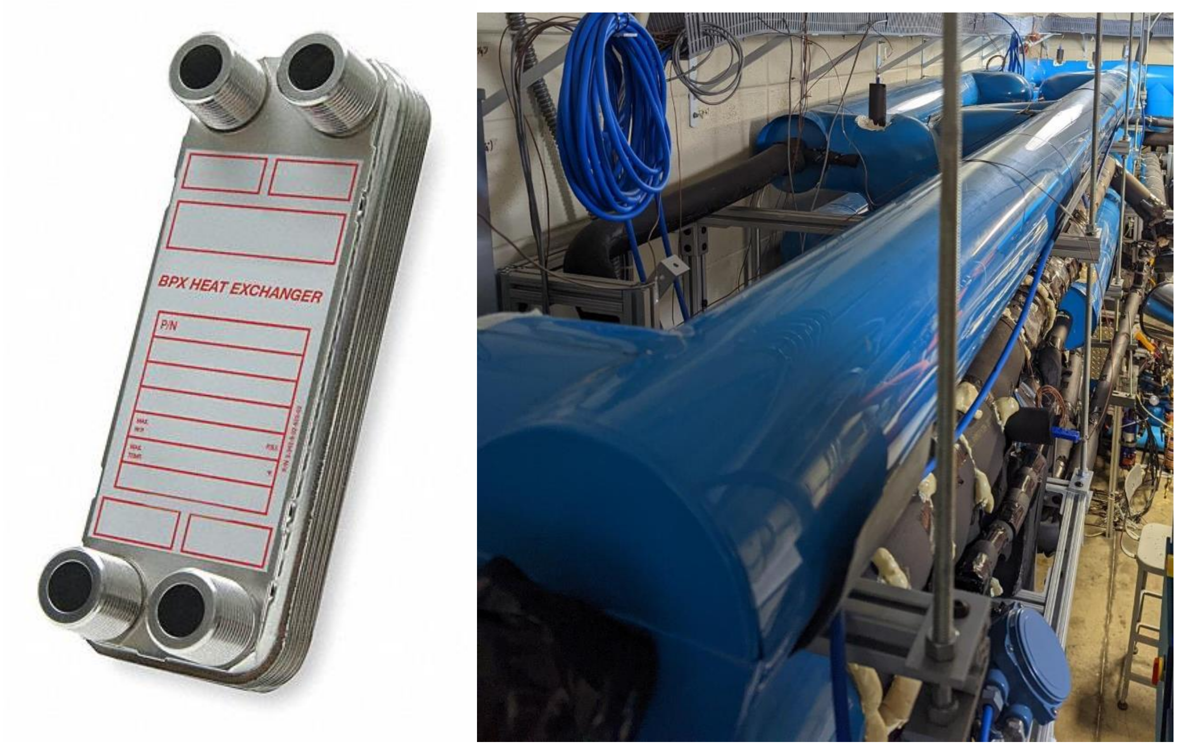

Figure 3.16: Ethylene glycol brazed plate preheater (left) and tube-in-tube preheater (right)

Electric Preheater Section

The electric preheater section consisted of a section of curved stainless steel and copper tubing wrapped with three electric resistance band heaters. The entire preheater section featured tubing with an inner diameter of 17.2 mm and had an equivalent straight length of 6.7 m. The three band heaters were manufactured by BriskHeat with part number BSAT101008. Each heater tape was made of silicone rubber, was 2.44 m long and 25.4 mm wide, and was rated for a maximum heating capacity of 576 W for a total of 1.728 kW. The electric preheater section was used to raise and fine tune the temperature of the refrigerant beyond that of the cooled EGW, usually to within only a few degrees Celsius of the saturation temperature at the given pressure, immediately before entry into the test section. The electric preheater section is pictured in Figure 3.17.

Figure 3.17: Electric preheater section

Secondary Liquid Refrigerant Pump

The refrigerant loop featured a second, smaller liquid pump positioned directly below the test section to assist with liquid flow back to the primary pump. This secondary pump was of the centrifugal type, constructed of cast iron, and was connected directly to the test section's liquid drain. It was manufactured by Wilo and marketed as a Star S 21 F with part number 4105032. It is pictured in Figure 3.18.

Figure 3.18: Secondary refrigerant centrifugal pump

Tube-in-tube Condenser

The tube-in-tube condenser is virtually identical to the tube-in-tube preheater. It features an inner stainless steel tube of inner diameter 9.5 mm and an outer stainless steel tube with an inner diameter of 25.4 mm with a total length of approximately 3.35 m. This heat exchanger also received a supply of cooled EGW from the pump module which was used to condense the vapor refrigerant after it had exited from the upper part of the test section. The heat exchanger is pictured in Figure 3.19a.

Shell-and-tube Condenser

The second condenser heater exchanger was a shell-and-tube type made of brass and manufactured by Standard Xchange with model number SN503006024005. It was rated for a capacity of 381 kW in a water-to-water application at a flow rate of 215 LPM on the tube side and 276 LPM on the shell side. The heat exchanger received a supply of cooled EGW from the pump module on the tube side which was used to cool and condense the vapor refrigerant immediately after exiting from the top of the test section. After initial shakedown tests using only the tube-in-tube condenser proved troublesome, the much larger shell-and-tube heat exchanger was installed to increase cooling capacity for the vapor refrigerant. It is pictured in Figure 3.19b.

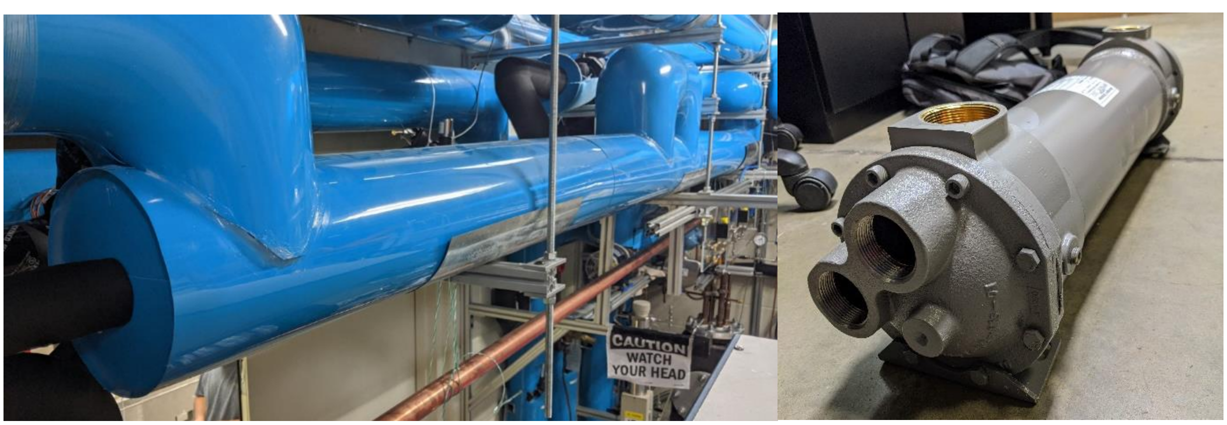

Figure 3.19: Tube-in-tube condenser (left, insulated) and shell-and-tube condenser (right)

Liquid Receiver

The liquid receiver was positioned just before the inlet to the subcooler heat exchanger to ensure a supply of refrigerant in liquid phase to the subcooler and primary pump. It was manufactured by Henry Group with part number S-8510. It is pictured in Figure 3.20.

Figure 3.20: Liquid receiver

Brazed-plate Subcooler Heat Exchanger

Immediately before the inlet of both primary refrigerant pumps was a 316L stainless steel brazed-plate heat exchanger similar to the one used in the ethylene glycol preheater section. It was manufactured by Bell & Gossett, Inc. with part number BPN410-60 LCA. The subcooler heat exchanger featured 60 plates and was rated for a maximum capacity of 352 kW in a water-to-water application at a flow rate of 190 LPM. The subcooler received a supply of cooled Syltherm directly from the chiller that was usually 15 °C to 30 °C colder than the EGW supply and thus ensured that the primary refrigerant pumps received a supply of subcooled liquid refrigerant for proper operation.

Coriolis Mass Flowmeter

The instrument that was used to measure total refrigerant mass flow rate in the loop was a Coriolis mass flowmeter manufactured by Micro Motion, Inc. and marketed as a Micro Motion Elite with product code CMFS025M319N2BAEKZZ. The flowmeter features a body made of 316 stainless steel and was calibrated with a maximum measurement uncertainty of ±0.1% up to a maximum flow rate of 17.5 kg/min. The instrument is pictured in Figure 3.21.

Figure 3.21: Coriolis mass flowmeter

Watt Transducers

To measure the electrical power input to the cartridge heaters, two AC watt transducers were wired in series with two different heater delta groups. The watt transducers were three phase, three wire 50/60 Hertz (two element) transducers manufactured by FLEX-CORE® with model number PC5-014EY24. Each transducer returned a 4 – 20 mA signal to the data acquisition system corresponding to a full scale output of 4 kW, and each was calibrated to an output accuracy within ±0.5% of the full scale output. The watt transducers are pictured in Figure 3.22.

Figure 3.22: AC watt transducers

Pressure Transducers

A number of pressure transducers were used throughout the system to measure refrigerant pressure at various locations. Among those were three Model 205 absolute pressure transducers manufactured by Setra with part number 2051500PG2F2B25WNN. These transducers returned a 0 – 5 VDC signal to the data acquisition system corresponding to a designed pressure range of 100 kPa – 3550 kPa (0 – 500 psig). Transducers of this type were used to measure system pressure at the outlet of the primary refrigerant pump, before the electric preheater section, and at the inlet of the subcooler. Each of these transducers was calibrated from the manufacturer to an accuracy within ±0.073% of the full scale. Additionally, a Model 206 absolute pressure transducer, also manufactured by Setra with part number 2061050PG2M11258NN, was used to measure refrigerant pressure within the test section. This instrument returned a 4 – 20 mA signal to the data acquisition system corresponding to a designed pressure range of 100 kPa – 450 kPa (0 – 50 psig) and was calibrated from the manufacturer to an accuracy within ±0.13% of the full scale. Examples of these pressure transducers are pictured in Figure 3.23.

Figure 3.23: Model 205 pressure transducer (left) and Model 206 pressure transducer (right)

T-type Thermocouples

All temperature measurements recorded throughout the system were taken using T-type copper/constantan thermocouples that interfaced directly with the data acquisition system. Those used to instrument the heater tubes were equipped with a thermocouple probe manufactured by Omega with part number TMQSS-062G-12. These probes featured a sheath made of 304 stainless steel with a length of 305 mm and a nominal diameter of 1.57 mm. All thermocouples were calibrated in the laboratory to within an accuracy of ±0.2 °C. An example of this type of probe is pictured in Figure 3.24.

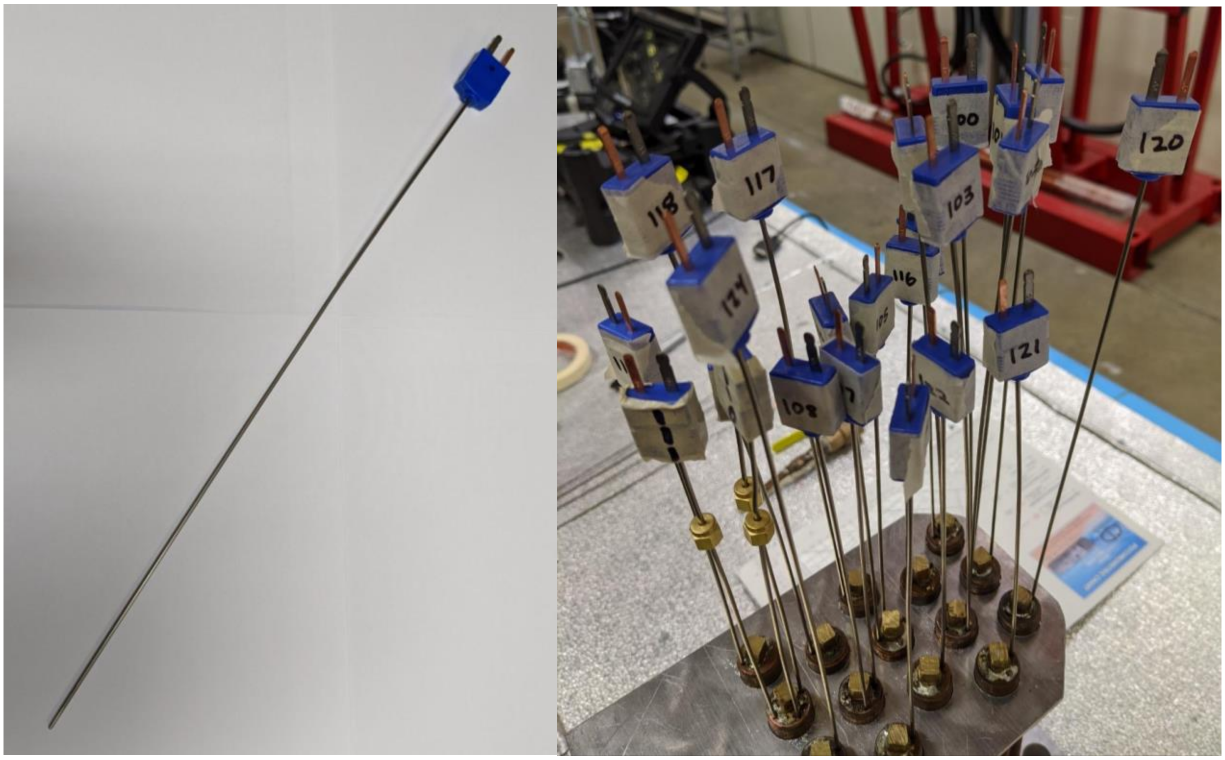

Figure 3.24: A T-type thermocouple probe (left) and thermocouple probes inserted into the copper heater tubes (right)

As mentioned previously, the thermocouple probes used to instrument the heater tubes were inserted into channels drilled into the tubes from the closed ends. These probes were supported by a flange affixed to the right side of the test section and were fixed in place by Swagelok compression-style fittings. These fittings were screwed into threaded holes in the flange and, when tightened on the probes, formed a seal around the perimeter of each probe thus holding them firmly in place and preventing refrigerant exfiltration from the test section. The compression fittings were configured such that the probes could be fixed and sealed at any point along their length, but their lengthwise positions could not be adjusted after tightening the fittings as installation was permanent. Therefore, to ensure that the tip of each thermocouple probe was in direct contact with the copper surface at the end of its respective tube channel at the time of installation, the probes were inserted into their channels with the bundle installed in the test section and held firmly in place with light pressure applied at the ends while the compression fittings were tightened. This procedure ensured that the probes would always be positioned correctly, even if the bundle had to be removed and later reinstalled in the test section. A 3D rendering of the thermocouple probe arrangement, including a cutaway view of the probes as installed and a depiction of the supporting flange, are depicted in Figure 3.25. All dimensions in Figure 3.25 are in centimeters unless otherwise noted.

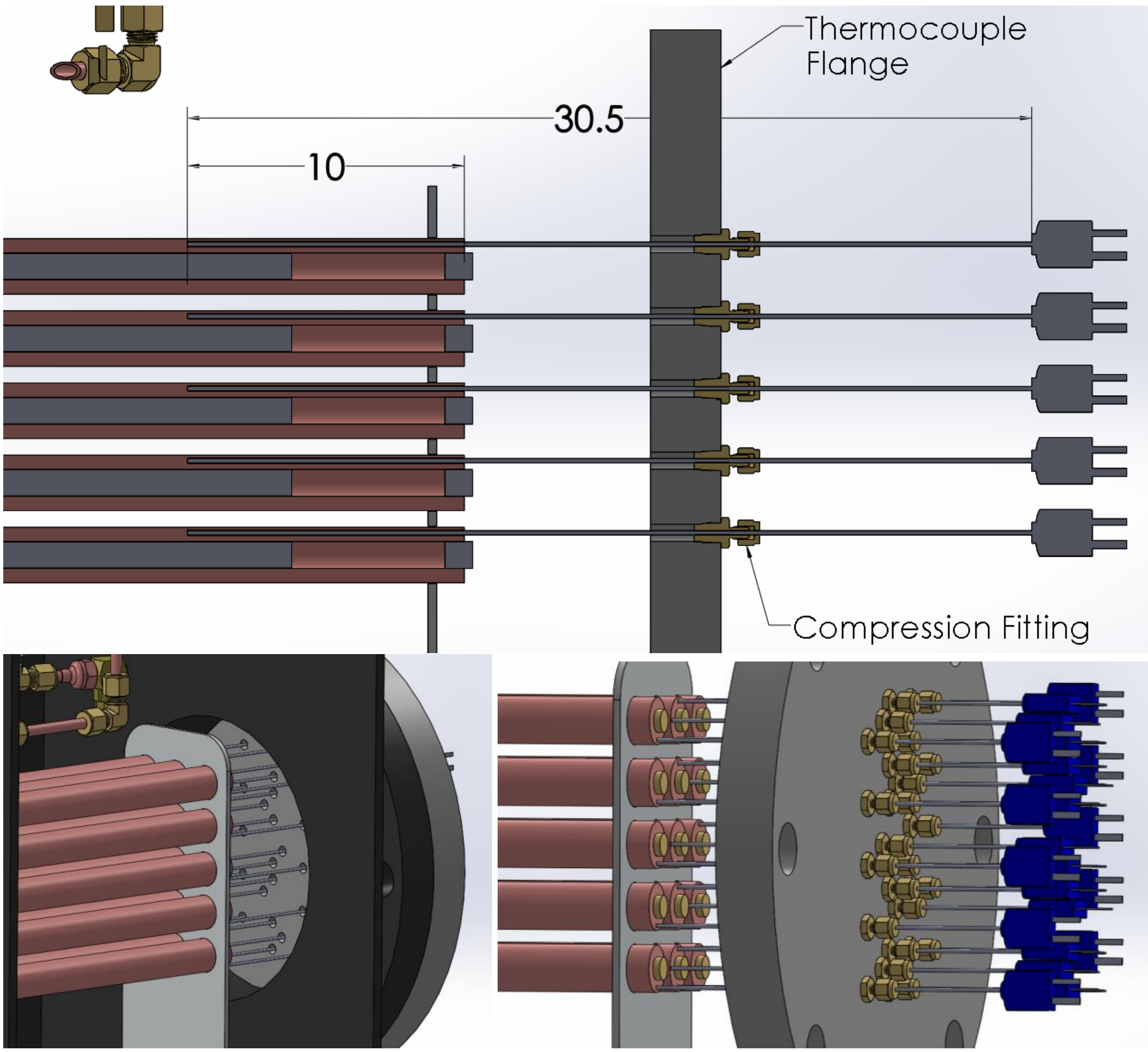

Figure 3.25: Cutaway view of the thermocouple probes as installed (top), and the inside (bottom left) and outside (bottom right) of the thermocouple flange

Ethylene Glycol Pump Module

A PM180 Pump Module manufactured by Mydax, Inc. was used to cycle a cooled 50/50 ethylene-glycol/water solution (EGW) through the brazed plate preheater, the tube-in-tube preheater, the tube-in-tube condenser, and the shell-and-tube condenser in the refrigerant loop. The pump module was rated for a maximum flow rate of approximately 76 LPM (20 GPM) at a pressure of 310 kPa (45 psia). The pump module is pictured in Figure 3.26a.

Cryogenic Chiller

A Cryodax 25 water-cooled chiller/heater manufactured by Mydax, Inc. was used to provide cooling to the refrigerant loop both directly and indirectly. The chiller used a self-contained R507 vapor-compression refrigeration cycle to cool a low temperature heat transfer fluid called Syltherm™, a specially-formulated silicone polymer oil. Heat was rejected from the cycle to the campus chilled water supply. The cooled Syltherm was circulated through the brazed-plate subcooler heat exchanger, where it cooled refrigerant in the refrigerant loop directly, and through the ethylene glycol pump module where it was used to cool the ethylene glycol/water solution. The chiller was rated for a nominal cooling capacity of 17300 Watts at -30 °C with a fluid temperature setpoint range of -70 °C to 30 °C. The chiller module is pictured in Figure 3.26b.

Figure 3.26: Mydax PM 180 Pump Module (left) and Mydax Cryodax 25 chiller (right)

3.2 Test Conditions

The independent variables controlled for the basic test matrix for this work are as follows: Type of refrigerant, refrigerant saturation temperature and pressure, refrigerant inlet subcooling, refrigerant mass flow rate, bundle heat flux, inlet spray nozzle type and configuration, heater tube enhanced surface type, and bundle configuration. Three refrigerants, R134a, R1234ze(E), and R1233zd(E) were used throughout the experimental campaign. Refrigerant mass flow rate, $\dot{m}$, was controlled via variation of the speed of the primary refrigerant pump using a variable frequency drive to within ±0.01 kg/s of the desired value. Refrigerant saturation temperature and pressure, T_{sat} and P_{sat}, in the test section were controlled via variation of the temperatures and flow rates of the EGW and Syltherm passing through the refrigerant loop heat exchangers, positions of various valves in the loop, and total refrigerant charge in the loop to within ±0.5 °C and ±7 kPa, respectively. Refrigerant inlet subcooling was controlled by varying the power input to the electric band heaters on the electric preheater section of the loop to within ±0.25 °C. The two different nozzle types were used in only two configurations, illustrated in Figures 3.9 and 3.11, which were constructed and installed separately. Each of the two sets of heater tubes, Tube-C and Tube-B, were tested in the triangular bundle and in the square bundle configurations for a total of four different tube bundle types. Bundle heat flux was controlled via variation of electric heater input to the tube cartridge heaters to within ±0.35 kW/m^2 of the desired value. Table 3.1 below contains the matrix of test conditions used in the experimental campaign.

Table 3.1: Experimental test matrix

Independent Variable	Units	Nominal Range
Refrigerants	[-]	R134a, R1234ze(E), R1233zd(E)
Saturation Temperature	[°C]	-12, -6, 2, 10, 16
Bundle Heat Flux	[kW/m^2]	3.5, 7, 10, 14, 17, 20, 24, 30
Refrigerant Inlet Subcooling	[°C]	Between 0 and 5
Refrigerant Mass Flow Rate	[kg/min]	Between 0.7 and 7.5
Enhanced Surface Type	[-]	Tube-C and Tube-B
Bundle Configuration	[-]	Triangular and Square
Nozzle Type	[-]	Deflected Flat Spray and Full Circular Cone

3.3 Experimental Test Procedure

The following is a description of the data collection procedure used throughout the entirety of the experimental campaign. After refrigerant flow was established in the loop, desired refrigerant saturation temperature and pressure conditions were achieved by adjusting EGW and Syltherm temperatures and flow rates in the heat exchangers while the electric cartridge heaters were powered up simultaneously. Tests were separated into distinct series which contained between 4 and 8 tests. For each series, refrigerant mass flow rate, inlet subcooling, and saturation temperature and pressure were held constant while bundle heat flux was varied at the different levels prescribed in the test matrix. Usually, small adjustments were required to EGW and Syltherm temperatures and refrigerant flow valve positions to maintain constant conditions throughout a series as heat flux varied. Temperature, pressure, flow rate, and electric power input data were read and recorded by the data acquisition system every 2 seconds for a total of between 30 and 40 minutes for each individual test. Usually, either one or two test series could be performed over the course of a single day of testing.

When only a single tube was tested at either the top-middle or bottom-middle position in the bundle, electric power input to the heater was controlled with a variable autotransformer and measured using a series of multimeters capable of reading voltage and current. All conditions were maintained and all other data were collected in the manners described previously.

3.4 Data Reduction

The parameters of particular interest in an experimental test are tube wall temperatures and refrigerant inlet temperature, measured by the thermocouples; refrigerant pressure at the inlet just before the nozzles and inside the test section, measured by pressure transducers; and heater power input, measured by the watt transducers. Heat flux on the surface of each tube is based on the recorded heater power input and a nominal tube length of 310 mm and diameter of 20 mm. The following equation is used to calculate the wall heat flux.

$$q" = \frac{Q_{htr}}{A} \tag{3.1}$$

where Q_{htr} is the average power supplied to a single cartridge heater and A is the nominal outer surface area of a heater tube. The shell-side heat transfer coefficient for a given heater tube was determined using the equation for Newton's Law of Cooling.

$$h_{tube} = \frac{q"}{T_{wall} - T_{ref}} \tag{3.2}$$

where T_{wall} is the average wall temperature of a given tube and T_{ref} is the refrigerant reference temperature which was determined using the following procedure. It was discovered during the course of testing that, because of the configuration of the pressure transducers, the pressure in the test section, P_{box}, was occasionally higher than that recorded before the inlet nozzles, P_{inlet}, especially during tests with a low saturation temperature, T_{sat}. For these tests, the reference temperature T_{ref} was chosen as the minimum of the measured inlet temperature, T_{inlet}, and the saturation temperature T_{sat}, which was approximated using the temperature of the saturated liquid refrigerant exiting the test section. For the majority of tests in which test section pressure was recorded as being lower than the inlet pressure, T_{ref} was determined using an isenthalpic expansion calculation in EES. This procedure is summarized in the equation below.

$$T_{ref} = \begin{cases} \min(T_{inlet}, T_{sat})\ if\ P_{box} \geq P_{inlet} \\ T_{EES}\ if\ P_{box} < P_{inlet} \end{cases} \tag{3.3}$$

The isenthalpic expansion formulation utilized in EES is detailed in Equation 3.4.

$$T_{EES} = \begin{cases} T_{EES} = T_{out} \\ T_{out} = Temperature(h_{out}, P_{box}) \\ h_{out} = h_{in} \\ h_{in} = Enthalpy(T_{inlet}, P_{inlet}) \end{cases} \tag{3.4}$$

where T_{EES} is the reference temperature calculated using the Engineering Equation Solver (EES) software, h_{out} is the enthalpy of the refrigerant after passing through the inlet nozzles, and h_{in} is the enthalpy of the refrigerant just before the inlet nozzles. Because the heater tube thermocouples were not mounted on the outside walls of the tubes but instead embedded in the walls at a finite distance from the outer surface, a correction was applied to each wall temperature measurement to account for the difference in temperature due to conduction through the tube wall. This is illustrated in the simple schematic shown in Figure 3.27.

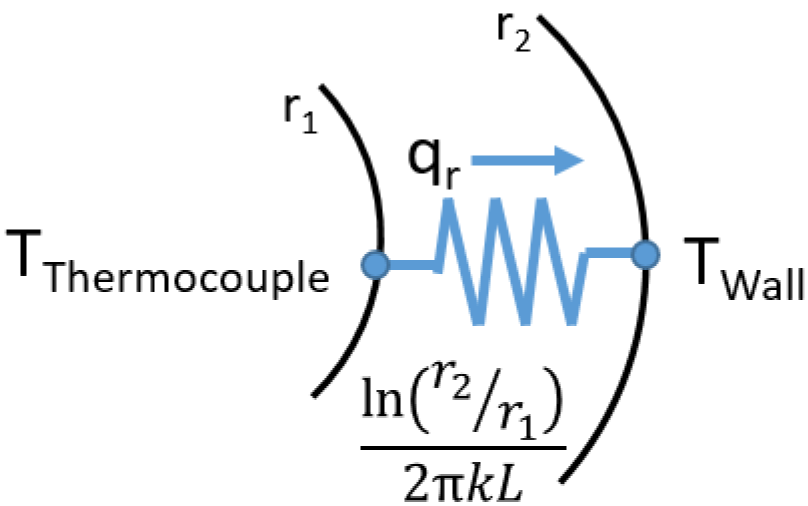

Figure 3.27: Conduction heat loss in a cylinder

As such, the quantity T_{wall} for each data point was calculated using the following formula.

$$T_{wall} = T_{Thermocouple} - \frac{Q_r ln\left({}^{r_2}/_{r_1}\right)}{2\pi k_{copper} L_{tube}} \tag{3.5}$$

where $T_{Thermocouple}$ is the temperature recorded by the embedded thermocouple, Q_r is the total heat provided by the cartridge heater in the tube, r_2 is the nominal radius of the tube outer surface, r_1 is the nominal radius of the thermocouple location within the wall, k_{copper} is the thermal conductivity of the copper wall (nominally 390 W/m-K), and L_{tube} is the nominal length of the heater tube. For heater tubes that contained more than one embedded thermocouple, the temperature T_{wall} was determined as the average of the thermocouple readings as in the following equation.

$$T_{wall} = \frac{\sum_{i=1}^{n} T_i}{n} \tag{3.6}$$

where n is the number of thermocouples embedded in a given tube. For each test, the convective heat transfer coefficient calculated for each tube is an average of all instantaneous heat transfer coefficients calculated for each data point in a test.

$$h_{tube} = \frac{\sum_{i=1}^{m} h_{instantaneous}}{m} \tag{3.7}$$

where m is the total number of data points collected during a test, usually somewhere between 900 and 1200 points for a test lasting 30 to 40 minutes. The row heat transfer coefficients for each test are the average of the individual tube heat transfer coefficients for the tubes in the given row.

$$h_{row} = \frac{\sum_{i=1}^{k} h_{i^{th}\ tube}}{k} \tag{3.8}$$

where k is the number of tubes in a row, either 2 or 3 depending on bundle configuration. The overall bundle heat transfer coefficient reported for each test is the average of the row heat transfer coefficients calculated for that test.

$$h_{bundle} = \frac{\sum_{i=1}^{j} h_{j^{th} row}}{j} \tag{3.9}$$

where the number of rows j is 5 in a full bundle test and 3 in a partial bundle test.

3.5 Uncertainty Analysis

The error analysis and uncertainty propagation procedures outlined in Taylor and Kuyatt (1994) were used to calculate the experimental uncertainty for this work using EES. The uncertainty propagation for each individual tube heat transfer coefficient is given in Equation 3.10.

$$\Delta h_{tube} = \left[\left(\frac{\partial h}{\partial q"}\Delta q"\right)^2 + \left(\frac{\partial h}{\partial T_{wall}}\Delta T_{wall}\right)^2 + \left(\frac{\partial h}{\partial T_{ref}}\Delta T_{ref}\right)^2\right]^{0.5} \tag{3.10}$$

where Δh_{tube} is the uncertainty in the calculated heat transfer coefficient for a given tube; $\partial h/\partial q''$, $\partial h/\partial T_{wall}$, and $\partial h/\partial T_{ref}$ are the partial derivatives of the heat transfer coefficient with respect to wall heat flux, tube wall temperature, and refrigerant reference temperatures, respectively; and $\Delta q''$, ΔT_{wall}, and ΔT_{ref} are the uncertainties associated with the wall heat flux, tube wall temperature, and refrigerant reference temperature, respectively. The partial derivative of the heat transfer coefficient with respect to wall heat flux is given in Equation 3.11.

$$\frac{\partial h}{\partial q''} = \frac{1}{T_{wall} - T_{ref}} \tag{3.11}$$

The uncertainty of the wall heat flux is given in Equation 3.12.

$$\Delta q'' = \frac{\Delta Q_{htr}}{A} \tag{3.12}$$

where ΔQ_{htr} is the uncertainty associated with the power provided to a single cartridge heater. This uncertainty is equal to ±6.67 W, or one-third the uncertainty associated with each AC watt transducer, which was given by the manufacturer as ±0.5% of FS (FS = 4 kW), or ±20 W. The partial derivative of the heat transfer coefficient with respect to the tube wall temperature is defined in Equation 3.13.

$$\frac{\partial h}{\partial T_{wall}} = -\frac{q''}{\left(T_{wall} - T_{ref}\right)^2} \tag{3.13}$$

The uncertainty of the wall temperature is given by Equation 3.14.

$$\Delta T_{wall} = \frac{\Delta T}{\sqrt{n}} \tag{3.14}$$

where n is the number of thermocouples embedded in a given tube and ΔT is the uncertainty associated with the embedded thermocouples, which is ±0.2 °C. It can be seen that, for tubes with only one embedded thermocouple, Equation 3.14 simplifies so that the total uncertainty associated with the average wall temperature ΔT_{wall} is equal to that of the single embedded thermocouple, or ±0.2 °C. The partial derivative of the heat transfer coefficient with respect to the reference temperature is defined in Equation 3.15.

$$\frac{\partial h}{\partial T_{ref}} = \frac{q"}{\left(T_{wall} - T_{ref}\right)^2} \tag{3.15}$$

The uncertainty of the reference temperature is given in Equation 3.16.

$$\Delta T_{ref} = \begin{cases} \Delta T_{inlet} \ if \ T_{ref} = T_{inlet} \\ \Delta T_{sat} \ if \ T_{ref} = T_{sat} \\ \Delta T_{EES} \ if \ T_{ref} = T_{EES} \end{cases} \tag{3.16}$$

where ΔT_{inlet}, ΔT_{sat}, and ΔT_{EES} are the uncertainties associated with the measured inlet temperature (±0.2 °C), the calculated saturation temperature, and the reference temperature calculated using EES as described in Equation 3.4, respectively. The uncertainties in T_{sat} and T_{EES} were functions of the uncertainties of the pressure transducers and thermocouples used to measure the quantities that were used in the calculations and therefore varied slightly with variations in measured quantities and refrigerant type. The uncertainty associated with each row heat transfer coefficient is given in Equation 3.17.

$$\Delta h_{row} = \frac{\Delta h_{tube}}{\sqrt{k}} \tag{3.17}$$

where k is the number of active tubes in a given row. Similarly, the uncertainty associated with the overall bundle heat transfer coefficient is given by Equation 3.18.

$$\Delta h_{bundle} = \frac{\Delta h_{tube}}{\sqrt{j}} \tag{3.18}$$

where j is the number of active rows in a given test. The specifications of the various instruments used in the experimental test setup, including their accuracies, are summarized in Table 3.2.

Table 3.2: Instrument specifications including associated uncertainties

Component	Manufacturer [Model] {Range} (Accuracy)
Thermocouples	Omega Engineering, Inc. [TMQSS-062G-12] {-20°C to 60°C} (±0.2°C)
Pressure Transducers	Setra [2051500PG2F2B25WNN] {0-500 psig} (±0.073% FS or 0.365 psi (2.5 kPa)) Setra [2061050PG2M11258NN] {0-50 psig} (±0.13% FS or 0.065 psi (0.45 kPa))
AC Watt Transducers	FLEX-CORE [PC5-014EY24] {0-4 kW} (±0.5% FS or 0.02 kW)
Coriolis Mass Flow Meter	Micro Motion, Inc. [CMFS025M319N2BAEKZZ] {0-17.5 kg/min} (±0.1%)

Because the uncertainties of the pressure transducers and the AC watt transducers were based on the full scales of the instruments, lower measured values had higher associated relative uncertainties. Based on uncertainty propagation calculations performed in EES, it was found that variations in experimental uncertainty due to the range of saturation pressures tested (from approximately 80 kPa to 450 kPa) were negligible. The greatest variations in uncertainty, then, were attributed to variations in wall heat flux. This variation is represented in Figure 3.28.

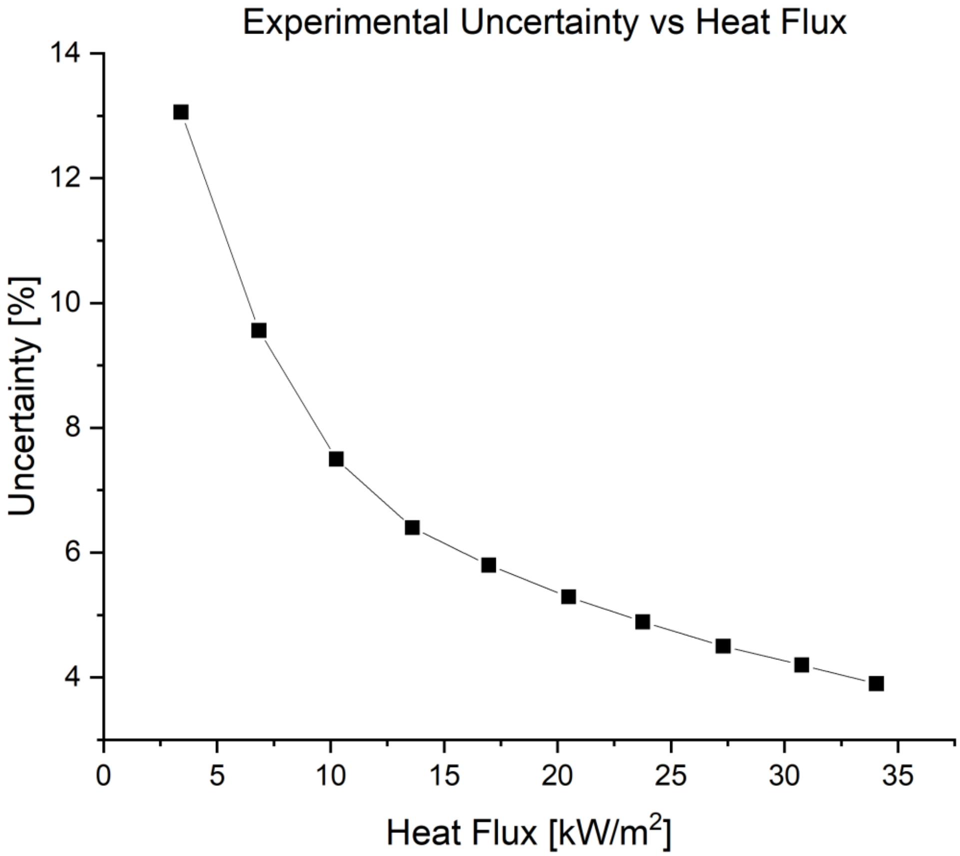

Figure 3.28: Experimental uncertainty in bundle heat transfer coefficient vs applied heat flux

As shown, experimental uncertainty in the overall bundle heat transfer coefficient decreased as wall heat flux increased, ranging from just over 13% for wall heat fluxes below 5 kW/m^2 to just under 4% for wall heat fluxes nearing 35 kW/m^2. For this reason, greater emphasis was placed on higher heat flux tests during experimentation.

Chapter 4: Results and Discussion

The experimental test results and discussion of the findings are presented in this chapter. The experimental campaign for this project consisted of five main phases characterized by spray nozzle type, tube enhanced surface type, and tube bundle configuration. Each phase included the use of at least two and at most three different refrigerants, each of which was tested at different saturation temperatures and various degrees of inlet subcooling. Phase 1 consisted of the use of the Tube-C condenser tubes in the triangular configuration with the circular cone spray nozzles. In Phase 2, the Tube-C condenser tubes were arranged in the square configuration with the circular cone nozzles. For Phase 3, the same triangular configuration as in Phase 1 was utilized with the second set of heater tubes, the Tube-B evaporator tubes. For Phase 4, the Tube-B evaporator tubes were used in the same square configuration from Phase 2. The circular cone nozzles were used for Phases 3 and 4, as well. All three refrigerants, R134a, R1234ze(E), and R1233zd(E), were tested in Phases 1, 2, 3, and 4. Phase 5 consisted of the use of the Tube-C condenser tubes in the same triangular configuration as Phases 1 and 3, but with the deflected flat spray nozzles. This was the only phase to utilize the flat spray nozzles as it was desired to use the circular full cone nozzles for the majority of the experimental campaign and for correlation development. Only two refrigerants, R134a and R1234ze(E), were tested in Phase 5. Many tests were conducted in which all or only some of the heater tubes were utilized, and these configurations included "full bundle" tests, "partial bundle" tests, "three tube" tests, and "single tube" tests. These various levels of utilization were achieved by powering either all or only some of the electric resistance heaters in the bundle according to the desired test conditions, and the configurations were different depending on bundle geometry. The two bundle geometries with color-coded tube rows and numbered tubes are represented in Figure 4.1.

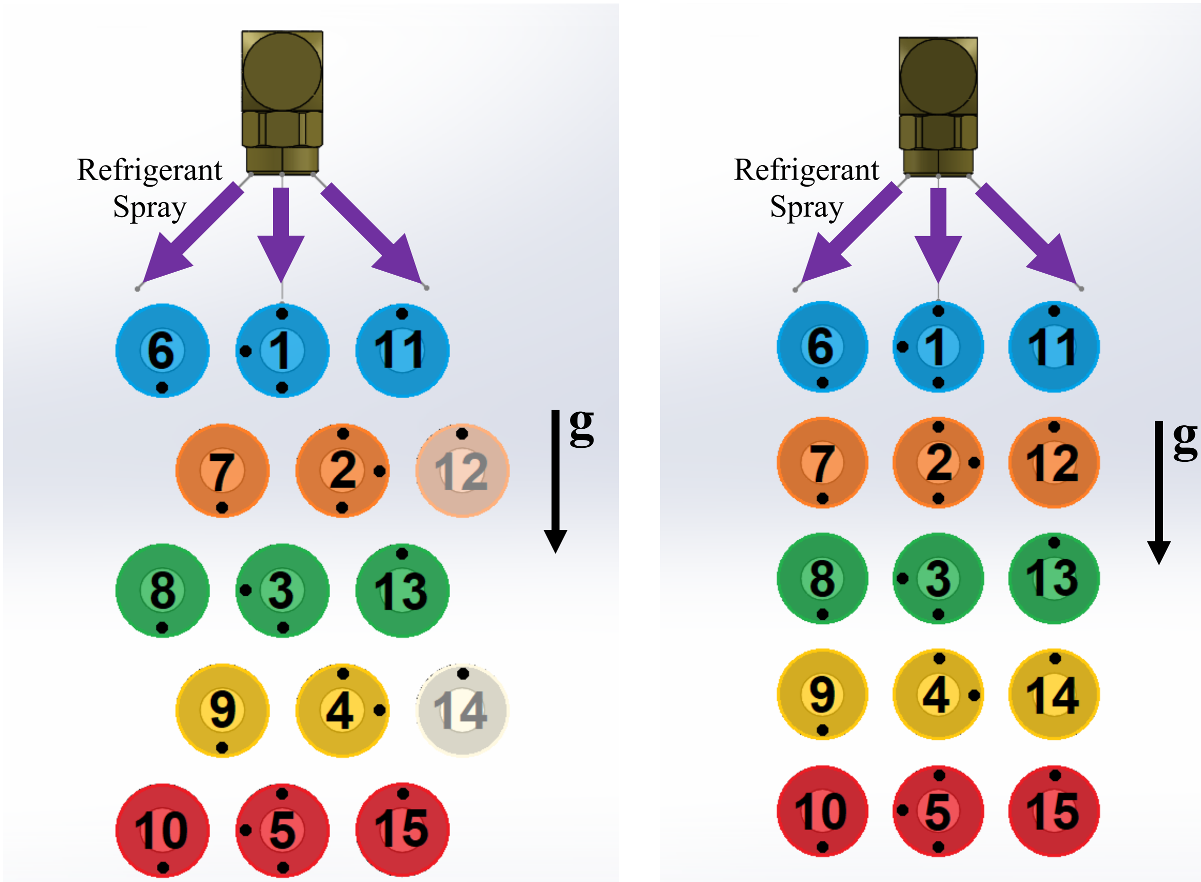

Figure 4.1: Triangular (left) and Square (right) bundle configurations

For full bundle tests in the triangular geometry, all tubes except numbers 12 and 14 were heated for a total of thirteen operating tubes. For full bundle tests in the square geometry, all fifteen tubes were heated. For partial bundle tests in both the triangular and square geometries, only the tubes in Rows 1, 3, and 5 (meaning Tubes 1, 3, 5, 6, 8, 10, 11, 13, and 15) were heated for a total of nine operating tubes. For the three tube tests in both geometries, only the tubes in Row 5 (meaning Tubes 5, 10, and 15) were heated. All single tube tests utilized only a single tube heater either in the Tube 1 (top row, middle tube) or Tube 5 (bottom row, middle tube) location. Though most tests were conducted in the spray evaporation mode with minimal liquid refrigerant present in the bottom of the test section, some pool boiling tests were conducted in both the single tube (Tube 5) and three tube (Row 5) configurations in which the bottom row of tubes was completely submerged in a pool of liquid refrigerant. These pool boiling tests will be referred to as "Flooded Tests" in the results. All results presented are spray evaporation tests unless otherwise noted. Generally, the results will be separated by experimental phase, refrigerant type, and saturation temperature.

4.1 Phase 1 Results

The experimental test results for Phase 1 using the Tube-C condenser tubes in the triangular geometry with the full circular cone nozzles are presented in Figures 4.2 through 4.13. For Phase 1, refrigerant R134a was tested in the single tube, three tube, partial bundle, and full bundle configurations at saturation temperatures of approximately 10 °C, 2 °C, and -6 °C. The R134a results are shown in Figures 4.2, 4.3, 4.4, 4.5, and 4.6. Refrigerant R1234ze(E) was tested in both partial bundle and full bundle configurations at saturation temperatures of approximately 10 °C, 3 °C, and -8.5 °C, and these results are shown in Figures 4.8, 4.9, 4.10, 4.11, and 4.12. Also, refrigerant R1233zd(E) was tested at a saturation temperatures between 9 °C and 13 °C, shown in Figure 4.13.

For the R134a tests in Phase 1, refrigerant mass flow rate was varied between 3.25 kg/min and 4.61 kg/min, and inlet subcooling was varied between 0.5 °C and 2.5 °C. Phase 1 was the first phase in which flooded tests were performed with any refrigerant. For the single tube flooded tests with R134a, tube heat transfer coefficients varied between 0.4 kW/m^2-K and 14.1 kW/m^2-K for heat fluxes between 1 kW/m^2 and 39 kW/m^2. For the three tube flooded tests, Row 5 heat transfer coefficients varied between 3.0 kW/m^2-K and 12.9 kW/m^2-K for heat fluxes between 3 kW/m^2 and 38 kW/m^2. For all flooded tests, heat transfer coefficients increased steadily with an increase in heat flux as shown in Figures 4.2 and 4.3. This behavior was to be expected based on prior knowledge of nucleate boiling phenomena and correlations developed to characterize such

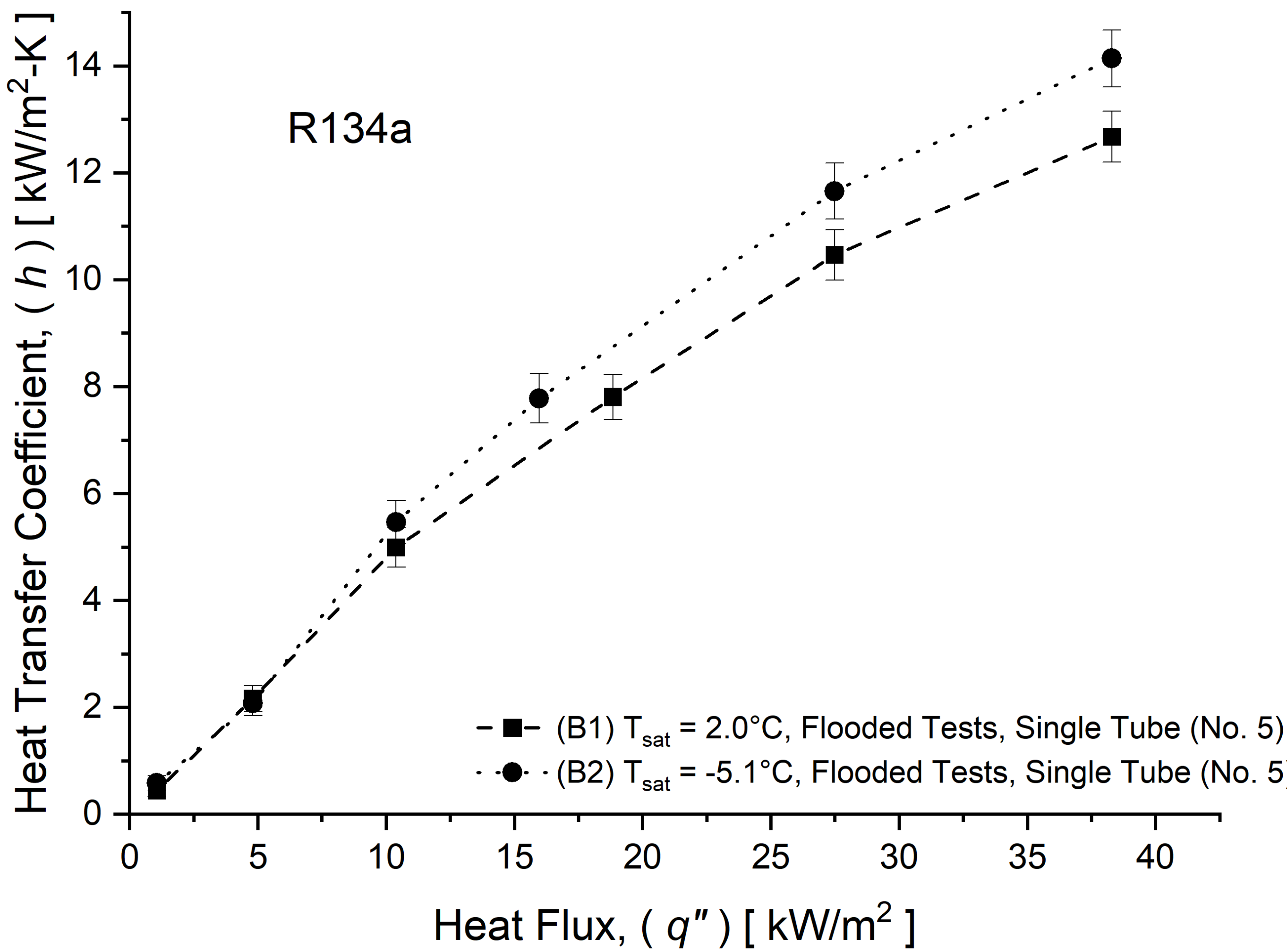

Figure 4.2: Heat transfer coefficient vs heat flux (Phase 1, R134a, single tube flooded tests)

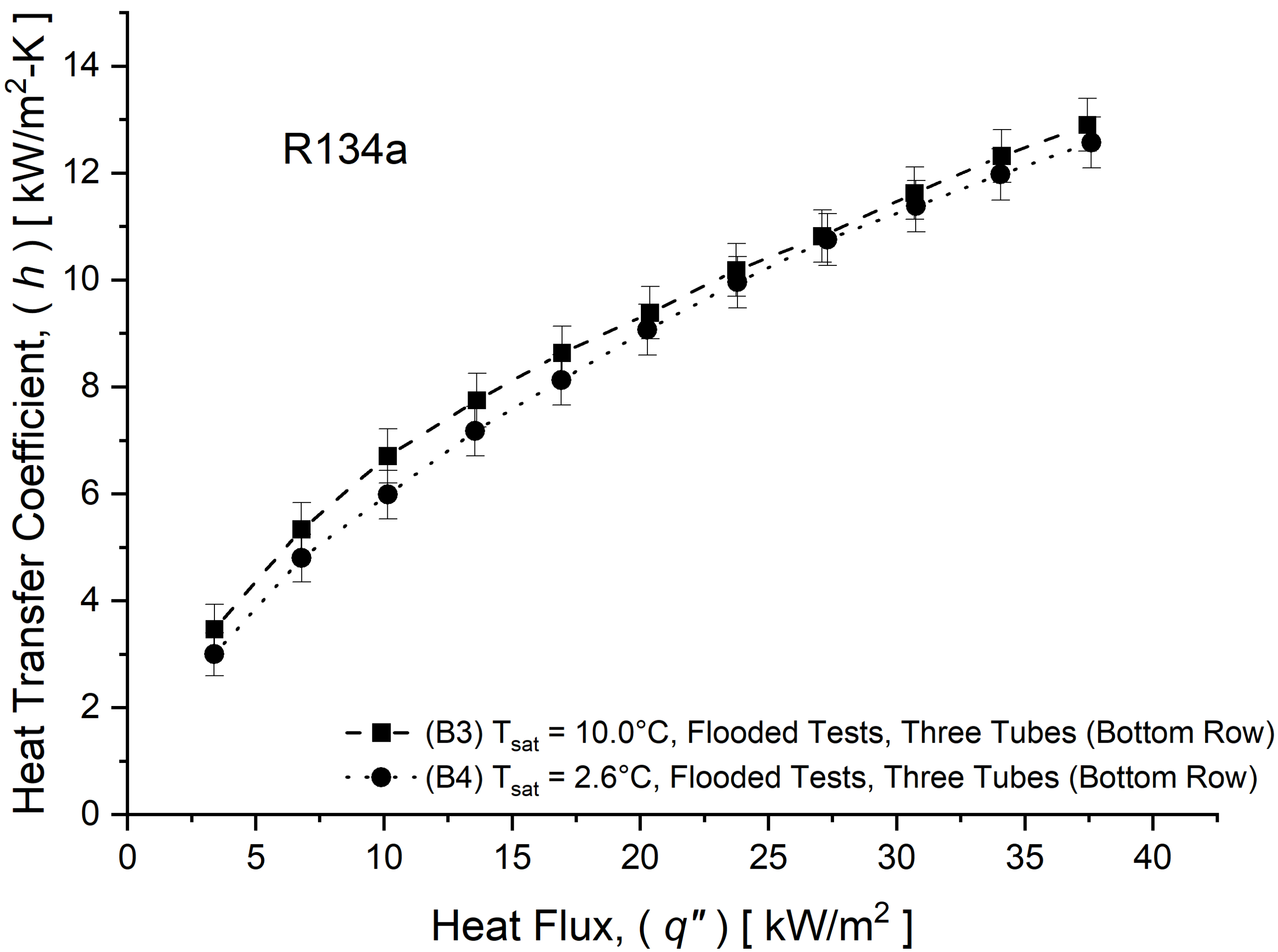

Figure 4.3: Heat transfer coefficient vs heat flux (Phase 1, R134a, three tube flooded tests)

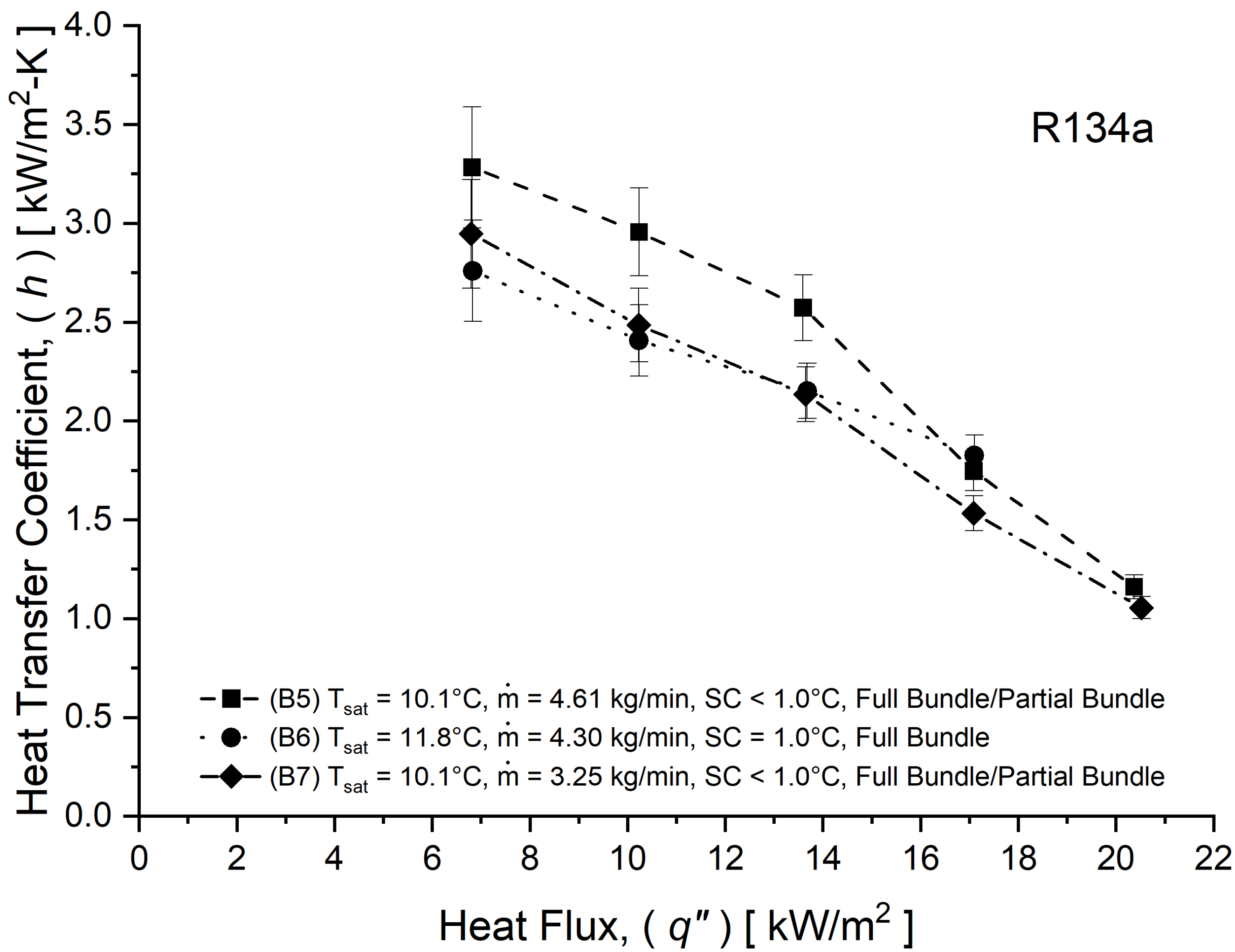

Figure 4.4: Heat transfer coefficient vs heat flux (Phase 1, R134a, T_{sat} = 10 °C)

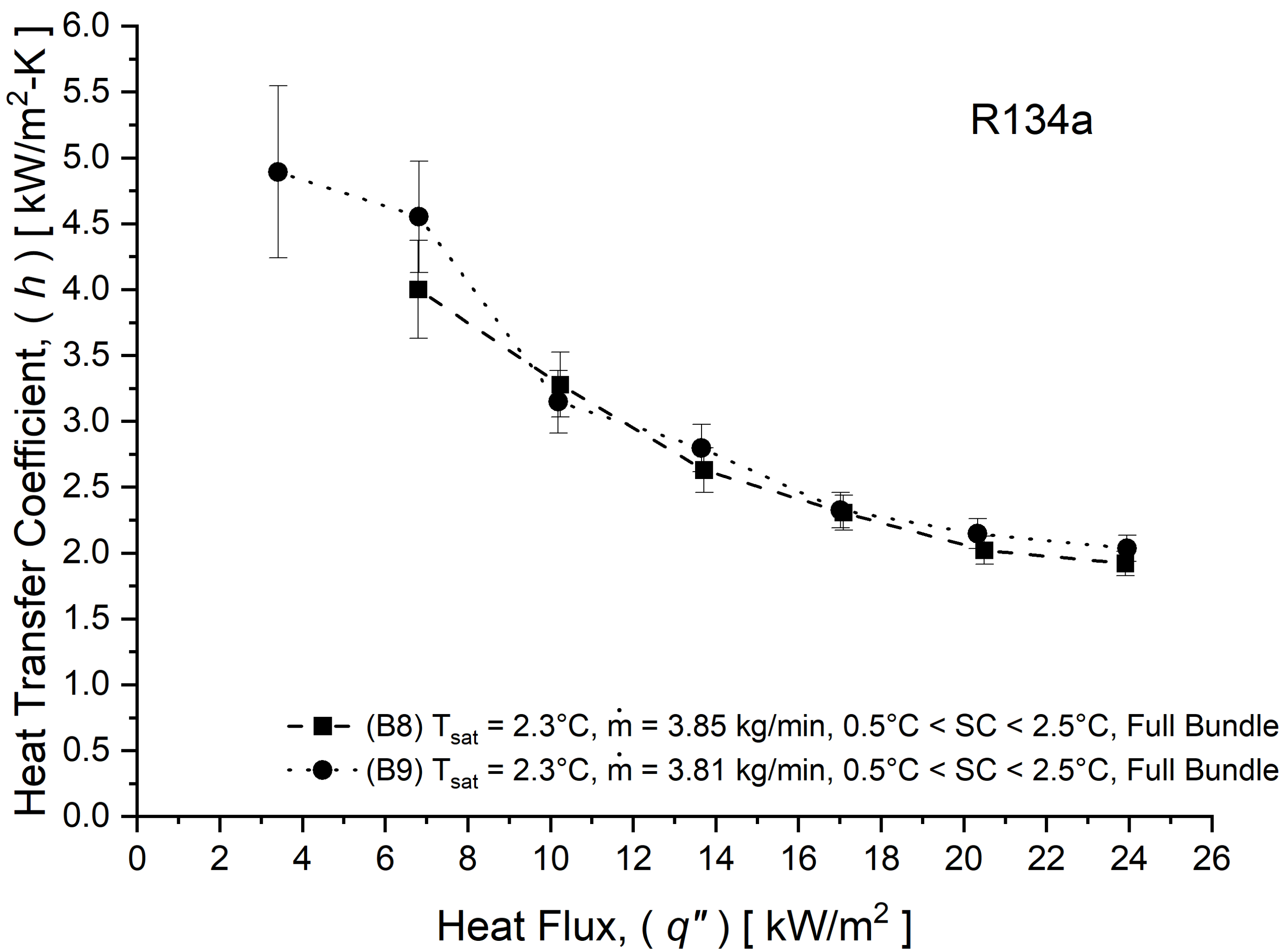

Figure 4.5: Heat transfer coefficient vs heat flux (Phase 1, R134a, T_{sat} = 2 °C)

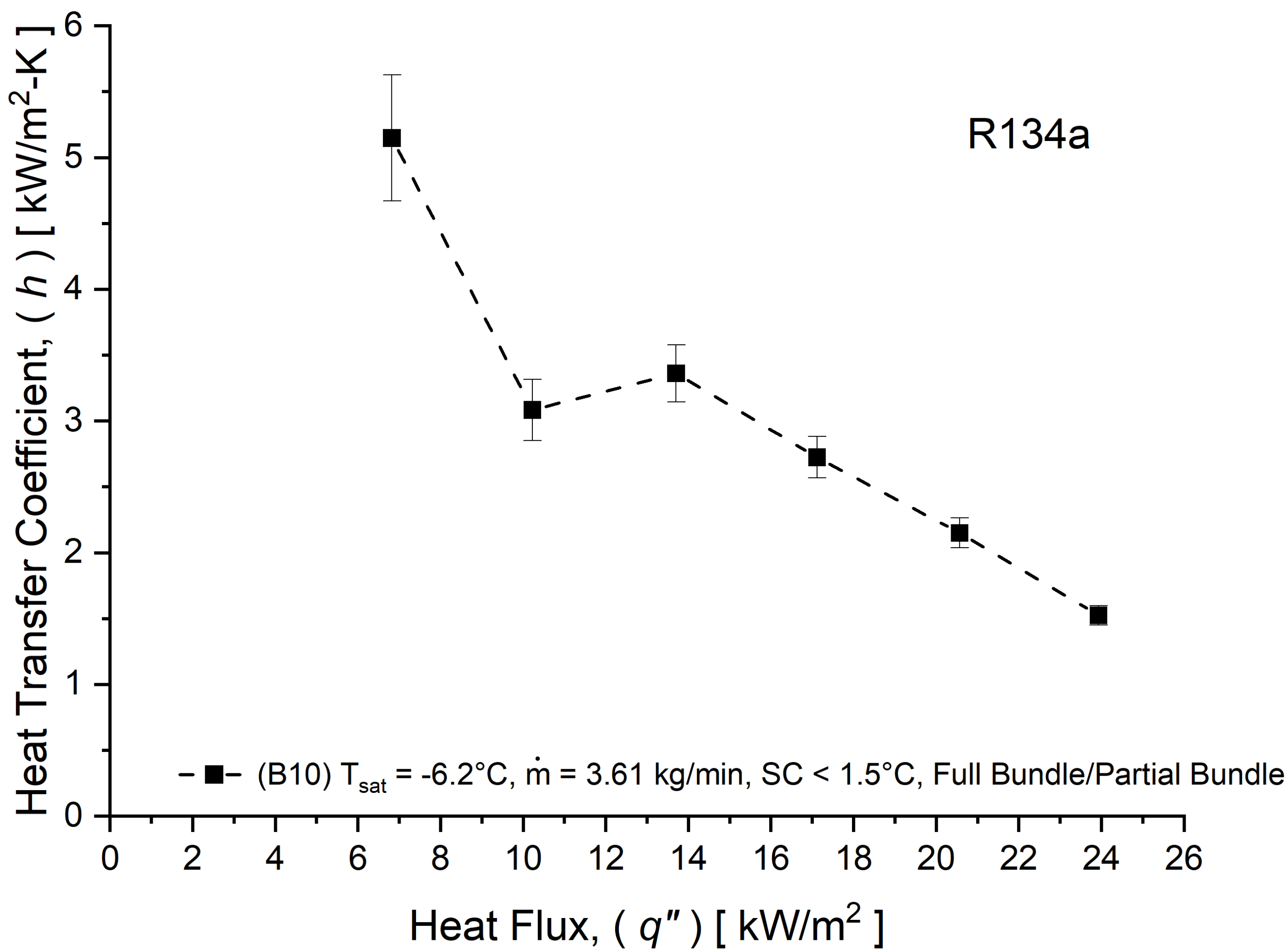

Figure 4.6: Heat transfer coefficient vs heat flux (Phase 1, R134a, T_{sat} = -6 °C)

phenomena. There was no significant dependence of heat transfer coefficients on refrigerant saturation temperature to be observed in these data. Bundle heat transfer coefficients for the 10 °C series varied between 1.1 kW/m^2-K and 3.3 kW/m^2-K for heat fluxes between 6 kW/m^2 and 21 kW/m^2. Those for the 2 °C series varied between 1.9 kW/m^2-K and 4.9 kW/m^2-K for heat fluxes between 2 kW/m^2 and 29 kW/m^2. Those for the -6 °C series varied between 1.5 kW/m^2-K and 5.1 kW/m^2-K for heat fluxes between 5 kW/m^2 and 24 kW/m^2. All of the series performed in the spray evaporation regime with R134a exhibited a steady decrease in bundle heat transfer coefficient with an increase in heat flux. This behavior was caused by a phenomenon known as "dryout," in which liquid refrigerant was partially evaporated and perhaps deflected by the upper rows of tubes in the bundle such that very little or, in some cases, no liquid refrigerant reached the bottommost row of tubes. This phenomenon was examined by plotting the row-by-row heat transfer coefficients for a representative series, B9, as shown in Figure 4.7.

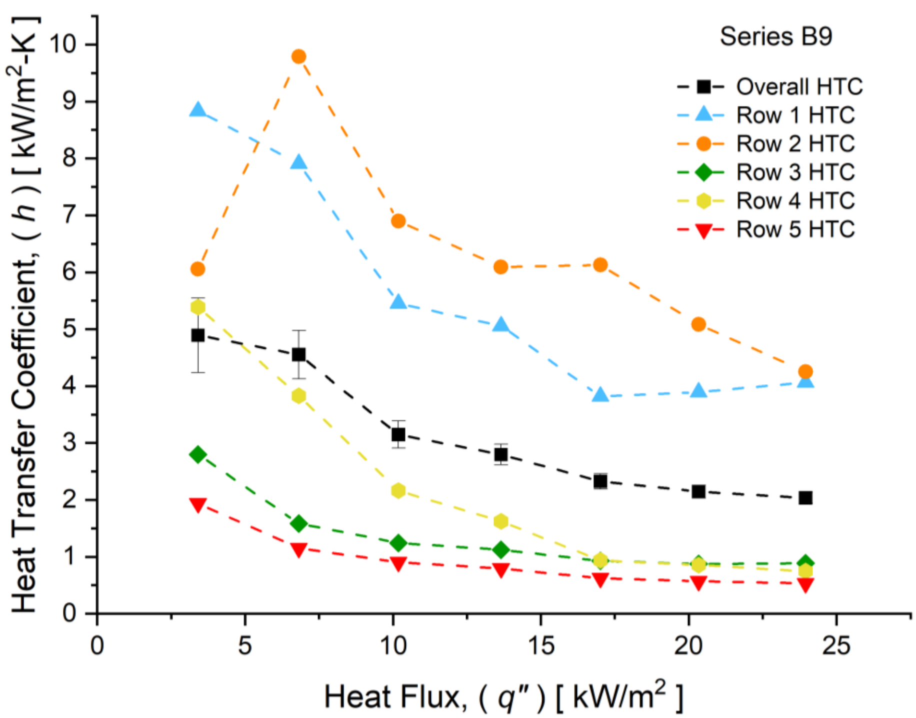

Figure 4.7: Row-by-row heat transfer coefficients vs heat flux, Series B9

It was observed that, for the majority of the series, the Row 2 heat transfer coefficient was the highest, followed by those for Row 1, Row 4, Row 3, and Row 5, in that order. The heat transfer coefficient for Row 2 was the highest in the bundle likely because, in the triangular bundle geometry, the tubes in Row 2 were mostly unobstructed by those in Row 1 and therefore received a steady supply of liquid refrigerant directly from the nozzles in addition to some extra liquid refrigerant that was deflected to Row 2 by the tubes in Row 1. It may also be expected that the Row 3 heat transfer coefficient should have been generally higher than that of Row 4, though that was not the case in this series. Because Row 2 contained only two heated tubes in this bundle geometry versus three heated tubes in Row 1, the tubes in Row 4 received a greater supply of liquid refrigerant dripping from Row 2 directly above than those in Row 3 received from Row 1. However, this effect was only noticed at low heat fluxes as the heat transfer coefficients for the lower Rows 3, 4, and 5 dropped to very low and nearly equal values at higher heat flux levels. These extremely low heat transfer coefficients of the lower tube rows most likely indicate a significantly decreased refrigerant supply to these rows at higher heat fluxes consistent with the dryout condition. It is because of these lower heat transfer coefficients that the overall bundle heat transfer coefficient decreased with increasing heat flux.

For the R1234ze(E) tests in Phase 1, refrigerant mass flow rate was varied between 2.08 kg/min and 6.83 kg/min, and inlet subcooling was varied between 0.3 °C and 2.4 °C. Bundle heat transfer coefficients for the 10 °C series varied between 1.0 kW/m^2-K and 9.1 kW/m^2-K for heat fluxes between 3 kW/m^2 and 30 kW/m^2. Those for the 3 °C series varied between 1.2 kW/m^2-K and 11.7 kW/m^2-K for heat fluxes between 3 kW/m^2 and 33 kW/m^2. Those for the -8.5 °C series varied between 1.0 kW/m^2-K and 6.2 kW/m^2-K for heat fluxes between 6 kW/m^2 and 24 kW/m^2. Contrary to the trends observed in the Phase 1 R134a tests, these Phase 1 R1234ze(E) tests were such that most series exhibited either a plateau or an increase in heat transfer coefficient with an increase in heat flux. A general increase in heat transfer coefficient with increasing heat flux was readily apparent in series B11. Though the heat transfer coefficient values were low (between 1.5 kW/m^2-K and 3.5 kW/m^2-K) due to the high degree of subcooling (2.3 °C), the high mass flow rate of 6.83 kg/min and the extremely low heat flux levels below 11 kW/m^2 meant that the entire series was performed in the regime before the onset of dryout. Among the series that exhibited a plateau or slight decrease in heat transfer coefficient were B14, B17, B22 and B23. Series B14 and B23 were extremely similar in terms of refrigerant mass flow rate (2.30 kg/min and 2.57 kg/min, respectively) and inlet subcooling (0.7 °C), and both series returned bundle heat transfer coefficient values between 1 kW/m^2-K and 2 kW/m^2-K within a difference of 0.5 kW/m^2-K at similar heat flux levels. These relatively low heat transfer coefficients were likely the result of the low refrigerant mass flow rates for both series, and the closeness of the values supports the observation that the bundle heat transfer coefficient for this configuration showed little correlation with refrigerant saturation temperature. Series B22, performed with similar subcooling (0.8 °C) exhibited larger values of bundle heat transfer coefficient between 5 kW/m^2-K and 6 kW/m^2-K due to a higher flow rate of 3.96 kg/min. Of the four, the highest bundle heat transfer coefficients were observed for Series B17 due to a combination of low subcooling (0.3 °C), high refrigerant mass flow rate (5.36 kg/min), and moderate heat flux levels (below 18 kW/m^2). Among the series where the dryout phenomenon was most readily apparent were Series B12, B13, B21, and B25. For both Series B12 and B13, a sharp decrease in bundle heat transfer coefficient was observed above 23 kW/m^2-K, while in Series B21 and B25, a more moderate decrease was observed above approximately 20 kW/m^2-K. Series B21, in concert with Series B15, B16, B24, B26, and B27, are excellent examples of series that exhibited the dryout phenomenon in a different manner. In all of

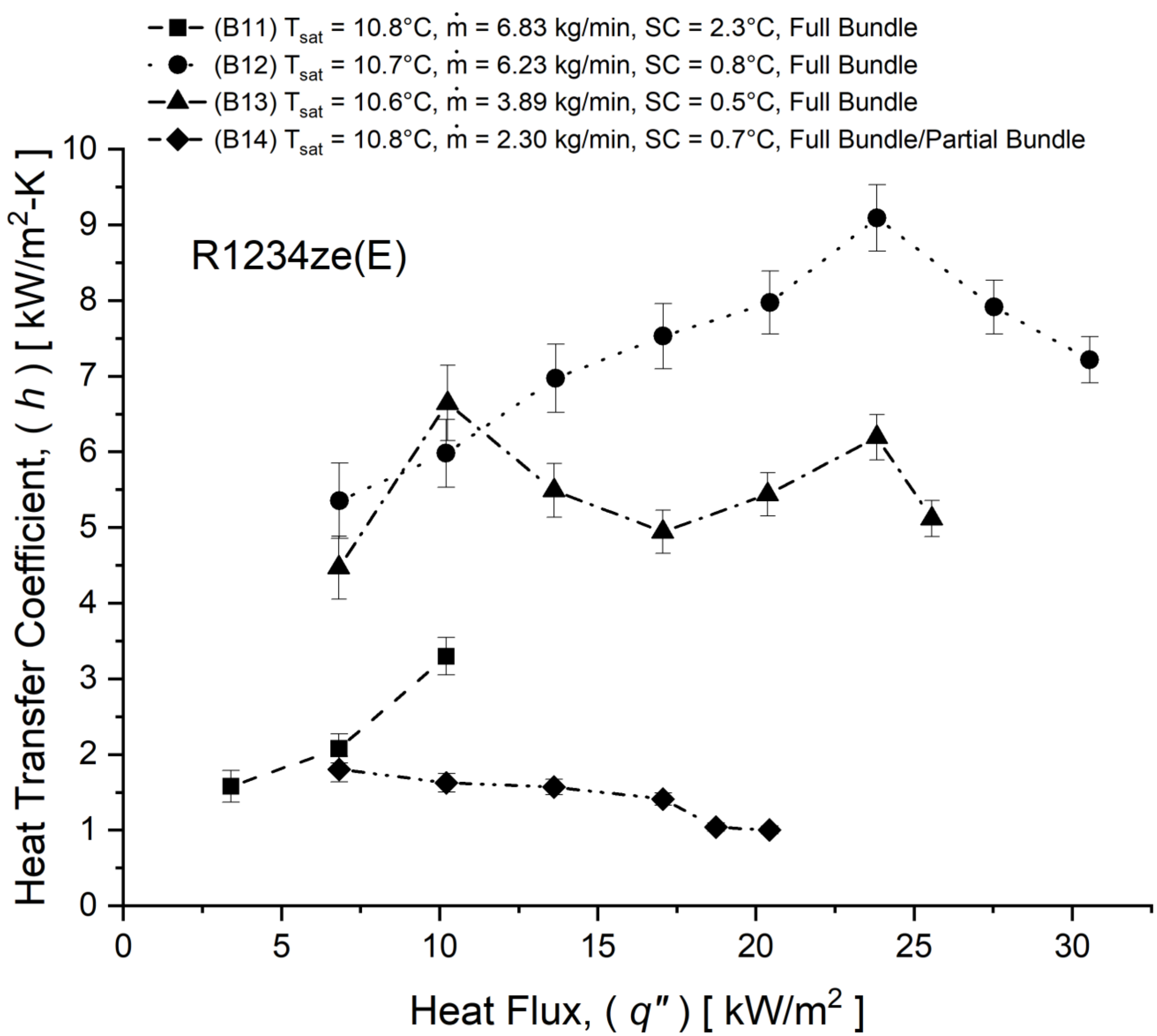

Figure 4.8: Heat transfer coefficient vs heat flux (Phase 1, R1234ze(E), T_{sat} = 10 °C)

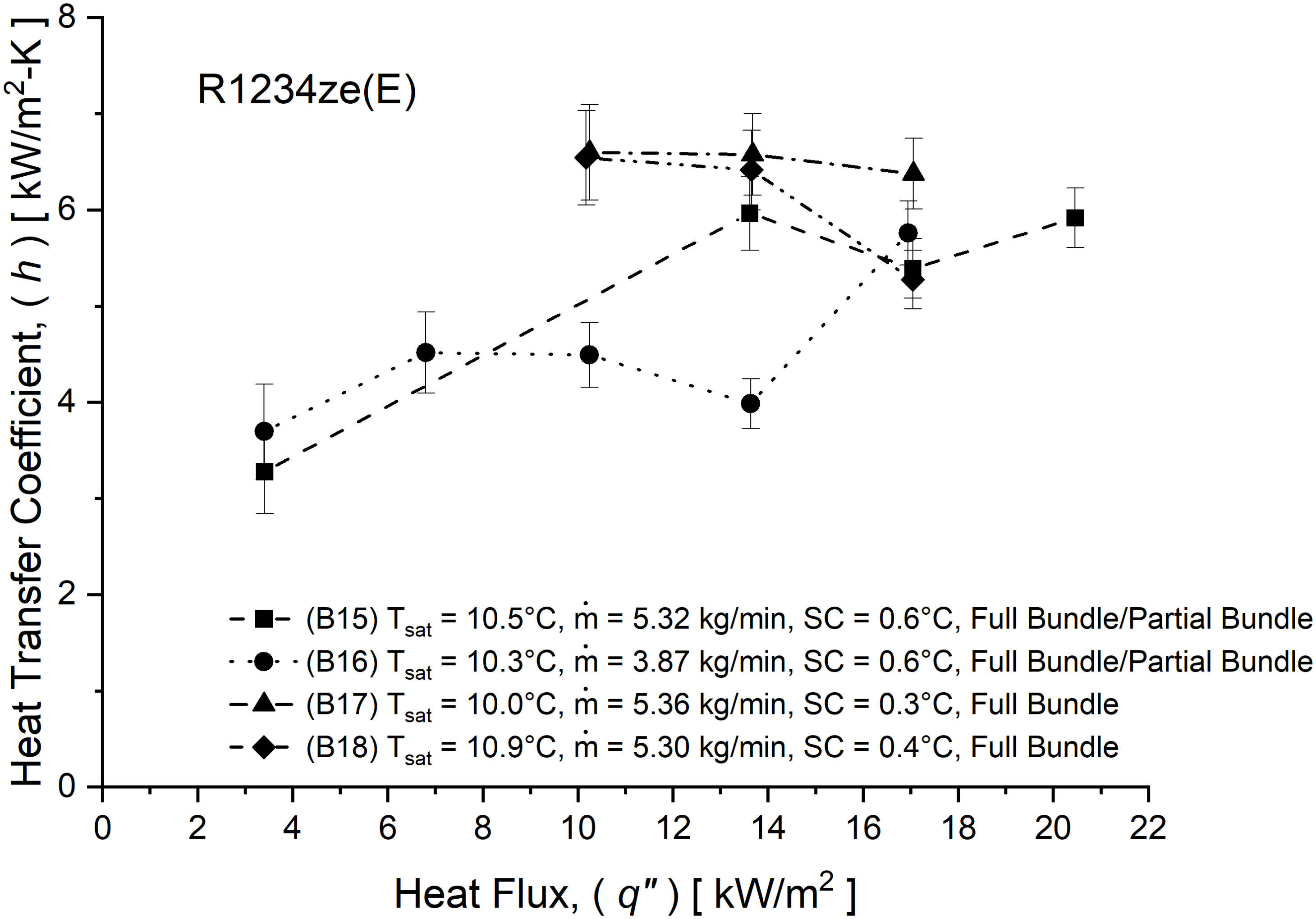

Figure 4.9: Heat transfer coefficient vs heat flux (Phase 1, R1234ze(E), T_{sat} = 10 °C)

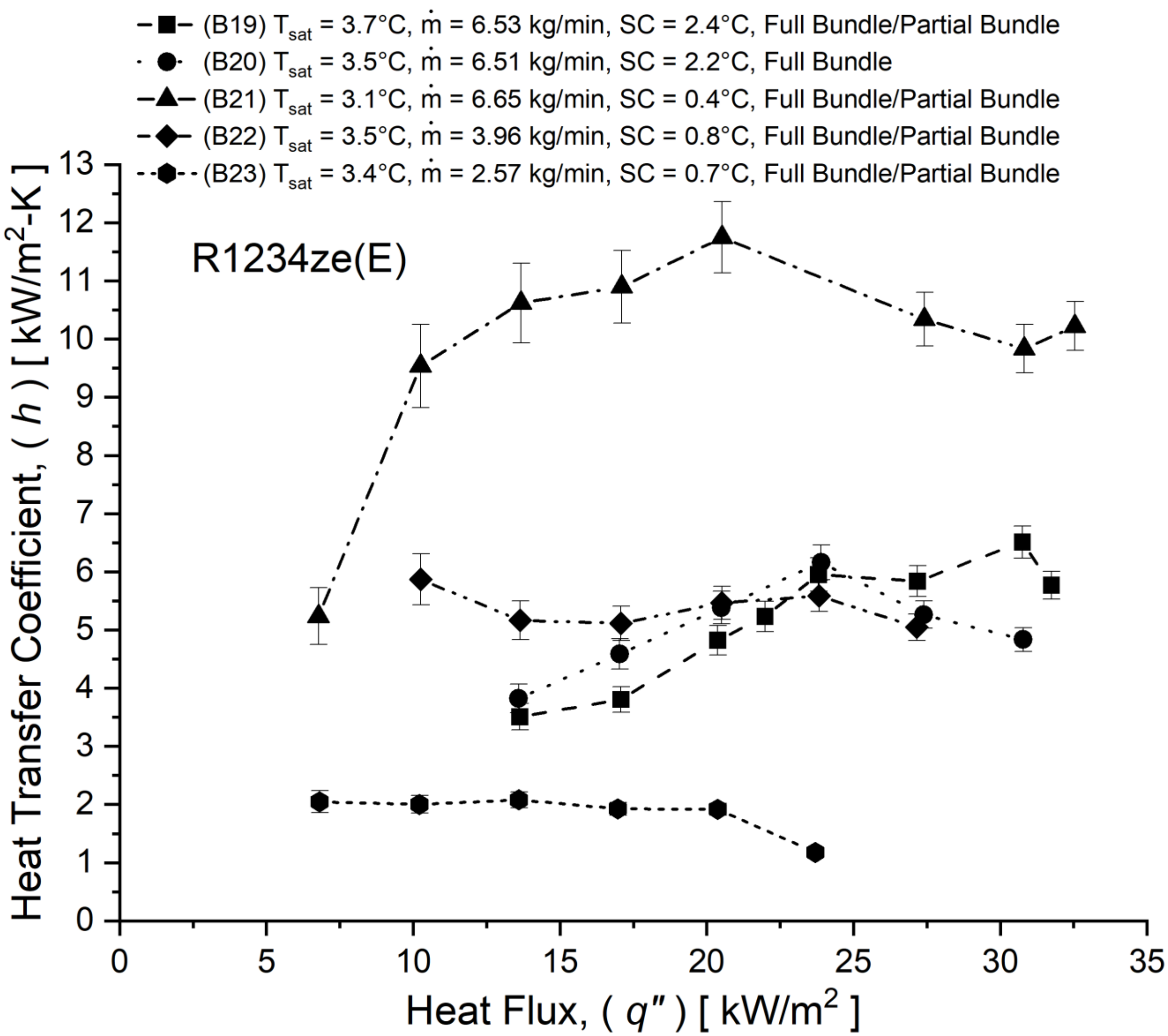

Figure 4.10: Heat transfer coefficient vs heat flux (Phase 1, R1234ze(E), T_{sat} = 3 °C)

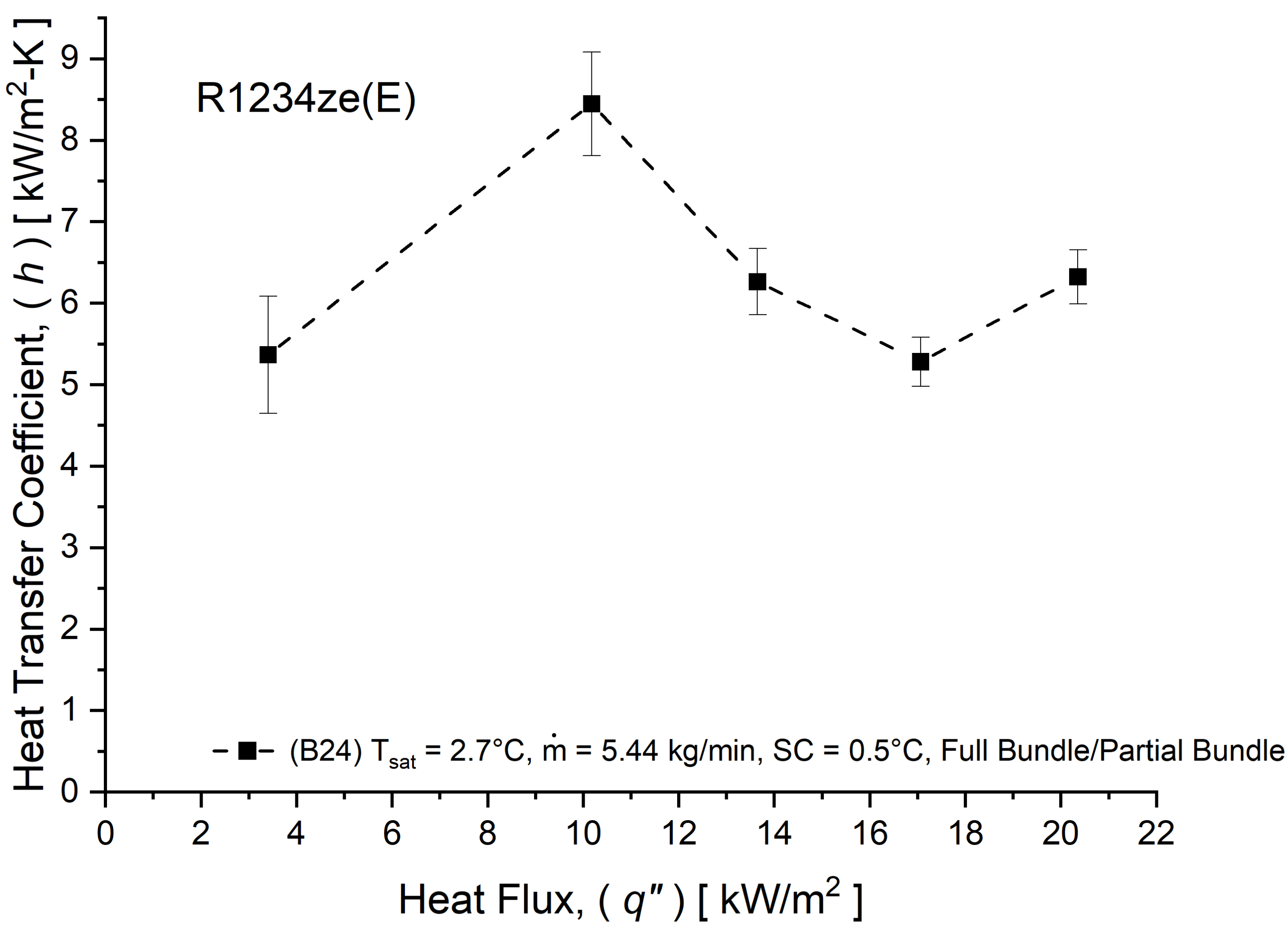

Figure 4.11: Heat transfer coefficient vs heat flux (Phase 1, R1234ze(E), T_{sat} = 3 °C)

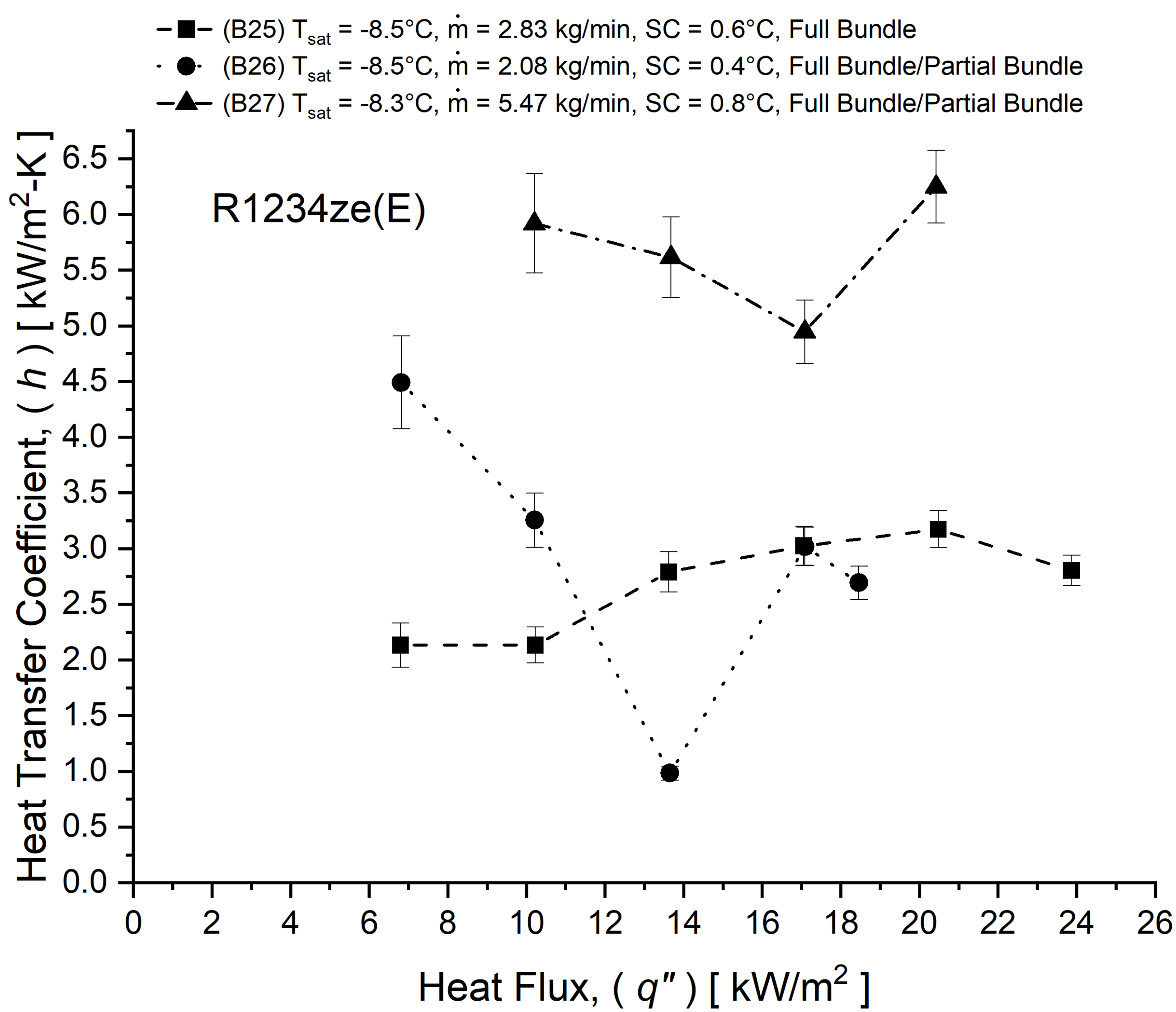

Figure 4.12: Heat transfer coefficient vs heat flux (Phase 1, R1234ze(E), T_{sat} = -8.5 °C)

the aforementioned series, an increase in heat transfer coefficient was observed at low heat fluxes which is consistent with conventional spray evaporation, followed by a decrease with increasing heat flux representing the onset of dryout, followed by a sharp increase for the single test at the highest heat flux. This sharp increase at the end of the series was due to the transition from the full bundle configuration to the partial bundle configuration in which only the last test was performed with the partial bundle. This change in configuration constituted by a decrease in the number of active tubes, specifically the deactivation of all tubes in Rows 2 and 4, meant a decrease in the total amount of heat input from the tube bundle to be transferred to the evaporating refrigerant. As a result, less liquid refrigerant was evaporated towards the top of the bundle so that more could reach the lower rows, thus increasing the bundle heat transfer coefficient and effectively delaying the onset of the dryout condition.

For the R1233zd(E) tests in Phase 1, refrigerant mass flow rate was varied between 1.53 kg/min and 3.26 kg/min, and inlet subcooling was varied between -0.5 °C and 12.1 °C. Bundle heat transfer coefficients varied between 0.9 kW/m^2-K and 5.6 kW/m^2-K for heat fluxes between 3 kW/m^2 and 21 kW/m^2. The only R1233zd(E) series to exhibit a plateau in bundle heat transfer coefficient was B29, in which inlet subcooling increased from 0.3 °C at the lowest heat flux of 7 kW/m^2 to 12.1 °C at the highest heat flux of 17 kW/m^2. This increase in subcooling with increasing heat flux was the largest contributing factor in keeping the bundle heat transfer coefficient nearly constant throughout the series. Lower refrigerant enthalpy at the inlet to the test section meant an increase in sensible heat of the refrigerant in addition to the ever-present latent heat. The result was an increase in simple convective heat transfer over the tubes in the upper rows and more liquid refrigerant available to the lower rows for evaporation than would otherwise be the case at a similar heat flux with a lesser degree of subcooling. Because of this effect, the plateau in heat transfer

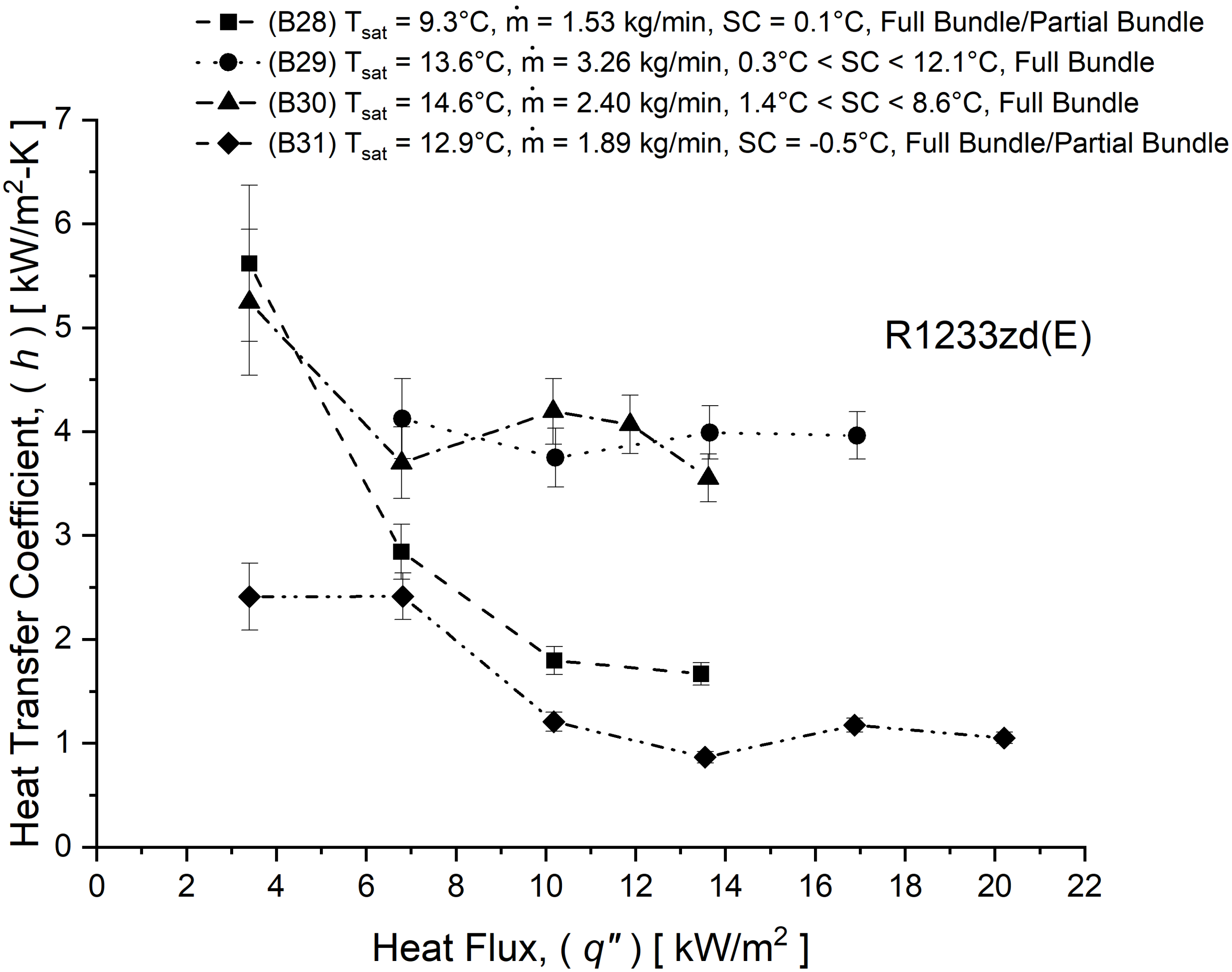

Figure 4.13: Heat transfer coefficient vs heat flux (Phase 1, R1233zd(E), 9 °C < T_{sat} < 15 °C)

coefficients was achieved at the expense of much higher potential heat transfer coefficients at high heat fluxes which could have been achieved with lesser degrees of subcooling at a higher refrigerant mass flow rate. A similar effect was observed in Series B30 in which subcooling was increased with increasing heat flux, though to a lesser degree such that the onset of the dryout condition was not fully compensated by the increase in refrigerant sensible heat. Series B29 and B31 demonstrated the effects of maintaining low or even no subcooling with low mass flow rates throughout the series, resulting in significantly lower bundle heat transfer coefficients especially at higher heat fluxes.

4.2 Phase 2 Results

The experimental test results for Phase 2, using the Tube-C condenser tubes in the square geometry with the full circular cone nozzles, are presented in Figures 4.14 through 4.31. For Phase 2, refrigerant R134a was tested in the single tube and full bundle configurations at saturation temperatures of approximately 10 °C and 2.5 °C. The R134a results are shown in Figures 4.14, 4.15, and 4.16. Refrigerant R1234ze(E) was tested in single tube, three tube, and full bundle configurations at saturation temperatures of approximately 10 °C, 2.5 °C, -6.5 °C, and -12 °C, and these results are shown in Figures 4.17 through 4.27. Also, refrigerant R1233zd(E) was tested in single tube, three tube, partial bundle, and full bundle configurations at saturation temperatures between 15 °C and 20 °C, shown in Figures 4.28 through 4.31.

For the R134a tests in Phase 2, refrigerant mass flow rate was varied between 4.25 kg/min and 6.07 kg/min, and inlet subcooling was varied between -0.6 °C and 2.1 °C. Phase 2 was the first phase in which single tube tests were performed in both pool boiling (flooded) and spray evaporation configurations. For the single tube tests with R134a, tube heat transfer coefficients varied between 3.0 kW/m^2-K and 11.9 kW/m^2-K for heat fluxes between 6 kW/m^2 and 35 kW/m^2. Bundle heat transfer coefficients for the 10 °C series varied between 1.6 kW/m^2-K and 4.8 kW/m^2-K for heat fluxes between 6 kW/m^2 and 17 kW/m^2. Those for the 3 °C series varied between 1.5 kW/m^2-K and 4.5 kW/m^2-K for heat fluxes between 3 kW/m^2 and 21 kW/m^2. For this bundle geometry, it was desired to perform single tube and three tube tests beyond the standard flooded tests in Phase 1 to highlight the differences in heat transfer coefficient recorded in different locations in the tube bundle. For the single tube flooded tests using Tube 5 in the bottom row, heat transfer coefficients increased steadily with increasing heat flux as expected, and the values were within ±20% of those observed in the similar Series B1 and B2 from Phase 1. However, in the single tube tests for Tube 1 and Tube 5 (Series C2 and C3, respectively), heat transfer coefficients showed a steady decrease with an increase in heat flux mostly due to the lack of inlet subcooling at the test section inlet. The saturated inlet condition meant that the tube wall temperatures could increase such that the difference between the wall temperatures and the refrigerant reference temperature grew more quickly than the heat flux, resulting in a net decrease in heat transfer coefficient. Of note is that the single tube heat transfer coefficients calculated for Tube 5 at the bottom of the bundle were between 10% and 50% lower than those calculated for Tube 1 at similar heat fluxes, which was well outside the experimental uncertainty. This difference was due to what will be known as the "bundle effect," wherein even when a given tube is the only one to be heated in a bundle, the supply of refrigerant to the tube is influenced significantly by bundle geometry and the tube's position within the bundle. In this case, Tube 1 was able to receive a direct supply of liquid refrigerant from the nozzles positioned directly above the bundle, whereas Tube 5 received a lesser supply at the same nominal flow rate and inlet subcooling condition due to deflection and dispersal of refrigerant by the upper tube rows. Based on these observations, the

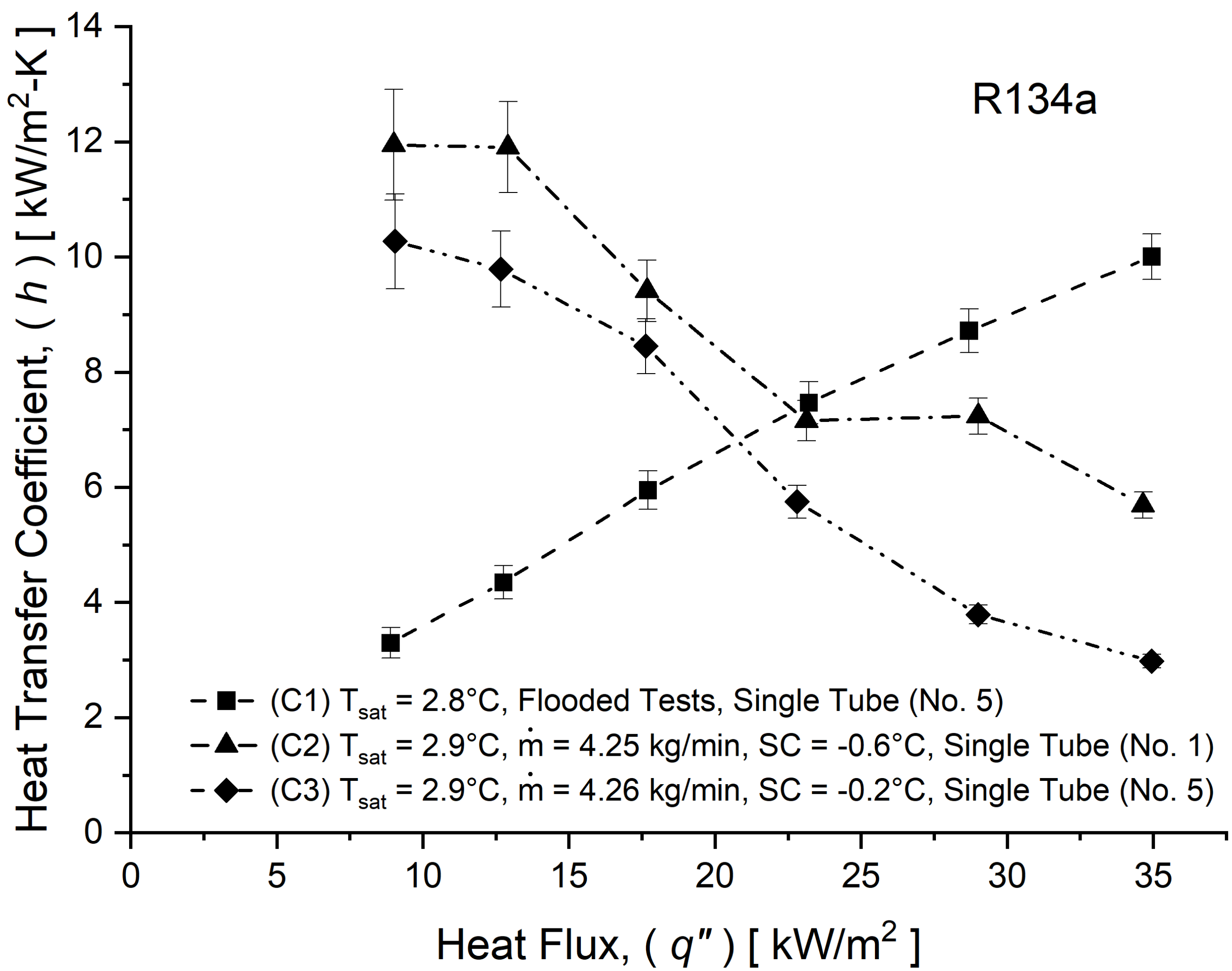

Figure 4.14: Heat transfer coefficient vs heat flux (Phase 2, R134a, single tube tests)

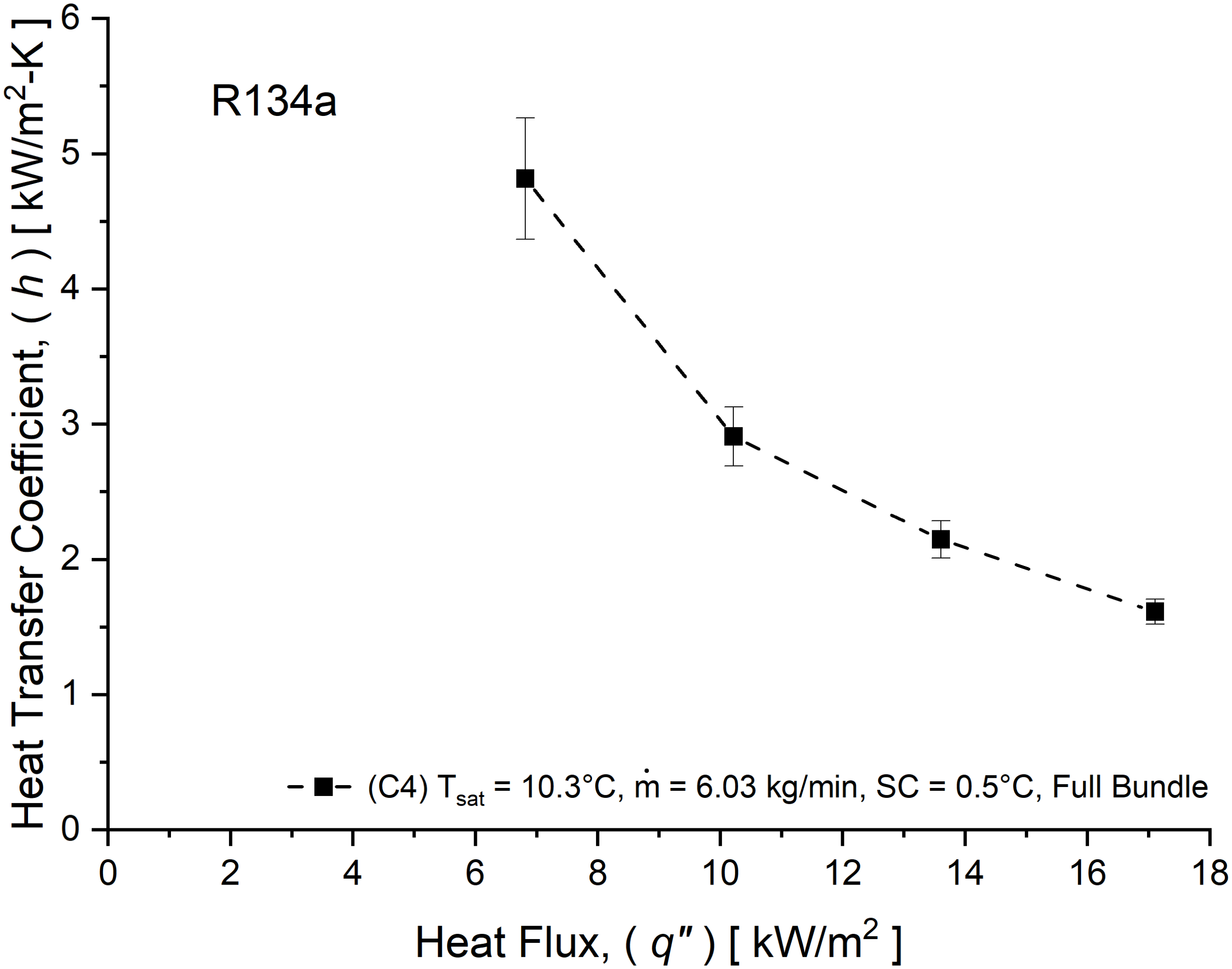

Figure 4.15: Heat transfer coefficient vs heat flux (Phase 2, R134a, T_{sat} = 10 °C)

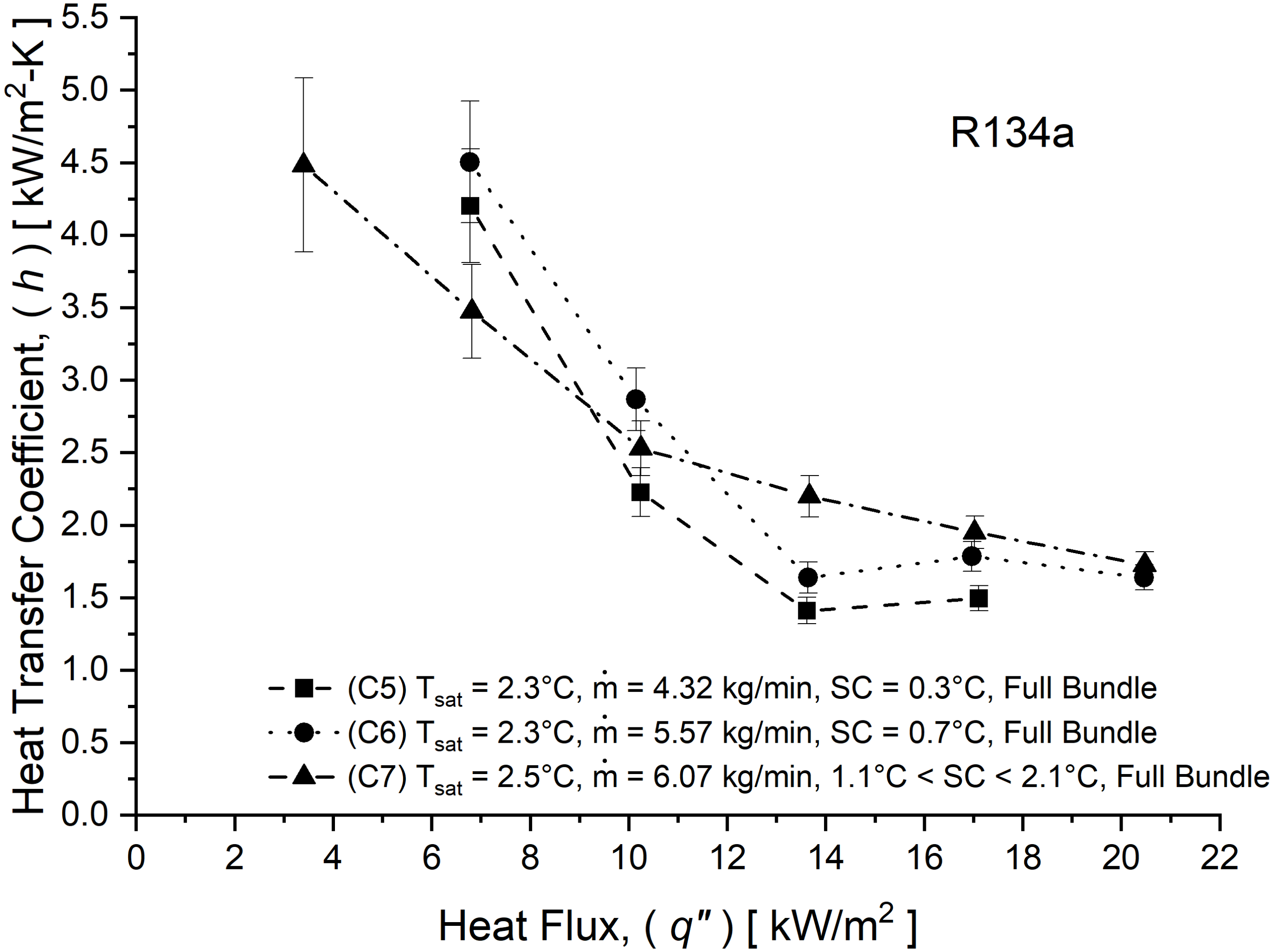

Figure 4.16: Heat transfer coefficient vs heat flux (Phase 2, R134a, T_{sat} = 3 °C)

bundle effect contributed significantly to the lower heat transfer coefficients at the lower tube rows and to the onset of the dryout condition. Similar to Phase 1, all of the full bundle series performed with R134a in the spray evaporation regime exhibited a decrease in heat transfer coefficient with increasing heat flux, consistent with an early onset of dryout.

For the R1234ze(E) tests in Phase 2, refrigerant mass flow rate was varied between 3.51 kg/min and 5.71 kg/min, and inlet subcooling was varied between -0.3 °C and 1.7 °C. For the single tube tests with R1234ze(E), tube heat transfer coefficients varied between 2.7 kW/m^2-K and 9.7 kW/m^2-K for heat fluxes between 1 kW/m^2 and 35 kW/m^2. For the three tube tests, heat transfer coefficients varied between 2.2 kW/m^2-K and 4.8 kW/m^2-K for heat fluxes between 10 kW/m^2 and 38 kW/m^2. Bundle heat transfer coefficients for the 10 °C series varied between 3.2 kW/m^2-K and 8.7 kW/m^2-K for heat fluxes between 3 kW/m^2 and 19 kW/m^2. Those for the 2.5 °C series varied between 1.9 kW/m^2-K and 9.8 kW/m^2-K for heat fluxes between 3 kW/m^2 and 19 kW/m^2. Those for the -6.5 °C series varied between 2.4 kW/m^2-K and 9.8 kW/m^2-K for heat fluxes between 3 kW/m^2 and 19 kW/m^2. Those for the -12 °C series varied between 2.4 kW/m^2-K and 6.1 kW/m^2-K for heat fluxes between 3 kW/m^2 and 19 kW/m^2. As with R134a, single tube flooded tests were again performed with R1234ze(E) in which heat transfer coefficients increased steadily with increasing heat flux and were within ±20% of those recorded in Series C1. Single tube tests were also repeated for this refrigerant, this time with two different series performed for each Tube 1 and Tube 5, shown in Figures 4.18 and 4.19, respectively. As before, the heat transfer coefficients calculated for the Tube 1 tests were between 10% and 30% higher than those calculated for the Tube 5 tests at similar heat fluxes in a demonstration of the bundle effect. For both the Tube 1 and Tube 5 tests, the two series for each set overlapped very closely, within ±10%, indicating excellent repeatability and reinforcing confidence in the test facility. As a further investigation into the

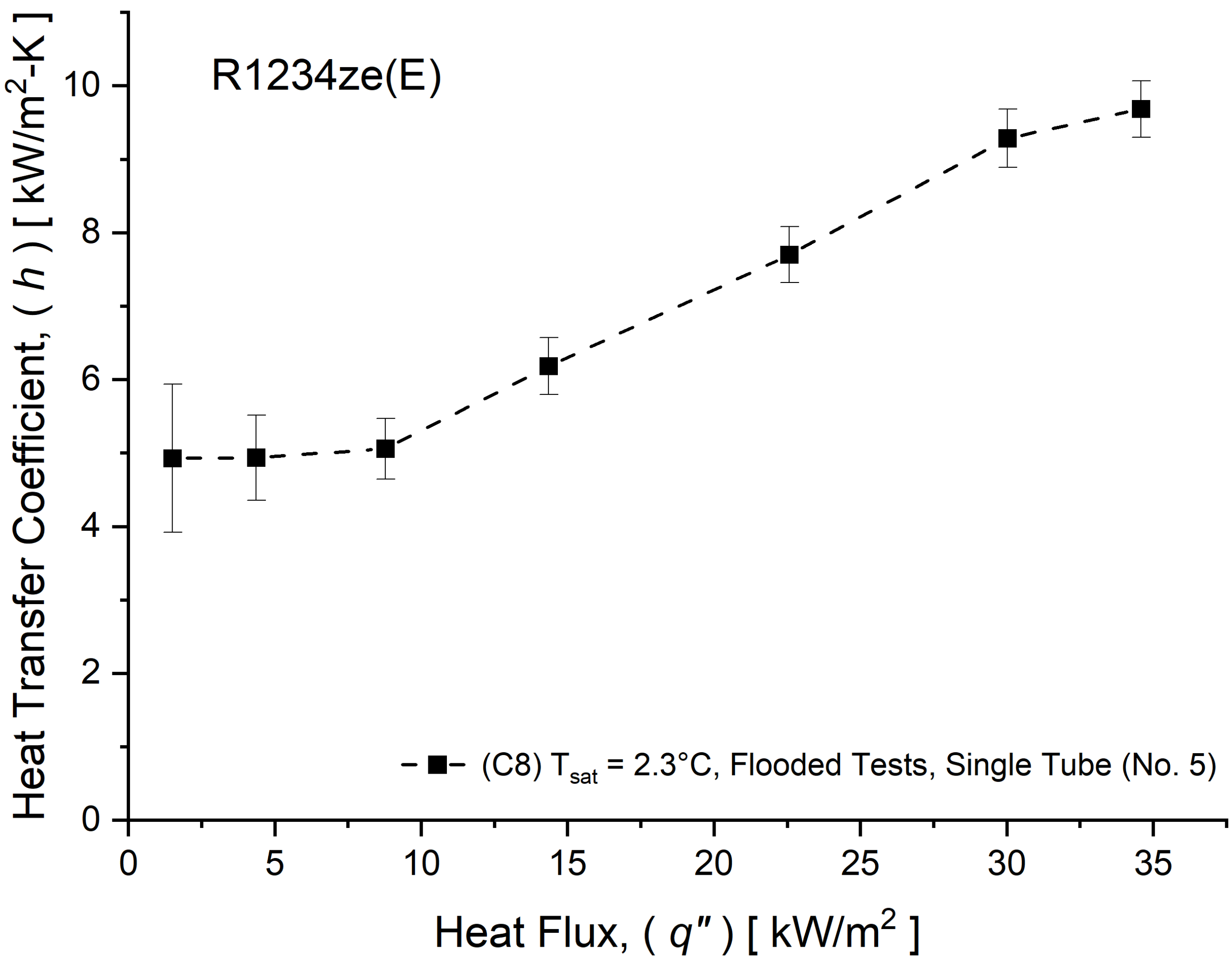

Figure 4.17: Heat transfer coefficient vs heat flux (Phase 2, R1234ze(E), single tube flooded tests)

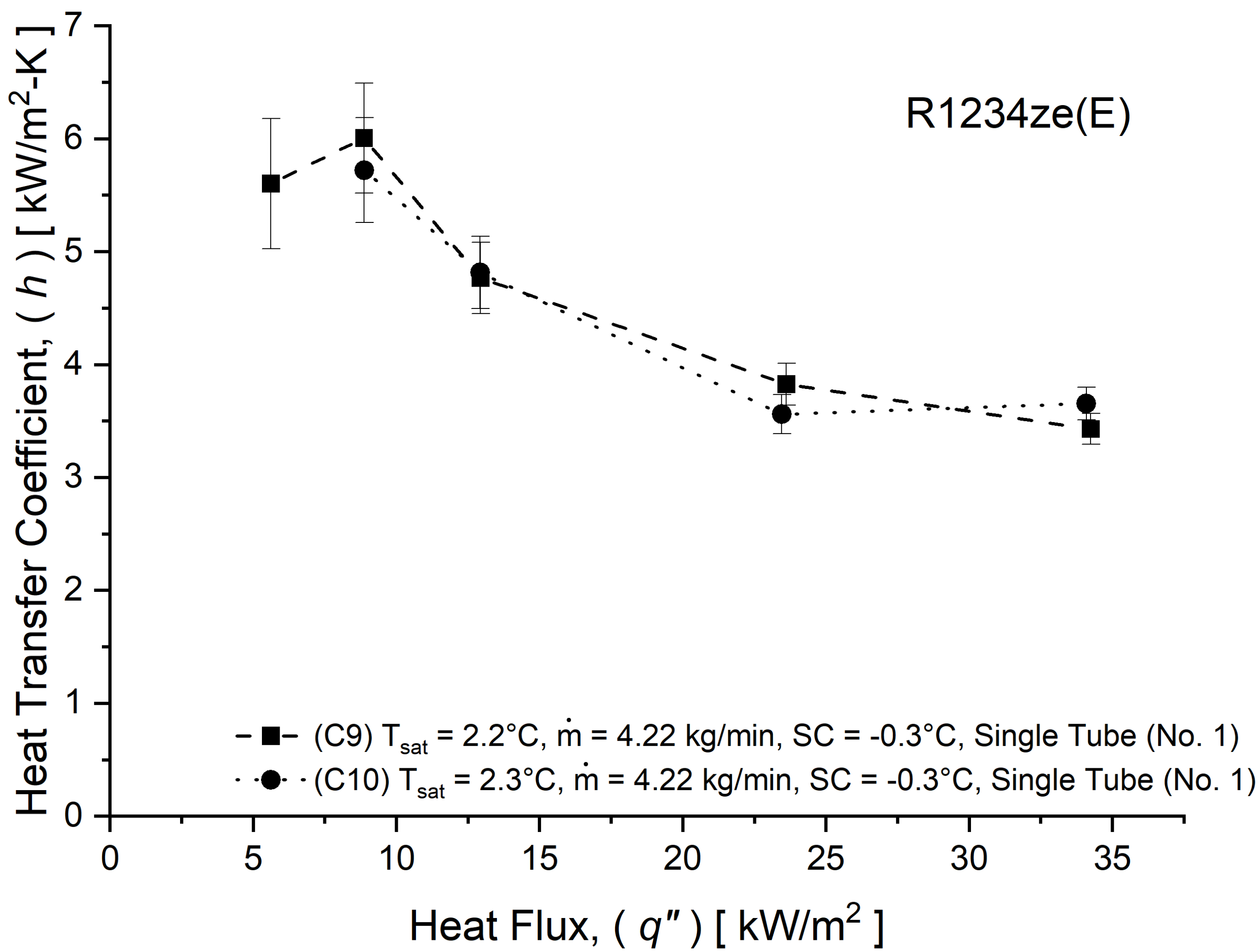

Figure 4.18: Heat transfer coefficient vs heat flux (Phase 2, R1234ze(E), single tube tests)

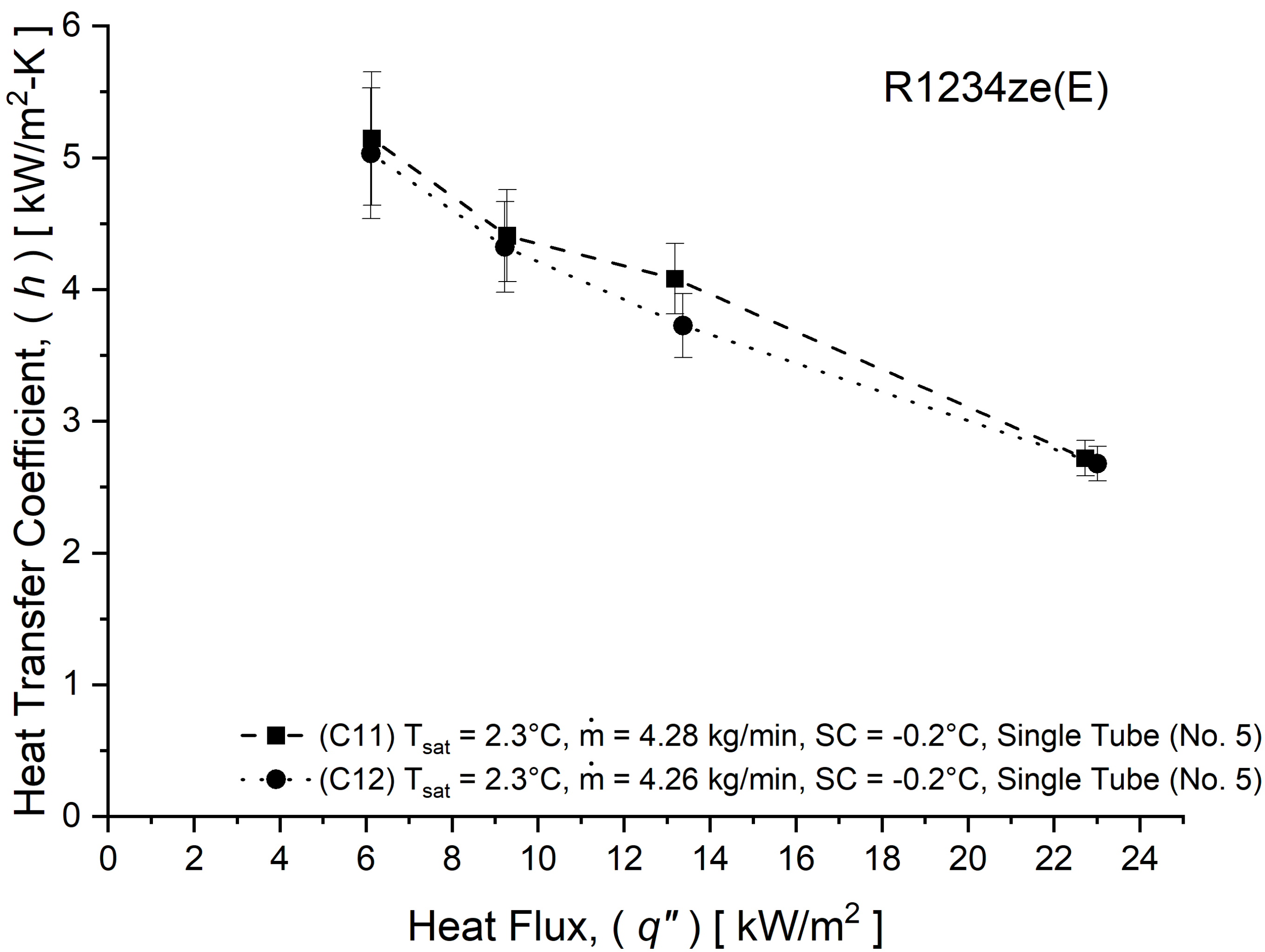

Figure 4.19: Heat transfer coefficient vs heat flux (Phase 2, R1234ze(E), single tube tests)

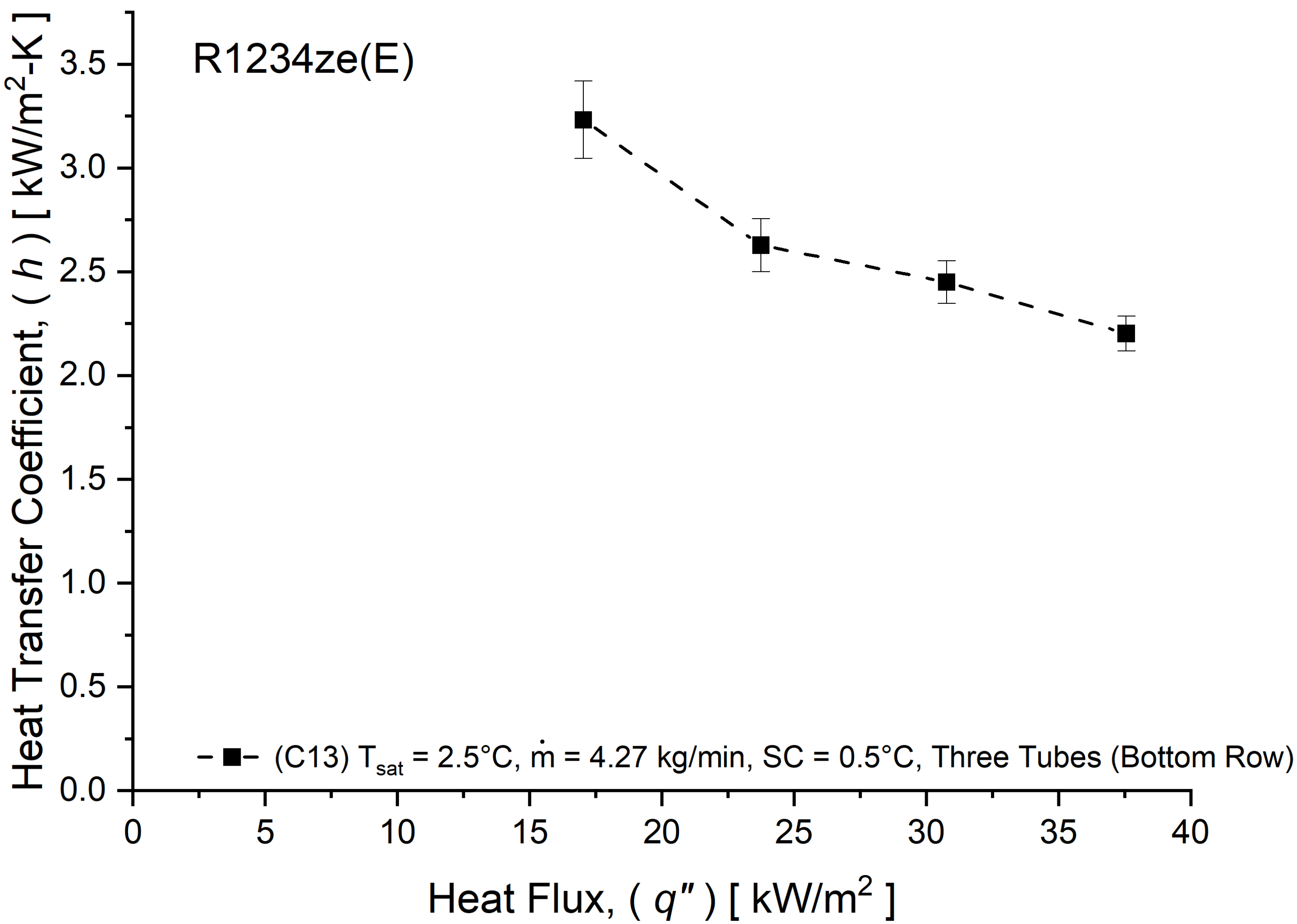

Figure 4.20: Heat transfer coefficient vs heat flux (Phase 2, R1234ze(E), T_{sat} = 2.5 °C)

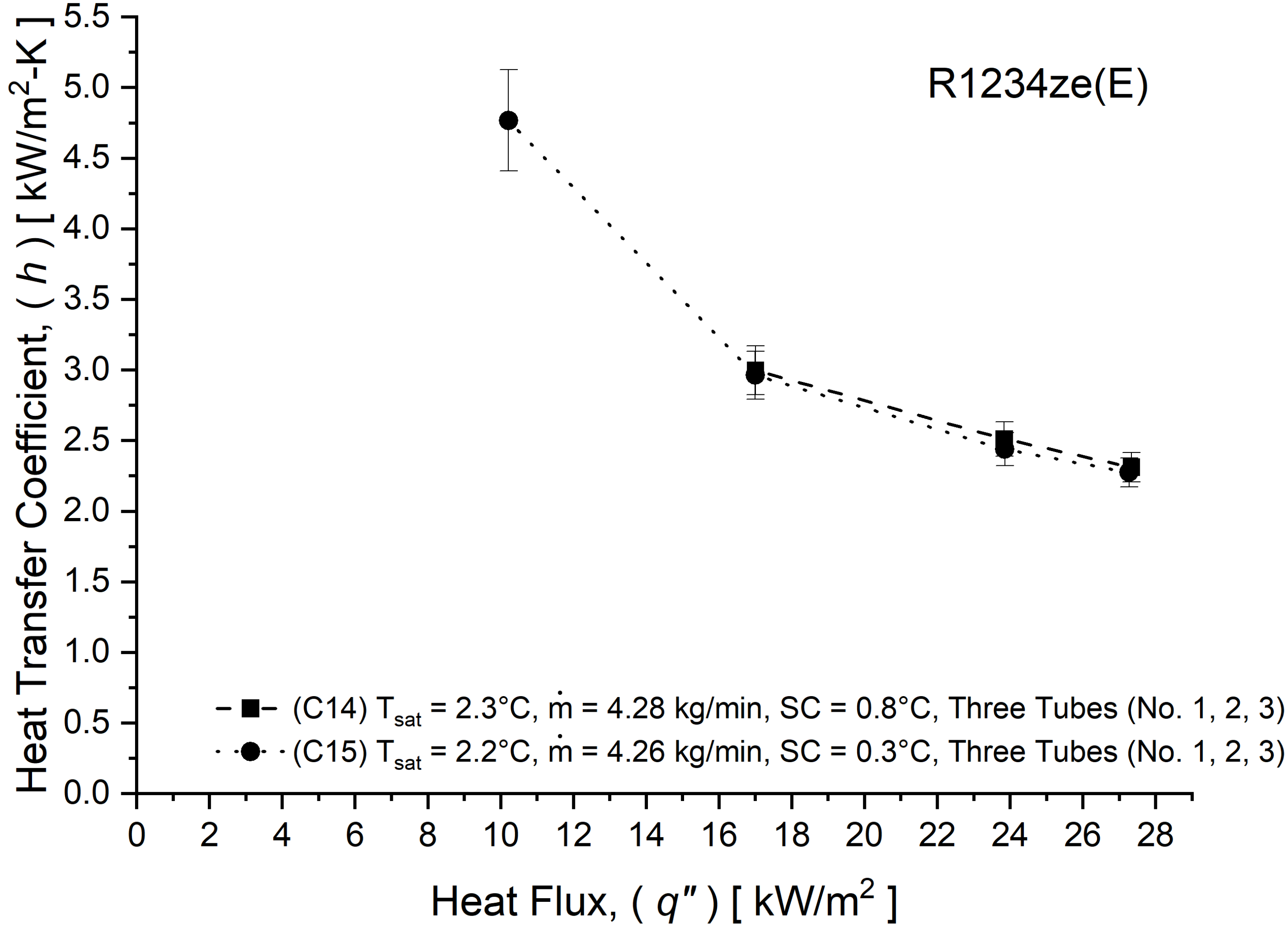

Figure 4.21: Heat transfer coefficient vs heat flux (Phase 2, R1234ze(E), T_{sat} = 2.5 °C)

bundle effect, a series of three tube tests using only the tubes in Row 5 and, separately, only the middle tube in Rows 1, 2, and 3 were performed. The results are shown in Figures 4.20 and 4.21, respectively. For the Row 5 series C13, heat transfer coefficients decreased steadily with increasing heat flux as observed in the single tube series C11 and C12 and were within ±10% for similar heat flux levels with very similar test conditions. For series C14 and C15 in which only Tubes 1, 2, and 3 were active, heat transfer coefficients generally fell between those observed for only Tube 1 (series C9 and C10) and those observed for only Tube 5 (series C11 and C12) for similar heat fluxes. To confirm the influence of the bundle effect, the row-by-row heat transfer coefficients for these series were plotted and are shown in Figures 4.22 and 4.23.

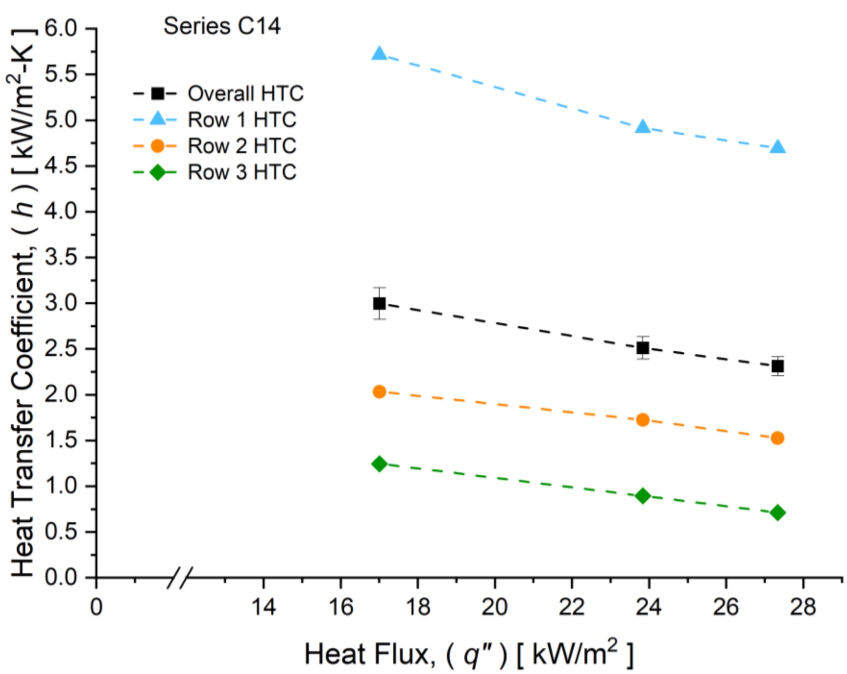

Figure 4.22: Row-by-row heat transfer coefficients vs heat flux, Series C14

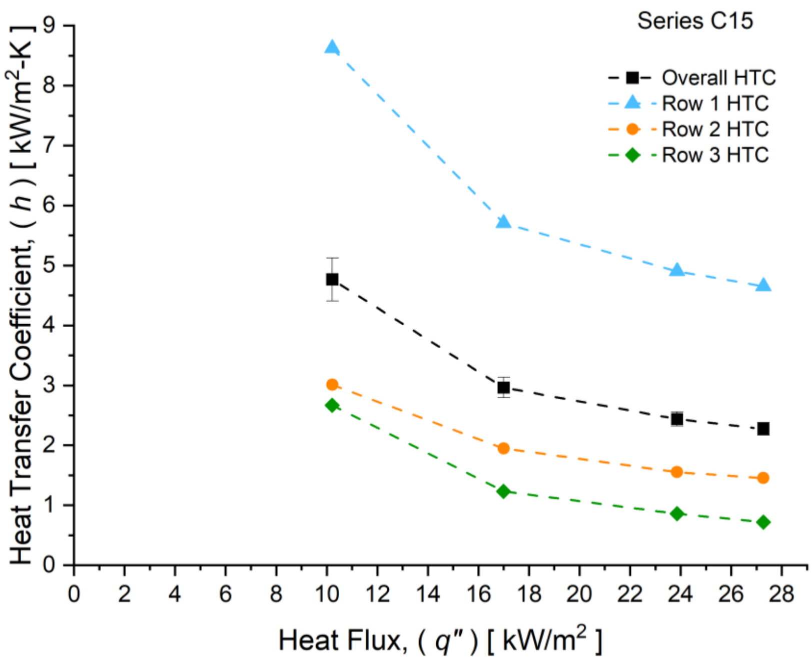

Figure 4.23: Row-by-row heat transfer coefficients vs heat flux, Series C15

It was observed in these series that the Row 1 heat transfer coefficients were within ±20% of those observed in the single tube series C9 and C10 and, importantly, that the Row 1 heat transfer coefficients were the highest at all heat fluxes, followed by those calculated for Row 2 and subsequently those for Row 3. These observations clearly illustrated the bundle effect by demonstrating the decrease in heat transfer coefficient for lower rows in the bundle, especially for the square bundle geometry in which the tubes in each row were aligned directly above those in subsequent rows such that only the first row received a direct supply of liquid refrigerant and lower rows received a lesser supply due to evaporation and deflection. For the full bundle tests at a saturation temperature of 10 °C, bundle heat transfer coefficients were observed to either plateau, such as in Series C17 and C18, or generally decrease with increasing heat flux, as in Series C16. Of note for these tests was the slight increase in heat transfer coefficient with the last test in both Series C16 and C17 despite the utilization of the full bundle for both entire series. Upon inspection of the data, it was determined that these sudden upticks in heat transfer coefficient were caused by

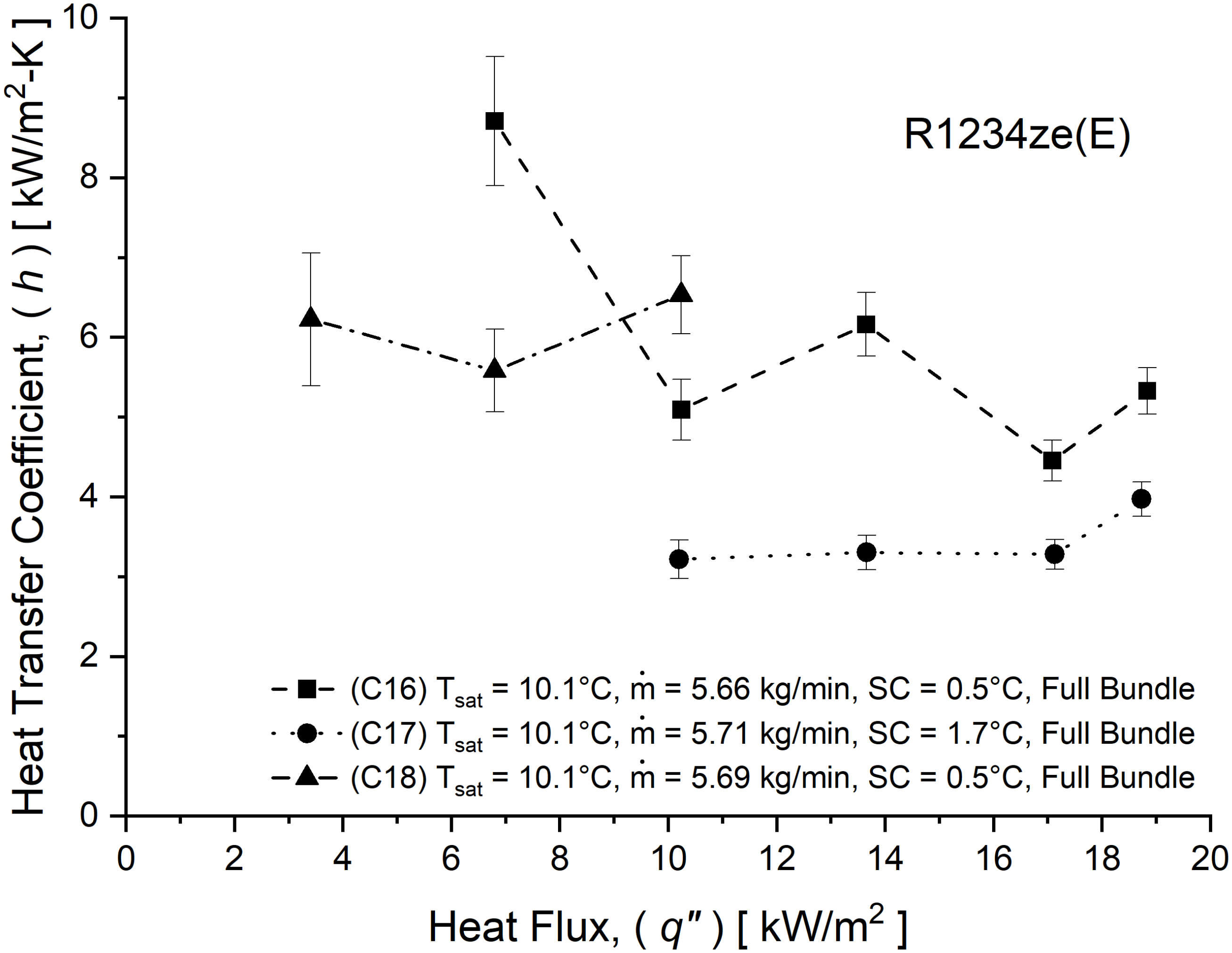

Figure 4.24: Heat transfer coefficient vs heat flux (Phase 2, R1234ze(E), T_{sat} = 10 °C)

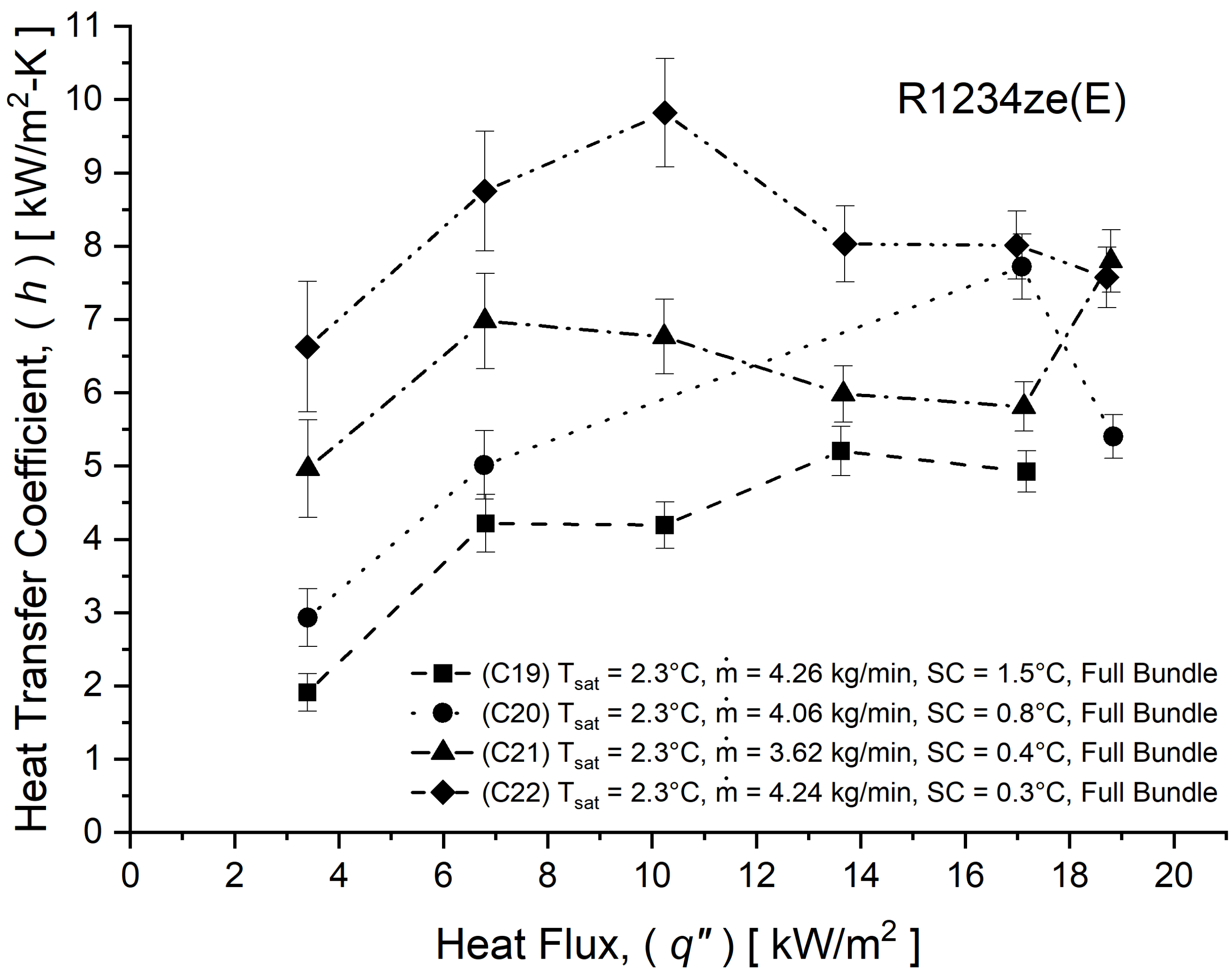

Figure 4.25: Heat transfer coefficient vs heat flux (Phase 2, R1234ze(E), T_{sat} = 2.5 °C)

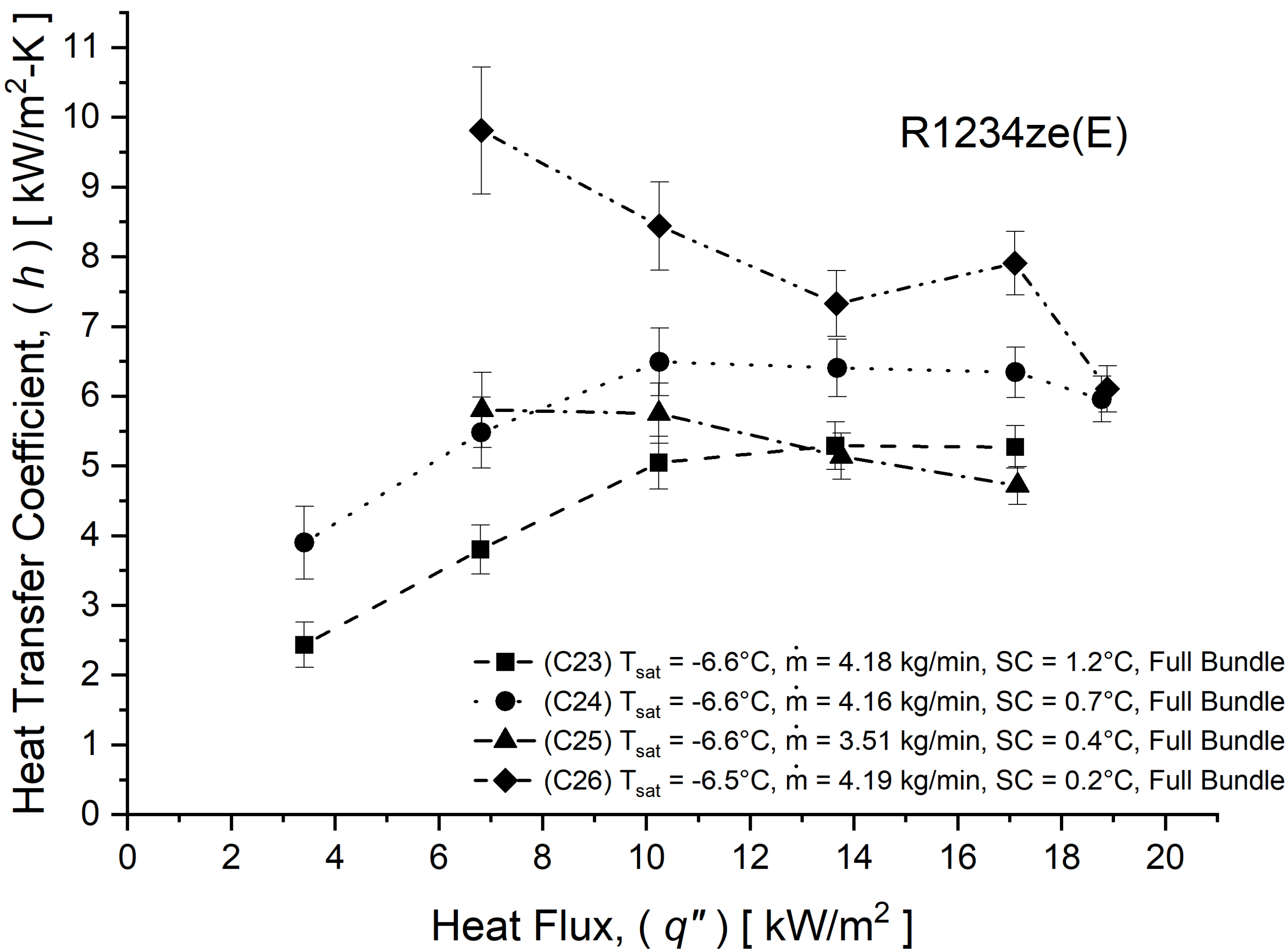

Figure 4.26: Heat transfer coefficient vs heat flux (Phase 2, R1234ze(E), T_{sat} = -6.5 °C)

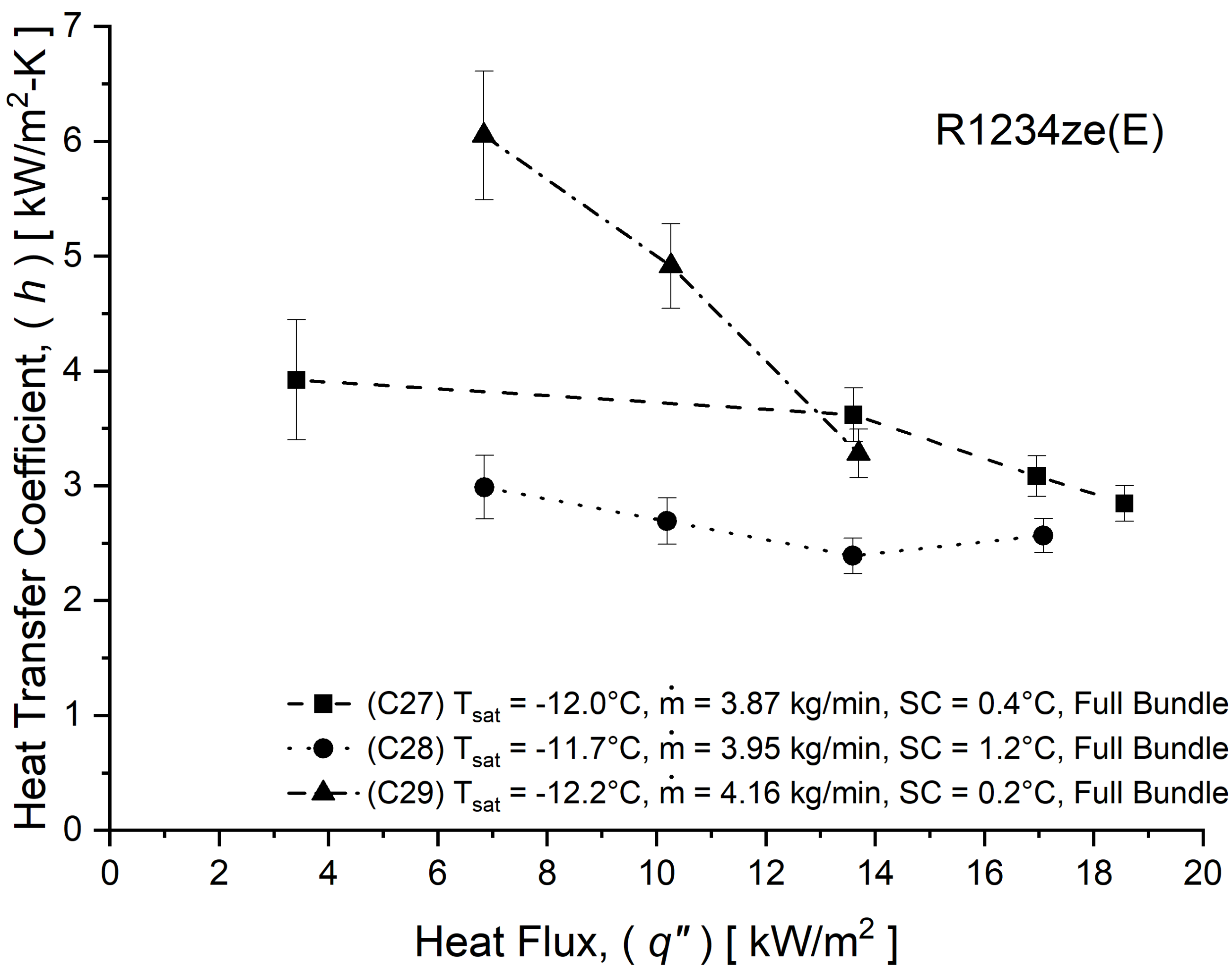

Figure 4.27: Heat transfer coefficient vs heat flux (Phase 2, R1234ze(E), T_{sat} = -12 °C)

a slight decrease in the amount of inlet subcooling for these tests. For Series C16, inlet subcooling decreased from 0.7 °C for the second-to-last test to 0.3 °C for the last test in the series. For Series C17, inlet subcooling decreased from 1.8 °C for the second-to-last test to 1.2 °C for the last test. This phenomenon highlighted to the investigators the importance of maintaining the degree of inlet subcooling as constant as possible for a given series and also the significant effect on heat transfer coefficient that a change of just 0.5 °C could have at such low levels of inlet subcooling. For these three series overall, it was observed that a decrease in subcooling of 1.2 °C caused an increase between 30% and 100% in bundle heat transfer coefficients. The trends observed in the 2.5 °C saturation temperature series were much more consistent with those observed previously in Phase 1. Series C22, which had the lowest degree of inlet subcooling at 0.3 °C, produced the highest bundle heat transfer coefficients of all four series and also displayed the earliest onset of the dryout condition at a heat flux of approximately 10 kW/m^2. The series with the next lowest inlet subcooling, C21, produced the next highest set of bundle heat transfer coefficients at lower heat fluxes and also exhibited an early onset of the dryout condition, earlier than that of C22 likely because of the lower refrigerant mass flow rate. The next highest heat transfer coefficients belonged to the series with the next lowest inlet subcooling, C20, which had a significantly delayed onset of dryout at a similar refrigerant mass flow rate as a result. The lowest heat transfer coefficients were calculated for the series with the highest inlet subcooling, C19, for which only a slight increase and then plateau was observed, thus allowing the entire series to be performed in the regime before the onset of dryout. The trends as described for the 2.5 °C series were mirrored almost exactly in the -6.5 °C series C23 through C26. It was noticed in Series C25 and C26, which had similar levels of inlet subcooling to Series C21 and C22, respectively, that dryout seemed to occur earlier than in the 2.5 °C series. The same was true for Series C27 and C29 in the -12 °C saturation temperature series, for which heat transfer coefficients only either plateaued or decreased without the increase at low heat fluxes. Based on these observations, it was concluded that, all other things equal, a decrease in saturation temperature generally promoted an earlier onset of the dryout condition. As in Phase 2, no significant changes in bundle heat transfer coefficients could be attributed solely to changes in refrigerant saturation temperature except for the very low saturation temperature of -12 °C, for which heat transfer coefficients at similar heat fluxes were between 35% and 60% lower.

For the R1233zd(E) tests in Phase 2, refrigerant mass flow rate was varied between 2.02 kg/min and 4.25 kg/min, and inlet subcooling was varied between -0.8 °C and 3.6 °C. For the single tube tests, tube heat transfer coefficients varied between 1.1 kW/m^2-K and 12.6 kW/m^2-K for heat fluxes between 3 kW/m^2 and 35 kW/m^2. For the three tube tests, heat transfer coefficients varied between 1.8 kW/m^2-K and 8.5 kW/m^2-K for heat fluxes between 7 kW/m^2 and 35 kW/m^2. Bundle heat transfer coefficients for the 16 °C series varied between 1.5 kW/m^2-K and 4.9 kW/m^2-K for heat fluxes between 3 kW/m^2 and 17 kW/m^2. It was decided in this phase of experimentation to test the R1233zd(E) refrigerant at much higher saturation temperatures than in Phase 1. Because R1233zd(E) is a "low pressure" refrigerant, meaning it has a low vapor pressure relative to other common refrigerants such as R134a, it was desired to test the refrigerant at temperatures corresponding to saturation pressures at or above standard atmospheric pressure to minimize the risk of air infiltration in the refrigerant loop. In the single tube tests, it was curiously observed that the heat transfer coefficients for the Tube 1 tests were higher than those for the Tube 5 flooded tests, opposite of the trend observed in earlier single tube tests in Phase 1. Given the low subcooling and relatively high flow rate of Series C30, it was concluded that, under the right conditions, the spray evaporation mode could potentially make possible higher heat transfer coefficients than

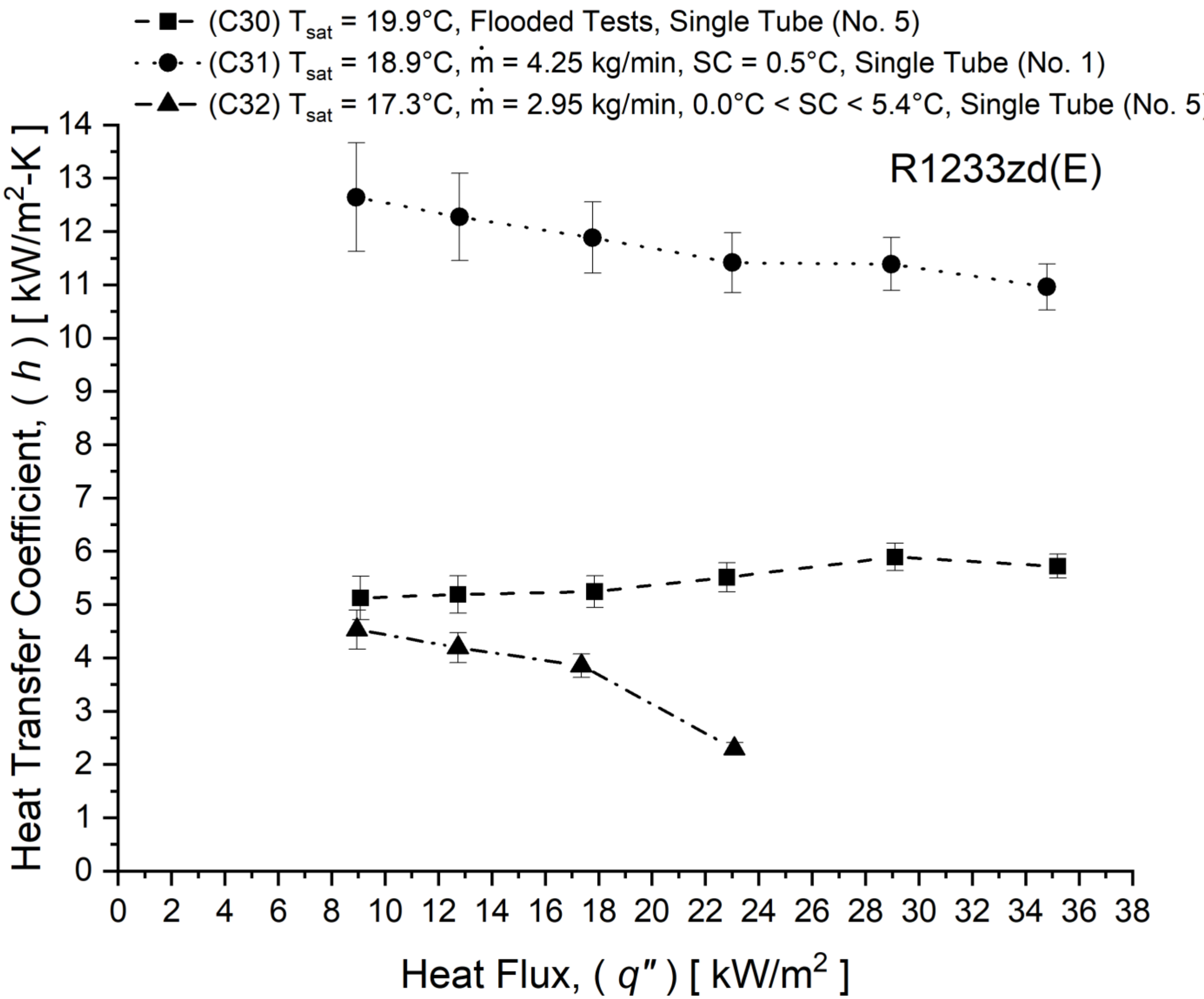

Figure 4.28: Heat transfer coefficient vs heat flux (Phase 2, R1233zd(E), single tube tests)

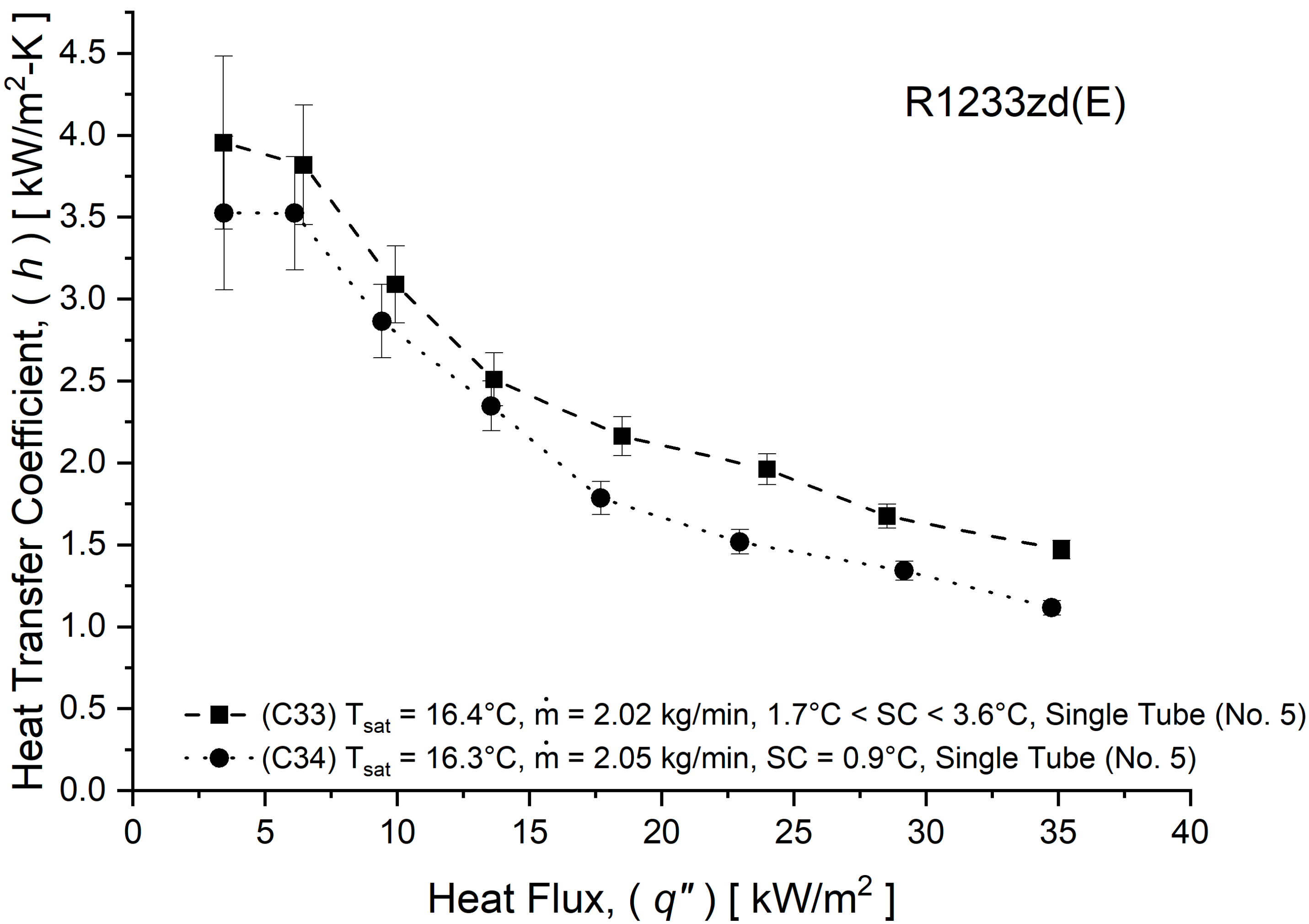

Figure 4.29: Heat transfer coefficient vs heat flux (Phase 2, R1233zd(E), single tube tests)

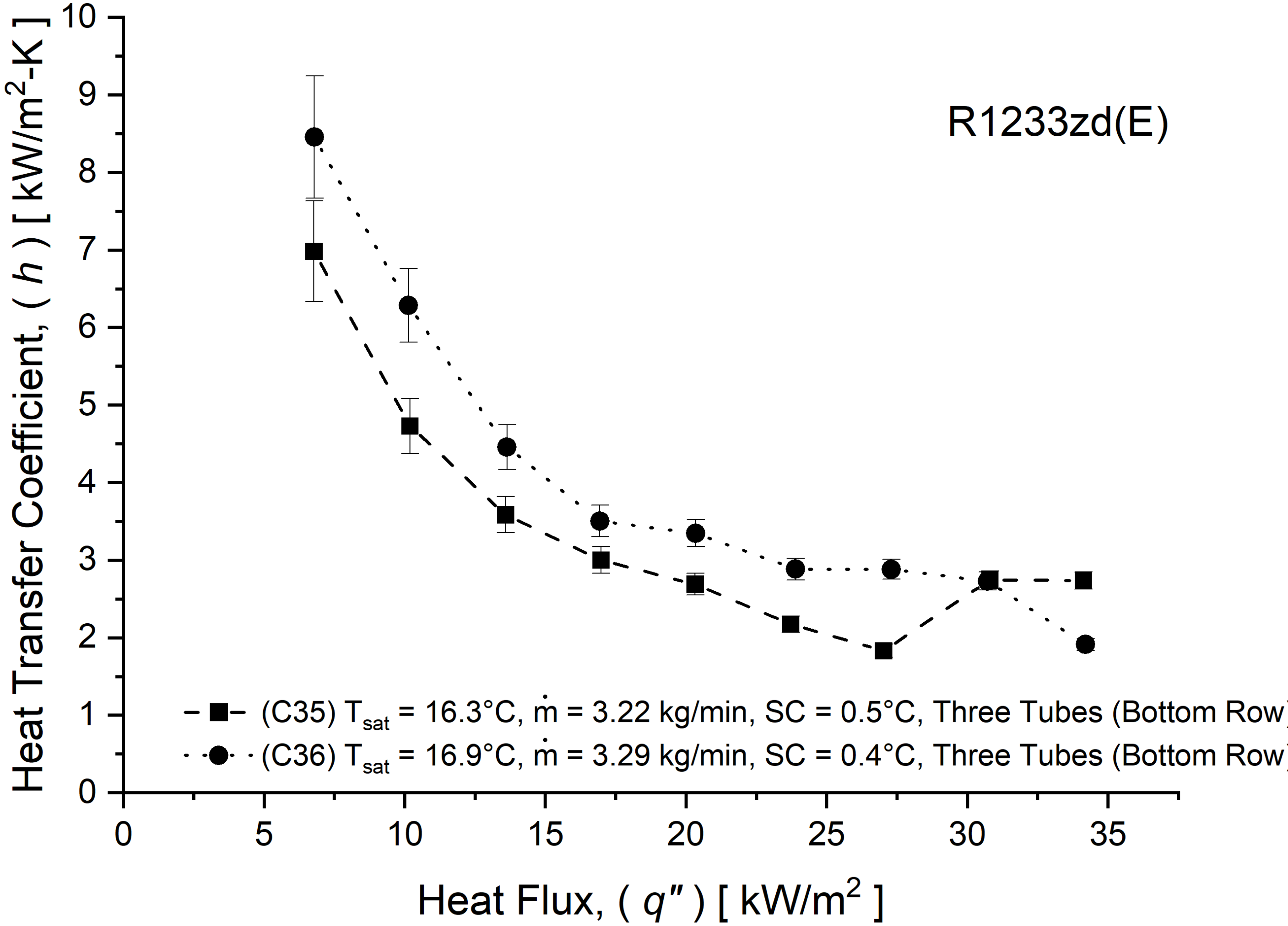

Figure 4.30: Heat transfer coefficient vs heat flux (Phase 2, R1233zd(E), three tube tests)

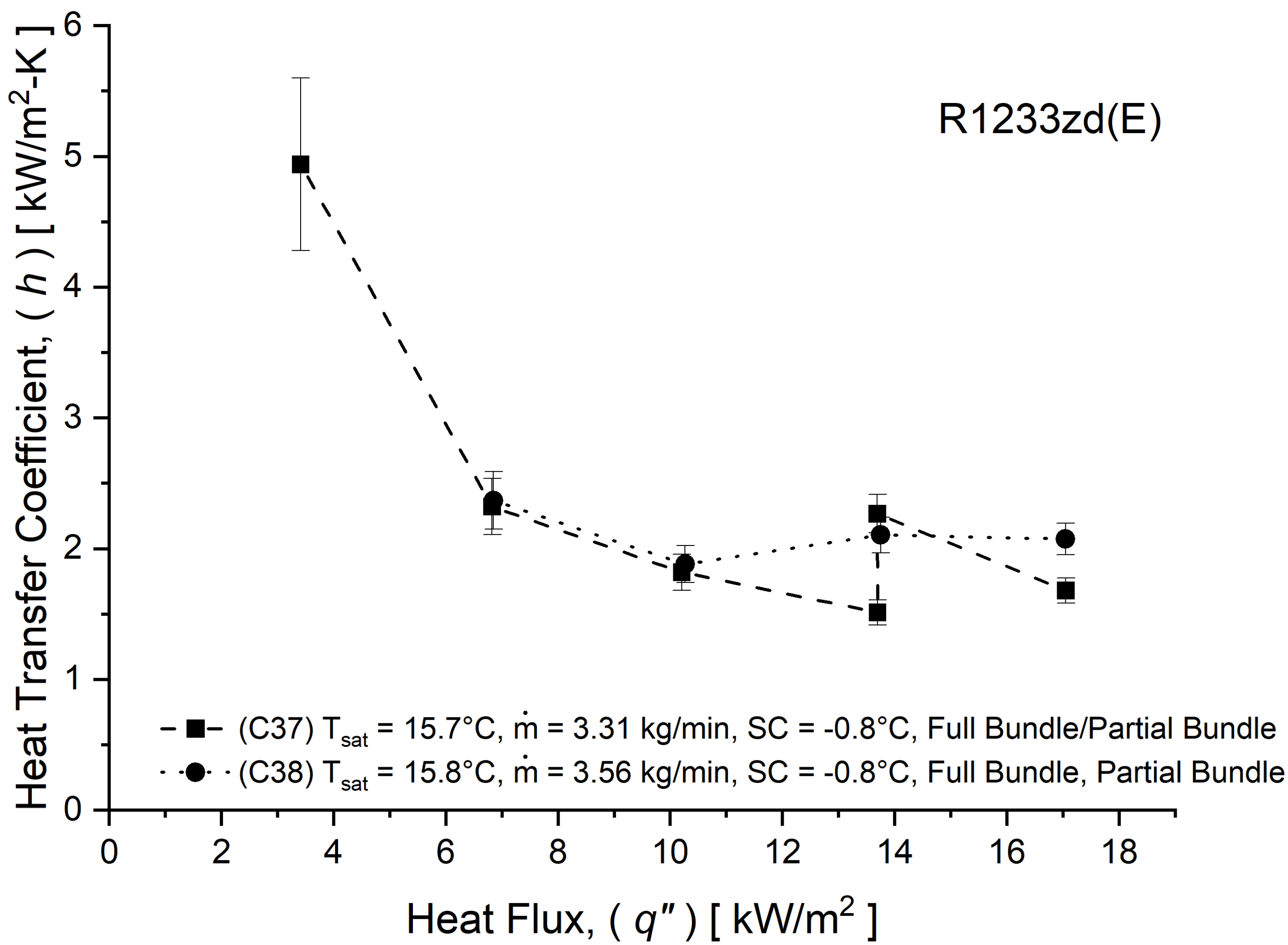

Figure 4.31: Heat transfer coefficient vs heat flux (Phase 2, R1233zd(E), T_{sat} = 16 °C)

those obtained in the nucleate boiling regime. Two series of single tube tests, C33 and C34, were performed in the spray evaporation regime using only Tube 5. In these series was observed a very strong influence of the bundle effect as heat transfer coefficients decreased with increasing heat flux. The same effect was observed in the Row 5 tests in Series C35 and C36 in which heat transfer coefficients also decreased with increasing heat flux. The full bundle tests for R1233zd(E) in this phase were performed with a moderately low refrigerant mass flow rate and no inlet subcooling, resulting in very low bundle heat transfer coefficients below 3.0 kW/m^2-K at higher heat fluxes in close agreement with the trend observed in the earlier Series B28 and B31.

4.3 Phase 3 Results

The experimental test results for Phase 3, using the Tube-B evaporator tubes in the triangular geometry with the full circular cone nozzles, are presented in Figures 4.32 through 4.40. For Phase 3, refrigerant R134a was tested in the single tube, partial bundle, and full bundle configurations at saturation temperatures of approximately 10 °C and 2.5 °C. The R134a results are shown in Figures 4.32 and 4.33. Refrigerant R1234ze(E) was tested in single tube, partial bundle, and full bundle configurations at saturation temperatures of 10 °C, 2.5 °C, and -6.5 °C, and these results are shown in Figures 4.34, 4.35, 4.36, and 4.37. Also, refrigerant R1233zd(E) was tested in single tube, partial bundle, and full bundle configurations at saturation temperatures of approximately 15 °C and 9 °C, shown in Figures 4.38, 4.39, and 4.40.

For the R134a tests in Phase 3, refrigerant mass flow rate was kept nearly constant around 4.30 kg/min, and inlet subcooling was varied between 0.0 °C and 1.5 °C. Phase 3 was the first phase in which the new Tube-B evaporator tubes were used. For the single tube tests with R134a, tube heat transfer coefficients varied between 6.1 kW/m^2-K and 22.4 kW/m^2-K for heat fluxes

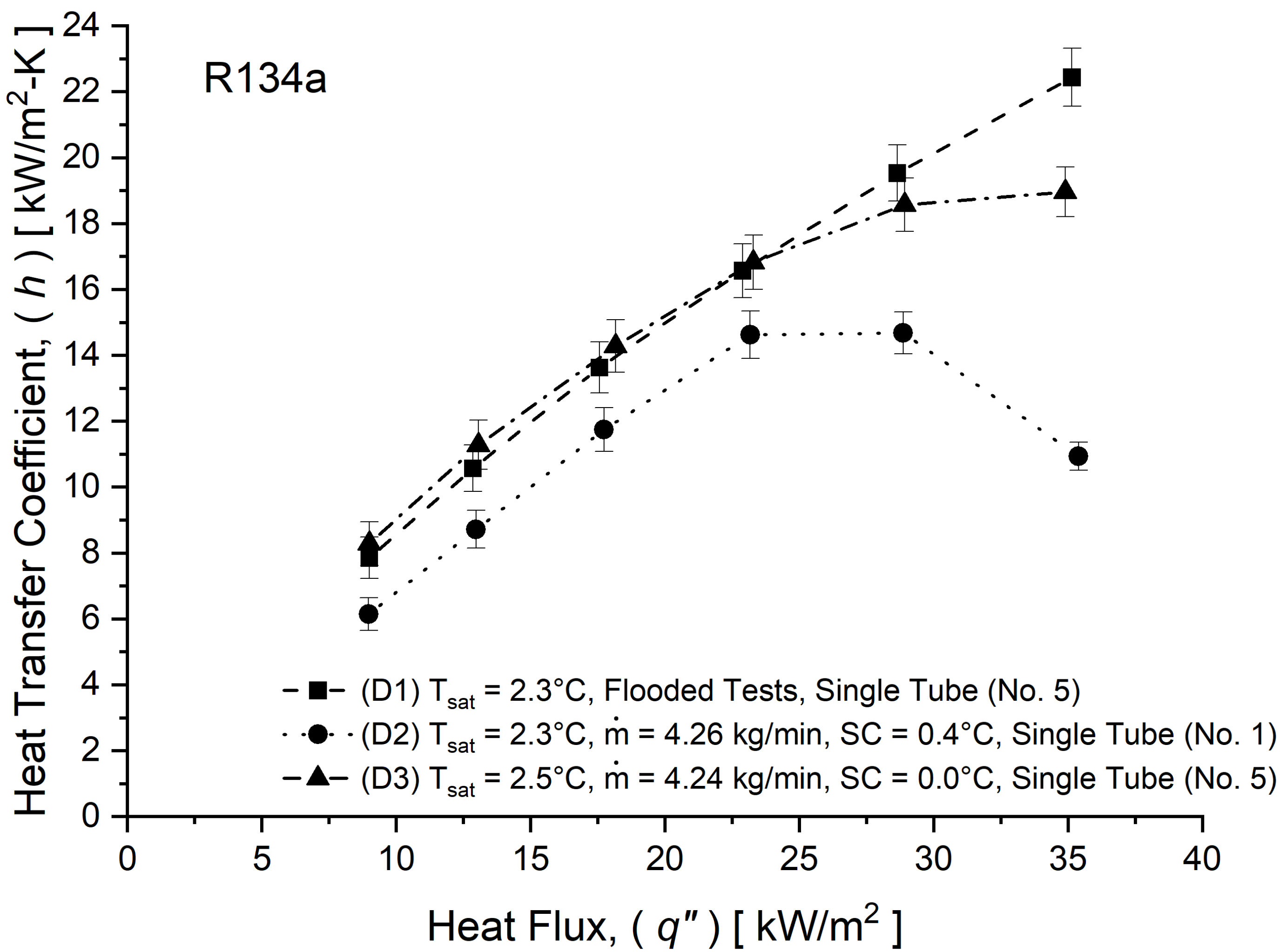

Figure 4.32: Heat transfer coefficient vs heat flux (Phase 3, R134a, single tube tests)

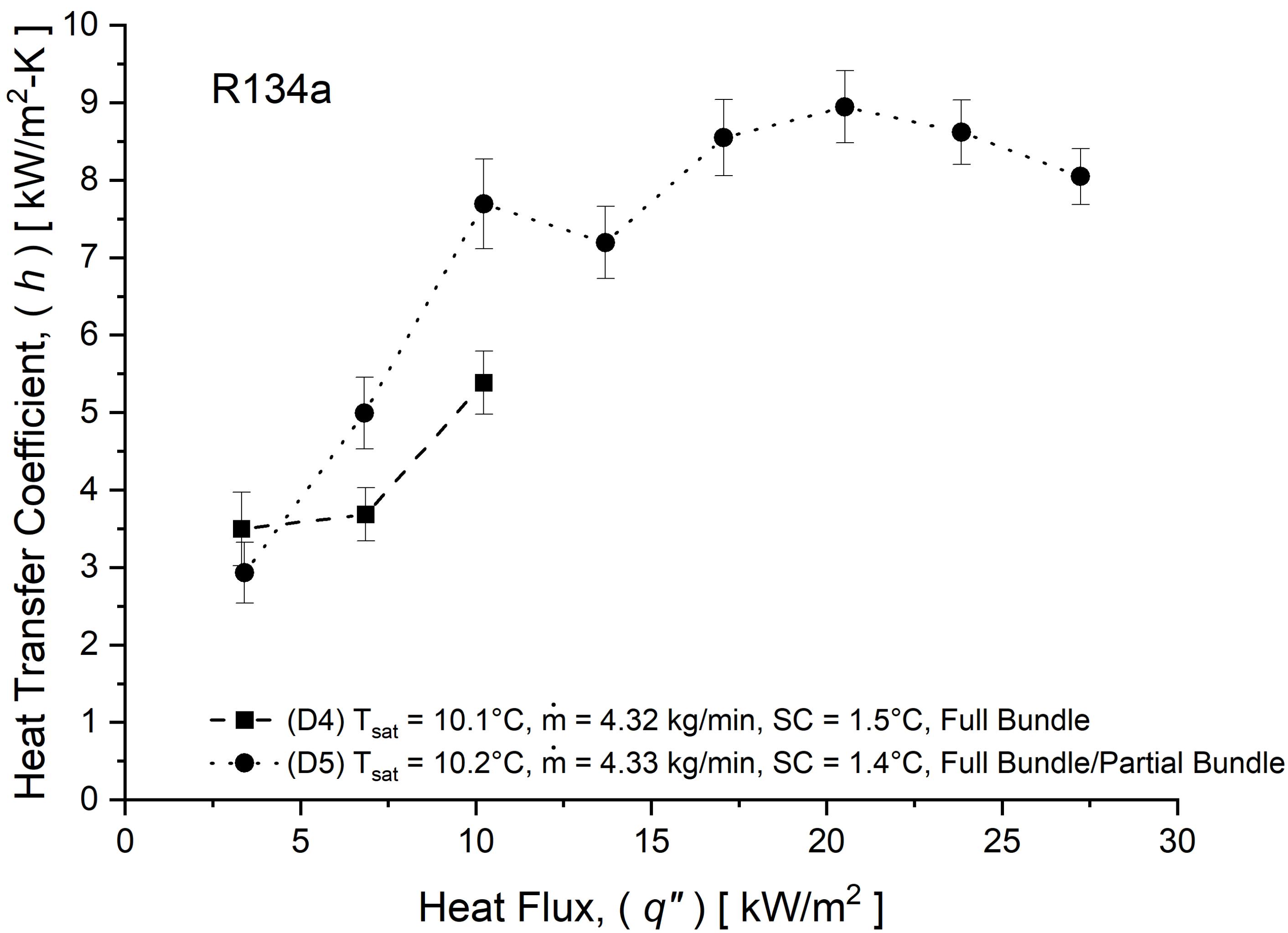

Figure 4.33: Heat transfer coefficient vs heat flux (Phase 3, R134a, T_{sat} = 10 °C)

between 9 kW/m^2 and 35 kW/m^2. Bundle heat transfer coefficients for the 10 °C series varied between 2.9 kW/m^2-K and 8.9 kW/m^2-K for heat fluxes between 3 kW/m^2 and 27 kW/m^2. Perhaps the most notable difference between Phase 3 and any data collected for previous configurations is the significantly higher heat transfer coefficients for the Tube-B evaporator tubes. The pool boiling heat transfer coefficients calculated for Series D1 were between 120% and 150% higher than those calculated for the equivalent flooded tests of Series C1 in Phase 2. In a reversal of the trend observed in Series C2 for the middle tube in Row 1, the heat transfer coefficients for Series D2 increased with increasing heat flux until approximately 20 kW/m^2, at which point the refrigerant mass flow rate was insufficient for the extremely low level of subcooling (0.0 °C) and dryout began to occur. Similarly for the Row 5 single tube tests in Series D3, heat transfer coefficients only increased with increasing heat flux until they began to plateau at approximately 35 kW/m^2. Tube heat transfer coefficients for Series D3 were approximately 10% to 30% higher than those for Series D2, seemingly in a reversal of previous trends. However, this difference was due to the lower degree of inlet subcooling for Series D3, again in a demonstration of the sensitivity of heat transfer coefficients to changes in inlet subcooling, even as small as 0.4 °C. For the full bundle/partial bundle Series D5, heat transfer coefficients generally increased with increasing heat flux until approximately 21 kW/m^2, at which point the onset of dryout occurred. Compared to the most similar data from Phase 1, Series B6, in which the bundle geometry and nozzle arrangement were the same, the heat transfer coefficients for series D5 were between 80% and 400% greater (or 2.2 kW/m^2-K to 6.7 kW/m^2-K greater) for similar levels of heat flux.

For the R1234ze(E) tests in Phase 3, refrigerant mass flow rate was kept nearly constant at approximately 4.60 kg/min, and inlet subcooling was varied between 0.0 °C and 1.3 °C. For the single tube tests with R1234ze(E), tube heat transfer coefficients varied between 9.6 kW/m^2-K and

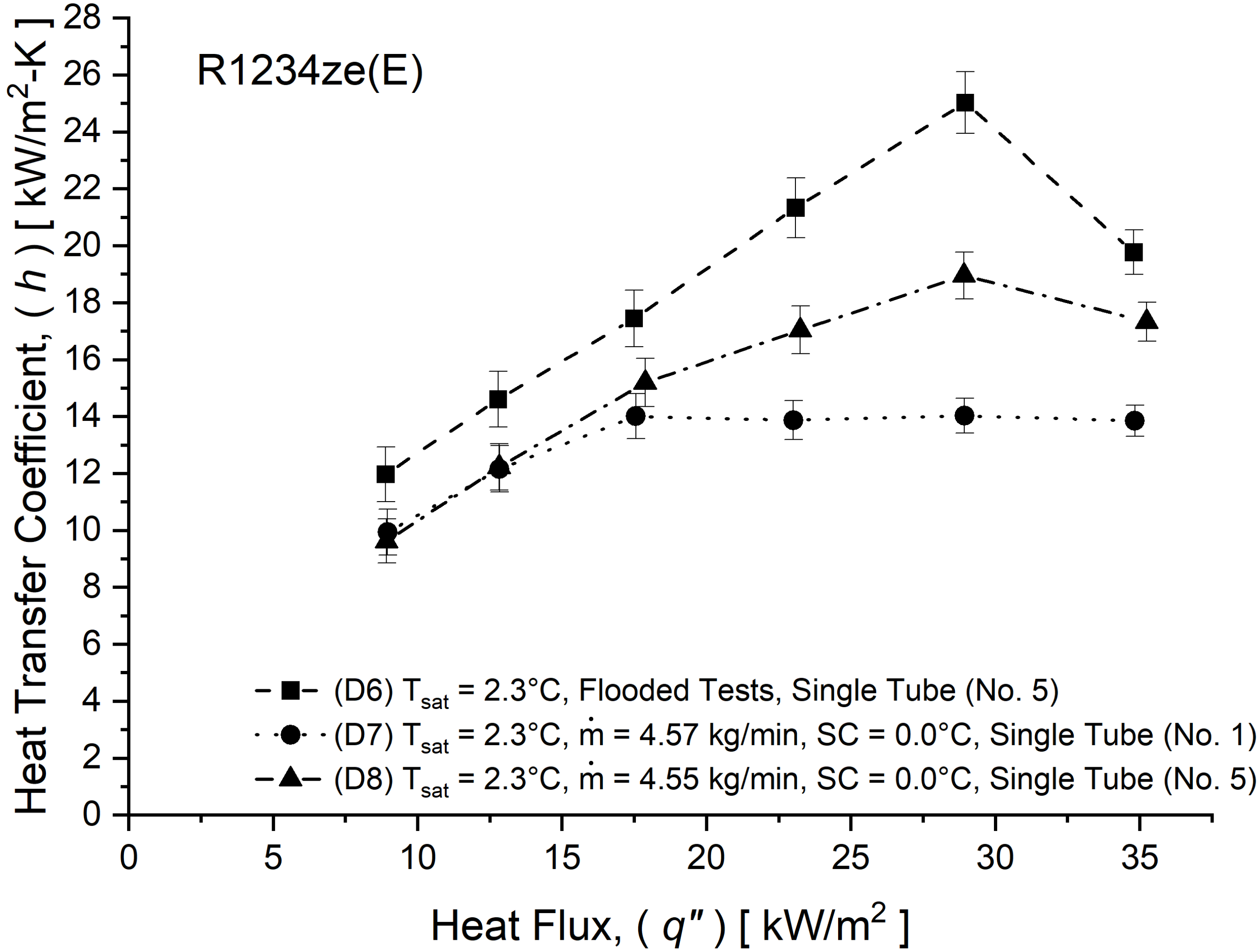

Figure 4.34: Heat transfer coefficient vs heat flux (Phase 3, R1234ze(E), single tube tests)

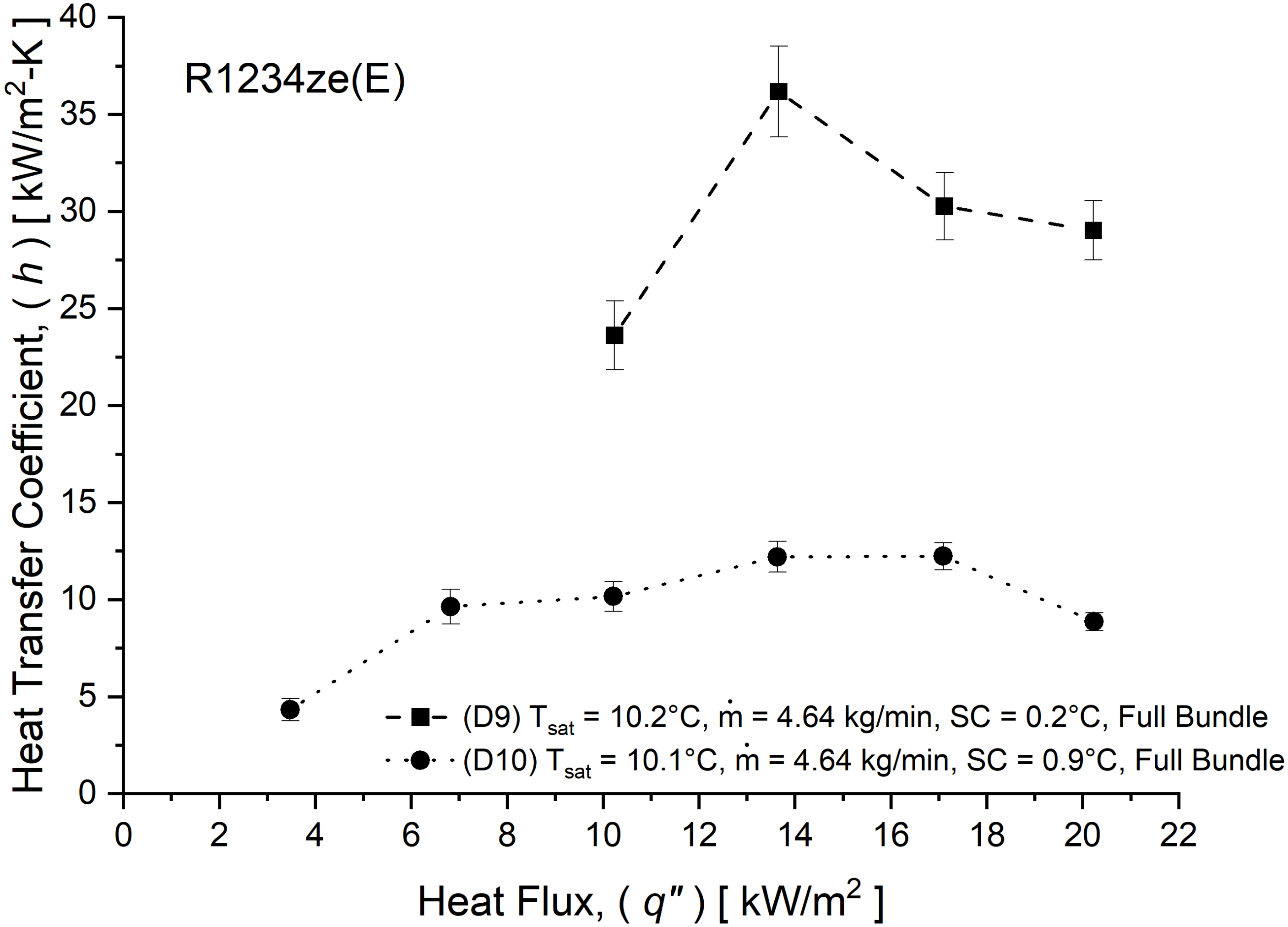

Figure 4.35: Heat transfer coefficient vs heat flux (Phase 3, R1234ze(E), T_{sat} = 10 °C)

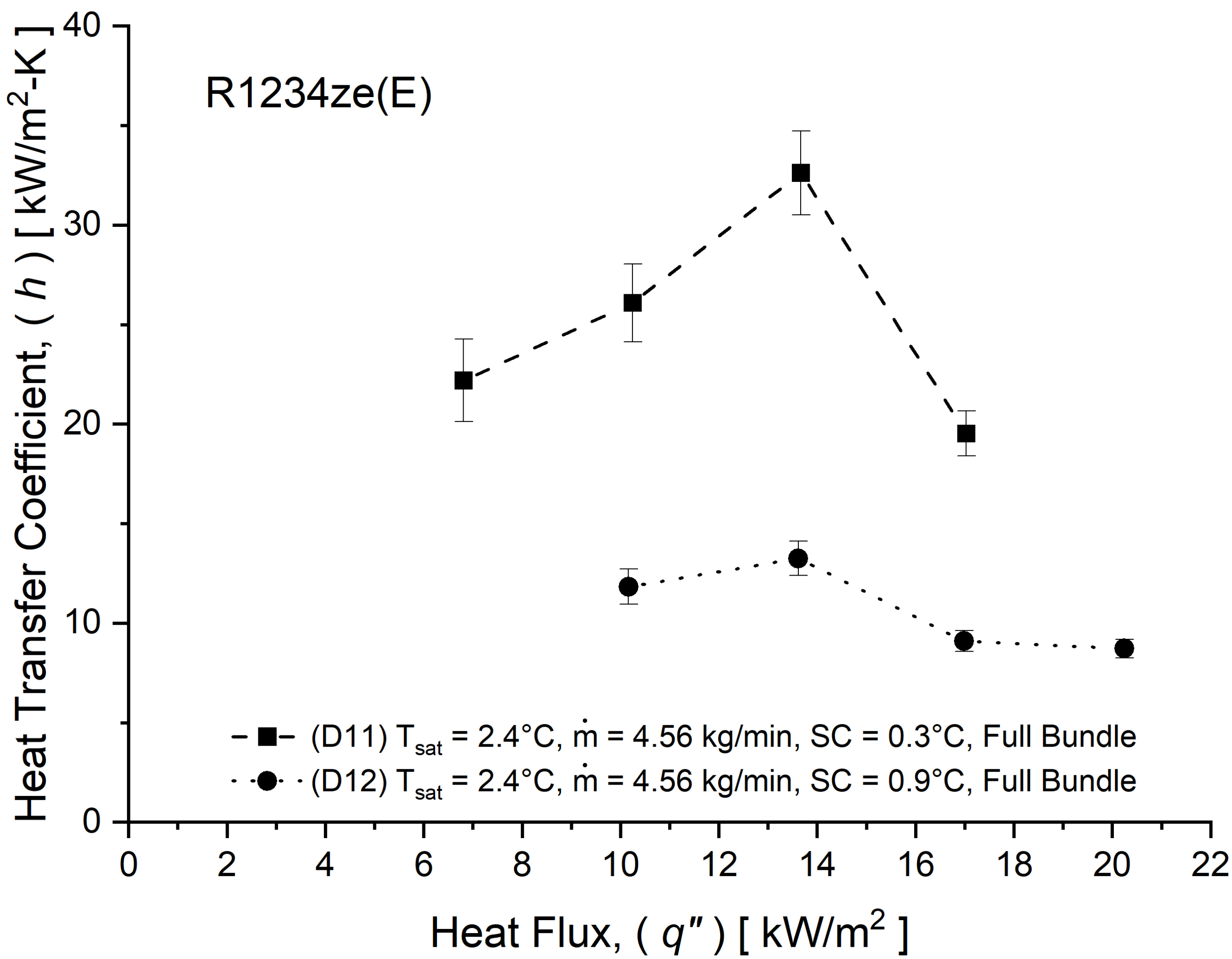

Figure 4.36: Heat transfer coefficient vs heat flux (Phase 3, R1234ze(E), T_{sat} = 2.5 °C)

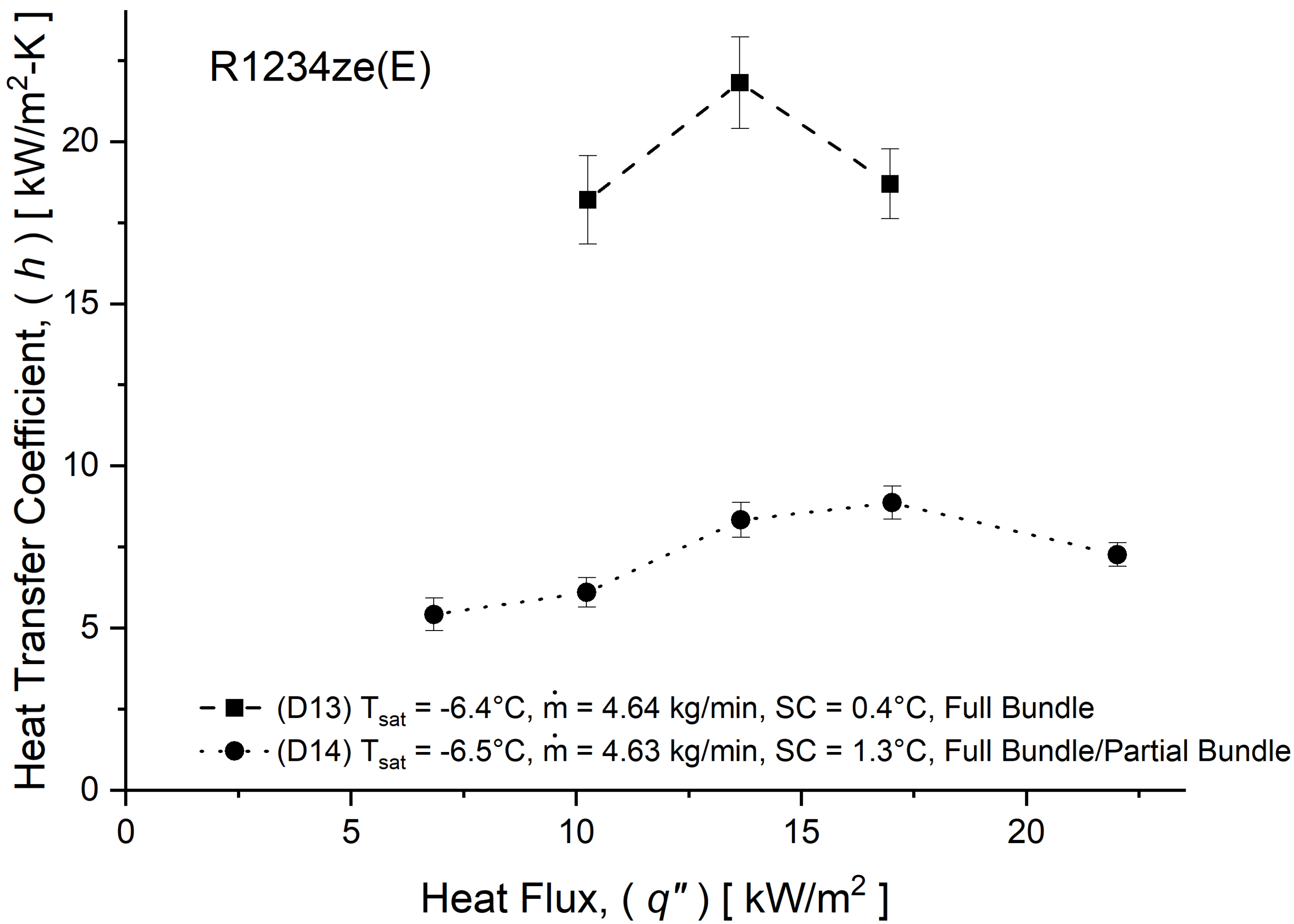

Figure 4.37: Heat transfer coefficient vs heat flux (Phase 3, R1234ze(E), T_{sat} = -6.5 °C)

25.0 kW/m^2-K for heat fluxes between 9 kW/m^2 and 35 kW/m^2. Bundle heat transfer coefficients for the 10 °C series varied between 4.3 kW/m^2-K and 36.2 kW/m^2-K for heat fluxes between 3 kW/m^2 and 20 kW/m^2. Those for the 2.5 °C series varied between 8.7 kW/m^2-K and 32.6 kW/m^2-K for heat fluxes between 6 kW/m^2 and 20 kW/m^2. Those for the -6.5 °C series varied between 5.4 kW/m^2-K and 21.8 kW/m^2-K for heat fluxes between 6 kW/m^2 and 22 kW/m^2. As in the R134a tests, very high heat transfer coefficients were observed in the single tube tests for R1234ze(E). For the flooded tests in Series D6, heat transfer coefficients were between 100% and 180% higher than those observed for the similar Series C8 in Phase 2. Similar trends to those in Series D2 and D3 were observed in the single tube Series D7 and D8, respectively, wherein heat transfer coefficients increased with increasing heat flux at low levels and then plateaued or began to decrease at higher levels with the onset of dryout. Interestingly, heat transfer coefficients for the Row 1 tests were generally equal to or lower than those for the Row 5 tests, counter to previous findings. This was due to minute variations in inlet subcooling, to which the heat transfer coefficients were extremely sensitive at such low levels as 0.0 °C. That said, heat transfer coefficients were between 60% and 300% greater for Series D7 than for the similar Series C9 and between 100% and 500% greater for Series D8 than for the similar Series C11 from Phase 2. Similarly, significantly increased values were also observed at all three refrigerant saturation temperatures for the full bundle/partial bundle tests. For low degrees of subcooling below 0.5 °C, Series D9 values were between 250% and 500% greater than those for the similar series B17, Series D11 values were between 200% and 450% greater than those for B24, and Series D13 values were between 400% and 600% greater than those for B26. Differences for the series with higher levels of subcooling between 0.9 °C and 1.3 °C were lesser, as Series D10 values were between 10% and 80% higher than those for B12, Series D12 values were between 50% and 150% greater than those for Series B22, and Series D14 values were between 3% and 80% greater than those for Series B27. For all three refrigerant saturation temperatures, it was observed that the onset of dryout occurred at slightly lower heat flux levels and was much more severe for lower levels of inlet subcooling, whereas dryout at higher subcooling caused a plateau and more gradual decline in heat transfer coefficient values.

For the R1233zd(E) tests in Phase 3, refrigerant mass flow rate was varied between 3.79 kg/min and 4.22 kg/min, and inlet subcooling was varied between 0.0 °C and 2.0 °C. For the single tube tests, tube heat transfer coefficients varied between 7.3 kW/m^2-K and 15.3 kW/m^2-K for heat fluxes between 9 kW/m^2 and 35 kW/m^2. Bundle heat transfer coefficients for the 15 °C series varied between 12.3 kW/m^2-K and 23.4 kW/m^2-K for heat fluxes between 3 kW/m^2 and 14 kW/m^2. Bundle heat transfer coefficients for the 9 °C series varied between 13.0 kW/m^2-K and 22.2 kW/m^2-K for heat fluxes between 3 kW/m^2 and 19 kW/m^2. As before, heat transfer coefficient values were significantly increased compared to those in Phase 2. For the flooded tests in Series D15, values were between 40% and 140% increased from those in the earlier Series C30. Values for the Row 5 single tube Series D17 were between 60% and 550% greater than those for the earlier Series C32. Interestingly, values for the Row 1 single tube Series D16 were only up to 30% greater than those calculated for the similar Series C31, likely due to the absence of any bundle effects. As observed in Series C30 through C32, Tube 1 heat transfer coefficients in the spray evaporation regime were higher than those for Tube 5 in the pool boiling regime which was indicative of the favorable conditions used for the spray evaporation tests in this phase. Heat transfer coefficients for full bundle tests seemed to be less sensitive to minute changes in inlet subcooling for R1233zd(E) as indicated in the results for Series D18 and D19. Values at similar heat fluxes were within ±10% despite the 0.8 °C difference in inlet subcooling. In this case, direct

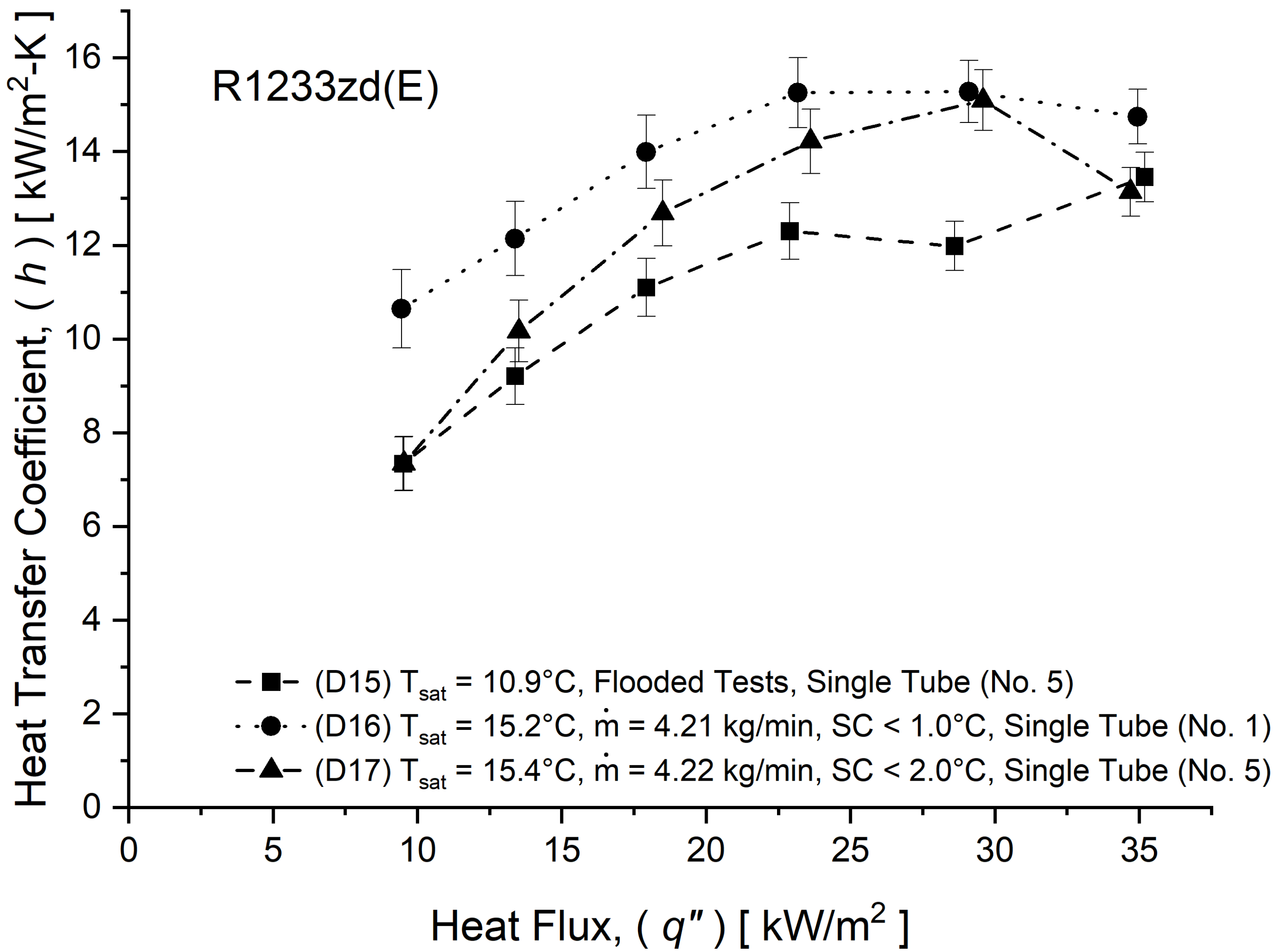

Figure 4.38: Heat transfer coefficient vs heat flux (Phase 3, R1233zd(E), single tube tests)

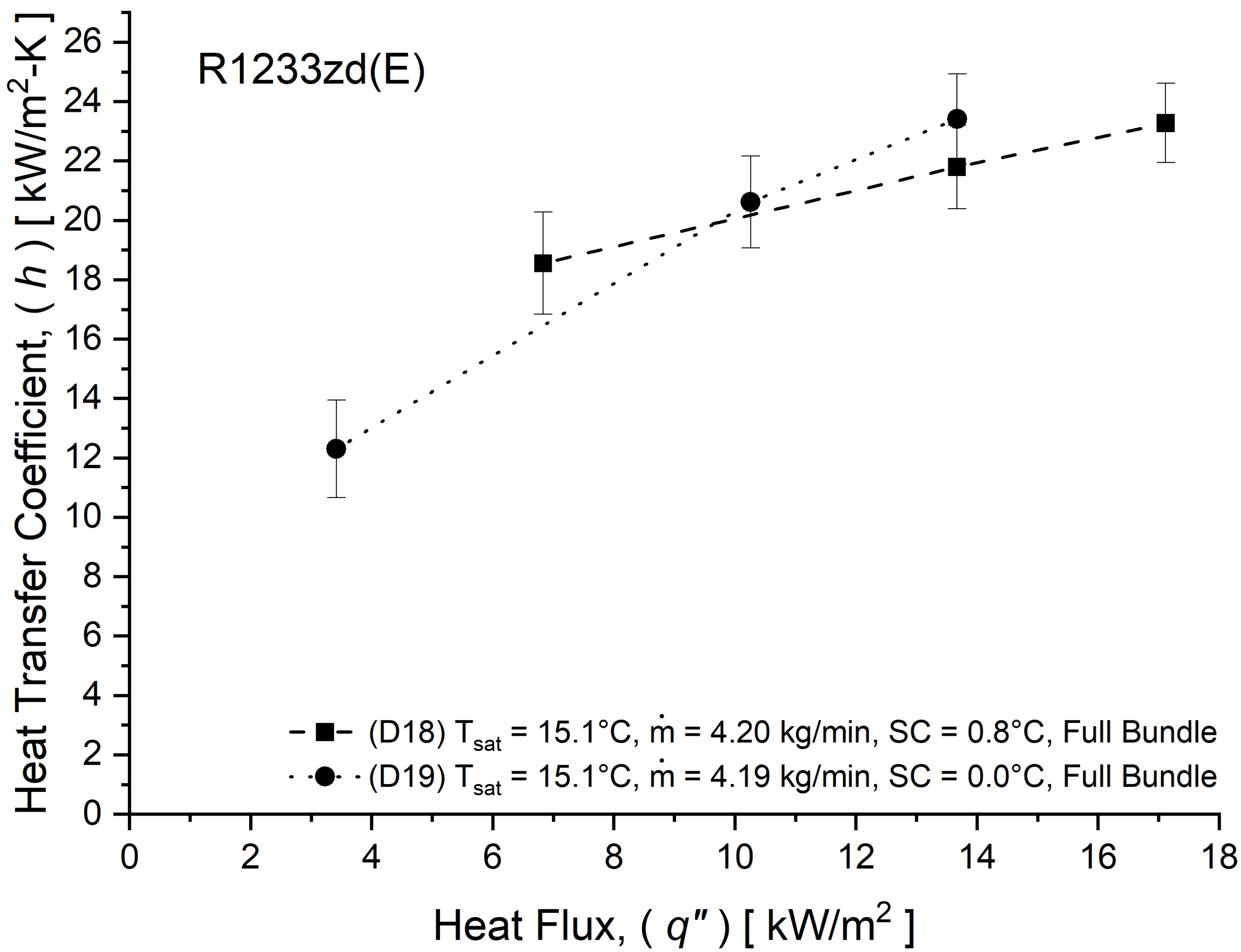

Figure 4.39: Heat transfer coefficient vs heat flux (Phase 3, R1233zd(E), T_{sat} = 15 °C)

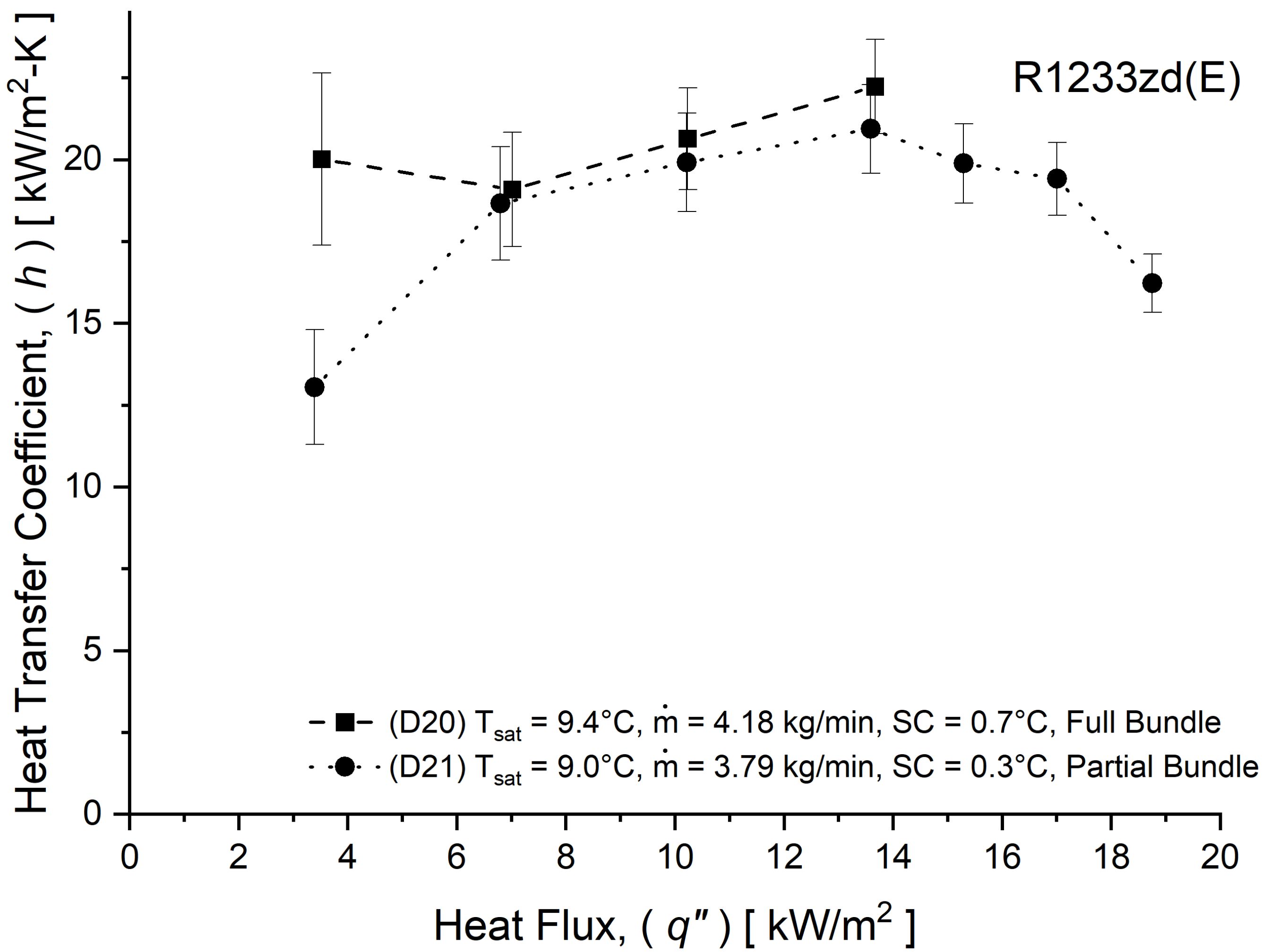

Figure 4.40: Heat transfer coefficient vs heat flux (Phase 3, R1233zd(E), T_{sat} = 9 °C)

comparisons could not be made to the earlier Tube-C enhanced surface tubes as those data were collected under different conditions. Worth noting is that, for these series, the onset of dryout was so severe that tests could not be performed at heat fluxes above approximately 20 kW/m^2. This was observed in the 9 °C saturation temperature series D21 with only 0.3 °C of subcooling in which heat transfer coefficient values began to decrease rapidly at heat fluxes above 13 kW/m^2. Values for Series D20 with a higher degree of subcooling were slightly higher than those for Series D21, though this was likely due to the difference in refrigerant mass flow rate between the two. As with the 15 °C series, direct comparisons could not be made to data in Phase 1, but more apt comparisons were made between Phase 4 and Phase 2 and are presented in the next section.

4.4 Phase 4 Results

The experimental test results for Phase 4, using the Tube-B evaporator tubes in the square geometry with the full circular cone nozzles, are presented in Figures 4.41 through 4.48. For Phase 4, refrigerant R134a was tested in the full bundle configuration at saturation temperatures of approximately 10 °C and 2.5 °C. The R134a results are shown in Figures 4.41 and 4.42. Refrigerant R1234ze(E) was tested in the full bundle configuration at saturation temperatures of 10 °C, 2.5 °C, -6.5 °C, and -12 °C, and these results are shown in Figures 4.43, 4.44, 4.45, and 4.46. Also, refrigerant R1233zd(E) was tested in the full bundle configuration at saturation temperatures of approximately 15 °C, 9 °C, and 5 °C, shown in Figures 4.47 and 4.48.

For the R134a tests in Phase 4, refrigerant mass flow rate was kept nearly constant around 4.60 kg/min, and inlet subcooling was varied between 1.1 °C and 1.9 °C. Bundle heat transfer coefficients for the 10 °C series varied between 3.5 kW/m^2-K and 13.5 kW/m^2-K for heat fluxes between 3 kW/m^2 and 21 kW/m^2. Those for the 2.5 °C series varied between 3.7 kW/m^2-K and

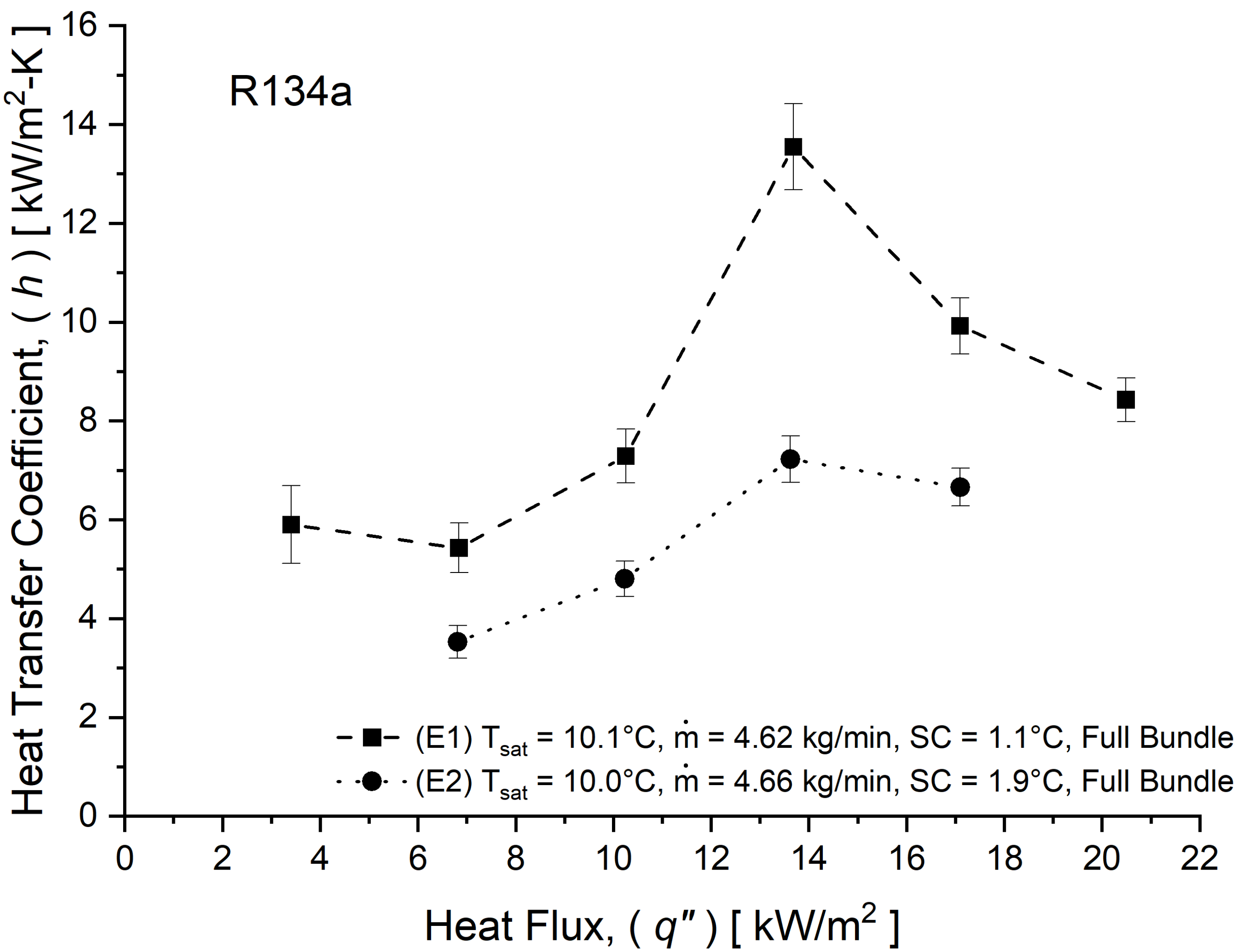

Figure 4.41: Heat transfer coefficient vs heat flux (Phase 4, R134a, T_{sat} = 10 °C)

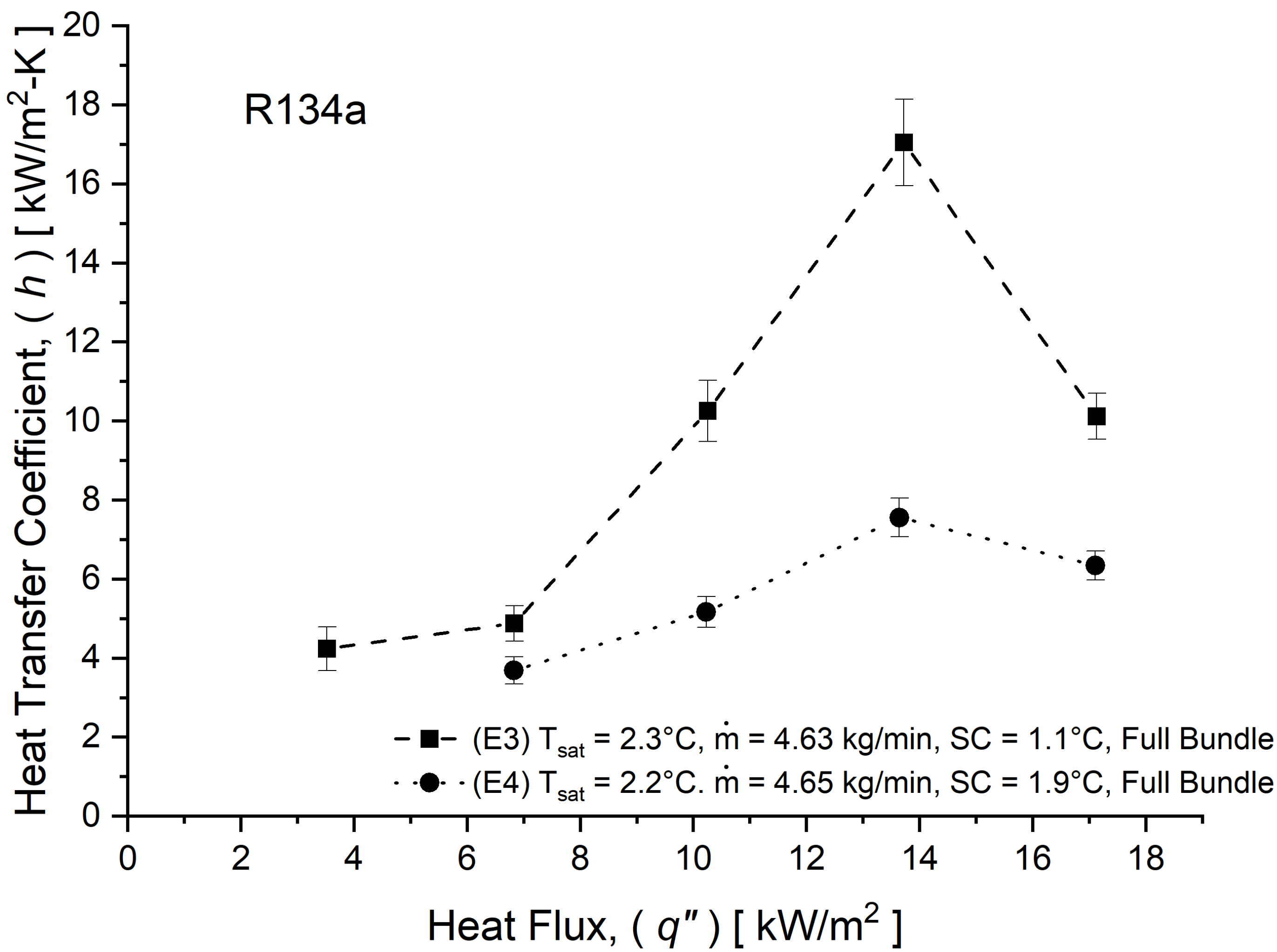

Figure 4.42: Heat transfer coefficient vs heat flux (Phase 4, R134a, T_{sat} = 2.5 °C)

17.0 kW/m^2-K for heat fluxes between 3 kW/m^2 and 17 kW/m^2. The most notable trend observed at both refrigerant saturation temperatures for lower degrees of subcooling, Series E1 and E3, was the large spike and relatively high peak in heat transfer coefficient values at approximately 14 kW/m^2. Careful review of the data revealed that, although the average subcooling for both series was 1.1 °C, both tests at 14 kW/m^2 were performed with a slightly lower subcooling of 0.7 °C. The result was an 85% increase and a 65% increase in bundle heat transfer coefficient from that calculated for the next lowest heat flux for Series E1 and Series E3, respectively. Values for higher degrees of subcooling were between 30% and 50% lower for Series E2 than in E1, and between 20% and 60% lower for Series E4 than in E3, for a difference of 0.8 °C between both sets. Though not a direct comparison, it was found that heat transfer coefficients were between 10% and 500% higher (with larger differences at higher heat fluxes) for Series E1 than for the earlier Series C4 performed at the same saturation temperature despite the higher refrigerant mass flow rate and lower subcooling of the latter. The values in Series E3 versus those in the similar Series C6 were only 5% higher at low heat fluxes, but were nearly 1000% higher at high heat fluxes (an absolute difference of 15.4 kW/m^2-K) due to the difference in enhanced surface type.

For the R1234ze(E) tests in Phase 4, refrigerant mass flow rate was kept nearly constant at approximately 4.65 kg/min except for the very low saturation temperature series at 2.89 kg/min, and inlet subcooling was varied between 0.7 °C and 1.8 °C. Bundle heat transfer coefficients for the 10 °C series varied between 3.2 kW/m^2-K and 9.5 kW/m^2-K for heat fluxes between 3 kW/m^2 and 21 kW/m^2. Those for the 2.5 °C series varied between 2.8 kW/m^2-K and 12.7 kW/m^2-K for heat fluxes between 3 kW/m^2 and 21 kW/m^2. Those for the -6.5 °C series varied between 4.4 kW/m^2-K and 13.5 kW/m^2-K for heat fluxes between 3 kW/m^2 and 19 kW/m^2. Those for the -12 °C series varied between 2.2 kW/m^2-K and 11.3 kW/m^2-K for heat fluxes between 3 kW/m^2 and

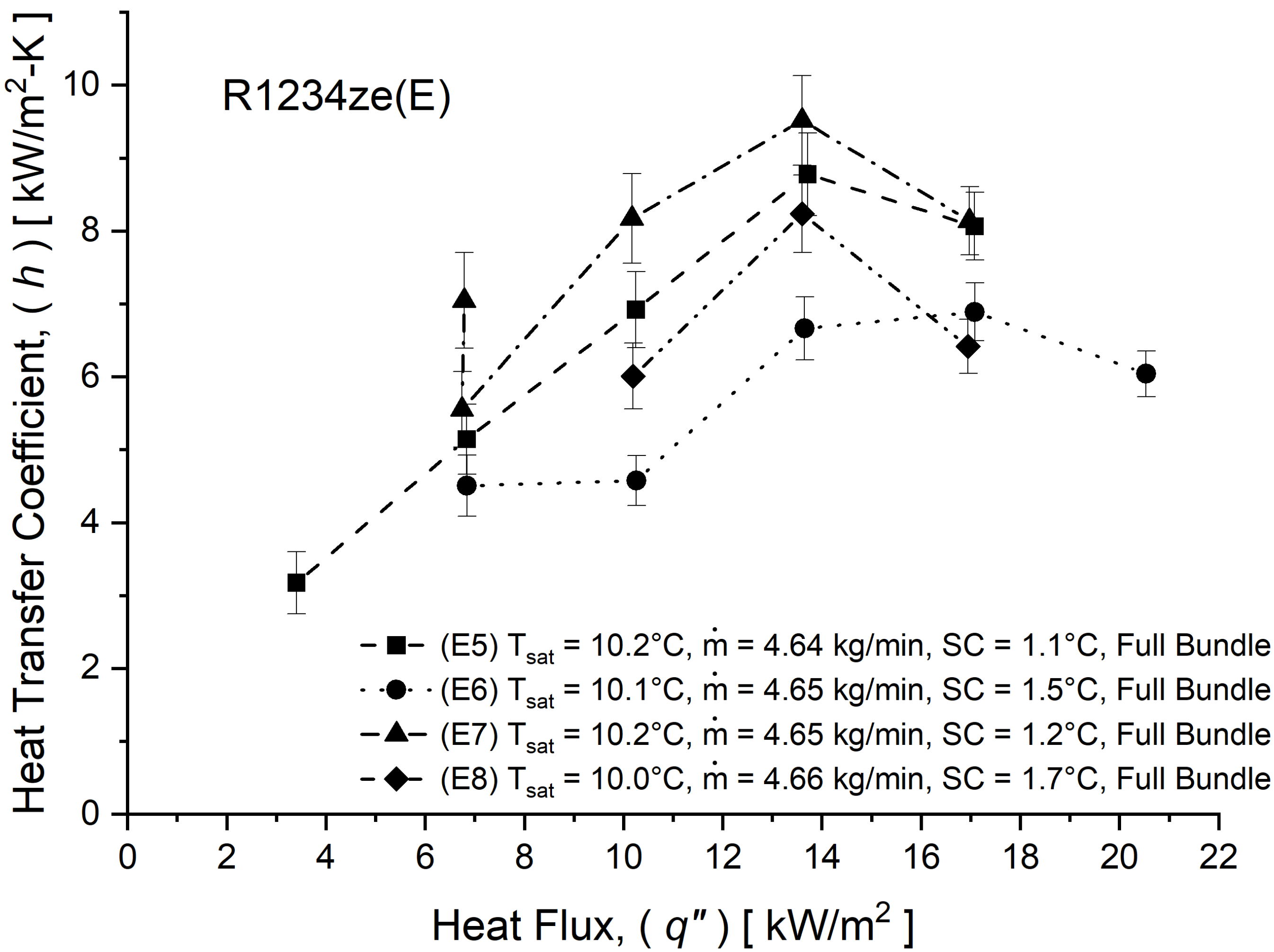

Figure 4.43: Heat transfer coefficient vs heat flux (Phase 4, R1234ze(E), T_{sat} = 10 °C)

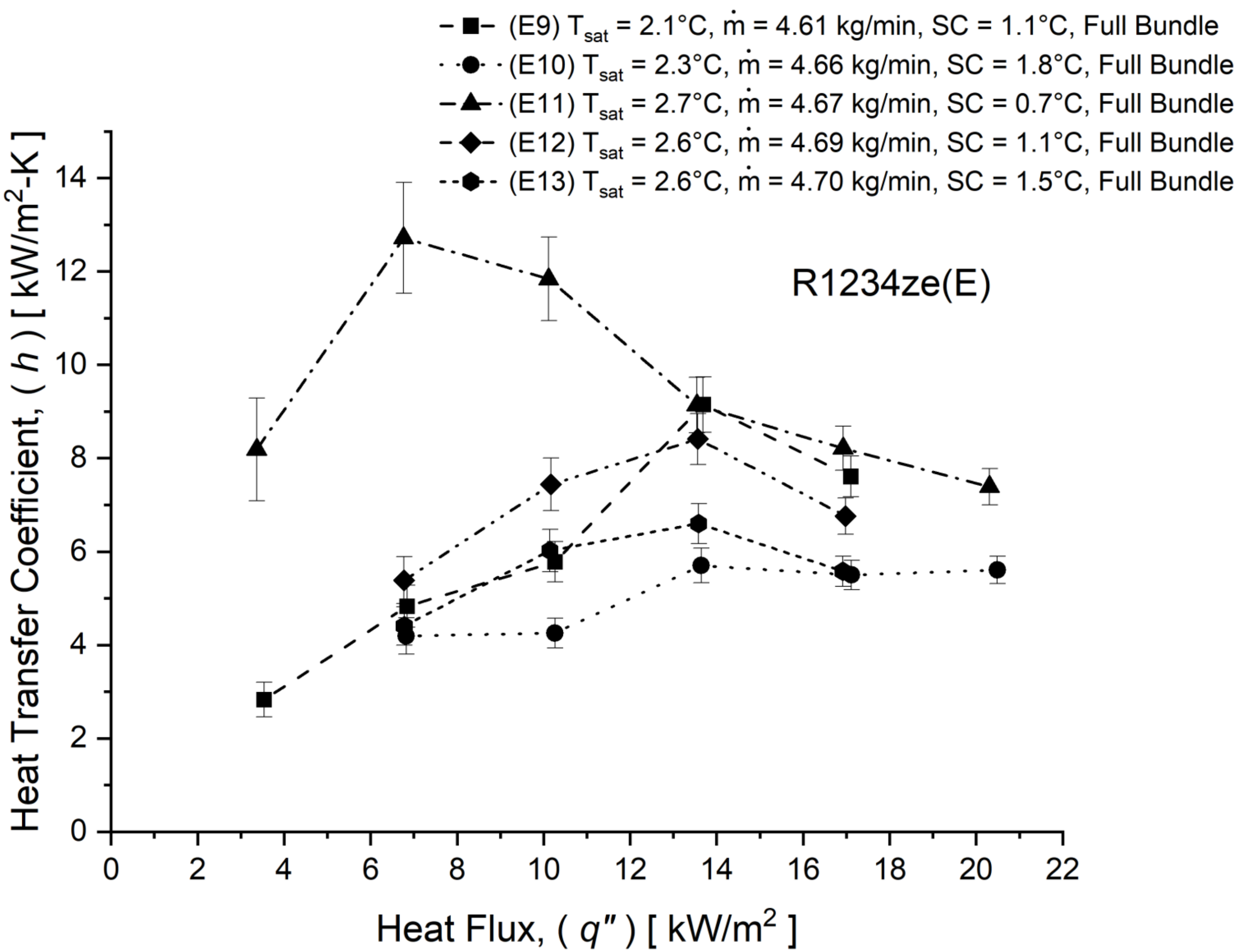

Figure 4.44: Heat transfer coefficient vs heat flux (Phase 4, R1234ze(E), T_{sat} = 2.5 °C)

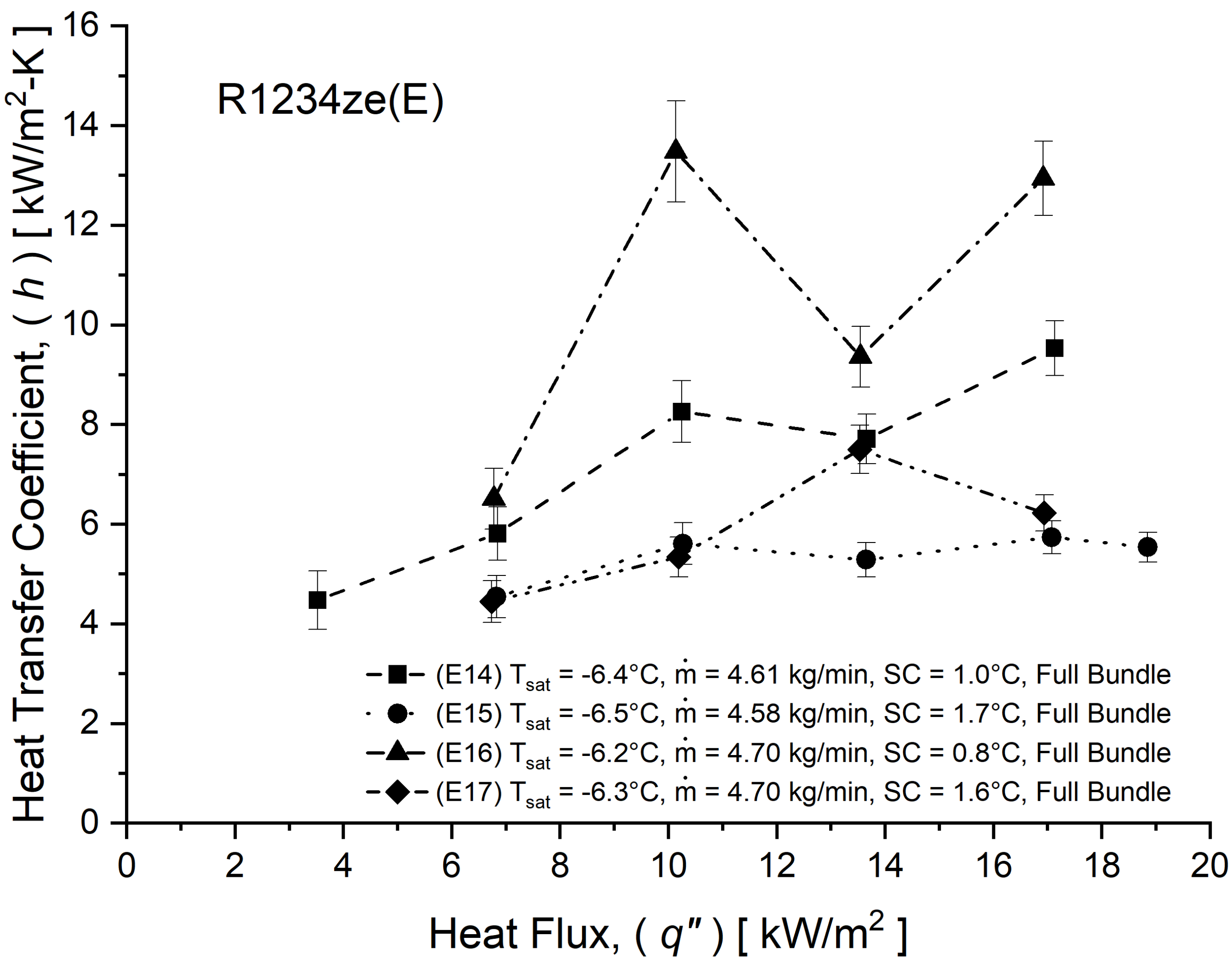

Figure 4.45: Heat transfer coefficient vs heat flux (Phase 4, R1234ze(E), T_{sat} = -6.5 °C)

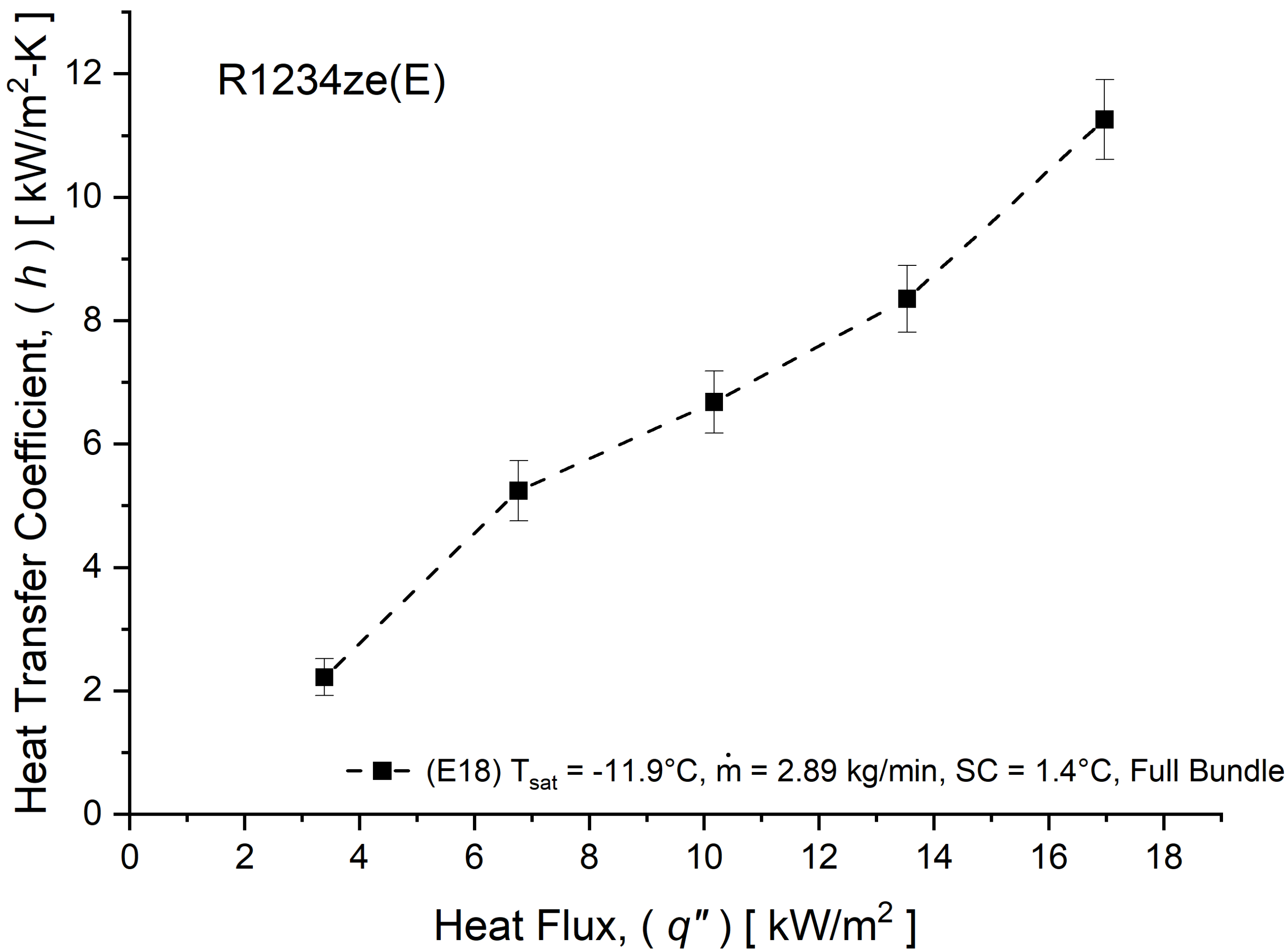

Figure 4.46: Heat transfer coefficient vs heat flux (Phase 4, R1234ze(E), T_{sat} = -12 °C)

17 kW/m^2. For all 10 °C series, the onset of the dryout condition was readily apparent in the sudden plateau or decrease in heat transfer coefficients above 14 kW/m^2 regardless of subcooling. Values for similar heat fluxes between series were generally more closely spaced than in previous phases, sometimes within the experimental uncertainty, most likely due to the closely spaced levels of subcooling. Heat transfer coefficients for Series E5 were between 25% and 50% lower than those for the most similar series from Phase 3, Series D10. However, because of the 0.2 °C difference in subcooling between the two, it was not clear whether the decrease was due more to the difference in subcooling or bundle geometry. Similarly, heat transfer coefficients for Series E11 were within ±35% of those for the similar Series D12, though the latter had an average subcooling that was higher by 0.2 °C. As in the 10 °C series, all but one of the 2.5 °C series exhibited the onset of dryout at approximately 14 kW/m^2. The one that did not, Series E11, had the lowest subcooling among the group and experienced dryout at a much lower heat flux of approximately 6.5 kW/m^2, similar to previous observations. For the -6.5 °C group, heat transfer coefficients for Series E14 with a subcooling of 1.0 °C were within ±30% of those for the most similar Series D14, which had a higher subcooling of 1.3 °C. Those values for D14 were in turn 10% to 45% higher than those for Series E17 with a subcooling of 1.6 °C. Given these comparisons, it seemed that the triangular bundle geometry provided a slight advantage in terms of bundle heat transfer coefficient values for similar levels of subcooling. Regarding the differences between enhanced surface type, heat transfer coefficient values for Series E8 were between 85% and 150% greater than those for Series C17 at the same level of inlet subcooling and slightly increased mass flow rate for the latter. Values for Series E13 were between 5% and 45% greater than those for Series C19, and values for Series E14 were between 50% and 85% greater than those for C23, indicating an overall significant advantage for the Tube-B surface over the Tube-C surface. In the lowest saturation temperature

series for R1234ze(E), heat transfer coefficients only increased with increasing heat flux due to a slightly decreasing level of inlet subcooling as the series progressed.

For the R1233zd(E) tests in Phase 4, refrigerant mass flow rate was varied between 3.54 kg/min and 4.09 kg/min, and inlet subcooling was varied between -1.3 °C and 1.1 °C. Bundle heat transfer coefficients for the 15 °C series varied between 8.3 kW/m^2-K and 17.1 kW/m^2-K for heat fluxes between 3 kW/m^2 and 14 kW/m^2. Bundle heat transfer coefficients for the lower saturation temperature series varied between 9.4 kW/m^2-K and 17.0 kW/m^2-K for heat fluxes between 10 kW/m^2 and 14 kW/m^2. The 15 °C series were an excellent illustration of the disadvantages of overly subcooling and overly saturating the refrigerant at the test section inlet. The highest bundle heat transfer coefficients recorded amongst the group were those for Series E20 for which inlet subcooling was 0.0 °C. All other series, with inlet subcooling both positive and negative, returned values between 10% and 35% lower at similar heat flux levels. Data for the lower saturation temperature series was quite sparse given the difficulty in testing R1233zd(E) at such low pressures, but the most noticeable trends were heat transfer coefficients that were approximately 35% to 40% lower for a decrease in refrigerant saturation temperature of around 4 °C. Bundle heat transfer coefficient values were between 30% and 40% lower for Series E20 than for the similar Series D19, and were between 35% and 70% lower for Series E19 that for Series D18. Similarly, for the 9 °C series, values were between 20% and 40% lower for Series E25 than for Series D21, again indicating slight advantages for the triangular geometry over the square geometry.

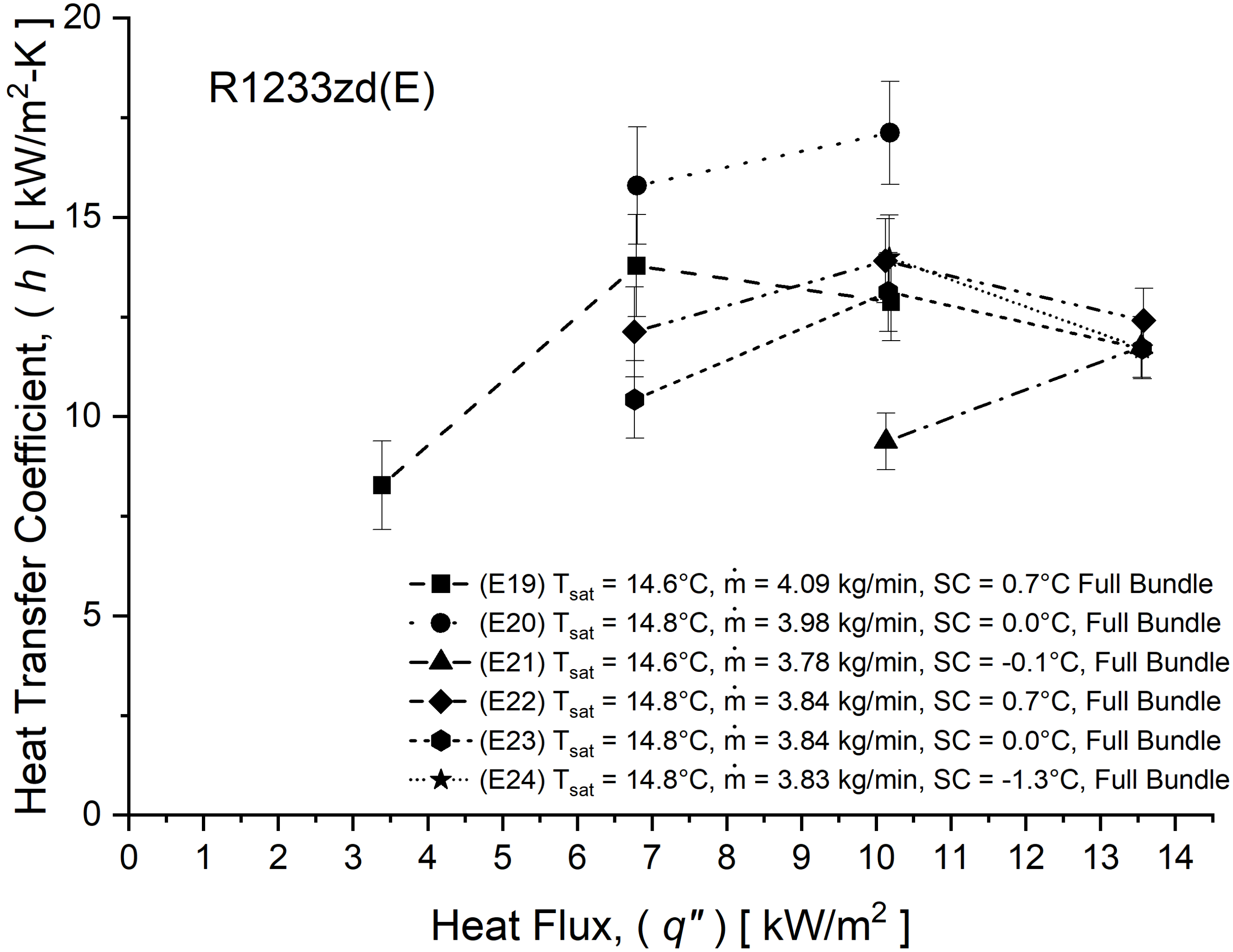

Figure 4.47: Heat transfer coefficient vs heat flux (Phase 4, R1233zd(E), T_{sat} = 15 °C)

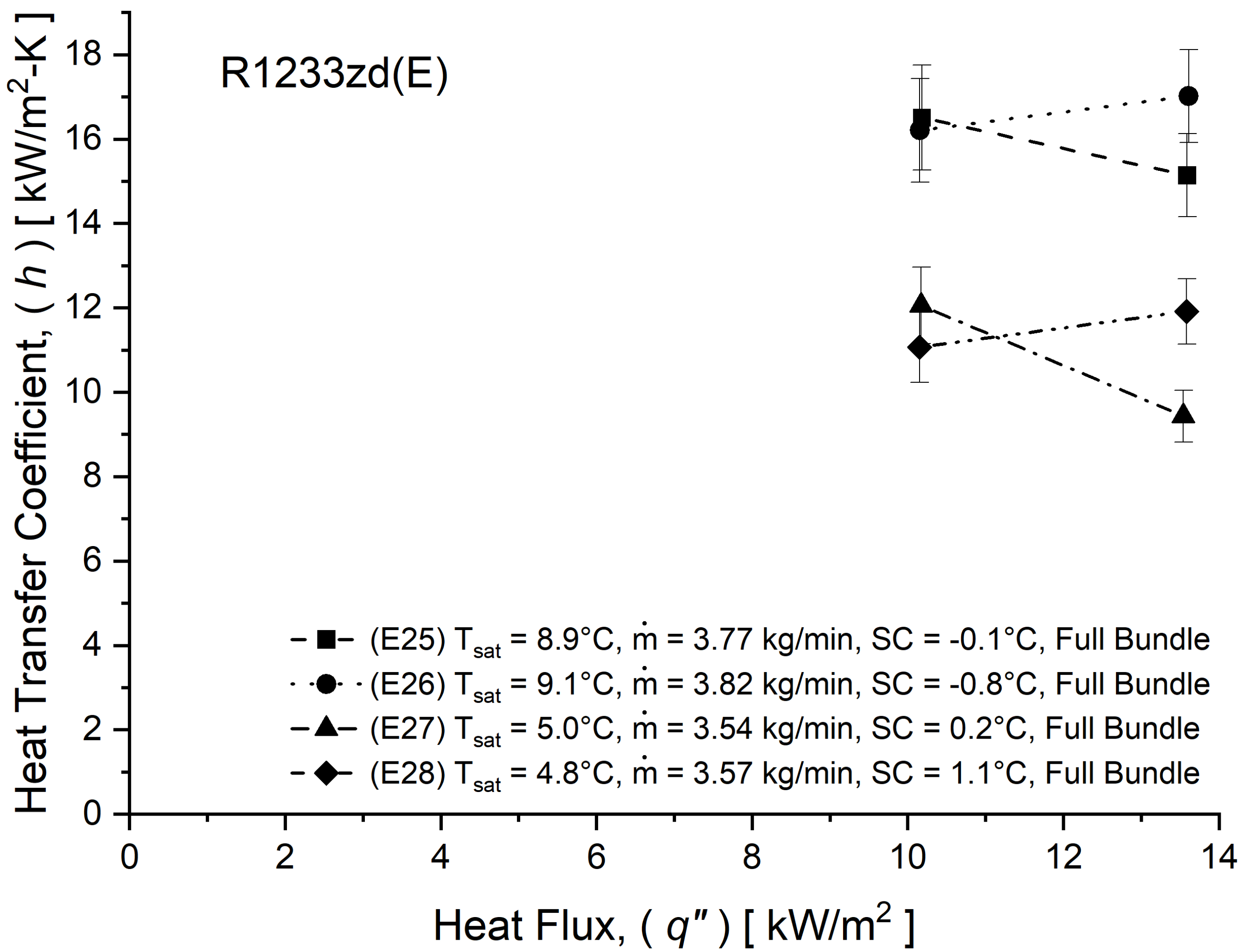

Figure 4.48: Heat transfer coefficient vs heat flux (Phase 4, R1233zd(E), 5 °C < T_{sat} < 9 °C)

4.5 Summary of Experimental Results

As described, tubes with two different enhanced surface types were tested in bundles with two different geometries and with three different refrigerants at varying levels of inlet subcooling. Via thorough investigation and systematic variations in these variables, the effect of each was quantified and the results are presented in this section. In general, it was found that the dependence of bundle heat transfer coefficients on enhanced surface type was very strong, amongst the strongest of the variables tested. Conversely, for the test setup used in these experiments, a much weaker correlation between bundle heat transfer coefficients and bundle geometry was noticed. The general effects of both enhanced surface type and bundle geometry are illustrated for refrigerants R134a and R1234ze(E) in Figure 4.49 and for R1233zd(E) in Figure 4.50.

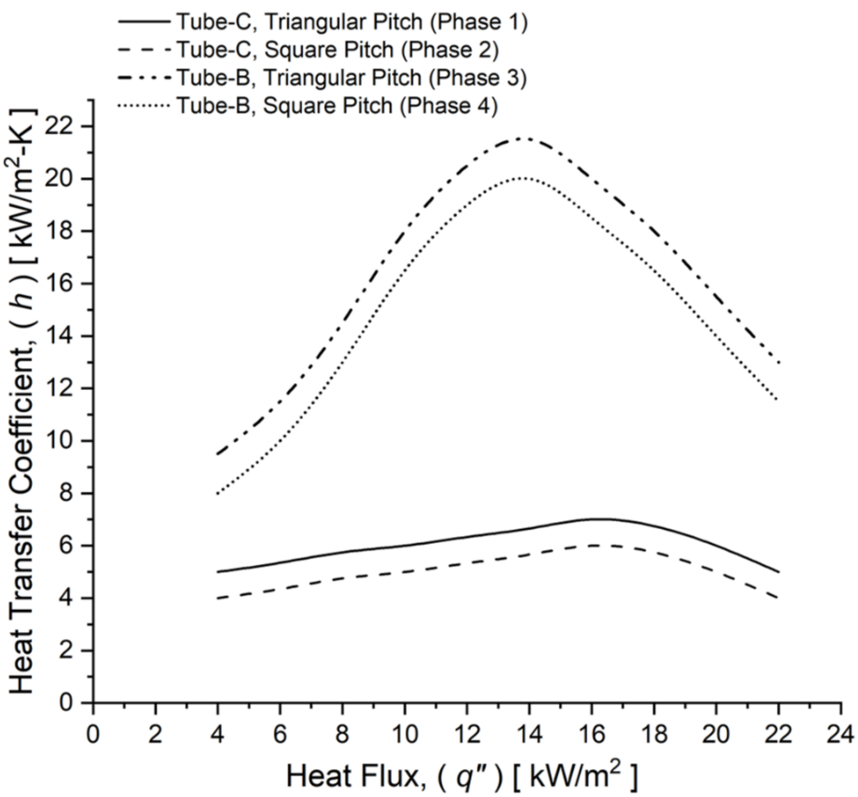

Figure 4.49: Effects of enhanced surface type and bundle geometry on overall heat transfer coefficients with R134a and R1234ze(E)

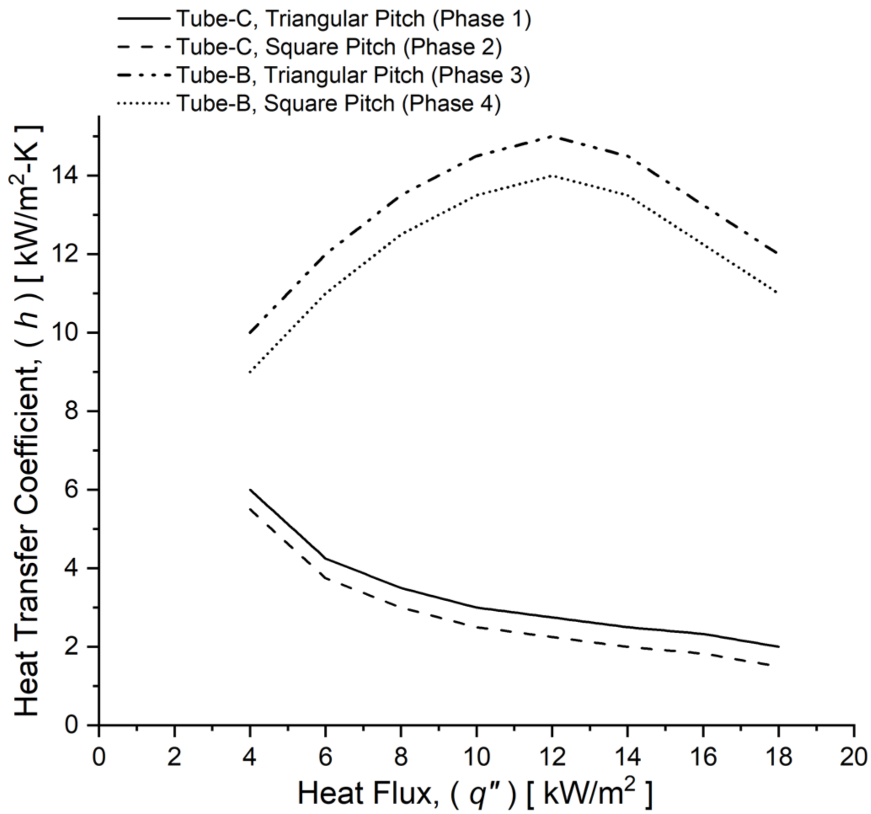

Figure 4.50: Effects of enhanced surface type and bundle geometry on overall heat transfer coefficients with R1233zd(E)

In general for all three refrigerants, the lowest bundle heat transfer coefficients were achieved with the Tube-C enhanced surface in the square bundle geometry. This was due to a combination of the significantly decreased performance of the Tube-C surface compared to the Tube-B surface and the slight decrease in bundle heat transfer coefficients attributed to the square geometry compared to the triangular geometry. The enhancement effect of the triangular geometry was found to be approximately 10% to 30% greater than that of the square geometry with larger relative differences recorded at lower bundle heat transfer coefficient values. The reasons for this modest enhancement were threefold: the triangular geometry allowed the tubes in the second row to receive direct impingement of the liquid refrigerant on their upper surfaces in addition to those in the first row; all tubes in the lower rows received a greater supply of refrigerant at the same nominal mass flow rate because a lesser amount was evaporated by the tubes directly above; and, two fewer tubes were heated in the triangular geometry compared to the square geometry, meaning a slightly decreased total power input for a given level of heat flux. Given these factors and similar results that had been reported in the literature, this finding was not unexpected. The enhancement effect of the Tube-B surface compared to the Tube-C surface was significantly greater at approximately 50% to 500%, depending on heat flux and refrigerant type. For R134a and R1234ze(E), the Tube-C surface produced bundle heat transfer coefficient curves that were generally flatter such that absolute variations with increasing heat flux were less than in the curves produced by the Tube-B surface. These absolute variations were generally on the order of 2 kW/m^2-K to 5 kW/m^2-K for the Tube-C surface and were often in excess of 10 kW/m^2-K for the Tube-B surface. The peaks in the heat transfer coefficient curves generally occurred at slightly lower heat flux levels, on the order of 10% to 15% lower, for the Tube-B surface compared to the Tube-C surface while curve slopes were much steeper for the Tube-B surface, indicating greater sensitivity to heat flux levels. For R1233zd(E), the peak trend was reversed such that the Tube-C surface produced curves that peaked at very low heat fluxes while the Tube-B curves peaked at moderate heat fluxes. As with the other refrigerants, however, the Tube-C curves were generally flatter such that absolute variations were lesser and the Tube-B surfaces showed greater sensitivity to changes in heat flux. Also, while absolute peaks for the Tube-C surfaces were nearly identical for all three refrigerants, those for the Tube-B surfaces were lower for R1233zd(E) at 12 kW/m^2-K to 15 kW/m^2-K compared to values in excess of 20 kW/m^2-K for R134a and R1234ze(E). Given these results, the highest heat transfer coefficients for all refrigerants intuitively belonged to the bundle with the Tube-B surfaces and the triangular geometry. Because curve shapes are highly dependent on test section geometry and refrigerant distribution within the bundle, generalizations for other applications could not be made. However, it can be concluded with relative confidence that, for heat exchangers with a similar refrigerant distribution setup, the triangular pitch geometry will yield slightly enhanced heat transfer coefficients compared to a square pitch geometry. It can also be generalized with great confidence that the Tube-B surface and other such low-finned surfaces that are designed to enhance evaporation and boiling heat transfer will produce much greater spray evaporation heat transfer coefficients than those surfaces like the Tube-C surface which are designed to enhance condensation.

Besides bundle geometry and enhanced surface type, it was also found that the degree of refrigerant subcooling at the test section inlet had a significant effect on bundle heat transfer coefficient peak values and curve shapes, as illustrated in Figure 4.51.

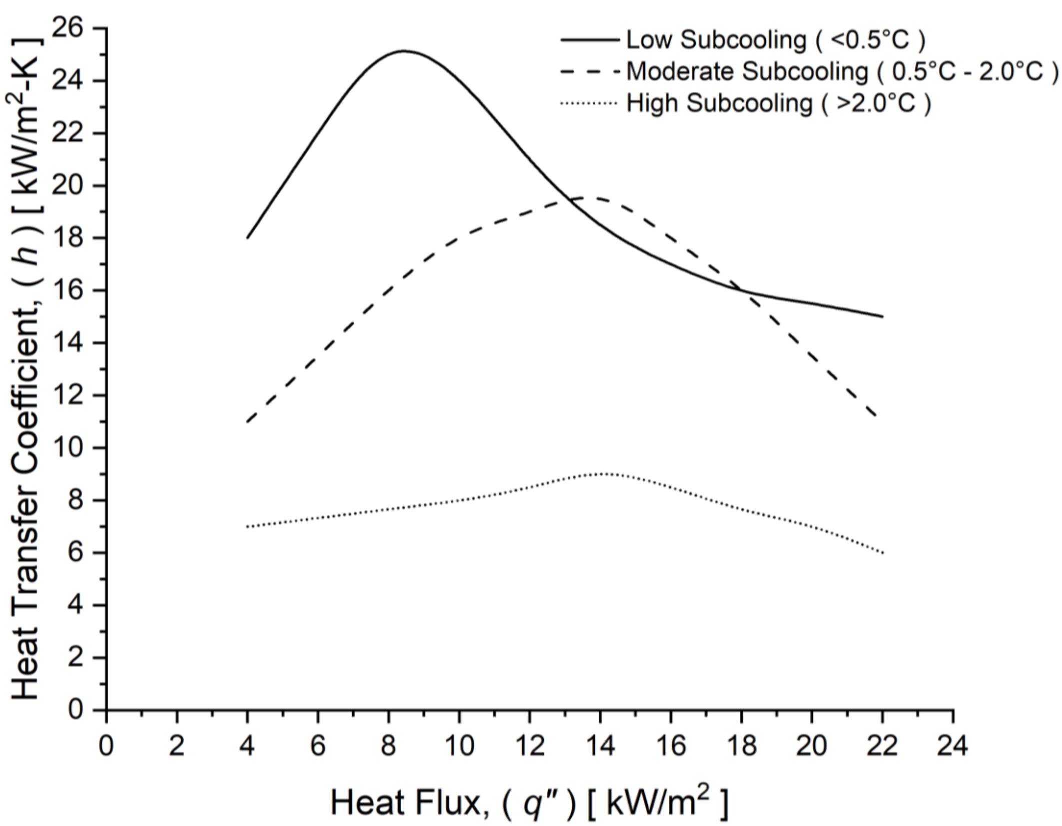

Figure 4.51: Effects of refrigerant inlet subcooling on bundle heat transfer coefficients

Though the specific values in the figure are more representative of the Tube-B surfaces, characteristics such as curve shapes and locations relative to each other can be applied to both enhanced surfaces and both bundle geometries tested. For all refrigerants, surface types, and bundle geometries, the highest peak heat transfer coefficients recorded during experimentation were those belonging to tests with relatively low levels of inlet subcooling. Generally, the highest peak values were attained with inlet subcooling levels less than 0.5 °C, with moderate performance often attained for subcooling between 0.5 °C and 2.0 °C, and decreased performance corresponding to subcooling levels greater than 2.0 °C. However, heat transfer coefficient curve shapes for these three regimes varied from each other significantly. In the low subcooling regime, peak heat transfer coefficients were often reached at relatively low heat flux levels with a steep increase below the peak and a sharp decrease after the peak. The steep increase was due to heat flux values that increased rapidly while the refrigerant reference temperature and tube wall temperatures remained nearly constant, while the sharp decrease was a result of the much earlier onset of the dryout condition in which tube wall temperatures spiked due to insufficient refrigerant supply. By comparison, a moderate degree of subcooling ensured a greater supply of liquid refrigerant to lower tube rows at higher heat fluxes, thus shifting the curve peak to the right, but also increased the difference between the refrigerant reference temperature and tube wall temperatures, thus resulting in slightly decreased peak performance compared to the low subcooling regime. The poorest performance was recorded in the high subcooling regime in which heat transfer coefficient curves were nearly flat and thus were not as sensitive to changes in heat flux. While high degrees of subcooling increased the supply of liquid refrigerant to all tube rows, it significantly diminished the effects of nucleate boiling on the tube outer surfaces in favor of convective heat transfer, resulting in lower heat transfer coefficient values over the entire range of heat fluxes. Though these values were low compared to those attained in the low and moderate subcooling spray evaporation regimes, they were quite similar to values reported in the literature for pool boiling on bundles of plain tubes. In that regard, the spray evaporator configuration with enhanced surfaces would provide the advantage of decreased refrigerant inventory compared to a flooded evaporator even if increases in heat transfer coefficients were not realized. Based on the findings, the greatest advantages of the spray evaporator configuration are realized when the heat exchanger operates with moderate to low levels of inlet subcooling at moderate to high heat fluxes. In these cases, heat transfer coefficients are comparable or slightly greater than those reported for pool boiling on enhanced surfaces with the added benefit of decreased refrigerant inventory in the system. It is for these reasons that spray evaporators implemented in real large-scale industrial processes are usually designed to operate in that regime and that heat transfer coefficient correlations formulated from research and development are valid primarily for those operating conditions.

4.6 Effect of Nozzle Type on Heat Transfer Performance

In addition to the preceding tests in which the circular cone nozzles were used, a number of tests were performed using the flat deflected spray nozzle arrangement. Even though these data were collected at the beginning of the experimental campaign, this phase of testing will be referred to as Phase 5. The experimental test results for Phase 5, using the Tube-C condenser tubes in the triangular geometry with the deflected flat spray nozzles, are presented in Figures 4.52 through 4.58. For Phase 5, refrigerant R134a was tested in the partial bundle configuration at saturation temperatures of approximately 10 °C, 5 °C, and 2 °C, shown in Figures 4.52, 4.53, and 4.54, respectively. Additionally, refrigerant R1234ze(E) was tested in both full bundle and partial bundle configurations at saturation temperatures of approximately 20 °C, 10 °C, 3 °C, and -10 °C, shown in Figures 4.55, 4.56, 4.57, and 4.58, respectively.

For the R134a tests in Phase 5, refrigerant mass flow rate was varied between 2.42 kg/min and 3.26 kg/min, and inlet subcooling was varied between 1.3 °C and 6.2 °C. Bundle heat transfer coefficients for the 10 °C series varied between 6.8 kW/m^2-K and 8.1 kW/m^2-K for heat fluxes between 20 kW/m^2 and 35 kW/m^2 with a general increase in heat transfer coefficient with heat flux. Those for the 5 °C series varied between 1.0 kW/m^2-K and 6.3 kW/m^2-K for heat fluxes between 7 kW/m^2 and 41 kW/m^2. Those for the 2 °C series varied between 4.3 kW/m^2-K and 10.6 kW/m^2-K for heat fluxes between 17 kW/m^2 and 40 kW/m^2. Inspection of the data revealed no obvious dependence of the bundle heat transfer coefficient on refrigerant saturation temperature, but instead indicated a significant correlation between bundle heat transfer coefficient and degree of inlet subcooling. In Figure 4.53, it can be seen that the highest bundle heat transfer coefficients were recorded for the series of tests A4 with the lowest degree of inlet subcooling, 3.3 °C. The next highest heat transfer coefficients were recorded for the series A2 with an intermediate degree of subcooling, 5.0 °C, while the lowest heat transfer coefficients correspond to the series A3 with the highest inlet subcooling, 6.2 °C. This pattern was observed again for the 2 °C saturation temperature series in Figure 4.54, where the highest heat transfer coefficients were recorded for the lowest inlet subcooling of 1.3 °C in series A5. It can also be seen that similar heat transfer coefficients were observed for the two series A6 and A7 given the similar degrees of inlet subcooling, despite a 14% difference in refrigerant mass flow rate between the two series. Both series A2 and A3 showed a general increase in bundle heat transfer coefficient with heat flux, while series A4 showed an increase up to approximately 26 kW/m^2, after which bundle heat transfer coefficients began to decrease. Similar increases in the bundle heat transfer coefficient

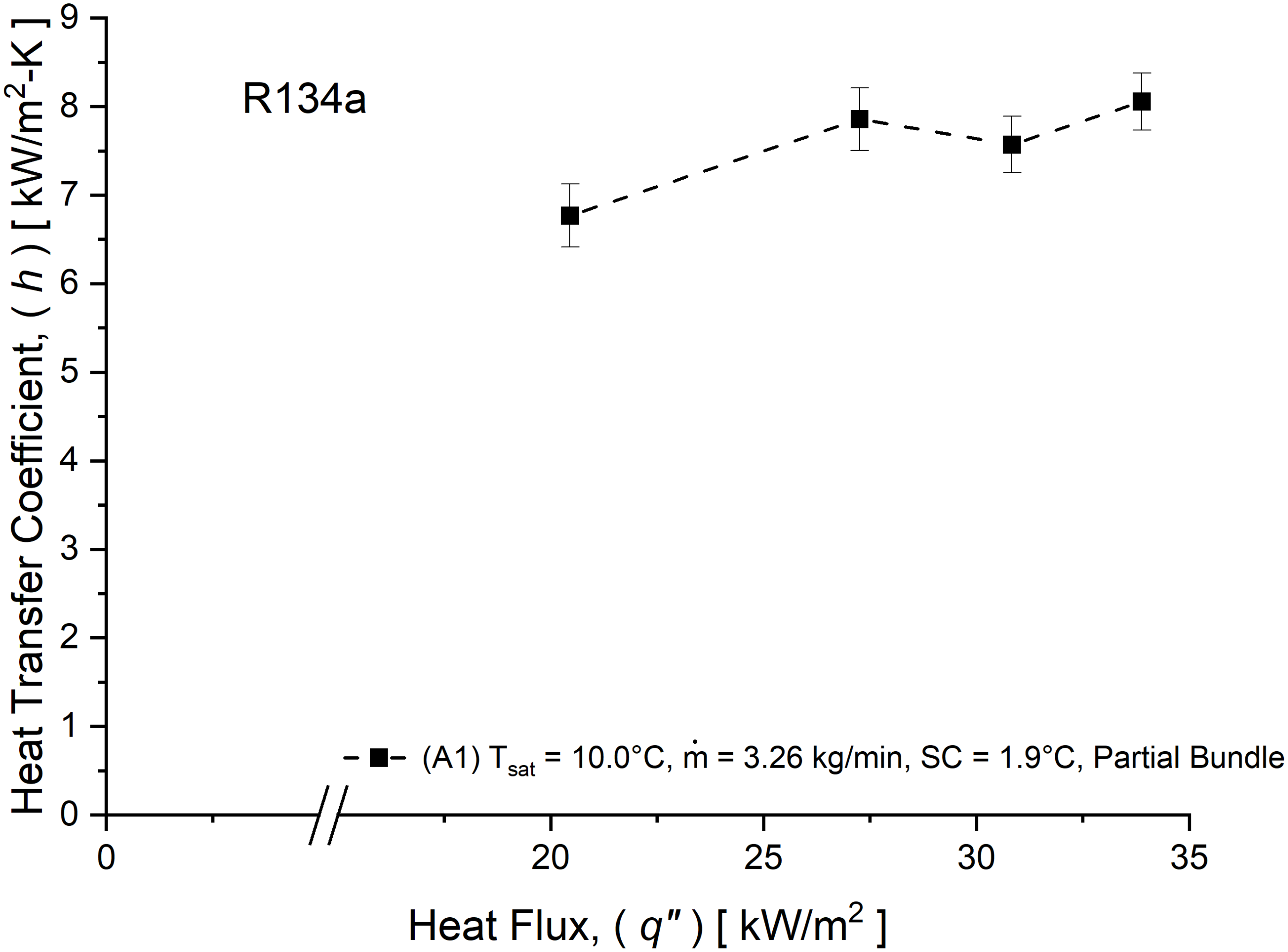

Figure 4.52: Heat transfer coefficient vs heat flux (Phase 5, R134a, T_{sat} = 10 °C)

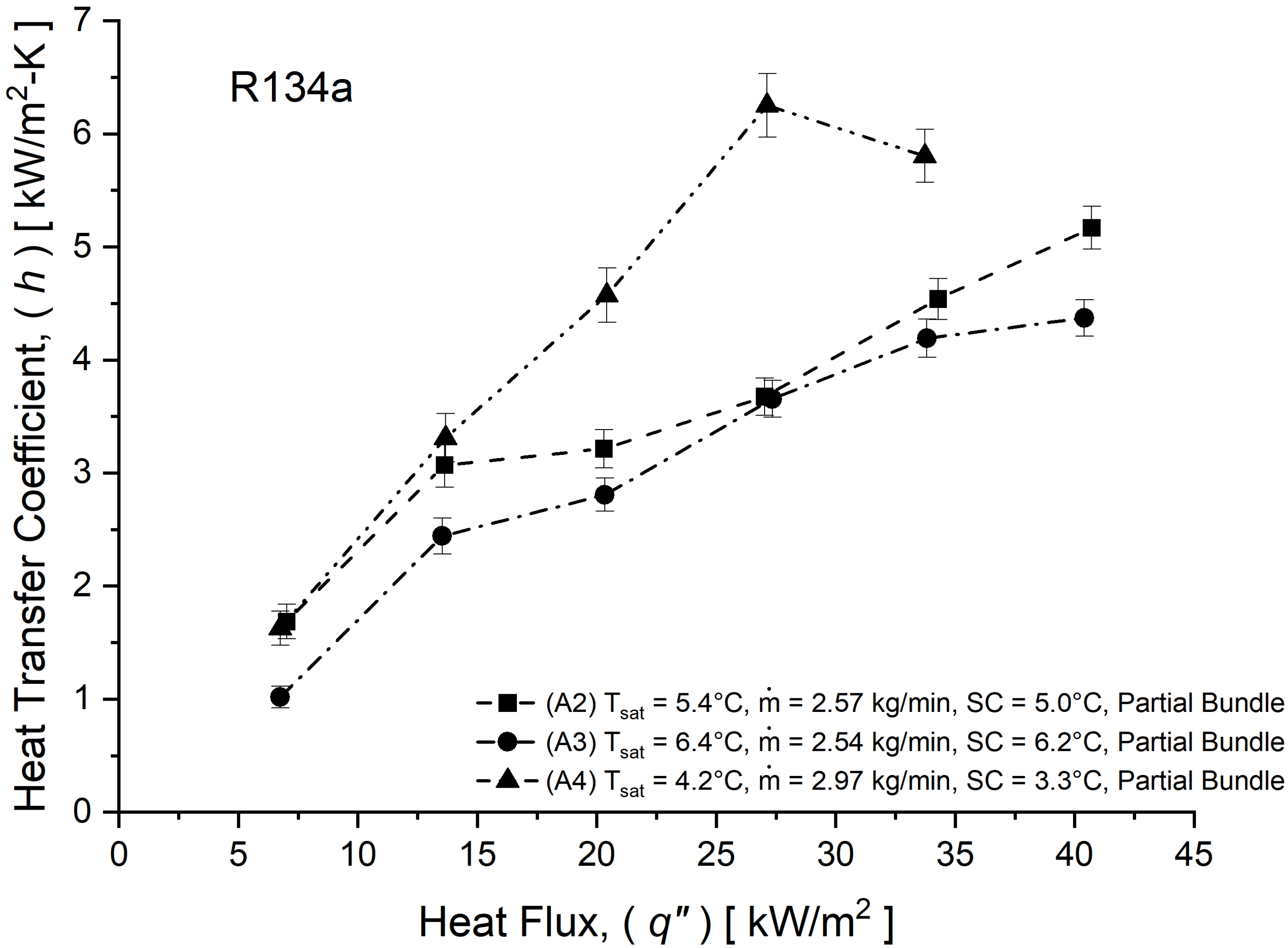

Figure 4.53: Heat transfer coefficient vs heat flux (Phase 5, R134a, T_{sat} = 5 °C)

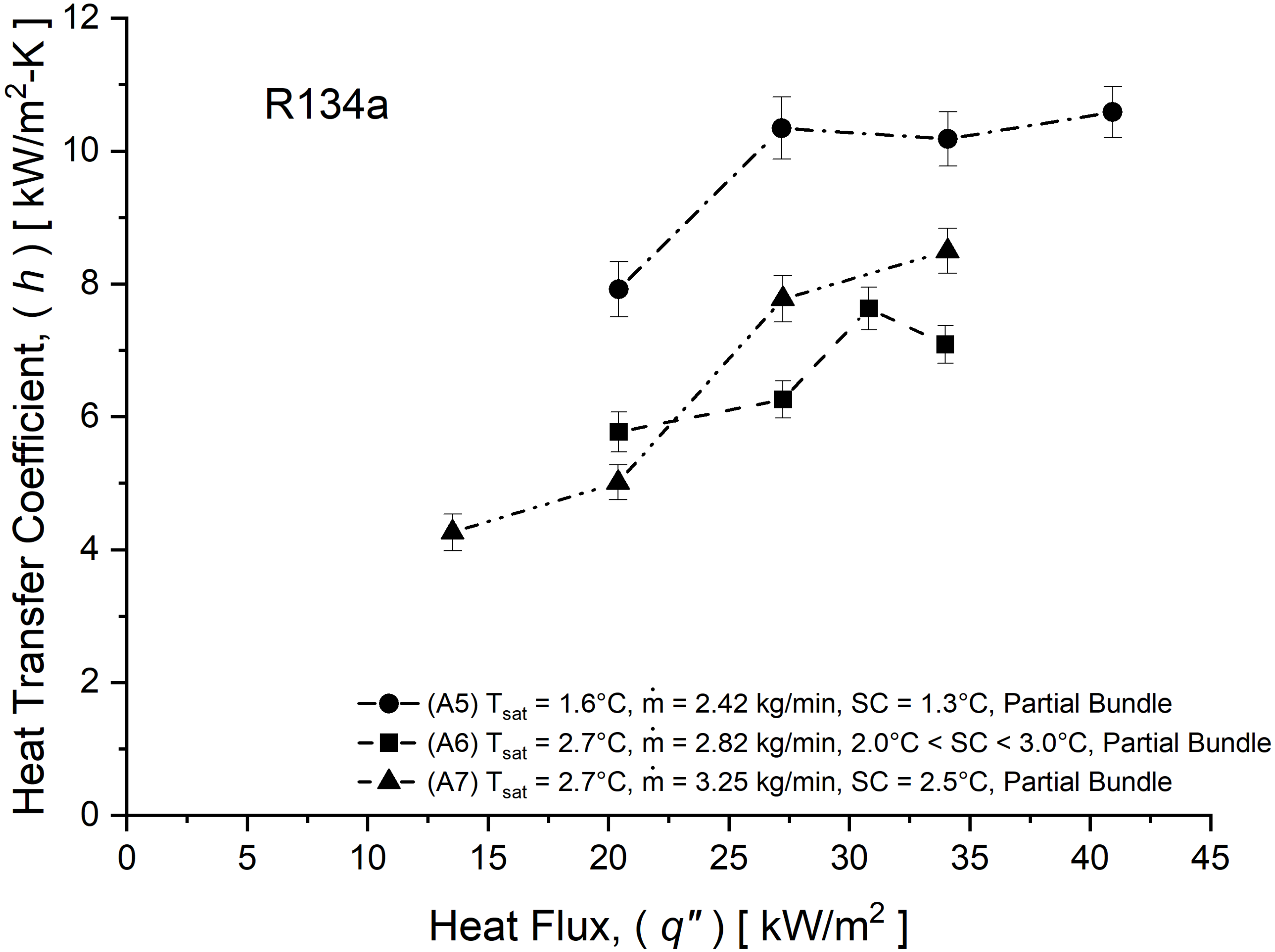

Figure 4.54: Heat transfer coefficient vs heat flux (Phase 5, R134a, T_{sat} = 2 °C)

with heat flux were observed for series A5, A6, and A7.

For the R1234ze(E) tests in Phase 5, refrigerant mass flow rate varied between 1.65 kg/min and 5.00 kg/min, and inlet subcooling was varied between -2.1 °C and 2.5 °C. Bundle heat transfer coefficients for the 20 °C series varied between 6.1 kW/m^2-K and 8.6 kW/m^2-K for heat fluxes between 14 kW/m^2 and 35 kW/m^2. Those for the 10 °C series varied between 3.5 kW/m^2-K and 9.6 kW/m^2-K for heat fluxes between 7 kW/m^2 and 33 kW/m^2. Those for the 3 °C series varied between 3.4 kW/m^2-K and 14.5 kW/m^2-K for heat fluxes between 7 kW/m^2 and 30 kW/m^2. Those for the -10 °C series varied between 9.1 kW/m^2-K and 14.2 kW/m^2-K for heat fluxes between 3 kW/m^2 and 20 kW/m^2. As before, bundle heat transfer coefficients showed no obvious dependence on refrigerant saturation temperature, but the inverse relationship between heat transfer coefficients and inlet subcooling was again observed here. Perhaps the most apt illustration of this phenomenon is in the 10 °C saturation temperature series depicted in Figure 4.56. For series A9 and A10, refrigerant mass flow rate was within 1.6% and saturation temperature was within 1%, but bundle heat transfer coefficients for similar levels of heat flux varied by as little as 20% at 20 kW/m^2 and as much as 60% at 14 kW/m^2. These differences were well outside the uncertainty and here were observed for a difference in inlet subcooling of only 0.7 °C. Similarly for the 3 °C series, bundle heat transfer coefficients were much higher (50% to 85%) for series A11 with an inlet subcooling below 1.5 °C than they were for series A12 with a subcooling of 1.5 °C. They were also approximately 27% higher for series A12 than for A13 at a similar heat flux for a difference in subcooling of only 0.4 °C. Series A9, A10, A12, and A13 showed a general increase or plateau in bundle heat transfer coefficients with increasing heat flux, while series A8, A11 and A14 showed a generally opposite trend. In series A8 and A11, this pattern was observed because the degree of inlet subcooling was inconsistent throughout the series with a general increase in inlet

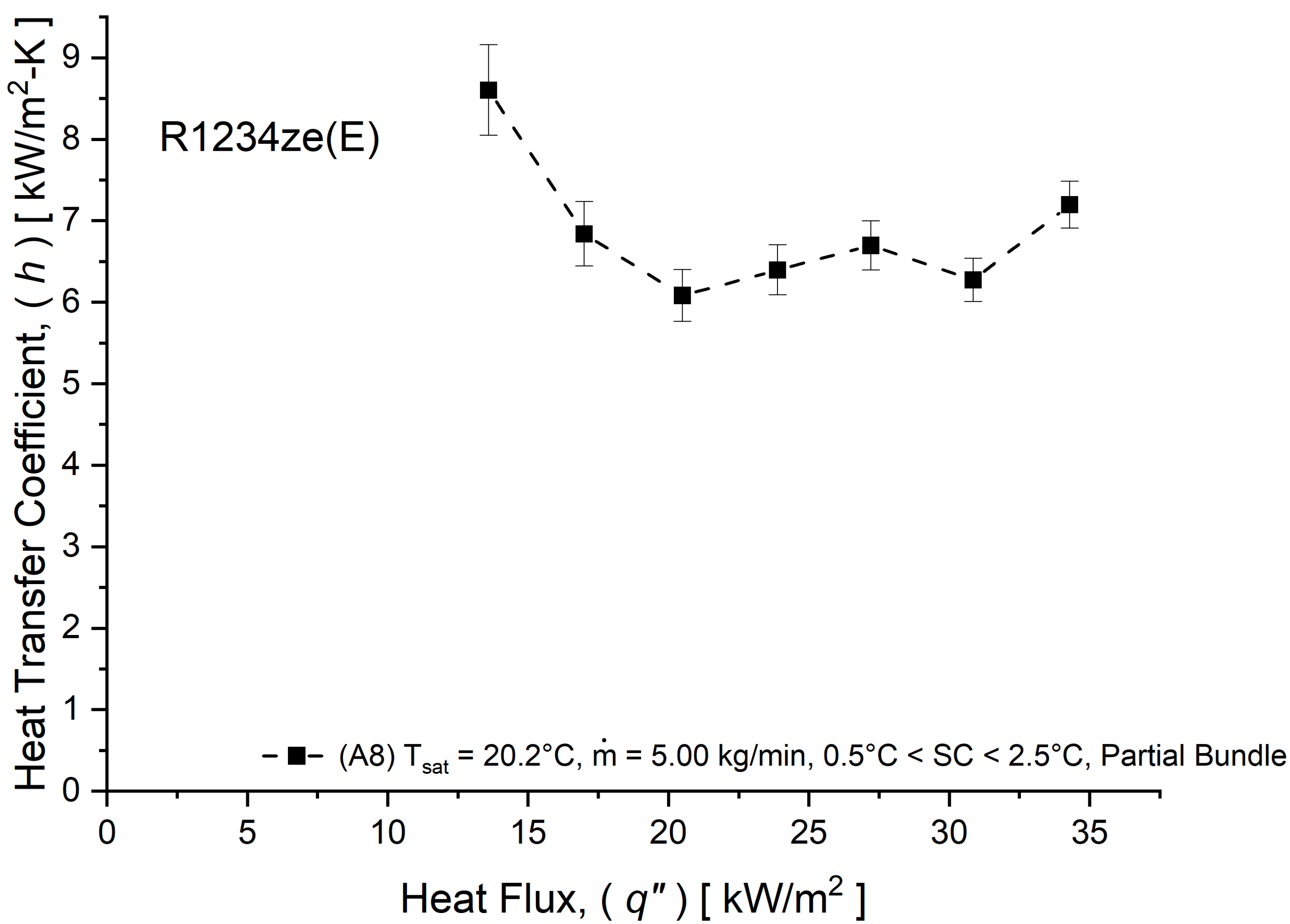

Figure 4.55: Heat transfer coefficient vs heat flux (Phase 5, R1234ze(E), T_{sat} = 20 °C)

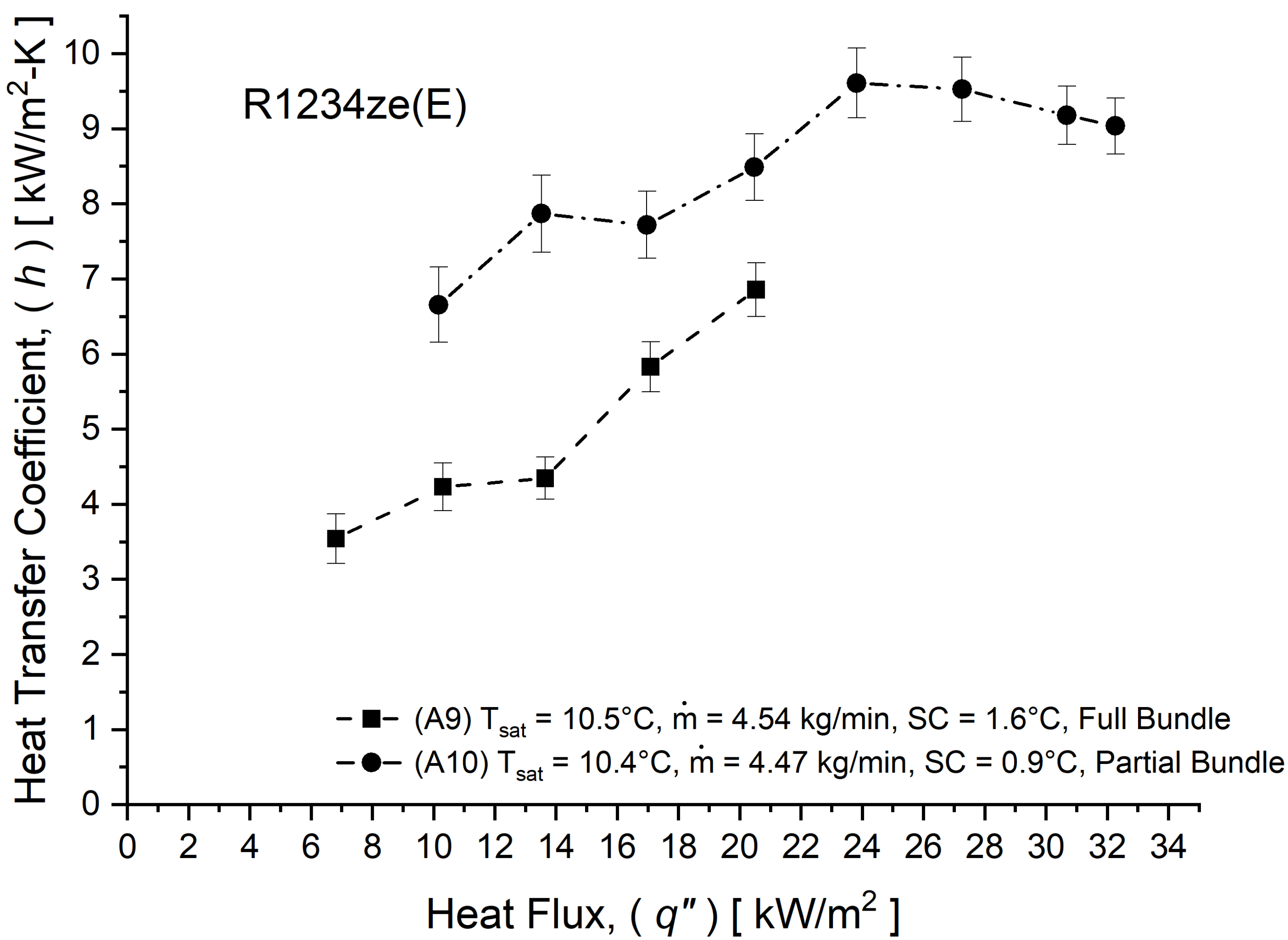

Figure 4.56: Heat transfer coefficient vs heat flux (Phase 5, R1234ze(E), T_{sat} = 10 °C)

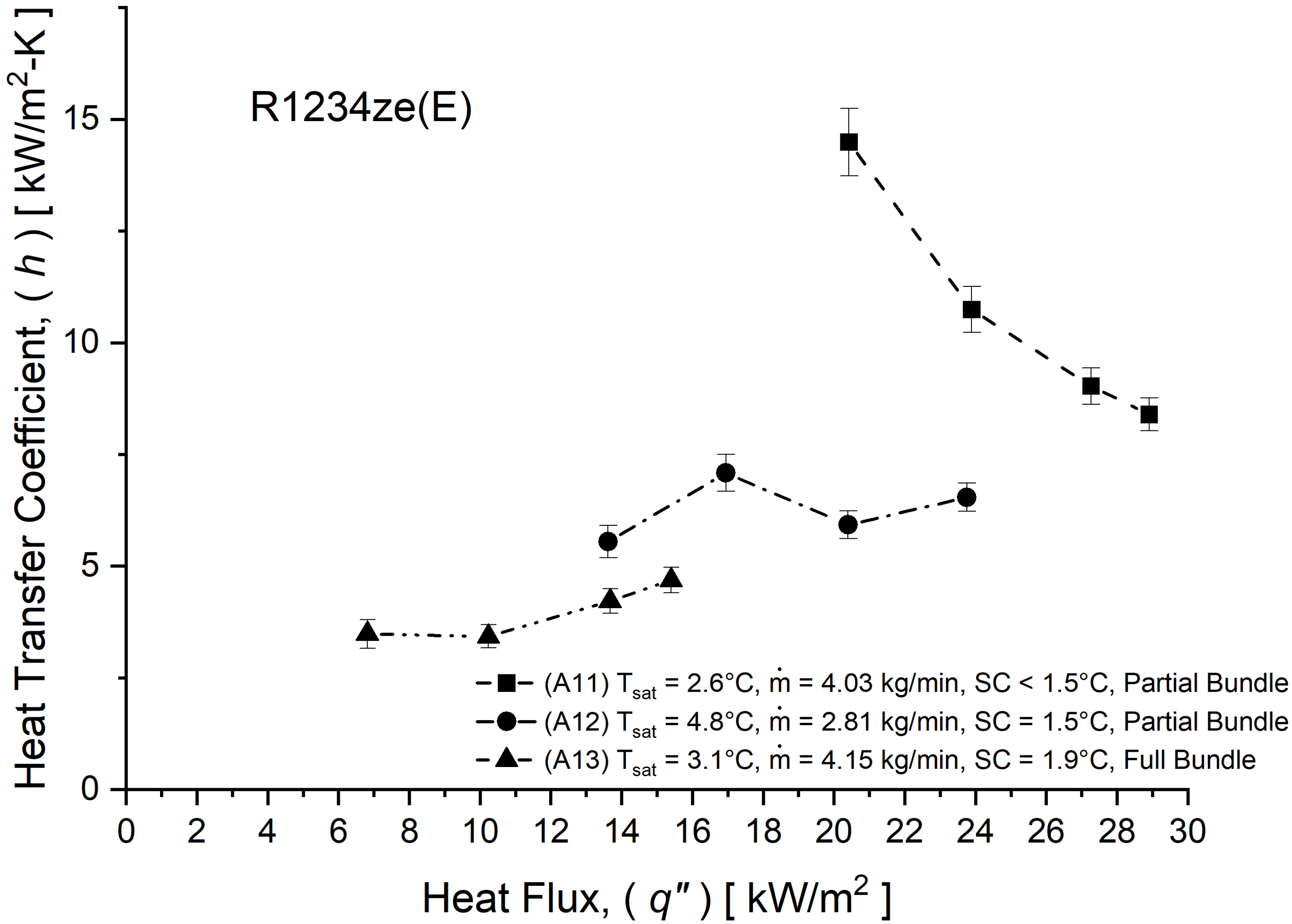

Figure 4.57: Heat transfer coefficient vs heat flux (Phase 5, R1234ze(E), T_{sat} = 3 °C)

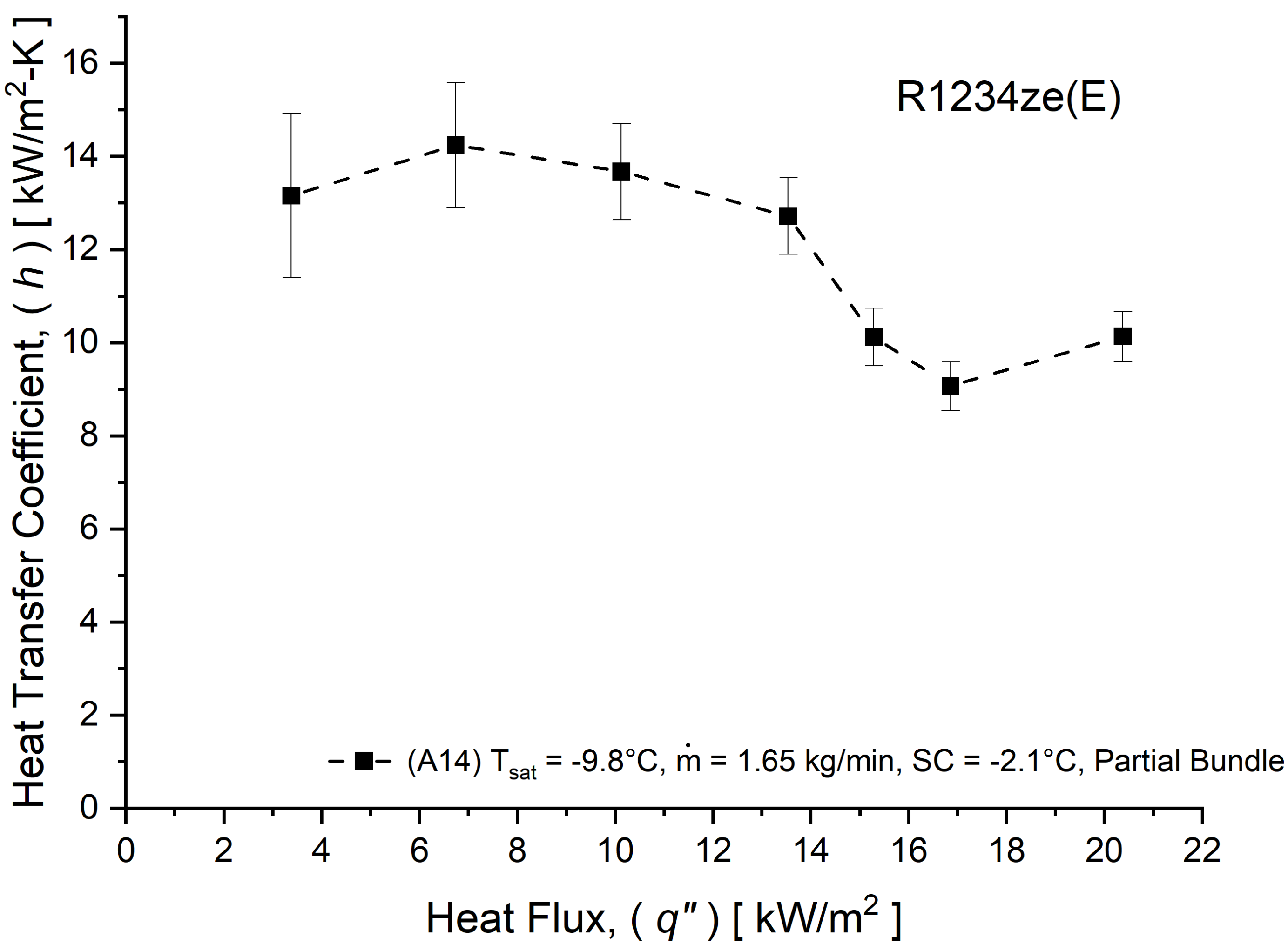

Figure 4.58: Heat transfer coefficient vs heat flux (Phase 5, R1234ze(E), T_{sat} = -10 °C)

subcooling with increasing heat flux and thus a decrease in bundle heat transfer coefficients. Series A14, however, was performed with a negative degree of subcooling, indicating that the refrigerant entered the test section as a saturated mixture instead of as a slightly subcooled liquid. It was observed in these and in later datasets that this condition was generally undesirable as it caused inconsistencies and general decreases in bundle heat transfer coefficients because of a decreased amount of liquid refrigerant available on the tube surfaces for boiling heat transfer. Due to the lack of directly comparable data in Phase 5, specific analysis of the variation in bundle heat transfer coefficients due to refrigerant type could not be made for these tests. However, observation of the most similar data revealed very similar heat transfer performance, within approximately 10%, between R134a and R1234ze(E) for this configuration.

Differences in heat transfer coefficients due to nozzle type and configuration were best illustrated with select full bundle series in Phases 1 and 5 with R1234ze(E). At a saturation temperature of 10 °C, series A9 with the flat deflected spray nozzles was most similar to series B11 and B12 from Phase 1 in which the circular cone nozzles were used. In series A9, inlet subcooling was steady at 1.6 °C and bundle heat transfer coefficients increased from approximately 3.5 kW/m^2-K to 6.8 kW/m^2-K with an increase in heat flux from 6 kW/m^2 to 21 kW/m^2. With the circular cone nozzles at a lower degree of subcooling of 0.8 °C in series B12, values increased from approximately 5.4 kW/m^2-K to 8.0 kW/m^2-K over the same heat flux range; with a higher subcooling of 2.3 °C in series B11, values were between 2.0 kW/m^2-K and 3.5 kW/m^2-K for heat fluxes between 6 kW/m^2 and 10 kW/m^2. It is likely that values would have been within ±10% if inlet subcooling had been the same for the two configurations. Similar results were obtained at a saturation temperature of 3 °C. In the Phase 5 series A13 with an inlet subcooling of 1.9 °C, bundle heat transfer coefficients were between 3.4 kW/m^2-K and 4.7 kW/m^2-K for heat fluxes between 6 kW/m^2 and 16 kW/m^2, while in the Phase 1 series B20 with a subcooling of 2.2 °C, values were between 3.8 kW/m^2-K and 6.2 kW/m^2-K for a heat flux range of 13 kW/m^2 to 24 kW/m^2. These results indicated a weak dependence of bundle heat transfer coefficients on nozzle type and configuration with slightly increased values attributed to the use of the circular cone nozzles. This slight enhancement was mostly due to the differences in refrigerant distribution patterns, as illustrated in Figure 4.59.

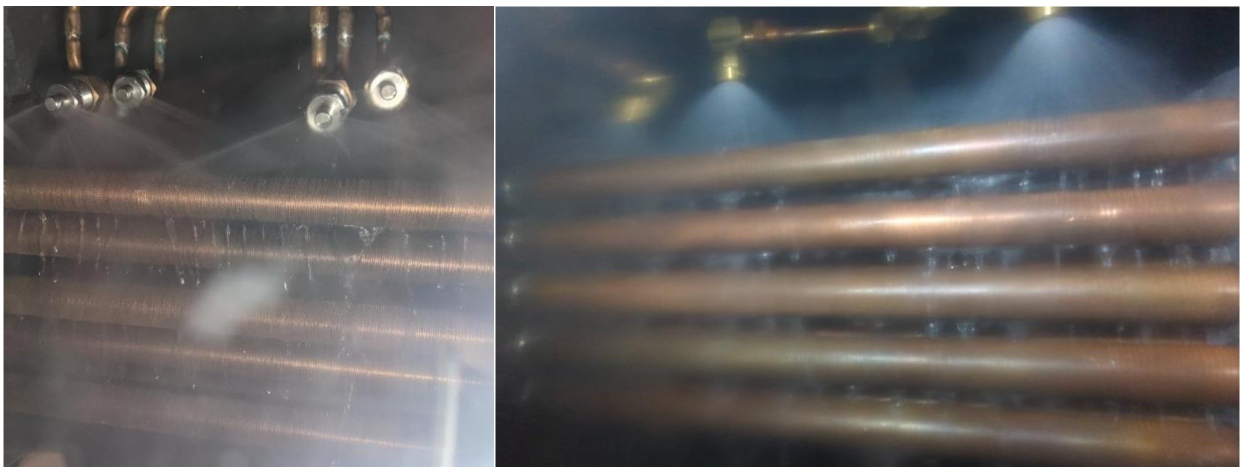

Figure 4.59: Refrigerant distribution of the deflected flat spray nozzles (left) and the circular cone nozzles (right)

As shown, the deflected flat spray nozzles emitted a thin, flat sheet of liquid refrigerant at large angles over each of the three tube columns while the circular cone nozzles sprayed the refrigerant in solid cones at slightly reduced angles. This meant that, for the deflected flat spray nozzles, proper refrigerant distribution was extremely sensitive to minute changes in nozzle position and orientation. Many fine adjustments were required in the early stages of testing to optimize the refrigerant distribution, and this configuration did not allow for concentration of the spray to more sensitive areas of the bundle. Additionally, because the nozzles were positioned directly above the top tubes in the triangular bundle, the amount of refrigerant impinging on the offset tubes in the second row was significantly reduced, thus reducing heat transfer performance of all offset rows in the bundle. Conversely, the solid cone spray pattern of the second nozzle arrangement provided a much improved distribution of refrigerant both within the bundle, especially to the offset tube rows, and to the more sensitive areas of the bundle near the mounting flange. Refrigerant distribution was not nearly as sensitive to minute changes in nozzle position or orientation, and few adjustments were required to optimize the spray pattern. In doing so, determination of the height of the nozzles above the bundle was amongst the most important factors: If the nozzles were placed too high above the bundle, a significant amount of refrigerant would bypass the bundle completely and would not contribute to heat transfer at all, while if the nozzles were placed too low, the supply of refrigerant to the upper rows would be insufficient. After the selection of the appropriate nozzles for these experiments, the optimal height of the nozzles was determined using simple calculations of spray pattern area on the top tubes given the spray cone angles, and the axial spacing was adjusted to achieve sufficient and uniform refrigerant supply along the entire length of the bundle. Often for nozzles of this type, spray cone angles, flow rates and pressure drops are specified by the manufacturers which facilitates selection, installation, and calibration. For these reasons, circular full cone nozzles of this type are much more common in industrial applications than the alternatives and have been more thoroughly utilized and studied in research applications.

Chapter 5: Modeling

The details of the preliminary mathematical model developed to correlate the data collected during the experimental campaign are presented in this chapter. Often in studies of this type, it is useful to generate some kind of correlation to serve as both a summary of the experimental data and perhaps a guideline for the design of similar test apparatuses or equipment for process applications. This chapter will describe the details of the model development process, an analysis of the model predictions, a comparison of the model with some data found in the literature, and then a comparison of the model with the experimental data collected in this work.

5.1 Model Development

The model developed for this project was a semi-empirical correlation based heavily on that proposed by Zeng, et al. (1997) as described previously in Equations 2.5 - 2.8 in Chapter 2. Their overall correlation was of the following form:

$$Nu = z_1 Re^{z_2} Pr^{z_3} P_{red}^{z_4} \Phi^{z_5} \tag{2.5}$$

where the Nusselt number averaged for the whole tube bundle is a function of the bundle film Reynolds number, the refrigerant Prandtl number and reduced pressure, and the bundle heat flux which was nondimensionalized using the refrigerant critical and saturation temperatures and some relevant bundle geometry. This correlation was a modification of that proposed by Parken, et al. (1990) to account for additional refrigerant properties such as refrigerant critical pressure and temperature, and the Parken model was itself a modification of that proposed by Chun and Seban (1971) to account for the effects of bundle heat flux on average heat transfer coefficients. It was desired that the model for this project account for all of the aforementioned factors while also accounting for the effects of enhanced surface type, bundle geometry, and refrigerant inlet subcooling on heat transfer coefficients, all of which were found to have significant influence on heat transfer performance. Additionally, it was desired to not only correlate the behavior of the tube bundle as a whole but also that of each individual row of tubes within the bundle to better account for the dryout phenomenon which tends to decrease bundle heat transfer coefficients at high heat fluxes and to make the model more applicable to the design of similar heat exchangers with different numbers of tube rows and a different number of tubes in each row. Only data from Phases 1 through 4 of the experimental campaign were used to develop the model since the data from Phase 5 was limited and because accounting for nozzle effects would have overly complicated the correlation. As such, the correlation is only valid for the Tube-C and Tube-B enhanced surfaces in the triangular and square bundle geometries using the solid cone spray nozzles, and only for full bundle tests. Given these objectives, the following function was found suitable to model the data collected in the experiment:

$$Nu_{Row\ j} = a_1 Re_{Row\ j}^{a_2} Pr^{a_3} P_{red}^{a_4} \Phi^{a_5} \tag{5.1}$$

where

$$Nu_{Row\ j} = \frac{h_{Row\ j}}{k_{ref}} \left(\frac{\nu^2}{g}\right)^{1/3} \tag{5.2}$$

$$a_1 = (EF)(BF)(SC) \tag{5.3}$$

$$Re_{Row\ j} = \frac{2\Gamma_{Row\ j}}{\mu} \tag{5.4}$$

$$P_{red} = \frac{P_{sat}}{P_{crit}} \tag{5.5}$$

$$\Phi = \frac{q''D}{(T_{crit} - T_{sat})k_{ref}} \tag{5.6}$$

In Equation 5.1, a_2, a_3, a_4, and a_5 are coefficients determined based on model fitting of the experimental data, and $Nu_{Row\ j}$ is the Nusselt number for a given row of tubes within the bundle. It was here that one of the most significant alterations was made from the Zeng model in order to account for the variations in heat transfer coefficient from row to row within the bundle. In Equation 5.2, k_{ref} is the thermal conductivity of the liquid refrigerant, v is the liquid refrigerant kinematic viscosity, g is the gravitational constant, and $h_{Row\ j}$ is the heat transfer coefficient for a row of tubes within the bundle as described earlier in Equation 3.8. In Equation 5.3, the multiplier coefficient a_1 is a product of three configuration factors which will be described later in greater detail. In Equation 5.5, P_{red} is the reduced pressure of the refrigerant calculated using the refrigerant saturation pressure, P_{sat}, and the refrigerant critical pressure, P_{crit}. In Equation 5.6, Φ is the nondimensionalized heat flux such that q'' is the dimensional heat flux at each tube wall, D is the tube diameter, T_{crit} is the refrigerant critical temperature, T_{sat} is the refrigerant saturation temperature in a given test, and k_{ref} is the same liquid refrigerant thermal conductivity used in Equation 5.2. For simplicity, it was assumed that refrigerant properties remained constant throughout the test section. To coincide with the row Nusselt number form of the model, the row Reynolds number, $Re_{Row\ j}$, was also utilized as described in Equation 5.4 in which μ is the dynamic viscosity of the liquid refrigerant and $\Gamma_{Row\ j}$ is the local mass flow rate of refrigerant per unit length of the tubes such that

$$\Gamma_{Row\ j} = \frac{\dot{m}_{Row\ j}}{L_t} \tag{5.7}$$

where $\dot{m}_{Row\ j}$ is the local mass flow rate of liquid refrigerant that reaches a given tube row and L_t is the total length of the heater tubes. Accordingly, the row Reynolds number effectively becomes

$$Re_{Row\ j} = \frac{2\dot{m}_{Row\ j}}{\mu L_t} \tag{5.8}$$

when appropriate substitutions are made for the quantity $\Gamma_{\mathrm{Row\ j}}$. The local mass flow rate $\dot{m}_{Row\ j}$ was determined separately and procedurally for each row of tubes in the bundle depending on how much refrigerant was expected to reach a given row. Naturally, it depended on various bundle geometries such as tube diameter, spacing, and layout and for this work was determined using a simplified thermodynamic model. First, it was necessary to calculate the approximate coverage area of the refrigerant spray such that the fraction of the total refrigerant mass flow rate that impinged on the bundle, as well as the complementary fraction of flow that bypassed the bundle, could be determined. Based on a nominal spray flow angle of 100° exiting the nozzles at an approximate height of the nozzles of 38.1 mm above the top row of tubes, a projection of the spray flow pattern on the bundle was generated as shown in Figure 5.1.

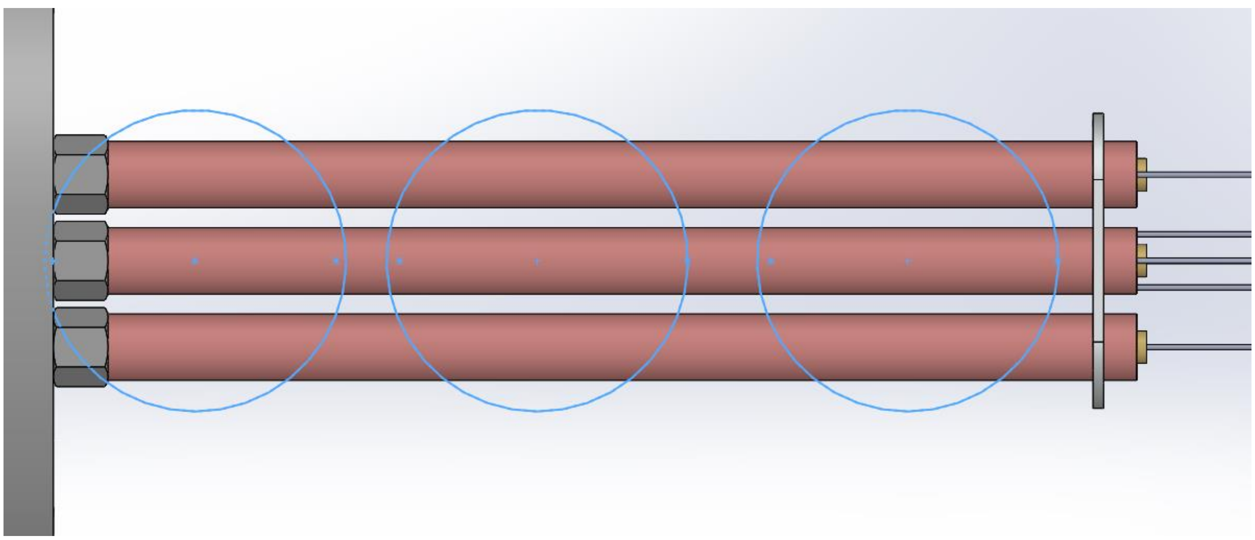

Figure 5.1: Projection of the spray flow pattern on the tube bundle

As shown and described previously, the nozzles were positioned for an optimal balance between the amount of flow interacting with the bundle and the distribution of the flow over the bundle. Given that the nozzles produced a solid cone spray pattern and based on the fraction of the total spray area that intersected with the tubes, it was determined that approximately 90% of the total flow exiting the nozzles contributed to heat transfer within the bundle while approximately 10% bypassed the bundle completely. It was then determined using the same method that approximately

60% of the flow that reached the bundle impinged directly on the tubes in Row 1, meaning effectively 54% of the total flow, such that

$$\dot{m}_{Row1} = 0.54\dot{m}_{total} \tag{5.9}$$

where $\dot{m}_{Row1}$ is the local mass flow rate of liquid refrigerant at the uppermost row of tubes, $\dot{m}_{total}$ is the total refrigerant mass flow rate entering the test section, and y = 0.54 is the value of the nozzle factor in this case, while the rest fell through the spaces between the tubes. From there, the calculations differed for the triangular-pitch geometry compared to the square-pitch geometry.

For the triangular bundle, it was assumed that the remaining 40% of the bundle flow that bypassed Row 1 impinged directly on the tubes in Row 2, effectively corresponding to 36% of the total flow such that

$$\dot{m}_{Row2} = 0.36\dot{m}_{total} \tag{5.10}$$

where $\dot{m}_{Row2}$ is the local mass flow rate of liquid refrigerant impinging on the second row of tubes, and y = 0.36 is the value of the nozzle factor for the second row. For subsequent rows, a thermodynamic model was applied in which the local flow rate at a given row could be approximated from an energy balance of the rows directly above. Using the number of tubes directly above a given row, the bundle heat flux, the nominal heat transfer area of a tube, and the enthalpy of vaporization, an energy balance was developed in the following form:

$$\dot{m}_{Row\ j} = y\dot{m}_{total} - (j-2)(k)\frac{q"A}{h_{fg}} \tag{5.11}$$

where $\dot{m}_{Row\ j}$ is the local refrigerant mass flow rate at a given row of interest, y is the percentage of the total mass flow that impinged on the topmost row directly above the row of interest (i.e. the nozzle factor), j is the number of the tube row within the bundle assuming the rows are numbered from the top, k is the number of active tubes in the relevant preceding tube rows, q'' is the bundle heat flux, A is the nominal heat transfer area of a single tube, and h_{fg} is the enthalpy of vaporization of the refrigerant. The model was formulated as such to account for the offset rows of tubes within the bundle and the varying proportions of refrigerant that would reach a lower row given that number of active tubes in each row was not constant for this configuration. For example, using the model, the local mass flow rate at Row 3, which had 3 active tubes and was positioned directly below Row 1, was calculated as follows:

$$\dot{m}_{Row3} = 0.54\dot{m}_{total} - (1)(3)\frac{q"A}{h_{fg}} \tag{5.12}$$

thus accounting for the percentage of the total flow impinging on the tube columns to which Row 3 belonged and the approximate amount of refrigerant that had been evaporated by the tubes in Row 1 and did not reach Row 3. Continuing the example, the local mass flow rate at Row 4 was determined as follows:

$$\dot{m}_{Row4} = 0.36\dot{m}_{total} - (1)(2)\frac{q"A}{h_{fg}} \tag{5.13}$$

which accounted for the different percentage of the total flow that impinged on Row 2, the uppermost row positioned directly above Row 4 (both of which were offset from the others) and the approximate amount of refrigerant that had been evaporated by the 2 active tubes in Row 2 and thus did not reach the tubes in Row 4. Finally, the calculation for the local flow rate at Row 5 was similar to that of Row 3 as follows:

$$\dot{m}_{Row5} = 0.54\dot{m}_{total} - (2)(3)\frac{q"A}{h_{fg}} \tag{5.14}$$

which accounted for the amount of liquid refrigerant impinging on Row 1 minus the approximate amount that was evaporated by the tubes in both Rows 1 and 3.

For the square bundle, it was assumed that the remaining 40% of the bundle flow that bypassed the tubes in Row 1 fell straight through the bundle and did not interact with the tubes. This assumption was made in order to simplify the mass flow rate calculations and to make the overall correlation a more conservative estimate of heat transfer performance. As such, the energy balance to determine the local flow rate at the lower tubes in the bundle was of the following form:

$$\dot{m}_{Row\ j} = 0.54\dot{m}_{total} - (j-1)(3)\frac{q"A}{h_{fg}} \tag{5.15}$$

where the y = 0.54 value of the nozzle factor was used for all rows since none were offset in this geometry, and all rows had 3 active tubes in a full bundle test such that k = 3. Following the examples from before, the local mass flow rates at Rows 2, 3, 4, and 5 were calculated as described in Equations 5.16, 5.17, 5.18, and 5.19, respectively.

$$\dot{m}_{Row2} = 0.54\dot{m}_{total} - (1)(3)\frac{q"A}{h_{fg}} \tag{5.16}$$

$$\dot{m}_{Row3} = 0.54\dot{m}_{total} - (2)(3)\frac{q"A}{h_{fg}} \tag{5.17}$$

$$\dot{m}_{Row4} = 0.54\dot{m}_{total} - (3)(3)\frac{q"A}{h_{fg}} \tag{5.18}$$

$$\dot{m}_{Row5} = 0.54\dot{m}_{total} - (4)(3)\frac{q"A}{h_{fg}} \tag{5.19}$$

In this way, the decrease in liquid refrigerant flow through the bundle due to evaporation, which was the essence of the dryout phenomenon, was integrated into the model such that values of the local flow rate per unit tube length $\Gamma_{Row\ j}$ and thus the local Reynolds number $Re_{Row\ j}$ were decreased for lower tube rows, especially at high heat fluxes. The result was a model with an improved correlation of the experimental data such that the increase in heat transfer coefficients at lower heat fluxes and subsequent decrease at higher heat fluxes, after the onset of dryout, were more accurately characterized. As mentioned previously, the coefficient a_1 in Equation 5.3 is the product of three different test section configuration factors: *EF* is called the enhancement factor and is a constant that is based on the enhanced surface type used in a given test; *BF* is called the bundle factor and is a constant that is based on the bundle geometry used; and *SC* is called the subcooling factor and is based on the degree of refrigerant inlet subcooling. The factors EF and BF were determined statistically by comparing the differences in mean heat transfer coefficient values for the different enhanced surface types and bundle geometries, respectively, under similar testing conditions. According to this approach, the values for each factor were prescribed as follows:

$$EF = \begin{cases} 1 & for\ the\ Tube - C\ surface \\ 2.97 & for\ the\ Tube - B\ surface \end{cases} \tag{5.20}$$

$$BF = \begin{cases} 1 & for\ the\ square\ bundle\ geometry \\ 1.26 & for\ the\ triangular\ bundle\ geometry \end{cases} \tag{5.21}$$

It was found from the analysis that the Tube-B enhanced surface resulted in heat transfer coefficient values that were an average of approximately 200% higher than those for the Tube-C surface under comparable testing conditions and, similarly, that the triangular bundle geometry produced values that were an average of approximately 26% higher than those for the square bundle geometry under similar conditions. Thus, the factors that resulted in the poorest performance were given the baseline unity value while the alternatives were given multipliers to raise the heat transfer coefficient curves to suite the enhancements observed. Meanwhile, the factor SC was assigned an algebraic expression since the degree of inlet subcooling was a continuous variable as opposed to the bundle geometry and enhanced surface type, which were categorical variables. Based on comparisons of mean heat transfer coefficient values in the data for tests with inlet subcooling between 0.5 °C and 2.0 °C, the following formula was found suitable:

$$SC = -0.49(T_{sat} - T_{inlet}) + 1.98 \tag{5.22}$$

where T_{sat} is the refrigerant saturation temperature and T_{inlet} is the temperature of the refrigerant at the inlet of the test section such that the quantity ($T_{sat} - T_{inlet}$) is the inlet subcooling in [°C] and the coefficient -0.49 has the units of [$°C^{-1}$] so that the factor SC is dimensionless. Thus, a subcooling value of 2.0 °C, which was used as the baseline, results in a value of unity while a subcooling of 0.5 °C results in a 74% increase in heat transfer coefficient values as observed in the data for similar test conditions. As such, the correlation as detailed in this chapter is only valid over a range of inlet subcooling values between approximately 0.5 °C and 2.0 °C. This combination of various configuration factors is unique to this particular model and, presently, makes it the only one known to the investigators to account for the effects of enhanced surface type, bundle geometry, and refrigerant inlet subcooling on heat transfer performance in one single, concise correlation. Given the procedures and values described, a nonlinear curve fit was performed using the Origin 2022 data analysis and graphing software on over 1100 data points resulting in the following values for the coefficients a_2, a_3, a_4, and a_5 in Equation 5.1:

$$a_2 = 0.155 \tag{5.23}$$

$$a_3 = -6.029 \tag{5.24}$$

$$a_4 = -2.109 \tag{5.25}$$

$$a_5 = 0.187 \tag{5.26}$$

The relatively small and similar positive values obtained for a_2 and a_5, the coefficients for the row Reynolds number and nondimensionalized heat flux, respectively, indicated a modest positive correlation between these quantities and the heat transfer coefficient such that heat transfer performance improved with increases in refrigerant flow rate and heat flux, all other things equal. The larger negative values obtained for a_3 and a_4, the coefficients for the Prandtl number and reduced refrigerant pressure, indicated negative correlations between these quantities and the row heat transfer coefficient such that heat transfer performance was diminished with increases in both.

5.2 Analysis of Model Predictions

In order to assess model adequacy, the fitted correlation was examined and compared to the data points that were used to inform the model. Of particular interest was an assessment of the fit to the data collected for the R1234ze(E) and R1233zd(E) refrigerants as those were the focus of the present work. Among the data points for R1234ze(E), an excellent fit was found in Series E6 from Phase 4, for which the refrigerant saturation temperature was 10.1 °C and inlet subcooling was steady at around 1.5 °C. The results of the comparison are shown in Figure 5.2.

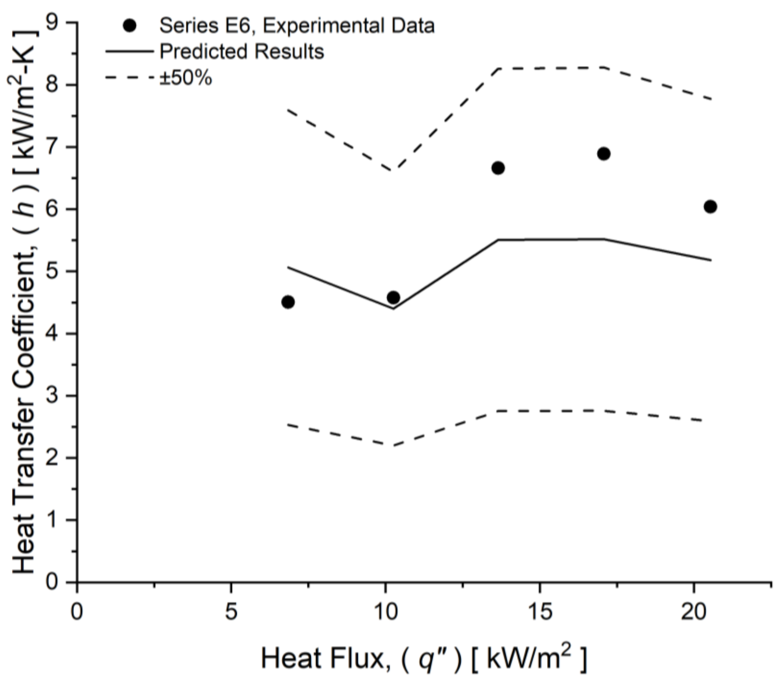

Figure 5.2: Correlation of the heat transfer coefficient experimental data from Series E6

For this series, the model followed the data closely such that all data points were well within the ±50% interval. The smallest relative deviation from the model was only 4% for the 10 kW/m^2 test, and the largest was 22% for the 17 kW/m^2 test. Importantly, the model accurately replicated the trend in the data in which a general increase in the bundle heat transfer coefficient was observed at low heat fluxes (in this case, up to about 13 kW/m^2) followed by a plateau in values at moderate heat fluxes (up to 17 kW/m^2), after which values began to decrease at the onset of refrigerant dryout (observed at heat fluxes higher than 17 kW/m^2 for this series). In this particular case, the correlation returned a conservative estimate for the bundle heat transfer coefficients observed during testing. Another case in which an excellent fit was observed was Series D18 from Phase 3 using R1233zd(E), for which the refrigerant saturation temperature was 15.1 °C and inlet subcooling was 0.8 °C. A comparison is shown in Figure 5.3.

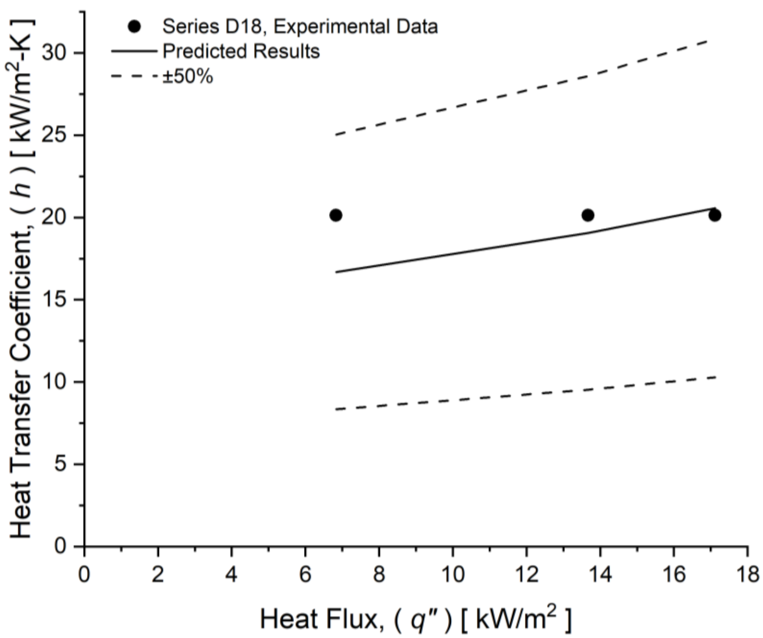

Figure 5.3: Correlation of the heat transfer coefficient experimental data from Series D18

As for Series E6, the data for Series D18 fell well within the ±50% interval such that the smallest relative deviation was only 2% for the 17 kW/m^2 test and the largest was 19% for the 7 kW/m^2 test. The data in this series exhibited a plateau in heat transfer coefficient values over the entire range of heat fluxes, which was more typical of tests in which R1233zd(E) was used, while the correlation predicted a gradual increase in values. For the tests conducted before the onset of dryout, the heat transfer coefficient prediction was moderately conservative.

Among the cases in which the fit of the model was considered good was Series D10 using R1234ze(E), for which the refrigerant saturation temperature was 10.1 °C and inlet subcooling was approximately 0.9 °C. A comparison of the experimental data for that series of tests is shown in Figure 5.4.

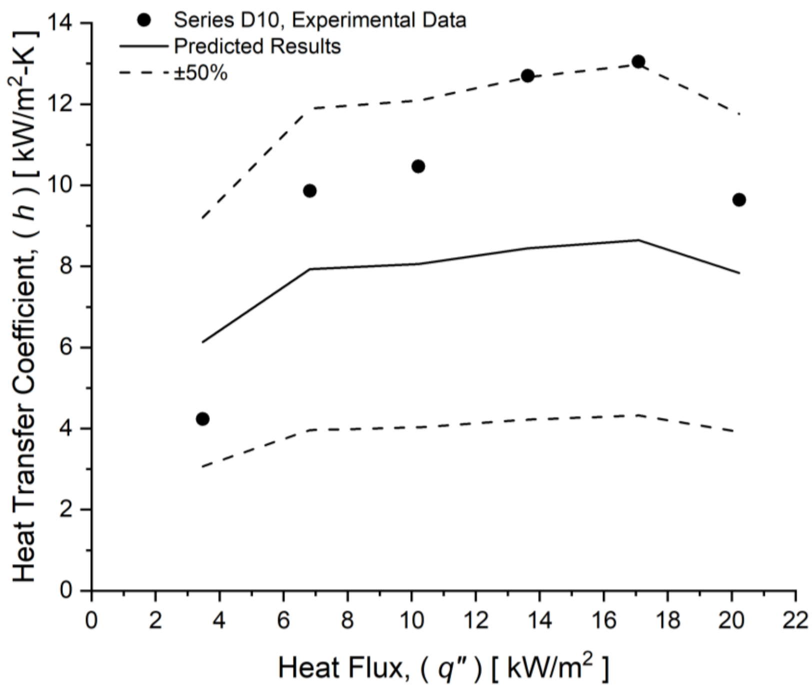

Figure 5.4: Correlation of heat transfer coefficient experimental data from Series D10

As shown, the model fit for this case, while not quite as good as that for the previous series, was still mostly within the ±50% interval. The minimum deviation from the model was for the 20 kW/m^2 test, for which the observed heat transfer coefficient was 23% greater than the prediction, and the maximum deviation was observed for the 17 kW/m^2 test, for which the observed value was 51% greater than the prediction. Though the correlation did not fit the data as closely in this case, the general trend of the heat transfer coefficient with increasing heat flux was still reflected in the prediction. For the data as well as the prediction, values increased with increasing heat flux up to approximately 18 kW/m^2, after which the onset of dryout occurred and values began to decrease. The only test for which the prediction exceeded the observed heat transfer coefficient value was the lowest heat flux, 3 kW/m^2, as the predictions were conservative at higher heat fluxes. For these tests, the model did not fit the data as closely because of the large deviation among heat transfer coefficient values within a single series, as opposed to Series E6 in which the deviation in values between individual tests was much less. For R1233zd(E), a good fit was observed for Series D20 in which the refrigerant saturation temperature was 9.4 °C and inlet subcooling was 0.7 °C. That comparison is shown in Figure 5.5.

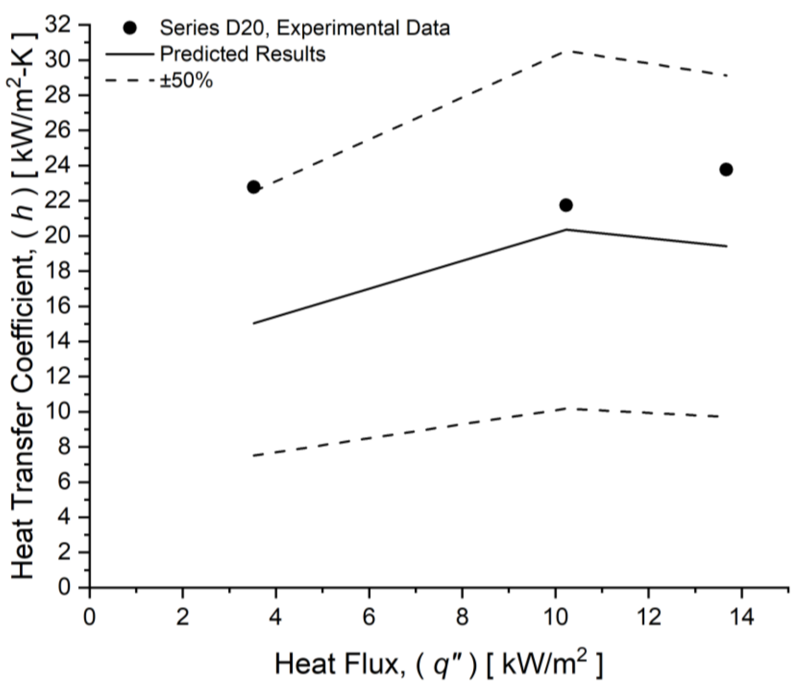

Figure 5.5: Correlation of heat transfer coefficient experimental data from Series D20

As before, the fit for this case was not as good as in Series D18 but still mostly within the ±50% interval. The minimum deviation from the model was for the 10 kW/m^2 test, for which the observed value was only 7% greater than the prediction, and the maximum deviation was observed for the 3 kW/m^2 test for which the observed value was 52% greater than the prediction. In this case, the goodness of fit of the model was diminished because of the peculiar trend observed in the data:

namely, a decrease in heat transfer coefficient values from 4 kW/m^2 to 10 kW/m^2, followed by an increase up to 14 kW/m^2. This trend was opposite to that usually observed under similar conditions, which was reflected in the increase and subsequent decrease in values predicted by the correlation. Still, in all tests for this case, the correlation provided a conservative estimate of heat transfer coefficient values.

Among all the data used to inform the correlation, there were some for which the model fit was considered marginal or poor. One such series for R1234ze(E) was B12, for which the refrigerant saturation temperature was 10.7 °C and inlet subcooling was 0.8 °C. A comparison of these data is shown in Figure 5.6.

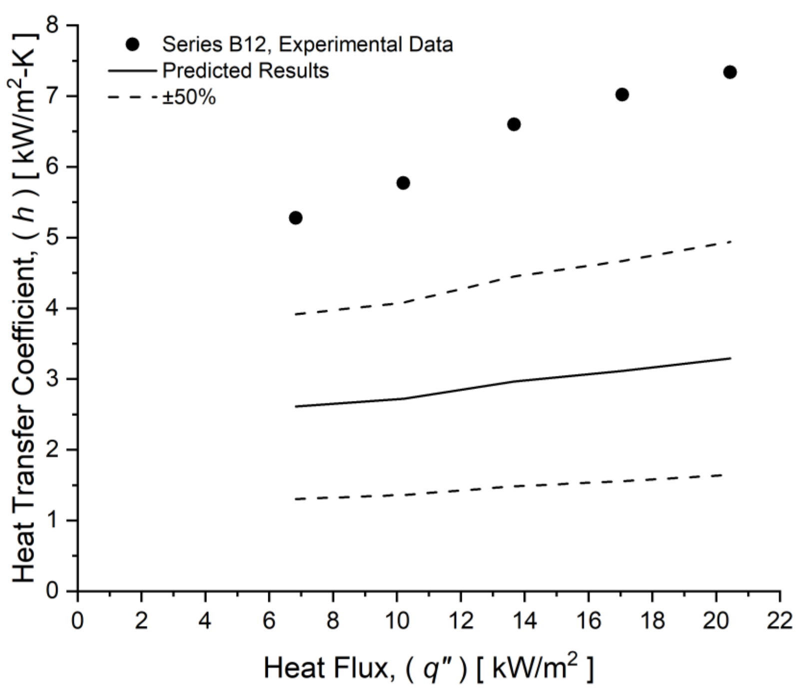

Figure 5.6: Correlation of heat transfer coefficient experimental data from Series B12

For this series, the departure of the experimental data from the predicted results was significant such that all of the data points fell outside of the ±50% interval. The minimum deviation observed was for the 6 kW/m^2 test, for which the heat transfer coefficient value was 102% greater than the prediction, and the maximum deviation corresponded to the 17 kW/m^2 test, for which the data point was 125% greater than the prediction. After examination of the data for that series, it was discovered that this significant deviation was due to the unusually high heat transfer coefficients obtained during those tests which were outliers among the data collected for the Tube-C enhanced surface. The unusually high refrigerant mass flow rate of 6.23 kg/min, combined with the relatively low inlet subcooling, was a likely contributor to these exceptionally high values. From the tests with R1233zd(E), one series for which the model fit was particularly poor was B30, for which the refrigerant saturation temperature was 14.6 °C and inlet subcooling varied from 1.4 °C to 2.0 °C for the first two tests in the series. A comparison of those first two tests is shown in Figure 5.7.

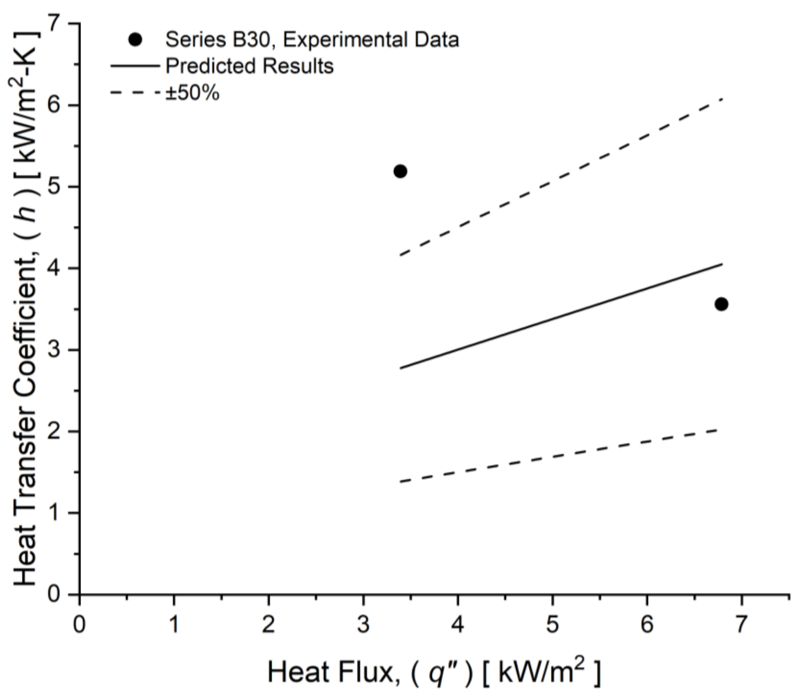

Figure 5.7: Correlation of heat transfer coefficient experimental data from Series B30

For these tests, only one fell within the ±50% interval while the other was well above the interval. The minimum deviation was for the 7 kW/m^2 test, which was 12% below the prediction, while the maximum deviation was for the 3.5 kW/m^2 test, which was 87% above the prediction. After examining these data, it was determined that the large deviation for the lower heat flux test was also due to a much higher than expected heat transfer coefficient calculated from the data for that test, which was conducted with a low refrigerant mass flow rate of 2.40 kg/min and a high inlet subcooling of 2.0 °C. For the higher heat flux test, in which the inlet subcooling was a more moderate 1.4 °C and the heat transfer coefficient was within the expected range, the prediction was much more accurate.

Given these results and the comparisons made with the rest of the data, it was concluded that the best fit of the correlation was generally observed for data that fell closer to the mean for some key operating conditions tested throughout the experimental campaign. For example, even though refrigerant mass flow rate varied from less than 2.00 kg/min to greater than 6.00 kg/min throughout the campaign, the best predictions were made for those tests for which flow rate was around a more moderate value of 4.00 kg/min. Incidentally, a large majority of data points were collected for flow rates close to this moderate value, meaning those tests had a much greater influence on the fitted curve coefficient values that those that fell closer to the upper and lower extremes. Similarly, a large majority of tests considered for the model were conducted with inlet subcooling between 1.0 °C and 1.5 °C, meaning those closer to the extreme values of 0.5 °C at the lower end and 2.0 °C at the upper end were sometimes not as well predicted by the model. Those tests for which heat transfer coefficient values were unusually high or low for a given enhanced surface type or bundle geometry were also not as well accounted for in the predictions as they fell farther from the mean values observed throughout the campaign. Unexpected trends were also not well predicted by the correlation, such as those in which heat transfer coefficients decreased at low heat fluxes, those in which they increased sharply at high heat fluxes, or those in which the individual values in a single series of tests under constant operating conditions varied greatly from each other. Thus, the bundle heat transfer coefficient curves that were most accurately predicted by the correlation were those that followed the trend seen in the majority of the data in which values increased at low heat fluxes and then began to decrease at the onset of dryout, for which the correlation was specifically modified to account.

5.3 Comparison with Data from the Literature

As another examination of model adequacy, versatility, and general applicability, the fitted correlation was also compared to some of the experimental data reported in the literature and presented earlier in Chapter 2. Of particular interest were data from spray evaporation experiments with enhanced-surface tubes and bundle geometries similar to those utilized in this work. One particularly pertinent dataset was that which was reported in Moeykens and Pate (1995) for spray evaporation of R134a over a low finned-triangular pitch tube bundle. Using the operating conditions and bundle geometry specified in that study, the correlation from the current work was used to predict bundle heat transfer coefficients over the same range of heat fluxes for two series of tests in which circular cone spray nozzles were used and the refrigerant saturation temperature was 10 °C. The results of those predictive calculations are compared to the reported experimental data in Figure 5.8.

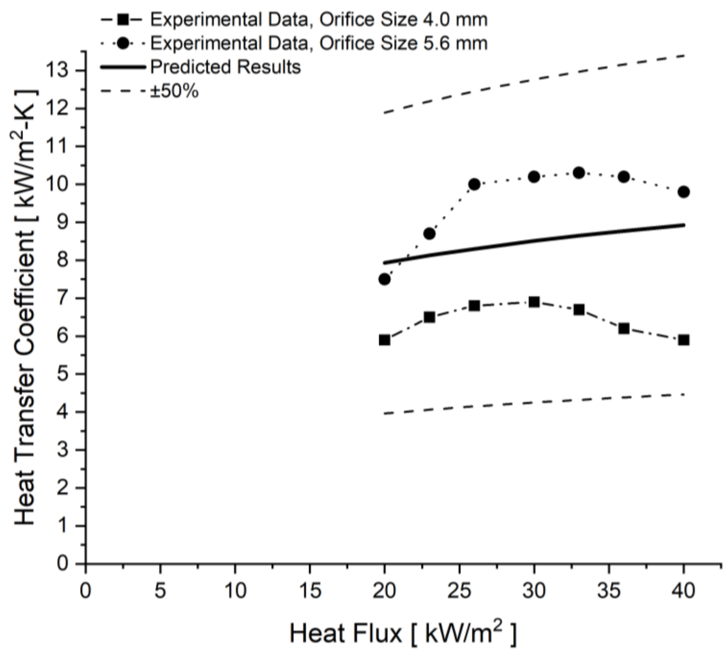

Figure 5.8: Correlation of experimental data from Moeykens and Pate (1995) using the model from the present work

As shown, the model successfully predicted the experimental data from that study very closely and well within the ±50% interval for both datasets, with the higher-performance large nozzle orifice data falling mostly above the prediction and the lower-performance small nozzle orifice data falling just below it. For the 5.6 mm data, the maximum deviation was for the 26 kW/m^2 test value which was 20% greater than the prediction, and for the 4.0 mm data, the maximum deviation was for the 40 kW/m^2 test value, which was 34% less than the prediction. Though the prediction curve was not strictly linear in the range of interest, it failed to capture the severity of the onset of dryout that was reported in the data, likely due to differences in that experimental test setup. Despite that, the recorded shell-side heat transfer performance was consistent with that of the Tube-B surfaces in the triangular-pitch bundle reported in the current work. Another dataset found to be apt for comparison was that reported in the study by Chang (2006) for spray evaporation of R141b over a set of low-finned tubes in a triangular pitch bundle. The results of those calculations are compared with the experimental data from that study in Figure 5.9.

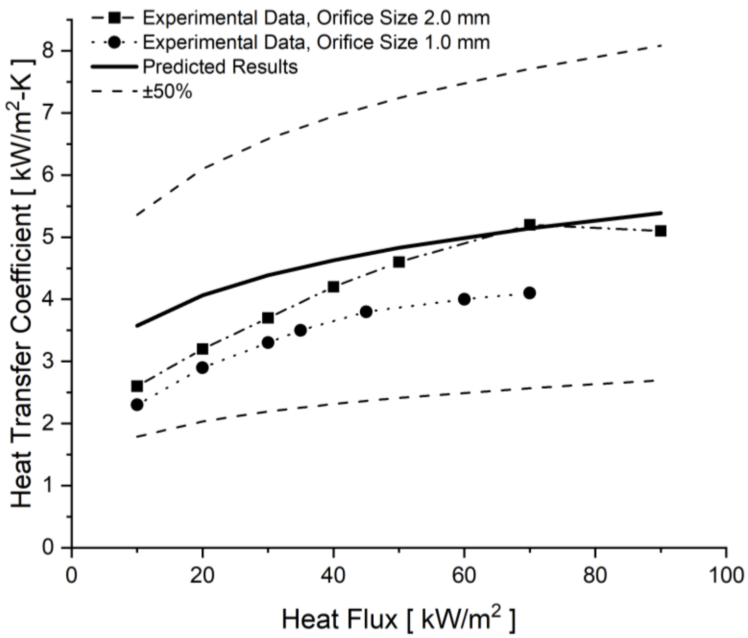

Figure 5.9: Correlation of experimental data from Chang (2006) using the model from the present work

Using that test setup geometry and operating conditions for a refrigerant saturation temperature of 20 °C, predictive calculations were made over a range of heat fluxes from 10 kW/m^2 to 90 kW/m^2. The model again proved successful for these datasets, with all points falling well within the ±50% interval, despite being applied to an HCFC refrigerant that was not used in the current work. The maximum deviation for both series was the 10 kW/m^2 data point, with the 2.0 mm data falling 27% below the prediction and the 1.0 mm data falling 36% below the prediction. For these data more than in the previous comparison, the prediction curve appeared to be more nonlinear such that the magnitude of the positive slope decreased with increasing heat flux thus reflecting the diminishing returns on heat transfer performance at heat fluxes approaching the onset of dryout. Worth noting is that the correlation from the current work was also used to predict bundle heat transfer coefficients based on the experimental data reported in Zeng, et al. (1997) for plain-surface tubes in a square-pitch bundle. However, because of the marked differences between R717 and the HFC and HFO refrigerants used to calibrate the correlation in the current work, the model fit was very poor to the extent that the predictions were not useful. Thus, the applicability of the model was deemed to be limited only to HFO, HFC, and perhaps some HCFC and CFC refrigerants with properties similar to those used in the current work.

5.4 Comparison with Data from the Present Work

As previously mentioned, the correlation as prescribed was compared to all of the experimental data used in the model fitting procedure, as is shown in Figure 5.10. All coefficients were indicated to be statistically significant from the model diagnostics with an overall R^2 value of 0.581 for the correlation.

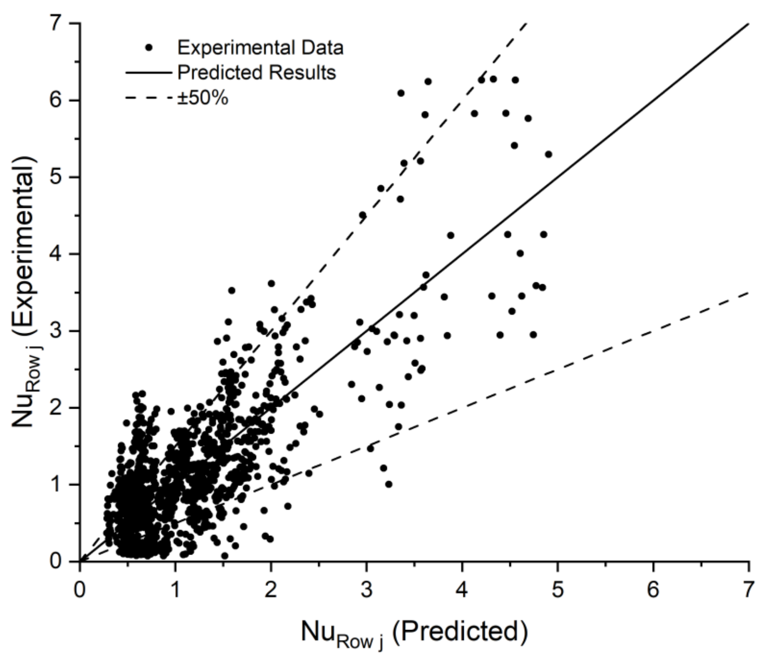

Figure 5.10: Correlation of the row Nusselt number experimental data

It was shown that the correlation covered a majority of the experimental data, determined to be 62.6% of it, within ±50% of the prediction and showed significantly better agreement with the data for which row Nusselt numbers were greater than approximately 1.0, which corresponded to a row heat transfer coefficient of approximately 5.0 kW/m^2-K depending on test conditions. Where the correlation was deemed especially useful was in predicting average bundle Nusselt numbers and, as a result, overall bundle heat transfer performance. Given values of the row Nusselt numbers for each row in the bundle, the average bundle Nusselt number could be determined as the simple average of these values as follows:

$$Nu_{bundle} = \frac{\sum_{j=1}^{5} Nu_{Row\ j}}{5} \tag{5.27}$$

where Nu_{bundle} is the Nusselt number for the whole tube bundle which consisted of 5 active tube rows in any given full bundle test. The correlation in this form was also compared to the experimental data, as shown in Figure 5.11.

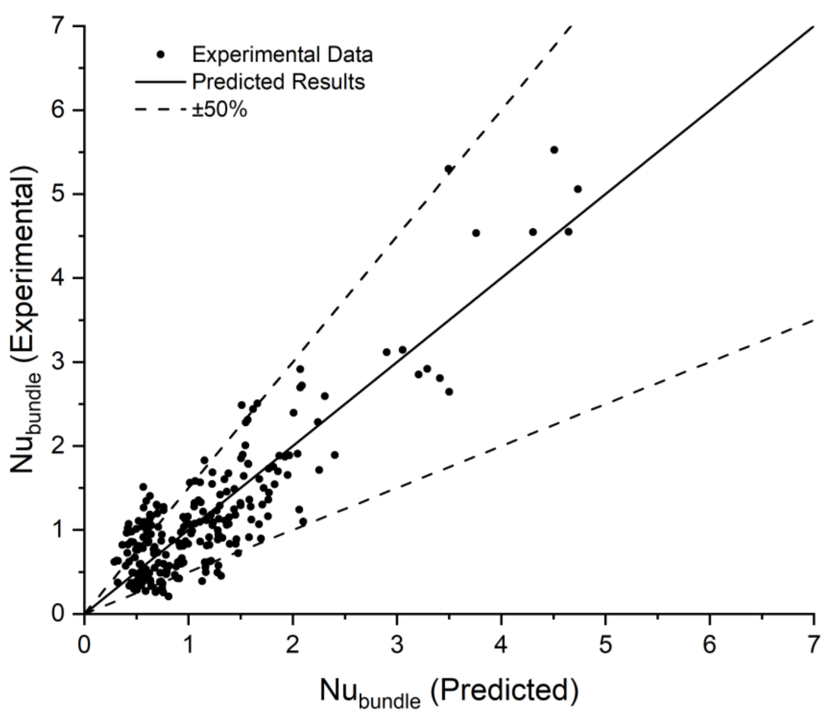

Figure 5.11: Correlation of the overall bundle Nusselt number experimental data

In this form, the correlation covered a larger percentage of the experimental data, determined to be approximately 73.2% of it, within ±50% of the prediction. Similarly, predictions tended to be more accurate for the data in which bundle Nusselt numbers were greater than 1.5, which corresponded to a bundle heat transfer coefficient of approximately 7.5 kW/m^2-K depending on conditions. As a preliminary model, the correlation as described was deemed an adequate fit for the data collected as part of this work.

Chapter 6: Conclusions

Increasingly stringent regulation of high global-warming-potential refrigerants coupled with the continuous desire to lower costs associated with the manufacture and operation of HVAC&R equipment have led to the development of new, more environmentally-friendly and as yet relatively untested low-GWP refrigerant alternatives and heat exchanger configurations that allow for the reduction of refrigerant inventory in a system. As new equipment is designed to accommodate these refrigerants and new techniques in refrigerant distribution are utilized, development engineers will need data on the heat transfer performance of such configurations to inform their design decisions. New HFO refrigerants with global warming potentials similar to that of carbon dioxide have the potential to serve as drop-in replacements with equal or improved performance compared to the HFC refrigerants currently in widespread use, especially in North America. Spray evaporation as a mode of heat transfer and refrigerant distribution in a shell-and-tube heat exchanger also has the potential to improve shell-side heat transfer performance compared to the nearly ubiquitous flooded evaporator configuration while simultaneously decreasing the refrigerant charge inside the heat exchanger, especially when coupled with cutting-edge enhanced-surface tubes that have only recently been introduced. The literature on the performance of HFO refrigerants, new enhanced surfaces, and spray evaporation as separate factors in the design of shell-and-tube heat exchangers is limited, and literature on the intersection of all three factors is nearly non-existent. The experiments performed and correlations developed as part of this work were designed to fill that gap.

In order to do so, a specialized shell-and-tube heat exchanger test section was constructed and instrumented to allow for measurements of refrigerant and tube wall temperatures and heat input so that shell-side heat transfer coefficients could be calculated. Two different low-finned enhanced-surface tube types, called Tube-C and Tube-B, were used in two different tube pitch configurations, square-pitch and triangular-pitch, for a total of four bundle arrangements. The Tube-C surface was one that had been specifically designed to enhance condensation heat transfer while the Tube-B surface was designed to enhance boiling heat transfer. The square-pitch pattern consisted of 15 tubes arranged in three columns of five tubes, and the triangular-pitch pattern consisted of 12 tubes arranged in five rows with every other row offset horizontally from the one above it. Spray nozzles with a solid cone spray pattern were used for the majority of the experimental campaign, though nozzles with a deflected flat spray pattern also saw limited use for the sake of comparison. Three different refrigerants were used: R134a, an HFC refrigerant commonly found in automotive air-conditioning systems and some residential cooling applications; R1234ze(E), an experimental HFO refrigerant designed as a near drop-in replacement for R134a; and R1233zd(E), another experimental HFO refrigerant designed to replace the HCFC R123 commonly found in large industrial-type centrifugal chillers. The test section was operated at tube heat fluxes between 3.5 kW/m^2 and 30 kW/m^2, at refrigerant saturation temperatures between -12 °C and 16 °C, at refrigerant mass flow rates between 0.7 kg/min and 7.5 kg/min, and with refrigerant inlet subcooling varying between 0 °C to over 5 °C. A total of over 900 tests were performed to investigate the heat transfer performance of the spray evaporation configuration and to compare the relative performance of the two different bundle configurations, the two different enhanced-surface types, and the three different refrigerants.

For the first bundle tested, the Tube-C surfaces in the triangular-pitch geometry, heat transfer coefficients ranged from approximately 1.0 kW/m^2-K to 6.0 kW/m^2-K for R134a, 1.0 kW/m^2-K to 12.0 kW/m^2-K for R1234ze(E), and 0.5 kW/m^2-K to 6.0 kW/m^2-K for R1233zd(E). Most tests were performed for heat fluxes ranging from 3 kW/m^2 to 24 kW/m^2 with some higher heat flux tests up to 35 kW/m^2 performed with R1234ze(E). For the second bundle tested, the Tube-C surfaces in the square-pitch geometry, heat transfer coefficients ranged from approximately 1.0 kW/m^2-K to 6.0 kW/m^2-K for R134a, 2.0 kW/m^2-K to 10.0 kW/m^2-K for R1234ze(E), and 1.0 kW/m^2-K to 5.0 kW/m^2-K for R1233zd(E) with all tests performed between 3 kW/m^2 and 22 kW/m^2. Single-tube pool boiling tests were also performed in R134a and R1234ze(E) with the Tube-C surface in which heat transfer coefficients increased from 2.0 kW/m^2-K to 14.0 kW/m^2-K for increases in heat flux from 5 kW/m^2 to 37 kW/m^2, but in R1233zd(E), values remained steady between 5.0 kW/m^2-K and 6.0 kW/m^2-K over a similar range. As such, peak spray evaporation heat transfer coefficients were comparable to those observed during nucleate boiling and demonstrated the viability of the spray evaporator configuration. The nucleate pool boiling results compared favorably to other results found in the literature for similar low-finned enhanced surfaces and thus were an excellent verification for the test facility and the methods used.

For the third bundle tested, the Tube-B surfaces in the triangular-pitch geometry, heat transfer coefficients ranged from approximately 3.0 kW/m^2-K to 9.0 kW/m^2-K for R134a, 5.0 kW/m^2-K to 37.0 kW/m^2-K for R1234ze(E), and 7.0 kW/m^2-K to 24.0 kW/m^2-K for R1233zd(E) with most tests performed at heat fluxes between 3 kW/m^2 and 27 kW/m^2. For the fourth bundle tested, the Tube-B surfaces in the square-pitch geometry, heat transfer coefficients ranged from 3.0 kW/m^2-K to 18.0 kW/m^2-K for R134a and 3.0 kW/m^2-K to 14.0 kW/m^2-K for R1234ze(E) with all tests performed between 3 kW/m^2 and 22 kW/m^2, and 7.0 kW/m^2-K to 17.0 kW/m^2-K for R1233zd(E) with no tests performed above 14 kW/m^2. As before, single-tube pool boiling tests were also performed using the Tube-B enhanced surface. Heat transfer coefficient values between 8 kW/m^2-K and 25 kW/m^2-K were observed for heat fluxes ranging from 7 kW/m^2 to 35 kW/m^2

in R134a and R1234ze(E), and values between 7 kW/m^2-K and 14 kW/m^2-K were observed over a similar range for R1233zd(E). As before, peak spray evaporation heat transfer coefficients were similar to those obtained in the nucleate pool boiling regime and were much higher than those reported in the literature for plain-surface boiling heat transfer coefficients.

The experiments showed significantly improved heat transfer performance for the Tube-B surface compared to the Tube-C surface and a modest improvement in performance for the triangular-pitch bundle arrangement compared to the square-pitch arrangement. For tests performed under similar conditions for all three refrigerants, the enhancement of heat transfer performance attributed to the triangular pitch bundle arrangement was between approximately 10% and 30% compared to the square-pitch arrangement. In modeling the data for which the inlet subcooling was between 0.5 °C and 2.0 °C, the average enhancement attributed to the triangular geometry was found to be 26%. Enhancements attributed to the Tube-B surface ranged from 50% to over 500% in some cases compared to the Tube-C surface with an average enhancement of approximately 200% calculated in later model development work.

In general, bundle heat transfer performance was found to be relatively insensitive to changes in refrigerant saturation temperature. Under similar flow rate and subcooling conditions for the Tube-C surfaces, bundle heat transfer coefficients for R134a and R1234ze(E) were usually within approximately ±15% for saturation temperatures between 12 °C and -6 °C and it was only for the R1234ze(E) tests at -12 °C that values were between 15% and 50% lower than those observed at -6 °C. Very low temperature data for the Tube-B surfaces was much more limited, but heat transfer coefficient values for R134a and R1234ze(E) were observed to be most independent of refrigerant saturation temperature as well. Because R1233zd(E) was almost exclusively tested at saturation temperatures around 15 °C, such comparisons could not be made for tube Tube-C surfaces. However, tests performed using the Tube-B surfaces with saturation temperatures around 15 °C and 9 °C showed that values were comparable within ±15%, all else being equal.

Bundle heat transfer performance was also found to be relatively insensitive to the type of spray nozzle used in the test section provided that sufficient refrigerant distribution was ensured for both the deflected flat nozzle type and the solid circular cone type. For tests performed under similar conditions using R1234ze(E), heat transfer coefficients for both nozzle types were within ±10%. Though both nozzle types had advantages associated with their differing spray patterns, it was ultimately decided to use the circular cone nozzles because of their relative ease of adjustment and improved distribution of refrigerant to the offset tube rows within the bundle. Nozzles of this type are much more common in real process applications likely for these reasons.

In all full bundle tests, and even in partial bundle tests to a lesser extent, heat transfer performance at high tube heat fluxes was significantly affected by the dryout phenomenon in which the tubes in the lower rows received a decreased supply of cooling liquid refrigerant due to both the bundle effect and an increased amount of refrigerant having been evaporated by the tubes in the upper rows. The bundle effect was a phenomenon in which impingement of the refrigerant on the highest tubes in the bundle caused deflection and dispersal of the spray such that, even in an unheated bundle, the lower tubes received a lesser supply of liquid refrigerant than the upper tubes. This bundle effect was observed in a number of single tube tests in the spray evaporation regime in which heat transfer coefficients were higher for the topmost tube than for the bottommost tube in the bundle even when all other tubes were inactive. In most cases, the dryout phenomenon was responsible for the change in slope of the heat transfer coefficient curves from positive to negative with the increase in bundle heat flux and necessitated the development of a new correlation technique to more accurately model this behavior. This effect represents a major hurdle in the design of similar spray evaporator shell-and-tube heat exchangers and emphasizes the need for sufficient refrigerant flow rate to suit the amount of heat being dissipated and proper refrigerant distribution on the shell side of the bundle.

Bundle heat transfer performance was also found to be extremely sensitive to the level of refrigerant inlet subcooling, a measure of the difference in temperature of the refrigerant at the test section inlet and its saturation temperature inside the test section. In general, decreases in the amount of inlet subcooling corresponded to increased bundle heat transfer coefficients due to the increased contribution of boiling heat transfer (and the excellent heat transfer performance associated with it) as opposed to the greater contribution of simple convective heat transfer observed with increases in inlet subcooling. This enhancement effect was observed for decreases in inlet subcooling down to a difference of 0.5 °C, below which heat transfer performance suffered due to partial evaporation of the refrigerant before even entering the test section. Diminished heat transfer enhancement was observed for inlet subcooling levels up to approximately 2.0 °C, and the enhancement effect of spray evaporation compared to nucleate pool boiling were largely negated at subcooling levels above 5.0 °C. Higher levels of inlet subcooling were observed to delay the onset of refrigerant dryout to higher heat fluxes, but this effect was not enough to counter the overall decrease in performance. Later model development showed an average enhancement in bundle heat transfer performance of 74% for an inlet subcooling of 0.5 °C compared to a subcooling of 2.0 °C. For this reason, it was concluded that the optimal operating range for a spray evaporator in a real process application would be one in which inlet subcooling was limited to the range of approximately 0.5 °C to 2.0 °C such that dryout is avoided.

In addition to the experimental work, some modeling development was also performed in which a semi-empirical mathematical model was developed to correlate the experimental data for full bundle tests with inlet subcooling between 0.5 °C and 2.0 °C. The correlation was adapted from an earlier model found in the literature for a similar investigation into shell-side spray evaporation heat transfer coefficients which accounted for the effects of tube heat flux, refrigerant mass flow rate, and refrigerant properties such as viscosity, Prandtl number, reduced pressure, and critical temperature on average bundle heat transfer coefficients. In the current work, that model was modified to correlate individual row heat transfer coefficients to the aforementioned factors while also accounting for the additional effects of enhanced surface type, bundle geometry, and the degree of inlet subcooling. To accompany the new model, a method for calculating the refrigerant flow rate at each tube row was developed so that row Reynolds numbers could be correlated to row Nusselt numbers. The overall correlation was of the form

$$Nu_{Row\ j} = a_1 Re_{Row\ j}^{a_2} Pr^{a_3} P_{red}^{a_4} \Phi^{a_5} \tag{5.1}$$

where the coefficient a_1 was a product of the enhanced surface factor, bundle factor, and subcooling factor, and the constants a_2, a_3, a_4, and a_5 were prescribed based on curve fitting of the experimental data. Changing the model to this form allowed for more detailed predictions of individual row heat transfer coefficients, which in turn potentially makes it applicable in applications with a different number of tubes, tube rows or columns. It also still allowed for relatively simple determination of overall bundle heat transfer coefficients which could be calculated as an average of individual row heat transfer coefficients. Model diagnostics found that the final correlation was a good fit for the experimental data and had an associated R^2 value of 0.581.

Recommendations for Future Work

Data collected during these experiments was much more limited for R1233zd(E) than for either R134a or R1234ze(E) due to the difficulty in working with a low-pressure refrigerant and the limitations of the test setup. The primary refrigerant diaphragm pump was installed to help alleviate this, but problems with testing the refrigerant at saturation pressures below atmospheric pressure persisted. For a more complete investigation, multiple series of tests with R1233zd(E) at pressures below standard atmospheric pressure are needed. Additionally, the use of a similar refrigerant already in widespread use, such as R123, would have allowed for heat transfer performance comparisons between the two refrigerants using R123 as a baseline.

Although outside the scope of the current project, the use of plain-surface tubes in the current test setup and in both bundle geometries would provide an excellent baseline for the performance of the Tube-B and Tube-C enhanced surfaces used throughout. In a survey of the literature, no studies could be found in which spray evaporation heat transfer coefficients of new HFO refrigerants were measured on bundles of plain-surface tubes.

Often in studies of this type, it is useful to measure heat transfer coefficients of not only the pure refrigerants but also mixtures of the refrigerants with lubricating oils commonly found in real process compressors. Such results could be reported using the data presented in this work as a set of baselines in order to quantify the heat transfer enhancement or attenuation. Modifications could be made to the correlation developed in this work to account for the effects of different lubricating oils on shell-side heat transfer performance.

References

Abed, A. M., Alghoul, M. A., Yazdi, M. A., Al-Shamani, A. N., & Sopian, K. (2015). The role of enhancement techniques on heat and mass transfer characteristics of shell and tube spray evaporator: a detailed review. *Applied Thermal Engineering*, 923-940.

Bergles, A. E. (1988). Heat Transfer Augmentation. In S. Kakac, A. E. Bergles, & E. O. Fernandes, *Two-Phase Flow Heat Exchangers, Thermal-Hydraulic Fundamentals and Design* (pp. 343-373). Dordrecht: Kluwer Academic Publishers.

Bock, B. D., Meyer, J. P., & Thome, J. R. (2019). Falling film boiling and pool boiling on plain circular tubes: Influence of surface roughness, surface material and saturation temperature on heat transfer and dryout. *Experimental Thermal and Fluid Science*.

Browne, M. W., & Bansal, P. K. (1999). Heat transfer characteristics of boiling phenomenon in flooded refrigerant evaporators. *Applied Thermal Engineering*, 595-624.

Byun, H.-W., Kim, D. H., Yoon, S. H., Sing, C. H., Lee, K. H., & Kim, O. J. (2017). Pool boiling performance of enhanced tubes on low GWP refrigerants. *Applied Thermal Engineering*, 791-798.

Chang, T. B., & Chiou, J. S. (1999). Spray evaporation heat transfer of R-141b on a horizontal tube bundle. *International Journal of Heat and Mass Transfer*, 1467-1478.

Chang, T.-B. (2006). Effects of nozzle configuration on a shell-and-tube spray evaporator with liquid catcher. *Applied Thermal Engineering*, 814-823.

Chen, J. C. (1966). Correlation for boiling heat transfer to saturated fluids in convective flow. *Industrial and Engineering Chemistry Process Design and Development*, 322-329.

Chien, L.-H., Tsai, Y.-L., & Chang, C.-H. (2019). A study of pool boiling and falling-film vaporization with R-245fa/oil mixtures on horizontal tubes. *International Journal of Heat and Mass Transfer*, 940-950.

Chiou, C.-B., Lu, D.-C., & Wang, C.-C. (1997). Pool boiling of R-22, R-124 and R-134a on a plain tube. *International Journal of Heat and Mass Transfer*, 1657-1666.

Chongrungreong , S., & Sauer, H. J. (1980). Nucleate Boiling Performance of Refrigerants and Refrigerant-Oil Mixtures. *Journal of Heat Transfer*, 701-705.

Chun, K. R., & Seban, R. A. (1971). Heat Transfer to Evaporating Liquid Films. *Journal of Heat Transfer*, 391-396.

Chyu, M.-C., & Bergles, A. E. (1989). Horizontal-Tube Falling-Film Evaporation With Structured Surfaces. *Journal of Heat Transfer*, 518-524.

Chyu, M.-C., Zeng, X., & Ayub, Z. H. (1995). Nozzle-sprayed flow rate distribution on a horizontal tube bundle. *ASHRAE Transactions*, 443-453.

Cornwell, K., & Einarrson, J. G. (1990). Influence of fluid flow on nucleate boiling from a tube. *Experimental Heat Transfer*, 101-116.

Cornwell, K., & Houston, S. D. (1994). Nucleate pool boiling on horizontal tubes: a convection-based correlation. *International Journal of Heat and Mass Transfer*, 303-309.

Dewangan, A. K., Sajjan, S. K., Kumar, A., & Kumar, R. (2020). Pool boiling heat transfer on a plain tube in saturated R-134a and R-410A. *Heat and Mass Transfer*, 1179-1188.

Dukler, A. E. (1960). Fluid Mechanics and Heat Transfer in Vertical Falling Film Systems. *Chemical Engineering Progress Symposium Series*, 1-10.

Fletcher, L. S., Sernas, V., & Galowin, L. S. (1974). Evaporation from Thin Water Films on Horizontal Tubes. *Industrial & Engineering Chemistry Process Design and Development*, 265-269.

Fujita, Y., & Tsutsui, M. (1998). Experimental investigation of falling film evaporation on horizontal tubes. *Heat Transfer - Japanese Research*, 609-618.

Hwang, T., & Yao, S. (1986). Crossflow boiling heat transfer in tube bundles. *International Communications in Heat and Mass Transfer*, 493-502.

Jensen, M. K. (1988). Boiling on the Shellside of Horizontal Tube Bundles. In S. Kakac, A. E. Bergles, & E. O. Fernandes, *Two-Phase Flow Heat Exchangers: Thermal-Hydraulic Fundamentals and Design* (pp. 707-746). Dordrecht: Kluwer Academic Publishers.

Jige, D., Miyata, H., & Inoue, N. (2019). Falling film evaporation of R1234ze(E) and R245fa on a horizontal smooth tube. *Experimental Thermal and Fluid Science*, 58-66.

Jin, P.-H., Zhang, Z., Mostafa, I., Zhao, C.-Y., Ji, W.-T., & Tao, W.-Q. (2019). Heat transfer correlations of refrigerant falling film evaporation on a single horizontal smooth tube. *International Journal of Heat and Mass Transfer*, 96-106.

Jung, D., An, K., & Park, J. (2004). Nucleate boiling heat transfer coefficients of HCFC22,HFC134a, HFC125, and HFC32 on various enhanced tubes. *International Journal of Refrigeration*, 202-206.

Jung, D., Kim, Y., Ko, Y., & Song, K. (2003). Nucleate boiling heat transfer coefficients of purehalogenated refrigerants. *International Journal of Refrigeration*, 240-248.

Katz, D. L., Myers, J. E., Young, E. H., & Balekjian, G. (1955). Boiling outside finned tubes. *Petroleum Refiner*, 113-116.

Krasowski, K., & Cieśliński, J. T. (2011). Nucleate pool boiling heat transfer from small horizontal smooth tube bundles. *Transactions of the Institute of Fluid-Flow Machinery*, 85-98.

Kumar, A., & Wang, C.-C. (2022). Nucleate pool boiling heat transfer of R-1234ze(E) and R-134a on GEWA-B5H and smooth tube with the influence of POE oil. *Applied Thermal Engineering*.

Leong, L. S., & Cornwell, K. (1979). Heat Transfer Coefficients in a Reboiler Tube Bundle. *The Chemical Engineer*, 219-221.

Li, W., Wu, X.-Y., Luo, Z., & Webb, R. L. (2011). Falling water film evaporation on newly-designed enhanced tube bundles. *International Journal of Heat and Mass Transfer*, 2990-2997.

Lin, L., & Kedzierski, M. A. (2019). Review of low-GWP refrigerant pool boiling heat transfer on enhanced surfaces. *International Journal of Heat and Mass Transfer*, 1279-1303.

Liu, P. (1975). The Evaporating Falling Film on Horizontal Tubes. *Ph.D. Thesis*. Madison: University of Wisconsin.

Marto, P. J., & Anderson, C. L. (1992). Nucleate Boiling Characteristics of R-113 in a Small Tube Bundle. *Journal of Heat Transfer*, 425-433.

Memory, S. B., Akcasayar, N., Eraydin, H., & Marto, P. J. (1995b). Nucleate pool boiling of R-114 and R-114-oil mixtures from smooth and enhanced surfaces—II. Tube bundles. *International Journal of Heat and Mass Transfer*, 1363-1376.

Memory, S. B., Sugiyama, D. C., & Marto, P. J. (1995a). Nucleate pool boiling of R-114 and R-114-oil mixtures from smooth and enhanced surfaces—I. Single tubes. *International Journal of Heat and Mass Transfer*, 1347-1361.

Mitrovic, J. (1986). Influence of tube spacing and flow rate on heat transfer from a horizontal tube to a falling liquid film. *Proceedings of the eighth international heat transfer conference*, (pp. 1949-1956). San Francisco.

Moeykens, S. A., & Pate, M. B. (1994). Spray Evaporation Heat Transfer of R-134a on Plain Tubes. *ASHRAE Transactions*, 173-184.

Moeykens, S. A., & Pate, M. B. (1995). The effects of nozzle height and orifice size on spray evaporation heat transfer performance for a low-finned, triangular-pitch tube bundle with R-134a. *ASHRAE Transactions*, 420-433.

Moeykens, S. A., Newton, B. J., & Pate, M. B. (1995). Effects of surface enhancement, film-feed supply rate, and bundle geometry on spray evaporation heat transfer performance. *ASHRAE Transactions*, 408-419.

Molina, M. J., & Rowland, F. S. (1974). Stratospheric sink for chlorofluoromethanes : chlorine atomc-atalysed destruction of ozone. *Nature*, 810-812.

Nagata, R., Kondou, C., & Koyama, S. (2016). Comparative assessment of condensation and pool boiling heat transfer on horizontal plain single tubes for R1234ze(E), R1234ze(Z), and R1233zd(E). *International Journal of Refrigeration*, 157-170.

Nelson, P. J., & Burnside, B. M. (1985). Boiling the immiscible water/n-nonane system from a tube bundle. *International Journal of Heat and Mass Transfer*, 1257-1267.

Owens, W. L. (1978). Correlation of Thin Film Evaporation Heat Transfer Coefficients for Horizontal Tubes. *Proceedings of the Fifth Annual Conference on Ocean Thermal Energy Conversion.* Miami Beach, FL.

Palen, J. W., & Taborek, J. (1962). Refinery Kettle Reboilers - Proposed Method for Design and Optimization. *Chemical Engineering Progress*, 37-46.

Parken, W. H., Fletcher, L. S., Sernas, V., & Han, J. C. (1990). Heat Transfer Through Falling Film Evaporation and Boiling on Horizontal Tubes. *Transactions of the ASME*, 744-750.

Ribatski, G., & Jacobi, A. M. (2005). Falling-film evaporation on horizontal tubes - A critical review. *International Journal of Refrigeration*, 635-653.

Ribatski, G., & Thome, J. R. (2007). Experimental study on the onset of local dryout in an evaporating falling film on horizontal plain tubes. *Experimental Thermal and Fluid Science*, 483-493.

Rohsenow, W. M. (1952). A Method of Correlating Heat-Transfer Data for Surface Boiling of Liquids. *Transactions of the American Society of Mechanical Engineers*, 969-975.

Saiz-Jabardo, J. M., da Silva, E. F., Ribatski, G., & de Barros, S. F. (2004). Evaluation of the Rohsenow Correlation Through Experimental Pool Boiling of Halocarbon Refrigerants on Cylindrical Surfaces. *Journal of the Brazilian Society of Mechanical Sciences and Engineering*, 218-230.

Stephan, K. (1995). Two-phase heat exchange for new refrigerants and their mixtures. *International Journal of Refrigeration*, 198-209.

Stephan, K., & Abdelsalam, M. (1980). Heat-transfer correlations for natural convection boiling. *International Journal of Heat and Mass Transfer*, 73-87.

Swain, A., Mohanty, R. L., & Das, M. K. (2017). Pool boiling of distilled water over tube bundle with variable heat flux. *Heat and Mass Transfer*, 2487-2495.

Taborek, J. (2014). *Shell-and-Tube Heat Exchanger Design: Objectives and Background.* Retrieved from HEDH Multimedia: https://hedhme.com/

Tatara, R. A., & Payvar, P. (2001). Measurement of spray boiling refrigerant coefficients in an integral-fin tube bundle segment simulating a full bundle. *International Journal of Refrigeration*, 744-754.

Taylor, B. N., & Kuyatt, C. E. (1994). *Guidelines for Evaluating and Expressing the Uncertainty of NIST Measurement Results.* Gaithersburg: National Institute of Standards and Technology.

Thome, J. R. (1989). Nucleate pool boiling of hydrocarbon mixtures on a GEWA-TX tube. *Heat Transfer Engineering*, 37-44.

Thome, J. R. (1996). Boiling of new refrigerants: a state-of-the-art review. *International Journal of Refrigeration*, 435-457.

Ubara, T., Asano, H., & Sugimoto, K. (2020). Heat Transfer Enhancement of Falling Film Evaporation on a Horizontal Tube by Thermal Spray Coating. *Applied Sciences*.

Ubara, T., Asano, H., & Sugimoto, K. (2021). Falling film evaporation and pool boiling heat transfer of R1233zd(E) on thermal spray coated tube. *Applied Thermal Engineering*.

van Rooyen, E., & Thome, J. R. (2013). Pool boiling data and prediction method for enhanced boiling tubes with R-134a, R-236fa and R-1234ze(E). *International Journal of Refrigeration*, 447-455.

Webb, R. L., & Pais, C. (1992). Nucleate pool boiling data for five refrigerants on plain, integral-fin and enhanced tube geometries. *International Journal of Heat and Mass Transfer*, 1893-1904.

Webb, R. L., Choi, K.-D., & Apparao, T. R. (1989). A Theoretical Model for Prediction of the Heat Load in Flooded Refrigerant Evaporators. *ASHRAE Transactions* (pp. 326-338). Chicago: ASHRAE.

Yan, W.-M., Pan, C.-W., Yang, T.-F., & Ghalambaz, M. (2019). Experimental study on fluid flow and heat transfer characteristics of falling film over tube bundle. *International Journal of Heat and Mass Transfer*, 9-24.

Yang, L., & Wang, W. (2011). The heat transfer performance of horizontal tube bundles in large falling film evaporators. *International Journal of Refrigeration*, 303-316.

Yilmaz, S., & Westwater, J. W. (1980). Effect of Velocity on Heat Transfer to Boiling Freon-113. *Journal of Heat Transfer*, 26-31.

Zeng, X., Chyu, M.-C., & Ayub, Z. (1994). Characteristic study of sprayed fluid flow in a tube bundle. *ASHRAE Transactions*.

Zeng, X., Chyu, M.-C., & Ayub, Z. H. (1995). Evaporation heat transfer performance of nozzle-sprayed ammonia on a horizontal tube. *ASHRAE Transactions*, 136-149.

Zeng, X., Chyu, M.-C., & Ayub, Z. H. (1997). Performance of Nozzle-Sprayed Ammonia Evaporator with Square-Pitch Plain-Tube Bundle. *ASHRAE Transactions*, 68-81.

Zeng, X., Chyu, M.-C., & Ayub, Z. H. (2001a). Experimental investigation on ammonia spray evaporator with triangular-pitch plain-tube bundle, Part I: tube bundle effect. *International Journal of Heat and Mass Transfer*, 2299-2310.

Zeng, X., Chyu, M.-C., & Ayub, Z. H. (2001b). Experimental investigation on ammonia spray evaporator with triangular-pitch plain-tube bundle, Part II: evaporator performance. *International Journal of Heat and Mass Transfer*, 2081-2092.

Zhao, C.-Y., Ji, W.-T., Jin, P.-H., & Tao, W.-Q. (2016). Heat transfer correlation of the falling film evaporation on a single horizontal smooth tube. *Applied Thermal Engineering*, 177-186.

Zheng, Y., Ma, X., Li, Y., Jiang, R., Wang, K., Lan, Z., & Liang, Q. (2017). Experimental study of falling film evaporation heat transfer on superhydrophilic horizontal-tubes at low spray density. *Applied Thermal Engineering*, 1548-1556.

Appendix A

Test Summary Data

Reported in this section are the summary data for all tests performed during the experimental campaign using pure refrigerants. Though a large majority of these data were presented in Chapter 4: Results and Discussion, some were not presented because of invalid results due to testing irregularities such as equipment malfunction, refrigerant contamination, or operator error. All data are presented in the chronological order in which they were collected such that the Phase 5 data appear first, followed by Phases 1, 2, 3, and 4. Each table contains the following columns: a Date column, indicating the day on which each test was performed; a Test Condition column containing a brief note about the operating condition for each test; a Power Setting column indicating the input value used by the investigators in the system controls; a Heat Flux column indicating the local heat flux on each active tube outer surface for each test; two Pressure columns, the first one indicating the average refrigerant pressure at the test section inlet and the second indicating the average refrigerant pressure inside the test section; four Temperature columns, the first of which indicates the average refrigerant temperature at the test section inlet, the second which indicates the average refrigerant saturation temperature inside the test section, the third which indicates the average refrigerant reference temperature used in the data analysis, and the fourth which indicates the average degree of subcooling of the refrigerant at the test section inlet; one Flow Rate column, indicating the average total refrigerant mass flow rate into the test section; and six Heat Transfer Coefficient columns, indicating the average heat transfer coefficients for tube rows 1, 2, 3, 4, and 5, and the overall average bundle heat transfer coefficient for the test, respectively. All dates are presented in the [MM/DD/YYYY] format, all heat flux values are presented in units of [kW/m^2], all pressures are in [kPa], all temperatures are in [°C], all flow rates are in [kg/min], and all heat transfer coefficients are in [kW/m^2-K]. The data in this section are split identically to those in Appendix B such that each table in this section corresponds exactly to a table containing test average local temperature data in that section.

Date	Test Condition	Power Setting	Heat Flux [kW/m^2]	Pressure [kPa]		Temperature [°C]				Flow Rate [kg/min]	Heat Transfer Coefficient [kW/m^2-K]					
				P_{inlet}	P_{box}	T_{inlet}	T_{sat}	T_{ref}	Subcooling		Row 1	Row 2	Row 3	Row 4	Row 5	Overall
PHASE 5 - R134a, deflected flat spray nozzles, triangular pitch, Tube-C condenser tubes (Bundle 1)																
2/12/2021	Full Bundle Tubes 1, 2, 3, 4, 5 maxed out	1.0kW	17.14	367.3	355.1	1.5	5.4	1.5	3.9	4.07	3.72	3.48	3.20	3.65	3.65	3.54
		1.0kW (2)	17.10	367.4	352.6	-1.6	5.2	-1.6	6.8	4.22	2.23	2.18	2.05	2.25	2.23	2.19
		1.0kW (3)	17.11	360.4	346.1	-1.5	4.7	-1.5	6.2	4.19	2.43	2.36	2.21	2.45	2.41	2.37
		1.0kW (4)	17.17	351.1	340.4	-0.8	4.2	-0.8	5.0	3.98	2.98	2.85	2.65	2.97	2.91	2.87
		1.0kW (5)	17.14	338.3	332.4	0.3	3.5	0.3	3.3	3.67	4.37	3.97	3.65	4.19	4.10	4.06
		1.0kW (6)	17.12	330.7	325.9	-5.3	3.0	-5.3	8.3	3.61	1.87	1.84	1.75	1.89	1.86	1.84
		1.0kW (7)	17.08	328.7	324.1	-7.5	2.8	-7.5	10.3	3.60	1.53	1.51	1.45	1.54	1.52	1.51
2/26/2021	Partial Bundle, Preheater ON, Increased Charge	0.4kW	6.76	321.2	331.8	1.0	3.5	1.0	2.5	2.29	2.41	-	2.36	-	-	2.39
		0.4kW (2)	7.02	341.1	351.7	1.0	5.1	1.0	4.1	2.29	1.69	-	1.67	-	-	1.69
		0.8kW	13.63	349.4	358.4	0.7	5.7	0.7	5.0	2.37	3.13	-	2.98	-	-	3.07
		0.8kW (2)	13.77	329.8	340.6	0.9	4.2	0.9	3.3	2.21	3.43	-	3.22	-	-	3.35
		1.2kW	20.30	341.7	351.3	0.2	5.1	0.2	4.9	2.39	3.26	-	3.15	-	-	3.22
		1.6kW	27.02	348.1	355.5	-0.1	5.5	-0.1	5.5	2.61	3.72	-	3.61	-	-	3.67
		2.0kW	34.29	351.2	356.4	0.2	5.5	0.2	5.3	2.79	4.62	-	4.41	-	-	4.54
		2.4kW	40.71	353.7	356.5	0.3	5.5	0.3	5.2	2.99	5.26	-	5.03	-	-	5.17
3/1/2021	Partial Bundle, Preheater ON, Increased Charge	0.4kW	6.75	355.9	367.6	0.0	6.4	0.0	6.4	2.28	1.01	-	1.02	-	1.03	1.02
		0.4kW (2)	6.74	354.8	366.9	0.3	6.4	0.3	6.0	2.25	1.06	-	1.08	-	1.09	1.07
		0.8kW	13.53	339.6	351.2	0.1	5.1	0.1	5.0	2.31	2.35	-	2.49	-	2.50	2.44
		1.2kW	20.34	357.1	366.4	0.0	6.3	0.0	6.3	2.54	2.67	-	2.90	-	2.87	2.81
		1.6kW	27.35	361.8	369.6	0.5	6.6	0.5	6.1	2.69	3.48	-	3.86	-	3.61	3.66
		2.0kW	33.81	367.0	375.1	0.8	7.0	0.8	6.2	2.66	3.96	-	4.47	-	4.06	4.19
	Row 5 Inactive	2.4kW	40.41	370.1	376.7	0.1	7.1	0.1	7.0	2.80	4.07	-	4.67	-	-	4.37
3/2/2021	Partial Bundle, Preheater ON, Increased Charge	0.4kW	6.77	397.9	409.5	0.0	9.6	0.0	9.6	2.27	0.69	-	0.68	-	0.69	0.69
		0.8kW	13.54	382.1	392.5	0.6	8.3	0.6	7.7	2.39	1.66	-	1.60	-	1.65	1.64
		1.2kW	20.42	309.0	314.3	0.5	2.0	0.5	1.5	2.42	7.99	-	7.41	-	8.20	7.92
		1.6kW	27.18	306.4	309.5	0.5	1.5	0.5	1.1	2.40	10.49	-	9.92	-	10.48	10.35
		2.0kW	34.10	305.0	307.6	0.3	1.4	0.3	1.1	2.40	11.38	-	10.70	-	7.87	10.18
		2.4kW	40.94	307.2	311.0	0.2	1.7	0.2	1.5	2.44	10.79	-	10.28	-	-	10.59
		2.4kW (2)	40.98	308.5	317.4	-4.9	2.2	-4.9	7.2	2.54	3.99	-	3.69	-	-	3.87
3/12/2021	Partial Bundle, Preheater ON, Increased Charge	0.4kW	6.75	332.5	339.6	0.6	4.1	0.6	3.5	2.63	1.77	-	1.81	-	1.30	1.63
		0.8kW	13.53	318.3	327.1	0.4	3.1	0.4	2.7	2.32	4.30	-	4.08	-	4.34	4.26
		0.8kW (2)	13.65	326.0	333.3	0.7	3.6	0.7	2.9	2.54	4.31	-	4.04	-	4.39	4.27
		1.2kW	20.39	319.4	324.7	0.1	2.9	0.1	2.7	2.79	5.05	-	4.89	-	5.05	5.01
		1.6kW	27.23	320.4	320.2	0.6	2.5	0.6	1.9	2.99	7.84	-	7.45	-	7.92	7.78
		2.0kW	34.07	322.6	318.8	0.5	2.4	0.5	1.9	3.18	8.74	-	8.33	-	8.36	8.50
3/15/2021	Partial Bundle, Preheater ON, Increased Charge	0.4kW	6.75	425.0	436.9	8.2	11.5	8.2	3.3	2.19	1.87	-	1.86	-	1.93	1.89
		1.2kW	20.45	414.5	415.2	8.1	10.0	8.1	1.9	3.13	6.60	-	6.43	-	7.16	6.77
		1.6kW	27.25	415.2	413.9	8.1	9.9	8.1	1.9	3.25	7.86	-	7.55	-	8.06	7.86
		1.8kW	30.84	415.3	412.7	7.7	9.8	7.7	2.2	3.36	7.71	-	7.53	-	7.46	7.57
		2.0kW	33.88	416.6	412.4	8.0	9.8	8.0	1.9	3.30	8.82	-	8.20	-	7.20	8.06

Date	Test Condition	Power Setting	Heat Flux [kW/m^2]	Pressure [kPa] P_{inlet}	Pressure [kPa] P_{box}	Temperature [°C] T_{inlet}	Temperature [°C] T_{sat}	Temperature [°C] T_{ref}	Temperature [°C] Subcooling	Flow Rate [kg/min]	Heat Transfer Coefficient [kW/m^2-K] Row 1	Row 2	Row 3	Row 4	Row 5	Overall
PHASE 5 - R134a, deflected flat spray nozzles, triangular pitch, Tube-C condenser tubes (Bundle 1)																
3/16/2021	Partial Bundle, Preheater ON, Increased Charge	0.8kW	13.67	339.6	344.5	1.0	4.6	1.0	3.5	2.92	3.30	-	3.17	-	3.41	3.31
		1.2kW	20.42	316.6	318.4	-0.2	2.3	-0.2	2.5	3.20	5.71	-	5.57	-	5.97	5.77
		1.6kW	27.25	318.7	319.1	-0.4	2.4	-0.4	2.7	3.25	6.35	-	6.10	-	6.27	6.26
		1.8kW	30.81	331.0	329.0	1.0	3.2	1.0	2.2	3.25	7.86	-	7.47	-	7.50	7.63
		2.0kW	33.98	326.1	323.9	0.1	2.8	0.1	2.7	3.31	7.41	-	7.07	-	6.78	7.09
3/17/2021	Partial Bundle, Preheater ON, Increased Charge	1.2kW	20.43	352.0	355.6	1.8	5.5	1.8	3.6	3.03	4.56	-	4.43	-	4.68	4.57
		1.2kW (2)	20.45	330.4	341.8	0.1	4.3	0.1	4.2	2.28	3.80	-	3.63	-	3.44	3.62
3/18/2021	Partial Bundle, Preheater ON, Increased Charge	0.4kW	6.76	352.8	363.1	0.3	6.1	0.3	5.8	2.48	1.15	-	1.13	-	0.96	1.07
		1.2kW	20.76	334.7	338.8	-0.3	4.1	-0.3	4.3	3.02	3.79	-	3.72	-	3.84	3.79
		1.6kW	27.13	328.5	329.2	0.5	3.3	0.5	2.8	3.22	6.43	-	6.09	-	6.18	6.25
		1.6kW (2)	27.30	317.5	322.6	0.2	2.7	0.2	2.4	2.47	7.02	-	6.65	-	5.95	6.53
		2.0kW	33.73	331.4	332.3	0.3	3.5	0.3	3.2	3.04	6.75	-	6.43	-	4.44	5.80
PHASE 5 - R1234ze(E), deflected flat spray nozzles, triangular pitch, Tube-C condenser tubes (Bundle 1)																
3/26/2021	Partial Bundle, Preheater OFF, Increased Charge	0.2kW	3.39	441.9	400.5	18.6	17.8	17.8	-0.8	5.20	128.19	-	23.99	-	62.61	71.59
		0.4kW	6.78	446.3	407.3	18.6	18.3	18.3	-0.2	5.15	24.58	-	25.62	-	26.13	25.44
		0.6kW	10.15	449.6	411.9	18.6	18.7	18.6	0.1	5.10	15.03	-	17.50	-	16.23	16.25
		0.8kW	13.59	458.0	420.8	18.6	19.4	18.6	0.8	5.08	8.39	-	8.97	-	8.44	8.60
		1.0kW	17.00	466.2	429.9	18.6	20.1	18.6	1.5	5.06	6.68	-	7.10	-	6.73	6.84
		1.2kW	20.50	467.5	431.8	18.1	20.2	18.1	2.1	5.04	5.92	-	6.30	-	6.02	6.08
	Preheater ON	1.4kW	23.88	470.0	434.9	18.2	20.4	18.2	2.2	5.02	6.16	-	6.69	-	6.33	6.40
		1.6kW	27.21	464.1	430.5	17.9	20.1	17.9	2.3	4.95	6.49	-	7.18	-	6.43	6.70
		1.8kW	30.86	468.3	434.9	17.7	20.4	17.7	2.7	4.94	6.30	-	6.83	-	5.68	6.27
		2.0kW	34.29	467.3	434.5	18.3	20.4	18.3	2.1	4.93	7.46	-	8.14	-	5.99	7.20
3/29/2021	Full Bundle, Preheater OFF, Increased Charge	0.2kW	3.40	336.7	311.9	9.9	10.1	9.9	0.3	4.55	7.24	6.18	6.87	6.60	7.49	6.95
		0.4kW	6.81	337.6	313.3	8.9	10.3	8.9	1.4	4.53	3.72	3.15	3.68	3.07	3.80	3.54
	Preheater ON	0.6kW	10.30	338.9	314.4	8.7	10.4	8.7	1.6	4.55	4.53	3.53	4.62	3.31	4.63	4.23
		0.8kW	13.65	342.0	317.9	8.8	10.7	8.8	2.0	4.53	4.72	3.32	4.90	3.26	4.83	4.35
		1.0kW	17.08	342.0	317.7	9.2	10.7	9.2	1.5	4.54	6.40	3.99	6.78	4.20	6.62	5.83
		1.2kW	20.53	340.1	315.5	9.2	10.5	9.2	1.3	4.56	7.64	4.11	8.22	4.73	7.97	6.86
3/30/2021	Full Bundle, Preheater OFF, Increased Charge	0.2kW	3.39	260.6	229.0	5.0	1.3	2.9	-3.7	4.02	11.57	5.79	9.17	4.43	10.40	8.76
		0.2kW (2)	3.41	270.5	241.6	5.3	2.8	2.8	-2.5	4.62	20.68	12.69	18.35	10.08	20.63	17.27
		0.8kW	13.72	257.9	240.6	2.1	2.7	2.1	0.6	4.18	8.85	2.11	9.80	4.53	9.52	7.52
	Partial Bundle	1.0kW	17.08	240.9	228.0	1.9	1.2	1.2	-0.7	3.92	21.01	-	16.90	-	15.95	17.95
		1.2kW	20.43	247.9	233.2	1.8	1.8	1.8	0.0	4.03	13.40	-	15.99	-	14.07	14.49
		1.4kW	23.89	252.9	237.8	1.8	2.4	1.8	0.5	4.05	10.33	-	11.60	-	10.30	10.74
		1.6kW	27.27	256.9	242.2	1.9	2.9	1.9	1.0	4.04	8.84	-	9.77	-	8.48	9.03
		1.7kW	28.91	259.1	244.9	1.8	3.2	1.8	1.4	4.02	8.28	-	9.20	-	7.70	8.39

Date	Test Condition	Power Setting	Heat Flux [kW/m^2]	Pressure [kPa]		Temperature [°C]				Flow Rate [kg/min]	Heat Transfer Coefficient [kW/m^2-K]					
				P_{inlet}	P_{box}	T_{inlet}	T_{sat}	T_{ref}	Subcooling		Row 1	Row 2	Row 3	Row 4	Row 5	Overall
PHASE 5 - R1234ze(E), deflected flat spray nozzles, triangular pitch, Tube-C condenser tubes (Bundle 1)																
3/31/2021	Partial Bundle, Preheater OFF, Increased Charge	0.2kW	3.38	132.5	142.4	-8.8	-11.2	-11.2	-2.4	0.97	13.79	-	13.36	-	12.30	13.15
		0.4kW	6.74	138.5	145.9	-8.1	-10.6	-10.6	-2.5	1.24	14.39	-	15.09	-	13.25	14.24
		0.6kW	10.12	141.6	146.6	-7.7	-10.4	-10.4	-2.7	1.48	13.76	-	14.59	-	12.68	13.68
		0.8kW	13.54	146.9	151.1	-7.2	-9.7	-9.7	-2.4	1.71	13.80	-	12.99	-	11.36	12.72
		0.9kW	15.29	145.9	153.3	-7.5	-9.3	-9.3	-1.8	1.86	13.16	-	9.35	-	7.84	10.12
		1.0kW	16.86	148.3	155.5	-7.1	-8.9	-8.9	-1.8	1.87	12.68	-	8.75	-	5.77	9.07
		1.2kW	20.37	152.0	159.7	-7.4	-8.3	-8.3	-0.9	2.43	12.73	-	11.25	-	6.43	10.14
4/1/2021	Partial Bundle, Preheater OFF, Increased Charge	0.2kW	3.39	227.4	235.0	3.6	2.0	2.0	-1.6	1.76	16.06	-	16.91	-	17.39	16.79
		0.4kW	6.79	231.3	240.9	3.7	2.7	2.7	-1.0	1.81	13.20	-	18.74	-	18.39	16.77
		0.6kW	10.14	235.5	247.4	3.7	3.5	3.5	-0.2	1.87	12.62	-	13.45	-	8.50	11.53
		0.7kW	11.88	238.8	251.4	3.7	3.9	3.7	0.2	1.87	9.84	-	10.01	-	4.43	8.09
		0.8kW	13.62	250.4	253.4	2.6	4.1	2.6	1.5	2.82	5.26	-	5.79	-	5.60	5.55
	Preheater ON	1.0kW	16.95	263.0	266.0	4.4	5.5	4.4	1.2	2.81	6.79	-	7.57	-	6.90	7.09
		1.2kW	20.40	255.5	258.4	2.8	4.7	2.8	1.9	2.81	5.90	-	6.32	-	5.55	5.92
		1.4kW	23.76	255.6	258.6	3.1	4.7	3.1	1.6	2.81	6.87	-	7.32	-	5.43	6.54
		1.6kW	27.30	281.0	259.5	3.4	4.8	3.4	1.4	4.41	8.04	-	8.80	-	7.87	8.23
		1.8kW	30.73	279.5	258.4	3.4	4.7	3.4	1.3	4.39	8.79	-	9.68	-	7.79	8.75
4/2/2021	Partial Bundle, Preheater OFF, Increased Charge	0.2kW	3.38	341.8	316.1	10.9	10.5	10.6	-0.3	4.50	20.24	-	18.15	-	22.70	20.37
		0.4kW	6.78	338.1	313.3	10.1	10.3	10.1	0.2	4.49	10.84	-	11.56	-	12.45	11.62
		0.6kW	10.17	336.9	312.4	9.3	10.2	9.3	0.9	4.49	6.33	-	6.81	-	6.83	6.66
	Preheater ON	0.8kW	13.53	338.7	314.5	9.6	10.4	9.6	0.8	4.48	7.42	-	8.25	-	7.94	7.87
		1.0kW	16.96	339.2	315.1	9.4	10.4	9.4	1.1	4.48	7.29	-	8.11	-	7.77	7.72
		1.2kW	20.48	339.8	315.9	9.5	10.5	9.5	1.0	4.47	7.96	-	8.95	-	8.56	8.49
		1.4kW	23.82	340.5	316.5	9.7	10.6	9.7	0.8	4.48	8.95	-	10.39	-	9.48	9.61
		1.6kW	27.26	337.7	313.8	9.4	10.3	9.5	0.9	4.48	9.16	-	10.60	-	8.81	9.52
		1.8kW	30.69	339.9	316.0	9.5	10.5	9.5	1.0	4.48	9.19	-	10.42	-	7.93	9.18
		1.9kW	32.27	338.5	316.3	9.7	10.6	9.7	0.9	4.40	9.69	-	11.07	-	6.35	9.04
4/12/2021	Full Bundle, Preheater OFF, Increased Charge	0.4kW	6.81	263.8	247.0	2.0	3.4	2.0	1.4	4.14	3.87	2.55	3.86	2.52	3.97	3.48
		0.6kW	10.24	248.2	235.4	0.0	2.1	0.0	2.1	3.90	3.90	1.84	4.08	2.29	4.12	3.43
		0.8kW	13.64	262.6	244.6	-0.2	3.1	-0.2	3.3	4.22	3.30	1.87	3.39	2.20	3.37	2.95
	Preheater ON	0.8kW (2)	13.67	270.6	251.1	1.7	3.9	1.7	2.1	4.28	4.76	2.39	5.01	2.92	4.97	4.22
		0.9kW	15.40	263.1	243.6	1.1	3.0	1.1	2.0	4.30	5.40	2.14	5.74	3.17	5.65	4.69
4/13/2021	Partial Bundle	0.6kW	10.19	247.6	230.2	2.3	1.4	2.1	-0.9	3.90	-2.26	-	-2.59	-	-2.24	-2.36
		0.8kW	13.53	254.4	235.1	1.6	2.0	1.4	0.5	4.21	16.43	-	4.07	-	0.82	7.10
PHASE 1 - R1234ze(E), circular cone nozzles, triangular pitch, Tube-C condenser tubes (Bundle 1)																
5/13/2021	Full Bundle, Preheater ON	0.2kW	3.41	324.5	316.0	8.6	10.5	8.6	1.9	6.80	1.66	1.31	1.63	1.64	1.65	1.58
		0.4kW	6.82	327.6	318.9	8.1	10.8	8.1	2.7	6.83	2.25	1.65	2.20	2.05	2.24	2.08
		0.6kW	10.21	331.1	322.2	8.9	11.1	8.9	2.2	6.85	3.83	2.53	3.67	2.79	3.67	3.30
	Partial Bundle	0.6kW	10.18	318.4	314.7	9.4	10.4	9.4	1.0	6.16	6.86	-	6.52	-	6.36	6.58

Date	Test Condition	Power Setting	Heat Flux [kW/m²]	Pressure [kPa]		Temperature [°C]				Flow Rate [kg/min]	Heat Transfer Coefficient [kW/m²-K]					
				P_{inlet}	P_{box}	T_{inlet}	T_{sat}	T_{ref}	Subcooling		Row 1	Row 2	Row 3	Row 4	Row 5	Overall
PHASE 1 - R1234ze(E), circular cone nozzles, triangular pitch, Tube-C condenser tubes (Bundle 1)																
5/15/2021	Full Bundle, Preheater OFF, Increased Charge	0.2kW	3.41	239.2	229.6	2.7	1.4	2.5	-1.4	5.64	-4.53	-3.52	-1.11	-3.25	-2.10	-2.90
		0.4kW	4.41	246.4	240.8	2.6	2.7	2.6	0.1	6.12	21.36	11.67	16.20	14.93	15.69	16.38
		0.6kW	5.41	250.4	243.7	1.5	3.0	1.5	1.5	6.46	5.20	4.10	4.80	3.05	4.77	4.51
	Preheater ON	0.8kW	6.41	245.8	240.0	1.7	2.6	1.5	0.9	5.44	6.76	8.76	4.16	5.06	3.33	5.41
		0.8kW (2)	7.41	260.6	253.1	1.4	4.1	1.4	2.8	6.60	3.98	3.16	3.86	2.24	3.75	3.51
		1.0kW	8.41	260.7	253.5	1.3	4.1	1.3	2.9	6.57	4.59	3.00	4.39	2.10	4.11	3.80
		1.2kW	9.41	263.2	256.2	2.2	4.5	2.2	2.2	6.55	6.36	3.16	5.96	2.10	5.08	4.82
		1.3kW	10.41	253.1	240.8	0.5	2.7	0.5	2.3	7.18	6.69	3.31	6.26	0.94	5.45	5.23
	Partial Bundle	1.4kW	11.41	247.9	245.7	1.1	3.3	1.1	2.2	5.94	7.20	-	6.18	-	4.48	5.95
		1.6kW	12.41	252.3	247.3	1.0	3.5	1.0	2.5	6.31	7.26	-	6.16	-	4.10	5.84
		1.8kW	13.41	259.1	251.3	1.9	3.9	1.9	2.0	6.66	8.95	-	7.10	-	3.48	6.51
		1.9kW	14.41	251.5	245.4	1.1	3.2	1.1	2.2	6.44	8.60	-	6.41	-	2.29	5.77
5/17/2021	Full Bundle, Preheater ON, Increased Charge	0.6kW	15.41	246.3	242.9	1.5	3.0	1.5	1.4	6.11	5.11	4.14	5.01	3.13	4.96	4.60
		0.8kW	16.41	252.6	247.2	1.2	3.4	1.2	2.3	6.37	4.35	3.28	4.25	2.31	4.24	3.82
		1.0kW	17.41	251.7	245.7	1.3	3.3	1.3	2.0	6.45	5.60	3.36	5.37	2.11	5.26	4.59
		1.2kW	18.41	256.2	249.1	1.9	3.7	1.9	1.7	6.60	7.04	3.41	6.71	1.91	6.04	5.38
		1.4kW	19.41	254.7	248.2	1.8	3.6	1.8	1.8	6.50	7.59	3.17	7.09	-	5.80	6.16
		1.6kW	20.41	255.2	248.5	1.1	3.6	1.1	2.5	6.55	6.82	2.77	6.18	-	4.46	5.26
		1.8kW	21.41	256.6	249.6	1.0	3.7	1.0	2.7	6.61	6.93	2.60	5.95	-	3.10	4.83
	Partial Bundle	1.9kW	22.41	237.6	242.0	0.9	2.9	0.9	1.9	5.04	8.88	-	5.06	-	1.18	5.04
5/24/2021	Preheater OFF	0.2kW	23.41	322.3	316.2	10.5	10.6	10.5	0.1	6.28	11.33	9.57	12.05	13.25	12.45	11.78
	Full Bundle, Preheater ON, Increased Charge	0.4kW	24.41	322.8	317.1	9.8	10.6	9.8	0.8	6.25	5.52	4.79	5.62	4.77	5.70	5.36
		0.6kW	25.41	323.9	318.0	9.8	10.7	9.8	0.9	6.28	6.69	5.14	6.64	3.67	6.71	5.98
		0.8kW	26.41	321.1	315.6	9.7	10.5	9.7	0.8	6.24	8.35	5.00	8.19	3.36	8.11	6.97
		1.0kW	27.41	323.2	317.9	10.0	10.7	10.0	0.8	6.23	9.79	4.48	9.34	2.94	8.54	7.53
		1.2kW	28.41	326.9	321.8	10.4	11.1	10.4	0.6	6.21	11.38	3.87	10.52	2.57	8.35	7.97
		1.4kW	29.41	320.5	315.4	9.9	10.5	9.9	0.6	6.22	12.88	3.39	11.10	-	7.08	9.09
		1.6kW	30.41	321.7	316.9	9.8	10.6	9.8	0.8	6.20	12.15	2.95	9.65	-	5.25	7.91
		1.8kW	31.41	323.1	318.4	9.8	10.8	9.8	0.9	6.19	12.59	2.62	8.98	-	3.15	7.22
5/25/2021	Preheater OFF	0.2kW	32.41	308.9	318.3	10.8	10.8	10.8	0.0	3.92	15.29	12.47	15.26	17.69	14.27	14.98
		0.4kW	33.41	311.1	320.4	10.1	11.0	10.1	0.9	3.94	4.88	4.53	4.46	4.50	4.02	4.47
	Full Bundle, Preheater ON, Increased Charge	0.6kW	34.41	307.6	317.2	10.3	10.6	10.3	0.4	3.92	9.71	7.09	6.21	5.35	4.57	6.64
		0.8kW	35.41	308.0	317.7	10.1	10.7	10.1	0.6	3.91	8.76	5.89	4.80	4.12	3.54	5.49
		1.0kW	36.41	309.2	319.0	10.2	10.8	10.2	0.6	3.90	9.30	4.86	4.44	2.32	2.91	4.95
		1.2kW	37.41	301.9	312.1	9.6	10.2	9.6	0.6	3.85	10.17	4.09	4.47	-	2.57	5.44
		1.4kW	38.41	306.0	316.2	10.5	10.5	10.5	0.1	3.85	13.71	3.41	4.72	-	2.00	6.19
		1.5kW	39.41	303.1	313.4	9.8	10.3	9.8	0.5	3.84	11.18	2.74	4.12	-	1.65	5.12

Date	Test Condition	Power Setting	Heat Flux [kW/m^2]	Pressure [kPa]		Temperature [°C]				Flow Rate [kg/min]	Heat Transfer Coefficient [kW/m^2-K]					
				P_{inlet}	P_{box}	T_{inlet}	T_{sat}	T_{ref}	Subcooling		Row 1	Row 2	Row 3	Row 4	Row 5	Overall
PHASE 1 - R1234ze(E), circular cone nozzles, triangular pitch, Tube-C condenser tubes (Bundle 1)																
5/26/2021	Preheater OFF	0.2kW	3.42	304.2	318.8	11.1	10.8	10.8	-0.3	2.21	7.86	12.80	4.59	14.63	3.56	7.91
		0.4kW	6.83	304.5	320.8	10.4	11.0	10.4	0.6	2.31	1.84	3.45	1.20	2.17	1.05	1.81
	Full Bundle, Preheater ON, Increased Charge	0.6kW	10.22	304.3	320.7	10.2	11.0	10.2	0.8	2.31	1.72	3.22	1.11	1.76	0.89	1.62
		0.8kW	13.62	306.4	322.8	10.5	11.2	10.5	0.7	2.31	1.73	3.25	1.08	1.56	0.80	1.57
		1.0kW	17.06	307.0	323.6	10.6	11.2	10.6	0.6	2.31	1.72	3.10	1.03	0.87	0.71	1.41
	Partial Bundle	1.1kW	18.73	292.7	309.4	9.1	9.9	9.1	0.8	2.27	1.54	-	0.94	-	0.64	1.04
		1.2kW	20.43	297.3	314.0	9.6	10.3	9.6	0.7	2.27	1.57	-	0.92	-	0.53	1.00
5/27/2021	Preheater OFF	0.2kW	3.41	245.9	240.7	2.6	2.7	2.6	0.1	6.26	9.88	8.68	10.60	11.30	10.82	10.30
		0.4kW	6.77	243.3	237.3	1.5	2.3	1.5	0.8	6.39	5.32	4.79	5.51	4.60	5.61	5.24
	Full Bundle, Preheater ON, Increased Charge	0.6kW	10.17	240.1	236.5	2.3	2.2	2.1	-0.1	6.04	-4.89	9.90	18.62	5.60	11.34	8.17
		0.6kW (2)	10.25	245.8	241.2	2.4	2.8	2.4	0.4	6.22	11.45	7.28	10.94	4.35	11.18	9.54
		0.8kW	13.64	248.3	242.8	2.8	2.9	2.7	0.2	6.24	21.49	8.32	6.50	4.76	16.96	12.38
		0.8kW (2)	13.68	251.1	243.9	2.7	3.1	2.7	0.3	6.52	13.11	7.13	12.68	3.54	13.11	10.62
		1.0kW	17.11	248.5	241.8	2.5	2.8	2.5	0.3	6.49	14.05	6.13	13.63	3.15	13.36	10.90
		1.2kW	20.53	257.4	246.1	3.1	3.3	3.1	0.2	7.04	15.56	6.21	15.37	2.97	13.85	11.75
		1.2kW (2)	20.53	257.5	245.9	2.8	3.3	2.8	0.5	7.07	12.63	5.62	12.40	2.78	11.41	9.70
		1.4kW	23.90	256.7	245.2	2.2	3.2	2.2	1.0	7.06	10.16	4.57	9.71	-	8.40	8.54
		1.6kW	27.42	255.6	244.2	2.6	3.1	2.6	0.5	7.07	13.89	4.82	12.67	-	8.15	10.34
		1.8kW	30.82	258.1	246.6	3.0	3.4	3.0	0.4	7.09	15.08	4.46	12.65	-	5.35	9.83
	Partial Bundle	1.9kW	32.55	249.9	246.2	3.6	3.3	3.5	-0.2	6.01	21.31	-	9.79	-	1.55	10.88
		1.9kW (2)	32.54	255.1	249.7	3.5	3.7	3.5	0.2	6.35	17.21	-	11.58	-	1.87	10.22
5/28/2021	Preheater OFF	0.2kW	3.41	232.2	239.4	3.0	2.5	2.5	-0.4	4.27	26.97	15.50	32.32	28.36	25.12	26.23
		0.4kW	6.83	234.4	243.4	2.7	3.0	2.6	0.4	4.03	9.48	7.24	7.70	7.61	6.07	7.65
	Full Bundle, Preheater ON, Increased Charge	0.6kW	10.26	235.9	245.8	2.6	3.3	2.5	0.7	3.97	8.46	5.94	5.73	4.48	4.30	5.87
		0.8kW	13.65	237.9	248.0	2.6	3.5	2.6	0.9	3.99	7.97	4.87	5.07	3.59	3.71	5.17
		1.0kW	17.08	240.3	250.5	2.9	3.8	2.9	0.9	3.99	9.23	3.98	4.93	2.64	3.59	5.11
		1.2kW	20.52	235.1	245.5	2.4	3.3	2.4	0.9	3.96	9.97	3.39	4.68	-	3.12	5.47
		1.4kW	23.83	236.1	246.8	2.8	3.4	2.8	0.6	3.95	11.51	2.87	4.67	-	2.39	5.59
	Partial Bundle	1.6kW	27.15	240.0	250.7	2.9	3.8	2.9	1.0	3.93	9.81	-	3.77	-	1.57	5.05
6/1/2021	Full Bundle, Preheater OFF, Increased Charge	0.2kW	3.39	227.7	242.6	3.2	2.9	2.9	-0.2	2.28	9.08	13.33	5.26	12.71	4.09	8.26
		0.4kW	6.81	227.8	244.4	2.5	3.1	2.5	0.6	2.50	2.12	3.75	1.29	2.77	1.11	2.05
		0.6kW	10.21	232.0	248.2	2.6	3.6	2.6	1.0	2.57	2.14	3.83	1.28	2.53	1.01	2.00
	Preheater ON	0.8kW	13.60	232.3	248.6	2.8	3.6	2.8	0.8	2.59	2.25	4.48	1.29	2.32	0.95	2.08
		1.0kW	16.97	234.8	251.2	3.2	3.9	3.2	0.6	2.60	2.27	4.59	1.24	1.37	0.86	1.93
		1.2kW	20.38	225.9	242.5	2.3	2.9	2.3	0.6	2.59	2.19	4.48	1.17	-	0.69	1.92
	Partial Bundle	1.4kW	23.70	230.0	246.4	2.4	3.3	2.4	1.0	2.58	1.98	-	1.02	-	0.53	1.18

Date	Test Condition	Power Setting	Heat Flux [kW/m²]	Pressure [kPa]		Temperature [°C]				Flow Rate [kg/min]	Heat Transfer Coefficient [kW/m²-K]					
				P_{inlet}	P_{box}	T_{inlet}	T_{sat}	T_{ref}	Subcooling		Row 1	Row 2	Row 3	Row 4	Row 5	Overall
PHASE 1 - R1234ze(E), circular cone nozzles, triangular pitch, Tube-C condenser tubes (Bundle 1)																
6/2/2021	Full Bundle, Preheater OFF, Increased Charge	0.2kW	3.39	143.5	157.1	-7.5	-8.7	-8.7	-1.1	1.99	5.32	10.69	3.51	15.04	2.52	6.58
		0.4kW	6.80	140.2	157.0	-9.0	-8.7	-9.0	0.3	2.35	2.15	4.19	1.31	2.83	1.12	2.13
		0.6kW	10.23	139.9	156.8	-9.4	-8.7	-9.4	0.6	2.63	2.19	4.10	1.36	2.85	1.06	2.13
	Preheater ON	0.8kW	13.62	140.2	156.4	-9.5	-8.8	-9.5	0.7	2.89	2.95	5.73	1.62	3.79	1.18	2.79
		1.0kW	17.06	142.9	158.7	-9.1	-8.4	-9.1	0.7	3.00	3.46	6.92	1.75	3.12	1.20	3.02
		1.2kW	20.48	142.5	158.4	-8.9	-8.5	-8.9	0.5	2.97	3.64	7.72	1.76	-	1.09	3.17
		1.4kW	23.87	147.6	163.1	-8.6	-7.7	-8.6	0.9	3.13	3.91	5.74	1.76	-	0.78	2.80
6/3/2021	Full Bundle, Preheater OFF, Increased Charge	0.2kW	3.40	143.9	158.6	-7.5	-8.4	-8.4	-1.0	1.80	5.63	12.98	3.41	16.05	2.45	7.12
		0.4kW	6.82	143.3	159.2	-8.6	-8.3	-8.6	0.3	2.02	4.73	7.72	2.60	7.49	1.99	4.49
		0.6kW	10.21	143.6	159.4	-9.1	-8.3	-9.1	0.8	2.12	3.79	5.47	2.02	4.59	1.59	3.25
		0.8kW	13.65	140.8	159.3	-9.2	-8.3	-9.2	0.9	2.22	1.15	1.57	0.80	1.02	0.58	0.98
		1.0kW	17.09	138.6	154.6	-9.3	-9.1	-9.3	0.2	2.02	6.11	0.62	3.18	-	1.36	3.02
	Partial Bundle	1.1kW	18.46	143.8	159.8	-8.3	-8.2	-8.3	0.1	2.01	5.75	-	1.72	-	0.61	2.69
6/4/2021	Full Bundle, Preheater OFF, Increased Charge	0.2kW	3.39	94.4	113.6	-16.2	-16.6	-16.6	-0.4	0.70	2.40	3.74	1.10	0.91	0.84	1.72
		0.4kW	6.81	95.7	114.3	-16.1	-16.5	-16.5	-0.4	1.05	2.98	4.32	1.31	0.67	0.94	1.97
		0.6kW	10.20	97.7	114.2	-15.8	-16.5	-16.5	-0.7	1.36	3.30	5.63	1.46	0.16	1.13	2.43
6/6/2021	Full Bundle, Preheater OFF, Increased Charge	0.2kW	3.41	233.6	227.9	2.7	1.2	2.5	-1.5	5.40	-3.72	-2.99	-4.22	-2.74	-1.59	-3.05
		0.2kW (2)	3.43	225.8	236.6	2.1	2.2	2.1	0.1	3.95	10.33	8.98	10.08	12.20	9.28	10.11
		0.4kW	6.80	240.0	237.5	2.0	2.3	2.0	0.3	6.02	10.59	7.77	10.08	7.95	10.63	9.64
		0.4kW (2)	6.83	228.2	231.6	2.1	1.6	1.8	-0.5	3.61	3.02	-4.01	2.18	1.55	3.65	1.66
6/7/2021	Full Bundle, Preheater OFF, Increased Charge	0.2kW	3.41	93.3	116.3	-15.7	-16.0	-16.0	-0.4	0.71	2.55	3.72	1.17	0.89	0.87	1.77
		0.4kW	6.82	102.1	120.7	-14.9	-15.2	-15.2	-0.3	1.01	3.00	4.56	1.41	0.73	1.04	2.07
		0.6kW	10.24	104.2	122.2	-14.6	-14.9	-14.9	-0.3	1.20	2.86	3.22	1.55	-	1.16	2.11
	Partial Bundle	0.7kW	11.85	102.7	120.6	-14.8	-15.2	-15.2	-0.4	1.21	2.89	-	1.56	-	1.03	1.82
PHASE 1 - R134a, circular cone nozzles, triangular pitch, Tube-C condenser tubes (Bundle 1)																
7/1/2021	Single Tube Flooded Tests	16%	1.06	321.2	312.3	1.7	1.8	1.2	0.1	1.25	-	-	-	-	0.44	0.44
		34%	4.80	324.8	316.4	2.0	2.2	1.6	0.2	1.22	-	-	-	-	2.16	2.16
		50%	10.39	321.4	321.6	2.3	2.6	2.1	0.3	1.21	-	-	-	-	4.99	4.99
		68%	18.84	326.4	317.2	2.0	2.2	1.8	0.2	1.09	-	-	-	-	7.80	7.80
		84%	27.49	319.5	309.7	1.4	1.5	1.3	0.2	0.98	-	-	-	-	10.46	10.46
		100%	38.29	320.6	311.0	1.5	1.7	1.4	0.2	0.96	-	-	-	-	12.67	12.67
7/2/2021	Single Tube Flooded Tests	16%	1.06	245.7	237.8	-6.4	-5.6	-5.6	0.7	1.01	-	-	-	-	0.58	0.58
		34%	4.80	243.6	236.0	-6.6	-5.8	-5.8	0.7	0.82	-	-	-	-	2.08	2.08
		50%	10.39	248.0	240.7	-6.1	-5.3	-5.3	0.8	0.79	-	-	-	-	5.46	5.46
		64%	15.97	249.9	242.2	-6.0	-5.1	-5.1	0.9	0.73	-	-	-	-	7.78	7.78
		84%	27.49	256.6	245.4	-5.2	-4.8	-4.8	0.4	1.23	-	-	-	-	11.66	11.66
		100%	38.29	261.6	250.9	-4.7	-4.2	-4.2	0.5	1.19	-	-	-	-	14.14	14.14

Date	Test Condition	Power Setting	Heat Flux [kW/m²]	Pressure [kPa]		Temperature [°C]				Flow Rate [kg/min]	Heat Transfer Coefficient [kW/m²-K]					
				P_{inlet}	P_{box}	T_{inlet}	T_{sat}	T_{ref}	Subcooling		Row 1	Row 2	Row 3	Row 4	Row 5	Overall
PHASE 1 - R134a, circular cone nozzles, triangular pitch, Tube-C condenser tubes (Bundle 1)																
7/20/2021	Bottom Row (Three Tubes) Pool Boiling Series	0.2kW	3.39	397.2	397.3	8.4	8.7	8.7	0.3	1.22	-	-	-	-	3.47	3.47
		0.4kW	6.79	414.4	415.5	9.8	10.0	10.0	0.3	1.12	-	-	-	-	5.33	5.33
		0.6kW	10.15	393.8	406.7	8.8	9.4	9.4	0.6	1.72	-	-	-	-	6.71	6.71
		0.8kW	13.63	407.6	405.7	9.0	9.3	9.3	0.4	1.50	-	-	-	-	7.75	7.75
		1.0kW	16.95	413.2	411.4	9.3	9.7	9.7	0.4	1.51	-	-	-	-	8.63	8.63
		1.2kW	20.38	408.5	406.3	8.9	9.4	9.4	0.4	1.54	-	-	-	-	9.39	9.39
		1.4kW	23.75	414.0	412.2	9.3	9.8	9.8	0.5	1.53	-	-	-	-	10.18	10.18
		1.6kW	27.10	417.5	415.9	9.5	10.1	10.1	0.5	1.55	-	-	-	-	10.82	10.82
		1.8kW	30.70	415.5	414.1	9.4	9.9	9.9	0.5	1.51	-	-	-	-	11.62	11.62
		2.0kW	34.10	413.3	411.5	9.2	9.7	9.7	0.6	1.57	-	-	-	-	12.32	12.32
		2.2kW	37.44	416.4	414.6	9.4	10.0	10.0	0.6	1.57	-	-	-	-	12.90	12.90
7/21/2021	Bottom Row (Three Tubes) Pool Boiling Series	0.2kW	3.38	323.3	323.7	2.5	2.8	2.8	0.3	1.31	-	-	-	-	3.00	3.00
		0.4kW	6.80	328.7	325.3	2.6	2.9	2.9	0.3	1.21	-	-	-	-	4.80	4.80
		0.6kW	10.15	331.1	321.5	2.4	2.6	2.6	0.2	1.10	-	-	-	-	5.98	5.98
		0.8kW	13.55	333.8	324.2	2.6	2.8	2.8	0.3	1.12	-	-	-	-	7.17	7.17
		1.0kW	16.93	329.6	319.7	2.2	2.4	2.4	0.2	1.10	-	-	-	-	8.13	8.13
		1.2kW	20.28	330.7	320.7	2.3	2.5	2.5	0.2	1.09	-	-	-	-	9.07	9.07
		1.4kW	23.79	329.6	319.7	2.2	2.4	2.4	0.3	1.02	-	-	-	-	9.96	9.96
		1.6kW	27.30	331.6	321.7	2.3	2.6	2.6	0.3	1.08	-	-	-	-	10.76	10.76
		1.8kW	30.76	330.4	320.0	2.1	2.5	2.5	0.3	1.09	-	-	-	-	11.38	11.38
		2.0kW	34.05	332.8	322.5	2.3	2.7	2.7	0.4	1.18	-	-	-	-	11.98	11.98
		2.2kW	37.59	334.5	324.0	2.4	2.8	2.8	0.4	1.21	-	-	-	-	12.57	12.57
10/1/2021	Full Bundle, Preheater ON, Normal Charge, Unstable Flow	0.2kW	3.40	451.1	416.6	9.3	10.1	9.3	0.8	3.85	17.76	5.87	2.99	9.23	1.87	7.54
		0.4kW	6.82	466.0	425.5	9.7	10.7	9.7	1.0	4.89	4.86	5.91	1.62	4.01	1.13	3.28
		0.6kW	10.23	464.4	424.2	9.8	10.7	9.8	0.9	4.77	4.88	6.02	1.19	2.92	0.78	2.96
		0.6kW (2)	10.28	461.7	420.1	9.9	10.4	9.9	0.5	4.79	5.43	7.44	1.16	2.69	0.75	3.25
		0.8kW	13.59	458.4	415.4	9.9	10.0	9.9	0.1	4.64	3.77	7.49	0.87	1.40	0.58	2.57
		1.0kW	17.09	452.6	412.5	9.4	9.8	9.4	0.4	4.15	2.55	4.75	0.74	0.91	0.51	1.75
	Partial Bundle	1.2kW	20.37	448.3	407.2	9.2	9.4	9.2	0.2	4.61	2.34	-	0.66	-	0.48	1.16
10/2/2021	Full Bundle, Preheater ON, Slightly Increased Charge, Unstable Flow	0.2kW	3.40	476.5	442.2	11.2	11.9	11.2	0.7	4.78	38.01	12.91	3.30	7.48	2.36	13.22
		0.4kW	6.83	480.9	452.8	11.5	12.6	11.5	1.1	3.76	4.09	5.35	1.37	2.93	0.99	2.76
		0.4kW (2)	6.87	482.2	451.6	11.5	12.6	11.5	1.1	4.07	4.18	5.46	1.45	3.20	1.05	2.87
		0.6kW	10.24	466.9	433.2	10.3	11.3	10.3	1.0	4.21	3.63	5.05	1.11	2.37	0.75	2.41
		0.8kW	13.68	473.2	438.8	10.6	11.7	10.6	1.0	4.55	3.25	5.00	0.92	1.81	0.62	2.15
		1.0kW	17.10	474.8	438.8	10.9	11.7	10.9	0.8	4.67	2.72	4.67	0.76	1.17	0.53	1.82

Date	Test Condition	Power Setting	Heat Flux [kW/m^2]	Pressure [kPa] P_{inlet}	Pressure [kPa] P_{box}	Temperature [°C] T_{inlet}	Temperature [°C] T_{sat}	Temperature [°C] T_{ref}	Temperature [°C] Subcooling	Flow Rate [kg/min]	Heat Transfer Coefficient [kW/m^2-K] Row 1	Row 2	Row 3	Row 4	Row 5	Overall
PHASE 1 - R134a, circular cone nozzles, triangular bundle, condenser tubes (Bundle 1)																
10/4/2021	Full Bundle, Preheater ON, Increased Charge, Unsteady Flow	0.2kW	3.41	342.2	319.6	2.1	2.4	2.1	0.3	3.05	22.81	36.88	3.71	6.52	2.42	13.36
		0.4kW	6.80	346.9	322.0	1.8	2.6	1.8	0.8	3.39	6.34	7.82	1.71	4.21	1.26	4.00
		0.6kW	10.23	350.1	323.2	2.0	2.7	2.0	0.8	3.52	5.56	6.79	1.31	2.80	0.94	3.28
		0.8kW	12.34	346.5	329.0	1.7	3.2	1.7	1.5	3.77	4.81	5.32	1.29	3.30	0.91	2.94
		0.8kW (2)	13.70	342.6	322.5	1.0	2.6	1.0	1.6	3.84	4.45	5.29	1.30	1.93	0.92	2.65
		0.8kW (3)	13.72	340.2	308.9	0.5	1.5	0.5	1.0	3.80	4.64	5.64	1.11	1.68	0.77	2.63
		1.0kW	17.09	345.6	313.8	1.3	1.9	1.3	0.6	3.91	3.89	5.82	0.93	0.99	0.63	2.31
		1.2kW	20.50	353.6	321.4	1.3	2.6	1.3	1.3	4.12	3.55	4.85	0.87	0.78	0.57	2.02
		1.4kW	23.91	353.2	321.3	0.5	2.6	0.5	2.1	4.39	3.73	4.13	0.87	0.68	0.51	1.92
10/5/2021	Full Bundle, Preheater ON, Increased Charge	0.2kW	3.41	328.2	304.7	0.2	1.1	0.2	0.9	3.09	10.14	11.00	2.75	4.61	2.01	5.84
		0.2kW (2)	3.41	339.3	313.4	1.1	1.9	1.1	0.8	3.10	8.83	6.06	2.80	5.39	1.94	4.89
		0.4kW	6.82	346.4	315.2	1.6	2.0	1.6	0.4	3.33	7.91	9.79	1.59	3.83	1.15	4.55
		0.6kW	10.18	343.9	311.1	1.0	1.7	1.0	0.7	3.55	5.45	6.90	1.24	2.16	0.91	3.15
		0.8kW	13.65	348.7	317.4	1.3	2.2	1.3	0.9	3.83	5.06	6.09	1.12	1.62	0.79	2.80
		1.0kW	17.01	360.0	325.9	2.4	3.0	2.4	0.6	3.96	3.82	6.13	0.93	0.94	0.62	2.33
		1.2kW	20.34	357.6	322.0	1.3	2.6	1.3	1.3	4.35	3.89	5.09	0.87	0.86	0.57	2.15
		1.4kW	23.95	351.9	318.9	0.1	2.4	0.1	2.2	4.55	4.07	4.25	0.88	0.75	0.53	2.04
10/6/2021	Full Bundle, Preheater ON, Increased Charge, Unsteady Flow	0.2kW	3.41	258.6	231.3	-6.4	-6.4	-6.5	0.1	3.21	-20.61	50.72	6.68	30.72	3.30	10.07
		0.4kW	6.83	255.5	229.5	-7.1	-6.6	-7.1	0.6	3.41	8.75	9.45	2.10	5.68	1.38	5.15
		0.6kW	10.23	257.2	231.4	-7.6	-6.3	-7.6	1.3	3.58	5.23	4.99	1.57	3.22	1.10	3.08
		0.8kW	13.70	263.7	234.9	-6.5	-5.9	-6.5	0.6	3.84	6.23	7.17	1.30	2.04	0.90	3.36
		1.0kW	17.12	265.5	235.5	-6.6	-5.9	-6.6	0.7	4.06	5.03	6.09	1.12	1.28	0.75	2.72
	Normal Charge	1.2kW	20.57	261.5	235.1	-6.7	-5.9	-6.7	0.8	3.40	4.18	4.92	0.97	0.51	0.55	2.15
	Partial Bundle	1.4kW	23.93	256.1	227.9	-7.0	-6.7	-7.0	0.2	3.41	3.34	-	0.82	-	0.41	1.52
10/7/2021	Full Bundle, Preheater ON, Normal Charge	0.2kW	3.41	442.4	415.0	9.9	10.0	9.9	0.1	3.11	9.91	-2.60	2.66	8.46	1.73	3.85
		0.4kW	6.80	436.7	413.0	9.1	9.9	9.1	0.7	3.12	4.59	4.93	1.42	4.17	1.09	2.95
		0.6kW	10.23	438.2	414.9	9.1	10.0	9.1	0.9	3.11	4.06	4.49	1.18	2.47	0.88	2.48
		0.6kW (2)	10.26	448.1	416.7	9.4	10.1	9.4	0.7	3.59	3.88	4.64	1.11	2.26	0.80	2.41
		0.8kW	13.65	449.4	416.7	9.4	10.1	9.4	0.7	3.78	3.39	4.55	0.96	1.55	0.64	2.13
		0.8kW (2)	13.68	440.3	416.4	9.4	10.1	9.4	0.7	3.09	3.14	4.28	0.96	1.18	0.68	2.01
		1.0kW	17.09	443.8	419.0	9.8	10.3	9.8	0.5	3.05	2.50	3.05	0.80	0.74	0.54	1.53
	Partial Bundle	1.2kW	20.52	447.6	419.6	10.1	10.3	10.1	0.2	3.21	2.02	-	0.68	-	0.47	1.05
PHASE 1 - R1234ze(E), circular cone nozzles, triangular pitch, Tube-C condenser tubes (Bundle 1)																
11/5/2021	Full Bundle, Preheater ON, Normal Charge	0.2kW	3.41	314.2	316.6	9.8	10.6	9.8	0.8	5.26	3.31	3.05	3.36	3.06	3.39	3.28
		0.4kW	6.81	315.4	312.5	10.9	10.2	10.8	-0.6	5.34	-7.61	38.74	15.16	83.01	16.29	19.33
		0.6kW	10.22	308.6	309.5	10.0	9.9	9.9	-0.1	5.21	13.44	4.73	12.99	1.19	10.40	10.09
		0.8kW	13.62	311.7	313.6	9.8	10.3	9.8	0.5	5.28	8.79	2.98	8.11	0.83	4.69	5.96
		1.0kW	17.05	313.2	314.9	9.8	10.4	9.8	0.6	5.34	9.76	2.22	7.69	0.40	2.49	5.39
	Partial Bundle	1.2kW	20.46	314.2	315.4	10.0	10.5	10.0	0.5	5.40	11.11	-	5.64	-	0.99	5.92

Date	Test Condition	Power Setting	Heat Flux [kW/m²]	Pressure [kPa]		Temperature [°C]				Flow Rate [kg/min]	Heat Transfer Coefficient [kW/m²-K]					
				P_{inlet}	P_{box}	T_{inlet}	T_{sat}	T_{ref}	Subcooling		Row 1	Row 2	Row 3	Row 4	Row 5	Overall
PHASE 1 - R1234ze(E), circular cone nozzles, triangular pitch, Tube-C condenser tubes (Bundle 1)																
11/8/2021	Full Bundle, Preheater ON, Normal Charge	0.2kW	3.41	292.4	304.8	9.2	9.5	9.2	0.2	3.36	7.55	6.58	5.93	6.47	4.68	6.18
		0.2kW (2)	3.40	291.6	304.5	9.0	9.4	9.0	0.4	3.39	4.38	4.57	3.28	4.76	2.48	3.69
		0.4kW	6.80	301.8	314.5	10.0	10.4	10.0	0.4	3.37	6.43	6.29	3.75	4.14	2.31	4.52
	Preheater OFF	0.6kW	10.24	311.7	320.2	10.5	10.9	10.5	0.5	3.66	7.50	6.04	3.88	1.59	2.03	4.49
		0.8kW	13.64	310.2	317.2	9.6	10.6	9.6	1.1	4.46	6.52	3.44	4.50	0.66	2.40	3.98
	Partial Bundle	1.0kW	16.95	305.0	311.3	9.6	10.1	9.6	0.5	4.48	10.46	-	4.74	-	2.07	5.76
11/9/2021	Full Bundle, Preheater ON, Normal Charge	0.2kW	3.40	242.6	243.4	2.6	3.0	2.6	0.4	5.56	5.54	4.64	5.61	4.60	5.68	5.37
		0.4kW	6.79	215.9	210.7	0.2	-1.0	0.1	-1.2	5.18	-6.61	-21.92	2.99	-13.98	7.71	-3.79
11/10/2021	Full Bundle, Preheater OFF, Normal Charge	0.4kW	6.76	239.2	237.4	2.8	2.3	2.8	-0.5	5.47	14.43	24.85	137.67	49.10	23.87	52.23
		0.6kW	10.18	236.0	237.0	2.1	2.3	2.1	0.2	5.46	10.07	4.98	10.32	1.11	9.70	8.45
		0.6kW (2)	10.24	234.1	237.5	2.3	2.3	2.3	0.0	4.75	14.13	6.02	12.36	1.18	8.98	9.97
		0.6kW (3)	10.23	248.0	248.6	3.8	3.6	3.6	-0.2	5.12	14.33	7.12	12.05	1.59	8.48	10.03
	Preheater ON	0.8kW	13.60	237.8	239.2	1.9	2.5	1.9	0.7	5.43	7.93	3.29	7.81	0.78	6.28	6.12
	Preheater OFF	0.8kW (2)	13.68	229.8	236.2	1.6	2.2	1.6	0.6	4.64	8.85	3.16	7.90	0.54	5.30	6.08
		0.8kW (3)	13.65	244.6	248.3	3.0	3.6	3.0	0.6	5.08	8.80	3.11	8.19	0.71	5.74	6.26
	Preheater ON	1.0kW	17.06	237.9	238.8	1.8	2.5	1.8	0.7	5.50	8.61	2.53	7.68	0.36	3.02	5.28
	Partial Bundle	1.2kW	20.36	234.7	234.9	1.6	2.0	1.6	0.4	5.59	11.35	-	6.33	-	1.28	6.32
11/11/2021	Full Bundle, Preheater OFF, Normal Charge	0.2kW	3.38	165.6	156.2	-6.2	-8.8	-6.5	-2.6	4.28	-2.24	-1.68	-2.66	-1.55	2.31	-1.14
		0.4kW	6.79	160.4	159.9	-7.4	-8.2	-7.6	-0.9	5.04	-3.21	29.95	20.58	-15.50	6.37	9.64
		0.4kW (2)	6.98	160.7	160.2	-7.4	-8.2	-7.5	-0.8	5.08	-27.33	2.76	26.19	-26.64	8.42	0.06
		0.6kW	10.20	154.2	157.4	-9.3	-8.6	-9.3	0.7	5.35	6.88	3.97	6.99	1.04	6.81	5.92
		0.6kW (2)	10.19	151.5	159.0	-9.0	-8.4	-9.0	0.7	4.52	7.25	3.82	6.74	0.93	5.99	5.71
		0.8kW	13.62	154.4	157.9	-9.5	-8.6	-9.5	0.9	5.30	7.06	3.18	6.74	0.74	5.70	5.47
	Preheater ON	0.8kW (2)	13.67	160.1	162.0	-8.8	-7.9	-8.8	0.9	5.53	7.14	3.44	6.89	0.78	5.88	5.61
		1.0kW	17.08	159.4	161.7	-9.0	-7.9	-9.0	1.1	5.51	7.37	2.69	6.64	0.37	3.86	4.95
	Partial Bundle	1.2kW	20.42	154.6	157.0	-9.4	-8.7	-9.4	0.7	5.50	9.73	-	7.00	-	2.01	6.25
11/12/2021	Full Bundle, Preheater OFF	1.0kW	17.00	242.2	242.5	0.4	2.9	0.4	2.5	5.67	4.53	2.16	4.31	0.52	2.46	3.23
	Preheater ON	1.0kW (2)	17.08	245.3	245.4	2.7	3.2	2.7	0.5	5.65	9.83	2.92	8.20	0.45	2.93	5.76
		1.0kW (3)	16.98	242.1	237.0	1.7	2.3	1.7	0.5	6.36	9.56	3.60	8.49	0.69	2.88	5.89
11/20/2021	Full Bundle, Preheater ON, Normal Charge	0.6kW	10.21	306.6	307.9	9.9	9.8	9.8	-0.1	5.16	13.57	5.41	11.35	1.26	7.65	9.15
		0.6kW (2)	10.25	305.6	308.0	9.4	9.8	9.4	0.4	5.16	8.89	4.57	7.97	1.24	6.07	6.60
11/21/2021		0.6kW (3)	10.20	310.7	310.0	10.0	10.0	9.9	0.0	5.54	14.28	5.56	12.39	1.28	9.19	10.00
11/22/2021		0.6kW (4)	10.17	319.0	321.3	10.6	11.0	10.6	0.5	5.22	8.83	4.68	7.92	1.26	5.88	6.54
		0.8kW	13.59	321.9	324.5	10.7	11.3	10.7	0.6	5.20	8.56	3.32	7.10	0.86	3.73	5.47
		0.8kW (2)	13.67	309.4	312.0	9.8	10.2	9.8	0.3	5.22	10.86	3.49	8.75	0.84	4.09	6.58
		0.8kW (3)	13.65	310.3	311.1	9.7	10.1	9.7	0.4	5.48	10.40	3.42	8.63	0.92	4.04	6.41
		1.0kW	17.04	323.5	326.1	11.0	11.5	11.0	0.5	5.20	10.31	2.46	6.65	0.46	2.34	5.27
		1.0kW (2)	17.06	312.9	311.8	10.0	10.1	10.0	0.2	5.71	13.07	2.77	8.31	0.55	2.09	6.38

Date	Test Condition	Power Setting	Heat Flux [kW/m^2]	Pressure [kPa] P_{inlet}	Pressure [kPa] P_{box}	Temperature [°C] T_{inlet}	Temperature [°C] T_{sat}	Temperature [°C] T_{ref}	Temperature [°C] Subcooling	Flow Rate [kg/min]	Heat Transfer Coefficient [kW/m^2-K] Row 1	Row 2	Row 3	Row 4	Row 5	Overall
PHASE 1 - R1234ze(E), circular cone nozzles, triangular pitch, Tube-C condenser tubes (Bundle 1)																
11/29/2021	Full Bundle, Preheater ON, Increased Charge	0.6kW	10.25	155.0	156.6	-9.2	-8.8	-9.2	0.5	5.29	7.88	4.15	8.13	1.02	7.38	6.63
		0.6kW (2)	10.24	154.1	158.1	-9.1	-8.5	-9.1	0.6	4.95	7.28	3.67	7.37	0.93	6.55	5.99
		0.6kW (3)	10.22	155.7	156.3	-9.3	-8.8	-9.3	0.5	5.45	7.84	4.31	8.11	1.09	7.47	6.66
		0.6kW (4)	10.20	161.1	161.8	-8.6	-7.9	-8.6	0.6	5.48	7.09	4.04	7.27	1.19	6.69	6.04
		0.8kW	13.61	164.9	166.7	-7.7	-7.2	-7.7	0.6	5.32	8.34	3.25	8.24	0.72	6.46	6.36
		0.8kW (2)	13.58	154.5	156.2	-9.4	-8.8	-9.4	0.5	5.33	8.32	3.29	8.16	0.71	6.36	6.32
		0.8kW (3)	13.59	154.0	156.9	-9.2	-8.7	-9.2	0.5	5.14	8.55	3.11	8.33	0.60	6.22	6.34
		0.8kW (4)	13.64	157.1	156.5	-9.3	-8.8	-9.3	0.6	5.67	8.04	3.60	8.05	0.86	6.71	6.37
PHASE 1 - R1233zd(E), circular cone nozzles, triangular pitch, Tube-C condenser tubes (Bundle 1)																
1/19/2022	Full Bundle, Preheater ON, Normal Charge	0.2kW	3.40	80.3	73.7	9.3	9.2	9.2	-0.1	1.48	11.48	6.11	3.62	3.34	2.19	5.62
		0.4kW	6.78	78.9	73.7	8.9	9.2	9.2	0.3	1.53	6.41	2.60	2.05	0.40	1.05	2.84
		0.6kW	10.19	78.6	74.1	9.4	9.4	9.4	0.0	1.56	4.74	1.11	1.25	0.23	0.37	1.80
	Partial Bundle	0.8kW	13.46	75.6	74.4	9.3	9.4	9.4	0.1	1.57	4.05	-	0.66	-	0.30	1.67
1/20/2022	Full Bundle, Preheater ON, Increased Charge	0.2kW	3.39	68.3	76.1	10.5	9.8	9.8	-0.7	3.12	6.32	6.99	2.84	8.11	2.05	4.64
		0.4kW	6.80	70.7	80.3	10.9	11.3	11.3	0.3	3.07	5.82	6.55	2.26	7.32	1.61	4.12
		0.6kW	10.22	78.5	81.8	9.4	11.8	11.8	2.4	3.18	6.39	6.02	1.91	4.10	1.31	3.75
		0.8kW	13.65	86.1	88.4	7.2	13.7	13.7	6.5	3.39	7.71	5.35	2.52	1.41	1.70	3.99
		0.8kW (2)	13.61	89.5	89.7	4.2	14.0	14.0	9.8	4.03	8.94	5.26	3.60	1.89	2.37	4.76
		1.0kW	16.93	90.5	102.6	5.5	17.6	17.6	12.1	3.40	9.06	2.66	3.56	0.46	1.30	3.96
1/28/2022	Full Bundle, Preheater ON, Increased Charge	0.2kW	3.39	99.9	88.8	11.4	13.4	13.4	2.0	2.04	9.59	5.39	4.00	4.26	2.70	5.25
		0.4kW	6.79	104.1	91.7	13.1	14.5	14.5	1.4	1.86	8.61	4.55	2.48	0.76	1.40	3.70
		0.6kW	10.16	108.3	91.4	6.5	14.3	14.3	7.7	2.66	9.16	4.94	3.21	0.96	1.88	4.19
		0.7kW	11.88	113.4	95.9	6.9	15.6	15.6	8.6	2.79	8.95	4.80	3.11	0.82	1.83	4.07
		0.8kW	13.62	112.6	95.5	7.3	15.4	15.4	8.1	2.67	8.33	3.78	2.78	0.35	1.55	3.55
	Partial Bundle	0.8kW	13.49	111.2	93.9	7.0	14.9	14.9	7.9	2.76	7.82	-	2.69	-	1.51	4.01
2/4/2022	Full Bundle, Preheater ON, Increased Charge	0.2kW	3.40	97.4	81.2	12.3	11.8	11.8	-0.5	1.53	3.61	4.37	1.37	2.57	0.90	2.41
		0.4kW	6.81	98.1	88.9	14.3	14.4	14.4	0.1	2.19	3.70	4.98	1.09	2.43	0.74	2.41
		0.6kW	10.18	93.5	85.9	14.6	13.6	13.6	-1.0	1.88	2.02	2.27	0.68	0.62	0.41	1.21
		0.8kW	13.54	90.5	82.7	13.7	12.6	12.6	-1.1	1.81	1.56	1.30	0.56	0.42	0.34	0.86
	Partial Bundle	1.0kW	16.88	89.8	80.9	12.2	11.9	11.9	-0.3	2.04	1.78	-	0.56	-	-	1.17
		1.2kW	20.21	93.0	84.7	13.4	13.1	13.1	-0.2	1.92	1.61	-	0.49	-	-	1.05
PHASE 2 - R134a, circular cone nozzles, square pitch, Tube-C condenser tubes (Bundle 2)																
3/7/2022	Full Bundle, Preheater ON, Normal Charge	0.2kW	3.40	354.6	314.6	1.7	2.0	1.7	0.3	4.57	98.01	7.46	4.60	-35.82	-1.59	14.53
		0.4kW	6.78	365.0	319.0	1.8	2.4	1.8	0.5	5.48	5.41	3.82	6.22	4.16	1.40	4.20
		0.6kW	10.24	350.1	311.7	1.4	1.7	1.4	0.4	4.05	3.45	2.12	3.74	1.15	0.67	2.23
		0.6kW (2)	10.24	348.4	320.2	2.2	2.5	2.2	0.3	2.76	2.68	1.49	2.57	0.81	0.56	1.62
		0.8kW	13.62	358.0	322.3	2.7	2.7	2.6	-0.1	3.39	2.14	1.32	2.41	0.69	0.49	1.41
		1.0kW	17.11	358.3	317.9	1.8	2.3	1.8	0.5	4.36	2.25	1.44	2.55	0.73	0.50	1.50

Date	Test Condition	Power Setting	Heat Flux [kW/m²]	Pressure [kPa]		Temperature [°C]				Flow Rate [kg/min]	Heat Transfer Coefficient [kW/m²-K]					
				P_{inlet}	P_{box}	T_{inlet}	T_{sat}	T_{ref}	Subcooling		Row 1	Row 2	Row 3	Row 4	Row 5	Overall
PHASE 2 - R134a, circular cone nozzles, square pitch, Tube-C condenser tubes (Bundle 2)																
3/8/2022	Full Bundle, Preheater ON, Normal Charge	0.2kW	3.41	361.7	314.0	1.8	1.9	1.8	0.1	6.36	-9.22	6.83	39.11	-60.19	480.59	91.42
		0.4kW	6.78	362.7	317.6	1.6	2.3	1.6	0.6	6.20	5.32	3.58	7.08	5.11	1.43	4.50
		0.6kW	10.15	363.7	319.2	1.9	2.4	1.9	0.5	5.89	3.49	2.46	5.54	1.97	0.87	2.87
		0.8kW	13.64	350.5	314.0	1.3	1.9	1.3	0.7	3.99	2.34	1.62	2.82	0.86	0.55	1.64
		0.8kW (2)	13.69	344.0	316.4	1.9	2.2	1.9	0.3	6.04	2.86	2.05	4.79	1.27	0.71	2.34
		1.0kW	16.96	361.4	320.5	1.9	2.5	1.9	0.6	5.63	2.39	1.73	3.25	0.97	0.59	1.78
		1.2kW	20.46	345.3	317.6	1.2	2.3	1.2	1.1	6.13	2.24	1.67	2.79	0.93	0.56	1.64
3/14/2022	Full Bundle, Preheater ON, Normal Charge	0.2kW	3.39	448.8	418.2	9.7	10.2	9.7	0.5	5.85	14.57	8.84	22.65	12.40	6.61	13.01
		0.4kW	6.82	454.0	422.0	10.0	10.5	10.0	0.5	6.18	5.91	3.86	6.79	5.88	1.64	4.82
		0.6kW	10.22	440.6	416.6	9.5	10.1	9.5	0.6	6.01	4.10	2.74	4.51	2.19	1.01	2.91
		0.8kW	13.61	439.9	418.1	9.9	10.2	9.9	0.4	5.64	2.56	1.84	4.51	1.16	0.67	2.15
		0.8kW (2)	13.69	452.0	417.2	10.1	10.2	10.1	0.1	6.14	1.99	1.44	3.98	0.99	0.63	1.80
		1.0kW	17.11	450.0	418.6	9.6	10.3	9.6	0.7	6.29	1.98	1.51	2.98	0.99	0.59	1.61
3/15/2022	Full Bundle, Preheater ON, Normal Charge	0.2kW	3.40	348.5	322.5	2.2	2.7	2.2	0.4	6.25	8.80	38.48	-25.80	-81.23	9.94	-9.96
		0.2kW (2)	3.39	344.4	324.1	1.9	2.8	1.9	0.9	5.98	6.81	4.64	7.13	7.55	4.03	6.03
		0.2kW (3)	3.40	341.0	321.6	1.5	2.6	1.5	1.1	6.00	4.95	3.79	4.97	5.34	3.36	4.48
		0.4kW	6.81	349.0	317.4	1.0	2.2	1.0	1.3	6.04	4.01	3.23	4.22	4.27	1.65	3.48
		0.6kW	10.24	347.7	319.5	0.9	2.4	0.9	1.5	6.04	3.45	2.44	3.41	2.35	0.99	2.53
		0.8kW	13.67	342.4	319.0	0.6	2.4	0.6	1.8	6.10	3.17	2.19	3.25	1.58	0.80	2.20
		1.0kW	17.02	346.2	321.5	0.5	2.6	0.5	2.1	6.18	2.86	2.00	2.91	1.27	0.71	1.95
		1.2kW	20.48	347.3	320.7	0.6	2.5	0.6	2.0	6.08	2.46	1.77	2.79	1.03	0.59	1.73
PHASE 2 - R1234ze(E), circular cone nozzles, square pitch, Tube-C condenser tubes (Bundle 2)																
3/25/2022	Full Bundle, Preheater ON, Normal Charge	0.2kW	3.40	316.7	312.0	9.3	10.2	9.3	0.8	6.03	3.94	3.56	3.49	3.60	3.27	3.57
		0.4kW	6.82	311.8	306.3	9.1	9.6	9.1	0.5	6.12	9.12	7.58	6.63	6.25	4.54	6.82
		0.6kW	10.26	302.6	280.9	8.9	7.1	7.1	-1.8	6.37	2.28	1.78	3.48	1.39	0.70	1.92
3/29/2022	Full Bundle, Preheater ON, Normal Charge	0.2kW	3.42	327.0	314.9	11.3	10.4	10.4	-0.8	6.21	106.47	11.74	15.74	14.69	6.83	31.09
		0.4kW	6.80	314.2	309.4	9.7	9.9	9.7	0.2	5.73	14.40	9.52	8.15	7.18	4.30	8.71
		0.6kW	10.24	311.5	310.4	9.3	10.0	9.3	0.8	5.42	7.68	6.26	4.99	4.20	2.33	5.09
		0.8kW	13.64	318.7	318.5	9.6	10.8	9.6	1.2	5.42	6.57	5.17	3.70	2.90	1.68	4.00
		0.8kW (2)	13.65	314.4	310.2	9.7	10.0	9.7	0.3	5.72	12.06	7.40	5.17	4.09	2.09	6.16
		1.0kW	17.09	317.4	314.7	9.7	10.4	9.7	0.7	5.69	9.38	5.67	3.34	2.61	1.29	4.46
		1.1kW	18.84	316.5	312.3	9.9	10.2	9.9	0.3	5.73	12.60	6.29	3.70	2.86	1.19	5.33
3/30/2022	Full Bundle, Preheater ON, Normal Charge	0.2kW	3.41	314.4	311.6	9.7	10.1	9.7	0.4	5.72	7.95	5.96	5.94	6.09	5.19	6.23
		0.2kW (2)	3.40	313.5	310.8	9.4	10.0	9.4	0.6	5.71	5.05	4.28	4.25	4.35	3.83	4.35
		0.4kW	6.80	311.6	309.0	9.2	9.9	9.2	0.6	5.62	7.49	6.02	5.47	5.20	3.74	5.58
		0.6kW	10.20	314.0	311.7	8.3	10.1	8.3	1.9	5.68	4.23	3.79	3.24	2.91	1.92	3.22
		0.6kW (2)	10.24	317.1	313.0	9.8	10.3	9.8	0.4	5.72	11.41	8.03	5.78	4.75	2.70	6.53
		0.8kW	13.66	313.0	310.6	8.2	10.0	8.2	1.8	5.72	5.17	4.19	3.13	2.49	1.53	3.30
		1.0kW	17.13	312.9	310.5	8.2	10.0	8.2	1.8	5.72	5.95	4.28	2.75	2.19	1.22	3.28
		1.1kW	18.73	314.1	311.8	8.9	10.1	8.9	1.2	5.71	7.85	4.78	2.84	2.19	1.30	3.97

Date	Test Condition	Power Setting	Heat Flux [kW/m^2]	Pressure [kPa]		Temperature [°C]				Flow Rate [kg/min]	Heat Transfer Coefficient [kW/m^2-K]					
				P_{inlet}	P_{box}	T_{inlet}	T_{sat}	T_{ref}	Subcooling		Row 1	Row 2	Row 3	Row 4	Row 5	Overall
PHASE 2 - R1234ze(E), circular cone nozzles, square pitch, Tube-C condenser tubes (Bundle 2)																
4/6/2022	Full Bundle, Preheater ON, Normal Charge	0.2kW	3.40	317.6	312.5	10.6	10.2	10.2	-0.4	4.16	235.85	15.29	21.01	14.85	6.09	58.62
		0.4kW	6.82	308.8	308.2	10.0	9.8	10.0	-0.2	4.00	25.16	10.53	12.42	7.23	2.91	11.65
		0.4kW (2)	6.81	312.6	311.2	10.1	10.1	10.1	0.0	4.21	18.03	9.38	9.95	6.49	3.08	9.38
		0.6kW	10.25	307.6	311.3	9.3	10.1	9.3	0.8	4.19	7.60	5.49	4.90	4.00	2.40	4.88
4/7/2022		0.8kW (2)	13.61	316.5	313.2	10.1	10.3	10.1	0.2	4.17	13.20	11.42	7.47	5.08	1.35	7.70
		1.0kW (2)	17.08	320.5	318.2	10.1	10.7	10.1	0.7	4.16	10.37	8.73	5.46	4.40	1.02	6.00
4/12/2022	Full Bundle, Preheater ON, Normal Charge	0.2kW	3.40	234.6	235.8	0.5	2.1	0.5	1.6	4.26	1.99	1.97	1.85	1.93	1.82	1.91
		0.2kW (2)	3.40	236.4	237.7	1.4	2.3	1.4	1.0	4.24	3.11	3.06	2.78	2.98	2.72	2.93
		0.2kW (3)	3.40	237.1	237.8	2.0	2.4	2.0	0.3	4.29	7.48	7.22	5.78	7.17	5.50	6.63
		0.2kW (4)	3.40	231.0	237.7	1.8	2.3	1.8	0.5	3.48	5.46	5.35	4.53	5.23	4.27	4.97
		0.4kW	6.79	238.9	238.1	2.0	2.4	2.0	0.4	4.23	10.24	9.74	7.56	10.09	6.14	8.75
		0.4kW (2)	6.78	236.5	237.0	1.3	2.3	1.3	0.9	4.24	5.53	5.37	4.62	5.24	4.30	5.01
		0.4kW (3)	6.81	235.7	236.6	1.0	2.2	1.0	1.2	4.25	4.54	4.50	3.94	4.38	3.73	4.22
		0.4kW (4)	6.80	232.3	236.3	1.7	2.2	1.7	0.4	3.48	8.14	7.89	6.60	8.21	4.05	6.98
4/13/2022		0.6kW	10.24	239.8	238.1	2.1	2.4	2.1	0.3	4.22	12.28	12.46	9.63	11.17	3.55	9.82
		0.6kW (2)	10.24	237.0	237.3	1.3	2.3	1.3	1.0	4.25	6.73	6.77	5.80	6.50	3.85	5.93
		0.6kW (3)	10.24	236.1	237.4	0.6	2.3	0.6	1.7	4.26	4.64	4.64	4.13	4.43	3.12	4.19
		0.6kW (4)	10.23	233.5	237.3	1.8	2.3	1.8	0.5	3.48	9.19	8.82	7.14	7.00	1.68	6.77
		0.8kW	13.62	238.5	239.2	1.0	2.5	1.0	1.5	4.28	6.29	6.29	5.04	5.46	2.94	5.21
		0.8kW (2)	13.66	238.9	238.4	1.5	2.4	1.5	1.0	4.24	8.31	8.39	6.71	7.49	3.22	6.83
		0.8kW (3)	13.69	240.9	238.2	2.2	2.4	2.2	0.2	4.21	11.53	12.18	8.75	6.11	1.58	8.03
		0.8kW (4)	13.66	236.6	239.1	2.2	2.5	2.2	0.4	3.52	9.50	8.43	7.05	3.86	1.07	5.98
4/14/2022		1.0kW	17.17	235.5	236.8	0.6	2.2	0.6	1.6	4.27	6.82	6.77	4.95	4.47	1.61	4.92
		1.0kW (2)	17.09	238.4	237.6	1.7	2.3	1.7	0.7	4.26	10.66	11.04	7.58	7.51	1.80	7.72
		1.0kW (3)	16.99	239.3	237.5	2.0	2.3	2.0	0.3	4.26	12.75	12.56	7.78	5.63	1.34	8.01
		1.0kW (4)	17.09	235.5	237.1	0.5	2.3	0.5	1.8	4.26	6.46	6.29	4.69	4.18	1.57	4.64
		1.0kW (5)	17.12	234.8	238.0	2.1	2.4	2.1	0.3	3.52	10.10	8.66	6.67	2.92	0.71	5.81
		1.1kW	18.71	239.6	237.6	2.2	2.3	2.1	0.2	4.24	12.80	12.12	7.74	4.26	0.94	7.57
		1.1kW (2)	18.79	238.4	237.4	1.8	2.3	1.8	0.5	4.24	12.40	12.02	7.15	6.20	1.22	7.80
		1.1kW (3)	18.85	241.6	238.3	2.5	2.4	2.4	-0.1	4.23	11.24	11.21	7.96	3.31	0.89	6.92
		1.1kW (4)	18.84	233.1	237.2	1.7	2.3	1.7	0.6	3.49	10.14	8.17	5.52	2.48	0.70	5.40

Date	Test Condition	Power Setting	Heat Flux [kW/m²]	Pressure [kPa]		Temperature [°C]				Flow Rate [kg/min]	Heat Transfer Coefficient [kW/m²-K]					
				P_{inlet}	P_{box}	T_{inlet}	T_{sat}	T_{ref}	Subcooling		Row 1	Row 2	Row 3	Row 4	Row 5	Overall
PHASE 2 - R1234ze(E), circular cone nozzles, square pitch, Tube-C condenser tubes (Bundle 2)																
5/6/2022	Full Bundle, Preheater ON, Normal Charge	0.2kW	3.41	164.0	169.3	-7.5	-6.8	-7.5	0.7	4.01	4.28	4.13	3.65	4.00	3.43	3.90
		0.2kW (2)	3.41	166.7	170.6	-6.6	-6.6	-6.7	0.1	3.98	70.31	30.12	12.08	14.45	9.28	27.25
		0.2kW (3)	3.41	163.6	169.1	-8.0	-6.8	-8.0	1.3	3.99	2.60	2.53	2.34	2.47	2.24	2.43
		0.2kW (4)	3.41	164.2	169.8	-6.8	-6.7	-6.8	0.1	3.51	-141.26	34.33	13.37	0.96	7.17	-17.09
		0.4kW	6.80	166.9	170.0	-8.0	-6.7	-8.0	1.4	4.19	4.19	4.10	3.63	3.92	3.16	3.80
		0.4kW (2)	6.82	169.0	170.9	-7.4	-6.5	-7.4	0.9	4.19	6.33	6.13	5.17	5.85	3.91	5.48
		0.4kW (3)	6.82	170.6	170.9	-6.8	-6.5	-6.8	0.3	4.20	12.12	12.39	8.70	11.63	4.21	9.81
		0.4kW (4)	6.83	165.7	170.7	-7.1	-6.6	-7.1	0.6	3.53	7.11	6.88	5.82	6.53	2.67	5.80
5/9/2022		0.6kW	10.24	168.6	170.9	-7.6	-6.5	-7.6	1.1	4.27	6.00	5.89	4.67	5.49	3.19	5.05
		0.6kW (2)	10.25	170.2	171.0	-6.7	-6.5	-6.7	0.2	4.17	11.34	11.40	7.22	8.82	3.43	8.44
		0.6kW (3)	10.25	168.5	170.4	-7.2	-6.6	-7.2	0.6	4.18	8.03	7.89	5.79	7.13	3.62	6.49
		0.6kW (4)	10.24	165.1	169.9	-7.0	-6.7	-7.0	0.3	3.51	8.29	8.27	5.59	5.19	1.43	5.75
		0.8kW	13.64	169.8	172.3	-7.5	-6.3	-7.5	1.2	4.23	6.76	6.57	4.97	5.55	2.59	5.29
		0.8kW (2)	13.66	170.0	170.6	-6.8	-6.6	-6.8	0.2	4.17	11.48	11.45	6.38	5.70	1.63	7.33
		0.8kW (3)	13.67	168.7	170.5	-7.3	-6.6	-7.3	0.7	4.18	8.61	8.45	5.71	6.61	2.65	6.41
		0.8kW (4)	13.76	166.4	170.8	-6.7	-6.5	-6.7	0.2	3.46	8.18	8.65	5.06	2.87	0.92	5.14
5/10/2022		1.0kW	17.10	168.9	170.0	-6.8	-6.7	-6.8	0.2	4.22	12.84	12.51	6.70	6.00	1.48	7.91
		1.0kW (2)	17.11	166.9	169.9	-7.8	-6.7	-7.8	1.1	4.21	7.61	7.31	5.18	4.79	1.47	5.27
		1.0kW (3)	17.11	169.5	170.8	-7.0	-6.5	-7.0	0.4	4.20	10.92	10.65	6.37	5.71	1.46	7.02
		1.0kW (4)	17.15	165.2	170.5	-7.1	-6.6	-7.1	0.5	3.52	8.59	7.51	4.25	2.55	0.70	4.72
		1.0kW (5)	17.11	168.0	169.4	-7.3	-6.8	-7.3	0.6	4.19	9.90	9.57	5.44	5.42	1.38	6.34
		1.1kW	18.85	176.4	173.2	-5.2	-6.2	-5.3	-0.9	4.08	6.24	30.52	4.14	2.31	0.66	8.77
		1.1kW (2)	18.78	169.2	171.0	-7.4	-6.5	-7.4	0.9	4.20	9.23	8.92	5.31	5.33	1.01	5.96
		1.1kW (3)	18.88	171.0	171.6	-6.7	-6.4	-6.7	0.3	4.16	11.42	10.09	5.05	3.13	0.83	6.10
5/18/2022	Full Bundle	0.2kW	3.41	123.8	137.6	-12.5	-12.0	-12.5	0.5	2.85	3.96	3.89	3.90	4.63	3.23	3.92
		0.2kW (2)	3.41	123.2	137.3	-12.1	-12.1	-12.2	0.1	2.77	8.51	9.16	8.31	14.46	5.45	9.18
		0.4kW	6.79	114.7	133.8	-12.6	-12.7	-12.7	-0.1	1.14	2.19	2.75	1.00	0.95	0.31	1.44
5/19/2022		0.4kW (2)	6.82	132.9	136.5	-11.6	-12.2	-12.2	-0.6	3.99	6.71	7.81	8.65	8.58	1.30	6.61
		0.4kW (3)	6.86	130.8	137.0	-12.1	-12.1	-12.2	0.0	3.86	6.89	8.60	8.60	8.03	1.33	6.69
		0.6kW	10.18	132.3	137.3	-12.0	-12.1	-12.1	0.0	4.01	5.11	7.05	6.27	3.73	0.93	4.62
		0.8kW	13.60	133.4	138.3	-12.1	-11.9	-12.1	0.3	4.17	4.69	5.65	4.54	2.44	0.77	3.62
		1.0kW	16.96	131.9	137.3	-12.7	-12.1	-12.7	0.6	4.27	4.65	4.77	3.49	1.88	0.62	3.08
		1.1kW	18.56	132.1	137.3	-12.4	-12.0	-12.4	0.3	4.18	4.30	4.89	2.97	1.55	0.51	2.85
PHASE 2 - R1233zd(E), circular cone nozzles, square pitch, Tube-C condenser tubes (Bundle 2)																
6/3/2022	Full Bundle, Preheater OFF, Normal Charge	0.2kW	3.39	75.2	81.4	-14.5	12.6	-14.5	27.2	2.05	0.189	0.138	0.127	0.117	0.107	0.136
		0.4kW	6.82	133.3	136.4	-15.4	26.4	-15.4	41.8	2.40	0.167	0.155	0.156	0.158	0.137	0.155
		0.6kW	10.20	165.4	162.8	-15.1	31.5	-15.1	46.6	2.34	0.218	0.203	0.205	0.201	0.170	0.200
		0.8kW	13.65	168.3	168.4	-15.2	32.5	-15.2	47.7	2.42	0.279	0.262	0.261	0.250	0.212	0.253
		1.0kW	17.03	171.0	166.3	-16.7	32.1	-16.7	48.8	3.19	0.349	0.336	0.329	0.314	0.255	0.317

Date	Test Condition	Power Setting	Heat Flux [kW/m^2]	Pressure [kPa]		Temperature [°C]				Flow Rate [kg/min]	Heat Transfer Coefficient [kW/m^2-K]					
				P_{inlet}	P_{box}	T_{inlet}	T_{sat}	T_{ref}	Subcooling		Row 1	Row 2	Row 3	Row 4	Row 5	Overall
PHASE 2 - R1233zd(E), circular cone nozzles, square pitch, Tube-C condenser tubes (Bundle 2)																
6/8/2022	Partial Bundle, Preheater OFF, Normal Charge	0.4kW	6.80	106.1	112.0	-13.5	21.0	-13.5	34.5	1.96	0.23	-	0.20	-	0.20	0.21
		0.6kW	10.18	145.8	151.0	-13.9	29.3	-13.9	43.2	2.07	0.22	-	0.21	-	0.18	0.20
		0.8kW	13.59	161.1	160.6	-14.5	31.1	-14.5	45.5	2.12	0.29	-	0.27	-	0.22	0.26
6/8/2022	Partial Bundle, Preheater ON, Normal Charge	0.4kW	6.75	153.2	160.6	11.7	31.1	11.7	19.3	1.90	0.36	-	0.35	-	0.33	0.35
		0.6kW	10.20	161.5	166.9	11.2	32.2	11.2	21.0	1.98	0.47	-	0.47	-	0.41	0.45
		0.8kW	13.61	164.5	170.7	10.1	32.9	10.1	22.8	2.09	0.58	-	0.55	-	0.45	0.53
6/9/2022	Partial Bundle, Preheater OFF, Increased Charge	0.4kW	6.79	72.4	96.4	-15.2	17.0	-15.2	32.2	2.42	0.30	-	0.24	-	0.19	0.24
		0.6kW	10.22	84.9	107.6	-16.2	19.9	-16.2	36.2	2.83	0.39	-	0.29	-	0.25	0.31
		0.8kW	13.51	95.9	115.6	-16.4	21.9	-16.4	38.3	3.35	0.40	-	0.35	-	0.33	0.36
		1.0kW	16.99	127.7	148.0	-16.5	28.7	-16.5	45.3	3.34	0.37	-	0.36	-	0.33	0.36
6/9/2022	Partial Bundle, Preheater ON, Increased Charge	0.4kW	6.81	112.2	136.0	3.7	26.4	3.7	22.6	2.73	0.38	-	0.31	-	0.28	0.32
		0.6kW	10.24	170.0	194.3	3.5	36.8	3.5	33.3	2.73	0.30	-	0.29	-	0.26	0.29
		0.8kW	13.63	235.1	258.9	3.9	21.9	3.9	18.0	2.65	0.30	-	0.29	-	0.27	0.29
6/10/2022	Full Bundle, Preheater OFF, Increased Charge	0.4kW	6.83	83.8	103.5	-16.4	18.9	-16.4	35.3	3.35	0.41	0.26	0.20	0.20	0.19	0.25
		0.6kW	10.20	128.6	148.9	-16.5	28.9	-16.5	45.4	3.36	0.23	0.22	0.22	0.22	0.20	0.22
7/13/2022	Single Tube (No. 5), Preheater OFF, Normal Charge, Variable Autotransformer	30%	3.42	103.9	94.6	14.8	16.5	14.8	1.7	2.01	-	-	-	-	3.95	3.95
		40%	6.46	105.0	95.9	15.0	16.9	15.0	1.9	2.05	-	-	-	-	3.82	3.82
		50%	9.93	102.6	94.4	14.2	16.4	14.2	2.3	2.08	-	-	-	-	3.09	3.09
		60%	13.66	101.4	94.5	13.7	16.5	13.7	2.8	1.97	-	-	-	-	2.51	2.51
		70%	18.51	100.5	94.0	13.3	16.3	13.3	3.0	1.99	-	-	-	-	2.16	2.16
		80%	23.99	99.1	93.5	13.0	16.2	13.0	3.2	2.01	-	-	-	-	1.96	1.96
		90%	28.52	98.9	94.4	13.1	16.4	13.1	3.3	2.02	-	-	-	-	1.68	1.68
		100%	35.12	96.9	93.6	12.6	16.2	12.6	3.6	2.04	-	-	-	-	1.47	1.47
7/14/2022	Single Tube (No. 5), Variable Autotransformer, Preheater ON, Normal Charge	30%	3.45	99.1	93.4	15.1	16.2	14.7	1.1	2.04	-	-	-	-	3.52	3.52
		40%	6.13	99.9	94.6	15.5	16.5	15.2	1.0	2.04	-	-	-	-	3.52	3.52
		50%	9.42	99.1	94.4	15.5	16.5	15.2	1.0	2.04	-	-	-	-	2.86	2.86
		60%	13.55	98.3	94.3	15.6	16.4	15.3	0.8	2.05	-	-	-	-	2.35	2.35
		70%	17.70	97.1	93.9	15.7	16.3	15.2	0.6	2.05	-	-	-	-	1.78	1.78
		80%	22.95	95.5	93.3	15.4	16.1	15.1	0.7	2.06	-	-	-	-	1.52	1.52
		90%	29.16	95.2	94.3	15.5	16.4	15.4	1.0	2.06	-	-	-	-	1.34	1.34
		100%	34.75	93.3	93.7	15.6	16.3	15.3	0.7	2.07	-	-	-	-	1.12	1.12
7/15/2022	Three Tubes (Bottom Row), Box 1, Preheater ON, Normal Charge	0.4kW	6.78	103.5	94.4	15.8	16.5	15.8	0.7	3.26	-	-	-	-	6.98	6.98
		0.6kW	10.19	100.4	93.0	15.5	16.1	15.5	0.6	3.27	-	-	-	-	4.73	4.73
		0.8kW	13.59	98.5	93.6	15.8	16.2	15.8	0.5	3.28	-	-	-	-	3.59	3.59
		1.0kW	16.98	97.4	93.8	16.1	16.3	16.1	0.2	3.29	-	-	-	-	3.00	3.00
		1.2kW	20.33	94.3	94.2	15.7	16.4	15.7	0.7	3.29	-	-	-	-	2.69	2.69
		1.4kW	23.72	90.5	94.0	16.3	16.4	16.3	0.1	3.17	-	-	-	-	2.17	2.17
		1.6kW	27.02	89.2	93.3	15.7	16.1	15.7	0.5	2.79	-	-	-	-	1.83	1.83
	Normal Charge (+5lbm)	1.8kW	30.80	82.2	94.7	15.8	16.5	15.8	0.8	3.31	-	-	-	-	2.75	2.75
		2.0kW	34.13	80.7	93.7	15.7	16.3	15.7	0.6	3.31	-	-	-	-	2.74	2.74

Date	Test Condition	Power Setting	Heat Flux [kW/m^2]	Pressure [kPa]		Temperature [°C]				Flow Rate [kg/min]	Heat Transfer Coefficient [kW/m^2-K]					
				P_{inlet}	P_{box}	T_{inlet}	T_{sat}	T_{ref}	Subcooling		Row 1	Row 2	Row 3	Row 4	Row 5	Overall
PHASE 2 - R1233zd(E), circular cone nozzles, square pitch, Tube-C condenser tubes (Bundle 2)																
7/18/2022	Three Tubes (Bottom Row), Box 1, Preheater ON, Normal Charge (+5lbm)	0.4kW	6.80	89.8	96.1	16.2	16.9	16.2	0.8	3.28	-	-	-	-	8.46	8.46
		0.6kW	10.14	88.9	96.2	16.5	16.9	16.5	0.5	3.29	-	-	-	-	6.29	6.29
		0.8kW	13.64	88.5	97.1	17.0	17.2	17.0	0.2	3.29	-	-	-	-	4.46	4.46
		1.0kW	16.94	88.6	96.9	17.1	17.1	17.1	0.0	3.29	-	-	-	-	3.51	3.51
		1.2kW	20.34	87.3	96.8	16.5	17.1	16.5	0.7	3.30	-	-	-	-	3.35	3.35
		1.4kW	23.90	87.3	96.7	16.6	17.1	16.6	0.4	3.30	-	-	-	-	2.88	2.88
		1.6kW	27.30	84.6	95.1	15.9	16.6	15.9	0.8	3.30	-	-	-	-	2.88	2.88
7/19/2022		1.8kW	30.72	83.9	95.2	15.9	16.7	15.9	0.7	3.29	-	-	-	-	2.73	2.73
		2.0kW	34.20	85.5	95.5	17.0	16.8	16.8	-0.2	3.29	-	-	-	-	1.91	1.91
7/20/2022	Full Bundle, Preheater ON, Normal Charge (+5lbm)	0.2kW	3.41	87.9	96.0	16.7	15.9	15.9	-0.8	3.31	4.70	6.13	5.94	6.49	2.28	4.94
		0.4kW	6.82	88.1	94.8	16.8	15.6	15.6	-1.2	3.31	2.88	3.20	3.14	1.59	0.83	2.32
		0.6kW	10.21	89.2	95.9	16.8	15.9	15.9	-0.9	3.31	2.61	2.71	1.91	0.92	0.67	1.82
		0.8kW	13.69	90.1	96.4	16.8	16.0	16.0	-0.8	3.32	2.36	2.33	1.23	0.69	0.58	1.51
		0.8kW (2)	13.70	90.4	95.6	15.6	15.8	15.8	0.2	3.80	3.20	3.06	1.66	0.86	0.67	1.99
	Partial Bundle	0.8kW	13.69	90.9	94.5	15.6	15.4	15.4	-0.2	3.30	2.70	-	3.47	-	1.03	2.27
		1.0kW	17.05	93.2	95.1	16.3	15.6	15.6	-0.7	3.30	2.20	-	2.25	-	0.78	1.68
7/21/2022	Full Bundle, Preheater ON, Increased Charge	0.2kW	3.42	83.4	94.3	15.3	15.4	15.4	0.1	3.32	8.90	9.18	6.79	7.92	3.14	7.16
		0.4kW	6.85	85.8	95.7	15.9	15.8	15.8	0.0	3.32	4.22	4.74	4.33	2.20	1.06	3.32
		0.4kW (2)	6.85	88.0	96.1	17.0	16.0	16.0	-1.0	3.31	3.06	3.22	3.16	1.52	0.85	2.37
		0.6kW	10.27	89.6	97.0	17.1	16.2	16.2	-0.9	3.32	2.69	2.77	2.04	0.96	0.69	1.88
		0.8kW	13.75	91.4	97.1	16.2	16.2	16.2	0.0	3.80	3.21	3.02	1.65	0.83	0.66	1.97
	Partial Bundle	0.8kW	13.75	89.0	93.7	16.3	15.3	15.3	-1.0	3.80	2.31	-	3.43	-	1.02	2.10
		1.0kW	17.05	90.2	95.8	16.3	15.9	15.9	-0.4	3.80	2.55	-	3.11	-	0.90	2.07
PHASE 2 - R1234ze(E), circular cone nozzles, square pitch, Tube-C condenser tubes (Bundle 2)																
7/28/2022	Full Bundle, Preheater ON, Normal Charge	0.4kW	6.85	131.2	136.3	-13.2	-12.2	-13.2	0.9	3.91	3.42	3.05	3.86	3.49	1.12	2.99
		0.6kW	10.19	131.9	137.3	-13.3	-12.1	-13.3	1.3	3.89	3.35	2.76	3.65	2.85	0.84	2.69
		0.8kW	13.60	132.5	138.2	-13.5	-11.9	-13.5	1.6	3.91	3.37	2.34	3.28	2.27	0.68	2.39
7/29/2022	Full Bundle, Preheater ON, Normal Charge	0.4kW	6.84	133.9	136.7	-12.3	-12.2	-12.3	0.1	4.09	5.94	5.26	8.99	8.83	1.24	6.05
		0.6kW	10.26	136.8	137.0	-12.1	-12.1	-12.2	0.0	4.20	6.02	4.22	9.04	4.46	0.83	4.91
		0.8kW	13.70	135.5	136.4	-12.6	-12.2	-12.6	0.4	4.18	4.67	2.84	5.82	2.41	0.67	3.28
		1.0kW	17.08	145.0	145.8	-11.5	-10.6	-11.5	0.9	4.11	3.49	2.32	4.94	1.54	0.53	2.57
		1.0kW (2)	17.10	135.4	139.7	-14.0	-11.6	-14.0	2.3	4.38	3.15	2.09	2.67	1.68	0.55	2.03
		1.0kW (3)	17.07	138.3	139.5	-12.5	-11.7	-12.5	0.8	4.24	3.51	2.38	4.34	1.64	0.56	2.48

Date	Test Condition	Power Setting	Heat Flux	Pressure [kPa]		Temperature [°C]				Flow Rate	Heat Transfer Coefficient [kW/m^2-K]					
			[kW/m^2]	P_{inlet}	P_{box}	T_{inlet}	T_{sat}	T_{ref}	Subcooling	[kg/min]	Row 1	Row 2	Row 3	Row 4	Row 5	Overall
PHASE 2 - R1234ze(E), circular cone nozzles, square pitch, Tube-C condenser tubes (Bundle 2)																
8/1/2022	Three tubes (bottom row), Preheater OFF, Normal Charge	0.6kW	10.18	246.7	236.0	2.4	2.1	2.1	-0.3	4.25	-	-	-	-	4.48	4.48
		1.0kW	17.03	245.6	238.0	2.0	2.4	2.0	0.4	4.27	-	-	-	-	3.23	3.23
		1.4kW	23.75	245.1	237.8	1.8	2.4	1.9	0.5	4.26	-	-	-	-	2.63	2.63
		1.4kW (2)	23.94	244.5	237.4	1.4	2.3	1.4	0.9	4.27	-	-	-	-	2.55	2.55
		1.8kW	30.77	242.0	238.0	0.9	2.4	0.9	1.5	4.32	-	-	-	-	2.49	2.49
		1.8kW (2)	30.77	244.2	239.4	2.3	2.6	2.3	0.3	4.27	-	-	-	-	2.45	2.45
	Preheater ON	2.2kW	37.56	240.3	239.1	1.8	2.5	1.8	0.7	4.30	-	-	-	-	2.20	2.20
		2.2kW (2)	31.45	262.2	234.9	4.9	2.0	4.2	-2.9	3.61	-	-	-	-	4.22	4.22
8/2/2022	Three tubes (No. 1, 2, & 3), Preheater OFF, Normal Charge	0.6kW	10.22	241.5	233.6	1.8	1.9	1.8	0.1	4.28	8.62	3.01	2.67	-	-	4.77
		1.0kW	17.01	243.5	238.8	1.8	2.5	1.8	0.7	4.29	5.71	2.03	1.24	-	-	3.00
		1.0kW (2)	17.00	242.4	237.6	2.0	2.3	2.0	0.3	4.28	5.70	1.95	1.23	-	-	2.96
		1.4kW	23.84	238.9	237.3	1.3	2.3	1.3	1.0	4.27	4.91	1.73	0.89	-	-	2.51
		1.4kW (2)	23.86	241.4	239.1	2.2	2.5	2.2	0.3	4.24	4.90	1.55	0.86	-	-	2.44
		1.6kW	27.34	237.1	236.4	1.4	2.2	1.4	0.8	4.27	4.70	1.53	0.71	-	-	2.31
		1.6kW (2)	27.27	237.8	236.9	1.8	2.3	1.8	0.5	4.26	4.65	1.45	0.72	-	-	2.27
8/3/2022	Single Tube (No. 1), Preheater OFF, Normal Charge	40%	5.62	240.7	233.9	2.4	1.9	1.4	-0.5	4.26	5.60	-	-	-	-	5.60
		50%	8.87	244.4	238.0	2.7	2.4	1.9	-0.4	4.27	6.01	-	-	-	-	6.01
		50% (2)	8.88	244.7	238.1	2.9	2.4	1.9	-0.6	4.25	5.72	-	-	-	-	5.72
		60%	12.94	243.3	237.2	2.7	2.3	1.8	-0.4	4.24	4.77	-	-	-	-	4.77
		60% (2)	12.93	243.3	236.0	2.5	2.1	1.7	-0.3	4.18	4.81	-	-	-	-	4.81
		80%	23.62	246.7	236.2	2.4	2.2	1.8	-0.2	4.18	3.83	-	-	-	-	3.83
		80% (2)	23.46	247.6	236.8	2.6	2.2	1.8	-0.4	4.22	3.56	-	-	-	-	3.56
		100%	34.25	246.4	237.8	2.5	2.4	2.0	-0.1	4.16	3.43	-	-	-	-	3.43
		100% (2)	34.10	244.9	236.7	2.1	2.2	1.8	0.1	4.22	3.65	-	-	-	-	3.65
8/4/2022	Single Tube (No. 5), Preheater OFF, Normal Charge, Variable Autotransformer	40%	6.13	241.9	235.6	2.4	2.1	1.6	-0.3	4.30	-	-	-	-	5.15	5.15
		40% (2)	6.11	244.2	237.5	3.0	2.3	1.8	-0.7	4.28	-	-	-	-	5.03	5.03
		50%	9.28	244.4	238.5	2.9	2.4	2.0	-0.5	4.28	-	-	-	-	4.41	4.41
		50% (2)	9.23	243.6	237.5	2.7	2.3	1.9	-0.3	4.29	-	-	-	-	4.32	4.32
		60%	13.19	242.4	237.7	2.4	2.3	1.9	-0.1	4.30	-	-	-	-	4.08	4.08
		60% (2)	13.37	243.2	238.3	2.7	2.4	2.0	-0.2	4.28	-	-	-	-	3.73	3.73
		80%	22.73	239.6	236.3	1.9	2.2	1.8	0.2	4.24	-	-	-	-	2.72	2.72
		80% (2)	23.01	239.2	235.0	1.6	2.0	1.6	0.4	4.20	-	-	-	-	2.68	2.68
8/5/2022	Single Tube (No. 2), Preheater OFF, Normal Charge, Variable Autotransformer	40%	6.31	231.5	235.8	1.7	2.1	1.7	0.4	4.34	-	10.01	-	-	-	10.01
		40% (2)	5.89	232.4	238.0	2.1	2.4	2.1	0.3	4.38	-	11.89	-	-	-	11.89
		80%	23.25	242.1	236.4	2.4	2.2	2.2	-0.2	4.24	-	3.33	-	-	-	3.33
		80% (2)	23.13	242.2	235.6	2.2	2.1	2.1	-0.1	4.21	-	3.23	-	-	-	3.23
	Two Tube (No. 1 & 2), Preheater OFF, Normal Charge, Variable Autotransformer	40%	5.92	251.0	239.0	3.3	2.5	2.5	-0.8	4.37	10.54	3.24	-	-	-	6.89
		40% (2)	5.90	250.3	238.6	3.1	2.5	2.4	-0.6	4.40	10.82	3.46	-	-	-	7.14
		80%	22.81	244.8	238.7	1.8	2.5	1.8	0.7	4.27	4.87	1.67	-	-	-	3.27
		80% (2)	23.01	245.4	239.1	2.0	2.5	2.0	0.5	4.26	4.86	1.64	-	-	-	3.25

Date	Test Condition	Power Setting	Heat Flux	Pressure [kPa]		Temperature [°C]				Flow Rate	Heat Transfer Coefficient [kW/m²-K]					
			[kW/m²]	P_{inlet}	P_{box}	T_{inlet}	T_{sat}	T_{ref}	Subcooling	[kg/min]	Row 1	Row 2	Row 3	Row 4	Row 5	Overall
PHASE 2 - R1234ze(E), circular cone nozzles, square pitch, Tube-C condenser tubes (Bundle 2)																
8/12/2022	Single Tube (No. 5), FLOODED Tests, Variable Autotransformer	20%	1.51	223.1	238.3	1.9	2.4	1.8	0.5	2.33	-	-	-	-	4.93	4.93
		35%	4.37	237.4	237.6	1.8	2.3	1.9	0.5	1.86	-	-	-	-	4.94	4.94
		35% (2)	4.41	223.5	238.7	1.8	2.5	1.9	0.7	2.33	-	-	-	-	5.65	5.65
		50%	8.78	238.4	238.6	1.8	2.5	2.0	0.6	1.86	-	-	-	-	5.06	5.06
		64%	14.35	235.1	235.6	1.5	2.1	1.7	0.6	1.85	-	-	-	-	6.18	6.18
		80%	22.57	237.0	237.0	0.8	2.3	1.9	1.5	1.98	-	-	-	-	7.15	7.15
		80% (3)	22.57	238.4	238.4	1.7	2.4	2.1	0.8	1.84	-	-	-	-	7.70	7.70
		92%	30.02	239.0	237.8	1.6	2.4	2.1	0.7	1.79	-	-	-	-	9.28	9.28
		100%	34.59	236.5	236.8	1.4	2.2	2.0	0.9	1.83	-	-	-	-	9.68	9.68
PHASE 2 - R1233zd(E), circular cone nozzles, square pitch, Tube-C condenser tubes (Bundle 2)																
8/19/2022	Single Tube (No. 5), Spray Tests, Variable Autotransformer	50%	8.95	86.2	102.9	14.1	18.7	17.1	4.6	3.17	-	-	-	-	4.53	4.53
		60%	12.73	89.7	106.3	14.2	19.6	18.1	5.4	3.21	-	-	-	-	4.19	4.19
		70%	17.35	88.6	93.9	16.3	16.3	15.2	0.0	3.18	-	-	-	-	3.86	3.86
		80%	23.09	91.5	87.4	13.5	14.4	13.4	1.0	2.23	-	-	-	-	2.29	2.29
8/22/2022	Single Tube (No. 5), Flooded Tests, Variable Autotransformer	50%	8.90	88.3	97.0	15.2	17.2	15.6	1.9	4.26	-	-	-	-	5.58	5.58
		50% (2)	9.08	97.3	108.8	16.4	20.2	18.5	3.8	4.28	-	-	-	-	5.12	5.12
		60%	12.88	88.2	95.7	14.8	16.8	15.4	2.0	4.26	-	-	-	-	5.54	5.54
		60% (2)	12.73	95.4	107.0	15.4	19.8	18.0	4.4	4.29	-	-	-	-	5.19	5.19
		70%	17.85	96.9	108.3	14.3	20.1	18.4	5.8	4.31	-	-	-	-	5.24	5.24
		80%	22.81	97.1	109.1	13.4	20.3	18.6	6.9	4.20	-	-	-	-	5.51	5.51
		90%	29.10	95.5	107.2	11.5	19.8	18.2	8.4	4.32	-	-	-	-	5.89	5.89
		100%	35.20	93.2	104.9	9.5	19.3	17.7	9.8	4.33	-	-	-	-	5.72	5.72
8/23/2022	Single Tube (No. 1), Spray Tests, Variable Autotransformer, Preheater ON	50%	8.92	91.1	103.2	18.4	18.8	17.9	0.5	4.23	12.64	-	-	-	-	12.64
		60%	12.79	91.6	103.7	18.3	18.9	18.0	0.6	4.24	12.27	-	-	-	-	12.27
		70%	17.77	91.4	103.4	18.3	18.9	18.0	0.6	4.26	11.89	-	-	-	-	11.89
		80%	23.01	91.3	103.3	18.4	18.8	18.0	0.5	4.26	11.42	-	-	-	-	11.42
		90%	28.96	91.5	103.4	18.4	18.9	18.0	0.5	4.26	11.39	-	-	-	-	11.39
		100%	34.80	91.8	103.6	18.5	18.9	18.0	0.5	4.26	10.96	-	-	-	-	10.96
8/23/2022	Single Tube (No. 1), Hysteresis Testing, Variable Autotransformer	90% (D)	29.19	91.2	103.1	18.4	18.8	18.4	0.4	4.26	15.13	-	-	-	-	15.13
		80% (D)	23.09	90.7	102.5	18.5	18.6	18.5	0.2	4.27	19.39	-	-	-	-	19.39
		70% (D)	17.85	90.2	101.9	18.5	18.5	18.4	0.0	4.26	29.77	-	-	-	-	29.77
		60% (D)	12.91	90.0	101.6	18.4	18.4	18.3	0.0	4.27	88.59	-	-	-	-	88.59
		70% (I)	17.88	90.4	102.2	18.4	18.5	18.4	0.2	4.27	25.79	-	-	-	-	25.79
		80% (I)	23.29	90.8	102.5	18.4	18.6	18.4	0.3	4.27	17.98	-	-	-	-	17.98
		90% (I)	29.37	91.3	103.0	18.3	18.8	18.3	0.4	4.27	14.13	-	-	-	-	14.13
		100% (I)	35.20	92.0	103.7	18.4	18.9	18.4	0.6	4.26	12.26	-	-	-	-	12.26

Date	Test Condition	Power Setting	Heat Flux [kW/m^2]	Pressure [kPa]		Temperature [°C]				Flow Rate [kg/min]	Heat Transfer Coefficient [kW/m^2-K]					
				P_{inlet}	P_{box}	T_{inlet}	T_{sat}	T_{ref}	Subcooling		Row 1	Row 2	Row 3	Row 4	Row 5	Overall
PHASE 2 - R134a, circular cone nozzles, square pitch, Tube-C condenser tubes (Bundle 2)																
8/29/2022	Single Tube (No. 5), FLOODED Tests, Variable Autotransformer	50%	8.90	314.6	321.0	-0.4	2.5	1.4	2.9	1.47	-	-	-	-	3.30	3.30
		60%	12.76	317.7	326.4	-0.4	3.0	2.0	3.4	1.50	-	-	-	-	4.35	4.35
		70%	17.70	331.2	321.7	-0.5	2.6	1.9	3.1	1.38	-	-	-	-	5.95	5.95
		80%	23.21	334.1	327.3	-0.8	3.1	2.5	3.9	1.60	-	-	-	-	7.47	7.47
		90%	28.69	329.9	319.9	-1.0	2.5	1.9	3.4	1.49	-	-	-	-	8.72	8.72
		100%	34.95	337.1	327.2	-0.8	3.1	2.6	3.9	1.44	-	-	-	-	10.01	10.01
8/30/2022	Single Tube (No. 5), Spray Tests, Variable Autotransformer	50%	8.75	310.9	317.9	2.9	2.3	2.0	-0.6	4.08	-	-	-	-	9.66	9.66
		60%	12.79	311.0	317.7	2.9	2.3	2.0	-0.6	4.06	-	-	-	-	8.82	8.82
		70%	18.06	316.2	325.1	3.0	2.9	2.6	-0.1	4.08	-	-	-	-	8.67	8.67
		80%	22.73	315.0	327.2	2.4	3.1	2.9	0.7	4.30	-	-	-	-	9.96	9.96
		80% (2)	22.81	313.7	325.3	2.7	2.9	2.7	0.3	4.23	-	-	-	-	10.19	10.19
		90%	28.82	313.3	324.5	2.8	2.9	2.7	0.1	4.13	-	-	-	-	8.25	8.25
		100%	34.70	312.9	323.9	2.7	2.8	2.7	0.1	4.19	-	-	-	-	7.26	7.26
8/31/2022	Single Tube (No. 1), Spray Tests, Variable Autotransformer	50% (2)	9.00	317.0	323.0	3.4	2.7	2.5	-0.7	4.29	11.95	-	-	-	-	11.95
		60% (2)	12.91	318.8	325.1	3.5	2.9	2.6	-0.5	4.28	11.91	-	-	-	-	11.91
		70% (2)	17.67	319.3	325.3	3.4	2.9	2.7	-0.5	4.29	9.41	-	-	-	-	9.41
		80%	23.13	318.4	323.2	3.5	2.7	2.5	-0.7	4.24	7.16	-	-	-	-	7.16
		90%	29.01	320.6	326.2	3.5	3.0	2.8	-0.5	4.23	7.24	-	-	-	-	7.24
		100%	34.65	320.4	325.4	3.6	2.9	2.7	-0.6	4.18	5.69	-	-	-	-	5.69
	Single Tube (No. 5), Spray Tests, Variable Autotransformer	50%	9.05	313.3	325.5	2.4	2.9	2.7	0.5	4.26	-	-	-	-	10.27	10.27
		60%	12.67	315.0	325.4	2.8	2.9	2.7	0.2	4.27	-	-	-	-	9.79	9.79
		70%	17.63	317.5	326.0	3.1	3.0	2.8	-0.1	4.23	-	-	-	-	8.45	8.45
		80% (2)	22.81	318.7	323.2	3.4	2.7	2.5	-0.7	4.27	-	-	-	-	5.75	5.75
9/1/2022		90%	29.01	321.9	327.2	3.7	3.1	2.9	-0.6	4.28	-	-	-	-	3.79	3.79
		100%	34.95	320.4	324.1	3.6	2.8	2.6	-0.8	4.28	-	-	-	-	2.98	2.98
PHASE 3 - R134a, circular cone nozzles, triangular pitch, Tube-B evaporator tubes (Bundle 3)																
9/19/2022	Single Tube (No. 1), Spray Tests, Variable Autotransformer	50%	8.97	333.6	315.2	1.6	2.0	0.6	0.4	4.35	6.14	-	-	-	-	6.14
		60%	12.97	332.8	317.5	1.8	2.2	0.8	0.5	4.40	8.72	-	-	-	-	8.72
		70%	17.74	335.1	319.5	1.9	2.4	1.1	0.5	4.30	11.74	-	-	-	-	11.74
		80%	23.17	338.0	319.1	1.9	2.4	1.2	0.5	4.22	14.62	-	-	-	-	14.62
		90%	28.87	339.7	318.5	1.9	2.3	1.2	0.4	4.17	14.68	-	-	-	-	14.68
		100%	35.40	341.0	315.8	1.8	2.1	1.1	0.3	4.14	10.93	-	-	-	-	10.93
9/20/2022	Single Tube (No. 5), Spray Tests, Variable Autotransformer	50%	9.00	347.3	318.7	2.5	2.4	1.3	-0.2	4.14	-	-	-	-	8.28	8.28
		60%	13.06	349.7	321.5	2.6	2.6	1.6	0.0	4.17	-	-	-	-	11.28	11.28
		70%	18.17	350.6	320.9	2.6	2.5	1.5	0.0	4.36	-	-	-	-	14.28	14.28
		70% (2)	17.70	348.9	318.9	2.5	2.4	1.3	-0.1	4.24	-	-	-	-	14.02	14.02
		80%	23.29	349.7	318.3	2.5	2.3	1.3	-0.1	4.26	-	-	-	-	16.83	16.83
		90%	28.91	351.1	320.3	2.5	2.5	1.5	0.0	4.26	-	-	-	-	18.57	18.57
		100%	34.90	351.9	320.3	2.5	2.5	1.6	0.0	4.26	-	-	-	-	18.96	18.96

Date	Test Condition	Power Setting	Heat Flux [kW/m²]	Pressure [kPa]		Temperature [°C]				Flow Rate [kg/min]	Heat Transfer Coefficient [kW/m²-K]					
				P_{inlet}	P_{box}	T_{inlet}	T_{sat}	T_{ref}	Subcooling		Row 1	Row 2	Row 3	Row 4	Row 5	Overall
PHASE 3 - R134a, circular cone nozzles, triangular pitch, Tube-B evaporator tubes (Bundle 3)																
9/21/2022	Single Tube (No. 5), FLOODED Tests, Variable Autotransformer	50%	9.00	329.9	318.8	0.6	2.4	1.3	1.8	2.49	-	-	-	-	7.85	7.85
		60%	12.85	331.1	319.4	0.5	2.4	1.4	1.9	2.56	-	-	-	-	10.57	10.57
		70%	17.56	329.1	317.1	0.3	2.2	1.2	1.9	2.51	-	-	-	-	13.63	13.63
		80%	22.89	330.0	318.0	0.3	2.3	1.4	2.0	2.50	-	-	-	-	16.56	16.56
		90%	28.64	331.3	319.0	0.3	2.4	1.5	2.1	2.48	-	-	-	-	19.53	19.53
		100%	35.15	330.6	318.0	0.2	2.3	1.5	2.1	2.45	-	-	-	-	22.44	22.44
9/22/2022	Full Bundle, Preheater ON, Normal Charge	0.2kW	3.32	414.3	424.0	9.5	10.6	9.5	1.2	4.35	3.90	3.37	3.71	2.52	3.63	3.50
		0.2kW (2)	3.41	408.0	419.0	9.6	10.3	9.6	0.7	4.31	5.33	4.74	5.19	3.10	5.11	4.82
		0.4kW	6.85	419.6	430.9	9.1	11.1	9.1	2.1	4.36	3.16	2.78	3.20	3.38	3.17	3.13
		0.4kW (2)	6.86	400.7	412.0	8.0	9.8	8.0	1.8	4.34	3.74	3.12	3.83	4.03	3.75	3.69
		0.6kW	10.22	403.2	414.8	8.3	10.0	8.3	1.7	4.27	5.68	3.75	5.75	6.16	5.55	5.39
9/23/2022		0.8kW	10.03	418.1	412.6	9.9	9.8	9.8	-0.1	4.37	41.49	16.33	53.02	15.18	34.08	37.94
9/29/2022	Full Bundle, Preheater ON, Normal Charge	0.2kW	3.41	425.4	417.1	8.9	10.1	8.9	1.3	4.54	3.19	3.19	2.90	2.44	2.85	2.93
		0.4kW	6.82	439.7	418.5	8.9	10.2	8.9	1.3	4.23	5.39	5.52	5.12	3.72	4.97	4.99
		0.6kW	10.23	437.7	415.7	8.9	10.1	8.9	1.2	4.32	8.11	8.87	8.06	4.92	7.98	7.70
		0.8kW	13.69	437.3	417.9	8.6	10.2	8.6	1.6	4.27	7.93	8.78	7.90	2.73	7.67	7.19
		1.0kW	17.06	434.1	414.1	8.3	9.9	8.3	1.6	4.28	9.18	10.40	9.13	1.47	8.45	8.55
		1.2kW	20.52	437.9	420.8	8.9	10.4	8.9	1.5	4.19	10.97	13.13	10.42	0.42	5.50	8.95
9/30/2022	Partial Bundle	1.4kW	23.84	433.1	415.9	8.5	10.1	8.5	1.5	4.39	11.80	-	10.59	-	3.47	8.62
		1.6kW	27.24	435.3	417.4	8.6	10.2	8.6	1.6	4.45	12.29	-	10.86	-	0.99	8.05
10/5/2022	Full Bundle, Preheater ON, Normal Charge (corrected)	0.2kW	3.40	333.2	315.1	1.2	2.0	1.1	0.9	4.35	4.20	5.18	3.70	5.87	3.53	4.21
		0.4kW	6.82	343.6	320.5	1.8	2.5	1.6	0.7	4.19	7.62	8.07	6.84	9.05	6.40	7.32
		0.6kW	10.22	345.4	320.5	2.2	2.5	1.6	0.3	4.46	10.64	11.51	9.06	13.38	8.76	10.15
		0.8kW	13.66	348.2	321.6	2.2	2.6	1.7	0.4	4.44	13.20	15.16	10.86	18.16	10.10	12.58
		1.0kW	17.04	347.3	322.5	1.9	2.7	1.8	0.8	4.43	14.54	17.68	11.96	21.83	5.77	12.83
		1.2kW	20.43	345.9	322.3	1.7	2.7	1.6	1.0	4.40	14.60	18.35	10.76	23.10	3.31	12.15
10/6/2022	Full Bundle, Preheater ON, Normal Charge (corrected)	0.4kW	6.77	330.9	317.4	2.3	2.2	1.3	-0.1	4.21	7.83	8.21	7.03	9.14	6.48	7.46
		0.6kW	10.21	338.8	319.2	2.3	2.4	1.5	0.1	4.26	10.95	11.68	9.18	13.38	8.72	10.27
		0.8kW	13.64	341.9	317.8	2.1	2.3	1.4	0.1	4.40	13.40	14.87	10.63	17.56	9.23	12.25
		1.0kW	17.00	345.3	320.8	2.3	2.5	1.6	0.3	4.46	15.25	18.02	11.59	21.95	5.20	12.84
		1.2kW	20.51	343.3	318.2	1.9	2.3	1.4	0.5	4.45	16.67	21.07	11.04	26.61	2.70	13.33

Date	Test Condition	Power Setting	Heat Flux	Pressure [kPa]		Temperature [°C]				Flow Rate	Heat Transfer Coefficient [kW/m^2-K]					
			[kW/m^2]	P_{inlet}	P_{box}	T_{inlet}	T_{sat}	T_{ref}	Subcooling	[kg/min]	Row 1	Row 2	Row 3	Row 4	Row 5	Overall
PHASE 3 - R1234ze(E), circular cone nozzles, triangular pitch, Tube-B evaporator tubes (Bundle 3)																
10/11/2022	Single Tube (No. 1), Spray Tests, Variable Autotransformer	50%	8.98	232.6	232.6	1.6	1.7	1.2	0.1	4.54	10.20	-	-	-	-	10.20
10/12/2022		50%	8.96	237.9	237.3	2.3	2.3	1.7	0.0	4.53	9.94	-	-	-	-	9.94
		60%	12.84	238.7	238.8	2.3	2.5	1.9	0.2	4.57	12.16	-	-	-	-	12.16
		70%	17.56	240.7	235.9	2.3	2.1	1.6	-0.1	4.57	14.01	-	-	-	-	14.01
		80%	23.01	241.9	236.2	2.3	2.2	1.7	-0.1	4.60	13.87	-	-	-	-	13.87
		90%	28.93	243.2	237.8	2.3	2.4	1.9	0.1	4.58	14.03	-	-	-	-	14.03
		100%	34.84	244.3	237.7	2.3	2.3	1.9	0.1	4.55	13.85	-	-	-	-	13.85
	Single Tube (No. 5), Spray Tests, Variable Autotransformer	50% (2)	8.92	239.4	236.0	2.3	2.1	1.6	-0.2	4.54	-	-	-	-	9.63	9.63
		60% (2)	12.82	241.3	237.0	2.3	2.3	1.7	0.0	4.56	-	-	-	-	12.23	12.23
		70% (2)	17.88	242.7	238.7	2.3	2.5	1.9	0.2	4.58	-	-	-	-	15.19	15.19
		80% (2)	23.25	244.2	236.8	2.3	2.2	1.8	0.0	4.54	-	-	-	-	17.04	17.04
		90% (2)	28.91	245.5	238.6	2.3	2.5	2.0	0.2	4.56	-	-	-	-	18.95	18.95
		100% (2)	35.25	246.4	236.7	2.2	2.2	1.8	0.0	4.54	-	-	-	-	17.33	17.33
10/13/2022	Single Tube (No. 5), FLOODED Tests, Variable Autotransformer	50%	8.90	246.8	236.7	1.7	2.2	1.8	0.5	1.80	-	-	-	-	11.97	11.97
		60%	12.79	246.9	236.4	1.6	2.2	1.8	0.6	1.78	-	-	-	-	14.60	14.60
		70%	17.49	247.7	237.1	1.7	2.3	1.9	0.6	1.77	-	-	-	-	17.44	17.44
		80%	23.09	248.2	237.5	1.7	2.3	1.9	0.7	1.75	-	-	-	-	21.33	21.33
		90%	28.96	248.8	237.9	1.7	2.4	2.0	0.7	1.73	-	-	-	-	25.03	25.03
		100%	34.80	248.9	237.8	1.6	2.4	2.0	0.8	1.71	-	-	-	-	19.77	19.77
10/14/2022	Full Bundle, Preheater ON, Normal Charge	0.2kW	3.40	245.9	238.8	2.7	2.5	2.5	-0.2	4.45	-37.09	-36.44	46.70	128.24	41.90	26.01
		0.4kW	6.77	249.7	239.9	2.6	2.6	2.6	0.0	4.48	-9.30	57.26	32.59	56.66	24.51	28.56
		0.4kW (2)	6.82	247.2	234.6	2.5	2.0	2.0	-0.5	4.51	-1369.60	-141.40	47.43	-19.35	27.70	-323.45
		0.4kW (3)	6.81	246.2	235.7	1.9	2.1	1.9	0.2	4.55	27.95	27.54	17.29	31.55	14.65	22.19
		0.6kW	10.17	248.9	238.8	1.9	2.5	1.9	0.6	4.57	13.88	11.13	10.82	15.31	10.10	11.83
		0.6kW (2)	10.25	249.8	239.3	2.3	2.5	2.3	0.2	4.58	33.50	31.43	19.52	41.26	16.61	26.08
		0.8kW	13.62	247.5	237.8	1.7	2.4	1.7	0.7	4.58	15.74	12.65	12.17	18.48	10.50	13.25
		0.8kW (2)	13.67	249.1	238.9	2.3	2.5	2.3	0.2	4.57	38.60	46.13	23.79	63.24	16.28	32.62
		1.0kW	17.03	244.6	239.2	2.2	2.5	2.2	0.4	4.56	26.18	22.15	16.95	36.37	8.10	19.53
10/15/2022		1.0kW	16.98	240.8	239.3	1.4	2.5	1.4	1.1	4.54	11.33	8.64	9.14	13.40	5.65	9.09
		1.2kW	20.24	238.9	237.3	1.2	2.3	1.2	1.1	4.54	12.76	8.62	9.43	15.77	1.68	8.72

Date	Test Condition	Power Setting	Heat Flux [kW/m^2]	Pressure [kPa]		Temperature [°C]				Flow Rate [kg/min]	Heat Transfer Coefficient [kW/m^2-K]					
				P_{inlet}	P_{box}	T_{inlet}	T_{sat}	T_{ref}	Subcooling		Row 1	Row 2	Row 3	Row 4	Row 5	Overall
PHASE 3 - R1234ze(E), circular cone nozzles, triangular pitch, Tube-B evaporator tubes (Bundle 3)																
10/17/2022	Full Bundle, Preheater ON, Normal Charge	0.2kW	3.47	307.7	311.6	9.1	10.1	9.1	1.0	4.51	5.17	3.31	4.33	4.14	4.23	4.33
		0.4kW	6.09	317.0	311.5	10.2	10.1	10.1	-0.1	4.65	133.27	1.02	88.37	-50.96	54.28	64.90
		0.4kW (2)	5.92	317.4	311.8	10.3	10.1	10.1	-0.2	4.65	41.97	-17.66	72.71	-68.21	54.83	33.75
		0.4kW (3)	6.82	313.8	310.4	9.4	10.0	9.4	0.6	4.73	11.06	8.98	9.01	11.67	8.60	9.64
		0.6kW	10.22	313.4	310.7	9.2	10.0	9.2	0.8	4.66	11.24	9.55	9.59	12.73	9.20	10.16
		0.6kW (2)	10.24	316.7	312.3	9.9	10.2	9.9	0.3	4.65	28.39	26.04	19.41	36.20	17.21	23.61
		0.8kW	13.64	315.2	312.4	9.4	10.2	9.4	0.8	4.65	13.61	11.54	11.47	16.25	10.63	12.20
		0.8kW (2)	13.66	318.6	313.6	10.1	10.3	10.1	0.2	4.64	37.88	51.62	26.95	77.04	19.78	36.18
		1.0kW	17.12	314.8	309.3	9.7	9.9	9.7	0.2	4.63	36.50	43.35	23.80	61.00	11.54	30.27
		1.0kW (2)	17.09	314.5	311.4	9.2	10.1	9.2	0.9	4.65	14.51	12.29	11.94	18.35	8.16	12.23
		1.2kW	20.24	313.0	310.9	8.8	10.0	8.8	1.2	4.66	12.06	8.44	9.83	14.91	2.98	8.86
		1.2kW (2)	20.22	319.1	313.5	10.1	10.3	10.1	0.2	4.63	32.53	48.28	25.01	68.63	3.47	29.02
10/22/2022	Full Bundle, Preheater ON, Normal Charge	0.4kW (2)	6.84	171.8	172.1	-7.4	-6.3	-7.4	1.1	4.69	5.82	4.89	5.36	6.18	5.17	5.42
		0.6kW	10.23	169.0	170.1	-8.0	-6.6	-8.0	1.4	4.70	6.56	5.33	5.89	7.14	6.02	6.10
		0.6kW (2)	10.26	173.0	171.1	-6.9	-6.5	-6.9	0.4	4.71	19.78	17.49	16.22	25.86	16.52	18.20
10/24/2022		0.8kW	13.66	176.2	172.9	-7.5	-6.2	-7.5	1.2	4.58	8.42	7.41	8.79	10.54	7.67	8.33
		0.8kW (2)	13.63	179.4	173.5	-6.4	-6.1	-6.4	0.3	4.60	19.45	25.86	22.47	37.20	15.68	21.81
		1.0kW	16.97	177.5	171.4	-6.8	-6.4	-6.8	0.4	4.61	18.08	23.64	20.36	37.19	8.17	18.69
		1.0kW (2)	17.02	173.7	169.8	-7.9	-6.7	-7.9	1.2	4.60	9.56	8.85	9.90	13.13	5.73	8.87
	Partial Bundle	1.2kW	22.02	174.5	170.9	-7.9	-6.5	-7.9	1.4	4.60	10.16	-	9.68	-	1.95	7.26
PHASE 3 - R1233zd(E), circular cone nozzles, triangular pitch, Tube-B evaporator tubes (Bundle 3)																
11/2/2022	Single Tube (No. 1), Spray Tests, Variable Autotransformer	50%	9.30	89.0	92.9	15.7	16.0	14.9	0.3	4.50	10.75	-	-	-	-	10.75
		50% (2)	9.45	86.8	88.6	14.7	14.8	13.6	0.1	4.21	10.65	-	-	-	-	10.65
		60%	13.39	87.0	88.6	14.6	14.8	13.6	0.2	4.20	12.14	-	-	-	-	12.14
		70%	17.93	87.5	90.0	14.6	15.2	14.1	0.6	4.21	13.99	-	-	-	-	13.99
		80%	23.18	88.0	90.7	14.6	15.4	14.3	0.8	4.21	15.26	-	-	-	-	15.26
		90%	29.10	88.4	90.8	14.6	15.4	14.3	0.8	4.21	15.28	-	-	-	-	15.28
		100%	34.94	88.6	90.3	14.6	15.3	14.2	0.6	4.21	14.74	-	-	-	-	14.74
	Single Tube (No. 5), Spray Tests, Variable Autotransformer	50% (3)	9.53	86.8	89.0	14.7	14.9	13.7	0.2	4.21	-	-	-	-	7.34	7.34
		60% (2)	13.51	87.4	90.8	14.7	15.4	14.2	0.7	4.21	-	-	-	-	10.17	10.17
		70% (2)	18.50	87.9	90.1	14.7	15.2	14.1	0.6	4.21	-	-	-	-	12.69	12.69
		80% (2)	23.62	88.3	91.1	14.7	15.5	14.4	0.9	4.21	-	-	-	-	14.22	14.22
		90% (2)	29.59	88.6	90.6	14.7	15.4	14.3	0.7	4.22	-	-	-	-	15.10	15.10
11/4/2022		100%	34.60	83.9	92.3	13.9	15.9	14.9	2.0	4.22	-	-	-	-	11.15	11.15
		100% (2)	34.70	85.6	92.5	13.9	15.9	14.9	2.0	4.23	-	-	-	-	13.14	13.14
	Single Tube (No. 5), Flooded/Spray Tests	50%	9.48	80.1	89.8	11.9	15.1	14.2	3.3	4.19	-	-	-	-	13.60	13.60
		90%	28.74	85.9	91.3	9.8	15.6	14.8	5.8	4.94	-	-	-	-	17.51	17.51

Date	Test Condition	Power Setting	Heat Flux [kW/m^2]	Pressure [kPa]		Temperature [°C]				Flow Rate [kg/min]	Heat Transfer Coefficient [kW/m^2-K]					
				P_{inlet}	P_{box}	T_{inlet}	T_{sat}	T_{ref}	Subcooling		Row 1	Row 2	Row 3	Row 4	Row 5	Overall
PHASE 3 - R1233zd(E), circular cone nozzles, triangular pitch, Tube-B evaporator tubes (Bundle 3)																
11/7/2022	Full Bundle, Preheater ON, Normal Charge (corrected)	0.2kW	3.42	81.8	91.4	14.7	14.9	14.9	0.2	4.20	11.86	19.56	7.86	18.95	10.14	12.30
		0.2kW (2)	3.52	61.7	73.3	8.3	9.3	9.3	0.9	4.09	15.34	49.15	10.78	26.17	12.46	20.02
		0.4kW	6.83	83.2	93.3	14.7	15.5	15.5	0.8	4.22	18.82	27.72	13.04	25.79	15.28	18.56
		0.4kW (2)	7.02	63.0	73.8	9.1	9.4	9.4	0.3	4.23	18.49	29.15	13.41	26.18	16.31	19.09
		0.6kW	10.26	84.4	92.8	15.5	15.4	15.4	-0.1	4.19	22.36	29.12	15.86	24.44	16.67	20.62
		0.8kW	13.67	82.6	91.3	14.1	14.9	14.9	0.8	4.19	23.20	34.61	17.24	29.23	13.92	21.79
		0.8kW (2)	13.67	84.0	91.6	15.3	15.0	15.0	-0.4	4.19	23.87	37.42	18.69	30.59	15.95	23.41
		1.0kW	17.12	82.2	91.0	14.1	14.8	14.8	0.7	4.20	23.52	35.45	16.60	34.38	7.07	23.27
11/8/2022	Full Bundle, Preheater ON	0.6kW	10.23	67.0	73.4	8.7	9.3	9.3	0.6	4.18	22.76	31.97	15.31	23.26	15.43	20.64
		0.8kW	13.67	69.6	74.2	8.7	9.6	9.6	0.9	4.22	24.82	35.81	17.25	27.01	14.00	22.24
11/9/2022	Partial Bundle (Box 1), Preheater ON, Normal Charge (corrected)	0.2kW	3.39	63.6	74.7	8.7	9.5	9.5	0.8	3.55	17.31	-	9.95	-	10.85	13.05
		0.4kW	6.80	63.2	73.0	8.2	9.0	9.0	0.7	3.82	21.56	-	15.02	-	18.20	18.66
		0.6kW	10.22	63.6	73.5	8.3	9.1	9.1	0.7	3.81	22.25	-	18.91	-	18.26	19.92
11/10/2022		0.8kW	13.59	67.9	73.9	8.9	8.7	8.7	-0.2	3.78	22.72	-	24.69	-	16.67	20.94
		0.9kW	15.30	68.0	73.2	8.6	8.3	8.3	-0.3	3.87	22.51	-	25.58	-	13.48	19.89
		1.0kW	17.01	69.6	75.3	8.8	9.1	9.1	0.3	3.87	23.36	-	26.56	-	10.70	19.41
		1.1kW	18.76	70.3	74.8	9.1	8.9	8.9	-0.2	3.88	21.56	-	24.84	-	5.15	16.23
11/11/2022	Single Tube (No. 5), FLOODED Tests, Variable Autotransformer	50%	9.50	79.9	75.9	8.5	10.9	8.6	2.4	5.70	-	-	-	-	7.34	7.34
		60%	13.39	80.7	76.0	8.6	10.9	8.7	2.3	5.58	-	-	-	-	9.21	9.21
		70%	17.93	81.8	75.5	8.6	10.8	8.6	2.2	5.61	-	-	-	-	11.10	11.10
		80%	22.90	83.0	76.2	8.6	11.0	8.8	2.4	5.57	-	-	-	-	12.30	12.30
		90%	28.60	78.8	75.9	6.2	10.9	8.5	4.7	5.71	-	-	-	-	11.99	11.99
		100%	35.19	81.3	76.4	6.5	11.1	8.8	4.6	5.49	-	-	-	-	13.46	13.46
PHASE 4 - R134a, circular cone nozzles, square pitch, Tube-B evaporator tubes (Bundle 4)																
11/22/2022	Preheater OFF	0.2kW	3.40	444.8	413.9	9.3	9.9	9.3	0.7	4.70	6.44	6.19	5.65	6.00	5.22	5.90
	Full Bundle, Preheater ON, Normal Charge	0.4kW	6.81	443.6	414.7	8.1	10.0	8.1	1.9	4.67	3.62	3.63	3.52	3.53	3.34	3.53
		0.4kW (2)	6.84	449.4	419.5	9.1	10.3	9.1	1.2	4.62	5.63	5.66	5.39	5.47	5.00	5.43
		0.6kW	10.23	443.0	414.1	8.0	9.9	8.0	2.0	4.66	4.92	4.95	4.82	4.78	4.54	4.80
		0.6kW (2)	10.25	444.1	415.4	8.8	10.0	8.8	1.2	4.66	7.55	7.61	7.28	7.34	6.66	7.29
11/23/2022		0.8kW	13.62	439.7	416.4	8.5	10.1	8.5	1.6	4.65	7.47	7.44	7.07	7.49	6.67	7.23
		0.8kW (2)	13.68	441.7	417.0	9.4	10.1	9.4	0.7	4.59	14.28	14.65	13.41	14.51	10.89	13.55
		1.0kW	17.09	434.9	414.3	8.7	9.9	8.7	1.2	4.64	11.19	11.41	10.69	10.20	6.12	9.92
		1.0kW (2)	17.10	435.5	415.7	8.0	10.1	8.0	2.0	4.66	7.23	7.20	6.92	6.79	5.16	6.66
		1.2kW	20.49	430.8	418.9	8.9	10.3	8.9	1.4	4.53	10.94	11.37	9.79	7.25	2.79	8.43

Date	Test Condition	Power Setting	Heat Flux $[kW/m^2]$	Pressure [kPa] P_{inlet}	Pressure [kPa] P_{box}	Temperature [°C] T_{inlet}	Temperature [°C] T_{sat}	Temperature [°C] T_{ref}	Temperature [°C] Subcooling	Flow Rate [kg/min]	Heat Transfer Coefficient $[kW/m^2\text{-}K]$ Row 1	Row 2	Row 3	Row 4	Row 5	Overall
PHASE 4 - R134a, circular cone nozzles, square pitch, Tube-B evaporator tubes (Bundle 4)																
11/28/2022	Full Bundle, Preheater ON, Normal Charge	0.2kW	3.52	348.4	317.2	1.2	2.2	1.2	1.1	4.64	5.62	3.91	4.01	3.63	4.00	4.23
		0.4kW	6.83	347.5	318.0	0.5	2.3	0.5	1.8	4.62	3.77	3.78	3.62	3.72	3.52	3.68
		0.4kW (2)	6.83	348.6	319.4	1.0	2.4	1.0	1.4	4.61	5.04	5.04	4.77	4.94	4.59	4.88
		0.6kW	10.23	343.5	318.5	0.5	2.3	0.5	1.9	4.65	5.29	5.30	5.11	5.20	4.94	5.17
		0.6W (2)	10.25	343.9	319.1	1.4	2.4	1.4	1.0	4.63	10.80	10.85	9.79	10.71	9.12	10.25
		0.8kW	13.64	331.7	315.2	0.4	2.0	0.4	1.6	4.66	7.87	7.70	7.46	7.68	7.06	7.55
		0.8kW (2)	13.72	335.0	318.3	1.6	2.3	1.6	0.7	4.61	17.74	18.48	16.33	19.16	13.52	17.05
		1.0kW	17.13	330.5	317.8	1.0	2.3	1.0	1.3	4.66	11.39	11.54	10.81	10.51	6.34	10.12
		1.0kW (2)	17.11	325.6	315.0	-0.3	2.0	-0.2	2.3	4.68	6.83	6.71	6.49	6.56	5.13	6.34
PHASE 4 - R1234ze(E), circular cone nozzles, square pitch, Tube-B evaporator tubes (Bundle 4)																
12/6/2022	Full Bundle, Preheater ON, Normal Charge	0.2kW	3.41	323.8	308.7	8.8	9.8	8.8	1.0	4.59	3.37	3.31	3.06	3.13	3.01	3.18
		0.4kW	6.85	331.7	312.5	8.9	10.2	8.9	1.3	4.57	4.65	4.66	4.44	4.53	4.25	4.50
		0.4kW (2)	6.84	332.4	313.3	9.2	10.3	9.2	1.1	4.57	5.32	5.35	5.04	5.19	4.81	5.14
		0.6kW	10.26	326.3	311.8	8.3	10.1	8.3	1.8	4.64	4.81	4.84	4.65	4.30	4.27	4.58
		0.6kW (2)	10.25	328.7	313.5	9.2	10.3	9.2	1.1	4.65	7.35	7.58	7.06	6.68	5.94	6.92
		0.8kW	13.65	331.4	311.9	8.8	10.1	8.8	1.4	4.65	7.56	7.69	7.23	6.60	4.23	6.66
		0.8kW (2)	13.71	333.0	313.1	9.3	10.3	9.3	0.9	4.63	9.98	10.51	9.55	9.24	4.61	8.78
		1.0kW	17.08	327.6	310.5	8.5	10.0	8.6	1.5	4.66	8.36	8.63	7.80	7.03	2.62	6.89
12/7/2022		1.0kW (2)	17.08	325.8	312.6	9.2	10.2	9.2	1.1	4.77	9.78	10.48	8.86	8.52	2.69	8.06
		1.2kW	20.54	322.2	311.0	8.4	10.1	8.4	1.7	4.75	8.30	8.45	6.84	5.08	1.54	6.04
	Full Bundle, Preheater ON, Normal Charge	0.2kW	3.54	259.9	228.8	0.1	1.3	0.1	1.2	4.47	3.23	2.77	2.78	2.60	2.75	2.83
		0.4kW	6.83	269.0	235.7	0.8	2.1	0.8	1.3	4.66	4.37	4.34	4.12	4.19	3.96	4.19
		0.4kW (2)	6.84	270.2	236.5	1.1	2.2	1.1	1.1	4.69	5.03	5.03	4.73	4.85	4.51	4.83
		0.6kW	10.26	268.1	238.0	0.5	2.4	0.5	1.9	4.56	4.50	4.52	4.32	4.01	3.93	4.26
		0.6kW (2)	10.26	269.0	238.2	1.1	2.4	1.1	1.3	4.53	6.21	6.26	5.92	5.50	5.01	5.78
		0.8kW	13.64	261.2	238.4	0.8	2.4	0.8	1.7	4.71	6.41	6.45	6.09	5.53	4.04	5.70
		0.8kW (2)	13.69	263.3	239.2	1.7	2.5	1.7	0.8	4.68	10.47	10.99	9.74	9.74	4.80	9.15
		1.0kW	17.12	248.3	237.4	0.3	2.3	0.3	2.0	4.70	6.71	6.73	6.20	5.48	2.38	5.50
12/8/2022		1.0kW (3)	17.10	248.9	237.4	1.1	2.3	1.1	1.2	4.66	9.52	9.74	8.50	7.93	2.36	7.61
		1.2kW	20.49	246.9	237.3	0.4	2.3	0.4	1.9	4.67	7.83	7.79	6.18	4.89	1.35	5.61
	Full Bundle, Preheater ON, Normal Charge	0.2kW	3.53	184.7	170.4	-7.4	-6.6	-7.4	0.8	4.69	5.79	4.27	4.14	4.02	4.15	4.47
		0.4kW	6.85	192.7	170.6	-7.5	-6.6	-7.5	1.0	4.36	6.24	6.00	5.42	5.97	5.41	5.81
		0.4kW (2)	6.83	195.5	169.8	-8.0	-6.7	-8.0	1.3	4.25	4.80	4.66	4.32	4.64	4.28	4.54
		0.6kW	10.27	186.7	171.4	-7.9	-6.4	-7.9	1.5	4.82	5.75	5.81	5.37	5.66	5.44	5.61
		0.6kW (2)	10.25	187.7	171.9	-7.3	-6.4	-7.3	0.9	4.80	8.52	8.77	7.81	8.41	7.78	8.26
12/9/2022		0.8kW	13.65	197.1	172.3	-8.2	-6.3	-8.2	1.9	4.47	5.94	5.87	5.49	5.05	4.06	5.28
		0.8kW (2)	13.66	198.8	173.2	-7.3	-6.2	-7.3	1.2	4.46	8.90	9.05	8.03	7.80	4.77	7.71
		1.0kW	17.08	183.9	171.9	-8.3	-6.4	-8.3	2.0	4.74	7.00	6.87	6.28	5.71	2.81	5.74
		1.0kW (2)	17.13	186.4	173.0	-7.2	-6.2	-7.2	1.0	4.74	11.66	12.32	10.27	10.10	3.30	9.53
		1.1kW	18.85	184.7	170.8	-8.6	-6.5	-8.6	2.0	4.62	7.19	7.13	6.24	5.21	1.91	5.53

Date	Test Condition	Power Setting	Heat Flux $[kW/m^2]$	Pressure [kPa] P_{inlet}	P_{box}	Temperature [°C] T_{inlet}	T_{sat}	T_{ref}	Subcooling	Flow Rate [kg/min]	Heat Transfer Coefficient $[kW/m^2\text{-}K]$ Row 1	Row 2	Row 3	Row 4	Row 5	Overall
PHASE 4 - R1234ze(E), circular cone nozzles, square pitch, Tube-B evaporator tubes (Bundle 4)																
1/5/2023	Full Bundle, Preheater ON, Normal Charge	0.4kW	6.79	441.2	311.1	9.1	10.1	9.1	1.0	4.72	7.49	7.12	6.81	7.43	6.37	7.05
		0.4kW (2)	6.74	440.1	310.7	8.8	10.0	8.8	1.2	4.73	5.87	5.60	5.41	5.78	5.11	5.55
		0.6kW	10.19	436.6	310.1	8.4	10.0	8.4	1.6	4.60	6.27	5.95	5.89	6.38	5.57	6.01
		0.6kW (2)	10.17	440.1	312.3	9.1	10.2	9.1	1.1	4.57	8.57	8.01	7.96	8.84	7.47	8.17
		0.8kW	13.60	439.8	311.1	8.7	10.1	8.7	1.4	4.62	8.61	8.19	8.18	8.85	7.35	8.24
		0.8kW (2)	13.60	441.7	312.1	9.0	10.2	9.1	1.1	4.60	10.01	9.55	9.47	10.39	8.16	9.52
		1.0kW	16.95	438.6	310.7	7.8	10.0	7.9	2.2	4.75	6.77	6.50	6.39	6.81	5.60	6.42
		1.0kW (2)	16.97	442.7	313.8	8.8	10.3	8.8	1.6	4.66	8.82	8.56	8.36	8.76	6.21	8.14
1/6/2023	Full Bundle, Preheater ON, Normal Charge	0.2kW	3.39	262.4	134.4	-14.3	-12.6	-14.3	1.7	2.61	2.35	2.24	2.18	2.20	2.14	2.22
		0.4kW	6.77	266.9	137.4	-13.4	-12.0	-13.4	1.4	2.64	5.52	5.29	5.07	5.49	4.85	5.24
		0.6kW	10.17	266.4	136.0	-13.8	-12.3	-13.7	1.5	2.99	7.35	6.66	6.38	7.00	6.02	6.68
		0.8kW	13.53	270.4	139.8	-13.0	-11.6	-13.0	1.4	3.01	9.84	8.67	8.31	8.90	6.04	8.35
		1.0kW	16.97	277.1	144.0	-11.7	-10.9	-11.7	0.9	3.18	16.48	14.15	13.77	10.46	1.44	11.26
PHASE 4 - R1233zd(E), circular cone nozzles, square pitch, Tube-B evaporator tubes (Bundle 4)																
1/10/2023	Full Bundle, Preheater ON, Normal Charge	0.2kW	3.39	84.3	93.5	14.3	14.7	14.7	0.4	4.28	12.08	8.42	7.53	6.79	6.55	8.27
		0.4kW	6.79	83.4	93.9	13.9	14.9	14.9	0.9	4.04	19.95	13.78	12.62	12.38	10.20	13.78
		0.4kW (2)	6.80	84.3	94.1	14.9	14.9	14.9	0.1	4.06	21.51	15.35	14.43	15.24	12.43	15.79
		0.6kW	10.18	83.8	92.6	14.7	14.6	14.6	-0.1	3.91	25.06	16.71	16.08	16.15	11.60	17.12
		0.6kW (2)	10.20	80.8	91.5	13.5	14.3	14.3	0.8	3.94	22.87	14.17	12.96	9.02	5.36	12.87
1/12/2023	Full Bundle, Preheater ON, Increased Charge	0.6kW	10.13	80.6	92.7	14.6	14.6	14.6	0.0	3.97	16.21	9.58	9.73	6.76	4.57	9.37
		0.6kW (2)	10.15	65.2	74.5	9.6	8.9	8.9	-0.7	3.94	24.00	15.04	15.05	14.51	12.42	16.20
		0.6kW (3)	10.13	61.8	73.9	7.9	8.6	8.6	0.7	3.90	21.48	14.39	13.97	12.26	10.53	14.53
		0.6kW (4)	10.18	62.8	74.1	8.8	8.7	8.7	-0.1	3.60	23.89	15.75	15.69	15.21	11.98	16.51
		0.8kW	13.54	79.2	92.3	14.1	14.5	14.5	0.4	3.78	19.68	10.95	11.41	6.08	3.74	10.37
		0.8kW (2)	13.55	78.6	92.6	14.8	14.6	14.6	-0.3	3.59	20.58	12.15	12.87	8.74	4.40	11.75
		0.8kW (3)	13.59	65.9	75.7	9.6	9.2	9.2	-0.4	3.80	24.52	15.63	15.99	13.35	6.05	15.11
		0.8kW (4)	13.61	66.6	75.7	10.1	9.2	9.2	-0.9	3.70	24.74	16.88	17.73	15.81	9.94	17.02
		0.8kW (5)	13.59	65.8	75.5	9.3	9.2	9.2	-0.1	3.95	24.39	16.23	16.39	13.96	4.73	15.14
1/13/2023	Full Bundle, Preheater ON, Increased Charge	0.6kW	10.15	49.9	63.9	4.1	4.9	4.9	0.8	3.41	15.60	10.40	10.80	10.06	8.50	11.07
		0.6kW (2)	10.17	52.0	64.1	4.7	5.0	5.0	0.3	3.36	18.38	11.51	12.21	10.96	7.23	12.06
		0.8kW	13.54	53.3	64.3	5.0	5.0	5.0	0.0	3.72	19.95	11.01	10.05	4.44	1.71	9.43
		0.8kW (2)	13.58	51.2	63.9	3.5	4.8	4.8	1.3	3.73	19.71	12.31	11.95	9.48	6.14	11.92
1/16/2023	Full Bundle, Preheater ON, Normal Charge	0.4kW	6.77	83.1	94.5	14.8	14.8	14.8	0.0	3.85	16.34	10.90	9.20	8.71	6.99	10.43
		0.4kW (2)	6.76	83.4	94.8	14.6	14.9	14.9	0.3	3.85	18.78	12.31	10.68	10.42	8.42	12.12
		0.6kW	10.16	83.6	95.0	15.0	15.0	15.0	-0.1	3.86	20.86	12.72	12.65	11.11	8.27	13.12
		0.6kW (2)	10.12	82.8	94.1	13.7	14.7	14.7	1.0	3.86	21.46	13.24	13.39	12.08	9.36	13.91
		0.6kW (3)	10.17	83.1	94.4	16.0	14.8	14.8	-1.2	3.86	21.98	13.64	13.61	11.95	8.80	13.99
		0.8kW	13.56	82.1	93.7	14.5	14.6	14.6	0.1	3.81	22.46	13.22	12.06	6.83	3.96	11.70
		0.8kW (2)	13.56	82.7	94.3	16.1	14.8	14.8	-1.3	3.81	22.80	13.50	12.14	6.47	3.61	11.70
		0.8kW (3)	13.58	82.5	94.0	14.0	14.7	14.7	0.7	3.81	23.03	14.15	12.69	7.74	4.44	12.41

Date	Test Condition	Power Setting	Heat Flux [kW/m^2]	Pressure [kPa] P_{inlet}	Pressure [kPa] P_{box}	Temperature [°C] T_{inlet}	T_{sat}	T_{ref}	Subcooling	Flow Rate [kg/min]	Heat Transfer Coefficient [kW/m^2-K] Row 1	Row 2	Row 3	Row 4	Row 5	Overall
PHASE 4 - R1234ze(E), circular cone nozzles, square pitch, Tube-B evaporator tubes (Bundle 4)																
1/27/2023	Full Bundle, Preheater ON, Normal Charge	0.2kW	3.37	248.6	237.5	1.7	2.3	1.7	0.6	4.71	10.57	7.98	7.51	7.76	7.12	8.19
		0.4kW	6.77	249.4	239.7	1.3	2.6	1.3	1.2	4.73	5.67	5.47	5.28	5.55	4.97	5.39
		0.4kW (2)	6.78	248.8	239.2	1.0	2.5	1.0	1.5	4.75	4.61	4.47	4.35	4.51	4.10	4.41
		0.4kW (3)	6.76	252.3	242.3	2.3	2.9	2.3	0.6	4.70	14.87	12.58	11.97	13.27	10.90	12.72
		0.6kW	10.15	243.2	238.7	1.0	2.5	1.0	1.5	4.75	6.33	6.26	6.12	6.25	5.17	6.03
		0.6kW (2)	10.17	244.8	239.6	1.4	2.6	1.4	1.1	4.72	7.92	7.84	7.70	7.76	5.97	7.44
1/28/2023	Full Bundle, Preheater ON, Normal Charge	0.6kW (3)	10.12	249.4	242.2	2.2	2.9	2.2	0.7	4.68	13.77	12.21	12.21	12.48	8.54	11.84
		0.8kW	13.58	244.3	239.5	1.2	2.6	1.2	1.4	4.65	8.16	7.84	7.44	6.06	3.50	6.60
		0.8kW (2)	13.54	247.6	241.3	2.0	2.8	2.0	0.8	4.65	12.37	11.51	11.13	7.48	3.21	9.14
		0.8kW (3)	13.57	247.4	241.1	1.8	2.7	1.8	0.9	4.67	11.30	10.59	10.17	6.98	3.02	8.41
		1.0kW	16.92	245.2	240.5	1.1	2.7	1.1	1.6	4.65	8.26	7.89	6.52	3.59	1.63	5.58
		1.0kW (2)	16.98	246.5	240.6	1.6	2.7	1.6	1.1	4.63	10.64	10.10	7.98	3.55	1.54	6.76
		1.0kW (3)	16.92	248.3	241.7	2.1	2.8	2.1	0.7	4.59	14.29	12.45	9.43	3.38	1.52	8.21
1/30/2023	Full Bundle, Preheater ON, Normal Charge	1.2kW	20.31	249.5	241.5	2.2	2.8	2.2	0.6	4.71	15.48	11.07	7.05	2.31	1.04	7.39
		0.4kW	6.74	179.5	172.1	-7.9	-6.3	-7.9	1.5	4.78	4.73	4.52	4.24	4.53	4.20	4.45
		0.4kW (2)	6.78	180.4	173.5	-7.2	-6.1	-7.2	1.1	4.78	7.07	6.51	6.17	6.66	6.14	6.51
		0.6kW	10.19	172.3	172.0	-8.1	-6.3	-8.1	1.8	4.68	5.62	5.25	5.25	5.47	5.11	5.34
		0.6kW (2)	10.14	177.1	174.0	-6.7	-6.0	-6.7	0.6	4.67	14.88	12.87	12.91	14.67	12.06	13.48
		0.8kW	13.56	179.1	179.1	-6.5	-5.3	-6.5	1.2	4.62	9.83	9.14	9.16	8.80	5.68	8.52
		0.8kW (2)	13.54	172.5	172.8	-7.6	-6.2	-7.6	1.4	4.66	8.45	8.08	8.04	7.76	5.16	7.50
		0.8kW (3)	13.55	173.5	173.3	-7.2	-6.2	-7.2	1.0	4.65	10.65	10.04	10.13	9.81	6.16	9.36
		1.0kW	16.94	173.0	173.3	-8.0	-6.1	-8.0	1.9	4.71	7.52	7.32	7.25	6.02	3.01	6.22
		1.0kW (2)	16.92	176.0	171.1	-7.1	-6.5	-7.1	0.6	4.70	17.08	16.85	16.36	10.80	3.58	12.94
1/31/2023	Full Bundle, Preheater ON, Normal Charge	0.8kW	13.50	242.5	238.1	1.3	2.4	1.3	1.1	4.67	9.92	9.22	8.86	7.28	3.65	7.78
		0.8kW (2)	13.55	253.1	243.5	3.6	3.0	2.7	-0.5	4.60	18.53	15.84	15.46	8.52	3.69	12.41
		0.8kW (3)	13.59	251.9	240.7	3.5	2.7	2.3	-0.8	4.64	17.73	14.91	13.86	7.50	3.28	11.46
		0.8kW (4)	13.53	238.5	239.2	-0.2	2.5	-0.2	2.7	4.61	4.50	4.42	4.27	3.85	2.46	3.90
		0.8kW (5)	13.60	234.6	237.2	-1.5	2.3	-1.5	3.8	4.70	3.32	3.23	3.18	2.90	2.00	2.92

Appendix B

Test Local Temperature Data

Reported in this section are the summary average local temperature data for all tests performed during the experimental campaign using pure refrigerants. Though a large majority of these data were presented in Chapter 4: Results and Discussion, some were not presented because of invalid results due to testing irregularities such as equipment malfunction, refrigerant contamination, or operator error. All data are presented in the chronological order in which they were collected such that the Phase 5 data appear first, followed by Phases 1, 2, 3, and 4. Each table contains 24 columns, the first of which indicates the day on which the data were collected, and the remaining 23 of which indicate the average local temperature reported by each thermocouple in each instrumented location throughout the tube bundle over the course of the test. A diagram of the thermocouple locations within the bundle can be found in Figure 4.1. Tubes 1, 2, and 5 were all instrumented in the top, side, and bottom locations around the outer surface circumference. Tube 3 was instrumented in the side and bottom locations while Tube 4 was instrumented in the top and side locations. Tubes 6, 7, 8, 9, and 10 were all instrumented in the bottom location while Tubes 11, 12, 13, 14, and 15 were all instrumented in the top location. All dates are presented in the [MM/DD/YYYY] format and all temperatures are in units of [°C]. The data in these tables are split identically to the data contained in Appendix A such that each table in this section corresponds exactly to a matching table containing the test summary data in that section.

Date	Row 1					Row 2					Row 3					Row 4					Row 5				
	Tube 1			Tube 6	Tube 11	Tube 2			Tube 7	Tube 12	Tube 3		Tube 8	Tube 13	Tube 4		Tube 9	Tube 14	Tube 5			Tube 10	Tube 15
	T_{top}	T_{side}	T_{bottom}	T_{bottom}	T_{top}	T_{top}	T_{side}	T_{bottom}	T_{bottom}	T_{top}	T_{side}	T_{bottom}	T_{bottom}	T_{top}	T_{top}	T_{side}	T_{bottom}	T_{top}	T_{top}	T_{side}	T_{bottom}	T_{bottom}	T_{top}
PHASE 5 - R134a, deflected flat spray nozzles, triangular pitch, Tube-C condenser tubes (Bundle 1)																								
2/12/2021	24.7	24.7	24.7	5.3	7.8	24.7	24.7	24.7	7.2	6.2	24.7	24.7	7.6	6.5	24.7	24.7	6.6	6.2	24.5	24.7	24.7	6.5	6.1
	24.7	24.7	24.7	5.1	7.5	24.7	24.7	24.7	7.0	5.9	24.7	24.7	7.4	6.3	24.7	24.7	6.3	6.0	24.5	24.7	24.7	6.3	5.9
	24.7	24.7	24.7	4.5	7.0	24.7	24.7	24.7	6.4	5.4	24.7	24.7	6.9	5.7	24.7	24.7	5.8	5.5	24.5	24.7	24.7	5.9	5.4
	24.7	24.7	24.7	4.1	6.5	24.7	24.7	24.7	6.0	4.9	24.7	24.7	6.3	5.2	24.7	24.7	5.3	5.0	24.5	24.7	24.7	5.4	4.9
	24.7	24.7	24.7	3.4	5.8	24.7	24.7	24.7	5.3	4.3	24.7	24.7	5.6	4.6	24.7	24.7	4.6	4.4	24.5	24.7	24.7	4.8	4.3
	24.7	24.7	24.7	2.8	5.2	24.7	24.7	24.7	4.7	3.7	24.7	24.7	5.0	4.0	24.7	24.7	4.1	3.8	24.5	24.7	24.7	4.2	3.7
	24.7	24.7	24.7	2.7	5.0	24.7	24.7	24.7	4.6	3.5	24.7	24.7	4.8	3.8	24.7	24.7	3.9	3.6	24.5	24.7	24.7	4.0	3.5
2/26/2021	3.6	3.7	3.9	3.7	4.1	35.6	35.6	35.7	7.4	3.4	3.7	3.9	4.0	3.6	3.4	3.4	4.6	3.4	3.4	3.4	3.3	3.4	3.4
	5.3	5.3	5.5	5.4	5.9	5.0	5.0	5.0	5.0	5.0	5.4	5.6	5.7	5.3	5.0	5.0	6.0	5.0	5.0	5.0	5.0	5.0	5.0
	6.0	6.1	6.5	6.3	7.2	5.5	5.5	5.5	5.5	5.5	6.4	6.6	6.9	6.1	5.5	5.5	17.4	5.5	5.5	5.5	5.5	5.5	5.5
	4.6	4.5	5.1	4.9	5.8	4.1	4.1	4.1	4.1	4.0	5.1	5.4	5.5	4.6	4.1	4.1	4.1	4.1	4.1	4.1	4.0	4.1	4.1
	5.7	6.2	6.5	6.2	7.5	5.0	5.0	5.0	4.9	4.9	6.5	6.8	7.0	6.0	5.0	5.0	5.0	5.0	5.0	5.0	4.9	5.0	5.0
	6.4	6.9	7.2	6.9	8.6	5.3	5.3	5.3	5.3	5.3	7.2	7.5	7.9	6.7	5.3	5.3	5.3	5.3	5.3	5.3	5.3	5.3	5.3
	6.9	7.3	7.7	7.3	9.3	5.4	5.4	5.4	5.3	5.3	7.7	8.2	8.5	7.4	5.4	5.4	5.4	5.4	5.4	5.4	5.3	5.4	5.4
	7.2	7.7	8.0	7.5	10.1	5.4	5.4	5.4	5.4	5.3	8.1	8.6	8.9	8.1	5.4	5.4	5.4	5.4	5.4	5.4	5.4	5.4	5.4
3/1/2021	6.6	6.5	6.7	6.6	7.0	6.3	6.3	6.3	6.3	6.3	6.6	6.9	7.0	6.3	6.3	6.3	6.3	6.3	6.5	6.7	7.3	6.8	6.5
	6.5	6.6	6.6	6.6	7.0	6.2	6.2	6.2	6.2	6.2	6.5	6.8	6.9	6.3	6.3	6.2	6.2	6.2	6.4	6.6	7.2	6.7	6.4
	5.5	5.5	5.7	5.7	6.7	4.9	4.9	4.9	4.9	4.9	5.7	6.2	6.3	4.9	4.9	4.9	4.9	4.9	5.7	6.3	7.1	6.0	5.3
	7.1	7.3	7.5	7.5	8.6	6.2	6.2	6.2	6.2	6.1	7.2	7.9	8.1	6.2	6.2	6.2	6.2	6.2	7.6	9.0	9.9	7.6	6.9
	7.7	8.0	8.1	8.1	9.7	6.4	6.4	6.4	6.4	6.4	8.0	8.7	8.9	6.4	6.4	6.4	6.4	6.4	9.0	11.2	12.0	8.7	7.7
	8.6	8.9	8.9	8.8	11.4	6.9	6.9	6.9	6.9	6.8	9.4	10.3	9.8	6.9	6.9	6.9	6.9	6.9	10.8	14.8	15.8	6.9	9.3
	9.1	9.4	9.4	9.3	13.1	7.0	7.0	7.0	7.0	7.0	10.1	11.1	10.5	7.0	7.0	7.0	7.0	7.0	20.5	25.4	29.6	7.0	7.0
3/2/2021	9.6	9.8	9.9	9.8	10.0	9.4	9.4	9.4	9.4	9.4	9.7	10.0	10.0	9.4	9.4	9.4	9.4	9.4	9.7	9.8	10.0	9.9	9.7
	8.6	8.6	8.8	8.9	9.5	8.1	8.1	8.1	8.1	8.1	8.9	9.4	9.5	8.1	8.1	8.1	8.1	8.1	9.2	9.5	9.5	9.2	8.7
	2.5	2.8	3.4	3.1	3.6	1.8	1.8	1.8	1.8	1.7	2.7	3.4	3.8	1.8	1.8	1.8	1.8	1.8	3.0	3.4	3.3	3.4	2.8
	2.4	2.8	3.4	3.1	4.1	1.3	1.3	1.3	1.3	1.3	2.6	3.5	3.9	1.3	1.4	1.4	1.3	1.3	3.3	3.7	3.5	3.2	3.0
	2.5	3.0	3.5	3.2	4.8	1.2	1.2	1.1	1.1	1.1	2.9	3.8	4.1	1.2	1.2	1.2	1.2	1.2	6.0	6.9	7.9	1.2	3.8
	3.1	3.6	4.2	3.8	6.3	1.5	1.5	1.5	1.5	1.4	3.6	4.6	4.9	1.5	1.5	1.5	1.5	1.5	1.5	1.5	1.4	1.5	3.2
	3.7	4.2	4.7	4.4	10.0	2.1	2.1	2.0	2.0	2.0	6.9	8.0	5.6	2.1	2.1	2.1	2.1	2.1	2.1	2.1	2.0	2.1	2.1
3/12/2021	4.3	4.4	4.5	4.5	4.5	4.1	4.1	4.1	4.1	4.1	4.4	4.6	4.7	4.1	4.1	4.2	4.2	4.1	5.9	5.8	5.7	5.8	6.0
	3.5	3.6	4.1	3.9	4.2	3.0	3.0	3.0	3.0	3.0	3.7	4.2	4.3	3.0	3.0	3.0	3.0	3.0	4.0	4.3	4.4	4.1	3.6
	4.0	4.0	4.2	4.4	4.8	3.5	3.5	3.5	3.5	3.5	4.2	4.7	4.7	3.5	3.5	3.5	3.5	3.5	4.3	4.5	4.6	4.5	4.0
	3.5	3.9	4.4	4.2	4.9	2.8	2.8	2.8	2.8	2.8	3.8	4.5	4.7	2.8	2.8	2.8	2.8	2.8	4.4	5.0	4.8	4.4	3.8
	3.5	3.9	4.4	4.1	5.1	2.4	2.4	2.4	2.4	2.4	3.8	4.6	4.9	2.4	2.4	2.4	2.4	2.4	4.8	4.8	4.7	4.2	4.0
	3.7	4.2	4.7	4.3	5.7	2.3	2.3	2.3	2.3	2.3	4.0	4.9	5.3	2.3	2.3	2.3	2.3	2.3	6.4	5.4	5.5	4.5	4.3
3/15/2021	11.7	11.8	12.0	11.9	12.1	11.5	11.5	11.5	11.5	11.5	11.8	12.0	12.0	11.5	11.5	11.5	11.5	11.5	11.8	11.9	12.0	11.9	11.7
	10.7	11.0	11.5	11.1	12.1	9.9	9.9	9.9	9.9	9.9	10.9	11.6	11.7	9.9	9.9	9.9	9.9	9.9	11.3	11.6	11.4	11.1	10.8
	10.9	11.4	11.8	11.4	12.7	9.8	9.8	9.8	9.8	9.8	11.2	12.0	12.2	9.8	9.8	9.8	9.8	9.8	12.8	12.1	12.1	11.4	11.3
	11.0	11.4	11.9	11.5	13.1	9.7	9.7	9.7	9.7	9.7	11.2	12.1	12.4	9.7	9.7	9.7	9.7	9.7	14.6	12.9	13.1	11.6	11.5
	11.1	11.6	12.0	11.6	13.2	9.7	9.7	9.7	9.7	9.7	11.7	12.5	12.6	9.7	9.7	9.7	9.7	9.7	21.6	19.9	21.4	11.9	11.7

Date	Row 1					Row 2					Row 3				Row 4				Row 5				
	Tube 1			Tube 6	Tube 11	Tube 2			Tube 7	Tube 12	Tube 3		Tube 8	Tube 13	Tube 4		Tube 9	Tube 14	Tube 5			Tube 10	Tube 15
	T_{top}	T_{side}	T_{bottom}	T_{bottom}	T_{top}	T_{top}	T_{side}	T_{bottom}	T_{bottom}	T_{top}	T_{side}	T_{bottom}	T_{bottom}	T_{top}	T_{top}	T_{side}	T_{bottom}	T_{top}	T_{top}	T_{side}	T_{bottom}	T_{bottom}	T_{top}
PHASE 5 - R134a, deflected flat spray nozzles, triangular pitch, Tube-C condenser tubes (Bundle 1)																							
3/16/2021	4.9	4.9	5.1	5.3	5.7	4.4	4.4	4.4	4.4	4.3	5.0	5.6	5.6	4.4	4.4	4.4	4.4	4.4	5.2	5.4	5.5	5.3	4.9
	2.9	3.2	3.8	3.5	4.1	2.1	2.1	2.1	2.1	2.1	3.1	3.8	4.0	2.1	2.1	2.1	2.1	2.1	3.5	3.8	3.7	3.5	3.1
	3.3	3.7	4.2	3.9	4.8	2.2	2.2	2.2	2.2	2.2	3.6	4.4	4.7	2.2	2.2	2.2	2.2	2.2	5.0	4.9	4.7	4.0	3.8
	4.3	4.8	5.3	4.9	5.9	3.1	3.0	3.0	3.0	3.0	4.6	5.5	5.8	3.1	3.1	3.1	3.1	3.1	6.9	6.0	6.1	5.0	4.9
	4.0	4.5	5.0	4.6	5.9	2.6	2.6	2.6	2.6	2.6	4.3	5.2	5.6	2.6	2.6	2.6	2.6	2.6	7.6	6.2	6.5	4.9	4.8
3/17/2021	6.1	6.4	6.9	6.6	7.3	5.3	5.3	5.3	5.3	5.2	6.3	6.9	7.2	5.3	5.3	5.3	5.3	5.3	6.8	7.1	6.9	6.8	6.2
	4.9	5.2	5.7	5.5	6.3	4.1	4.1	4.1	4.1	4.1	5.4	6.0	6.1	4.1	4.1	4.1	4.1	4.1	7.5	9.3	9.0	5.7	5.2
3/18/2021	6.0	6.2	6.4	6.2	6.4	5.8	5.8	5.8	5.8	5.8	6.1	6.4	6.4	5.8	5.8	5.8	5.8	5.8	7.3	7.4	7.3	7.5	7.3
	4.6	4.9	5.5	5.2	6.0	3.8	3.8	3.8	3.8	3.8	4.9	5.5	5.8	4.7	3.8	3.8	3.8	3.8	5.3	5.5	5.4	5.4	5.0
	4.1	4.5	5.0	4.7	5.6	3.0	3.0	3.0	3.0	3.0	4.4	5.3	5.5	4.2	3.0	3.0	3.0	3.0	5.5	5.2	5.2	5.0	4.9
	3.5	3.9	4.5	4.1	5.0	2.4	2.4	2.4	2.4	2.4	3.8	4.6	5.0	3.7	2.5	2.5	2.4	2.5	4.5	5.2	5.0	4.5	5.9
	4.7	5.1	5.6	5.2	6.6	3.3	3.3	3.3	3.3	3.2	5.0	6.0	6.3	5.0	3.3	3.3	3.3	3.3	7.2	6.9	6.8	10.9	13.7
PHASE 5 - R1234ze(E), deflected flat spray nozzles, triangular pitch, Tube-C condenser tubes (Bundle 1)																							
3/26/2021	17.9	18.0	18.1	18.0	17.8	17.7	17.7	17.7	17.7	17.7	17.9	18.0	18.1	17.9	17.7	17.7	17.7	17.7	18.0	17.9	17.9	17.9	17.9
	18.6	18.7	19.0	18.7	18.6	18.3	18.3	18.3	18.3	18.3	18.6	18.8	18.9	18.6	18.3	18.3	18.3	18.3	18.7	18.6	18.8	18.8	18.6
	19.2	19.4	19.8	19.3	19.3	18.7	18.6	18.7	18.6	18.6	19.1	19.5	19.7	19.1	18.6	18.7	18.6	18.6	19.2	19.2	19.5	19.6	19.1
	20.1	20.4	20.7	20.2	20.4	19.3	19.3	19.3	19.3	19.3	20.0	20.5	20.7	19.9	19.3	19.3	19.3	19.3	20.1	20.2	20.5	20.6	20.1
	20.9	21.3	21.6	21.1	21.4	20.0	20.0	20.0	20.0	20.0	20.8	21.5	21.6	20.7	20.0	20.0	20.0	20.0	21.1	21.2	21.4	21.5	21.0
	21.2	21.7	22.0	21.4	22.1	20.2	20.2	20.2	20.2	20.1	21.2	21.9	22.0	21.0	20.2	20.2	20.2	20.2	21.6	21.6	21.7	21.9	21.4
	21.6	22.1	22.4	21.9	22.9	20.4	20.4	20.4	20.4	20.4	21.6	22.3	22.5	21.5	20.4	20.4	20.4	20.4	22.3	22.2	22.1	22.2	22.0
	21.5	22.0	22.3	21.8	23.3	20.1	20.1	20.1	20.1	20.0	21.4	22.2	22.5	21.3	20.1	20.1	20.0	20.1	23.2	22.9	23.1	21.9	22.0
	22.0	22.5	22.8	22.3	24.2	20.4	20.4	20.4	20.4	20.4	22.0	22.8	23.1	22.0	20.4	20.4	20.4	20.4	26.6	25.6	26.4	22.5	22.7
	22.1	22.7	22.9	22.4	25.2	20.4	20.4	20.4	20.4	20.3	22.4	23.2	23.3	22.2	20.4	20.4	20.3	20.3	32.5	30.1	31.0	22.7	23.4
3/29/2021	10.4	10.4	10.5	10.4	10.3	10.4	10.5	10.5	10.5	10.5	10.3	10.5	10.5	10.3	10.5	10.5	10.4	10.3	10.4	10.3	10.4	10.4	10.3
	10.6	10.8	11.0	10.8	10.6	10.9	11.2	11.1	11.1	10.9	10.6	10.9	11.0	10.6	11.8	11.5	10.8	10.6	10.7	10.7	10.8	10.8	10.6
	10.9	11.1	11.4	11.0	11.1	11.6	11.8	11.5	11.9	11.2	10.9	11.3	11.3	10.8	13.9	13.4	11.1	10.8	10.9	11.0	11.2	11.4	10.8
	11.4	11.7	12.1	11.6	11.9	12.8	12.9	12.3	13.4	11.8	11.4	12.0	12.0	11.3	16.3	15.7	11.8	11.3	11.5	11.6	11.9	12.1	11.3
	11.5	11.9	12.3	11.8	12.2	12.9	12.8	12.3	15.3	12.1	11.5	12.2	12.3	11.4	18.3	17.6	12.0	11.5	11.8	11.8	12.1	12.3	11.5
	11.5	11.9	12.3	11.8	12.4	13.4	13.1	12.5	17.4	12.1	11.5	12.3	12.4	11.4	22.3	21.6	11.9	11.4	12.0	11.8	12.0	12.2	11.6
3/30/2021	1.5	1.5	1.6	1.5	1.4	1.5	1.6	1.6	1.7	1.6	1.4	1.6	1.6	1.4	2.2	2.0	1.5	1.4	1.6	1.5	1.5	1.5	1.4
	3.0	3.1	3.2	3.0	2.9	3.0	3.1	3.1	3.1	3.1	3.0	3.1	3.1	3.0	3.8	3.6	3.0	2.9	3.1	3.0	3.0	3.0	2.9
	3.4	3.7	4.1	3.6	3.9	28.5	29.3	29.2	5.9	3.9	3.4	4.0	4.1	3.2	10.1	9.6	4.1	3.6	3.5	3.5	3.9	4.1	3.3
	2.0	2.4	2.9	2.4	3.0	1.2	1.2	1.2	1.2	1.2	2.1	2.8	2.9	2.0	1.2	1.2	1.2	1.2	2.3	2.4	2.6	2.6	2.0
	2.8	3.2	3.8	3.3	4.2	1.8	1.8	1.8	1.8	1.8	3.0	3.9	4.0	2.8	1.8	1.8	1.8	1.8	3.4	3.3	3.6	3.7	3.1
	3.5	4.0	4.6	4.1	5.1	2.4	2.4	2.4	2.4	2.4	3.8	4.7	4.8	3.6	2.4	2.4	2.4	2.4	4.5	4.1	4.3	4.4	4.2
	4.2	4.7	5.2	4.8	6.2	2.9	2.9	2.9	2.9	2.9	4.5	5.4	5.6	4.3	2.9	2.9	2.9	2.9	6.1	5.2	5.4	5.1	5.1
	4.6	5.1	5.6	5.2	6.6	3.2	3.2	3.2	3.2	3.2	4.7	5.5	6.0	4.6	3.2	3.2	3.2	3.2	7.1	6.1	6.2	5.3	5.6

Date	Row 1					Row 2					Row 3				Row 4				Row 5				
	Tube 1			Tube 6	Tube 11	Tube 2			Tube 7	Tube 12	Tube 3		Tube 8	Tube 13	Tube 4		Tube 9	Tube 14	Tube 5			Tube 10	Tube 15
	T_{top}	T_{side}	T_{bottom}	T_{bottom}	T_{top}	T_{top}	T_{side}	T_{bottom}	T_{bottom}	T_{top}	T_{side}	T_{bottom}	T_{bottom}	T_{top}	T_{top}	T_{side}	T_{bottom}	T_{top}	T_{top}	T_{side}	T_{bottom}	T_{bottom}	T_{top}
PHASE 5 - R1234ze(E), deflected flat spray nozzles, triangular pitch, Tube-C condenser tubes (Bundle 1)																							
3/31/2021	-11.0	-10.9	-10.7	-10.9	-10.9	-11.1	-11.1	-11.1	-11.1	-11.1	-10.9	-10.8	-10.8	-10.9	-11.1	-11.1	-11.1	-11.1	-10.8	-10.9	-10.8	-10.8	-10.9
	-10.2	-10.1	-9.8	-10.0	-10.0	-10.5	-10.5	-10.5	-10.5	-10.5	-10.2	-9.8	-9.8	-10.2	-10.5	-10.5	-10.5	-10.5	-10.1	-10.1	-9.8	-9.7	-10.1
	-10.0	-9.8	-9.2	-9.6	-9.4	-10.4	-10.4	-10.4	-10.4	-10.4	-9.8	-9.3	-9.3	-9.9	-10.4	-10.4	-10.4	-10.4	-9.6	-9.5	-9.1	-9.3	-9.8
	-9.1	-8.8	-8.1	-8.7	-8.2	-9.6	-9.6	-9.6	-9.6	-9.6	-8.7	-8.0	-8.0	-8.8	-9.6	-9.6	-9.6	-9.6	-8.4	-8.3	-7.8	-8.1	-8.7
	-8.6	-8.3	-7.6	-8.1	-7.3	-9.3	-9.3	-9.3	-9.3	-9.3	-7.7	-7.2	-7.3	-7.7	-9.3	-9.3	-9.3	-9.3	-6.7	-6.5	-6.8	-7.8	-6.9
	-8.2	-7.9	-7.0	-7.5	-6.5	-8.9	-8.9	-8.9	-8.9	-8.9	-7.2	-6.7	-6.7	-6.8	-8.9	-8.9	-8.9	-8.9	-6.3	-5.9	-6.2	-7.2	18.8
	-7.4	-6.9	-6.0	-6.7	-5.4	-8.3	-8.3	-8.3	-8.3	-8.3	-6.3	-5.6	-5.9	-6.7	-8.3	-8.3	-8.3	-8.3	-4.7	-3.3	-3.3	-6.6	10.0
4/1/2021	2.2	2.3	2.4	2.3	2.2	2.1	2.1	2.1	2.1	2.1	2.2	2.4	2.4	2.2	2.1	2.1	2.1	2.1	2.3	2.2	2.3	2.3	2.2
	3.0	3.2	3.4	3.2	3.7	2.8	2.8	2.8	2.8	2.8	3.1	3.4	3.4	3.0	2.8	2.8	2.8	2.8	3.3	3.2	3.4	3.3	3.0
	3.9	4.1	4.5	4.2	5.3	3.5	3.5	3.5	3.5	3.5	4.7	5.1	4.5	4.0	3.5	3.5	3.5	3.5	6.6	6.3	6.5	4.5	4.4
	4.4	4.7	5.1	4.8	6.2	4.0	3.9	3.9	3.9	3.9	5.7	6.1	5.2	4.5	4.0	3.9	3.9	3.9	8.1	8.1	8.2	5.2	9.3
	4.8	5.1	5.5	5.1	5.9	4.2	4.2	4.2	4.2	4.2	4.9	5.5	5.5	4.7	4.2	4.2	4.2	4.2	5.2	5.3	5.6	5.3	4.9
	6.3	6.6	7.2	6.7	7.7	5.5	5.5	5.5	5.5	5.5	6.5	7.2	7.3	6.3	5.5	5.5	5.5	5.5	7.1	7.1	7.2	6.9	6.7
	5.6	6.0	6.6	6.1	7.3	4.7	4.7	4.7	4.7	4.7	5.9	6.6	6.8	5.7	4.7	4.7	4.7	4.7	7.0	6.9	6.9	6.4	6.7
	5.8	6.2	6.8	6.4	7.8	4.7	4.7	4.7	4.7	4.7	6.2	6.9	7.1	6.0	4.7	4.7	4.7	4.7	7.9	8.0	7.9	6.5	9.2
	6.2	6.7	7.1	6.7	7.9	4.8	4.8	4.8	4.8	4.8	6.3	7.2	7.4	6.2	4.8	4.8	4.8	4.8	8.1	7.4	7.9	6.6	6.9
	6.2	6.7	7.2	6.8	8.4	4.7	4.7	4.7	4.7	4.7	6.4	7.3	7.6	6.3	4.7	4.7	4.7	4.7	9.9	8.6	9.9	6.7	7.5
4/2/2021	10.7	10.8	10.9	10.8	10.7	10.6	10.6	10.6	10.6	10.6	10.7	10.9	10.8	10.7	10.6	10.6	10.6	10.6	10.8	10.7	10.7	10.8	10.7
	10.7	10.8	11.0	10.8	10.7	10.3	10.3	10.3	10.3	10.3	10.6	10.9	10.9	10.6	10.3	10.3	10.3	10.3	10.7	10.7	10.9	10.8	10.6
	10.8	11.0	11.3	10.9	11.1	10.2	10.2	10.3	10.2	10.2	10.8	11.2	11.2	10.6	10.3	10.2	10.2	10.2	10.8	10.9	11.2	11.1	10.7
	11.1	11.4	11.8	11.3	11.7	10.4	10.4	10.4	10.4	10.4	11.2	11.8	11.7	11.0	10.5	10.4	10.4	10.4	11.3	11.5	11.8	11.6	11.1
	11.4	11.7	12.1	11.6	12.3	10.5	10.5	10.5	10.5	10.5	11.4	12.1	12.1	11.2	10.5	10.5	10.5	10.5	11.7	11.8	12.0	11.9	11.4
	11.6	12.0	12.4	11.9	12.9	10.6	10.6	10.6	10.6	10.6	11.7	12.5	12.4	11.5	10.6	10.6	10.6	10.6	12.2	12.2	12.3	12.2	11.7
	11.8	12.3	12.7	12.2	13.9	10.6	10.6	10.6	10.6	10.6	11.9	12.7	12.8	11.8	10.6	10.6	10.6	10.6	13.0	12.7	12.9	12.3	12.1
	11.7	12.2	12.6	12.1	14.5	10.4	10.4	10.4	10.4	10.4	11.9	12.7	12.8	11.8	10.4	10.4	10.4	10.4	14.6	13.8	14.6	12.2	12.4
	12.1	12.6	13.0	12.5	15.5	10.6	10.6	10.6	10.6	10.6	12.3	13.1	13.4	12.2	10.6	10.6	10.6	10.6	17.8	16.2	17.7	12.5	13.3
	12.2	12.7	13.1	12.6	16.2	10.6	10.6	10.6	10.6	10.6	12.4	13.3	13.6	12.3	10.6	10.6	10.6	10.6	19.4	17.4	18.8	12.7	21.2
4/12/2021	3.7	3.8	4.0	3.8	3.7	5.3	5.6	5.2	4.3	4.0	3.7	3.9	3.9	3.6	6.6	6.4	4.0	3.6	3.8	3.7	3.8	3.8	3.6
	2.5	2.7	3.0	2.7	2.8	18.4	18.9	18.5	3.8	2.9	2.5	2.9	2.9	2.4	8.0	7.6	3.2	2.5	2.5	2.6	2.9	2.8	2.4
	3.7	4.0	4.4	3.9	4.2	17.0	17.2	16.3	5.7	4.3	3.7	4.3	4.3	3.6	10.6	10.1	4.3	3.8	3.8	4.0	4.3	4.3	3.6
	4.4	4.7	5.1	4.7	4.9	17.8	18.0	17.3	6.5	5.0	4.5	5.1	5.0	4.3	11.3	10.8	5.0	4.6	4.5	4.7	5.1	5.0	4.4
	3.7	4.0	4.4	3.9	4.3	26.2	26.7	25.8	6.3	4.3	3.7	4.4	4.4	3.5	12.5	12.0	4.3	3.9	3.8	4.0	4.4	4.3	3.6
4/13/2021	1.9	2.1	2.4	2.1	2.1	1.4	1.4	1.4	1.4	1.4	2.0	2.4	2.4	1.8	1.4	1.4	1.4	1.4	2.2	2.1	2.4	2.3	1.9
	2.7	3.0	3.4	3.0	3.3	2.0	2.0	2.0	2.0	2.0	2.8	3.4	3.3	2.5	2.0	2.0	2.0	2.0	3.2	3.0	3.4	3.3	2.7
PHASE 1 - R1234ze(E), circular cone nozzles, triangular pitch, Tube-C condenser tubes (Bundle 1)																							
5/13/2021	10.6	10.7	10.8	10.7	10.7	10.7	10.8	10.8	10.8	13.6	10.7	10.8	10.8	10.7	10.7	10.7	10.7	10.9	10.8	10.7	10.7	10.8	10.7
	11.0	11.2	11.5	11.2	11.1	11.1	11.3	11.4	11.5	18.5	11.1	11.4	11.4	11.1	11.4	11.3	11.2	12.1	11.2	11.3	11.3	11.3	11.0
	11.5	11.5	12.1	11.8	11.5	11.5	12.0	12.0	12.2	23.5	11.6	12.1	12.0	11.5	13.0	12.8	11.9	13.8	11.7	11.9	12.0	12.0	11.5
	10.8	10.8	11.4	11.1	10.9	10.4	10.4	10.4	10.4	10.4	10.9	11.4	11.3	10.7	10.4	10.4	10.4	10.4	11.0	11.3	11.4	11.3	10.8

Date	Row 1					Row 2					Row 3				Row 4				Row 5				
	Tube 1			Tube 6	Tube 11	Tube 2			Tube 7	Tube 12	Tube 3		Tube 8	Tube 13	Tube 4		Tube 9	Tube 14	Tube 5			Tube 10	Tube 15
	T_{top}	T_{side}	T_{bottom}	T_{bottom}	T_{top}	T_{top}	T_{side}	T_{bottom}	T_{bottom}	T_{top}	T_{side}	T_{bottom}	T_{bottom}	T_{top}	T_{top}	T_{side}	T_{bottom}	T_{top}	T_{top}	T_{side}	T_{bottom}	T_{bottom}	T_{top}
PHASE 1 - R1234ze(E), circular cone nozzles, triangular pitch, Tube-C condenser tubes (Bundle 1)																							
5/15/2021	1.5	1.6	1.9	1.9	1.6	1.5	1.6	1.6	1.7	1.3	2.1	2.4	1.8	1.6	1.5	1.5	1.6	1.3	2.7	3.6	3.3	1.7	1.6
	2.9	2.9	3.3	3.1	2.9	3.0	3.2	3.2	3.5	2.7	3.0	3.3	3.3	3.0	3.2	3.1	3.1	2.7	3.1	3.2	3.3	3.2	3.0
	3.4	3.4	3.9	3.7	3.4	3.5	3.9	4.0	4.5	3.0	3.6	4.0	4.0	3.5	6.3	5.6	4.4	3.0	3.6	4.0	3.9	3.9	3.5
	3.6	4.0	4.4	4.4	4.0	3.7	3.9	4.0	4.8	2.6	6.0	6.3	6.8	5.4	7.4	6.7	5.2	2.6	6.7	8.7	8.2	7.9	7.7
	4.6	4.8	5.2	4.9	4.8	5.1	5.3	5.3	6.4	4.1	4.8	5.2	5.4	4.6	10.1	8.7	6.4	4.1	5.1	5.5	5.3	5.2	4.8
	4.7	5.0	5.5	5.2	5.0	6.0	6.0	6.2	8.8	4.2	5.1	5.5	5.7	4.8	15.7	14.1	7.3	4.2	5.9	6.4	6.0	5.5	5.1
	5.1	5.4	6.0	5.6	5.5	7.1	7.2	7.3	12.3	4.5	5.6	6.0	6.3	5.3	25.6	24.2	8.6	4.4	7.9	7.7	7.2	6.1	5.8
	3.5	3.8	4.3	3.9	3.9	5.4	5.3	5.4	11.5	2.7	3.9	4.4	4.7	3.7	24.9	23.2	2.7	2.7	5.9	5.4	5.1	4.5	4.2
	4.1	4.4	4.9	4.6	4.6	3.3	3.2	3.2	3.2	3.3	5.1	5.4	5.6	4.5	3.3	3.2	3.2	3.2	9.5	8.6	8.1	6.0	5.7
	4.4	4.8	5.3	4.9	5.0	3.4	3.4	3.4	3.4	3.4	5.7	6.0	6.1	4.9	3.4	3.4	3.4	3.4	14.1	9.9	10.2	7.1	6.6
	5.0	5.4	6.0	5.5	5.7	3.9	3.9	3.9	3.9	3.9	7.0	7.5	6.9	5.5	3.9	3.9	3.9	3.9	23.5	16.7	21.1	10.6	8.2
	4.4	4.8	5.5	5.0	5.1	3.2	3.2	3.2	3.2	3.2	7.8	8.5	6.7	5.2	3.2	3.2	3.2	3.2	39.3	35.3	38.6	18.5	11.5
5/17/2021	3.3	3.3	3.9	4.0	3.4	3.7	3.9	3.8	4.5	2.9	3.6	3.8	3.9	3.4	6.0	5.2	4.4	2.9	3.5	4.2	4.1	3.8	3.4
	3.9	4.1	4.7	4.8	4.1	4.7	4.7	4.6	6.6	3.4	4.3	4.7	4.8	4.1	9.8	8.3	6.1	3.4	4.3	5.1	4.9	4.6	4.1
	3.9	4.2	4.7	4.9	4.2	5.3	5.1	5.3	9.0	3.3	4.5	4.9	4.9	4.1	16.8	15.4	7.0	3.3	4.8	5.6	5.2	4.7	4.1
	4.4	4.7	5.4	5.5	4.8	6.4	6.1	6.2	13.0	3.7	5.1	5.6	5.7	4.6	25.9	24.4	9.1	3.7	6.8	7.0	6.5	5.4	4.8
	4.4	4.8	5.5	5.6	4.9	7.2	6.8	6.9	17.7	3.6	5.3	5.8	5.9	4.7	3.6	3.6	3.6	3.6	9.1	7.9	7.5	5.7	5.3
	4.6	5.0	5.7	5.8	5.1	8.0	7.6	7.8	22.9	3.6	6.0	6.3	6.3	5.0	3.6	3.6	3.6	3.6	14.5	9.7	10.2	6.7	6.3
	4.8	5.3	6.0	6.0	5.5	8.9	8.5	8.8	29.1	3.7	7.1	7.6	6.7	5.3	3.7	3.7	3.7	3.7	23.9	17.2	21.9	10.5	8.1
	4.0	4.5	5.1	5.1	4.8	2.8	2.8	2.8	2.8	2.8	8.4	9.0	8.8	6.0	2.8	2.8	2.8	2.8	55.0	55.0	55.0	42.9	18.0
5/24/2021	10.7	10.7	10.9	11.0	10.7	10.8	10.8	10.8	10.9	10.6	10.8	10.8	10.8	10.7	10.8	10.7	10.7	10.6	10.9	10.8	10.8	10.8	10.7
	10.9	10.9	11.3	11.4	11.0	11.1	11.2	11.3	11.4	10.7	11.0	11.2	11.2	10.9	11.5	11.4	11.2	10.7	11.1	11.2	11.2	11.2	10.9
	11.1	11.1	11.7	11.8	11.3	11.6	11.6	11.8	12.2	10.7	11.4	11.6	11.7	11.2	14.3	13.4	12.1	10.7	11.4	11.7	11.7	11.6	11.1
	11.0	11.2	11.7	11.8	11.2	11.8	11.7	11.9	14.1	10.5	11.4	11.8	11.8	11.1	17.2	15.6	12.8	10.5	11.6	12.0	11.9	11.6	11.1
	11.3	11.6	12.1	12.3	11.7	12.7	12.5	12.7	17.6	10.7	11.9	12.3	12.4	11.5	24.3	22.9	13.8	10.7	12.8	13.1	12.9	12.1	11.6
	11.8	12.1	12.6	12.8	12.2	14.1	13.9	14.0	22.2	11.1	12.5	12.9	13.0	12.0	34.0	32.6	15.4	11.1	15.3	14.7	14.4	12.7	12.4
	11.4	11.7	12.2	12.2	11.9	14.7	14.5	14.6	26.3	10.5	12.4	12.7	12.8	11.6	10.5	10.5	10.5	10.5	16.5	14.8	14.5	12.9	12.9
	11.6	12.0	12.6	12.5	12.2	16.0	15.7	15.9	32.7	10.6	13.3	13.6	13.3	12.1	10.6	10.6	10.6	10.6	21.6	16.7	17.6	14.3	14.4
	11.9	12.3	12.9	12.8	12.6	17.4	17.3	17.6	38.8	10.8	14.6	15.1	13.9	12.6	10.8	10.8	10.8	10.8	37.6	33.6	38.6	19.3	16.3
5/25/2021	10.9	11.0	11.1	11.3	10.9	11.0	11.1	11.1	11.1	10.8	11.0	11.1	11.1	10.9	11.0	11.0	11.0	10.8	11.1	11.3	11.3	11.1	10.9
	11.2	11.3	11.6	11.9	11.3	11.4	11.5	11.6	11.7	11.0	11.6	11.8	11.9	11.3	11.9	11.7	11.5	11.0	11.8	12.9	12.6	11.9	11.4
	11.1	11.1	11.7	12.0	11.3	11.5	11.6	11.7	12.1	10.7	11.9	12.2	12.4	11.7	13.7	12.8	11.8	10.7	12.7	14.6	13.8	12.5	12.1
	11.3	11.4	12.1	12.4	11.6	12.1	12.0	12.1	13.3	10.7	12.8	13.0	13.6	12.8	18.6	17.9	12.3	10.7	13.8	16.4	15.4	13.4	14.0
	11.5	11.8	12.4	12.7	11.9	13.0	12.6	12.7	16.3	10.9	13.5	13.7	15.0	14.0	52.7	52.5	14.5	10.9	15.1	17.8	16.9	16.0	16.1
	11.1	11.4	11.9	12.3	11.6	13.4	12.9	12.9	19.7	10.2	13.4	13.6	15.5	14.2	10.2	10.2	10.2	10.2	15.7	19.4	18.2	18.3	17.2
	11.6	12.0	12.5	12.9	12.4	15.3	14.9	15.1	26.7	10.6	14.5	14.7	17.4	15.7	10.6	10.6	10.6	10.6	26.3	33.0	33.9	21.3	19.9
	11.5	11.9	12.4	12.8	12.3	16.2	15.6	15.9	32.9	10.3	14.7	15.0	18.0	16.4	10.3	10.3	10.3	10.3	54.5	55.0	55.0	22.2	21.1

Date	Row 1					Row 2					Row 3				Row 4				Row 5				
	Tube 1			Tube 6	Tube 11	Tube 2			Tube 7	Tube 12	Tube 3		Tube 8	Tube 13	Tube 4		Tube 9	Tube 14	Tube 5			Tube 10	Tube 15
	T_{top}	T_{side}	T_{bottom}	T_{bottom}	T_{top}	T_{top}	T_{side}	T_{bottom}	T_{bottom}	T_{top}	T_{side}	T_{bottom}	T_{bottom}	T_{top}	T_{top}	T_{side}	T_{bottom}	T_{top}	T_{top}	T_{side}	T_{bottom}	T_{bottom}	T_{top}
PHASE 1 - R1234ze(E), circular cone nozzles, triangular pitch, Tube-C condenser tubes (Bundle 1)																							
	11.0	11.1	11.3	11.9	11.2	11.0	11.1	11.1	11.1	10.8	11.5	11.6	11.7	11.5	11.1	11.1	11.0	10.8	11.9	12.7	12.4	11.7	11.6
	13.0	13.3	13.4	15.8	14.2	12.0	12.1	12.3	12.9	11.0	15.2	15.3	16.5	16.9	13.8	14.0	13.4	11.0	16.3	18.0	17.4	16.5	17.2
	14.3	14.7	14.8	18.6	16.5	12.8	12.8	13.0	14.2	11.0	17.8	17.8	20.1	20.8	16.4	16.7	15.7	11.0	19.0	21.7	20.8	21.7	23.2
5/26/2021	15.8	16.3	16.4	21.9	19.2	13.9	13.8	14.2	16.0	11.2	20.4	20.5	24.6	25.7	19.6	20.1	18.8	11.2	21.9	25.6	24.5	29.8	30.8
	17.0	17.8	18.0	25.2	21.9	15.1	15.0	15.7	17.8	11.3	22.9	23.1	30.0	31.4	36.5	37.6	26.7	11.3	25.5	30.4	29.2	40.4	39.5
	17.1	18.0	18.2	27.1	23.0	9.9	9.9	9.9	9.9	9.9	23.7	23.9	33.2	34.5	9.9	9.9	9.9	9.9	29.5	35.1	33.8	45.2	40.6
	18.0	19.1	19.3	29.0	24.7	10.3	10.3	10.3	10.3	10.4	25.3	25.6	37.1	38.2	10.4	10.3	10.3	10.3	42.6	48.4	47.1	55.0	46.2
	2.8	2.9	3.0	3.1	2.9	2.9	3.0	3.0	3.0	2.7	2.9	3.0	3.0	2.9	2.9	2.9	2.9	2.7	3.0	3.0	3.0	2.9	2.8
	2.6	2.7	3.0	3.1	2.6	2.7	2.9	2.9	3.0	2.3	2.7	2.9	2.9	2.6	3.2	3.0	2.9	2.3	2.8	2.8	2.9	2.8	2.6
	2.6	2.6	3.1	3.3	2.7	3.0	3.1	3.2	3.6	2.2	2.8	3.1	3.1	2.6	6.2	5.2	3.5	2.2	2.9	3.1	3.2	3.0	2.6
	3.1	3.1	3.7	3.8	3.2	3.5	3.6	3.8	4.2	2.7	3.4	3.6	3.7	3.2	7.0	5.9	4.1	2.7	3.4	3.6	3.7	3.6	3.2
	3.4	3.5	4.0	4.3	3.7	4.0	4.2	4.2	5.6	2.9	3.9	4.2	4.3	3.5	10.6	9.3	5.0	2.9	4.1	4.8	4.6	4.1	3.6
	3.5	3.6	4.2	4.4	3.8	4.1	4.3	4.4	5.9	3.1	3.9	4.3	4.3	3.6	11.9	10.5	5.4	3.1	4.0	4.3	4.2	4.1	3.6
5/27/2021	3.4	3.7	4.2	4.4	3.7	4.5	4.4	4.6	8.6	2.8	4.0	4.4	4.4	3.5	19.3	18.0	5.9	2.8	4.4	4.6	4.4	4.1	3.6
	4.0	4.4	5.0	5.1	4.5	5.5	5.2	5.4	11.8	3.3	4.7	5.2	5.2	4.1	26.1	24.7	7.4	3.3	6.0	5.7	5.5	4.8	4.3
	4.0	4.4	5.0	5.1	4.5	5.4	5.1	5.3	11.7	3.3	4.7	5.2	5.2	4.1	25.7	24.2	7.4	3.3	6.0	5.6	5.4	4.7	4.3
	4.1	4.5	5.1	5.2	4.6	6.0	5.4	5.6	15.0	3.2	4.9	5.3	5.5	4.3	3.2	3.2	3.2	3.2	7.5	6.2	6.1	4.9	4.7
	4.1	4.5	5.2	5.3	4.7	6.7	5.9	6.2	19.8	3.1	5.2	5.5	5.6	4.4	3.1	3.1	3.1	3.1	12.0	7.7	8.5	5.4	5.6
	4.5	5.0	5.6	5.7	5.2	7.7	7.0	7.3	25.5	3.4	6.3	6.7	6.2	4.9	3.4	3.4	3.4	3.4	19.5	11.4	14.3	7.7	8.1
	4.7	5.2	5.7	5.8	5.5	3.3	3.3	3.3	3.3	3.3	8.7	9.2	9.0	7.0	3.3	3.3	3.3	3.3	15.4	15.1	14.8	55.0	55.0
	4.9	5.4	5.9	5.9	5.7	3.7	3.7	3.7	3.7	3.7	8.0	8.5	6.9	5.6	3.7	3.7	3.7	3.7	15.2	10.1	10.1	55.0	55.0
	2.6	2.7	2.8	3.0	2.7	2.7	2.8	2.8	2.8	2.5	2.8	2.9	2.8	2.6	2.7	2.7	2.7	2.5	2.9	3.1	3.1	2.8	2.6
	3.2	3.3	3.6	3.9	3.3	3.5	3.6	3.6	3.7	3.0	3.7	3.9	3.8	3.4	4.1	3.8	3.5	3.0	4.0	5.0	4.7	4.0	3.6
	3.6	3.6	4.2	4.4	3.8	4.2	4.2	4.3	4.7	3.2	4.5	4.7	4.8	4.1	6.8	5.9	4.4	3.2	5.1	7.0	6.3	5.0	4.7
5/28/2021	4.0	4.2	4.7	4.8	4.2	5.0	4.8	4.9	6.7	3.5	5.3	5.6	5.8	4.9	12.7	11.8	5.1	3.5	6.0	8.4	7.5	5.9	6.3
	4.4	4.7	5.2	5.3	4.7	6.3	5.8	5.9	10.9	3.7	6.2	6.4	7.3	6.1	50.6	50.2	6.5	3.7	7.4	9.6	8.7	7.2	7.9
	4.0	4.4	4.9	5.0	4.5	6.9	6.3	6.4	15.2	3.2	6.2	6.4	8.3	6.6	3.2	3.2	3.2	3.2	8.3	11.3	10.2	9.0	8.7
	4.3	4.7	5.3	5.4	4.9	8.7	8.1	8.3	21.1	3.3	7.0	7.2	10.0	7.8	3.3	3.3	3.3	3.3	16.5	21.8	23.1	11.9	10.5
	5.0	5.5	6.1	6.3	5.8	3.8	3.8	3.8	3.8	3.8	8.7	9.0	13.1	10.0	3.8	3.8	3.8	3.7	55.0	55.0	55.0	17.1	15.2
	3.1	3.2	3.4	3.9	3.3	3.1	3.2	3.2	3.2	2.9	3.5	3.7	3.7	3.5	3.3	3.3	3.2	2.9	3.9	4.6	4.4	3.7	3.6
	4.7	5.0	5.1	7.7	5.7	3.9	4.0	4.3	5.0	3.1	7.2	7.2	8.1	8.3	4.9	5.1	5.1	3.1	8.0	9.8	9.3	8.5	8.5
	5.9	6.3	6.4	10.0	7.3	4.8	4.8	5.0	6.1	3.6	9.3	9.4	11.2	11.4	6.9	7.1	6.5	3.6	10.4	13.1	12.5	13.3	13.3
6/1/2021	6.8	7.3	7.4	12.5	9.2	5.3	5.2	5.5	7.2	3.6	11.3	11.4	14.8	14.9	8.4	8.8	9.2	3.6	12.4	16.1	15.3	19.7	18.6
	8.0	8.7	8.8	15.5	11.3	6.2	6.0	6.3	8.8	3.9	13.5	13.7	19.5	19.6	13.5	15.3	18.2	3.9	15.4	20.2	19.3	28.8	25.1
	8.1	8.9	9.3	17.6	12.8	6.0	5.6	6.2	9.4	2.9	15.1	15.4	24.0	23.5	2.9	2.9	2.9	2.9	24.6	30.8	30.0	37.9	31.5
	9.7	10.9	11.4	22.0	15.7	3.3	3.3	3.3	3.3	3.4	19.6	20.1	31.2	30.0	3.3	3.3	3.3	3.3	55.0	55.0	55.0	51.2	38.8

Date	Row 1					Row 2					Row 3				Row 4				Row 5				
	Tube 1			Tube 6	Tube 11	Tube 2			Tube 7	Tube 12	Tube 3		Tube 8	Tube 13	Tube 4		Tube 9	Tube 14	Tube 5			Tube 10	Tube 15
	T_{top}	T_{side}	T_{bottom}	T_{bottom}	T_{top}	T_{top}	T_{side}	T_{bottom}	T_{bottom}	T_{top}	T_{side}	T_{bottom}	T_{bottom}	T_{top}	T_{top}	T_{side}	T_{bottom}	T_{top}	T_{top}	T_{side}	T_{bottom}	T_{bottom}	T_{top}
PHASE 1 - R1234ze(E), circular cone nozzles, triangular pitch, Tube-C condenser tubes (Bundle 1)																							
6/2/2021	-8.4	-8.2	-7.9	-7.4	-8.1	-8.4	-8.3	-8.3	-8.3	-8.6	-7.7	-7.6	-7.4	-7.9	-8.5	-8.4	-8.4	-8.6	-7.4	-6.4	-6.7	-7.5	-7.4
	-6.9	-6.6	-6.3	-3.9	-5.6	-7.8	-7.6	-7.4	-6.5	-8.6	-4.4	-4.3	-3.4	-3.4	-6.5	-6.3	-6.3	-8.6	-3.6	-1.8	-2.3	-3.0	-2.8
	-6.3	-5.9	-5.7	-1.8	-4.6	-7.4	-7.3	-7.0	-5.9	-8.7	-2.9	-2.8	-1.1	-1.2	-5.7	-5.4	-5.7	-8.7	-2.0	0.9	0.1	0.6	1.0
	-6.5	-6.0	-5.9	-2.0	-4.7	-7.5	-7.5	-7.2	-6.5	-8.8	-2.6	-2.5	0.0	-0.1	-5.8	-5.6	-5.9	-8.8	-1.7	2.2	1.3	3.5	2.9
	-6.0	-5.4	-5.2	-1.0	-3.9	-6.8	-7.0	-6.8	-6.0	-8.4	-1.5	-1.4	2.5	2.0	-4.6	-4.4	-1.7	-8.4	0.0	4.9	3.9	7.9	6.1
	-5.5	-4.8	-4.6	0.6	-2.8	-6.4	-6.8	-6.6	-5.3	-8.5	-0.3	-0.1	5.9	4.6	-8.5	-8.5	-8.5	-8.5	3.2	9.6	8.6	14.1	10.5
	-4.7	-4.0	-3.8	1.6	-2.1	-5.3	-5.9	-5.8	0.4	-7.7	1.5	1.9	8.5	7.0	-7.7	-7.8	-7.8	-7.8	51.9	55.0	55.0	18.8	13.5
6/3/2021	-8.2	-8.0	-7.7	-7.2	-7.8	-8.2	-8.2	-8.1	-8.1	-8.4	-7.5	-7.4	-7.1	-7.6	-8.3	-8.2	-8.1	-8.4	-7.1	-6.2	-6.4	-7.2	-7.1
	-7.8	-7.5	-7.1	-6.2	-7.2	-7.9	-7.8	-7.7	-7.6	-8.3	-6.3	-6.1	-5.6	-6.1	-7.9	-7.8	-7.4	-8.3	-5.7	-3.8	-4.3	-5.3	-5.5
	-7.3	-6.9	-6.4	-5.2	-6.4	-7.5	-7.4	-7.2	-6.9	-8.3	-4.7	-4.5	-3.1	-4.1	-7.0	-7.0	-6.6	-8.3	-4.1	-1.2	-2.0	-2.8	-2.5
	-1.4	-0.7	-0.7	9.8	3.7	-2.2	-2.1	-1.6	2.2	-8.3	4.4	4.6	9.8	10.5	4.6	4.8	4.0	-8.3	7.1	10.9	10.0	21.1	16.1
	-7.5	-7.0	-6.7	-5.5	-6.1	34.1	34.7	35.7	55.0	-9.1	-3.4	-3.2	-3.7	-3.8	-9.1	-9.1	-9.1	-9.1	55.0	55.0	55.0	-0.7	0.3
	-6.4	-5.8	-5.4	-3.6	-4.6	-8.2	-8.2	-8.3	-8.2	-8.2	7.5	8.8	2.1	1.6	-8.2	-8.2	-8.3	-8.3	55.0	55.0	55.0	6.8	55.0
6/4/2021	-15.7	-15.5	-15.4	-14.5	-15.1	-15.8	-15.9	-15.8	-15.3	-16.5	-14.1	-14.1	-12.9	-13.2	-13.0	-12.9	-12.5	-16.5	-13.5	-12.7	-13.0	-12.1	-12.3
	-14.9	-14.6	-14.4	-13.4	-13.9	-15.1	-15.1	-15.0	-14.4	-16.3	-12.3	-12.3	-10.2	-10.6	-5.6	-5.3	-6.6	-16.4	-11.4	-9.5	-10.1	-8.0	-8.4
	-14.5	-14.0	-13.7	-12.2	-13.0	-15.0	-15.0	-14.7	-14.1	-16.4	-10.9	-10.8	-8.1	-8.5	-16.4	-16.4	46.2	-16.4	-10.6	-7.5	-8.4	-6.6	-5.8
6/6/2021	1.4	1.5	1.6	1.8	1.4	1.4	1.5	1.4	1.5	1.2	1.9	2.1	1.6	1.3	1.3	1.3	1.4	1.2	2.3	3.2	2.9	1.5	1.4
	2.4	2.4	2.6	2.7	2.4	2.4	2.5	2.5	2.5	2.2	2.5	2.6	2.5	2.4	2.4	2.4	2.4	2.2	2.7	2.9	2.8	2.5	2.4
	2.5	2.7	2.9	3.0	2.6	2.8	2.9	2.9	3.1	2.3	2.7	2.9	2.9	2.6	3.0	2.9	2.9	2.3	2.8	2.8	2.9	2.8	2.6
	2.0	2.2	2.6	3.0	2.2	2.1	2.2	2.3	2.5	1.6	3.5	3.7	3.4	2.7	2.2	2.2	2.2	1.6	4.3	5.8	5.3	3.9	3.5
6/7/2021	-15.1	-15.0	-14.9	-14.1	-14.6	-15.3	-15.3	-15.2	-14.8	-15.9	-13.7	-13.7	-12.6	-12.8	-12.4	-12.3	-11.9	-15.9	-13.1	-12.3	-12.6	-11.6	-11.9
	-13.5	-13.3	-13.1	-12.4	-12.5	-13.8	-13.8	-13.8	-13.3	-15.1	-11.4	-11.4	-9.2	-9.8	-4.9	-4.7	-6.1	-15.1	-10.6	-8.8	-9.3	-7.7	-7.9
	-12.1	-11.7	-11.5	-11.3	-10.0	-12.5	-12.6	-12.4	3.4	-14.8	-10.0	-10.0	-5.7	-7.5	-14.8	-14.8	-14.8	-14.8	-8.5	-5.3	-6.1	-5.7	-5.1
	-12.2	-11.8	-11.5	-10.5	-9.9	-15.1	-15.1	-15.1	-15.1	-15.1	-9.9	-9.8	-4.4	-5.5	-15.1	-15.1	-15.1	-15.1	-6.3	-2.5	-3.2	-0.4	-1.9
PHASE 1 - R134a, circular cone nozzles, triangular pitch, Tube-C condenser tubes (Bundle 1)																							
7/1/2021	1.2	1.2	1.2	1.2	1.2	1.2	1.6	1.2	1.2	1.2	1.2	1.2	1.1	1.2	1.2	1.3	1.3	1.2	3.4	3.7	3.6	1.4	1.5
	1.6	1.5	1.6	1.6	1.5	1.6	-18.6	1.6	1.6	1.6	1.6	1.6	1.5	1.6	1.9	1.9	1.9	1.7	3.6	4.1	3.8	1.9	1.9
	2.0	2.0	2.0	2.0	2.0	2.0	-24.5	2.1	2.0	2.0	2.1	2.1	2.0	2.1	2.3	2.4	2.4	2.1	4.0	4.6	4.1	2.4	2.5
	1.7	1.7	1.7	1.7	1.7	1.7	-24.5	1.7	1.7	1.7	1.8	1.8	1.7	1.7	2.1	2.1	2.1	2.1	4.1	4.8	4.0	2.0	2.1
	1.1	1.1	1.1	1.1	1.1	1.1	-24.5	1.2	1.1	1.1	1.3	1.4	1.2	1.2	1.5	1.5	1.4	1.4	3.8	4.7	3.8	1.4	1.5
	1.2	1.2	1.2	1.3	1.2	1.2	-24.5	1.3	1.3	1.3	1.4	1.5	1.3	1.4	1.6	1.6	1.5	1.6	4.3	5.4	4.2	1.6	1.6
7/2/2021	-6.4	-6.4	-6.4	-6.4	-6.4	-6.4	-24.5	-6.4	-6.4	-6.4	-6.4	-6.4	-6.4	-6.4	-6.1	-6.1	-6.1	-6.1	-4.0	-3.6	-3.7	-6.0	-6.0
	-6.6	-6.6	-6.6	-6.6	-6.6	-6.6	-24.5	-6.5	-6.6	-6.6	-6.4	-6.3	-6.5	-6.5	-6.1	-6.1	-6.1	-6.1	-3.4	-3.5	-3.5	-6.1	-6.1
	-6.0	-6.0	-6.0	-6.0	-6.0	-6.0	-24.5	-6.0	-6.0	-6.0	-5.7	-5.6	-5.8	-5.8	-5.5	-5.5	-5.5	-5.5	-3.4	-3.2	-3.4	-5.5	-5.5
	-5.8	-5.8	-5.8	-5.8	-5.9	-5.8	-24.5	-5.8	-5.8	-5.8	-5.5	-5.4	-5.6	-5.6	-5.3	-5.3	-5.3	-5.3	-3.1	-2.8	-3.1	-5.3	-5.3
	-5.5	-5.5	-5.5	-5.5	-5.5	-5.5	-24.5	-5.4	-5.5	-5.5	-5.2	-5.1	-5.3	-5.2	-5.0	-5.0	-5.0	-5.0	-2.4	-2.0	-2.4	-5.0	-5.0
	-4.8	-4.8	-4.8	-4.8	-4.8	-4.8	-24.5	-4.7	-4.8	-4.8	-4.5	-4.4	-4.7	-4.6	-4.4	-4.4	-4.4	-4.4	-1.4	-1.0	-1.4	-4.4	-4.4

Date	Row 1					Row 2					Row 3				Row 4				Row 5				
	Tube 1			Tube 6	Tube 11	Tube 2			Tube 7	Tube 12	Tube 3		Tube 8	Tube 13	Tube 4		Tube 9	Tube 14	Tube 5			Tube 10	Tube 15
	T_{top}	T_{side}	T_{bottom}	T_{bottom}	T_{top}	T_{top}	T_{side}	T_{bottom}	T_{bottom}	T_{top}	T_{side}	T_{bottom}	T_{bottom}	T_{top}	T_{top}	T_{side}	T_{bottom}	T_{top}	T_{top}	T_{side}	T_{bottom}	T_{bottom}	T_{top}
PHASE 1 - R134a, circular cone nozzles, triangular pitch, Tube-C condenser tubes (Bundle 1)																							
7/20/2021	8.1	8.1	8.1	8.1	8.1	8.1	-24.5	8.1	8.1	8.1	8.1	8.1	8.1	8.1	8.2	8.3	8.3	8.2	9.5	9.6	9.7	9.8	9.8
	9.5	9.5	9.5	9.5	9.5	9.5	-24.5	9.5	9.5	9.5	9.6	9.6	9.5	9.6	9.7	9.8	9.8	9.7	11.0	11.2	11.5	11.4	11.5
	8.7	8.7	8.7	8.7	8.7	8.7	-24.5	8.7	8.7	8.7	8.8	8.8	8.7	8.7	8.9	8.9	9.1	8.9	10.7	10.9	11.2	11.0	11.1
	8.8	8.8	8.8	8.8	8.8	8.8	-24.5	8.8	8.8	8.8	8.9	8.9	8.8	8.9	9.0	9.1	9.1	9.0	10.8	11.0	11.4	11.1	11.3
	9.2	9.2	9.2	9.2	9.2	9.2	-24.5	9.3	9.2	9.2	9.4	9.4	9.2	9.4	9.5	9.6	9.5	9.5	11.4	11.7	12.1	11.8	12.0
	8.9	8.9	8.9	8.9	8.9	8.9	-24.5	8.9	8.9	8.9	9.0	9.1	8.9	9.1	9.2	9.2	9.2	9.1	11.2	11.6	12.1	11.6	11.8
	9.3	9.3	9.3	9.3	9.3	9.3	-24.5	9.4	9.3	9.4	9.5	9.5	9.4	9.5	9.6	9.7	9.6	9.5	11.7	12.2	12.8	12.2	12.4
	9.6	9.6	9.6	9.6	9.6	9.6	-24.5	9.7	9.6	9.6	9.8	9.8	9.7	9.8	9.9	9.9	9.9	9.8	12.1	12.7	13.4	12.7	12.8
	9.5	9.5	9.5	9.5	9.5	9.5	-24.5	9.6	9.5	9.5	9.6	9.7	9.6	9.7	9.8	9.8	9.8	9.7	12.1	12.8	13.5	12.7	12.8
	9.3	9.3	9.3	9.3	9.3	9.3	-24.5	9.4	9.3	9.4	9.5	9.5	9.4	9.5	9.6	9.6	9.6	9.5	12.1	12.8	13.6	12.6	12.8
	9.5	9.5	9.5	9.6	9.6	9.5	-24.5	9.6	9.6	9.6	9.7	9.8	9.6	9.8	9.9	9.9	9.9	9.8	12.5	13.2	14.1	13.0	13.2
7/21/2021	2.1	2.0	2.1	2.1	2.0	2.1	-24.5	2.1	2.1	2.1	2.2	2.3	2.2	2.2	2.6	2.6	2.6	2.6	3.6	3.9	4.0	4.0	4.0
	2.3	2.3	2.3	2.3	2.3	2.3	-24.5	2.3	2.3	2.3	2.5	2.6	2.5	2.5	2.8	2.8	2.8	2.8	4.0	4.3	4.5	4.5	4.5
	2.1	2.1	2.1	2.1	2.1	2.1	-24.5	2.1	2.1	2.1	2.3	2.4	2.3	2.3	2.5	2.5	2.5	2.5	3.9	4.3	4.5	4.4	4.6
	2.3	2.3	2.3	2.4	2.3	2.3	-24.5	2.4	2.4	2.4	2.6	2.7	2.6	2.6	2.8	2.8	2.8	2.8	4.3	4.7	5.0	4.8	5.0
	2.0	2.0	2.0	2.0	2.0	2.0	-24.5	2.1	2.0	2.0	2.3	2.4	2.3	2.3	2.4	2.4	2.4	2.3	4.1	4.5	4.9	4.6	4.9
	2.1	2.1	2.1	2.1	2.1	2.1	-24.5	2.2	2.2	2.1	2.4	2.5	2.4	2.4	2.5	2.5	2.5	2.4	4.4	4.8	5.3	4.8	5.2
	2.0	2.0	2.0	2.0	2.0	2.1	-24.5	2.2	2.2	2.1	2.3	2.4	2.3	2.4	2.4	2.4	2.4	2.3	4.4	4.9	5.5	4.9	5.2
	2.2	2.2	2.2	2.2	2.2	2.2	-24.5	2.4	2.3	2.2	2.5	2.5	2.5	2.5	2.6	2.5	2.5	2.5	4.7	5.3	5.9	5.2	5.6
	2.1	2.1	2.1	2.1	2.1	2.1	-24.5	2.2	2.2	2.1	2.4	2.4	2.4	2.4	2.4	2.4	2.4	2.4	4.7	5.4	6.0	5.2	5.6
	2.3	2.3	2.3	2.3	2.3	2.3	-24.5	2.4	2.4	2.3	2.6	2.6	2.6	2.6	2.6	2.6	2.6	2.6	5.0	5.8	6.5	5.6	5.9
	2.4	2.4	2.4	2.5	2.4	2.5	-24.5	2.6	2.6	2.5	2.7	2.7	2.7	2.7	2.8	2.7	2.7	2.7	5.2	6.1	6.8	6.0	6.2
10/1/2021	9.5	9.7	9.8	10.7	9.6	9.4	9.7	9.6	9.7	9.1	10.5	10.6	10.4	10.7	9.9	9.9	10.3	9.1	10.9	12.1	11.8	11.4	11.1
	10.8	10.9	11.5	13.3	10.8	10.5	11.0	10.8	11.3	10.0	13.7	13.8	14.6	13.8	11.2	11.2	12.0	10.0	15.3	17.6	17.0	16.1	15.0
	11.2	11.2	12.6	16.0	11.4	10.9	11.2	11.3	12.6	10.1	17.6	17.8	19.4	18.3	12.5	12.6	15.2	10.1	20.7	24.0	23.2	23.9	22.4
	10.9	11.1	12.6	16.2	11.5	10.7	11.0	11.0	12.8	9.8	18.0	18.1	19.7	18.8	12.7	12.8	16.5	9.8	21.4	24.8	24.0	24.4	23.4
	11.9	13.4	14.2	20.2	13.0	10.8	11.5	11.6	15.8	9.6	24.0	24.2	26.5	26.6	17.8	18.3	23.5	9.6	29.5	33.8	33.0	35.0	33.9
	14.4	15.7	16.0	23.5	14.5	11.2	12.1	12.3	19.5	9.4	29.8	30.1	34.5	33.9	25.2	25.7	34.0	9.4	36.7	42.1	41.2	46.1	43.6
	15.9	17.4	17.8	27.0	16.4	8.9	9.0	8.9	9.0	9.0	36.1	36.4	42.6	42.8	9.1	9.1	9.2	9.0	47.0	52.6	51.9	53.3	51.7
10/2/2021	11.3	11.4	11.6	12.3	11.3	11.3	11.6	11.4	11.5	11.0	12.2	12.3	12.5	12.2	11.6	11.6	12.4	11.0	12.5	13.6	13.4	12.7	12.5
	13.2	13.2	13.8	16.1	13.2	12.8	13.2	13.1	14.1	11.8	16.5	16.5	18.0	17.0	14.6	14.7	16.0	11.9	17.9	20.1	19.6	19.8	18.5
	12.8	12.9	13.4	15.6	12.7	12.4	12.8	12.7	13.4	11.7	15.8	15.8	17.3	16.3	13.4	13.5	14.7	11.7	17.1	19.4	18.9	18.8	17.6
	12.3	13.2	13.3	17.2	12.4	11.6	12.2	12.0	13.8	10.6	18.7	18.8	21.0	19.7	14.3	14.5	17.5	10.6	21.5	24.8	24.1	25.8	23.4
	13.5	15.1	15.0	20.5	14.0	12.3	13.2	12.8	16.1	11.1	24.1	24.3	27.5	26.0	17.9	18.2	23.2	11.1	28.2	32.5	31.8	36.4	32.7
	15.8	17.3	17.2	24.5	15.9	13.1	13.9	13.9	19.6	11.2	30.9	31.1	35.3	34.9	24.1	24.6	31.7	11.2	37.3	42.6	41.8	46.4	43.6

Date	Row 1					Row 2					Row 3				Row 4				Row 5				
	Tube 1			Tube 6	Tube 11	Tube 2			Tube 7	Tube 12	Tube 3		Tube 8	Tube 13	Tube 4		Tube 9	Tube 14	Tube 5			Tube 10	Tube 15
	T_{top}	T_{side}	T_{bottom}	T_{bottom}	T_{top}	T_{top}	T_{side}	T_{bottom}	T_{bottom}	T_{top}	T_{side}	T_{bottom}	T_{bottom}	T_{top}	T_{top}	T_{side}	T_{bottom}	T_{top}	T_{top}	T_{side}	T_{bottom}	T_{bottom}	T_{top}
PHASE 1 - R134a, circular cone nozzles, triangular bundle, condenser tubes (Bundle 1)																							
10/4/2021	2.0	2.1	2.3	3.0	2.0	2.0	2.3	2.1	2.2	1.7	2.8	3.0	3.4	3.0	2.3	2.3	2.6	1.7	3.1	4.2	4.0	3.6	3.4
	2.7	3.0	3.3	4.8	2.7	2.5	2.9	2.8	3.3	2.0	5.3	5.4	6.7	5.9	3.2	3.2	4.4	2.0	6.1	8.3	7.8	8.0	6.9
	3.2	3.9	4.2	7.0	3.3	2.9	3.4	3.2	4.5	2.2	8.8	8.9	11.0	9.9	4.6	4.6	8.8	2.2	10.3	13.5	12.9	14.8	12.2
	3.8	4.7	4.7	8.2	4.1	3.5	3.8	3.8	4.7	2.8	11.5	11.6	14.4	13.0	4.5	4.5	7.0	2.8	13.2	17.3	16.7	21.7	16.0
	3.3	4.3	4.3	7.8	3.6	3.1	3.5	3.6	5.4	2.2	10.9	11.1	13.7	12.4	7.3	7.4	13.2	2.2	12.9	16.9	16.3	21.1	15.8
	2.3	3.6	3.5	8.0	2.7	2.2	2.2	2.4	4.8	1.0	11.2	11.3	14.7	13.3	6.3	6.5	14.5	1.0	13.8	17.9	17.3	22.8	17.4
	4.3	5.7	5.7	11.8	4.5	3.4	3.1	3.3	8.9	1.5	16.8	17.0	22.3	20.6	14.5	15.2	25.8	1.5	21.6	27.0	26.2	34.4	27.4
	5.4	7.0	7.1	14.0	5.7	4.2	3.9	4.0	13.7	2.2	21.0	21.3	28.7	26.1	21.9	22.7	36.8	2.2	29.7	36.0	35.2	43.7	36.2
	5.1	6.6	6.7	14.1	5.4	4.5	4.0	4.1	17.2	2.2	23.4	23.8	33.5	29.0	28.0	28.9	48.1	2.2	40.7	47.5	46.7	53.6	44.8
10/5/2021	0.5	0.6	0.8	1.5	0.5	0.5	0.7	0.7	0.8	0.2	1.3	1.4	1.7	1.4	0.9	0.9	1.2	0.2	1.5	2.5	2.4	2.0	1.8
	1.2	1.4	1.5	2.3	1.3	1.2	1.4	1.4	1.6	0.9	2.1	2.2	2.6	2.3	1.6	1.6	2.3	0.9	2.4	3.5	3.3	3.0	2.8
	2.1	2.4	3.1	4.8	2.3	1.9	2.1	2.2	3.1	1.3	5.1	5.2	7.0	6.0	2.9	3.0	4.8	1.3	5.9	8.2	7.8	8.5	7.1
	1.9	2.8	3.6	6.6	2.5	1.9	2.1	2.5	4.0	1.1	7.9	8.0	10.6	9.5	4.3	4.5	9.4	1.0	9.5	12.7	12.2	14.2	11.7
	2.7	4.3	4.3	9.0	3.5	2.7	3.1	3.4	5.6	1.8	11.8	11.9	15.7	13.7	7.4	7.8	15.2	1.7	14.1	18.3	17.7	22.9	17.5
	4.9	7.2	7.2	13.6	5.8	4.0	4.2	4.5	10.2	2.6	17.9	18.1	23.9	21.3	16.7	17.3	27.3	2.5	23.1	28.5	27.8	36.0	28.8
	3.8	7.1	7.2	14.3	5.6	3.8	3.9	4.1	12.3	2.2	21.0	21.3	28.4	25.6	20.0	20.8	33.9	2.2	29.3	35.5	34.7	43.4	35.7
	3.2	6.2	6.3	13.6	5.0	3.7	3.7	3.9	15.4	1.9	22.9	23.3	32.6	27.9	24.8	25.8	44.9	2.0	38.5	45.4	44.6	51.9	42.1
10/6/2021	-6.9	-6.7	-6.6	-6.0	-6.8	-6.9	-6.7	-6.7	-6.4	-7.2	-6.0	-5.9	-5.9	-5.9	-6.5	-6.5	-6.3	-7.2	-5.8	-4.8	-4.9	-5.4	-5.4
	-6.6	-6.3	-6.0	-4.7	-6.5	-6.6	-6.5	-6.3	-5.6	-7.1	-4.4	-4.3	-3.4	-3.6	-6.2	-6.1	-5.2	-7.2	-3.4	-1.3	-1.6	-1.5	-2.5
	-6.1	-5.8	-5.4	-3.4	-6.1	-6.2	-6.0	-5.6	-4.6	-6.8	-1.7	-1.6	-0.6	-0.7	-5.2	-5.2	-2.6	-6.9	-0.7	2.4	1.9	3.4	1.2
	-5.3	-4.2	-4.4	-0.5	-4.8	-5.5	-4.9	-4.6	-2.8	-6.3	2.4	2.6	5.4	4.7	-2.0	-1.8	7.0	-6.3	4.5	8.8	8.2	12.5	8.1
	-4.7	-3.2	-3.3	1.8	-3.7	-4.9	-24.5	-4.3	-0.2	-6.2	6.6	6.7	10.8	9.5	3.3	3.8	14.3	-6.2	10.4	15.6	14.9	22.8	15.0
	-4.1	-1.9	-1.7	5.1	-2.6	-4.4	-24.5	-4.0	9.7	-6.2	10.8	11.1	18.7	15.5	26.7	26.9	43.8	-6.2	24.7	30.6	29.9	38.1	27.9
	-2.5	-0.3	0.1	9.1	-1.3	-7.1	-24.5	-7.1	-7.1	-7.0	17.2	17.6	28.1	23.5	-6.9	-7.0	-7.0	-7.1	47.2	53.5	52.8	55.0	47.1
10/7/2021	9.7	9.9	10.1	10.8	9.9	9.6	-24.5	9.7	10.0	9.2	10.8	10.9	11.5	11.3	10.0	10.0	-24.5	9.2	11.3	12.4	12.1	12.1	11.7
	10.2	10.7	10.8	12.6	10.2	9.9	11.5	10.2	11.1	9.3	13.2	13.2	14.9	14.0	10.8	10.9	-24.5	9.3	14.1	16.2	15.8	16.4	14.8
	10.5	11.8	11.7	15.0	11.2	10.4	12.1	10.9	12.5	9.6	16.5	16.6	19.4	18.0	13.2	13.5	-24.5	9.6	18.4	21.3	20.8	23.1	19.9
	10.7	12.4	12.1	15.9	11.6	10.6	12.3	11.1	13.0	9.6	17.3	17.3	20.3	19.0	13.9	14.1	-24.5	9.6	19.5	22.6	22.1	24.4	21.5
	11.4	13.9	13.6	18.8	12.7	10.9	13.0	11.5	15.6	9.7	21.7	21.9	25.7	24.3	18.1	18.6	-24.5	9.7	26.0	30.3	29.7	34.4	30.0
	12.4	13.7	13.5	18.6	12.8	11.0	13.2	11.6	16.1	9.8	21.5	21.6	25.9	24.2	20.9	21.4	-24.5	9.7	24.8	29.0	28.4	34.4	28.2
	14.7	16.4	16.3	23.0	15.2	12.8	14.7	13.5	23.0	10.0	27.7	27.9	34.5	32.3	32.9	33.1	-24.5	10.0	34.4	39.7	39.1	48.1	39.9
	17.2	19.3	19.6	28.0	18.7	9.9	12.6	10.0	10.0	10.0	36.1	36.4	43.0	43.0	10.1	10.1	-24.5	10.0	49.1	54.9	54.4	55.0	54.9
PHASE 1 - R1234ze(E), circular cone nozzles, triangular pitch, Tube-C condenser tubes (Bundle 1)																							
11/5/2021	10.7	10.8	10.9	11.0	10.8	10.9	11.0	11.0	10.9	10.5	10.9	10.9	10.8	10.8	11.0	10.9	-24.5	10.5	10.8	11.0	10.9	10.8	10.8
	10.6	10.7	10.9	11.2	10.7	10.9	11.1	11.0	11.1	10.2	11.0	11.1	11.0	10.9	10.9	10.9	-24.5	10.2	11.2	12.4	12.0	11.4	11.1
	10.5	10.6	11.0	11.1	10.6	11.7	12.0	11.9	12.6	9.9	10.8	11.0	10.9	10.6	19.2	18.3	-24.5	9.9	10.8	11.5	11.1	11.1	10.8
	11.0	11.2	11.7	11.8	11.3	13.4	14.0	13.7	15.7	10.3	11.6	11.8	11.7	11.3	27.1	26.0	-24.5	10.3	13.7	13.3	12.7	12.9	12.3
	11.2	11.5	12.1	12.1	11.6	16.2	16.7	16.3	19.6	10.4	12.6	12.7	12.2	11.8	53.4	52.2	-24.5	10.4	19.2	15.8	16.1	16.7	16.9
	11.4	11.6	12.3	12.3	11.9	10.4	10.4	10.4	10.4	10.4	15.9	16.1	12.9	13.3	10.5	10.4	-24.5	10.4	31.1	26.3	28.1	46.7	26.1

Date	Row 1					Row 2					Row 3				Row 4				Row 5				
	Tube 1			Tube 6	Tube 11	Tube 2			Tube 7	Tube 12	Tube 3		Tube 8	Tube 13	Tube 4		Tube 9	Tube 14	Tube 5			Tube 10	Tube 15
	T_{top}	T_{side}	T_{bottom}	T_{bottom}	T_{top}	T_{top}	T_{side}	T_{bottom}	T_{bottom}	T_{top}	T_{side}	T_{bottom}	T_{bottom}	T_{top}	T_{top}	T_{side}	T_{bottom}	T_{top}	T_{top}	T_{side}	T_{bottom}	T_{bottom}	T_{top}
PHASE 1 - R1234ze(E), circular cone nozzles, triangular pitch, Tube-C condenser tubes (Bundle 1)																								
11/8/2021	9.6	9.7	9.8	10.2	9.7	9.8	9.9	9.8	9.8	9.4	9.9	10.0	9.9	9.9	9.8	9.8	-24.5	9.4	10.0	10.6	10.4	10.2	10.0
	9.6	9.7	9.8	10.3	9.7	9.8	9.8	9.8	9.8	9.4	10.0	10.1	10.0	10.1	9.7	9.7	-24.5	9.4	10.1	11.0	10.7	10.4	10.2
	10.8	10.9	11.1	11.9	10.9	11.1	11.2	11.1	11.1	10.4	11.7	11.8	11.9	12.1	11.8	11.7	-24.5	10.4	12.2	14.0	13.4	13.5	12.8
	11.5	11.6	12.0	12.7	11.7	11.9	12.4	12.3	12.3	10.9	12.8	13.0	13.1	13.6	17.0	17.2	-24.5	10.9	14.0	16.7	15.8	17.0	14.9
	11.3	11.5	11.9	12.2	11.5	12.7	13.3	13.2	14.5	10.6	12.4	12.6	12.7	12.8	30.7	30.2	-24.5	10.6	14.4	16.9	15.9	16.4	14.3
	10.9	11.1	11.5	11.8	11.3	10.1	10.1	10.1	10.1	10.1	13.0	13.1	13.5	13.5	10.1	10.1	-24.5	10.1	15.2	18.3	17.6	27.0	15.8
11/9/2021	3.1	3.2	3.3	3.4	3.2	3.3	3.4	3.4	3.4	3.0	3.3	3.3	3.2	3.2	3.4	3.4	-24.5	2.9	3.2	3.3	3.3	3.3	3.2
	-0.5	-0.3	0.0	0.8	-0.4	-0.3	-0.1	-0.2	0.1	-1.0	0.7	0.9	0.7	0.7	-0.1	-0.1	-24.5	-1.0	1.1	2.8	2.3	1.5	1.2
11/10/2021	2.7	2.8	3.0	3.3	2.8	3.0	3.2	3.1	3.2	2.3	3.0	3.1	3.0	2.8	3.1	3.1	-24.5	2.3	3.0	3.7	3.5	3.2	2.9
	2.8	2.9	3.4	3.6	3.0	3.6	4.0	3.8	4.8	2.3	3.1	3.3	3.3	2.9	11.7	11.0	-24.5	2.3	3.1	3.5	3.3	3.3	2.9
	2.8	2.9	3.4	3.6	3.0	3.4	3.9	4.2	4.6	2.3	3.2	3.4	3.3	3.0	11.4	10.8	-24.5	2.3	3.3	4.4	4.0	3.7	3.2
	4.1	4.2	4.6	4.9	4.3	4.6	4.9	5.3	5.5	3.6	4.5	4.7	4.7	4.4	10.5	9.9	-24.5	3.6	4.7	5.9	5.4	5.1	4.6
	3.2	3.4	4.0	4.2	3.5	4.8	5.6	5.4	7.7	2.5	3.7	4.0	3.9	3.4	20.0	19.1	-24.5	2.5	4.5	4.4	4.1	4.3	3.8
	2.8	3.0	3.6	3.8	3.0	4.6	5.3	5.3	7.9	2.1	3.5	3.7	3.6	3.2	27.5	26.8	-24.5	2.1	5.3	5.3	4.7	4.1	3.9
	4.2	4.4	4.9	5.1	4.4	6.1	6.9	6.8	9.1	3.5	4.8	5.0	4.9	4.5	22.8	22.1	-24.5	3.5	6.4	6.1	5.6	5.5	5.1
	3.3	3.6	4.3	4.3	3.6	6.6	7.5	7.3	11.7	2.5	4.3	4.6	4.3	3.7	50.0	49.2	-24.5	2.5	11.2	6.7	7.1	7.0	7.9
	3.0	3.3	4.1	4.1	3.4	2.0	2.0	2.0	2.0	2.0	7.0	7.2	4.3	4.6	2.0	2.0	-24.5	2.0	16.4	8.7	10.4	52.9	18.6
11/11/2021	-8.6	-8.4	-8.2	-7.5	-8.5	-8.6	-8.4	-8.4	-8.4	-8.9	-7.6	-7.5	-8.0	-7.8	-8.6	-8.6	-24.5	-8.9	-7.5	-6.3	-6.6	-7.8	-7.4
	-7.8	-7.7	-7.4	-6.7	-7.7	-7.6	-7.4	-7.2	-7.2	-8.3	-6.9	-6.7	-7.2	-6.9	-7.7	-7.6	-24.5	-8.3	-6.7	-5.0	-5.5	-6.5	-6.5
	-7.8	-7.7	-7.3	-6.7	-7.7	-7.6	-7.3	-7.1	-7.1	-8.2	-7.0	-6.7	-7.2	-7.0	-7.3	-7.3	-24.5	-8.2	-6.8	-5.2	-5.6	-6.5	-6.7
	-8.2	-8.0	-7.5	-7.3	-8.0	-7.5	-7.2	-6.9	-5.7	-8.7	-7.8	-7.6	-7.7	-8.1	1.0	0.3	-24.5	-8.7	-7.9	-7.4	-7.5	-7.6	-8.1
	-7.9	-7.8	-7.3	-7.0	-7.7	-7.1	-6.8	-6.5	-5.2	-8.4	-7.5	-7.2	-7.3	-7.6	2.6	1.9	-24.5	-8.4	-7.4	-6.7	-6.9	-7.1	-7.6
	-7.9	-7.7	-7.0	-6.9	-7.7	-6.6	-6.1	-5.8	-2.8	-8.6	-7.3	-6.9	-7.2	-7.7	9.8	8.9	-24.5	-8.6	-6.6	-6.9	-6.9	-6.7	-7.4
	-7.3	-7.1	-6.4	-6.3	-7.0	-6.2	-5.7	-5.4	-2.5	-7.9	-6.7	-6.3	-6.5	-7.1	9.4	8.5	-24.5	-8.0	-6.1	-6.3	-6.3	-6.1	-6.8
	-7.2	-6.9	-6.1	-5.8	-6.9	-4.7	-4.1	-4.0	1.5	-8.0	-6.1	-5.7	-6.2	-6.8	38.6	37.6	-24.5	-8.0	-1.6	-4.9	-4.8	-4.9	-4.3
	-7.8	-7.5	-6.6	-6.6	-7.4	-8.8	-8.8	-8.8	-8.8	-8.8	-5.7	-5.4	-6.5	-6.8	-8.8	-8.8	-24.5	-8.8	3.3	-2.8	-1.7	5.4	0.5
11/12/2021	3.7	4.0	4.7	4.7	4.0	6.2	6.9	7.1	11.6	2.9	4.6	4.9	4.6	4.1	33.9	32.8	-24.5	2.9	11.1	6.6	7.3	7.3	7.2
	4.1	4.4	5.1	5.1	4.4	6.7	7.6	7.8	12.2	3.2	5.2	5.5	5.2	4.6	42.2	41.3	-24.5	3.2	12.6	7.7	8.5	8.6	8.8
	3.1	3.4	4.1	4.1	3.4	4.8	5.3	5.8	9.5	2.3	3.9	4.2	4.1	3.4	27.0	26.2	-24.5	2.3	11.4	7.1	7.9	7.5	7.5
11/20/2021	10.3	10.4	10.8	10.9	10.5	11.1	11.5	11.6	12.3	9.7	10.7	10.9	10.8	10.6	18.6	17.5	-24.5	9.7	10.9	11.6	11.4	11.4	10.9
	10.3	10.4	10.8	10.9	10.5	11.1	11.4	11.5	12.2	9.8	10.7	10.9	10.8	10.6	18.2	17.3	-24.5	9.8	10.9	11.5	11.4	11.3	10.9
11/21/2021	10.5	10.6	11.0	11.0	10.6	11.2	11.7	11.7	12.5	9.9	10.8	11.0	11.0	10.7	18.7	17.6	-24.5	9.9	11.0	11.3	11.2	11.2	11.0
11/22/2021	11.5	11.6	12.0	12.1	11.7	12.2	12.6	12.6	13.4	11.0	11.9	12.1	12.0	11.8	19.4	18.4	-24.5	11.0	12.2	12.9	12.7	12.5	12.1
	12.0	12.2	12.7	12.7	12.2	13.7	14.0	14.1	16.8	11.3	12.7	12.9	12.8	12.5	27.5	26.1	-24.5	11.3	15.1	14.5	14.3	14.8	13.9
	10.8	11.0	11.5	11.5	11.1	12.6	13.0	13.1	15.9	10.1	11.5	11.7	11.6	11.3	27.1	25.8	-24.5	10.1	14.2	13.2	13.1	13.5	13.0
	10.7	10.9	11.4	11.4	11.0	12.5	12.9	13.0	16.0	10.0	11.4	11.6	11.5	11.1	25.6	24.1	-24.5	10.0	14.3	12.8	12.8	13.3	13.0
	12.3	12.5	13.1	13.0	12.6	16.1	16.4	16.5	21.5	11.4	14.1	14.2	13.6	13.3	49.5	47.7	-24.5	11.4	19.4	17.2	18.0	19.3	17.8
	11.0	11.2	11.8	11.7	11.3	14.4	14.8	14.9	19.7	10.1	13.0	13.1	12.0	11.8	42.2	40.6	-24.5	10.1	20.8	15.4	16.7	17.8	20.5

Date	Row 1					Row 2					Row 3					Row 4					Row 5				
	Tube 1			Tube 6	Tube 11	Tube 2			Tube 7	Tube 12	Tube 3		Tube 8	Tube 13	Tube 4		Tube 9	Tube 14	Tube 5			Tube 10	Tube 15
	T_{top}	T_{side}	T_{bottom}	T_{bottom}	T_{top}	T_{top}	T_{side}	T_{bottom}	T_{bottom}	T_{top}	T_{side}	T_{bottom}	T_{bottom}	T_{top}	T_{top}	T_{side}	T_{bottom}	T_{top}	T_{top}	T_{side}	T_{bottom}	T_{bottom}	T_{top}
PHASE 1 - R1234ze(E), circular cone nozzles, triangular pitch, Tube-C condenser tubes (Bundle 1)																									
11/29/2021	-8.2	-8.1	-7.6	-7.4	-8.0	-7.5	-7.1	-7.1	-5.6	-8.8	-7.8	-7.6	-7.7	-8.2	1.3	0.6	-24.5	-8.8	-7.8	-7.6	-7.5	-7.6	-8.0
	-8.0	-7.8	-7.3	-7.2	-7.8	-7.1	-6.7	-6.7	-5.1	-8.5	-7.6	-7.3	-7.4	-7.9	2.4	1.8	-24.5	-8.5	-7.5	-7.3	-7.2	-7.3	-7.7
	-8.3	-8.1	-7.6	-7.5	-8.1	-7.6	-7.3	-7.2	-5.9	-8.8	-7.9	-7.7	-7.8	-8.3	0.5	-0.1	-24.5	-8.8	-8.0	-7.8	-7.6	-7.7	-8.1
	-7.4	-7.3	-6.8	-6.6	-7.2	-6.7	-6.3	-6.3	-5.1	-7.9	-7.0	-6.8	-6.9	-7.4	0.5	-0.1	-24.5	-7.9	-7.0	-6.9	-6.7	-6.8	-7.2
	-6.5	-6.2	-5.6	-5.5	-6.2	-4.7	-4.1	-4.2	-1.7	-7.2	-5.8	-5.4	-5.7	-6.4	11.8	11.0	-24.5	-7.2	-4.9	-5.5	-5.4	-5.5	-5.8
	-8.1	-7.9	-7.2	-7.1	-7.9	-6.5	-5.9	-5.9	-3.1	-8.8	-7.4	-7.0	-7.3	-8.0	10.5	9.7	-24.5	-8.8	-6.5	-7.2	-7.0	-7.1	-7.4
	-8.0	-7.8	-7.1	-7.0	-7.7	-6.1	-5.6	-5.6	-2.5	-8.7	-7.3	-6.9	-7.2	-7.9	14.3	13.6	-24.5	-8.7	-6.1	-6.9	-6.8	-7.0	-7.1
	-8.0	-7.8	-7.1	-7.0	-7.8	-6.7	-6.1	-6.1	-3.9	-8.8	-7.4	-7.0	-7.3	-8.0	7.2	6.4	-24.5	-8.8	-6.8	-7.2	-7.1	-7.1	-7.5
PHASE 1 - R1233zd(E), circular cone nozzles, triangular pitch, Tube-C condenser tubes (Bundle 1)																									
1/19/2022	9.4	9.5	9.7	10.2	9.4	9.7	9.8	9.7	9.9	9.1	10.2	10.3	10.1	10.3	10.4	10.2	-24.5	9.2	10.4	11.3	11.0	10.8	10.8
	9.9	10.1	10.3	11.6	10.1	11.3	11.3	11.2	13.3	9.2	12.5	12.5	12.3	13.0	26.6	26.5	-24.5	9.2	14.6	16.3	15.8	16.3	15.4
	10.8	11.0	11.4	13.8	11.3	15.7	15.8	15.6	27.9	9.3	17.2	17.1	17.1	18.6	54.1	54.1	-24.5	9.3	28.8	32.1	31.4	42.6	39.2
	11.7	12.0	12.2	16.2	12.4	9.3	9.3	9.3	9.3	9.3	27.7	27.8	27.2	38.1	9.4	9.4	-24.5	9.4	54.8	55.0	55.0	55.0	55.0
1/20/2022	10.1	10.3	10.5	11.3	10.2	10.2	10.3	10.3	10.5	9.8	11.1	11.2	10.9	11.2	10.3	10.3	-24.5	9.9	11.0	12.1	11.8	11.4	11.5
	12.0	12.3	12.7	14.3	12.1	12.1	12.3	12.2	12.7	11.2	14.0	14.2	14.5	14.5	12.2	12.3	-24.5	11.3	14.2	16.4	16.0	15.9	15.4
	12.7	13.2	13.8	16.5	12.9	13.0	13.2	13.2	14.3	11.7	16.6	16.8	17.4	17.4	14.4	14.3	-24.5	11.8	17.1	20.3	19.8	20.8	19.1
	14.8	15.4	16.2	18.6	14.9	15.6	15.8	15.7	17.9	13.7	18.7	19.1	20.0	19.0	26.3	26.1	-24.5	13.8	19.0	23.0	22.5	23.8	20.9
	14.9	15.4	16.2	18.0	15.1	15.9	16.1	16.1	18.1	14.1	17.8	18.2	17.8	17.8	21.6	21.3	-24.5	14.2	17.8	21.1	20.8	21.1	18.9
	18.7	19.3	20.2	21.8	19.0	21.4	21.8	21.6	36.2	17.8	22.9	23.8	22.2	21.9	55.0	55.0	-24.5	17.8	43.2	43.8	45.1	26.6	30.1
1/28/2022	13.7	13.8	14.0	14.4	13.7	14.0	14.1	14.0	14.2	13.4	14.4	14.5	14.2	14.3	14.3	14.3	14.3	13.6	14.4	15.2	15.0	14.7	14.6
	15.0	15.2	15.5	16.4	15.1	15.6	15.7	15.7	16.7	14.4	17.1	17.2	17.1	17.4	20.4	20.3	34.7	14.6	18.1	20.0	19.5	19.9	19.0
	14.9	15.2	15.8	17.3	15.0	15.8	15.9	15.9	17.5	14.2	17.5	17.7	17.3	17.6	20.7	20.4	52.4	14.5	18.1	20.8	20.2	20.7	19.0
	16.3	16.7	17.4	19.1	16.5	17.3	17.5	17.4	19.7	15.5	19.4	19.6	19.2	19.6	24.9	24.5	55.0	15.8	20.2	23.4	22.7	23.6	21.0
	16.4	16.9	17.5	19.6	16.6	17.8	17.9	17.9	23.7	15.5	20.3	20.6	20.0	20.8	55.0	55.0	55.0	15.6	21.7	25.1	24.4	27.1	23.0
	16.0	16.4	17.1	19.3	16.2	14.9	14.9	15.0	15.0	14.9	19.9	20.2	19.6	20.5	15.2	15.2	15.2	15.1	21.6	25.3	24.6	26.5	22.4
2/4/2022	12.4	12.6	12.7	13.6	12.6	12.4	12.5	12.5	12.9	11.7	14.1	14.1	14.7	14.5	13.3	13.3	-24.5	11.8	14.7	15.8	15.6	16.1	15.6
	15.6	16.0	16.3	18.2	15.8	15.3	15.5	15.6	16.4	14.3	19.9	19.9	21.0	21.3	17.3	17.3	-24.5	14.4	20.7	22.9	22.5	25.9	23.6
	17.1	17.9	18.1	22.6	17.9	16.4	16.8	17.0	22.7	13.5	25.9	25.9	31.8	29.2	30.3	30.3	-24.5	13.5	32.8	35.8	35.3	43.1	38.4
	18.7	19.9	20.0	27.2	20.3	19.5	19.9	20.5	31.6	12.5	32.2	32.2	42.8	37.5	45.6	45.6	-24.5	12.6	46.8	50.5	50.0	55.0	55.0
	18.6	20.1	20.2	28.6	20.0	11.8	11.8	11.8	11.8	11.9	37.5	37.6	47.2	42.8	11.9	11.9	-24.5	11.9	12.7	12.8	12.8	12.7	12.8
	22.0	23.9	24.1	34.8	24.1	13.0	13.0	13.0	13.1	13.1	52.8	53.0	55.0	55.0	13.1	13.1	-24.5	13.2	14.5	14.6	14.5	14.3	14.6
PHASE 2 - R134a, circular cone nozzles, square pitch, Tube-C condenser tubes (Bundle 2)																									
3/7/2022	1.7	1.8	1.9	2.5	1.7	2.4	2.4	2.6	1.9	1.9	2.0	2.1	2.0	1.6	1.9	1.8	2.0	1.7	2.4	2.2	2.5	2.6	2.1
	2.6	2.9	3.2	4.7	2.9	4.9	5.0	4.8	3.2	3.6	4.1	4.3	3.5	2.5	4.4	4.2	4.2	3.0	7.1	7.7	8.9	7.9	5.4
	2.7	3.5	5.2	9.5	4.2	9.5	9.5	9.4	5.0	6.6	9.5	10.3	8.5	2.7	11.2	11.0	13.1	9.0	15.7	17.1	18.8	21.7	13.4
	3.8	4.7	7.0	12.4	6.2	11.1	11.0	11.1	7.9	9.5	11.3	12.3	13.4	4.1	13.7	13.6	19.5	13.7	18.6	20.4	22.1	27.2	16.5
	5.5	7.7	9.5	17.4	8.7	16.3	16.1	16.3	10.9	13.6	16.7	18.2	20.1	5.2	21.1	20.9	28.7	19.8	27.3	29.6	31.9	41.6	24.9
	5.8	7.7	10.0	18.8	8.6	17.8	17.6	17.8	11.3	14.4	20.2	22.0	22.7	4.8	25.5	25.3	32.3	21.4	32.3	35.3	38.1	49.2	28.7

Date	Row 1					Row 2					Row 3					Row 4					Row 5				
	Tube 1			Tube 6	Tube 11	Tube 2			Tube 7	Tube 12	Tube 3		Tube 8	Tube 13	Tube 4		Tube 9	Tube 14	Tube 5			Tube 10	Tube 15
	T_{top}	T_{side}	T_{bottom}	T_{bottom}	T_{top}	T_{top}	T_{side}	T_{bottom}	T_{bottom}	T_{top}	T_{side}	T_{bottom}	T_{bottom}	T_{top}	T_{top}	T_{side}	T_{bottom}	T_{top}	T_{top}	T_{side}	T_{bottom}	T_{bottom}	T_{top}
PHASE 2 - R134a, circular cone nozzles, square pitch, Tube-C condenser tubes (Bundle 2)																									
3/8/2022	1.5	1.6	1.8	2.4	1.6	2.3	2.3	2.5	1.8	1.8	1.7	1.9	1.8	1.4	1.7	1.6	1.8	1.5	1.8	1.7	2.0	2.3	1.9
	2.4	2.7	3.0	4.2	2.7	5.0	5.3	5.1	3.0	3.6	3.4	3.6	3.1	2.2	3.9	3.6	2.9	2.8	8.3	7.6	9.0	7.2	5.0
	3.0	3.9	5.5	8.6	4.4	9.3	9.3	9.3	4.8	6.4	7.3	8.0	6.4	2.8	8.5	8.1	8.4	5.7	15.8	14.9	16.7	16.3	10.8
	3.6	5.8	7.8	14.3	6.1	13.3	13.2	13.4	7.8	10.0	14.1	15.6	15.4	3.5	18.7	18.6	21.5	13.9	27.5	26.4	28.6	34.4	20.7
	3.3	5.1	7.5	13.3	6.1	12.5	12.4	12.7	6.8	8.9	12.1	13.5	12.0	3.2	14.3	14.1	15.5	10.3	23.8	22.7	25.0	25.6	17.4
	5.2	7.2	9.6	17.1	7.8	16.9	16.8	17.1	9.3	12.2	17.3	19.2	17.0	4.2	22.4	22.2	23.9	15.4	33.7	32.3	35.0	39.0	24.1
	6.1	8.0	11.0	19.9	8.8	19.3	19.1	19.6	10.6	13.7	21.7	24.1	21.5	4.5	27.3	27.1	28.7	17.7	40.4	38.7	42.0	49.8	29.8
3/14/2022	9.9	10.0	10.0	10.5	9.9	10.5	10.5	10.5	10.1	10.1	10.1	10.2	10.1	9.9	10.1	10.0	10.1	10.0	10.5	10.2	10.4	10.4	10.2
	10.7	10.9	11.4	12.7	11.0	13.1	13.5	12.9	11.4	11.7	12.0	12.2	11.6	10.6	12.1	11.9	11.0	11.0	14.7	15.4	16.5	14.9	13.1
	10.8	11.2	12.8	15.9	11.7	15.5	15.5	15.6	12.4	13.0	15.1	15.8	13.6	10.7	15.7	15.5	15.1	13.0	20.6	22.0	23.4	21.9	16.9
	12.5	13.9	15.9	22.0	14.7	21.4	21.4	21.5	15.3	17.6	21.1	22.4	20.1	11.2	23.8	23.5	24.2	19.0	29.1	31.3	33.1	36.7	25.7
	13.2	15.7	17.8	25.0	16.7	23.5	23.4	23.7	17.8	19.6	22.8	24.2	23.6	11.6	23.5	23.1	28.8	21.9	30.0	32.1	33.9	38.7	27.3
	14.4	16.3	18.7	27.2	17.2	25.5	25.5	25.8	18.4	21.5	25.7	27.5	26.4	12.2	28.8	28.5	32.1	22.9	36.3	39.1	41.3	48.2	32.4
3/15/2022	2.2	2.4	2.6	3.3	2.3	3.4	3.2	3.4	2.5	2.5	2.4	2.6	2.5	2.2	2.3	2.3	2.5	2.2	2.7	2.4	2.6	3.1	2.5
	2.3	2.4	2.6	3.2	2.3	3.1	3.1	3.2	2.6	2.6	2.5	2.7	2.5	2.3	2.5	2.4	2.5	2.3	2.9	2.6	2.8	3.1	2.6
	2.1	2.2	2.3	2.9	2.0	2.8	2.9	2.9	2.3	2.3	2.3	2.4	2.3	2.1	2.2	2.2	2.3	2.1	2.6	2.4	2.5	2.8	2.4
	2.3	2.5	2.9	3.9	2.3	3.6	4.3	4.1	2.8	3.0	3.1	3.3	2.7	2.3	3.4	3.2	2.6	2.4	6.0	6.6	7.7	5.6	4.1
	2.8	3.3	4.5	6.9	3.3	7.4	7.4	7.3	4.2	5.1	6.4	7.0	4.8	2.7	7.4	7.2	6.1	4.0	11.6	13.2	14.8	13.7	8.7
	3.2	3.9	6.2	10.2	4.1	10.0	10.1	10.3	5.4	7.0	10.2	11.4	7.5	2.8	12.3	12.1	10.6	7.0	17.1	19.4	21.4	22.5	13.6
	4.0	5.1	8.1	13.9	5.3	13.7	13.8	14.2	7.0	9.0	15.4	17.4	11.1	3.4	18.1	18.1	16.4	10.3	23.4	26.5	29.1	33.3	18.3
	5.4	7.3	10.5	18.4	7.4	18.2	18.2	18.8	9.4	12.3	21.2	23.7	18.0	3.9	24.6	24.7	27.0	15.0	33.6	37.4	40.4	48.3	26.8
PHASE 2 - R1234ze(E), circular cone nozzles, square pitch, Tube-C condenser tubes (Bundle 2)																									
3/25/2022	10.2	10.3	10.2	10.3	10.1	10.3	10.4	10.4	10.4	10.3	10.3	10.4	10.3	10.3	10.3	10.2	10.4	10.3	10.6	10.3	10.4	10.3	10.4
	9.9	10.2	10.0	10.1	9.8	10.0	10.2	10.2	10.2	10.0	10.1	10.3	10.1	10.3	10.3	10.2	10.3	10.3	11.3	10.6	11.0	10.3	10.9
	9.2	10.6	11.9	16.3	11.5	16.2	16.3	16.4	11.1	13.6	14.1	14.8	12.7	8.6	15.7	15.4	15.4	13.4	21.7	23.2	24.4	23.7	19.4
3/29/2022	10.6	10.7	10.6	10.9	10.5	10.8	10.9	10.9	10.8	10.7	10.8	10.9	10.7	10.6	10.8	10.7	10.7	10.7	11.3	11.1	11.4	10.8	11.0
	10.3	10.5	10.4	10.4	10.1	10.5	10.6	10.6	10.6	10.4	10.6	10.8	10.5	10.6	10.8	10.7	10.7	10.7	11.8	11.5	12.0	11.1	11.4
	10.6	10.9	10.8	10.9	10.4	11.0	11.1	11.2	11.0	10.8	11.4	11.7	11.1	11.4	12.2	12.2	11.5	11.7	15.3	14.5	15.2	12.5	14.3
	11.5	12.0	11.9	12.3	11.3	12.3	12.5	12.7	12.2	12.3	14.0	14.6	12.9	13.1	17.3	17.4	13.8	13.5	20.7	18.9	20.6	15.4	19.7
	10.8	11.2	11.1	11.6	10.5	11.6	11.8	12.1	11.5	11.6	12.8	13.7	12.3	12.0	14.4	14.4	13.0	12.5	19.0	18.3	19.8	14.2	17.7
	11.4	11.9	11.9	12.4	11.1	12.9	13.3	13.9	12.3	13.0	17.7	18.2	14.0	14.2	24.4	24.2	15.1	14.8	42.8	38.0	38.8	17.6	25.0
	11.3	11.7	11.8	12.6	11.0	13.2	13.7	14.7	12.5	13.0	18.6	19.8	14.4	14.0	22.4	22.5	15.6	15.1	53.7	49.8	49.8	18.6	30.9
3/30/2022	10.2	10.3	10.2	10.3	10.1	10.3	10.3	10.3	10.4	10.3	10.3	10.4	10.3	10.3	10.3	10.2	10.4	10.3	10.6	10.3	10.5	10.3	10.5
	10.1	10.2	10.1	10.2	10.0	10.2	10.3	10.3	10.3	10.2	10.2	10.3	10.2	10.2	10.2	10.2	10.3	10.2	10.5	10.2	10.4	10.2	10.4
	10.2	10.4	10.3	10.3	10.0	10.3	10.5	10.5	10.5	10.4	10.5	10.6	10.5	10.6	10.6	10.5	10.6	10.6	11.7	11.1	11.5	10.7	11.4
	10.7	11.0	10.9	10.9	10.4	10.9	11.2	11.3	11.1	10.9	11.5	11.7	11.2	11.5	12.3	12.3	11.6	11.7	15.4	14.4	15.2	12.4	14.0
	10.8	11.1	11.0	11.1	10.6	11.1	11.4	11.5	11.2	11.1	11.9	12.4	11.4	11.7	12.6	12.5	11.8	12.0	15.1	14.8	15.8	12.7	14.0
	10.8	11.2	11.1	11.5	10.5	11.5	11.8	12.0	11.4	11.6	13.4	14.1	12.1	12.5	16.8	16.9	13.2	12.8	20.5	18.0	19.7	14.7	19.2
	11.0	11.5	11.5	11.9	10.6	12.5	12.9	13.6	11.9	12.3	17.3	18.0	13.5	13.7	22.6	22.5	15.1	14.5	42.6	37.9	38.7	17.3	22.4
	11.2	11.7	11.8	12.3	10.8	13.0	13.5	14.3	12.5	13.2	20.7	21.1	14.4	14.5	25.9	26.4	16.2	15.7	55.0	55.0	55.0	18.6	38.3

Date	Row 1					Row 2					Row 3				Row 4				Row 5				
	Tube 1			Tube 6	Tube 11	Tube 2			Tube 7	Tube 12	Tube 3		Tube 8	Tube 13	Tube 4		Tube 9	Tube 14	Tube 5			Tube 10	Tube 15
	T_{top}	T_{side}	T_{bottom}	T_{bottom}	T_{top}	T_{top}	T_{side}	T_{bottom}	T_{bottom}	T_{top}	T_{side}	T_{bottom}	T_{bottom}	T_{top}	T_{top}	T_{side}	T_{bottom}	T_{top}	T_{top}	T_{side}	T_{bottom}	T_{bottom}	T_{top}
PHASE 2 - R1234ze(E), circular cone nozzles, square pitch, Tube-C condenser tubes (Bundle 2)																							
4/6/2022	10.3	10.4	10.4	10.6	10.2	10.6	10.6	10.6	10.5	10.4	10.6	10.7	10.4	10.4	10.7	10.6	10.5	10.4	11.3	11.4	11.7	10.7	10.7
	10.2	10.4	10.4	11.0	10.2	11.2	11.3	11.3	10.6	10.5	11.7	12.1	10.5	10.3	12.3	12.1	10.7	10.8	13.0	14.1	14.7	12.0	11.9
	10.4	10.6	10.6	11.1	10.4	11.2	11.3	11.3	10.8	10.7	11.6	12.0	10.8	10.6	12.4	12.2	11.0	11.0	13.1	14.2	14.8	11.9	12.0
	10.6	10.9	10.8	11.3	10.4	11.4	11.6	11.7	11.2	11.2	12.3	13.1	11.2	11.1	12.3	12.1	11.9	11.9	14.0	15.7	16.5	13.3	13.0
4/7/2022	11.0	11.4	11.4	12.0	10.9	11.1	11.2	11.2	11.0	15.7	14.0	15.1	11.7	11.5	12.1	12.0	15.9	12.7	16.9	19.6	20.7	24.6	19.1
	11.6	12.1	12.0	12.6	11.4	11.6	11.8	11.8	11.6	15.7	15.1	16.6	12.8	12.7	12.9	12.8	21.2	13.5	18.1	21.4	22.8	31.9	38.3
4/12/2022	2.3	2.4	2.3	2.3	2.2	2.2	2.2	2.2	2.2	2.5	2.3	2.4	2.4	2.3	2.2	2.2	2.7	2.2	2.5	2.3	2.5	2.4	2.4
	2.5	2.6	2.5	2.5	2.4	2.4	2.5	2.5	2.5	2.7	2.6	2.7	2.7	2.6	2.4	2.4	2.9	2.5	2.8	2.6	2.7	2.6	2.6
	2.5	2.6	2.5	2.6	2.4	2.5	2.5	2.5	2.5	2.7	2.6	2.7	2.7	2.6	2.4	2.4	3.0	2.5	2.8	2.6	2.7	2.7	2.6
	2.5	2.6	2.5	2.6	2.4	2.4	2.5	2.5	2.5	2.7	2.6	2.7	2.7	2.6	2.4	2.4	3.0	2.5	2.8	2.6	2.8	2.7	2.6
	2.7	2.8	2.8	2.8	2.6	2.6	2.7	2.6	2.7	3.2	2.8	3.0	3.1	2.9	2.6	2.6	3.6	2.6	3.3	3.1	3.5	3.1	3.1
	2.6	2.7	2.7	2.7	2.4	2.5	2.5	2.5	2.5	3.0	2.7	2.9	2.9	2.8	2.4	2.4	3.5	2.5	3.0	2.8	3.1	2.9	2.9
	2.5	2.8	2.7	2.7	2.4	2.4	2.5	2.5	2.5	3.0	2.6	2.8	2.9	2.8	2.4	2.4	3.5	2.5	3.0	2.7	3.0	2.8	2.9
	2.5	2.8	2.7	2.9	2.4	2.4	2.5	2.5	2.5	3.5	2.8	3.1	2.9	2.7	2.5	2.4	3.5	2.4	3.8	4.1	4.7	3.2	3.2
4/13/2022	2.9	3.2	3.1	3.4	2.7	2.7	2.8	2.8	2.8	4.3	3.2	3.6	3.4	2.9	3.0	2.9	4.2	2.8	5.3	6.5	7.4	4.4	4.8
	2.8	3.1	3.0	3.2	2.6	2.6	2.7	2.7	2.7	3.6	2.9	3.2	3.3	3.0	2.6	2.6	4.2	2.8	3.8	3.6	4.0	3.7	4.8
	2.8	3.1	3.0	3.2	2.6	2.6	2.7	2.7	2.7	3.6	2.9	3.1	3.2	3.2	2.6	2.5	4.1	2.8	3.8	3.4	3.8	3.5	5.0
	2.9	3.2	3.2	3.6	2.7	2.7	2.9	2.9	2.8	5.5	4.2	4.7	3.4	2.9	3.5	3.4	4.4	2.9	6.8	8.6	9.3	9.1	7.2
	3.2	3.5	3.6	3.7	2.9	2.9	3.0	3.1	3.0	4.4	3.3	3.7	3.8	4.3	3.1	3.0	5.0	3.6	6.7	4.7	4.9	4.7	8.9
	3.1	3.4	3.4	3.6	2.9	2.8	3.0	3.0	2.9	4.4	3.3	3.7	3.7	3.6	3.0	2.9	4.8	3.2	5.4	5.8	6.5	5.0	7.0
	3.2	3.6	3.8	4.4	3.0	3.1	3.2	3.3	3.0	6.8	5.3	6.3	3.7	3.3	4.4	4.2	6.1	4.0	8.5	11.3	12.4	15.1	8.9
	3.3	3.7	4.0	5.0	3.2	3.6	3.7	3.8	3.2	11.3	7.9	9.2	3.9	3.5	5.5	5.3	10.6	4.8	10.7	13.2	14.2	23.0	13.2
4/14/2022	3.0	3.4	3.7	3.7	2.8	2.7	2.9	2.9	2.8	5.1	3.3	3.6	3.8	6.2	4.1	3.7	5.5	4.7	12.1	7.0	7.9	8.5	41.2
	3.2	3.6	3.8	3.9	3.0	2.9	3.1	3.1	3.0	4.8	3.7	4.2	4.0	4.2	3.4	3.3	6.0	4.1	6.9	9.1	10.5	11.9	16.5
	3.2	3.6	3.9	4.3	3.0	3.1	3.2	3.3	3.1	6.7	5.1	6.2	4.0	4.0	4.5	4.2	8.0	5.0	8.7	12.1	13.5	20.7	15.3
	3.1	3.4	3.7	3.7	2.8	2.7	3.0	3.0	2.9	5.0	3.3	3.7	3.8	6.4	4.1	3.8	5.9	4.7	11.7	7.3	8.4	8.5	35.5
	3.4	3.8	4.3	5.5	3.4	4.0	4.2	4.1	3.3	15.1	8.9	10.7	4.2	4.1	6.2	5.9	21.7	7.3	13.0	16.5	17.8	35.1	54.8
	3.4	3.8	4.1	4.8	3.2	3.5	3.7	3.7	3.2	9.4	6.9	8.5	4.2	4.2	5.2	4.9	15.0	6.5	10.4	14.4	16.0	28.8	40.7
	3.3	3.7	3.9	4.1	3.0	3.0	3.2	3.2	3.2	5.9	5.0	5.9	4.1	4.5	4.1	3.9	8.0	5.1	8.1	11.4	13.0	21.2	45.1
	3.6	4.1	4.6	6.2	3.7	4.4	4.5	4.5	3.4	14.9	8.8	10.8	4.3	4.3	6.2	6.0	24.4	7.6	12.7	16.8	18.4	35.4	31.0
	3.3	3.7	4.1	5.0	3.2	3.7	3.9	3.9	3.3	13.9	8.6	10.5	4.6	4.5	5.8	5.6	23.6	13.5	13.9	17.7	19.0	41.8	55.0

Date	Row 1					Row 2					Row 3				Row 4				Row 5				
	Tube 1			Tube 6	Tube 11	Tube 2			Tube 7	Tube 12	Tube 3		Tube 8	Tube 13	Tube 4		Tube 9	Tube 14	Tube 5			Tube 10	Tube 15
	T_{top}	T_{side}	T_{bottom}	T_{bottom}	T_{top}	T_{top}	T_{side}	T_{bottom}	T_{bottom}	T_{top}	T_{side}	T_{bottom}	T_{bottom}	T_{top}	T_{top}	T_{side}	T_{bottom}	T_{top}	T_{top}	T_{side}	T_{bottom}	T_{bottom}	T_{top}
PHASE 2 - R1234ze(E), circular cone nozzles, square pitch, Tube-C condenser tubes (Bundle 2)																							
5/6/2022	-6.6	-6.5	-6.6	-6.6	-6.8	-6.7	-6.7	-6.7	-6.7	-6.4	-6.6	-6.5	-6.6	-6.5	-6.7	-6.7	-6.2	-6.7	-6.4	-6.5	-6.4	-6.5	-6.5
	-6.4	-6.3	-6.4	-6.4	-6.5	-6.5	-6.5	-6.5	-6.5	-6.2	-6.3	-6.3	-6.4	-6.3	-6.5	-6.5	-6.0	-6.5	-6.2	-6.3	-6.2	-6.3	-6.3
	-6.7	-6.6	-6.7	-6.7	-6.8	-6.7	-6.7	-6.7	-6.8	-6.4	-6.6	-6.5	-6.6	-6.6	-6.8	-6.8	-6.3	-6.7	-6.5	-6.6	-6.4	-6.5	-6.5
	-6.6	-6.5	-6.5	-6.4	-6.7	-6.6	-6.6	-6.6	-6.7	-6.1	-6.4	-6.4	-6.5	-6.5	-6.7	-6.7	-6.2	-6.6	-6.2	-6.2	-6.0	-6.3	-6.3
	-6.4	-6.2	-6.3	-6.3	-6.6	-6.5	-6.5	-6.5	-6.5	-5.8	-6.2	-6.1	-6.2	-6.1	-6.6	-6.6	-5.4	-6.4	-5.8	-6.0	-5.7	-5.9	-5.8
	-6.3	-6.1	-6.2	-6.1	-6.4	-6.3	-6.4	-6.4	-6.4	-5.6	-6.0	-5.9	-6.0	-6.1	-6.4	-6.4	-5.2	-6.3	-5.5	-5.5	-5.2	-5.7	-5.7
	-6.2	-6.0	-6.1	-5.9	-6.4	-6.3	-6.3	-6.3	-6.4	-5.1	-5.9	-5.7	-6.0	-6.1	-6.3	-6.3	-5.0	-6.3	-4.9	-4.6	-4.0	-5.4	-5.3
	-6.3	-6.1	-6.0	-5.7	-6.4	-6.3	-6.3	-6.3	-6.4	-4.3	-5.6	-5.4	-6.0	-6.1	-6.2	-6.2	-4.8	-6.3	-4.2	-3.6	-3.0	-4.9	-4.7
5/9/2022	-5.9	-5.6	-5.6	-5.6	-6.1	-6.1	-5.9	-6.0	-6.0	-4.8	-5.6	-5.4	-5.4	-5.1	-6.1	-6.0	-4.4	-5.8	-4.3	-4.8	-4.5	-4.7	-3.4
	-5.8	-5.5	-5.5	-5.4	-6.0	-6.0	-5.9	-5.9	-6.0	-4.5	-5.3	-5.1	-5.3	-5.2	-5.8	-5.8	-4.0	-5.7	-3.5	-2.7	-1.9	-4.2	-3.8
	-6.0	-5.7	-5.7	-5.7	-6.2	-6.1	-6.0	-6.1	-6.1	-4.9	-5.6	-5.4	-5.5	-5.3	-6.1	-6.1	-4.3	-5.9	-4.3	-4.1	-3.7	-4.6	-4.3
	-6.0	-5.6	-5.4	-4.9	-6.1	-6.0	-5.9	-5.9	-6.1	-2.3	-4.1	-3.6	-5.4	-5.5	-5.3	-5.4	-3.3	-5.3	-1.1	0.5	1.4	0.9	-0.3
	-5.6	-5.2	-5.0	-4.9	-5.8	-5.8	-5.6	-5.6	-5.7	-3.9	-5.1	-4.9	-4.7	-4.1	-5.6	-5.6	-3.2	-5.0	-2.4	-3.3	-2.9	-3.2	1.6
	-5.8	-5.4	-5.1	-4.7	-5.9	-5.9	-5.7	-5.6	-5.9	-2.7	-4.2	-3.5	-4.8	-4.8	-5.0	-5.0	-2.0	-4.5	-0.2	2.0	3.1	2.6	1.3
	-5.8	-5.4	-5.3	-5.2	-6.0	-6.0	-5.9	-5.8	-5.9	-4.0	-5.3	-4.9	-4.8	-4.5	-5.8	-5.8	-2.8	-5.2	-3.0	-2.1	-1.3	-3.1	-0.2
	-5.6	-5.1	-4.5	-3.1	-5.4	-5.1	-4.9	-4.9	-5.7	3.2	0.0	1.3	-4.3	-4.7	-3.0	-3.1	6.7	-2.8	2.9	5.8	6.9	18.1	6.6
5/10/2022	-5.6	-5.2	-4.9	-4.6	-5.8	-5.8	-5.5	-5.5	-5.8	-2.9	-3.9	-3.0	-4.5	-4.4	-4.8	-4.9	-0.5	-4.0	0.9	3.6	5.0	10.5	3.7
	-5.7	-5.3	-5.0	-4.8	-5.9	-5.9	-5.7	-5.7	-5.8	-3.1	-5.0	-4.7	-4.6	-3.4	-4.9	-5.1	-1.0	-4.5	2.9	0.3	1.3	0.7	26.8
	-5.5	-5.1	-4.8	-4.5	-5.7	-5.7	-5.4	-5.4	-5.6	-2.8	-4.1	-3.4	-4.4	-4.0	-4.7	-4.7	-0.4	-4.0	1.2	2.9	4.1	7.6	10.0
	-5.4	-5.0	-4.6	-3.5	-5.5	-5.3	-4.9	-4.9	-5.5	2.6	1.4	3.2	-3.7	-4.0	-2.4	-2.6	10.3	-0.7	4.4	7.8	9.0	22.3	55.0
	-5.7	-5.3	-5.0	-4.8	-6.0	-6.0	-5.7	-5.7	-5.9	-3.2	-3.9	-3.0	-4.4	-4.3	-4.8	-5.0	-0.8	-4.5	-0.3	2.8	4.1	9.2	7.1
	-3.8	-3.0	-1.1	3.4	-2.0	-1.7	-1.4	-1.5	-4.8	15.2	6.4	8.2	-0.2	-2.1	0.4	0.1	45.1	2.1	11.6	15.1	16.8	47.3	28.0
	-5.4	-5.0	-4.7	-4.6	-5.7	-5.8	-5.4	-5.4	-5.6	-2.9	-4.2	-3.6	-4.2	-2.8	-4.9	-5.0	0.6	-3.7	1.7	3.3	4.8	13.6	50.7
	-5.2	-4.8	-4.3	-3.8	-5.4	-5.0	-4.7	-4.7	-5.4	0.5	0.3	2.0	-3.7	-3.4	-2.3	-2.4	9.6	-1.2	4.7	8.5	10.0	22.8	31.9
5/18/2022	-11.7	-11.7	-11.6	-11.3	-11.8	-11.8	-11.8	-24.5	-11.7	-11.0	-11.6	-11.5	-11.6	-11.7	-11.9	-11.9	-11.4	-11.8	-11.6	-11.5	-11.3	-11.3	-11.5
	-11.8	-11.7	-11.6	-11.3	-11.8	-11.8	-11.8	-24.5	-11.8	-11.0	-11.7	-11.6	-11.6	-11.8	-11.9	-11.9	-11.3	-11.9	-11.6	-11.6	-11.3	-11.3	-11.6
	-10.9	-10.5	-9.8	-6.7	-9.4	-10.1	-10.2	-24.5	-11.2	4.6	-5.2	-4.6	-3.9	-6.8	-8.8	-8.9	54.0	-5.2	-0.3	1.0	2.3	55.0	8.8
5/19/2022	-11.6	-11.6	-10.8	-9.3	-11.3	-11.2	-11.2	-24.5	-11.7	-7.5	-10.2	-10.0	-11.1	-11.7	-11.3	-11.4	-8.5	-11.6	-7.4	-6.4	-5.7	-6.0	-8.0
	-11.8	-11.6	-10.5	-8.8	-11.0	-11.1	-11.2	-24.5	-11.7	-6.8	-10.1	-9.8	-11.0	-11.7	-11.4	-11.5	-8.3	-11.7	-7.6	-6.5	-5.7	-5.2	-8.0
	-11.0	-10.6	-9.5	-7.2	-10.3	-10.3	-10.4	-24.5	-11.3	-3.2	-7.6	-7.0	-9.9	-11.2	-10.0	-10.1	-3.9	-9.9	-3.6	-2.0	-0.8	2.9	-2.5
	-10.5	-9.9	-8.5	-5.5	-9.7	-9.2	-9.3	-24.5	-10.8	2.1	-5.0	-3.8	-8.6	-10.3	-8.3	-8.5	5.8	-7.3	-0.2	2.3	3.8	15.1	4.1
	-10.5	-9.8	-8.4	-4.8	-9.5	-8.5	-8.4	-24.5	-10.7	6.7	-1.2	0.3	-7.2	-9.7	-6.3	-6.5	19.6	-5.4	4.0	7.4	9.0	28.3	17.1
	-10.1	-9.3	-7.4	-2.7	-8.4	-7.4	-7.4	-24.5	-10.4	13.1	1.2	3.0	-4.9	-8.6	-4.6	-4.8	36.0	-2.1	9.2	12.9	14.7	41.1	31.1
PHASE 2 - R1233zd(E), circular cone nozzles, square pitch, Tube-C condenser tubes (Bundle 2)																							
6/3/2022	-0.3	0.0	0.4	11.8	1.9	5.5	-24.5	-24.5	11.2	16.7	11.1	11.3	15.0	10.8	11.2	11.2	24.0	11.8	14.1	14.7	15.1	22.3	15.6
	23.9	24.6	25.2	26.8	24.6	26.0	-24.5	-24.5	27.3	34.6	31.0	31.5	27.8	25.7	27.9	27.7	31.1	25.6	32.5	33.6	34.1	38.6	31.4
	30.3	30.9	32.0	33.6	30.2	31.7	-24.5	-24.5	33.2	42.2	38.8	39.7	34.2	30.9	34.3	34.0	43.5	31.1	41.6	43.0	43.7	53.0	39.8
	31.8	32.2	34.1	37.0	31.6	33.2	-24.5	-24.5	34.6	45.6	42.3	43.5	37.5	32.0	37.0	36.6	55.0	32.4	46.9	48.9	49.9	55.0	44.4
	31.0	31.6	32.6	33.9	30.6	32.5	-24.5	-24.5	32.1	38.7	37.9	39.3	33.9	33.0	35.4	35.3	48.6	32.3	44.4	47.6	48.8	55.0	48.7

Date	Row 1					Row 2					Row 3				Row 4				Row 5				
	Tube 1			Tube 6	Tube 11	Tube 2			Tube 7	Tube 12	Tube 3		Tube 8	Tube 13	Tube 4		Tube 9	Tube 14	Tube 5			Tube 10	Tube 15
	T_{top}	T_{side}	T_{bottom}	T_{bottom}	T_{top}	T_{top}	T_{side}	T_{bottom}	T_{bottom}	T_{top}	T_{side}	T_{bottom}	T_{bottom}	T_{top}	T_{top}	T_{side}	T_{bottom}	T_{top}	T_{top}	T_{side}	T_{bottom}	T_{bottom}	T_{top}
PHASE 2 - R1233zd(E), circular cone nozzles, square pitch, Tube-C condenser tubes (Bundle 2)																							
6/8/2022	15.4	16.4	16.8	17.1	15.8	17.5	-2.2	-24.5	16.8	17.3	20.5	20.7	20.5	20.1	19.4	19.4	19.2	18.9	21.2	21.4	21.8	20.9	20.7
	28.6	29.0	31.2	37.7	28.5	27.6	12.1	-24.5	28.2	28.0	40.0	40.8	34.4	28.7	28.3	28.2	28.3	28.1	42.0	43.1	43.3	50.9	39.0
	30.6	30.7	33.1	35.6	30.4	29.7	30.0	-24.5	29.9	29.9	44.2	45.4	36.4	30.6	30.2	30.2	30.2	30.1	47.2	49.0	49.6	52.9	42.7
6/8/2022	30.0	30.5	30.8	31.2	29.8	29.2	3.1	-24.5	29.1	29.2	31.5	31.8	31.0	30.5	29.8	29.8	29.7	29.6	32.8	33.6	34.0	31.6	31.6
	31.8	32.0	33.1	34.6	31.6	31.0	-9.5	-24.5	30.9	31.0	34.5	35.2	33.0	31.8	31.5	31.5	31.3	31.2	37.6	39.2	39.8	34.8	35.1
	32.5	32.7	34.3	36.2	32.5	31.8	-24.5	-24.5	31.7	31.9	37.3	38.4	34.4	32.6	32.3	32.3	32.1	32.0	41.8	44.3	45.5	38.7	38.4
6/9/2022	3.6	4.2	5.1	17.6	5.4	-1.4	-24.5	-24.5	2.4	-1.6	14.2	14.9	17.5	8.6	7.5	7.5	8.7	7.0	18.7	19.9	20.5	26.5	18.9
	7.0	8.2	9.4	15.0	8.6	7.3	-24.5	-24.5	7.6	6.3	21.6	22.2	19.8	17.4	18.0	17.9	17.9	17.7	23.1	24.5	25.5	27.3	22.8
	15.6	17.1	18.1	19.3	16.2	19.0	-24.5	-24.5	18.3	18.6	22.8	23.4	22.3	21.1	20.7	20.7	20.6	20.5	25.0	26.5	27.7	23.3	23.3
	27.3	28.0	29.5	31.6	27.6	27.1	-24.5	-24.5	26.8	27.2	32.2	33.4	30.3	28.2	27.9	27.8	27.8	27.7	35.7	38.4	39.6	33.5	33.3
6/9/2022	19.8	20.6	21.3	23.8	20.8	21.6	-24.5	-24.5	21.3	21.5	26.8	27.1	25.9	25.1	24.6	24.5	24.5	24.0	27.4	27.9	28.5	28.5	27.0
	36.3	36.5	37.9	40.7	36.3	35.4	-24.5	-24.5	35.4	35.5	40.2	40.8	38.5	36.4	36.0	35.9	36.0	35.7	42.1	43.4	44.3	43.0	40.7
	46.1	46.1	49.9	55.0	45.6	45.3	-24.5	-24.5	45.2	45.2	54.7	55.0	52.8	45.6	45.5	45.4	45.4	45.3	55.0	55.0	55.0	55.0	53.1
6/10/2022	-0.5	0.3	0.7	1.2	-0.5	8.6	-24.5	-24.5	6.9	17.7	17.0	17.4	16.4	16.8	17.1	17.1	18.8	17.1	18.7	18.9	19.3	19.4	18.5
	26.1	27.0	27.6	28.8	26.6	28.3	-24.5	-24.5	28.0	32.3	30.2	30.6	29.3	28.3	29.0	28.9	31.2	28.4	32.5	34.2	35.0	36.8	32.1
7/13/2022	14.8	14.8	14.8	14.8	14.8	14.8	-24.5	-24.5	14.8	14.8	14.8	14.8	14.7	14.8	14.8	14.8	14.8	14.8	15.9	15.6	15.7	14.8	14.8
	15.2	15.2	15.2	15.2	15.2	15.2	-24.5	-24.5	15.2	15.2	15.2	15.2	15.2	15.2	15.3	15.3	15.2	15.2	16.8	16.5	16.8	15.3	15.3
	14.9	14.9	14.9	14.9	14.9	14.9	-24.5	-24.5	14.9	14.9	14.9	14.9	14.9	14.9	15.0	15.0	14.9	14.9	17.4	17.1	17.9	15.0	15.1
	15.1	15.1	15.1	15.1	15.1	15.1	-24.5	-24.5	15.1	15.1	15.1	15.1	15.0	15.0	15.1	15.1	15.1	15.1	18.9	18.8	20.3	15.2	15.3
	15.0	15.0	15.0	15.0	15.0	15.0	-24.5	-24.5	15.0	15.0	15.0	15.0	15.0	15.0	15.1	15.1	15.0	15.0	20.7	21.6	24.4	15.1	15.2
	14.9	14.9	14.9	14.9	14.9	14.9	-24.5	-24.5	14.9	14.9	14.9	14.9	14.9	14.9	15.0	15.0	14.9	14.9	22.9	25.5	29.3	15.1	15.1
	15.2	15.2	15.2	15.2	15.2	15.2	-24.5	-24.5	15.2	15.2	15.2	15.2	15.2	15.2	15.3	15.3	15.3	15.2	26.6	31.0	35.7	15.4	15.4
	15.0	15.0	15.0	15.0	15.0	15.0	-24.5	-24.5	15.0	15.0	15.1	15.0	15.0	15.0	15.1	15.1	15.1	15.1	31.5	37.8	44.1	15.2	15.2
7/14/2022	14.7	14.7	14.7	14.7	14.7	14.7	-24.5	-24.5	14.7	14.7	14.7	14.7	14.7	14.7	14.7	14.7	14.7	14.7	15.7	15.6	15.8	14.7	14.7
	15.1	15.1	15.2	15.2	15.1	15.2	-24.5	-24.5	15.2	15.1	15.2	15.2	15.1	15.1	15.2	15.2	15.1	15.1	16.8	16.7	17.3	15.2	15.2
	15.2	15.2	15.2	15.3	15.2	15.2	-24.5	-24.5	15.3	15.2	15.3	15.2	15.2	15.2	15.3	15.3	15.2	15.2	18.1	18.2	19.5	15.3	15.3
	15.2	15.2	15.3	15.3	15.2	15.3	-24.5	-24.5	15.3	15.3	15.3	15.3	15.2	15.2	15.3	15.3	15.2	15.2	20.0	20.5	22.9	15.3	15.3
	15.2	15.2	15.2	15.3	15.2	15.2	-24.5	-24.5	15.3	15.2	15.3	15.3	15.2	15.2	15.3	15.3	15.2	15.2	22.7	24.7	28.3	15.3	15.3
	15.1	15.1	15.1	15.1	15.1	15.1	-24.5	-24.5	15.1	15.1	15.1	15.1	15.0	15.0	15.1	15.1	15.1	15.1	26.3	30.1	34.6	15.2	15.2
	15.4	15.4	15.4	15.4	15.4	15.4	-24.5	-24.5	15.5	15.4	15.5	15.4	15.4	15.4	15.5	15.5	15.4	15.4	31.8	37.3	42.8	15.5	15.5
	15.3	15.3	15.3	15.3	15.3	15.3	-24.5	-24.5	15.3	15.3	15.3	15.3	15.2	15.2	15.3	15.3	15.3	15.3	39.5	47.0	53.4	15.4	15.4
7/15/2022	15.3	15.3	15.3	15.3	15.3	15.3	-24.5	-24.5	15.3	15.3	15.3	15.3	15.2	15.3	15.3	15.3	15.3	15.2	16.6	16.3	16.6	17.9	16.7
	15.0	15.0	15.0	15.0	15.0	15.0	-24.5	-24.5	15.0	15.0	15.0	15.0	14.9	14.9	15.0	15.0	15.0	14.9	17.1	16.7	17.3	20.2	17.7
	15.2	15.2	15.2	15.2	15.2	15.2	-24.5	-24.5	15.2	15.2	15.2	15.2	15.2	15.2	15.2	15.2	15.2	15.2	18.4	18.0	19.0	23.5	19.6
	15.3	15.3	15.3	15.3	15.3	15.3	-24.5	-24.5	15.3	15.3	15.3	15.3	15.3	15.3	15.3	15.3	15.3	15.3	19.6	19.5	21.0	28.2	21.8
	15.4	15.4	15.4	15.5	15.4	15.5	-24.5	-24.5	15.5	15.5	15.5	15.5	15.4	15.4	15.5	15.5	15.5	15.4	20.5	20.7	22.8	30.3	23.0
	15.4	15.4	15.4	15.5	15.4	15.4	-24.5	-24.5	15.5	15.4	15.5	15.4	15.4	15.4	15.5	15.5	15.4	15.4	22.3	23.9	27.3	38.5	26.7
	15.2	15.2	15.2	15.3	15.2	15.2	-24.5	-24.5	15.3	15.2	15.3	15.3	15.2	15.2	15.3	15.3	15.3	15.2	24.5	27.6	31.7	43.2	28.7
	15.7	15.7	15.7	15.7	15.7	15.7	-24.5	-24.5	15.7	15.7	15.7	15.7	15.7	15.7	15.8	15.8	15.7	15.7	23.9	26.1	30.2	33.2	25.1
	15.4	15.4	15.4	15.5	15.4	15.4	-24.5	-24.5	15.4	15.4	15.5	15.5	15.4	15.4	15.5	15.5	15.5	15.4	24.7	27.8	32.4	34.7	25.8

Date	Row 1					Row 2					Row 3				Row 4				Row 5				
	Tube 1			Tube 6	Tube 11	Tube 2			Tube 7	Tube 12	Tube 3		Tube 8	Tube 13	Tube 4		Tube 9	Tube 14	Tube 5			Tube 10	Tube 15
	T_{top}	T_{side}	T_{bottom}	T_{bottom}	T_{top}	T_{top}	T_{side}	T_{bottom}	T_{bottom}	T_{top}	T_{side}	T_{bottom}	T_{bottom}	T_{top}	T_{top}	T_{side}	T_{bottom}	T_{top}	T_{top}	T_{side}	T_{bottom}	T_{bottom}	T_{top}
PHASE 2 - R1233zd(E), circular cone nozzles, square pitch, Tube-C condenser tubes (Bundle 2)																							
7/18/2022	15.8	15.8	15.8	15.8	15.8	15.8	-24.5	-24.5	15.8	15.8	15.8	15.8	15.8	15.8	15.8	15.8	15.8	15.8	17.1	16.7	17.0	17.7	16.9
	15.9	15.9	15.9	15.9	15.9	15.9	-24.5	-24.5	15.9	15.9	15.9	15.9	15.8	15.9	15.9	15.9	15.9	15.9	17.9	17.4	18.0	20.2	18.0
	16.1	16.1	16.2	16.2	16.1	16.2	-24.5	-24.5	16.2	16.2	16.2	16.2	16.1	16.1	16.2	16.2	16.1	16.1	19.2	18.7	19.7	24.0	19.9
	16.1	16.1	16.1	16.1	16.1	16.1	-24.5	-24.5	16.1	16.1	16.1	16.1	16.0	16.1	16.1	16.1	16.1	16.1	20.2	19.9	21.5	28.2	21.8
	16.1	16.1	16.1	16.1	16.1	16.1	-24.5	-24.5	16.1	16.1	16.1	16.1	16.1	16.1	16.1	16.1	16.1	16.1	20.8	20.5	22.3	27.9	22.1
	16.1	16.1	16.1	16.1	16.1	16.1	-24.5	-24.5	16.1	16.1	16.1	16.1	16.1	16.1	16.1	16.1	16.1	16.1	22.0	22.7	25.6	32.1	24.0
	15.7	15.7	15.7	15.7	15.7	15.7	-24.5	-24.5	15.7	15.7	15.7	15.7	15.7	15.7	15.7	15.7	15.7	15.7	22.6	24.0	27.4	31.4	23.8
7/19/2022	15.7	15.7	15.7	15.7	15.7	15.7	-24.5	-24.5	15.7	15.7	15.7	15.7	15.6	15.7	15.7	15.7	15.7	15.7	24.0	26.5	31.2	33.3	25.1
	15.8	15.8	15.8	15.8	15.8	15.8	-24.5	-24.5	15.8	15.8	15.9	15.8	15.8	15.8	15.8	15.8	15.8	15.8	28.1	33.1	37.8	47.6	31.6
7/20/2022	16.3	16.5	16.8	17.5	16.5	16.4	-24.5	-24.5	18.8	16.3	16.4	16.4	16.6	16.1	16.8	16.9	16.3	16.1	16.9	16.9	17.4	19.0	17.2
	16.4	17.3	18.3	20.7	17.7	17.3	-24.5	-24.5	27.3	17.0	17.1	17.1	19.9	15.8	22.5	22.6	18.8	16.1	22.8	23.9	24.8	29.8	21.4
	17.2	18.6	20.2	24.0	19.6	18.8	-24.5	-24.5	36.3	18.5	19.4	19.4	27.9	16.2	33.0	33.7	24.1	17.5	29.7	31.5	32.8	43.3	26.4
	18.1	19.9	22.3	27.8	21.6	20.5	-24.5	-24.5	51.4	20.1	23.2	23.6	39.6	16.8	46.7	47.5	30.8	20.3	38.4	41.0	42.8	55.0	32.2
	17.2	18.7	20.9	24.9	19.7	19.2	-24.5	-24.5	41.2	18.9	21.1	21.3	34.2	16.4	40.8	41.9	27.4	18.0	35.0	37.5	39.1	54.1	29.2
	17.2	18.8	21.1	25.9	20.3	15.5	-24.5	-24.5	15.5	15.5	19.0	19.2	19.9	15.9	15.5	15.5	15.5	15.5	24.2	26.6	28.5	35.8	27.3
	18.7	20.8	24.0	31.1	23.0	15.7	-24.5	-24.5	15.7	15.7	22.4	23.3	23.8	16.9	15.7	15.7	15.8	15.7	31.4	34.6	36.8	52.2	33.9
7/21/2022	15.7	15.9	16.1	16.7	15.7	15.8	-24.5	-24.5	17.2	15.7	15.9	15.9	16.0	15.6	16.3	16.4	15.8	15.6	16.3	16.2	16.5	17.3	16.4
	16.4	16.8	17.9	19.7	17.3	17.0	-24.5	-24.5	23.1	16.8	17.0	17.0	18.6	16.1	21.3	21.4	18.1	16.2	21.5	22.6	23.7	27.0	20.4
	16.7	17.2	18.7	21.0	18.2	17.7	-24.5	-24.5	27.4	17.4	17.5	17.5	20.2	16.2	22.9	23.0	19.4	16.5	22.9	24.0	25.0	29.9	21.8
	17.4	18.8	20.5	24.1	19.9	19.1	-24.5	-24.5	36.2	18.8	19.5	19.5	27.6	16.4	32.9	33.6	24.1	17.7	29.7	31.5	32.8	42.6	26.5
	17.4	19.1	21.4	25.3	20.1	19.6	-24.5	-24.5	42.0	19.4	21.6	21.9	34.4	16.8	41.6	42.7	28.4	18.8	35.8	38.3	39.9	54.8	30.0
	17.3	19.4	22.0	27.0	21.0	15.4	-24.5	-24.5	15.3	15.3	19.0	19.2	19.8	15.8	15.4	15.3	15.4	15.3	24.3	26.5	28.4	36.2	27.4
	18.0	20.3	23.6	29.0	22.3	15.9	-24.5	-24.5	15.9	15.9	21.1	21.6	21.5	16.9	15.9	15.9	16.0	15.9	29.5	32.8	34.9	45.9	31.4
PHASE 2 - R1234ze(E), circular cone nozzles, square pitch, Tube-C condenser tubes (Bundle 2)																							
7/28/2022	-11.9	-11.6	-10.6	-9.2	-11.5	-11.4	-24.5	-24.5	-5.9	-11.5	-11.1	-11.0	-9.8	-12.0	-6.6	-6.8	-10.7	-12.1	-7.6	-6.7	-6.0	-1.8	-9.1
	-11.5	-11.1	-9.3	-7.0	-10.8	-10.7	-24.5	-24.5	0.4	-10.4	-9.7	-9.7	-4.9	-11.8	0.3	0.6	-7.0	-11.6	-1.0	0.5	1.5	9.4	-5.5
	-11.3	-10.5	-8.3	-4.5	-9.9	-9.4	-24.5	-24.5	9.6	-8.9	-6.3	-5.9	4.5	-11.5	13.3	14.1	-1.5	-10.7	7.0	9.4	10.8	24.7	-0.9
7/29/2022	-11.8	-11.5	-10.5	-8.6	-11.2	-11.4	-24.5	-24.5	-5.1	-11.3	-11.2	-11.1	-9.8	-11.9	-7.6	-7.6	-10.3	-11.9	-7.6	-6.5	-5.8	-1.6	-8.6
	-11.6	-11.0	-9.2	-6.2	-10.2	-10.5	-24.5	-24.5	2.4	-10.2	-9.8	-9.9	-3.5	-11.6	1.1	1.8	-6.4	-11.1	-1.0	0.8	1.8	10.9	-3.7
	-11.5	-10.7	-8.2	-3.9	-9.5	-9.2	-24.5	-24.5	13.0	-8.9	-6.9	-6.7	6.1	-11.6	15.9	16.8	-0.6	-10.1	7.1	9.7	11.0	25.5	0.9
	-9.1	-8.0	-5.5	0.2	-6.8	-6.2	-24.5	-24.5	27.8	-5.9	-0.6	0.1	18.7	-10.0	32.1	32.9	7.9	-6.2	20.6	24.2	26.2	55.0	8.7
	-10.6	-9.8	-7.6	-2.9	-9.4	-8.1	-24.5	-24.5	22.0	-7.7	-2.3	-1.7	13.7	-11.0	28.5	29.6	3.4	-9.1	18.5	21.9	23.8	48.6	5.2
	-10.2	-9.0	-6.2	-0.1	-8.0	-7.6	-24.5	-24.5	25.5	-6.8	-2.1	-1.4	17.0	-10.8	27.5	28.3	5.4	-7.5	17.7	21.5	23.4	55.0	6.6

Date	Row 1					Row 2					Row 3				Row 4				Row 5				
	Tube 1			Tube 6	Tube 11	Tube 2			Tube 7	Tube 12	Tube 3		Tube 8	Tube 13	Tube 4		Tube 9	Tube 14	Tube 5			Tube 10	Tube 15
	T_{top}	T_{side}	T_{bottom}	T_{bottom}	T_{top}	T_{top}	T_{side}	T_{bottom}	T_{bottom}	T_{top}	T_{side}	T_{bottom}	T_{bottom}	T_{top}	T_{top}	T_{side}	T_{bottom}	T_{top}	T_{top}	T_{side}	T_{bottom}	T_{bottom}	T_{top}
PHASE 2 - R1234ze(E), circular cone nozzles, square pitch, Tube-C condenser tubes (Bundle 2)																							
8/1/2022	1.8	1.8	1.8	1.9	1.8	1.8	-24.5	-24.5	1.8	1.8	1.8	1.8	1.8	1.8	1.8	1.8	1.8	1.8	4.4	3.9	4.2	5.0	4.5
	2.1	2.1	2.1	2.2	2.1	2.1	-24.5	-24.5	2.1	2.1	2.1	2.1	2.1	2.1	2.1	2.1	2.1	2.1	6.7	6.5	7.0	9.1	6.8
	2.1	2.1	2.1	2.2	2.1	2.1	-24.5	-24.5	2.1	2.1	2.1	2.1	2.1	2.1	2.1	2.1	2.1	2.1	9.1	10.0	11.6	14.5	9.7
	2.0	2.0	2.0	2.1	2.0	2.1	-24.5	-24.5	2.1	2.1	2.1	2.1	2.0	2.0	2.1	2.1	2.0	2.0	9.2	10.2	11.8	14.0	9.5
	2.1	2.1	2.1	2.2	2.1	2.2	-24.5	-24.5	2.2	2.2	2.2	2.2	2.1	2.1	2.2	2.2	2.2	2.1	11.0	13.2	15.6	17.6	11.2
	2.3	2.3	2.3	2.4	2.3	2.3	-24.5	-24.5	2.3	2.4	2.4	2.4	2.3	2.3	2.4	2.4	2.3	2.3	11.5	14.0	16.9	21.7	12.6
	2.3	2.3	2.3	2.4	2.3	2.3	-24.5	-24.5	2.3	2.3	2.3	2.3	2.3	2.3	2.4	2.3	2.3	2.3	14.5	19.1	23.7	28.7	15.1
	4.2	4.2	4.2	4.3	4.2	4.2	-24.5	-24.5	4.2	4.2	4.2	4.2	4.1	4.2	4.2	4.2	4.2	4.2	14.5	18.4	22.3	27.4	15.2
8/2/2022	2.3	2.6	4.2	2.0	1.5	5.3	-24.5	-24.5	1.6	1.5	5.6	5.8	1.5	1.6	1.7	1.7	1.6	1.6	1.7	1.6	1.6	1.6	1.6
	3.8	4.2	6.7	3.2	2.2	10.3	-24.5	-24.5	2.3	2.2	15.2	16.0	2.2	2.3	2.4	2.4	2.3	2.3	2.4	2.3	2.3	2.3	2.3
	3.8	4.3	7.1	3.7	2.1	10.8	-24.5	-24.5	2.1	2.1	15.5	16.3	2.1	2.1	2.3	2.2	2.1	2.2	2.2	2.2	2.1	2.1	2.2
	4.6	5.5	9.0	3.7	2.1	15.3	-24.5	-24.5	2.2	2.1	27.5	28.8	2.1	2.2	2.3	2.2	2.1	2.2	2.2	2.2	2.1	2.1	2.2
	5.1	6.2	10.2	3.9	2.3	17.7	-24.5	-24.5	2.4	2.3	29.4	30.7	2.3	2.4	2.5	2.4	2.4	2.4	2.4	2.4	2.3	2.3	2.4
	5.3	6.3	10.5	3.6	1.9	19.5	-24.5	-24.5	2.1	2.0	39.1	40.7	2.0	2.1	2.2	2.2	2.0	2.0	2.2	2.1	2.0	2.0	2.1
	5.7	6.7	10.9	3.7	2.0	20.7	-24.5	-24.5	2.1	2.1	39.0	40.6	2.1	2.1	2.3	2.2	2.1	2.1	2.2	2.1	2.1	2.1	2.1
8/3/2022	2.1	2.2	2.9	1.9	1.4	1.5	-24.5	-24.5	1.4	1.4	1.4	1.5	1.4	1.4	1.4	1.4	1.4	1.4	1.5	1.4	1.4	1.4	1.4
	2.7	3.2	4.3	2.4	1.9	2.0	-24.5	-24.5	1.9	1.9	2.0	2.0	1.9	1.9	1.9	1.9	1.9	1.9	2.0	1.9	1.9	1.9	1.9
	2.8	3.2	4.5	2.4	1.9	2.0	-24.5	-24.5	2.0	1.9	2.0	2.0	1.9	2.0	2.0	2.0	1.9	1.9	2.0	2.0	1.9	1.9	2.0
	3.6	4.3	6.0	2.3	1.8	2.0	-24.5	-24.5	1.9	1.9	1.9	1.9	1.8	1.9	1.9	1.9	1.8	1.9	1.9	1.9	1.8	1.9	1.9
	3.3	4.0	6.0	2.1	1.7	1.8	-24.5	-24.5	1.7	1.7	1.8	1.8	1.7	1.7	1.7	1.7	1.7	1.7	1.8	1.7	1.7	1.7	1.7
	6.0	7.3	11.0	2.2	1.8	1.9	-24.5	-24.5	1.8	1.8	1.9	1.9	1.8	1.8	1.9	1.8	1.8	1.8	1.9	1.8	1.8	1.8	1.8
	6.3	7.7	11.7	2.3	1.8	2.0	-24.5	-24.5	1.9	1.9	1.9	1.9	1.8	1.9	1.9	1.9	1.8	1.9	1.9	1.9	1.9	1.9	1.9
	8.8	10.8	17.0	2.4	2.0	2.1	-24.5	-24.5	2.1	2.0	2.1	2.1	2.0	2.0	2.1	2.1	2.0	2.0	2.1	2.1	2.0	2.0	2.0
	8.1	9.9	16.1	2.3	1.8	2.0	-24.5	-24.5	1.9	1.9	2.0	2.0	1.9	1.9	1.9	1.9	1.9	1.9	2.0	1.9	1.9	1.9	1.9
8/4/2022	1.6	1.6	1.6	2.4	1.6	1.6	-24.5	-24.5	1.6	1.6	1.6	1.6	1.6	1.6	1.6	1.6	1.6	1.6	3.0	2.6	3.0	1.6	1.6
	1.9	1.8	1.9	2.5	1.8	1.9	-24.5	-24.5	1.9	1.9	1.9	1.9	1.8	1.9	1.9	1.9	1.8	1.8	3.2	2.8	3.2	1.9	1.9
	2.0	2.0	2.0	2.7	2.0	2.0	-24.5	-24.5	2.0	2.0	2.0	2.0	2.0	2.0	2.0	2.0	2.0	2.0	4.4	3.8	4.3	2.0	2.0
	1.9	1.9	1.9	2.6	1.9	1.9	-24.5	-24.5	1.9	1.9	1.9	1.9	1.8	1.9	1.9	1.9	1.9	1.9	4.3	3.7	4.2	1.9	1.9
	1.9	1.9	1.9	2.6	1.9	1.9	-24.5	-24.5	1.9	1.9	1.9	1.9	1.9	1.9	1.9	1.9	1.9	1.9	5.5	4.7	5.4	1.9	1.9
	2.0	2.0	2.0	2.8	2.0	2.0	-24.5	-24.5	2.0	2.0	2.0	2.0	1.9	2.0	2.0	2.0	2.0	2.0	5.7	5.1	6.2	2.0	2.0
	1.8	1.8	1.8	2.6	1.8	1.8	-24.5	-24.5	1.8	1.8	1.8	1.8	1.7	1.8	1.8	1.8	1.8	1.8	8.9	9.6	12.4	1.8	1.8
	1.6	1.6	1.6	2.3	1.6	1.6	-24.5	-24.5	1.6	1.6	1.6	1.6	1.6	1.6	1.6	1.6	1.6	1.6	9.0	9.6	12.4	1.7	1.6
8/5/2022	1.6	1.6	1.6	3.0	1.6	2.4	-24.5	-24.5	1.6	1.6	1.7	1.7	1.6	1.7	1.7	1.6	1.6	1.6	1.7	1.6	1.6	1.6	1.6
	1.9	1.9	1.9	3.4	1.8	2.6	-24.5	-24.5	1.9	1.9	1.9	1.9	1.8	1.9	1.9	1.9	1.9	1.9	1.9	1.9	1.8	1.9	1.9
	1.9	1.9	1.9	3.4	1.8	9.3	-24.5	-24.5	1.9	1.9	2.0	2.0	1.8	1.9	2.0	1.9	1.9	1.9	2.0	1.9	1.9	1.9	1.9
	1.8	1.8	1.8	3.3	1.7	9.4	-24.5	-24.5	1.8	1.8	1.9	1.9	1.7	1.8	1.9	1.8	1.8	1.8	1.9	1.8	1.8	1.8	1.8
	2.7	2.9	3.7	3.4	2.0	4.4	-24.5	-24.5	2.1	2.1	2.1	2.1	2.0	2.1	2.1	2.1	2.1	2.1	2.1	2.1	2.1	2.1	2.1
	2.7	2.9	3.6	3.4	2.0	4.2	-24.5	-24.5	2.0	2.0	2.1	2.1	2.0	2.0	2.1	2.0	2.0	2.0	2.1	2.1	2.0	2.0	2.0
	4.9	6.1	8.8	3.6	2.2	15.5	-24.5	-24.5	2.3	2.2	2.3	2.3	2.2	2.3	2.3	2.3	2.2	2.2	2.3	2.3	2.2	2.2	2.3
	5.1	6.3	9.3	3.6	2.2	16.1	-24.5	-24.5	2.3	2.3	2.4	2.4	2.2	2.3	2.3	2.3	2.3	2.3	2.4	2.3	2.3	2.3	2.3

Date	Row 1					Row 2					Row 3					Row 4					Row 5				
	Tube 1			Tube 6	Tube 11	Tube 2			Tube 7	Tube 12	Tube 3		Tube 8	Tube 13	Tube 4		Tube 9	Tube 14	Tube 5			Tube 10	Tube 15
	T_{top}	T_{side}	T_{bottom}	T_{bottom}	T_{top}	T_{top}	T_{side}	T_{bottom}	T_{bottom}	T_{top}	T_{side}	T_{bottom}	T_{bottom}	T_{top}	T_{top}	T_{side}	T_{bottom}	T_{top}	T_{top}	T_{side}	T_{bottom}	T_{bottom}	T_{top}
PHASE 2 - R1234ze(E), circular cone nozzles, square pitch, Tube-C condenser tubes (Bundle 2)																							
8/12/2022	1.8	1.8	1.8	-24.5	1.8	1.8	-24.5	-24.5	1.8	1.8	1.8	1.8	1.8	1.8	1.8	1.8	1.8	1.8	2.2	2.1	2.1	1.8	1.8
	1.9	1.9	1.9	-24.5	1.8	1.9	-24.5	-24.5	1.9	1.9	1.9	1.9	1.8	1.9	1.9	1.9	1.9	1.8	2.7	2.6	3.0	2.0	1.9
	1.9	1.9	1.9	-24.5	1.9	1.9	-24.5	-24.5	1.9	1.9	1.9	1.9	1.8	1.9	1.9	1.9	1.9	1.9	2.7	2.6	2.8	2.0	1.9
	2.0	2.0	2.0	-24.5	2.0	2.0	-24.5	-24.5	2.0	2.0	2.0	2.0	2.0	2.0	2.0	2.0	2.1	2.0	3.7	3.6	4.1	2.2	2.1
	1.7	1.7	1.7	-24.5	1.7	1.7	-24.5	-24.5	1.7	1.7	1.7	1.7	1.7	1.7	1.7	1.7	1.8	1.7	4.0	3.8	4.5	1.9	1.8
	1.9	1.9	1.9	-24.5	1.9	1.9	-24.5	-24.5	1.9	1.9	1.9	1.9	1.9	1.9	2.0	2.0	2.0	1.9	5.4	4.8	5.5	2.2	2.1
	2.1	2.1	2.1	-24.5	2.1	2.1	-24.5	-24.5	2.1	2.1	2.1	2.1	2.1	2.1	2.1	2.1	2.2	2.1	5.2	4.8	5.6	2.4	2.2
	2.1	2.1	2.1	-24.5	2.0	2.1	-24.5	-24.5	2.1	2.1	2.1	2.1	2.0	2.1	2.1	2.1	2.2	2.1	5.6	5.1	5.7	2.3	2.2
	2.0	2.0	2.0	-24.5	2.0	2.0	-24.5	-24.5	2.0	2.0	2.0	2.0	2.0	2.0	2.0	2.0	2.1	2.0	5.8	5.3	6.1	2.2	2.1
PHASE 2 - R1233zd(E), circular cone nozzles, square pitch, Tube-C condenser tubes (Bundle 2)																							
8/19/2022	17.1	17.1	17.1	-24.5	17.0	17.1	-24.5	-24.5	17.1	17.1	17.1	17.1	17.1	17.1	17.1	17.2	17.1	17.1	19.1	19.0	19.4	17.2	17.2
	17.9	17.9	18.0	-24.5	17.9	18.0	-24.5	-24.5	18.0	18.0	18.0	18.0	18.0	18.0	18.1	18.1	18.1	18.0	21.1	20.9	21.5	18.2	18.2
	15.1	15.1	15.1	-24.5	15.1	15.1	-24.5	-24.5	15.2	15.2	15.2	15.2	15.1	15.1	15.2	15.2	15.1	15.1	19.2	19.3	20.7	15.3	15.2
	13.3	13.3	13.3	-24.5	13.3	13.4	-24.5	-24.5	13.4	13.3	13.4	13.4	13.3	13.3	13.4	13.4	13.4	13.3	21.0	23.5	26.3	13.5	13.4
8/22/2022	15.6	15.6	15.6	-24.5	15.6	15.6	-24.5	-24.5	15.6	15.6	15.6	15.6	15.6	15.6	15.7	15.7	15.7	15.6	17.4	17.0	17.4	15.8	15.7
	18.4	18.4	18.4	-24.5	18.4	18.5	-24.5	-24.5	18.5	18.4	18.5	18.5	18.5	18.5	18.5	18.6	18.6	18.5	20.4	20.1	20.4	18.6	18.6
	15.3	15.3	15.3	-24.5	15.3	15.3	-24.5	-24.5	15.4	15.3	15.4	15.4	15.3	15.3	15.4	15.4	15.4	15.4	17.9	17.4	17.9	15.6	15.4
	18.0	18.0	18.0	-24.5	17.9	18.0	-24.5	-24.5	18.0	18.0	18.0	18.0	18.0	18.0	18.1	18.2	18.2	18.1	20.7	20.3	20.7	18.3	18.2
	18.3	18.3	18.3	-24.5	18.2	18.3	-24.5	-24.5	18.3	18.3	18.4	18.4	18.4	18.4	18.5	18.6	18.6	18.4	22.0	21.5	22.1	18.7	18.6
	18.5	18.5	18.5	-24.5	18.5	18.6	-24.5	-24.5	18.6	18.6	18.7	18.7	18.6	18.6	18.8	18.9	18.9	18.7	23.0	22.4	23.3	19.1	18.9
	18.1	18.1	18.1	-24.5	18.0	18.2	-24.5	-24.5	18.2	18.1	18.2	18.2	18.2	18.2	18.4	18.5	18.5	18.3	23.3	22.7	24.0	18.7	18.6
	17.5	17.5	17.5	-24.5	17.4	17.6	-24.5	-24.5	17.6	17.6	17.7	17.7	17.6	17.6	17.9	17.9	18.0	17.7	23.5	23.2	25.4	18.2	18.1
8/23/2022	18.4	18.5	19.1	-24.5	17.9	18.0	-24.5	-24.5	17.9	17.9	18.0	18.0	17.9	17.9	17.9	17.9	17.9	17.9	18.0	17.9	17.9	17.9	17.9
	18.7	19.0	19.8	-24.5	18.0	18.1	-24.5	-24.5	18.1	18.1	18.1	18.1	18.0	18.1	18.1	18.1	18.1	18.1	18.1	18.1	18.0	18.1	18.1
	18.9	19.3	20.5	-24.5	18.0	18.1	-24.5	-24.5	18.0	18.0	18.0	18.0	18.0	18.0	18.0	18.0	18.0	18.0	18.1	18.0	18.0	18.0	18.0
	19.2	19.7	21.3	-24.5	18.0	18.1	-24.5	-24.5	18.0	18.0	18.0	18.0	17.9	18.0	18.0	18.0	18.0	18.0	18.1	18.0	17.9	18.0	18.0
	19.6	20.3	22.1	-24.5	18.0	18.1	-24.5	-24.5	18.0	18.0	18.0	18.0	18.0	18.0	18.0	18.0	18.0	18.0	18.1	18.0	18.0	18.0	18.0
	20.2	21.1	22.9	-24.5	18.0	18.1	-24.5	-24.5	18.0	18.0	18.1	18.1	18.0	18.0	18.1	18.1	18.0	18.0	18.1	18.1	18.0	18.1	18.0
8/23/2022	19.5	20.2	21.9	-24.5	17.9	18.0	-24.5	-24.5	17.9	17.9	17.9	17.9	17.8	17.9	17.9	17.9	17.9	17.9	18.0	17.9	17.8	17.9	17.9
	19.0	19.5	20.9	-24.5	17.7	17.8	-24.5	-24.5	17.7	17.7	17.8	17.7	17.7	17.7	17.7	17.7	17.7	17.7	17.8	17.7	17.7	17.7	17.7
	18.5	18.9	20.0	-24.5	17.6	17.6	-24.5	-24.5	17.6	17.6	17.6	17.6	17.5	17.6	17.6	17.6	17.6	17.6	17.6	17.6	17.5	17.6	17.6
	18.2	18.4	19.2	-24.5	17.5	17.6	-24.5	-24.5	17.5	17.5	17.5	17.5	17.5	17.5	17.5	17.5	17.5	17.5	17.6	17.5	17.5	17.5	17.5
	18.6	18.9	20.1	-24.5	17.6	17.7	-24.5	-24.5	17.6	17.6	17.7	17.6	17.6	17.6	17.6	17.6	17.6	17.6	17.7	17.6	17.6	17.6	17.6
	19.0	19.5	21.0	-24.5	17.7	17.8	-24.5	-24.5	17.7	17.7	17.7	17.7	17.7	17.7	17.7	17.7	17.7	17.7	17.8	17.7	17.7	17.7	17.7
	19.5	20.3	22.0	-24.5	17.8	17.9	-24.5	-24.5	17.8	17.8	17.9	17.9	17.8	17.8	17.9	17.9	17.8	17.8	17.9	17.9	17.8	17.8	17.8
	20.2	21.1	23.0	-24.5	18.0	18.1	-24.5	-24.5	18.0	18.0	18.1	18.1	18.0	18.0	18.1	18.1	18.0	18.0	18.1	18.0	18.0	18.0	18.0

Date	Row 1					Row 2					Row 3				Row 4				Row 5				
	Tube 1			Tube 6	Tube 11	Tube 2			Tube 7	Tube 12	Tube 3		Tube 8	Tube 13	Tube 4		Tube 9	Tube 14	Tube 5			Tube 10	Tube 15
	T_{top}	T_{side}	T_{bottom}	T_{bottom}	T_{top}	T_{top}	T_{side}	T_{bottom}	T_{bottom}	T_{top}	T_{side}	T_{bottom}	T_{bottom}	T_{top}	T_{top}	T_{side}	T_{bottom}	T_{top}	T_{top}	T_{side}	T_{bottom}	T_{bottom}	T_{top}
PHASE 2 - R134a, circular cone nozzles, square pitch, Tube-C condenser tubes (Bundle 2)																							
8/29/2022	1.4	1.4	1.4	-24.5	1.4	1.4	-24.5	-24.5	1.4	1.4	1.4	1.5	1.4	1.4	1.8	1.9	1.7	1.6	4.5	4.0	4.0	2.0	2.0
	1.9	1.9	1.9	-24.5	1.9	1.9	-24.5	-24.5	2.0	1.9	2.0	2.0	1.9	2.0	2.3	2.4	2.3	2.1	5.4	4.7	4.8	2.6	2.6
	1.8	1.7	1.8	-24.5	1.7	1.8	-24.5	-24.5	1.8	1.8	1.9	2.0	1.8	1.8	2.3	2.4	2.2	2.1	5.4	4.6	4.8	2.4	2.4
	2.2	2.2	2.2	-24.5	2.2	2.3	-24.5	-24.5	2.3	2.3	2.6	2.6	2.4	2.4	2.8	2.9	2.7	2.6	6.2	5.3	5.7	3.0	2.9
	1.7	1.7	1.7	-24.5	1.7	1.8	-24.5	-24.5	1.8	1.8	2.0	2.0	1.9	1.8	2.4	2.4	2.3	2.3	5.9	4.9	5.4	2.4	2.3
	2.4	2.4	2.4	-24.5	2.4	2.4	-24.5	-24.5	2.5	2.5	2.7	2.7	2.6	2.5	3.0	3.0	3.0	2.9	6.9	5.7	6.3	3.0	3.0
8/30/2022	2.0	2.0	2.0	-24.5	2.0	2.0	-24.5	-24.5	2.0	2.0	2.0	2.0	2.0	2.0	2.0	2.0	2.0	2.0	3.0	2.7	3.1	2.0	2.0
	2.0	2.0	2.0	-24.5	1.9	2.0	-24.5	-24.5	2.0	2.0	2.0	2.0	1.9	2.0	2.0	2.0	2.0	1.9	3.6	3.2	3.6	2.0	2.0
	2.6	2.6	2.6	-24.5	2.6	2.6	-24.5	-24.5	2.6	2.6	2.6	2.6	2.6	2.7	2.6	2.6	2.6	2.6	5.1	4.5	4.8	2.6	2.6
	2.9	2.9	2.9	-24.5	2.9	2.9	-24.5	-24.5	2.9	2.9	2.9	2.9	2.9	2.9	2.9	2.9	2.9	2.9	5.8	4.9	5.2	2.9	2.9
	2.7	2.7	2.7	-24.5	2.7	2.7	-24.5	-24.5	2.7	2.7	2.7	2.8	2.7	2.8	2.7	2.7	2.7	2.7	5.7	4.7	5.0	2.8	2.7
	2.7	2.7	2.7	-24.5	2.7	2.7	-24.5	-24.5	2.7	2.7	2.7	2.7	2.7	2.7	2.7	2.7	2.7	2.7	6.5	5.8	6.9	2.7	2.7
	2.7	2.7	2.7	-24.5	2.7	2.7	-24.5	-24.5	2.7	2.7	2.7	2.7	2.7	2.7	2.7	2.7	2.7	2.7	7.0	6.8	9.3	2.7	2.7
8/31/2022	3.0	2.9	3.9	-24.5	2.5	2.5	-24.5	-24.5	2.5	2.5	2.5	2.5	2.5	2.5	2.5	2.5	2.5	2.5	2.5	2.5	2.4	2.5	2.5
	3.3	3.3	4.8	-24.5	2.6	2.7	-24.5	-24.5	2.7	2.7	2.7	2.7	2.6	2.7	2.7	2.7	2.7	2.7	2.7	2.7	2.6	2.7	2.7
	3.5	4.3	6.1	-24.5	2.7	2.7	-24.5	-24.5	2.7	2.7	2.7	2.7	2.7	2.7	2.7	2.7	2.7	2.7	2.7	2.7	2.6	2.7	2.7
	3.8	5.1	8.7	-24.5	2.5	2.6	-24.5	-24.5	2.5	2.5	2.5	2.5	2.5	2.5	2.5	2.5	2.5	2.5	2.6	2.5	2.5	2.5	2.5
	4.4	6.1	10.3	-24.5	2.8	2.8	-24.5	-24.5	2.8	2.8	2.8	2.8	2.8	2.8	2.8	2.8	2.8	2.8	2.8	2.8	2.8	2.8	2.8
	5.6	7.5	13.9	-24.5	2.7	2.8	-24.5	-24.5	2.7	2.7	2.7	2.8	2.7	2.7	2.7	2.7	2.7	2.7	2.8	2.7	2.7	2.7	2.7
	2.7	2.7	2.7	-24.5	2.7	2.7	-24.5	-24.5	2.7	2.7	2.7	2.7	2.7	2.7	2.7	2.7	2.7	2.7	3.5	3.4	4.0	2.7	2.7
	2.7	2.7	2.7	-24.5	2.7	2.7	-24.5	-24.5	2.7	2.7	2.7	2.7	2.7	2.7	2.7	2.7	2.7	2.7	4.0	3.8	4.5	2.7	2.7
	2.8	2.7	2.7	-24.5	2.7	2.8	-24.5	-24.5	2.8	2.8	2.8	2.8	2.7	2.8	2.8	2.7	2.7	2.7	5.0	4.6	5.3	2.8	2.8
	2.5	2.5	2.5	-24.5	2.5	2.5	-24.5	-24.5	2.5	2.5	2.5	2.5	2.5	2.5	2.5	2.5	2.5	2.5	6.2	5.8	7.8	2.5	2.5
9/1/2022	2.9	2.9	2.9	-24.5	2.9	2.9	-24.5	-24.5	2.9	2.9	2.9	2.9	2.8	2.9	2.9	2.9	2.9	2.9	8.0	10.4	13.7	2.9	2.9
	2.6	2.6	2.6	-24.5	2.6	2.6	-24.5	-24.5	2.6	2.6	2.6	2.6	2.6	2.6	2.6	2.6	2.6	2.6	10.1	14.7	18.9	2.6	2.6
PHASE 3 - R134a, circular cone nozzles, triangular pitch, Tube-B evaporator tubes (Bundle 3)																							
9/19/2022	2.1	2.1	2.0	0.6	0.6	0.6	0.6	0.6	0.6	0.6	0.6	0.6	0.6	0.6	-19.9	0.6	0.5	0.6	0.5	0.5	0.6	0.5	0.6
	2.5	2.4	2.3	0.8	0.8	0.9	0.8	0.8	0.8	0.8	0.9	0.9	0.8	0.9	-19.9	0.8	0.8	0.8	0.8	0.8	0.8	0.8	0.8
	2.9	2.7	2.6	1.1	1.1	1.1	1.1	1.1	1.1	1.1	1.2	1.2	1.1	1.1	-19.9	1.1	1.1	1.1	1.0	1.1	1.1	1.1	1.1
	3.1	2.8	2.8	1.2	1.2	1.2	1.2	1.2	1.2	1.2	1.2	1.2	1.2	1.2	-19.9	1.2	1.2	1.2	1.1	1.1	1.2	1.2	1.2
	3.4	3.4	3.3	1.2	1.2	1.3	1.2	1.2	1.3	1.2	1.3	1.3	1.2	1.3	-19.9	1.2	1.2	1.2	1.1	1.2	1.2	1.2	1.2
	4.1	4.8	4.7	1.1	1.1	1.1	1.1	1.1	1.1	1.1	1.1	1.1	1.1	1.1	-19.9	1.1	1.0	1.1	1.0	1.0	1.0	1.0	1.0
9/20/2022	1.3	1.3	1.3	1.3	1.3	1.3	1.3	1.3	1.3	1.3	1.3	1.3	1.3	1.3	-19.9	1.3	1.3	1.3	2.3	2.5	2.5	1.3	1.3
	1.6	1.6	1.5	1.6	1.6	1.6	1.5	1.5	1.5	1.6	1.5	1.5	1.5	1.6	-19.9	1.6	1.5	1.6	2.6	2.8	2.9	1.6	1.6
	1.5	1.5	1.5	1.5	1.5	1.5	1.5	1.5	1.5	1.5	1.5	1.5	1.5	1.5	-19.9	1.5	1.5	1.5	2.7	2.9	3.0	1.5	1.5
	1.4	1.4	1.3	1.4	1.4	1.4	1.3	1.3	1.3	1.4	1.3	1.3	1.3	1.4	-19.9	1.4	1.3	1.4	2.5	2.8	2.8	1.3	1.4
	1.3	1.3	1.3	1.4	1.3	1.4	1.3	1.3	1.3	1.4	1.3	1.3	1.3	1.4	-19.9	1.4	1.3	1.4	2.6	2.9	3.0	1.3	1.4
	1.5	1.5	1.5	1.6	1.5	1.5	1.5	1.5	1.5	1.6	1.5	1.5	1.5	1.6	-19.9	1.6	1.5	1.6	3.0	3.3	3.5	1.5	1.6
	1.6	1.6	1.5	1.6	1.6	1.6	1.6	1.6	1.6	1.6	1.6	1.6	1.6	1.6	-19.9	1.6	1.5	1.6	3.2	3.6	4.0	1.6	1.6

Date	Row 1					Row 2					Row 3				Row 4				Row 5				
	Tube 1			Tube 6	Tube 11	Tube 2			Tube 7	Tube 12	Tube 3		Tube 8	Tube 13	Tube 4		Tube 9	Tube 14	Tube 5			Tube 10	Tube 15
	T_{top}	T_{side}	T_{bottom}	T_{bottom}	T_{top}	T_{top}	T_{side}	T_{bottom}	T_{bottom}	T_{top}	T_{side}	T_{bottom}	T_{bottom}	T_{top}	T_{top}	T_{side}	T_{bottom}	T_{top}	T_{top}	T_{side}	T_{bottom}	T_{bottom}	T_{top}
PHASE 3 - R134a, circular cone nozzles, triangular pitch, Tube-B evaporator tubes (Bundle 3)																							
9/21/2022	1.3	1.3	1.3	1.3	1.3	1.3	1.3	1.3	1.3	1.3	1.3	1.3	1.3	1.3	-19.9	1.3	1.4	1.3	2.4	2.5	2.6	1.5	1.4
	1.4	1.4	1.4	1.4	1.4	1.4	1.4	1.4	1.4	1.4	1.4	1.4	1.4	1.4	-19.9	1.4	1.5	1.4	2.6	2.7	2.7	1.8	1.5
	1.2	1.2	1.2	1.3	1.2	1.2	1.2	1.2	1.2	1.2	1.2	1.2	1.3	1.2	-19.9	1.2	1.3	1.2	2.5	2.7	2.7	1.6	1.4
	1.4	1.4	1.3	1.4	1.3	1.3	1.3	1.3	1.4	1.4	1.3	1.3	1.4	1.4	-19.9	1.4	1.4	1.4	2.8	2.9	2.9	1.8	1.6
	1.5	1.5	1.5	1.5	1.5	1.5	1.5	1.5	1.5	1.5	1.5	1.5	1.5	1.5	-19.9	1.5	1.6	1.5	3.0	3.2	3.1	1.9	1.8
	1.5	1.5	1.5	1.5	1.4	1.4	1.4	1.4	1.5	1.5	1.4	1.4	1.5	1.5	-19.9	1.5	1.5	1.5	3.1	3.3	3.2	1.8	1.8
9/22/2022	10.6	10.7	10.6	10.6	10.6	10.6	10.6	10.6	10.9	10.4	10.7	10.7	10.7	10.6	-19.9	10.6	13.3	10.4	10.8	10.7	10.6	10.6	10.6
	10.3	10.4	10.3	10.3	10.3	10.3	10.2	10.3	10.6	10.1	10.3	10.3	10.3	10.3	-19.9	10.3	15.4	10.1	10.4	10.3	10.3	10.3	10.3
	11.2	11.3	11.2	11.2	11.3	11.2	11.1	11.1	12.3	10.9	11.3	11.3	11.3	11.2	-19.9	11.1	11.0	10.9	11.5	11.3	11.2	11.3	11.2
	9.9	10.0	9.8	9.8	10.0	9.8	9.7	9.8	11.2	9.6	9.9	9.9	9.9	9.8	-19.9	9.8	9.6	9.6	10.1	9.9	9.8	9.9	9.9
	10.2	10.3	10.1	10.1	10.2	10.1	10.0	10.0	16.2	9.8	10.2	10.2	10.2	10.1	-19.9	10.0	9.8	9.8	10.5	10.2	10.1	10.2	10.2
9/23/2022	10.2	10.2	10.1	10.2	10.4	10.2	10.1	10.2	9.6	9.6	10.2	10.2	10.6	10.1	-19.9	10.2	9.6	9.6	10.5	10.2	10.2	10.9	10.2
9/29/2022	10.0	10.0	10.0	10.1	9.9	10.0	9.9	9.9	10.1	9.4	10.2	10.1	10.1	10.0	-19.9	10.3	10.4	9.5	10.1	10.2	10.1	10.2	10.0
	10.2	10.3	10.3	10.3	10.1	10.2	10.1	10.1	10.3	9.7	10.2	10.4	10.4	10.2	-19.9	10.7	11.0	9.8	10.4	10.5	10.3	10.4	10.2
	10.1	10.3	10.2	10.2	10.2	10.1	9.9	9.9	10.2	9.6	10.1	10.3	10.5	10.0	-19.9	10.9	11.1	9.6	10.4	10.5	10.2	10.3	10.0
	10.3	10.6	10.5	10.4	10.5	10.2	10.1	10.1	10.5	9.8	10.3	10.5	10.9	10.3	-19.9	13.4	14.2	9.8	10.8	10.8	10.6	10.6	10.3
	10.2	10.4	10.3	10.3	10.4	10.0	9.9	9.9	10.3	9.6	10.1	10.4	10.8	10.1	-19.9	20.2	9.6	9.6	10.7	10.7	10.4	10.9	10.1
	10.8	11.0	10.8	10.9	11.0	10.6	10.4	10.4	10.8	10.1	10.6	10.9	12.6	10.6	-19.9	58.0	10.1	10.1	13.8	13.5	15.4	24.6	10.9
9/30/2022	10.5	11.0	10.5	10.7	10.7	9.6	9.6	9.6	9.6	9.7	10.6	10.5	14.5	10.3	-19.9	9.7	9.7	9.7	17.6	17.5	19.7	34.1	12.3
	10.7	11.1	10.7	11.0	11.0	9.8	9.7	9.7	9.7	9.8	10.7	10.6	18.2	10.5	-19.9	9.8	9.8	9.8	32.3	32.9	35.3	54.8	30.5
10/5/2022	1.9	2.0	2.0	2.0	1.8	1.6	1.6	1.6	2.0	1.4	2.2	2.1	2.0	1.9	-19.9	1.7	1.4	1.4	2.2	2.0	2.0	2.1	2.0
	2.5	2.7	2.6	2.6	2.4	2.4	2.3	2.4	2.7	2.0	2.9	2.7	2.6	2.5	-19.9	2.4	2.0	2.0	2.9	2.7	2.7	2.7	2.7
	2.6	2.9	2.7	2.7	2.5	2.5	2.4	2.4	2.8	2.1	3.3	2.9	3.0	2.5	-19.9	2.4	2.1	2.1	3.1	2.8	2.8	2.8	2.8
	2.8	3.2	2.9	3.0	2.6	2.6	2.5	2.5	3.0	2.2	3.8	3.3	3.4	2.6	-19.9	2.5	2.2	2.2	3.4	2.9	3.4	3.1	3.1
	3.0	3.6	3.2	3.3	2.8	2.7	2.6	2.6	3.2	2.3	4.4	3.7	3.9	2.7	-19.9	2.7	2.3	2.3	8.0	6.8	9.4	7.5	3.4
	2.9	3.8	3.5	3.4	2.8	2.7	2.6	2.6	3.3	2.3	5.8	4.6	5.1	2.8	-19.9	2.7	2.3	2.4	27.0	26.0	28.1	20.7	4.3
10/6/2022	2.2	2.4	2.3	2.3	2.1	2.1	2.1	2.1	2.4	1.7	2.6	2.4	2.4	2.2	-19.9	2.1	1.7	1.8	2.6	2.4	2.4	2.4	2.4
	2.5	2.8	2.6	2.6	2.3	2.3	2.3	2.3	2.7	2.0	3.1	2.7	2.9	2.4	-19.9	2.3	2.0	2.0	3.0	2.7	2.7	2.7	2.7
	2.4	2.7	2.6	2.6	2.3	2.2	2.2	2.2	2.7	1.9	3.4	2.8	3.2	2.3	-19.9	2.2	1.9	1.9	3.2	2.7	3.4	2.9	2.8
	2.8	3.1	3.1	3.1	2.6	2.5	2.5	2.5	3.0	2.2	4.3	3.4	4.3	2.6	-19.9	2.5	2.2	2.2	8.2	7.9	9.7	9.8	3.3
	2.6	3.5	3.2	3.0	2.4	2.3	2.2	2.3	3.0	2.0	5.8	4.8	6.3	2.4	-19.9	2.3	2.0	2.0	24.6	23.8	26.1	24.1	4.8

Date	Row 1					Row 2					Row 3				Row 4				Row 5				
	Tube 1			Tube 6	Tube 11	Tube 2			Tube 7	Tube 12	Tube 3		Tube 8	Tube 13	Tube 4		Tube 9	Tube 14	Tube 5			Tube 10	Tube 15
	T_{top}	T_{side}	T_{bottom}	T_{bottom}	T_{top}	T_{top}	T_{side}	T_{bottom}	T_{bottom}	T_{top}	T_{side}	T_{bottom}	T_{bottom}	T_{top}	T_{top}	T_{side}	T_{bottom}	T_{top}	T_{top}	T_{side}	T_{bottom}	T_{bottom}	T_{top}
PHASE 3 - R1234ze(E), circular cone nozzles, triangular pitch, Tube-B evaporator tubes (Bundle 3)																							
10/11/2022	1.9	2.2	2.1	1.2	1.2	1.2	1.2	1.2	1.2	1.2	1.2	1.2	1.2	1.2	-19.9	1.2	1.2	1.2	1.3	1.2	1.2	1.2	1.2
	2.4	2.9	2.8	1.7	1.7	1.8	1.8	1.8	1.8	1.8	1.8	1.8	1.8	1.8	-19.9	1.8	1.8	1.8	1.9	1.8	1.8	1.8	1.8
	2.7	3.4	3.1	1.9	1.9	2.0	2.0	2.0	2.0	2.0	2.0	2.0	2.0	2.0	-19.9	2.0	2.0	2.0	2.1	2.0	2.0	2.0	2.0
	2.5	3.5	3.0	1.6	1.6	1.7	1.7	1.7	1.7	1.7	1.7	1.7	1.7	1.7	-19.9	1.7	1.7	1.7	1.8	1.7	1.7	1.7	1.7
	2.6	4.0	3.7	1.7	1.7	1.8	1.7	1.7	1.7	1.7	1.8	1.8	1.7	1.7	-19.9	1.7	1.7	1.7	1.9	1.7	1.8	1.7	1.7
	3.0	4.8	4.5	1.9	1.9	2.0	2.0	2.0	2.0	1.9	2.0	2.0	1.9	1.9	-19.9	2.0	2.0	1.9	2.1	1.9	2.0	1.9	1.9
10/12/2022	3.1	5.5	5.2	1.9	1.9	2.0	2.0	2.0	2.0	1.9	2.0	2.0	1.9	2.0	-19.9	2.0	2.0	2.0	2.1	2.0	2.0	1.9	1.9
	1.6	1.6	1.6	1.6	1.6	1.6	1.6	1.6	1.6	1.6	1.6	1.6	1.6	1.6	-19.9	1.6	1.6	1.6	2.7	2.5	2.5	1.6	1.6
	1.7	1.7	1.7	1.7	1.7	1.7	1.7	1.7	1.7	1.7	1.7	1.7	1.7	1.7	-19.9	1.7	1.7	1.7	3.0	2.8	2.7	1.7	1.7
	1.9	1.9	1.9	1.9	1.9	1.9	1.9	1.9	1.9	1.9	1.9	1.9	1.9	1.9	-19.9	2.0	2.0	2.0	3.4	3.1	3.1	2.0	2.0
	1.7	1.7	1.7	1.7	1.7	1.8	1.7	1.7	1.7	1.8	1.8	1.8	1.7	1.8	-19.9	1.8	1.8	1.8	3.5	3.1	3.2	1.8	1.8
	1.9	2.0	1.9	1.9	1.9	2.0	1.9	2.0	2.0	2.0	2.0	2.0	2.0	2.0	-19.9	2.0	2.0	2.0	4.1	3.3	3.7	2.0	2.0
	1.8	1.8	1.7	1.8	1.8	1.8	1.8	1.8	1.8	1.8	1.8	1.8	1.8	1.8	-19.9	1.8	1.8	1.8	4.4	3.6	4.1	1.9	1.9
	1.8	1.8	1.8	1.8	1.8	1.8	1.8	1.8	1.8	1.8	1.8	1.8	1.8	1.8	-19.9	1.8	1.8	1.8	2.7	2.5	2.5	1.9	1.8
	1.8	1.8	1.8	1.8	1.8	1.8	1.8	1.8	1.8	1.8	1.8	1.8	1.8	1.8	-19.9	1.8	1.8	1.8	2.9	2.6	2.6	1.9	1.8
	1.9	1.9	1.9	1.9	1.9	1.9	1.9	1.9	1.9	1.9	1.9	1.9	1.9	1.9	-19.9	1.9	1.9	1.9	3.2	2.9	2.8	2.0	2.0
10/13/2022	2.0	2.0	1.9	2.0	1.9	2.0	1.9	1.9	1.9	1.9	1.9	1.9	2.0	2.0	-19.9	2.0	2.0	2.0	3.4	3.0	3.1	2.1	2.0
	2.0	2.0	2.0	2.0	2.0	2.0	2.0	2.0	2.0	2.0	2.0	2.0	2.0	2.0	-19.9	2.0	2.1	2.1	3.5	3.2	3.3	2.2	2.1
	2.0	2.0	2.0	2.0	2.0	2.0	2.0	2.0	2.0	2.0	2.0	2.0	2.0	2.0	-19.9	2.1	2.1	2.1	4.1	3.4	4.3	2.1	2.1
	2.5	2.5	2.5	2.5	2.4	2.4	2.4	2.5	2.9	2.1	2.6	2.6	2.6	2.5	-19.9	2.5	3.1	2.1	2.8	2.6	2.6	2.6	2.6
	2.8	2.7	2.8	2.9	2.6	2.6	2.6	2.7	3.4	2.3	2.9	2.9	2.9	2.7	-19.9	2.7	21.5	2.4	3.1	2.9	2.9	2.9	2.8
	2.2	2.1	2.2	2.2	2.0	2.0	2.0	2.0	2.7	1.7	2.3	2.2	2.3	2.1	-19.9	2.0	1.7	1.7	2.4	2.3	2.3	2.3	2.2
	2.3	2.2	2.3	2.3	2.1	2.2	2.1	2.1	2.9	1.8	2.4	2.4	2.4	2.2	-19.9	2.2	1.8	1.8	2.6	2.4	2.4	2.4	2.3
10/14/2022	2.8	2.6	2.8	2.8	2.5	2.6	2.5	2.5	3.7	2.2	3.0	2.9	3.1	2.7	-19.9	2.6	2.3	2.2	3.1	3.0	3.0	3.0	2.8
	2.9	2.7	2.9	2.9	2.6	2.7	2.5	2.6	3.7	2.3	3.0	3.0	3.2	2.8	-19.9	2.6	2.3	2.3	3.2	3.0	3.0	3.0	2.9
	2.8	2.5	2.8	2.9	2.4	2.5	2.4	2.4	4.2	2.1	3.1	2.9	3.2	2.6	-19.9	2.5	2.2	2.1	3.2	3.0	3.1	3.2	2.9
	2.9	2.7	3.0	3.0	2.6	2.7	2.5	2.5	4.3	2.2	3.2	3.0	3.4	2.8	-19.9	2.6	2.3	2.3	3.4	3.2	3.4	3.5	3.0
	3.1	2.8	3.4	3.3	2.7	2.8	2.6	2.6	6.7	2.3	3.6	3.2	4.6	2.9	-19.9	2.7	2.4	2.3	4.0	4.1	5.1	9.4	3.5
10/15/2022	3.0	2.9	3.5	3.3	2.7	2.8	2.6	2.7	6.8	2.3	3.6	3.3	4.1	2.9	-19.9	2.8	2.4	2.4	4.1	4.1	5.1	8.9	3.5
	2.9	2.8	3.6	3.3	2.6	2.6	2.4	2.5	35.2	2.1	3.7	3.2	5.8	2.8	-19.9	2.6	2.2	2.2	12.7	13.1	15.5	23.6	9.6

Date	Row 1					Row 2					Row 3				Row 4				Row 5				
	Tube 1			Tube 6	Tube 11	Tube 2			Tube 7	Tube 12	Tube 3		Tube 8	Tube 13	Tube 4		Tube 9	Tube 14	Tube 5			Tube 10	Tube 15
	T_{top}	T_{side}	T_{bottom}	T_{bottom}	T_{top}	T_{top}	T_{side}	T_{bottom}	T_{bottom}	T_{top}	T_{side}	T_{bottom}	T_{bottom}	T_{top}	T_{top}	T_{side}	T_{bottom}	T_{top}	T_{top}	T_{side}	T_{bottom}	T_{bottom}	T_{top}
PHASE 3 - R1234ze(E), circular cone nozzles, triangular pitch, Tube-B evaporator tubes (Bundle 3)																							
10/17/2022	10.1	10.0	10.1	10.1	10.0	10.0	10.0	10.1	10.7	9.7	10.2	10.2	10.2	10.1	-19.9	10.1	9.8	9.7	10.3	10.2	10.2	10.1	10.1
	10.2	10.1	10.3	10.3	10.0	10.1	10.0	10.1	10.9	9.7	10.4	10.3	10.3	10.2	-19.9	10.1	9.8	9.8	10.5	10.3	10.3	10.3	10.3
	10.3	10.2	10.3	10.3	10.1	10.1	10.1	10.1	10.8	9.8	10.4	10.4	10.4	10.2	-19.9	10.1	9.8	9.8	10.5	10.4	10.4	10.3	10.3
	10.1	10.0	10.2	10.2	9.9	10.0	9.9	10.0	10.7	9.6	10.3	10.2	10.2	10.1	-19.9	10.0	9.7	9.7	10.4	10.2	10.2	10.2	10.2
	10.2	10.1	10.5	10.3	10.0	10.0	10.0	10.1	11.1	9.7	10.5	10.4	10.5	10.2	-19.9	10.1	9.8	9.7	10.6	10.4	10.4	10.4	10.3
	10.4	10.3	10.7	10.5	10.2	10.2	10.1	10.2	11.3	9.8	10.6	10.6	10.6	10.3	-19.9	10.2	9.9	9.9	10.7	10.6	10.6	10.6	10.5
	10.5	10.4	11.0	10.6	10.3	10.2	10.2	10.3	11.8	9.9	10.9	10.7	10.9	10.4	-19.9	10.3	10.0	9.9	10.9	10.8	10.8	10.9	10.6
	10.6	10.5	11.1	10.8	10.4	10.3	10.3	10.4	11.9	10.0	11.0	10.8	11.1	10.5	-19.9	10.4	10.1	10.0	11.0	10.9	11.0	11.2	10.7
	10.3	10.2	11.0	10.6	10.1	10.0	9.9	10.0	12.7	9.6	10.9	10.6	11.7	10.2	-19.9	10.0	9.7	9.7	11.2	11.3	12.2	16.0	10.6
	10.5	10.4	11.2	10.7	10.3	10.2	10.1	10.3	12.9	9.8	11.1	10.8	11.4	10.4	-19.9	10.2	9.9	9.9	11.2	11.1	11.9	14.5	10.7
	10.6	10.5	11.3	10.9	10.3	10.2	10.1	10.3	28.1	9.7	11.2	10.9	12.5	10.4	-19.9	10.2	9.9	9.8	16.8	17.4	20.0	25.4	12.7
	10.8	10.8	11.6	11.3	10.6	10.4	10.3	10.5	27.5	10.0	11.5	11.1	14.5	10.6	-19.9	10.5	10.1	10.1	16.1	16.8	19.3	28.8	13.4
10/22/2022	-6.3	-6.2	-6.0	-6.1	-6.4	-6.3	-6.4	-6.3	-5.3	-6.7	-6.1	-6.0	-6.1	-6.3	-19.9	-6.3	-6.6	-6.6	-5.9	-6.1	-6.1	-6.0	-6.2
	-6.5	-6.3	-6.3	-6.3	-6.6	-6.6	-6.6	-6.6	-4.8	-6.9	-6.0	-6.1	-6.1	-6.5	-19.9	-6.5	-6.8	-6.8	-6.0	-6.2	-6.2	-6.1	-6.5
	-6.3	-6.2	-6.2	-6.1	-6.4	-6.5	-6.5	-6.5	-4.8	-6.8	-5.8	-6.0	-6.0	-6.4	-19.9	-6.4	-6.7	-6.7	-5.9	-6.1	-6.1	-6.0	-6.4
10/24/2022	-6.0	-5.7	-5.6	-5.6	-5.9	-6.1	-6.2	-6.1	-3.8	-6.5	-5.7	-5.7	-5.6	-6.1	-19.9	-6.1	-6.4	-6.4	-5.4	-5.6	-5.4	-5.3	-5.9
	-5.9	-5.6	-5.6	-5.5	-5.7	-6.0	-6.1	-6.0	-4.4	-6.4	-5.6	-5.7	-5.5	-5.9	-19.9	-6.0	-6.3	-6.4	-5.3	-5.5	-5.3	-5.2	-5.7
	-6.1	-5.7	-5.4	-5.6	-5.9	-6.3	-6.4	-6.4	-3.0	-6.7	-5.8	-5.9	-4.4	-6.2	-19.9	-6.3	-6.6	-6.7	-4.8	-4.8	-3.7	0.8	-5.6
	-6.3	-6.0	-5.7	-5.9	-6.1	-6.5	-6.6	-6.6	-3.5	-7.0	-6.1	-6.1	-5.3	-6.5	-19.9	-6.5	-6.9	-6.9	-5.2	-5.2	-4.1	0.1	-6.0
	-6.0	-5.5	-5.3	-5.4	-5.8	-6.9	-6.9	-6.9	-6.9	-6.8	-5.7	-5.7	-4.1	-6.0	-19.9	-6.8	-6.7	-6.8	4.6	5.0	7.1	14.9	-0.9
PHASE 3 - R1233zd(E), circular cone nozzles, triangular pitch, Tube-B evaporator tubes (Bundle 3)																							
11/2/2022	15.7	15.7	16.1	14.9	14.9	15.0	15.0	15.0	15.0	14.9	15.0	15.0	15.0	14.9	-19.9	15.0	15.0	15.0	15.0	15.0	15.0	15.0	14.9
	14.5	14.4	14.8	13.6	13.6	13.7	13.6	13.6	13.6	13.6	13.7	13.7	13.6	13.6	-19.9	13.6	13.6	13.6	13.7	13.6	13.6	13.6	13.6
	14.6	14.6	15.2	13.6	13.6	13.7	13.7	13.7	13.7	13.7	13.7	13.7	13.7	13.7	-19.9	13.7	13.7	13.7	13.7	13.7	13.7	13.7	13.6
	15.3	15.2	15.9	14.1	14.1	14.2	14.1	14.1	14.1	14.1	14.2	14.2	14.1	14.1	-19.9	14.1	14.1	14.1	14.2	14.1	14.1	14.1	14.1
	15.7	15.5	16.5	14.3	14.3	14.4	14.3	14.3	14.3	14.3	14.4	14.4	14.3	14.3	-19.9	14.3	14.3	14.3	14.4	14.3	14.4	14.3	14.3
	16.0	15.9	17.2	14.4	14.3	14.5	14.4	14.4	14.4	14.4	14.5	14.5	14.4	14.4	-19.9	14.4	14.4	14.4	14.5	14.4	14.4	14.4	14.4
	16.3	16.3	17.9	14.3	14.2	14.4	14.3	14.3	14.3	14.3	14.4	14.4	14.3	14.3	-19.9	14.3	14.3	14.3	14.4	14.3	14.3	14.3	14.3
	13.7	13.7	13.6	13.6	13.6	13.7	13.6	13.6	13.7	13.7	13.7	13.7	13.7	13.7	-19.9	13.7	13.7	13.7	14.9	14.8	15.3	13.7	13.7
	14.2	14.2	14.2	14.2	14.2	14.2	14.2	14.2	14.2	14.2	14.2	14.2	14.2	14.2	-19.9	14.3	14.3	14.3	15.6	15.5	15.8	14.3	14.3
	14.1	14.1	14.0	14.1	14.0	14.1	14.1	14.1	14.1	14.1	14.1	14.1	14.1	14.1	-19.9	14.1	14.1	14.1	15.6	15.5	15.8	14.2	14.2
	14.4	14.4	14.4	14.4	14.4	14.4	14.4	14.4	14.4	14.4	14.4	14.4	14.4	14.4	-19.9	14.4	14.4	14.5	16.2	15.9	16.5	14.5	14.5
	14.3	14.3	14.3	14.3	14.3	14.3	14.3	14.3	14.3	14.3	14.3	14.3	14.3	14.3	-19.9	14.3	14.3	14.3	16.3	16.2	16.8	14.4	14.4
11/4/2022	14.8	14.8	14.8	14.8	14.8	14.9	14.8	14.8	14.8	14.8	14.8	14.9	14.9	14.8	-19.9	14.9	14.9	14.9	17.9	17.4	19.2	14.9	14.9
	14.9	14.9	14.9	14.9	14.8	14.9	14.9	14.9	14.9	14.9	14.9	14.9	14.9	14.9	-19.9	14.9	15.0	14.9	17.6	17.1	18.6	15.0	14.9
	14.2	14.2	14.2	14.2	14.2	14.2	14.2	14.2	14.2	14.2	14.2	14.2	14.2	14.2	-19.9	14.2	14.2	14.2	14.9	14.9	15.2	14.2	14.2
	14.8	14.8	14.8	14.8	14.7	14.8	14.8	14.8	14.8	14.8	14.8	14.8	14.8	14.8	-19.9	14.8	14.8	14.8	16.3	16.2	17.4	14.8	14.8

Date	Row 1					Row 2					Row 3				Row 4				Row 5				
	Tube 1			Tube 6	Tube 11	Tube 2			Tube 7	Tube 12	Tube 3		Tube 8	Tube 13	Tube 4		Tube 9	Tube 14	Tube 5			Tube 10	Tube 15
	T_{top}	T_{side}	T_{bottom}	T_{bottom}	T_{top}	T_{top}	T_{side}	T_{bottom}	T_{bottom}	T_{top}	T_{side}	T_{bottom}	T_{bottom}	T_{top}	T_{top}	T_{side}	T_{bottom}	T_{top}	T_{top}	T_{side}	T_{bottom}	T_{bottom}	T_{top}
PHASE 3 - R1233zd(E), circular cone nozzles, triangular pitch, Tube-B evaporator tubes (Bundle 3)																							
11/7/2022	15.1	15.3	15.5	15.3	15.1	15.0	15.0	15.0	15.2	14.8	15.8	15.6	15.5	15.2	-19.9	15.1	14.9	14.9	15.5	15.3	15.3	15.3	15.2
	9.5	9.7	9.9	9.7	9.5	9.4	9.3	9.4	9.6	9.2	10.1	10.2	10.3	9.5	-19.9	9.4	9.2	9.2	9.9	9.9	9.9	9.9	9.6
	15.8	16.2	16.3	16.1	15.8	15.7	15.7	15.7	16.1	15.5	17.1	16.6	16.3	15.8	-19.9	15.8	15.5	15.5	16.5	16.3	16.1	16.1	15.8
	9.8	10.2	10.4	10.1	9.7	9.6	9.6	9.7	10.1	9.4	10.8	10.4	10.7	9.7	-19.9	9.8	9.4	9.4	10.3	10.2	10.1	10.1	9.7
	15.8	16.3	16.2	16.1	15.7	15.6	15.7	15.7	16.1	15.3	17.8	17.2	16.4	15.7	-19.9	15.8	15.4	15.4	16.7	16.5	16.5	16.2	15.8
	15.5	16.1	16.0	15.9	15.3	15.2	15.2	15.3	15.8	14.9	18.8	17.8	16.3	15.4	-19.9	15.5	15.0	14.9	20.3	20.1	20.1	16.3	15.5
	15.5	16.1	16.0	15.9	15.4	15.3	15.3	15.4	15.8	14.9	18.3	17.2	16.3	15.4	-19.9	15.5	15.0	15.0	19.4	19.3	19.6	16.2	15.5
	15.5	16.3	16.0	16.0	15.4	15.1	15.2	15.3	16.0	14.8	21.9	21.4	16.6	15.4	-19.9	15.4	14.9	14.8	15.0	14.9	14.9	17.3	14.8
11/8/2022	9.7	10.3	10.4	10.1	9.6	9.6	9.6	9.7	9.9	9.2	11.6	11.0	10.8	9.7	-19.9	9.8	9.3	9.3	10.9	10.8	10.8	10.4	9.7
	10.1	10.7	10.7	10.6	10.0	9.9	9.9	10.0	10.3	9.5	12.6	11.9	11.2	10.0	-19.9	10.2	9.6	9.6	11.9	11.9	12.2	11.3	10.1
11/9/2022	9.7	9.9	10.0	9.9	9.7	9.5	9.4	9.4	9.4	9.4	9.5	9.5	10.2	9.8	-19.9	9.5	9.5	9.5	10.0	9.9	9.9	10.2	9.8
	9.2	9.5	9.7	9.5	9.2	8.9	8.9	8.9	8.9	8.9	8.9	8.9	10.1	9.3	-19.9	8.9	8.9	8.9	9.6	9.5	9.5	9.5	9.2
	9.5	10.0	10.0	9.9	9.4	9.0	9.0	9.0	9.0	9.0	9.0	9.0	10.4	9.5	-19.9	9.0	9.0	9.0	9.9	9.8	9.8	10.0	9.5
11/10/2022	9.3	9.8	10.0	9.8	9.1	8.6	8.6	8.6	8.6	8.6	8.7	8.7	10.4	9.1	-19.9	8.7	8.7	8.7	9.8	9.7	9.8	11.0	9.3
	9.0	9.7	10.0	9.6	8.8	8.2	8.2	8.2	8.2	8.2	8.3	8.3	10.4	8.8	-19.9	8.3	8.3	8.3	9.6	9.4	9.4	13.5	9.1
	9.8	10.5	10.9	10.4	9.6	9.0	9.0	9.0	9.0	9.0	9.1	9.1	11.3	9.6	-19.9	9.1	9.1	9.1	10.4	10.2	10.3	18.9	10.4
	9.8	10.5	10.9	10.6	9.5	8.8	8.8	8.8	8.8	8.8	8.9	8.9	13.2	9.5	-19.9	8.9	8.9	8.9	10.5	10.4	11.0	33.4	16.3
11/11/2022	8.6	8.6	8.5	8.5	8.5	8.6	8.5	8.6	8.6	8.6	8.6	8.6	8.6	8.6	-19.9	8.6	8.6	8.6	10.0	9.8	9.9	8.9	8.7
	8.7	8.7	8.6	8.7	8.6	8.7	8.6	8.7	8.7	8.7	8.7	8.7	8.7	8.7	-19.9	8.7	8.8	8.7	10.3	10.1	10.2	9.0	8.8
	8.5	8.5	8.5	8.6	8.5	8.6	8.5	8.5	8.5	8.6	8.5	8.6	8.6	8.5	-19.9	8.6	8.7	8.6	10.4	10.1	10.3	8.9	8.7
	8.8	8.8	8.8	8.8	8.8	8.8	8.8	8.8	8.8	8.8	8.8	8.8	8.8	8.8	-19.9	8.8	8.9	8.8	10.9	10.6	10.8	9.1	8.9
	8.5	8.5	8.5	8.5	8.5	8.5	8.5	8.5	8.5	8.5	8.5	8.6	8.5	8.5	-19.9	8.6	8.8	8.6	11.3	10.9	11.1	9.0	8.7
	8.7	8.7	8.7	8.7	8.7	8.8	8.8	8.8	8.8	8.8	8.8	8.8	8.8	8.8	-19.9	8.9	9.0	8.8	11.8	11.4	11.6	9.2	8.9
PHASE 4 - R134a, circular cone nozzles, square pitch, Tube-B evaporator tubes (Bundle 4)																							
11/22/2022	9.8	10.0	9.9	10.0	9.7	9.9	9.8	9.8	9.8	10.1	9.9	9.9	10.0	9.8	-19.9	9.8	10.1	9.8	9.7	9.9	10.1	10.1	9.9
	9.9	10.3	10.1	10.2	9.8	10.1	9.9	9.9	9.9	10.3	10.1	10.1	10.3	10.0	-19.9	10.0	10.6	9.9	9.9	10.1	10.4	10.5	10.0
	10.3	10.6	10.5	10.6	10.2	10.5	10.3	10.3	10.3	10.7	10.5	10.4	10.6	10.3	-19.9	10.3	11.0	10.3	10.3	10.5	10.7	10.8	10.4
	10.0	10.4	10.2	10.3	9.9	10.2	9.9	9.9	9.9	10.5	10.2	10.1	10.4	10.0	-19.9	10.0	10.9	9.9	10.0	10.3	10.4	10.6	10.1
	10.1	10.5	10.3	10.4	10.0	10.3	10.0	10.0	10.0	10.6	10.3	10.2	10.5	10.1	-19.9	10.1	11.0	10.0	10.1	10.4	10.5	10.8	10.2
11/23/2022	10.2	10.7	10.5	10.6	10.1	10.5	10.1	10.2	10.2	10.9	10.4	10.4	10.9	10.2	-19.9	10.2	11.0	10.2	10.2	10.6	10.6	11.1	10.4
	10.3	10.9	10.5	10.7	10.2	10.5	10.2	10.2	10.3	11.0	10.5	10.4	11.0	10.3	-19.9	10.2	11.9	10.2	10.3	10.7	10.8	12.1	10.4
	10.2	11.0	10.4	10.7	10.1	10.2	10.0	10.2	10.1	11.1	10.4	10.3	11.0	10.2	-19.9	10.1	15.2	10.1	10.2	10.6	10.6	19.5	11.6
	10.3	11.0	10.5	10.7	10.1	10.2	10.2	10.3	10.2	11.3	10.5	10.4	11.1	10.3	-19.9	10.2	12.6	10.2	10.3	10.8	10.8	14.9	10.9
	10.6	11.6	10.8	11.5	10.4	10.5	10.4	10.6	10.5	12.1	10.8	10.8	11.9	10.9	-19.9	10.5	43.3	12.0	11.2	11.8	12.7	51.4	34.5

Date	Row 1					Row 2					Row 3				Row 4				Row 5				
	Tube 1			Tube 6	Tube 11	Tube 2			Tube 7	Tube 12	Tube 3		Tube 8	Tube 13	Tube 4		Tube 9	Tube 14	Tube 5			Tube 10	Tube 15
	T_{top}	T_{side}	T_{bottom}	T_{bottom}	T_{top}	T_{top}	T_{side}	T_{bottom}	T_{bottom}	T_{top}	T_{side}	T_{bottom}	T_{bottom}	T_{top}	T_{top}	T_{side}	T_{bottom}	T_{top}	T_{top}	T_{side}	T_{bottom}	T_{bottom}	T_{top}
PHASE 4 - R134a, circular cone nozzles, square pitch, Tube-B evaporator tubes (Bundle 4)																							
11/28/2022	2.0	2.3	2.1	2.1	1.9	2.2	2.0	2.0	2.0	2.3	2.2	2.1	2.2	2.1	-19.9	2.1	2.5	2.1	2.0	2.1	2.3	2.3	2.1
	2.2	2.7	2.3	2.5	2.1	2.4	2.2	2.2	2.2	2.6	2.4	2.3	2.5	2.3	-19.9	2.2	2.8	2.2	2.1	2.4	2.6	2.7	2.3
	2.3	2.8	2.4	2.6	2.2	2.5	2.3	2.3	2.3	2.8	2.5	2.4	2.7	2.4	-19.9	2.3	2.9	2.3	2.3	2.5	2.8	2.8	2.4
	2.3	3.0	2.5	2.6	2.2	2.5	2.3	2.3	2.3	2.9	2.6	2.5	2.8	2.4	-19.9	2.3	3.2	2.3	2.3	2.6	2.8	2.9	2.4
	2.4	3.0	2.5	2.6	2.3	2.6	2.3	2.3	2.3	3.0	2.6	2.5	2.8	2.4	-19.9	2.4	3.3	2.3	2.3	2.6	2.9	3.1	2.4
	2.1	2.9	2.3	2.4	2.0	2.3	2.0	2.0	2.1	2.9	2.3	2.3	2.7	2.1	-19.9	2.1	3.2	2.0	2.1	2.4	2.5	2.9	2.2
	2.4	3.2	2.5	2.8	2.3	2.6	2.3	2.3	2.3	3.2	2.6	2.5	3.0	2.4	-19.9	2.3	4.1	2.3	2.4	2.7	2.9	3.9	2.5
	2.4	3.3	2.6	3.0	2.3	2.6	2.3	2.3	2.4	3.5	2.6	2.6	3.2	2.4	-19.9	2.3	8.6	2.3	2.4	2.9	2.9	13.6	3.6
	2.1	2.9	2.5	2.6	2.0	2.4	2.0	2.1	2.1	3.3	2.4	2.4	3.0	2.2	-19.9	2.1	4.0	2.0	2.2	2.6	2.8	7.5	2.4
PHASE 4 - R1234ze(E), circular cone nozzles, square pitch, Tube-B evaporator tubes (Bundle 4)																							
12/6/2022	9.7	10.0	9.9	10.0	9.7	9.9	9.8	9.8	9.8	10.1	9.9	9.9	10.0	9.8	-19.9	9.8	10.3	9.8	9.7	9.9	10.1	10.1	9.8
	10.3	10.8	10.5	10.6	10.2	10.5	10.2	10.2	10.2	10.8	10.5	10.4	10.7	10.3	-19.9	10.3	11.1	10.3	10.2	10.5	10.8	10.9	10.3
	10.4	10.8	10.6	10.7	10.3	10.5	10.3	10.3	10.3	10.9	10.6	10.5	10.7	10.4	-19.9	10.4	11.2	10.3	10.3	10.6	10.9	11.0	10.4
	10.3	10.9	10.6	10.8	10.2	10.5	10.2	10.2	10.2	11.1	10.6	10.5	10.9	10.4	-19.9	10.3	13.4	10.2	10.3	10.6	11.1	11.5	10.4
	10.5	11.1	10.7	11.0	10.4	10.7	10.4	10.4	10.4	11.2	10.8	10.6	11.0	10.5	-19.9	10.4	14.3	10.4	10.4	10.8	11.2	12.3	10.6
	10.4	11.1	10.7	11.1	10.3	10.6	10.3	10.3	10.4	11.5	10.8	10.6	11.2	10.5	-19.9	10.3	18.9	10.3	10.5	11.0	11.7	15.7	11.9
	10.5	11.3	10.9	11.3	10.4	10.7	10.4	10.5	10.5	11.7	10.9	10.7	11.3	10.6	-19.9	10.5	20.0	10.5	10.7	11.1	11.9	16.4	12.6
	10.4	11.3	10.8	11.3	10.2	10.5	10.2	10.3	10.3	11.8	10.8	10.6	11.4	10.6	-19.9	10.3	25.6	10.5	10.9	11.7	12.9	23.8	20.8
12/7/2022	10.6	11.6	11.1	11.9	10.5	10.8	10.5	10.5	10.6	12.3	11.1	10.9	11.9	10.9	-19.9	10.5	29.8	10.8	11.4	12.2	13.5	26.0	20.3
	10.6	11.6	11.1	11.8	10.4	10.6	10.4	10.5	10.5	12.7	11.2	11.0	12.3	11.4	-19.9	10.5	43.4	13.3	12.7	14.1	16.3	50.7	41.5
	1.3	1.6	1.4	1.5	1.2	1.5	1.3	1.3	1.3	1.6	1.5	1.5	1.6	1.4	-19.9	1.4	1.8	1.4	1.3	1.5	1.6	1.7	1.4
	2.3	2.7	2.4	2.6	2.2	2.5	2.2	2.2	2.2	2.8	2.5	2.4	2.7	2.3	-19.9	2.3	3.1	2.3	2.2	2.5	2.8	2.9	2.3
	2.4	2.8	2.5	2.7	2.3	2.5	2.3	2.3	2.3	2.9	2.6	2.5	2.7	2.4	-19.9	2.4	3.2	2.3	2.3	2.6	2.8	3.0	2.4
	2.6	3.3	2.9	3.1	2.5	2.8	2.6	2.6	2.6	3.4	2.9	2.8	3.2	2.7	-19.9	2.6	5.9	2.6	2.6	3.0	3.3	4.0	2.7
	2.7	3.3	2.9	3.1	2.6	2.9	2.6	2.6	2.6	3.5	3.0	2.8	3.2	2.7	-19.9	2.6	6.5	2.6	2.6	3.0	3.4	4.6	2.8
	2.8	3.6	3.1	3.3	2.6	2.9	2.6	2.7	2.7	3.8	3.1	3.0	3.5	2.8	-19.9	2.7	10.3	2.7	2.8	3.3	3.9	7.9	3.8
	2.9	3.7	3.2	3.6	2.7	3.0	2.7	2.8	2.8	4.0	3.2	3.1	3.7	3.0	-19.9	2.8	12.3	2.8	3.0	3.4	4.1	9.1	4.8
	2.8	3.7	3.1	3.4	2.6	2.9	2.6	2.6	2.7	4.1	3.2	3.0	3.8	2.9	-19.9	2.6	16.2	2.8	3.4	4.2	5.5	16.5	10.3
12/8/2022	2.7	3.8	3.3	3.5	2.6	2.9	2.5	2.6	2.7	4.3	3.2	3.0	3.9	2.9	-19.9	2.6	21.8	2.8	3.8	4.7	5.9	20.4	13.6
	2.8	4.0	3.4	3.6	2.6	2.9	2.6	2.7	2.7	4.9	3.5	3.2	4.4	3.9	-19.9	2.7	38.4	5.0	5.3	7.1	9.2	56.2	34.6
	-6.7	-6.4	-6.5	-6.5	-6.7	-6.5	-6.6	-6.6	-6.6	-6.3	-6.4	-6.4	-6.3	-6.5	-19.9	-6.6	-6.1	-6.5	-6.6	-6.5	-6.3	-6.2	-6.5
	-6.4	-6.2	-6.3	-6.2	-6.5	-6.3	-6.5	-6.5	-6.5	-5.9	-6.2	-6.3	-6.0	-6.3	-19.9	-6.4	-6.0	-6.4	-6.5	-6.3	-6.0	-5.9	-6.4
	-6.6	-6.3	-6.5	-6.4	-6.6	-6.4	-6.6	-6.6	-6.6	-6.0	-6.3	-6.4	-6.2	-6.4	-19.9	-6.6	-6.1	-6.5	-6.6	-6.4	-6.1	-6.0	-6.5
	-6.2	-6.0	-6.1	-5.8	-6.2	-6.1	-6.3	-6.3	-6.3	-5.5	-5.9	-6.1	-5.7	-6.1	-19.9	-6.3	-5.2	-6.2	-6.2	-6.0	-5.6	-5.8	-6.1
	-6.1	-5.9	-6.0	-5.7	-6.2	-6.0	-6.2	-6.2	-6.2	-5.4	-5.8	-6.0	-5.7	-6.0	-19.9	-6.2	-5.0	-6.2	-6.1	-5.9	-5.6	-5.6	-6.0
12/9/2022	-5.9	-5.7	-5.8	-5.6	-6.0	-5.9	-6.1	-6.2	-6.1	-4.8	-5.6	-5.8	-5.3	-5.8	-19.9	-6.1	0.3	-6.1	-5.8	-5.5	-5.0	-2.7	-5.2
	-5.8	-5.6	-5.7	-5.5	-5.8	-5.8	-6.0	-6.0	-6.0	-4.6	-5.5	-5.7	-5.2	-5.7	-19.9	-6.0	1.8	-5.9	-5.7	-5.3	-4.8	-1.4	-4.5
	-5.9	-5.6	-5.7	-5.6	-6.0	-5.9	-6.2	-6.2	-6.1	-4.4	-5.6	-5.7	-5.1	-5.7	-19.9	-6.1	6.1	-6.0	-5.4	-5.1	-4.4	7.2	-0.3
	-5.7	-5.4	-5.5	-5.3	-5.8	-5.7	-6.0	-6.0	-5.9	-4.1	-5.4	-5.6	-5.0	-5.5	-19.9	-6.0	8.6	-5.7	-5.0	-4.7	-3.9	10.4	1.3
	-6.0	-5.6	-5.8	-5.6	-6.1	-6.0	-6.3	-6.3	-6.2	-4.2	-5.6	-5.8	-5.0	-5.5	-19.9	-6.3	13.0	-5.3	-4.5	-4.0	-2.8	30.1	6.9

Date	Row 1					Row 2					Row 3					Row 4					Row 5				
	Tube 1			Tube 6	Tube 11	Tube 2			Tube 7	Tube 12	Tube 3		Tube 8	Tube 13	Tube 4		Tube 9	Tube 14	Tube 5			Tube 10	Tube 15
	T_{top}	T_{side}	T_{bottom}	T_{bottom}	T_{top}	T_{top}	T_{side}	T_{bottom}	T_{bottom}	T_{top}	T_{side}	T_{bottom}	T_{bottom}	T_{top}	T_{top}	T_{side}	T_{bottom}	T_{top}	T_{top}	T_{side}	T_{bottom}	T_{bottom}	T_{top}
PHASE 4 - R1234ze(E), circular cone nozzles, square pitch, Tube-B evaporator tubes (Bundle 4)																									
1/5/2023	9.9	10.3	10.3	10.3	9.9	10.3	10.1	10.1	10.1	10.1	10.2	10.1	10.3	10.0	-19.9	10.1	10.2	10.0	10.0	10.2	10.4	10.8	10.0
	9.9	10.3	10.3	10.2	9.8	10.3	10.0	10.1	10.0	10.1	10.2	10.1	10.3	10.0	-19.9	10.1	10.1	10.0	10.0	10.2	10.4	10.7	10.0
	9.9	10.5	10.3	10.4	9.9	10.4	10.1	10.2	10.2	10.3	10.3	10.2	10.5	10.0	-19.9	10.1	10.2	10.0	10.1	10.3	10.5	11.1	10.0
	10.2	10.8	10.5	10.6	10.1	10.6	10.3	10.4	10.4	10.5	10.5	10.4	10.7	10.2	-19.9	10.3	10.4	10.2	10.3	10.5	10.7	11.3	10.2
	10.1	10.9	10.6	10.7	10.1	10.6	10.3	10.4	10.4	10.5	10.5	10.4	10.9	10.2	-19.9	10.3	10.5	10.2	10.4	10.6	11.0	11.8	10.1
	10.3	11.1	10.7	10.8	10.2	10.7	10.4	10.5	10.5	10.6	10.7	10.5	11.0	10.3	-19.9	10.4	10.7	10.3	10.7	10.8	11.3	12.0	10.3
	10.2	11.1	10.8	10.8	10.1	10.6	10.4	10.7	10.5	10.6	10.7	10.5	11.2	10.3	-19.9	10.4	10.7	10.3	10.8	11.0	11.6	12.4	10.2
	10.5	11.4	11.2	11.2	10.4	10.9	10.7	11.1	10.8	10.9	11.0	10.8	11.5	10.6	-19.9	10.8	11.2	10.6	11.7	12.0	13.0	13.9	10.6
1/6/2023	-12.9	-12.6	-12.6	-12.7	-12.9	-12.6	-12.8	-12.8	-12.8	-12.7	-12.7	-12.7	-12.5	-12.8	-19.9	-12.7	-12.7	-12.7	-12.8	-12.7	-12.5	-12.5	-12.7
	-12.2	-11.8	-11.9	-12.0	-12.2	-11.9	-12.1	-12.1	-12.1	-11.9	-11.9	-12.0	-11.7	-12.1	-19.9	-12.1	-12.0	-12.1	-12.1	-12.0	-11.8	-11.5	-12.1
	-12.3	-12.0	-12.1	-12.2	-12.4	-12.0	-12.2	-12.3	-12.2	-12.0	-12.0	-12.2	-11.7	-12.3	-19.9	-12.2	-12.1	-12.2	-12.1	-12.0	-11.7	-11.4	-12.3
	-11.6	-11.1	-11.2	-11.4	-11.6	-11.1	-11.4	-11.4	-11.3	-11.2	-11.1	-11.3	-10.8	-11.5	-19.9	-11.4	-11.1	-11.4	-11.2	-10.9	-10.4	-7.3	-11.3
	-10.7	-10.1	-10.3	-10.2	-10.8	-10.2	-10.6	-10.5	-10.4	-10.2	-10.1	-10.3	-10.0	-10.6	-19.9	-10.4	-5.8	-10.3	-3.0	-1.6	-0.4	21.7	-3.3
PHASE 4 - R1233zd(E), circular cone nozzles, square pitch, Tube-B evaporator tubes (Bundle 4)																									
1/10/2023	15.0	15.2	15.2	15.1	14.9	15.2	15.1	15.1	15.1	15.1	15.3	15.3	15.3	15.0	-19.9	15.2	15.4	15.1	15.1	15.2	15.6	15.5	15.0
	15.2	15.6	15.5	15.5	15.1	15.6	15.4	15.5	15.4	15.4	15.7	15.7	15.7	15.3	-19.9	15.5	15.7	15.3	15.5	15.9	16.2	16.4	15.3
	15.2	15.6	15.6	15.5	15.2	15.6	15.4	15.4	15.4	15.4	15.6	15.6	15.7	15.3	-19.9	15.4	15.6	15.3	15.4	15.6	15.9	16.2	15.3
	15.0	15.6	15.4	15.4	14.9	15.5	15.1	15.3	15.2	15.3	15.5	15.5	15.9	15.0	-19.9	15.5	15.4	15.1	15.6	16.1	16.7	16.9	15.1
	14.7	15.4	15.0	15.1	14.6	15.2	14.9	15.1	15.0	15.0	15.9	15.9	15.7	14.7	-19.9	17.0	16.1	14.9	18.3	19.2	19.8	20.3	15.2
1/12/2023	15.1	15.9	15.9	15.9	15.0	15.8	15.7	16.0	15.9	15.6	16.2	16.2	17.0	15.2	-19.9	17.1	16.6	15.6	18.9	19.8	20.4	19.0	15.8
	9.3	9.9	9.7	9.7	9.2	9.8	9.4	9.6	9.6	9.6	9.9	10.1	10.6	9.3	-19.9	9.9	10.0	9.4	10.0	10.5	11.3	11.6	9.3
	9.0	9.6	9.4	9.5	9.0	9.5	9.2	9.4	9.4	9.4	10.0	10.1	10.2	9.1	-19.9	11.0	9.7	9.1	11.4	12.4	13.1	12.3	9.1
	9.0	9.7	9.4	9.5	9.0	9.5	9.2	9.3	9.4	9.4	9.7	9.8	10.2	9.1	-19.9	9.7	9.6	9.1	9.7	10.1	10.9	11.3	9.1
	15.1	16.1	15.7	15.7	15.0	15.9	15.6	16.3	15.9	15.6	18.1	18.3	17.3	15.1	-19.9	22.9	17.9	15.7	25.4	26.5	27.4	24.7	16.1
	15.1	16.1	15.7	15.7	15.0	15.9	15.6	16.2	15.8	15.6	17.7	18.0	17.0	15.1	-19.9	22.2	16.5	15.4	26.1	27.3	28.1	22.2	16.0
	9.7	10.6	10.2	10.3	9.6	10.3	9.9	10.2	10.2	10.1	10.7	10.7	11.2	9.7	-19.9	11.1	10.6	9.9	11.9	12.9	13.8	13.0	10.8
	9.7	10.6	10.2	10.4	9.6	10.3	9.8	10.2	10.1	10.1	10.5	10.5	11.1	9.7	-19.9	10.6	10.4	9.9	10.9	11.6	12.5	12.6	10.0
	9.7	10.6	10.1	10.2	9.6	10.3	9.9	10.2	10.1	10.1	10.6	10.5	11.0	9.7	-19.9	11.0	10.4	9.9	12.8	13.7	14.6	13.4	11.1
1/13/2023	5.4	6.1	6.1	6.2	5.3	6.2	6.0	6.2	6.1	5.7	6.2	6.3	7.0	5.5	-19.9	5.8	6.8	5.8	6.1	6.6	7.2	8.0	5.6
	5.5	6.2	6.1	6.0	5.4	6.1	5.9	6.1	6.0	5.8	6.2	6.2	6.9	5.5	-19.9	6.1	6.1	5.8	6.7	7.4	8.1	7.2	5.9
	5.6	6.4	6.3	6.2	5.5	6.4	6.1	6.7	6.5	6.1	8.7	8.8	7.6	5.7	-19.9	13.4	9.1	6.8	16.9	17.8	18.7	17.3	10.3
	5.4	6.2	6.0	6.0	5.3	6.1	5.9	6.4	6.0	5.8	8.6	8.7	7.1	5.4	-19.9	12.5	6.5	5.6	13.6	14.6	15.4	12.1	5.8
1/16/2023	15.1	15.6	15.7	15.5	15.1	15.6	15.5	15.6	15.5	15.3	15.8	15.9	16.2	15.3	-19.9	15.7	15.9	15.4	15.7	15.9	16.5	17.0	15.4
	15.2	15.6	15.6	15.5	15.1	15.6	15.4	15.5	15.5	15.4	15.7	15.9	16.1	15.3	-19.9	15.7	15.7	15.4	15.7	15.8	16.5	16.9	15.4
	15.4	16.1	15.8	15.8	15.3	15.9	15.7	15.9	15.9	15.7	16.4	16.4	16.6	15.4	-19.9	17.5	16.0	15.5	18.2	19.1	19.7	18.6	15.5
	15.1	15.8	15.6	15.5	15.0	15.6	15.3	15.6	15.6	15.5	16.0	16.0	16.2	15.2	-19.9	16.9	15.7	15.2	17.6	18.5	19.0	18.2	15.2
	15.2	15.9	15.7	15.6	15.1	15.7	15.4	15.7	15.6	15.6	16.2	16.2	16.3	15.3	-19.9	17.5	15.8	15.3	18.1	19.0	19.5	18.5	15.4
	15.1	16.1	15.6	15.6	15.0	15.9	15.5	16.0	15.7	15.6	18.6	18.7	16.7	15.2	-19.9	23.8	17.4	15.6	25.5	26.4	27.1	24.2	16.1
	15.3	16.3	15.9	15.8	15.2	16.0	15.6	16.2	15.9	15.8	19.0	19.1	16.8	15.4	-19.9	24.0	17.7	15.9	26.2	27.1	27.9	24.5	16.5
	15.2	16.2	15.7	15.7	15.1	15.9	15.5	16.0	15.7	15.7	18.4	18.6	16.7	15.3	-19.9	23.4	17.2	15.6	25.1	26.0	26.7	23.7	16.1

Date	Row 1					Row 2					Row 3				Row 4				Row 5				
	Tube 1			Tube 6	Tube 11	Tube 2			Tube 7	Tube 12	Tube 3		Tube 8	Tube 13	Tube 4		Tube 9	Tube 14	Tube 5			Tube 10	Tube 15
	T_{top}	T_{side}	T_{bottom}	T_{bottom}	T_{top}	T_{top}	T_{side}	T_{bottom}	T_{bottom}	T_{top}	T_{side}	T_{bottom}	T_{bottom}	T_{top}	T_{top}	T_{side}	T_{bottom}	T_{top}	T_{top}	T_{side}	T_{bottom}	T_{bottom}	T_{top}
PHASE 4 - R1234ze(E), circular cone nozzles, square pitch, Tube-B evaporator tubes (Bundle 4)																							
	2.0	2.2	2.2	2.3	2.0	2.3	2.2	2.1	2.1	2.2	2.3	2.2	2.3	2.2	-19.9	2.2	2.2	2.2	2.1	2.2	2.3	2.5	2.1
	2.4	2.9	2.7	2.8	2.4	2.8	2.6	2.5	2.6	2.7	2.7	2.6	2.8	2.5	-19.9	2.6	2.7	2.5	2.5	2.7	2.8	3.3	2.5
	2.4	2.8	2.6	2.7	2.3	2.7	2.5	2.5	2.5	2.6	2.6	2.6	2.8	2.5	-19.9	2.6	2.6	2.4	2.5	2.6	2.8	3.2	2.4
1/27/2023	2.7	3.2	3.0	3.1	2.7	3.1	2.9	2.8	2.9	3.0	3.0	2.9	3.1	2.8	-19.9	2.9	3.0	2.8	2.8	3.0	3.1	3.6	2.8
	2.4	3.1	2.7	3.1	2.3	2.9	2.6	2.5	2.6	2.7	2.8	2.7	3.0	2.5	-19.9	2.8	2.8	2.5	2.8	3.0	3.2	4.0	2.6
	2.5	3.2	2.9	3.3	2.5	3.0	2.7	2.6	2.8	2.9	2.9	2.8	3.1	2.6	-19.9	2.9	3.0	2.6	3.0	3.2	3.4	4.3	2.7
	2.9	3.4	3.2	3.4	2.8	3.3	3.0	3.0	3.1	3.2	3.2	3.1	3.4	2.9	-19.9	3.2	3.3	2.9	3.2	3.4	3.7	5.0	3.1
	2.7	3.3	3.0	3.4	2.5	3.1	2.8	2.8	3.0	3.0	3.1	3.0	3.7	2.7	-19.9	3.7	4.4	2.9	5.0	5.3	6.0	8.5	3.8
	2.9	3.7	3.4	3.8	2.8	3.3	3.0	3.0	3.4	3.3	3.3	3.2	4.0	2.9	-19.9	4.0	5.1	3.3	5.4	5.6	6.4	9.5	5.2
1/28/2023	2.9	3.6	3.3	3.8	2.8	3.3	3.0	3.0	3.3	3.2	3.3	3.2	4.0	2.9	-19.9	4.0	5.1	3.3	5.5	6.1	6.5	9.3	5.4
	2.9	3.7	3.5	3.9	2.8	3.3	3.1	3.3	3.5	3.3	4.0	4.0	5.2	3.0	-19.9	5.9	8.2	4.7	10.5	10.9	12.0	15.6	9.6
	2.9	3.8	3.6	4.4	2.8	3.3	3.1	3.4	3.7	3.3	4.2	4.2	5.6	3.1	-19.9	6.4	9.2	5.3	11.0	11.4	12.5	17.3	11.0
	3.1	4.1	3.8	4.8	3.0	3.5	3.2	3.5	4.0	3.5	4.4	4.5	6.2	3.3	-19.9	6.8	10.7	6.0	11.3	11.7	12.7	18.8	11.9
	3.1	4.4	3.9	6.5	3.1	4.0	3.6	4.4	5.0	3.8	6.0	6.5	8.0	4.0	-19.9	9.9	16.7	9.4	18.2	18.6	20.0	37.0	17.7
	-6.5	-6.2	-6.3	-6.2	-6.6	-6.2	-6.4	-6.4	-6.4	-6.3	-6.2	-6.3	-5.9	-6.4	-19.9	-6.3	-6.3	-6.4	-6.4	-6.2	-6.0	-5.9	-6.4
	-6.3	-6.0	-6.1	-6.0	-6.3	-5.9	-6.2	-6.2	-6.2	-6.1	-6.0	-6.1	-5.8	-6.2	-19.9	-6.1	-6.1	-6.2	-6.2	-6.1	-5.9	-5.7	-6.2
	-6.4	-6.1	-6.2	-6.1	-6.4	-6.0	-6.3	-6.3	-6.1	-6.1	-6.1	-6.2	-5.9	-6.3	-19.9	-6.2	-6.1	-6.3	-6.2	-6.1	-5.8	-5.8	-6.3
1/30/2023	-6.1	-5.8	-5.9	-5.7	-6.1	-5.7	-6.0	-6.0	-5.8	-5.8	-5.8	-5.9	-5.6	-6.0	-19.9	-5.9	-5.8	-6.0	-5.9	-5.7	-5.5	-5.4	-6.0
	-5.2	-4.8	-5.0	-4.8	-5.2	-4.8	-5.1	-5.1	-4.8	-4.9	-4.8	-5.0	-4.6	-5.1	-19.9	-4.8	-4.4	-5.1	-4.0	-3.5	-2.8	-2.9	-4.8
	-6.1	-5.7	-5.9	-5.7	-6.1	-5.7	-6.0	-6.1	-5.8	-5.8	-5.8	-5.9	-5.6	-6.0	-19.9	-5.8	-5.3	-6.1	-4.9	-4.3	-3.6	-3.8	-5.7
	-6.0	-5.6	-5.8	-5.6	-6.0	-5.6	-5.9	-6.0	-5.7	-5.7	-5.7	-5.9	-5.5	-5.9	-19.9	-5.7	-5.3	-6.0	-4.9	-4.4	-3.6	-3.8	-5.7
	-5.9	-5.4	-5.7	-5.3	-5.9	-5.6	-5.9	-5.8	-5.5	-5.6	-5.5	-5.7	-5.2	-5.8	-19.9	-5.2	-3.7	-5.7	-2.0	-1.3	-0.2	1.3	-4.3
	-6.2	-5.7	-5.9	-5.4	-6.2	-5.9	-6.2	-6.1	-5.8	-5.9	-5.9	-6.0	-5.4	-6.1	-19.9	-5.7	-2.8	-5.8	-2.8	-2.1	-0.9	2.8	-3.9
	2.5	3.3	3.0	3.2	2.4	2.9	2.6	2.7	3.0	2.9	3.0	2.8	3.7	2.6	-19.9	3.2	4.5	2.7	4.6	5.0	5.7	8.8	3.9
	3.2	4.0	3.8	4.9	3.1	3.6	3.3	3.4	3.9	3.5	3.7	3.5	4.8	3.3	-19.9	3.9	6.5	4.0	5.5	5.7	6.6	11.2	5.4
1/31/2023	2.9	3.7	3.6	5.0	2.8	3.3	3.0	3.1	3.8	3.3	3.4	3.3	4.7	3.1	-19.9	3.7	6.5	4.0	5.2	5.4	6.4	11.2	5.8
	2.7	3.3	3.1	3.4	2.5	3.1	2.8	2.8	3.1	3.0	3.1	3.0	3.7	2.7	-19.9	3.5	4.2	2.8	5.5	6.0	6.9	8.0	3.8
	2.4	3.1	2.8	3.1	2.3	2.8	2.5	2.6	2.8	2.8	2.9	2.8	3.3	2.5	-19.9	3.5	3.9	2.5	5.6	6.2	7.0	7.3	3.7